

Advances in Acoustic Emission - 2007

**Proceedings of
The Sixth International Conference
on Acoustic Emission**

**Edited by
Kanji Ono**

**Published by
The Acoustic Emission Working Group
and Acoustic Emission Group, Encino, CA, USA**

The Sixth International Conference on Acoustic Emission ICAE-6

Commemorating
The 40th Anniversary and 50th Meeting of
The Acoustic Emission Working Group

Lake Tahoe, Nevada, USA
October 29 – November 2, 2007

Conference Organized by
The Acoustic Emission Working Group
Allen Green, Conference Chair

Sponsored by
The Acoustic Emission Working Group (AEWG),
The European Working Group on Acoustic Emission (EWGAE)
and
The Japanese Society for Non-Destructive Inspection (JSNDI)

Copyright © 2007 Acoustic Emission Working Group and Acoustic Emission Group
Printed in the United States of America

Purpose of Conference

This Conference was organized to provide an international forum for participants to present and discuss research and industrial applications of the science and technology of acoustic emission (AE). We wanted to explore both theoretical and practical aspects of acoustic emission associated with materials characterization, structural integrity monitoring, in-process monitoring, instrumentation development, as well as pertinent codes and standards and to set directions for future developments and applications in the field of acoustic emission.

About the Sponsoring Organizations

The Acoustic Emission Working Group

Founded in 1967, the Acoustic Emission Working Group (AEWG) is an independent organization dedicated to the advancement of acoustic emission technology through the exchange of technical information; defining and promoting standardized terminology in AE documentation; holding symposia, workshops, and primers; and, establishing technical interchange with other societies and organizations. Previous international meetings were sponsored by AEWG in 1979 (Anaheim, California); 1985 (Lake Tahoe, Nevada); 1989 (Charlotte, North Carolina); 1991 (Boston, Massachusetts); 1998 (Kamuela, Hawaii).

The Japanese Society for Non-Destructive Inspection (JSNDI) Ad Hoc Committee on Acoustic Emission

Japanese Committee on Acoustic Emission (JCAE) was originally organized in 1969 under the sponsorship of the High Pressure Institute of Japan and in cooperation with the Japanese Society for Non-Destructive Inspection (JSNDI). In 1979, JCAE became Committee 006 on Acoustic Emission of JSNDI, and currently is called the Ad Hoc Committee on Acoustic Emission. JCAE has sponsored biennial international symposia since 1972, and published 18 proceedings of these symposia.

The European Working Group on Acoustic Emission

European Working Group on Acoustic Emission (EWGAE) started as European Stress Wave Emission Working Group, holding its first meeting in 1972. Thus far, 27 meetings have been held, with published proceedings from the last six meetings. The Codes Subgroup has developed 10 codes. Five recent codes were published under TC138-WG7 and covered terminology, principles, equipment, equipment characterization and pressure vessel testing.

This Proceedings Volume Published by:

The proceedings volume is jointly published by the Acoustic Emission Working Group (AEWG) and the Acoustic Emission Group (aegroup7@gmail.com; PMB 409, 4924 Balboa Blvd, Encino, CA 91316 USA). For additional copies ordered after the conference (\$120 each including US shipping), contact Acoustic Emission Group (fax 818-990-1686).

Foreword

Welcome to the 6th International Conference on Acoustic Emission (ICAE-6), organized by the Acoustic Emission Working Group (AEWG). We are proud to have the Japanese Committee on Acoustic Emission (JCAE) and the European Working Group on Acoustic Emission (EWGAE) as cosponsors for marking AEWG's 40th anniversary and 50th meeting.

One objective of the conference is the exchange of information about AE with particular emphasis on recent scientific and technical developments. We wish to encourage experts, researchers, users, as well as those who are just interested in AE technology, to discuss their results with others, to learn from each other, to bring up new ideas together, and to inspire the continuously growing AE community with new visions. The program offers many opportunities for networking, to cultivate friendships, and to make new contacts. Needing special mention is an evening panel discussion on "Establishing the Integrity of Bridge Structures using Acoustic Emission".

The conference location is one of the most scenic places in the US and we hope all participants enjoy this unique area.

We wish to express our sincere thanks to all authors for their careful efforts in submitting papers. We also wish to thank all participants for attending the conference, especially those who have traveled a long distance to be with us.

Jochen Vallen, Chairman, AEWG

After I chaired the 2nd International Conference on Acoustic Emission, in this same hotel and meeting room, in 1985, I pledged that I would not do it again. Well, as you can see – here I am again. I truly did not remember just how much time is consumed in the details. However, it isn't just an 'I' that put this Conference together.

I have had some extraordinary assistance from the Editor of the *Journal of Acoustic Emission*, Prof. Kanji Ono, and from the Chairman of the Acoustic Emission Working Group, Jochen Vallen, and others from his company. We all owe them a thank you.

It is my hope that you take back with you a lot of valuable information about our technology, new acquaintances and renewals of old ones, and a thank you for being here from all of us who put this Conference together. Certainly, if you are one of the presenters, we owe you an additional sincere thank you for your own efforts.

Lastly, to the Japanese Committee on Acoustic Emission and The European Working Group on Acoustic Emission for your willingness to agree to the Conference and the support you have lent since the offer was first made in Berlin a few years ago.

My sincere gratitude to all.
In friendship,

Allen Green, Conference Chair

Review Processes of Conference Papers for ICAE6

All the papers appearing in this Proceedings volume, *Advances in Acoustic Emission – 2007*, have been peer-reviewed in accordance with the practice and standards for the *Journal of Acoustic Emission*. Reviews are primarily conducted by the Editor, Professor Kanji Ono and Associate Editors, Dr. A.G. Beattie, Mr. T.F. Drouillard, Professor M. Ohtsu and Dr. W.H. Prosser. When expertise on special topics are needed, the members of the Editorial Board and outside experts are consulted. Current Editorial Board includes the following members.

A.A. Anastassopoulos	(Greece)
F.C. Beall	(USA)
J. Bohse	(Germany)
P. Cole	(UK)
L. Golaski	(Poland)
M.A. Hamstad	(USA)
H.R. Hardy, Jr.	(USA)
K.M. Holford	(UK)
O.Y. Kwon	(Korea)
J.C. Lenain	(France)
P. Mazal	(Czech Republic)
S.L. McBride	(Canada)
A.A. Pollock	(USA)
F. Rauscher	(Austria)
I. Roman	(Israel)
Tomoki Shiotani	(Japan)
M. Takemoto	(Japan)
P. Tscheliesnig	(Austria)
H. Vallen	(Germany)
M. Wevers	(Belgium)
B.R.A. Wood	(Australia)

Conference Organizing Committee

Allen Green, Chair
Jochen Vallen, AEWG Chair
Dave Prine, AEWG Vice Chair
Tomoki Shiotani, AEWG Secretary
T.F. Drouillard, AEWG Historian
Kanji Ono, Proceedings Editor

EWGAE Representatives

V. Svoboda (Chair), C. Hervé, J-C. Lenain, L. Rogers, P. Tscheliesnig, H. Vallen

JCAE Representatives

M. Enoki (Chair), M. Ohtsu, M. Takemoto, K. Yoshida, S. Yuyama

Advances in Acoustic Emission - 2007

Proceedings of the 6th International Conference on Acoustic Emission

CONTENTS

AE Working Groups – Forums for Technology Exchange and Dissemination: Thomas F. Drouillard	1/A1
High-Temperature Acoustic Emission Sensing Using Aluminum Nitride Sensor: H. Noma, T. Tabaru, M. Akiyama, N. Miyoshi, T. Hayano and H. Cho	11
Recent Advances in the Mechanics of MEMS Acoustic Emission Sensors: D.W. Greve, I.J. Oppenheim, A.P. Wright, W. Wu	16
Film-Type PZT Sensor as AE Sensor and Active Guided Wave Transducer: Application for detecting wall reduction and corrosion of pipes: H. Cho and M. Takemoto	22
Heat Resistant Optical Fiber System for Monitoring AE in High Temperature Vacuum Chamber: T. Hayano, T. Matsuo, H. Cho and M. Takemoto	28
Immersion-Type Quadridirectional Optical Fiber AE Sensor for Liquid-Borne AE: T. Matsuo, H. Cho, T. Ogawa and M. Takemoto	34
Optical Fiber AE Sensor for Blockage Monitoring of Water Pipes of Power Generation Plant: T. Matsuo, H. Cho, T. Ogawa and M. Takemoto	40
Damage Identification of a Concrete Water-Channel in Service by Acoustic Emission; T. Suzuki, M. Ohtsu, M. Aoki and R. Nakamura	46
Temporal Evolution and 3D Locations of Acoustic Emissions Produced from the Drying Shrinkage of Concrete: G. C. McLaskey and S. D. Glaser	52
Demand on Flexural Tension Steel Reinforcement Anchorage Zones in Full-Scale Bridge Bent Caps Quantified by Means of Acoustic Emission: T. Schumacher, C. Higgins, S. Glaser and Christian Grosse	58
Damage Evaluation of Post-Tensioned Concrete Viaduct by AE During Proof Loading: E. Proverbio, G. Campanella and V. Venturi	64
Assessing Damage Evolution in Corroded Reinforced Concrete by Acoustic Emission: E. Proverbio, L. Golaski and R. Bonfiglio	70
Impact Imaging Method to Map Damage in Concrete Bridge Deck Slabs: S.D. Butt, V. Limaye and J.P. Newhook	76
High Performance User Code Processing Within Standard AE Software Environments: J. Vallen, H. Vallen, J. Forker and T. Shiotani	82
Reassigned Spectrogram and Sparse Non-Negative Tensor Factorization for Acoustic Emission Transient Analysis: E. Pomponi, G. Romiti and F. Piazza	88
Real-Time Denoising of AE Signals by Short Time Fourier Transform and Wavelet Transform: K. Ito and M. Enoki	94
Acoustic Emission Source Location on an Arbitrary Surface by Geodesic Curve Evolution: G. Prasanna, M.R. Bhat and C.R.L. Murthy	100

Thirty (30) Years Experience of Industrial Applications of Acoustic Emission Testing. Peter Tscheliesnig	106
Application of Acoustic Emission Technology to Monitor the Lubrication Condition of a Diesel Engine of an Armored Fire Supporting Vehicle: N. Jamaluddin, M.J. Mohd Nor, O. Inayatullah and B.I. Suraya Murat	115
Plastic-Region Tightening of Bolts Controlled by Acoustic Emission Method: Y. Mizutani, T. Onishi and M. Mayuzumi	120
Measurement of Memorized Stress After Various Loading Conditions by AE: S. Nambu, Y. Fujino, and M. Enoki	126
Damage Assessment of Gearbox Operating in High Noisy Environment Using Waveform Streaming Approach: D. Ozevin, J. Dong, V. Godinez and M. Carlos	131
Assessment of the Surface Condition at the Removal of Coatings by Dry Ice Blasting Using the Analysis and Location of Acoustic Emission Signals: C. Scheer, P. Brueggemann, W. Reimche and F-W. Bach	137
Using a Simplified Acoustic Emission Equipment to Rank Paper Materials With Respect to Their Fracture Toughness: H. Vallen, J. Vallen, P.A. Gradin and P. Nygård	143
Acoustic Emission Testing of Seam-Welded High Energy Piping Systems in Fossil Power Plants: J.M. Rodgers	149
Application of Acoustic Emission in Monitoring of Failure in Slide Bearings: I. Baran, M. Nowak and W. Darski	155
Threshold Independent Acoustic Emission Monitoring of a Crimping Process in Series Production: J. Forker, H. Vallen and K. Obrist	161
Probability of Detection for Acoustic Emission: A. Pollock	167
Acoustic Emission Waveform Analysis of Gas Leakage on Pipe With Various Types of Artificial Defects: L.R. Nunez, H. Nishino and K. Yoshida	173
Acoustic Emission Evaluation of Retrofits on the 1-80 Bryte Bend Bridge, Sacramento, California: D.E. Kosnik and D.R. Marron	179
Acoustic Emissions of Dehydrating Wood Related to Shrinkage Processes: S. Rosner	184
Use of Acousto-Ultrasonic Techniques to Determine Properties of Remanufactured Particleboards Made Solely From Recycled Particles: S. Kawamoto, J. H. Muehl and R. S. Williams	190
Inspection of Wooden Poles in Brazil Using Acousto-Ultrasonics Parameters: R. Gonçalves, R. Souza Jr. and S. Herrera	196
Analysis of Racking of Structural Assemblies Using Acoustic Emission: J. Li, F.C. Beall and T. A. Breiner	202
ISPESL Experience for Requalification of Small LPG Underground Vessels Using an Acoustic Emission-Based Procedure and Statistics: C. De Petris, F. Quaresima, A. Faragnoli, V. Mazzocchi and P. Lenzuni	208
Periodical Testing of LPG Vessels (Above and Underground) Based on a Validated Acoustic Emission Procedure Within Central Europe: P. Tscheliesnig	217
Potentials of AE Application in Testing Industrial Pipelines: M. Nowak, I. Baran, J. Schmidt and K. Ono	223
Unique AE Testing Applications; C. Allevato	229
Novel Acoustic Emission Source Location: R. Pullin, M. Baxter, M. Eaton, K. Holford and S. Evans	235

Fundamental Studies of Signal Strength and Source Location Using Simulated AE Sources Produced in Model Corrosion Pits Placed on the Bottom Plate of an Aboveground Tank: S. Murakami, R. Ogawa, T. Koike, M. Yamada, S. Yuyama and K. Homma	241
Lamb Modal Regions with Significant AE Energy in a Thick Steel Plate: M. A. Hamstad	247
A Simple Method to Compare the Sensitivity of Different AE Sensors for Tank Floor Testing: H. Vallen, J. Vallen and J. Forker	253
Investigation of AE from a Stepped Chemical Reaction: S. Azimov, A. Lakaev, F. Choriev and R. Nordstrom	259
Early Fault Detection at Gear Units by Acoustic Emission and Wavelet Analysis: C. Scheer, W. Reimche and F-W. Bach	265
Neural Network Analysis of Acoustic Emission Signals for Drill Wear Monitoring: K. Prasopchaichana and O-Y. Kwon	271
Evaluation of Impact Force of Melted Particle in Thermal Spraying Process: M. Enoki, K. Taniguchi, S. Oikawa, L. Shen, M. Watanabe and S. Kuroda	277
Investigation of Elastic Velocity in Anisotropic Shale for Correction of Hypocentral Location and Characterization of Acoustic Emission Events: N. Dyaur, I. Bayuk, Y. Mohamed, G. Kullman and E. Chesnokov	282
Source Mechanisms of Acoustic Emission Events Between Large Underground Cavities in a Salt Mine: G. Manthei, J. Eisenblätter and T. Spies	288
Clustering Analysis of AE in Rock: N. Iverson, C-S. Kao and J.F. Labuz	294
On Investigating Microcrack Events at CoCr Alloy and Acrylic Cement Interface in Shear Strength Tests: G. Qi and B. Zhang	300
Review of Acoustic Emission in China: G. Shen, G. Dai and S. Liu	305
An Investigation of Frequency as an Acoustic Emission Signal Discriminator in Carbon Fibre Composite Materials: M. Eaton, K. Holford, C. Featherston and R. Pullin	312
Monitoring the Evolution of Individual AE Sources in Cyclically Loaded FRP Composites: R. Unnthorsson, T.P. Runarsson and M.T. Jonsson	318
Neural Network Burst Pressure Prediction in Composite Overwrapped Pressure Vessels: E.v.K. Hill, S.-A. T. Dion, J.O. Karl, N.S. Spivey and J.L Walker, II	324
Ultimate Strength Prediction in Fiberglass/Epoxy Beams Using Acoustic Emission Amplitude Data: E.v.K. Hill, M.D. Dorfman and Y. Zhao	330
Analysis of Acoustic Emission From Impact and Fracture of CFRP Laminates: K. Ono, Y. Mizutani and M. Takemoto	336
On Using AE-Hit Patterns for Monitoring Cyclically Loaded CFRP: R. Unnthorsson, T.P. Runarsson and M.T. Jonsson	342
Analysis of the Hydrogen Degradation of Low-Alloy Steel by Acoustic Emission: K. Paradowski, W. Spychalski, K. Lublinska and K.J. Kurzdłowski	348
AE Analysis of Transformed Martensite Volume: V. Pawar, W. Wood and R. Nordstrom	354
Hydrogen Related Brittle Cracking of Metastable Type-304 Stainless Steel: H. Cho and M. Takemoto	360

Characterization of Titanium Hydrides Using a Hybrid Technique of AE and FEM During Indentation Test: Y. Taniyama, H. Cho, M. Takemoto and G. Nakayama	366
Can We Use AE Technique for Soil Corrosion Monitoring of Underground Pipeline? Monitoring Limit of AE Signals from Rust Fracture by Soil Corrosion: H. Cho and M. Takemoto	372
Development of an Acoustic Emission Diagnosis of Steel-Concrete Composite Decking: M. Shigeishi and M. Ohtsu	378
Defect Development and Failure Evaluation in Prestressed Concrete Girder by Acoustic Emission: M. Kalicka	384
Acoustic Emission of Full Scale Concrete Beams for Evaluation of Joint Effect: D.G. Aggelis, T. Shiotani, S. Momoki and M. Terazawa	390
Acoustic Emission and X-Ray Tomography Imaging of Shear Fracture Formation in Large Reinforced Concrete Beam: T. Katsaga and R.P. Young	396
Global Monitoring of Concrete Bridge Using Acoustic Emission: T. Shiotani, D.G. Aggelis and O. Makishima	402
Mapping of Wheel Flange Rubbing on Rail Using AE: Laboratory Test: N.A. Thakkar, R.L. Reuben and J.A. Steel	408
Contribution of Acoustic Emission to Stress Corrosion Cracking Research: Mikio Takemoto	414
Foreword	v
Review Processes of Conference Papers for ICAE-6	vi
Contents	vii
Author Index	xi

Advances in Acoustic Emission - 2007

Proceedings of the 6th International Conference on Acoustic Emission

Author Index

D.G. Aggelis	390, 402	M. A. Hamstad	247
M. Akiyama	11	T. Hayano,	11, 28
C. Allevato	229	S. Herrera	196
M. Aoki	46	C. Higgins	58
S. Azimov	259	E.v.K. Hill	324, 330
		K. Holford	235, 312
		K. Homma	241
F-W. Bach	137, 265		
I. Baran	155, 223	O. Inayatullah	115
M. Baxter	235	K. Ito	94
I. Bayuk	282	N. Iverson	294
F.C. Beall	202		
M.R. Bhat	100	N. Jamaluddin	115
R. Bonfiglio	70	M.T. Jonsson	318, 342
T. A. Breiner	202		
P. Brueggemann	137	M. Kalicka	384
S.D. Butt	76	C-S. Kao	294
		J.O. Karl	324
G. Campanella	64	T. Katsaga	396
M. Carlos	131	S. Kawamoto	190
E. Chesnokov	282	T. Koike	241
H. Cho	11, 22, 28, 34, 40, 360, 366, 372	D.E. Kosnik	179
F. Choriev	259	G. Kullman	282
		S. Kuroda	277
G. Dai	305	K.J. Kurzdowski	348
W. Darski	155	O-Y. Kwon	271
C. De Petris	208		
S.-A. T. Dion	324	J.F. Labuz	294
J. Dong	131	A. Lakaev	259
M.D. Dorfman	330	P. Lenzuni	208
Thomas F. Drouillard	1/A1	J. Li	202
N. Dyaur	282	V. Limaye	76
		S. Liu	305
M. Eaton	235, 312	K. Lublinska	348
J. Eisenblätter	288		
M. Enoki	94, 120, 277	O. Makishima	402
S. Evans	235	G. Manthei	288
		D.R. Marron	179
A. Faragnoli	208	T. Matsuo	28, 34, 40
C. Featherston	312	M. Mayuzumi	120
J. Forker	82, 161, 253	V. Mazzocchi	208
Y. Fujino	126	G. C. McLaskey	52
		N. Miyoshi	11
S. D. Glaser	52, 58	Y. Mizutani	120, 336
V. Godinez	131	Y. Mohamed	282
L. Golaski	70	S. Momoki	390
R. Gonçalves	196	J. H. Muehl	190
P.A. Gradin	143	S. Murakami	241
D.W. Greve	16	B.I. Suraya Murat	115
Christian Grosse	58	C.R.L. Murthy	100

R. Nakamura	46	T. Tabaru	11
G. Nakayama	366	M. Takemoto	22, 28, 34, 40, 336, 360, 366, 372, 414
S. Nambu	120	K. Taniguchi	277
J.P. Newhook	76	Y. Taniyama	366
H. Nishino	173	M. Terazawa	390
H. Noma	11	N.A. Thakkar	408
M.J. Mohd Nor	115	Peter Tscheliesnig	106, 217
R. Nordstrom	259, 354	R. Unnthorsson	318, 342
M. Nowak	155, 223	H. Vallen	82, 143, 161, 253
L.R. Nunez	173	J. Vallen	82, 143, 253
P. Nygård	143	V. Venturi	64
K. Obrist	161	J.L. Walker II	324
R. Ogawa	241	M. Watanabe	277
T. Ogawa	34, 40	R.S. Williams	190
S. Oikawa	277	W. Wood	354
T. Onishi	120	A.P. Wright	16
M. Ohtsu	46, 378	W. Wu	16
K. Ono	223, 336	M. Yamada	241
I.J. Oppenheim	16	K. Yoshida	173
D. Ozevin	131	R.P. Young	396
K. Paradowski	348	S. Yuyama	241
V. Pawar	354	B. Zhang	300
F. Piazza	88	Y. Zhao	330
A. Pollock	167		
E. Pomponi	82		
G. Prasanna	100		
K. Prasopchaichana	271		
E. Proverbio	64, 70		
R. Pullin	235, 312		
G. Qi	300		
F. Quaresima	208		
W. Reimche	137, 265		
R.L. Reuben	408		
J.M. Rodgers	149		
G. Romiti	82		
S. Rosner	184		
T.P. Runarsson	318, 342		
C. Scheer	137, 265		
J. Schmidt	223		
T. Schumacher	58		
G. Shen	305		
L. Shen	277		
M. Shigeishi	378		
T. Shiotani	82, 390, 402		
R. Souza Jr.	196		
T. Spies	288		
N.S. Spivey	324		
W. Spychalski	348		
J.A. Steel	408		
T. Suzuki	46		

ACOUSTIC EMISSION WORKING GROUPS: FORUMS FOR TECHNOLOGY EXCHANGE AND DISSEMINATION

THOMAS F. DROUILLARD

AEWG Archivist and Historian

Golden, Colorado, USA

Abstract

During the first half of the 20th century, a number of significant instrumented acoustic emission (AE) and seismic/microseismic (MS) experiments were conducted around the world. These rudimentary experiments were directed at enhancing the audible sounds, such as *tin cry*, which were incidental observations during experiments with a number of metals and from rockburst studies in mines.

The second half of the 20th century brought about experiments directed at probing into the fundamentals of AE phenomena and studying AE behavior during deformation and fracture of various materials with the hopes of one day developing industrial applications. Researchers delved into the fundamentals of acoustic emission, developed instrumentation specifically for AE, and characterized the AE behavior of many materials. Acoustic emission was starting to be recognized for its unique capabilities as a nondestructive testing (NDT) method for monitoring dynamic processes. All this stemmed from the research work following World War II of graduate student Joseph Kaiser at the Technische Hochschule München in Germany.

Next followed extensive research into AE phenomena performed in the United States by Bradford H. Schofield at Lessells and Associates in Boston, Massachusetts. His work had a profound impact on launching many careers in the field of AE, both research work and the development of applications of AE technology at a number of universities and U.S. government-sponsored programs at a number of laboratories and manufacturing facilities around the country.

The late 1960s ushered in *The Golden Age of Acoustic Emission* with the formation of three acoustic emission working groups: the *Acoustic Emission Working Group* (AEWG) in the United States and Canada in 1967, the *Japanese Committee on Acoustic Emission* (JCAE) in 1969; and the *European Working Group on Stress Wave Emission* in 1972, renamed a year later the *European Working Group on Acoustic Emission* (EWGAE).

These working groups have been largely responsible for the orchestrated development of AE technology throughout the world. They brought together people with expertise in all of the basic sciences that form the basis of AE technology; they provided forums for the exchange of ideas and information; and through critical peer review they helped coalesce the direction of research into a viable nondestructive testing method.

This paper will discuss the formation of these three working groups and the impact they have had in the development and progress of AE technology and application throughout the world. The paper will be concluded with a number of observations and thoughts of the author for continuation and growth of the working groups and the research and application of AE technology.

Keywords: Acoustic emission, working groups, microseismic activity, history

Introduction

Acoustic emissions are naturally occurring phenomena which man has observed from early times. The earliest recorded observation of audible acoustic emission found in the literature was in *The Works of Geber* published in 1678 [1]. Since then, in reporting the sounds they heard, researchers referred to them as *clicking, chatter, squeak, grinding, hissing, and snapping* noises and, in one case, the *tinkle of Japanese glass chimes*.

During the first half of the 20th century, four significant experiments were conducted and reported in the literature. These were a prelude to AE becoming a technology unto itself. In 1925, at the National Physical-Technical Röntgen Institute in Leningrad, Russia, M.V. Klassen-Neklyudova (aka Classen-Nekcludowa) investigated the phenomenon of plastic deformation, which was accompanied by very regular cracking noises reminiscent of the ticking of a clock [2]. In 1927, she employed a magnifying recording apparatus, which achieved an expansion factor of 10^4 times, thus permitting her to manually plot a sharp, stepwise deformation curve as a function of time, which she measured with a stopwatch [3].

The next report of a scientifically planned AE experiment was given in 1933 by Prof. Fuyuhiko Kishinouye at a meeting of the Earthquake Research Institute and published in 1934 [4], followed by an English version in 1937 [5]. Kishinouye designed and performed a series of *Gedanken* or thought experiments to amplify and record the AE from the fracture of wood in order to study fracture of the earth's crust as the cause of earthquakes, and solve the problem of time distribution of earthquakes.

During the 1930s, electronic instrumentation such as vacuum-tube amplifiers were beginning to be used to achieve much greater amplifications than were previously possible by mechanical means. At the recently founded Kaiser-Wilhelm-Institut für Metallforschung in Stuttgart, Germany, Dr. Friedrich Förster and metallurgist Erich Scheil conducted experiments on Ni-steel which they published in 1936 [6] and 1940 [7]. They used a Siemens-und-Halske Elektro-Kardiograph to detect and measure extremely small voltage changes due to resistance variations caused by sudden, jerky strain movements in the wire-shaped test specimen caused by martensitic transformations.

The short article by Drs. Warren P. Mason, Herbert J. McSkimin, and William Shockley, published in 1948 [8], reported on experiments suggested by Shockley that were performed with view to observing the effects of individual moving dislocations.

Common to the above four experiments was the development of instrumentation to enhance the *acoustic emissions* generated in the materials being studied. The oscillograms made by Kishinouye showing "...many rapid inaudible vibrations [acoustic emissions] and cracking sounds from fracture of wooden board" are the first acoustic emission waveforms ever recorded.

The science of seismology to study earthquake activity and the geomechanical study of microseismic activity in rock are strikingly similar to the AE study of deformation and fracture in metals. Experimental techniques, instrumentation, and emission-producing events are similar. The possibility of using "supersonic vibrations" to predict earthquakes and rockbursts was suggested in 1923 by Dr. Ernest A. Hodgson of the Dominion Observatory in Ottawa [9].

Dr. Leonard A. Obert at the Eastern Experimental Station of the U.S. Bureau of Mines in College Park, Maryland, and later Denver, Colorado, described the discovery of microseismic emission in rock as purely accidental [10]. In 1938, he was conducting seismic velocity tests in lead-zinc mines in northeastern Oklahoma to determine if the seismic velocity in mine pillars was dependent on pillar loading. Throughout the tests spurious signals kept triggering the interval time between two geophones. Dr. Obert and Wilbur I. Duvall, also with the Bureau of Mines, then conducted similar tests in copper mines in Upper Michigan [11,12]. The source of these microseisms was attributed to the rockbursts. Thus, they recognized that this phenomenon

provided the basis for a method of detecting and delineating areas of high stress that required no prior knowledge of the mechanical properties of the rock or the state of stress in the rock.

The Founding of Acoustic Emission Technology

The genesis of today's acoustic emission technology was the research work of graduate student Joseph Kaiser at the Technische Hochschule München [13], now Technische Universität München (TUM). His most notable discovery was the irreversibility phenomenon, which, thanks to Prof. Hans Maria Tensi, now bears his name, the *Kaiser Effekt*.

Following Kaiser's work, the arena of activity moved to the United States where researchers delved into the fundamentals of AE, developed instrumentation specifically for AE, and characterized the AE behavior of many materials. AE was starting to be recognized for its unique capabilities as an NDT method.

The first investigation into acoustic emission to follow and continue the foundation Kaiser had laid down was initiated in 1954 by Bradford H. Schofield at Lessells and Associates in Boston, Massachusetts. Schofield's interest was to direct his research towards the application of AE to the field of materials engineering. His initial efforts were to verify the findings of Kaiser, then establish the basic mechanisms of AE, identify source mechanisms, and develop experimental techniques and instrumentation. He published his work in a series of seminal reports entitled "Acoustic Emission under Applied Stress" [Refs. 14 and 15 being the first two reports]. In Schofield's first report [14] the term "acoustic emission" appeared in print for the first time, thus introducing the term to identify our technology.

In the fall of 1956 at Michigan State University, Prof. Lawrence E. Malvern came across a brief article in a book by Dr. Wilhelm Späth [16]. Interested in studying the asperity theory of friction, Malvern suggested to a new faculty member, Dr. Clement A. Tatro, that this acoustic technique would be interesting to look into. Consequently, Tatro began laboratory investigations into AE phenomena, thus initiating the second major effort in AE research [17]. A visionary, Tatro foresaw the unique potential of AE as a nondestructive testing procedure.

Acoustic Emission Working Groups

In the decade of the 1970s research activities became more coordinated and directed with the formation of the acoustic emission working groups, and the use of AE as an NDT method increased for industrial applications. The AE working groups have been indirectly responsible for the orchestrated development of AE throughout the world. They have brought together scientists, engineers, and technicians engaged in all areas of AE research, development, and application. They have provided forums for the exchange of ideas and information, an information network that has kept researchers informed on an international scale of one another's successes, as well as their failures, and helped coalesce the direction of research. They have provided a peer review system and, in the case of the Acoustic Emission Working Group, a set of awards for recognizing outstanding work in the field of acoustic emission.

The Acoustic Emission Working Group

The *Acoustic Emission Working Group* (AEWG) was conceived in the spring of 1967 by Jack C. Spanner of Battelle-Northwest and Allen T. Green of Aerojet-General Corp. They observed that research remained chiefly a decentralized and individualized activity, in which researchers communicated only through their technical reports and journal articles. Few in number, these publications showed evidence that there was a lack of communication, and differences

in terminology and experimental techniques, generally reflecting each researcher's educational background and field of expertise. Spanner and Green agreed that there was enough interest in AE to consider beginning some type of informal exchange of information. A formative meeting was set up to organize an informal working group that would serve not only the AE folks from the United States and Canada, but anyone involved or interested in AE.

The Formative Meeting of the AEWG was held November 2, 1967, in Alcoa, Tennessee. Twelve persons attended the meeting: Harold L. Dunegan of Lawrence Radiation Laboratory; Prof. Julian R. Frederick of the University of Michigan; Allen T. Green of Aerojet-General Corp.; Philip H. Hutton, Jack C. Spanner, and Herb N. Pedersen of Battelle-Northwest Laboratories; Dr. Harvey L. Balderston and Dr. Robert W. Moss of The Boeing Co., Seattle; Charles W. Musser of The Boeing Co., New Orleans; Dwight L. Parry and Norman K. Sowards of Phillips Petroleum Co.; and Bradford H. Schofield of Teledyne Materials Research (formerly Lessells and Associates). During the meeting each person gave a brief discussion of his activities in AE. A constitution and bylaws were drafted. The first slate of officers was elected: Dunegan chairman, Parry vice-chairman, and Green secretary-treasurer.

The first meeting was held February 8-9, 1968, in Idaho Falls, Idaho, with 19 people attending. In addition to the 12 founding members, eight persons were elected to membership to form the Charter Membership: T. Theodore Anderson and Dr. Robert G. Liptai of Argonne National Laboratory; Thomas F. Drouillard of Dow Chemical Co., Rocky Flats Plant; Dr. Robert B. Engle of Lawrence Radiation Laboratory; D.K. Mitchell of The Boeing Co., New Orleans; R. Neal Ord of Battelle-Northwest; Ronald E. Ringsmuth of the Jet Propulsion Laboratory; and Richard K. Steele of Aerojet-General Corp. The meeting consisted of a business meeting and technical presentations, followed by a tour of the host's facility. There was much discussion on instrumentation, test procedures, and how to eliminate noise.

The format of this meeting set the pace for future meetings. Informality of the technical program and presentations was, and still is, the *modus operandi* of the AEWG. From the beginning meetings were held every nine months; elected officers served for a three-meeting term of office. At the 27th meeting (San Antonio, Texas, 1985) the time interval between meetings was extended anywhere from nine months to a year and officers term of office was reduced to two meetings. At the 37th meeting (Sacramento, California, 1994), the Constitution was revised to hold regular meetings at nine to eighteen month intervals. Membership originally was by company with two voting members from each autonomous company location. At the 7th meeting (Atlanta, Georgia, 1971) the Constitution was revised to provide for individual memberships. Commercial presentations by vendors comprised part of the program between the 5th meeting (Las Vegas, Nevada, 1970) and the 22nd meeting (Boulder, Colorado, 1981), after which they were discontinued to provide more time for technical talks. They were reinstated at the 37th meeting (Sacramento, California, 1994).

AEWG Committees

Some of the first activities of the AEWG were accomplished through *ad hoc* committees, three of which will be briefly discussed. A *Terminology Committee* was established at the first meeting and chaired by Philip H. Hutton; it was chartered to establish a glossary of terms common to acoustic emission. The first glossary of eight terms was published as "Recommended Acoustic Terminology" in *Acoustic Emission, ASTM STP 505* [18]. By the 13th meeting (Laguna Hills, California, 1974), this activity was totally assimilated into ASTM Task Group E07.04.01. A current glossary of AE and NDT terminology may be found in the latest revision of the *Annual Book of ASTM Standards* [19].

Another *ad hoc* committee was the *Bibliography Committee*. At the first meeting it was unanimously agreed upon to have open and free exchange of information. Members began

exchanging reports and literature. Allen T. Green distributed a bibliography consisting of 81 references, which listed most of the AE literature published up to 1967 [20]. A significant expansion was made to this bibliography by Jack C. Spanner, which he distributed at the 5th meeting (Las Vegas, Nevada, 1970). Spanner had prepared his bibliography with 295 references for his masters thesis [21], which he later included as part of his book, *Acoustic Emission: Techniques and Applications* [22]. The committee ceased to function beyond the 10th meeting (Pasadena, California, 1972). This effort was, however, continued by Thomas F. Drouillard with the publication of his first bibliography in 1975 [23]. Over the next four years, Drouillard compiled some 2000 references, which were published with annotations in *Acoustic Emission: A Bibliography with Abstracts* [24]. Since then, over 8000 documents have been collected, many of which have been listed in the AE Literature section in the *Journal of Acoustic Emission* [see Refs. 25 to 34].

The *Committee on Equipment and Standardization* was proposed at the 8th meeting (Bal Harbour, Florida, 1971) with Dr. Robert B. Engle as chairman. Their first task was to prepare a specification for calibration of transducers. At the 10th meeting (Pasadena, California, 1972), this became the *Standardization Committee*. By the 13th meeting (Laguna Hills, California, 1974), the activity of this committee was absorbed into ASTM Task Groups E07.04.02 on AE Sensors and E07.04.03 on AE Instrumentation.

AE Sessions, International Conferences, and World Meetings

Organizing symposia-type technical sessions on acoustic emission has been one of the prime objectives of the AEWG. At the first meeting Secretary Green agreed to explore the mechanism of AEWG sponsoring a session on AE at a national conference. Subsequently, arrangements were made to sponsor a half-day session at the American Society for Metals Materials Engineering Congress in Philadelphia, Pennsylvania in October 1969, in conjunction with the 4th AEWG meeting. Since then, the AEWG has sponsored and supported numerous AE sessions at ASNT, ASTM, and ASME conferences.

The first major symposium on AE was the *Symposium on Acoustic Emission* held during ASTM Committee Week in Bal Harbour, Florida, December 7-8, 1971, in conjunction with the 8th AEWG meeting. The proceedings of this symposium became the first major publication on acoustic emission [18]. Revised versions of six of the papers were subsequently published in a special issue of *Materials Research and Standards* [35].

The first *International Conference on Acoustic Emission*, co-sponsored by AEWG and ASNT, was held September 10-13, 1979, in Anaheim, California, in conjunction with the 20th AEWG meeting. Harold L. Dunegan and William F. Hartman were co-chairmen and together published the proceedings [36].

The *Second International Conference on Acoustic Emission* was held in conjunction with the 28th AEWG meeting at Lake Tahoe, Nevada, October 28-November 1, 1985. Allen T. Green was chairman. Extended abstracts of the papers presented were published in a special issue of the *Journal of Acoustic Emission* [37].

The third international conference, called the *World Meeting on Acoustic Emission*, was held in conjunction with the 32nd AEWG meeting and the 1989 ASNT Spring Conference in Charlotte, North Carolina, March 20-23, 1989. Extended summaries of the papers presented were published in a special issue of the *Journal of Acoustic Emission* [38], with complete papers published later by ASTM [39].

The *4th World Meeting on Acoustic Emission and 1st International Conference on Acoustic Emission in Manufacturing* was held September 15-18, 1991, in Boston, Massachusetts in conjunction with the 35th AEWG meeting and the 1991 ASNT Fall Conference. Extended summaries of the papers presented at these meetings were published by ASNT [40].

The *5th Acoustic Emission World Meeting and 14th International Acoustic Emission Symposium* was held in conjunction with the 41st AEWG meeting in Kamuela, Hawaii, August 9-14, 1998. The proceedings were published as *Progress in Acoustic Emission IX: Transitions in AE for the 21st Century* [41].

This meeting at Lake Tahoe, Nevada is the *6th International Conference on Acoustic Emission*, chaired by Allen T. Green. The proceedings are being edited by Prof. Kanji Ono and will be published by the Acoustic Emission Group and AEWG.

Primers

At the 25th meeting (Princeton, New Jersey, 1983) Prof. Davis M. Egle proposed holding a one-day workshop/tutorial/primer on the basics of acoustic emission at the next AEWG meeting. As a result, the first primer was held at the 26th meeting in Reno, Nevada in 1984. Since then, primers have been held at twelve AEWG meetings. Additionally, at the 33rd meeting (Berkeley, California, 1990), Prof. David A. Dornfeld held a Workshop on Acoustic Emission in Manufacturing.

Awards of the AEWG

In preparation for celebrating the 10th anniversary of the AEWG, it became apparent that over the past decade there was no peer recognition for outstanding accomplishments in AE. The AEWG needed to institute some form of awards, similar to what other professional societies offered. At the 20th meeting (Anaheim, California, 1979) four awards were proposed: the *Gold Medal Award*, the *Achievement Award*, the *Publication Award*, and the *Fellow Award*. Approved at the 21st meeting (Ithaca, New York, 1980), the awards were inaugurated at the 24th meeting (Knoxville, Tennessee, 1982) with the Gold Medal Award being presented to Dr. Clement A. Tatro, the Achievement Award to Harold L. Dunegan, and Charter Fellow Awards to Clifford D. Bailey, Prof. Steve H. Carpenter, Thomas F. Drouillard, Harold L. Dunegan, Dr. Robert B. Engle, Allen T. Green, Philip H. Hutton, Prof. Kanji Ono, and Dr. Clement A. Tatro. At the 25th meeting (Princeton, New Jersey, 1983) the Inaugural Publication Award was presented to Thomas F. Drouillard. At the 40th meeting (Evanston, Illinois, 1997) the Achievement Award was renamed the *Joseph Kaiser Achievement Award* to honor Dr. Joseph Kaiser, "Father of Traditional AE."

Japanese Committee on Acoustic Emission

Until the formation of the *Japanese Committee on Acoustic Emission* (JCAE), there was little indigenous AE research in Japan except for the pioneering work on rocks by Prof. Kiyoo Mogi at the Earthquake Research Institute, University of Tokyo. In the summer of 1969, at the International Institute of Welding Conference in Kyoto, several papers on AE were presented, which generated considerable interest among many of the attendees. Later that year, Dr. Eiji Isono of Fuji Steel, together with Prof. Morio Onoe of the Institute of Industrial Science, University of Tokyo, organized the *Japanese Committee on Acoustic Emission* under sponsorship of the High Pressure Institute of Japan, in cooperation with the Japanese Society for Non-Destructive Inspection (JSNDI). Some of the early history of AE activities in Japan have been summarized in articles by Onoe [42, 43], Isono [44], Fuji [45], and Nakasa [46, 47].

The JCAE held its first meeting December 10, 1969 at Fuji Steel in Tokyo. This was followed by 20 meetings to April 1972. At the first meeting, Prof. Onoe was appointed chairman. In 1979 the JCAE became *Committee 006 on Acoustic Emission* of JSNDI. Upon the retirement of Prof. Onoe in 1986, Prof. Kusuo Yamaguchi of the Institute of Industrial Science, University of Tokyo, was appointed chairman. Upon his retirement in 1992, Prof. Teruo Kishi, Research

Center for Advanced Science and Technology, University of Tokyo, was appointed chairman. In 1994, Prof. Yasuhiko Mori of the College of Industrial Technology, Nihon University, was appointed chairman. During Prof. Mori's term of office, Committee 006 became the *Ad Hoc Committee on Acoustic Emission*. In 2002, Prof. Masayasu Ohtsu, Graduate School of Science and Technology, Kumamoto University, was appointed chairman. Prof. Manabu Enoki, Department of Materials Engineering, University of Tokyo, was appointed chairman in 2006 and will serve until 2008.

International Symposia and National Conference on AE

The biennial *International Acoustic Emission Symposia* (IAES), inaugurated in 1972, have become the foremost international meetings on AE today. The first was *The U.S.-Japan Joint Symposium on Acoustic Emission*, held in Tokyo, July 4-6, 1972. Some of the sessions were held in Japanese and some in English. The proceedings consisted of two volumes: a Japanese volume with 11 papers and an English volume with six papers [48]. The *Second AE Symposium* was held two years later (September 2-4, 1974) in Tokyo [49]. Starting with this meeting, all presentations and published proceedings were in English [see Refs. 50 and 51 for proceedings of the 3rd and 4th symposia, respectively]. Starting with the 5th symposium the name was changed to *International Acoustic Emission Symposium* [52; see also Ref. 46 for a review of the first five symposia]. Starting with the 6th symposium the title of the proceedings was changed to *Progress in Acoustic Emission* [53]. The proceedings of these symposia have become an ongoing documentation of the progress in AE throughout the world and comprise a major component of the permanent world literature on AE [see Refs. 41 and 54 to 65 for proceedings of the 7th through 18th IAES].

The *National Conference on AE* was established and held in odd years, the years between IAES, in order to better exchange information among Japanese researchers. Talks are presented in Japanese and cover all areas of AE research and application. Proceedings are published in Japanese for each conference. The first conference, sponsored by High Pressure Institute of Japan, was held December 8-9, 1977. The 2nd conference, held in 1979, and all subsequent conferences have been sponsored by JSNDI. The National Conference on AE continues to hold meetings to this day.

AE Short Courses and Tutorial Sessions

Starting in 1974, AE short courses were given yearly until 1980. The first was given October 28-29, 1974, at the Japanese Society of Civil Engineers Hall with demonstrations at Nippon Steel Corp. The second short course was given November 25-26, 1975. The results of the third short course, given December 6-7, 1976, were reported in a special issue on AE of *Pressure Engineering* (Japan) [66]. A textbook, entitled *Acoustic Emission Basics and Applications*, was prepared from lecture notes by Prof. Onoe and five other instructors [67]. This textbook, written in Japanese, was used at the 3rd and all subsequent AE short courses. A detailed schedule of lectures and demonstrations for the first seven short courses is given by Nakasa [46]. The JCAE also organized tutorial sessions on AE for various professional societies, e.g., the National Symposium on Atomic Energy in the spring of 1973, and the National Convention of Electrical Engineers in the fall of the same year.

European Working Group on Acoustic Emission

A series of events sparked AE interest in Europe and led to the founding of the *European Working Group on Acoustic Emission* (EWGAE). During the summer of 1971, Harold L. Duneagan toured England and a number of countries on the continent giving short courses on AE

and demonstrating Dunegan Research Corporation's new line of AE instrumentation. On March 14, 1972, Dr. Adrian A. Pollock of Cambridge Consultants, England conducted the *Institute of Physics Conference on Acoustic Emission* at Imperial College in London; fifteen papers from throughout Europe and the United States were presented. This meeting brought together the key people of Europe already involved in AE research; from England: in addition to Dr. Pollock, Dr. Don Birchon at the Admiralty Materials Laboratory, Drs. Ian L. Mogford and Ian G. Palmer at Central Electricity Research Laboratories, Peter G. Bentley at Risley Engineering and Materials Laboratory of the U.K. Atomic Energy Authority, and Dr. Brian Harris at the University of Sussex; from Germany: Drs. Jurgen Eisenblätter and Peter Jax at Battelle-Institut; from France: Dr. Paul F. Dumousseau at the Centre Technique des Industries Mecaniques and M. Nicole Chretien and Dr. E.G. Tomachevsky at the Centre d'Études Nucléaires de Saclay, Commissariat a l'Energie Atomique; from Italy: Dr. M. Mirabile at Centro Sperimentale Metallurgico; from Denmark: Arved Nielsen at the Research Establishment Risø, Danish Atomic Energy Commission; and from the Netherlands: Dr. J.C.F. DeKanter at the Technische Hogeschool Delft. As a result of this meeting and Dunegan's influence, Pollock and Birchon organized the *European Stress Wave Emission Working Group*, which held its first meeting November 1972, at the Admiralty Materials Laboratory in England. Fifty people from seven countries attended. Birchon was elected chairman and Pollock, secretary. The second meeting, co-chaired by Drs. Eisenblätter and Jax, was held September 1973, at Battelle-Institut in Frankfurt, Germany, at which the group adopted their present name, *European Working Group on Acoustic Emission*. Meetings were held yearly through 1989, and every other year since 1990 in different European countries.

The first EWGAE meeting, from which extended abstracts were published, was the 15th meeting held in Istanbul, Turkey, October 1986. Seven extended abstracts were included in a special issue of the *Journal of Acoustic Emission* [68]. This was followed by the proceedings of the 16th meeting at London, October 1987, in conjunction with the 4th European Conference on Non-Destructive Testing [69]. At the 20th meeting, held in Leuven, Belgium, host Prof. Martine Wevers handed out folders of all the papers presented at the meeting [70]. Starting with the 22nd meeting (Aberdeen, Scotland, 1996), proceedings have been published for each meeting [see Refs. 71 to 76]. Today, AE testing is being conducted throughout Europe in areas such as proof testing, in-service monitoring, and corrosion and leak detection.

Other Working Groups and AE Activities

The next four working groups founded were the Chinese Committee on Acoustic Emission (CCAIE) in 1978 as a technical committee of the Chinese Society for NDT, the Acoustic Emission Working Group (India) in 1985, the South African Working Group for Acoustic Emission in 1989, and the Korean Working Group on Acoustic Emission (KWGAE) in 1990. Since then other working groups have been organized throughout the world; Germany, Poland, France, Czech Republic, Russia, and South America.

In 1970, Prof. H. Reginald Hardy, Jr. at The Pennsylvania State University joined the Acoustic Emission Working Group, bringing to the AE community knowledge of geophysics and the beginning of cross-fertilization with geophysical scientists. In 1975, Prof. Hardy, with the late Frederick W. Leighton, organized the first of a series of six *Conferences on Acoustic Emission/Microseismic Activity in Geologic Structures and Materials* held at The Pennsylvania State University. The proceedings from these conferences are a valuable resource documenting the progress in the research and application of AE/MS technology throughout the world [see Refs. 77 to 82].

Concluding Remarks

I have only briefly touched on the histories of the first three working groups. These and the more recently formed working groups have been and continue to be largely responsible for the continued orchestrated development of AE technology throughout the world. They continue to bring together people with expertise in all of the basic sciences that form the foundation of AE technology; they provide forums for the exchange of ideas and information; and through critical peer review they help coalesce the direction of research.

Through the dedicated research of hundreds of scientists and engineers throughout the world, AE has become a mature, highly developed technology and recognized nondestructive test method. Reciprocal and synergistic gains have occurred from intellectual interactions of people from different fields of science and engineering working together, and through the exuberant exchange of literature, personal correspondence, and the world-wide travel of many people. AE has become an international fraternity of these scientists, engineers, and technicians. Foreign travel to international meetings, visiting each other's laboratories, attending each other's working group meetings, and presenting lectures, colloquia, and short courses, have indeed created a camaraderie and continuing working relationship throughout the world. The fact that the U.S., Japanese, and European working groups have existed for nearly half a century attests to the importance of AE. Language has never seemed to be a barrier. I have been fortunate over the past 40 years to have been a part of the international community of this exciting field of technology. I am honored and privileged to be invited to give this presentation here today. Thank you very much.

In closing, there are a few thoughts and observations I would like to share with you regarding future needs and directions in AE:

1. There is a need for a textbook and training manuals on AE, both of which should be translated into as many different languages as needed.
2. Being a person from the old school where a book is the most beautiful thing to hold in one's hand, and not everything can be found on the internet, I believe there is a need for the establishment of an international AE library or document center to house a complete collection of the world literature on AE and provide on-line search service. This became a reality in 1997, when Allen Green donated his library of technical papers to the Grainger Engineering Library at the University of Illinois in Urbana-Champaign, Illinois. Then in 2003, Alan Beattie added his collection to the library. Within the coming year, I will be moving my library of AE literature to the collection. This will make the combined collection the largest and most complete resource on AE in the world. I would encourage all of you to contribute copies of your documents and literature on AE to this collection. The AE collection can be searched online at <http://shiva.grainger.uiuc.edu/ae/opent1.asp>.
3. We must make a concerted effort to educate the layman, and particularly people in management, in order to take the mystery out of AE and its applications. This could be accomplished by putting together a compendium of reports on AE applications for each industry.
4. In research, we must explore the vast area of opportunity offered by the recent advancements in electronics and computers and the spinoff technology of the telecommunication and sound synthesizer industries, e.g., explore the possibility of performing signal analysis on the hetrodyned signal with the vast instrumentation and capability in the audio frequency range.
5. In applications, we need to develop effective techniques to inspect nuclear reactors and civil structures, particularly bridges and earthquake-prone buildings. With the growing demand for electric power throughout the world, nuclear power plants are being planned. NDT, and especially AE, must be an integral part of this planning. Nuclear materials are forever and we cannot afford to build and operate nuclear facilities with anything less than total quality control.

6. We need to couple and expand AE with other NDT methods and physical phenomena, such as was done in combining AE and ultrasonics in developing the acousto-ultrasonic technique.

7. We must learn to look outside the confines of traditional AE to meet the changing needs of the future. We have to realize that the AE frequency spectrum ranges from meter-size seismic events up into the MHz range of ultrasonics.

8. The ultimate goal in AE health monitoring of materials and structures must be related to fracture mechanics and the identification of source mechanisms such as: crack propagation, fatigue failure, phase transformation, corrosion and stress corrosion cracking, twinning, and inclusion fracture; structural failures such as: fracture in high stress areas or in defective welds versus heat-affected zone and base metal; and finally being able to sort out meaningful emission sources from noise sources.

9. We need to start looking into the fundamental physics of acoustic wave generation and propagation. Based on Newtonian physics, wave modes are predictable and identifiable. Better understanding of these waves can lead to better understanding of fracture mechanics, flaw growth in materials and structures, and material properties themselves.

10. We can no longer be satisfied to merely detect and report acoustic signals and events. Our goal must be to detect, identify, analyze, and quantify source mechanisms. Then AE will continue to be recognized as a valuable tool in the fields of metallurgy, structural engineering, naval architecture, aerospace, and geophysics. Remember, acoustic emission is the only NDT method to offer real-time, dynamic analysis of materials and structures while they are under service loads.

11. The working groups are only as valuable as you make them. Their function is to provide the forum in which each of us may participate. By participation, we become the more informed. Every working group I have attended provided me with one or more ideas by which I could improve what I was doing or solve a problem. Each of us becomes a winner by participation in our working group. Don't be just a passive listener. Take an active roll by presenting papers, by participating in open discussion, asking questions, posing problems, and sharing reports of your work. Remember, it is important to have input from the full gamut of AE activity: research, development, and application.

Acknowledgements: I would like to express my sincere appreciation to many colleagues who over the past half-century have provided input to my career and to this paper and for their valuable contributions to the field of acoustic emission. They include Allen T. Green, Harold L. Dunegan, Kanji Ono, Masayasu Ohtsu, H. Reginald Hardy, Jr., Hartmut Vallen, Jochen Vallen, David W. Prine, Marvin A. Hamstad, Clinton R. Heiple, Frank C. Beall, Adrian A. Pollock, Alan G. Beattie, and several who are no longer with us: Clement A. Tatro, Julian R. Frederick, and Robert B. Engle. Also included are those I have forgotten to mention you know who you are.

References: The listing of references is available in the CD-version of this article.

References

1. Geber, *The Works of Geber, Englished by Richard Russell, 1678, A New Edition with Introduction by E.J. Holmyard, M.A., D. Litt.*, J.M. Dent & Sons Ltd., London and E.P. Dutton & Co., New York, 1928, pp. 50, 66, 69, 139, and 149.
2. M. Classen-Neklyudowa, "Über die sprungartige Deformation [Sudden Deformation of Crystals under Strain]," *Zeitschrift für Physik*, **55**, 1929, pp. 555-568. (in German)
3. M.V. Klassen-Neklyudova, "On the Nature of Plastic Deformation [title in Russian]," *Zhurnal Russkogo Fiziko-Khimicheskogo Obshchestva, Chast Fizicheskaya*, **59**(5-6), 1927, pp. 509-515. (in Russian)
4. F. Kishinouye, "An Experiment on the Progression of Fracture (A Preliminary Report)," *Jishin*, **6**, 1934, pp. 25-31. (in Japanese). [see *Journal of Acoustic Emission*, **9**(3), 1990, pp. 177-180 for English translation]
5. F. Kishinouye, "Frequency-Distribution of the Ito Earthquake Swarm of 1930," *Bulletin of the Earthquake Research Institute, Tokyo Imperial University*, **15**(Part 2), 1937, pp. 785-826 and Plate LVL (Figs. 5 and 15).
6. F. Förster and E. Scheil, "Akustische Untersuchung der Bildung von Martensitnadeln [Acoustic Study of the Formation of Martensite Needles]," *Zeitschrift für Metallkunde*, **28**(9), 1936, pp. 245-247. (in German)
7. F. Förster and E. Scheil, "Untersuchung des zeitlichen Ablaufes von Umklappvorgängen in Metallen [Investigation of the Progress in Time of Magnetic Reversals in Metals]," *Zeitschrift für Metallkunde*, **32**(6), 1940, pp. 165-173. (in German)
8. W.P. Mason, H.J. McSkimin, and W. Shockley, "Ultrasonic Observations of Twinning in Tin," *Physical Review*, **73**(10), 1948, pp. 1213-1214.
9. E.A. Hodgson, "A Proposed Research into the Possibility of Earthquake Prediction," *Bulletin of the Seismological Society of America*, **13**(3), 1923, pp. 100-104.
10. L. Obert, "The Microseismic Method: Discovery and Early History," pp. 11-12 in *Proceedings, First Conference on Acoustic Emission/Microseismic Activity in Geologic Structures and Materials*, H.R. Hardy, Jr. and F.W. Leighton (eds.), Trans Tech Publications, Clausthal-Zellerfeld, Germany, 1977.
11. L. Obert, "Use of Subaudible Noises for Prediction of Rock Bursts," Report of Investigations 3555, U.S. Bureau of Mines, Washington, D.C., 1941.
12. L. Obert and W. Duvall, "Use of Subaudible Noises for the Prediction of Rock Bursts, Part II," Report of Investigations 3654, U.S. Bureau of Mines, Washington, D.C., 1942.
13. Joseph Kaiser, "Untersuchungen über das Auftreten Geräuschen beim Zugversuch [A Study of Acoustic Phenomena in Tensile Tests]," Dr.-Ing. Dissertation, Technische Hochschule München, Germany, 1950. (in German); Translation UCRL-Trans-1082(L), translated into English for Lawrence Radiation Laboratory, Livermore, California, June 1964.
14. B.H. Schofield, R.A. Bareiss, and A.A. Kyrala, "Acoustic Emission under Applied Stress," WADC Technical Report 58-194, Lessells and Associates, Boston, Massachusetts, April 30, 1958.
15. B.H. Schofield, "Acoustic Emission under Applied Stress," Report ARL-150, Lessells and Associates, Boston, Massachusetts, December 1961.
16. W. Späth, *Fleissen und Kriechen der Metalle*, Metall-Verlag GmbH, Berlin-Grunewald, Germany, 1955, pp. 37-38. (in German)
17. C.A. Tatro, "Sonic Techniques in the Detection of Crystal Slip in Metals," Progress Report, *Engineering Research*, Vol. 1, Engineering Experiment Station, College of Engineering, Michigan State University, East Lansing, Michigan, 1957.

18. *Acoustic Emission, ASTM STP 505*, American Society for Testing and Materials, Philadelphia, Pennsylvania, 1972. [proceedings of the Symposium on Acoustic Emission, held in Bal Harbour, Florida, December 7-8, 1971. (see pp. 335-337 for glossary of AE terminology)]
19. *Annual Book of ASTM Standards 2006, Section 3: Metals Test Methods and Analytical Procedures*, Vol. 03.03: Nondestructive Testing, American Society for Testing and Materials, Philadelphia, Pennsylvania, 2006. [see: E-1316-06A. Standard Terminology for Nondestructive Examination, Section B: Acoustic Emission, pp. 671-674]
20. A.T. Green and J. Ross, "Bibliography on Stress Wave/Acoustic Emission: 1932-1967," Aerojet General Corp., Sacramento, California, October 1967.
21. J.C. Spanner, "Selective Review on the Utilization of Acoustic Emission Techniques for Materials Research and Structural Integrity Analysis (A Literature Survey)," M.S. Thesis, Washington State University, Pullman, Washington, 1970.
22. J.C. Spanner, *Acoustic Emission: Techniques and Applications*, Intex Publishing Co., Evanston, Illinois, 1974.
23. T.F. Drouillard, "Acoustic Emission: A Bibliography for 1970-1972," pp. 241-284 in *Monitoring Structural Integrity by Acoustic Emission, ASTM STP 571*, J.C. Spanner and J.W. McElroy (eds.), American Society for Testing and Materials, Philadelphia, Pennsylvania, 1975.
24. T.F. Drouillard, *Acoustic Emission: A Bibliography with Abstracts*, F.J. Laner (ed.), IFI/Plenum Data Co., Division of Plenum Publishing Corp., New York, 1979.
25. T.F. Drouillard, "AE Literature," *Journal of Acoustic Emission*, **1**(1), 1982, pp. 45-65; **1**(2), 1982, pp. 121-140; **1**(3), 1982, pp. 195-210; and **1**(4), 1982, pp. 271-293.
26. T.F. Drouillard, "AE Literature," *Journal of Acoustic Emission*, **2**(1-2), 1983, pp. 129-142; **2**(3), 1983, pp. 221-238; and **2**(4), 1983, pp. 292-318.
27. T.F. Drouillard, "AE Literature," *Journal of Acoustic Emission*, **3**(1), 1984, pp. 46-50; **3**(2), 1984, pp. 90-99; **3**(3), 1984, pp. 164-171; and **3**(4), 1984, pp. 212-223.
28. T.F. Drouillard, "AE Literature," *Journal of Acoustic Emission*, **4**(1), 1985, pp. 41-59.
29. T.F. Drouillard, "AE Literature Concrete," *Journal of Acoustic Emission*, **5**(2), 1986, pp. 103-109.
30. T.F. Drouillard, "A Comprehensive Guide to the Literature on Acoustic Emission from Composites [Supplement II," *Journal of Acoustic Emission*, **9**(1), 1990, pp. 45-68.
31. T.F. Drouillard and F.C. Beall, "AE Literature Wood," *Journal of Acoustic Emission*, **9**(3), 1990, pp. 215-222.
32. T.F. Drouillard, "AE Literature Bibliography of Acoustic Emission of Bearings and Rotating Machinery," *Journal of Acoustic Emission*, **11**(1), 1993, pp. 53-59.
33. T.F. Drouillard and A. Vary, "AE Literature Acousto-Ultrasonics," *Journal of Acoustic Emission*, **12**(1-2), 1994, pp. 79-103.
34. K. Ono, "AE Literature Trends of Recent Acoustic Emission Literature," *Journal of Acoustic Emission*, **12**(3-4), 1994, pp. 177-198.
35. *Materials Research and Standards*, **11**(3), 1971. [special issue on AE]
36. H.L. Dunegan and W.F. Hartman (eds.), *Advances in Acoustic Emission*, Dunhart Publishers, Knoxville, Tennessee, 1981. [proceedings of first International Conference on Acoustic Emission, held in Anaheim, California, September 10-13, 1979]
37. *Journal of Acoustic Emission*, **4**(2/3), 1985. [special issue containing extended abstracts of papers presented at the Second International Conference on Acoustic Emission and 28th AEWG meeting, Lake Tahoe, Nevada, October 28-November 1, 1985]

38. *Journal of Acoustic Emission*, **8**(1-2), 1989. [special issue containing extended summaries of papers presented at the World Meeting on Acoustic Emission and 32nd AEWG meeting, Charlotte, North Carolina, March 20-23, 1989; see also Ref. 39]
39. W. Sachse, J. Roget, and K. Yamaguchi (eds.), *Acoustic Emission: Current Practice and Future Directions*, ASTM STP 1077, American Society for Testing and Materials, Philadelphia, Pennsylvania, 1991. [see also Ref. 38]
40. S.J. Vahaviolos (ed.), *4th World Meeting on Acoustic Emission and 1st International Conference on Acoustic Emission in Manufacturing*, American Society for Nondestructive Testing, Columbus, Ohio, 1991. [extended paper summaries and abstracts of papers presented at the meetings, held in Boston, Massachusetts, September 16-19, 1991]
41. M.A. Hamstad, T. Kishi, and K. Ono (eds.), *Progress in Acoustic Emission IX Transitions in AE for the 21st Century*, Acoustic Emission Working Group and Acoustic Emission Group, Encino, California, 1998. [proceedings of the 14th IAES and 5th AE World Meeting, held in Kamuela, Hawaii, August 9-14, 1998]
42. M. Onoe, "Acoustic Emission Research in Japan for Flaw Detection in Weld," pp. 22-47 in *Significance of Defects in Welded Structures*, T. Kanazawa and A.S. Kobayashi (eds.), University of Tokyo Press, Tokyo, 1974.
43. M. Onoe, "AE Events of Interest: The Acceptance Speech by Professor Onoe," *Journal of Acoustic Emission*, **5**(4), p.i, 1986. [acceptance speech for receiving the AEWG Gold Medal Award at the 8th International AE Symposium, Tokyo, October 22, 1986].
44. E. Isono, "History of the Acoustic Emission Method A New Tool for NDT," *Hihakai Kensa* [Journal of NDI], **19**(11), 1970, pp. 579-598. (in Japanese); RFP-Trans-79, translated into English for Dow Chemical U.S.A., Rocky Flats Division, Golden, Colorado, 1971.
45. T. Fuji, "Report of Acoustic Emission Study Group Visited to U.S.A," *Hihaki Kensa* [Journal of NDI], **21**(4), 1972, pp. 242-247. (in Japanese). [special issue on AE]
46. H. Nakasa, "An Overview of the Acoustic Emission Technology in Japan," Invited Lecture, pp. 20-46 in *The Fifth International Acoustic Emission Symposium*, Japanese Society for Non-Destructive Inspection, Tokyo, 1980. [proceedings of the 5th AE Symposium, held in Tokyo, Japan, November 18-20, 1980]
47. H. Nakasa, H. Kusanagi, and H. Ohno, "Review of Japanese Research and Development Activities on Acoustic Emission Applications in the Nuclear Industry," pp. 206-220 in *Nondestructive Evaluation in the Nuclear Industry*, R. Natesh (ed.), American Society for Metals, Metals Park, Ohio, 1978. [proceedings of conference held in Salt Lake City, Utah, February 13-15, 1978]
48. *Proceedings of the U.S.-Japan Joint Symposium on Acoustic Emission*, Japanese and English volumes, Japan Industrial Planning Assoc., Tokyo, 1972. [proceedings of the 1st AE Symposium, held in Tokyo, Japan, July 4-6, 1972. (2-vol. set)]
49. *The Second Acoustic Emission Symposium*, Japan Industrial Planning Assoc., Tokyo, 1974. [proceedings of the 2nd AE Symposium, held in Tokyo, Japan, September 2-4, 1974]
50. *The Third Acoustic Emission Symposium*, Japan Industrial Planning Assoc., Tokyo, 1976. [proceedings of the 3rd AE Symposium, held in Tokyo, Japan, September 16-18, 1976]
51. *The Fourth Acoustic Emission Symposium*, Japanese Society for Non-Destructive Inspection, Tokyo, 1978. [proceedings of the 4th AE Symposium, held in Tokyo, Japan, September 18-20, 1978]
52. *The Fifth International Acoustic Emission Symposium*, Japanese Society for Non-Destructive Inspection, Tokyo, 1980. [proceedings of the 5th International AE Symposium, held in Tokyo, Japan, November 18-20, 1980]

53. M. Onoe, K. Yamaguchi, and T. Kishi (eds.), *Progress in Acoustic Emission*, Japanese Society for Non-Destructive Inspection, Tokyo, 1982. [proceedings of the 6th International AE Symposium, held in Susono, Japan, October 31-November 3, 1982]
54. M. Onoe, K. Yamaguchi, and H. Takahashi (eds.), *Progress in Acoustic Emission II*, Japanese Society for Non-Destructive Inspection, Tokyo, 1984. [proceedings of the 7th International AE Symposium, held in Zao, Japan, October 23-26, 1984]
55. K. Yamaguchi, K. Aoki, and T. Kishi (eds.), *Progress in Acoustic Emission III*, Japanese Society for Non-Destructive Inspection, Tokyo, 1986. [proceedings of the 8th International AE Symposium, held in Tokyo, Japan, October 21-24, 1986]
56. K. Yamaguchi, I. Kimpara, and Y. Higo (eds.), *Progress in Acoustic Emission IV*, Japanese Society for Non-Destructive Inspection, Tokyo, 1988. [proceedings of the 9th International AE Symposium, held in Kobe, Japan, November 14-17, 1988]
57. K. Yamaguchi, H. Takahashi, and H. Niitsuma (eds.), *Progress in Acoustic Emission V*, Japanese Society for Non-Destructive Inspection, Tokyo, 1990. [proceedings of the 10th International AE Symposium, held in Sendai, Japan, October 22-25, 1990].
58. T. Kishi, K. Takahashi, and M. Ohtsu (eds.), *Progress in Acoustic Emission VI*, Japanese Society for Non-Destructive Inspection, Tokyo, 1992. [proceedings of the 11th International AE Symposium, held in Fukuoka, Japan, October 26-29, 1992]
59. T. Kishi, Y. Mori, and M. Enoki (eds.), *Progress in Acoustic Emission VII*, Japanese Society for Non-Destructive Inspection, Tokyo, 1994. [proceeding of the 12th International AE Symposium, held in Sapporo, Japan, October 17-20, 1994]
60. T. Kishi, Y. Mori, Y. Higo, and M. Enoke (eds.), *Progress in Acoustic Emission VIII*, Japanese Society for Non-Destructive Inspection, Tokyo, 1996. [proceeding of the 13th International AE Symposium, held in Nara, Japan, November 27-30, 1996]
61. T. Kishi, Y. Higo, M. Ohtsu, and S. Yuyama (eds.), *Progress in Acoustic Emission X*, Japanese Society for Non-Destructive Inspection, Tokyo, 2000. [proceeding of the 15th International AE Symposium, held in Tokyo, Japan, September 11-14, 2000]
62. T. Kishi, M. Ohtsu, and S. Yuyama (eds.), *Acoustic Emission Beyond the Millennium*, Elsevier Science Ltd., Oxford, New York, Tokyo, 2000. [proceeding of the Kishi Workshop 2000, held in conjunction with IAES-15 in Tokyo, Japan, September 13, 2000]
63. T. Kishi, M. Ohtsu, M. Enoki, and K. Yoshida (eds.), *Progress in Acoustic Emission XI*, Japanese Society for Non-Destructive Inspection, Tokyo, 2002. [proceeding of the 16th International AE Symposium, held in Tokushima, Japan, November 12-15, 2002]
64. M. Ohtsu, M. Enoki, and S. Wakayama (eds.), *Progress in Acoustic Emission XII*, Japanese Society for Non-Destructive Inspection, Tokyo, 2004. [proceeding of the 17th International AE Symposium, held in Tokyo, Japan, November 9-12, 2004]
65. M. Enoki, M. Takemoto, and H. Cho (eds.), *Progress in Acoustic Emission XIII*, Japanese Society for Non-Destructive Inspection, Tokyo, 2006. [proceeding of the 18th International AE Symposium, held in Kamagawa, Japan, July 25-27, 2006]
66. *Pressure Engineering* (Japan) [Atsuryoku Gijitsu Journal of Japan High Pressure Institute], 15(3), 1977. (in Japanese). [special issue on AE]
67. M. Onoe et al., *Acoustic Emission Basics and Applications*, Corona Publishing Co., Ltd., Tokyo, 1976. (in Japanese). [textbook used for JCAE AE short courses]
68. "The 15-th Meeting of European Working Group on Acoustic Emission," *Journal of Acoustic Emission*, 5(3), 1986, pp. 121 and S42-S68. [extended abstracts of seven papers presented at the 15th meeting of the European Working Group on Acoustic Emission, held in Istanbul, Turkey, October 7-10, 1986]
69. *Proceedings of the 16th Conference of the European Working Group on Acoustic Emission*, C.B. Scruby and R. Hill (eds.), in Vol. 4, pp. 2825-3100 of *Non-Destructive Testing*,

- J.M. Farley and R.W. Nichols (eds.), Pergamon Press, Oxford, England, 1988. [proceedings of the 4th European Conference on Non-Destructive Testing and 16th Conference of the European Working Group on Acoustic Emission, held in London, England, October 13-18, 1987]
70. *Proceedings of the EWGAE Symposium*, M. Wevers (ed.), Department of Metallurgy and Materials Engineering, Katholieke Universiteit Leuven, Belgium, (1992). [handout folder of papers presented at the 20th meeting of the European Working Group on Acoustic Emission, held at Katholieke Universiteit Leuven, Belgium, April 27-30, 1998]
71. *22nd European Conference on Acoustic Emission Testing*, L.M. Rogers and P. Tscheliesnig (eds.), Univation Ltd at The Robert Gordon University, Aberdeen, Scotland, 1996. [proceedings of the 22nd meeting of the European Working Group on Acoustic Emission, held at The Robert Gordon University, Aberdeen, Scotland, May 29-31, 1996]
72. *23rd European Conference on Acoustic Emission Testing (incorporating EWGAE)*, P. Tscheliesnig (ed.), TÜV Austria, Vienna, Austria, 1998. [proceedings of the 23rd European Conference on Acoustic Emission Testing, sponsored by EWGAE, held at TÜV Austria, Vienna, Austria, May 6-8, 1998]
73. *24th European Conference on Acoustic Emission Testing*, Centre Technique des Industries Mécaniques (CETIM), Senlis/Paris, France, 2000. [proceedings of the 24th European Conference on Acoustic Emission Testing, sponsored by EWGAE and CETIM, held in Senlis/Paris, France, May 22-24, 2000]
74. *25th European Conference on Acoustic Emission Testing*, Czech Society for Non-Destructive Testing, Prague, Czech Republic, 2002. [proceedings of the 25th European Conference on Acoustic Emission Testing, sponsored by EWGAE and CSNDT, held in Prague, Czech Republic, September 11-13, 2002. (2-vol. set)]
75. *26th European Conference on Acoustic Emission Testing*, Deutsche Gesellschaft für Zerstörungsfreie Prüfung, eV, Berlin, Germany, 2004. [proceedings of the 26th European Conference on Acoustic Emission Testing, sponsored by EWGAE and DGZfP, held in Berlin, Germany, September 15-17, 2004. (2-vol. set)]
76. *Acoustic Emission Testing: Proceedings of the 27th European Conference on Acoustic Emission Testing (EWGAE 2006)*, R. Pullin, K.M. Holford, S.L. Evans, and J.M. Dulieu-Barton (eds.), Trans Tech Publications Ltd, Uetikon-Zuerich, Switzerland, 2006. [proceedings of the 27th European Conference on Acoustic Emission Testing, sponsored by EWGAE, held in Cardiff, Wales, September 20-22, 2006]
77. H.R. Hardy, Jr. and F.W. Leighton (eds.), *Proceedings, First Conference on Acoustic Emission/Microseismic Activity in Geologic Structures and Materials*, Trans Tech Publications, Clausthal-Zellerfeld, Germany, 1977. [conference held at Pennsylvania State University, University Park, Pennsylvania, June 9-11, 1975]
78. H.R. Hardy, Jr. and F.W. Leighton (eds.), *Proceedings, Second Conference on Acoustic Emission/Microseismic Activity in Geologic Structures and Materials*, Trans Tech Publications, Clausthal-Zellerfeld, Germany, 1980. [conference held at Pennsylvania State University, University Park, Pennsylvania, November 13-15, 1978]
79. H.R. Hardy, Jr. and F.W. Leighton (eds.), *Acoustic Emission/Microseismic Activity in Geologic Structures and Materials, Proceedings of the Third Conference*, Trans Tech Publications, Clausthal-Zellerfeld, Germany, 1984. [conference held at Pennsylvania State University, University Park, Pennsylvania, October 5-7, 1981]
80. H.R. Hardy, Jr. (ed.), *Acoustic Emission/Microseismic Activity in Geologic Structures and Materials, Proceedings of the Fourth Conference*, Trans Tech Publications, Clausthal-Zellerfeld, Germany, 1989. [conference held at Pennsylvania State University, University Park, Pennsylvania, October 22-24, 1985]

81. H.R. Hardy, Jr. (ed.), *Acoustic Emission/Microseismic Activity in Geologic Structures and Materials, Proceedings of the Fifth Conference*, Trans Tech Publications, Clausthal-Zellerfeld, Germany, 1995. [conference held at Pennsylvania State University, University Park, Pennsylvania, June 11-13, 1991]
82. H.R. Hardy, Jr. (ed.), *Acoustic Emission/Microseismic Activity in Geologic Structures and Materials, Proceedings of the Sixth Conference*, Trans Tech Publications, Clausthal-Zellerfeld, Germany, 1998. [conference held at Pennsylvania State University, University Park, Pennsylvania, June 11-13, 1996]

HIGH-TEMPERATURE ACOUSTIC EMISSION SENSING USING ALUMINUM NITRIDE SENSOR

HIROAKI NOMA, TATSUO TABARU, MORITO AKIYAMA, NORIKO MIYOSHI,
TOMO HARU HAYANO* and HIDEO CHO*

Measurement Solution Research Center, National Institute of Advanced Industrial Science and
Technology (AIST), 807-1 Shuku, Tosu, Saga 841-0052, Japan;

* Faculty of Science and Engineering, Aoyama Gakuin University,
5-10-1, Fuchinobe, Sagami-hara, Kanagawa, 229-8558, Japan

Abstract

We developed a heat-resistant acoustic emission (AE) sensor using AlN thin films and detected AE signals from molten-salt attack of Type-304 stainless steel pipe. Aluminum nitride (AlN) is a promising AE sensor element for high-temperature environment, such as gas turbines and other plants because AlN maintains its piezoelectricity up to 1200°C. Highly *c*-axis-oriented AlN thin-film sensor elements were prepared on silicon single crystals by rf magnetron sputtering. The AE sensor sensitivity increased with d_{33} and thickness of AlN elements and the heat-resistant AE sensors were developed using AlN elements with high d_{33} values and thickness of 9 μm. The sensor showed a constant sensitivity across a frequency range of 100 kHz to 1 MHz at ambient temperature. The sensor characteristics were evaluated at elevated temperatures up to 700°C. It was confirmed that the AE sensor works well up to 700°C and does not deteriorate. The AE sensor detected AE signals from frequent cracking of oxide scales produced by molten-salt attack (85% V₂O₅ + Na₂SO₄) at 700°C during cooling of the pipe.

Keywords: AE sensor, high temperature, aluminum nitride, molten-salt attack

Introduction

Plant monitoring systems are on high demand due to a series of recent accidents of power stations and chemical plants in Japan. Thus, there is the need to monitor high-temperature members in large structures. The AE method offers advantages such as observing the progress of plastic deformation and microscopic fracture in real time, locating a flaw using several AE sensors, and diagnosis capability without shutdowns. The AE method is used in a wide range of fields, including the inspection of manufactured products, monitoring the safety of structures and detecting natural disasters such as landslides [1]. The most common detection material for application in AE sensors is lead-zirconate titanate (PZT). Its Curie point, the temperature above which a piezoelectric material loses its piezoelectricity, is approximately 300°C. When an AE sensor with a PZT element is applied in high-temperature environment, a waveguide and/or a cooling device are essential and so it is difficult to measure AE correctly. Therefore, the development of a heat-resistant AE sensor that can be used above 300°C is strongly desired.

Aluminum nitride (AlN) is a piezoelectric material, which has a piezoelectric strain constant d_{33} of 5.6 pm/V [2] and an ability to maintain piezoelectricity up to 1200°C [3]. AlN is a promising material as the active element of a heat-resistant AE sensor without a cooling device. However, the polarization of AlN cannot be controlled after preparation and sintered AlN polycrystals exhibit no piezoelectricity. This had been a major hindrance to the commercialization

of AlN piezoelectric devices. After trying several methods, we finally succeeded in making highly oriented AlN thin films by rf magnetron sputtering [4].

In our previous studies [5-7], we developed both ordinary AE sensors and heat-resistant AE sensors using the AlN elements. The sensor characteristics were evaluated at ambient temperature and at elevated temperatures. To evaluate of d_{33} and thickness of AlN elements on sensor sensitivity, AlN elements with d_{33} from 2 to 7 pm/V and thickness from 3 to 9 μm were prepared. It is confirmed that the AE sensor sensitivity increased with d_{33} and thickness of AlN elements [7]. The sensitivity of the heat-resistant AE sensor was also improved by a design of the sensor structure. The sensor characteristics were evaluated at elevated temperatures from 200 to 600°C. It was confirmed that the AE sensor works well at 600°C and does not deteriorate.

In this study, we developed a heat-resistant AlN AE sensor using AlN element of 9- μm thickness and Inconel-600 housing. The sensor characteristics were evaluated at elevated temperatures up to 700°C. Finally, using this AlN AE sensor, we succeeded in detecting AE signals from frequent cracking of the oxide scale produced by the molten salt attack (85% $\text{V}_2\text{O}_5 + \text{Na}_2\text{SO}_4$) at 700°C during cooling of the pipe.

Experimental Procedures and Results

Preparation of AlN Thin Films

AlN thin-film sensor elements were prepared on silicon single-crystal substrates (thickness: 0.625 mm) by rf magnetron sputtering. The sputtering conditions for the AlN thin film are reported in a previous study [4]. The thickness of AlN thin film was controlled by the sputtering time. The full width at half-maximum (FWHM) of the X-ray rocking curves of the film deposited under the optimized sputtering conditions was 2° and the film was highly oriented along the c -axis. A platinum (Pt) thin film used as the upper electrode was also prepared by rf magnetron sputtering. The crystal structure and orientation of the film were investigated by X-ray diffraction (XRD) analysis.

Development of Heat-resistant AlN AE Sensors

Disk-like AlN elements with 6-mm diameter were cut out from Si wafer for AE sensors. The d_{33} value of each AlN element was measured using d_{33} PiezoMeter System (Piezotest). The heat-resistant AlN AE sensors were developed using AlN element with high d_{33} values and thickness of 9 μm . The AlN elements were selected and directly fixed to the wear plate (alumina) by Ag paste just like an ordinary AE sensor. The diagram and the photo of the heat-resistant AlN AE sensor are shown in Fig. 1. The metal housing was made of Inconel 600, which has high thermal and corrosion resistances. A heat-resistant coaxial cable was developed for connecting the sensor to a preamplifier.

Evaluation of Characteristics of AlN AE Sensor

To measure the frequency responses of the AlN AE sensor, a commercial PZT AE sensor, AE-900S-WB (NF Corporation), was used to generate quasi-AE waves. This AE sensor is a wide-band model and possesses a constant sensitivity in the range of 100 kHz to 1 MHz (± 10

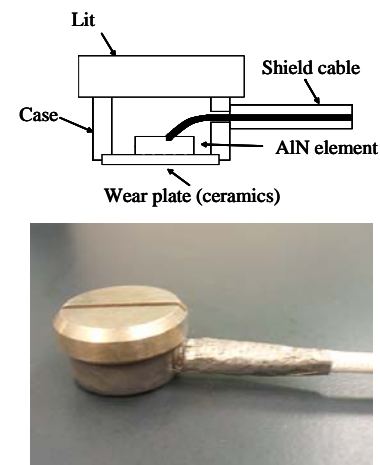


Fig. 1 Diagram and photo of a heat-resistant AlN AE sensor.

dB). A preamplifier (9913, NF Corporation) with a 40-dB gain in the frequency range of 100 Hz to 20 MHz was used for the AlN AE sensor. The AlN AE sensor was fixed to the PZT sensor using an acoustic coupler, Gelsonic (Nihon Kohden Corporation). Single-cycle sine wave (V_{p-p} : 20 V) was applied to the PZT sensor and the output from the AlN AE sensor was measured and expressed in dB (the ratio of the output to the input 20 V). The frequency of the sine wave was varied from 100 kHz to 1 MHz by 10 kHz intervals.

The frequency responses are shown in Fig. 2. It showed a constant sensitivity across the range of 100 kHz to 1 MHz (± 5 dB) like the PZT commercial AE sensor. While the PZT commercial AE sensor has a damper for constant wideband sensitivity, the AlN AE sensor shows a constant sensitivity without such a damper. The thickness of AlN element is 9 μm so that the resonance frequency must be much higher than 1 MHz. That is the reason why the AlN AE sensor shows a constant sensitivity, which is an advantageous feature of this heat-resistant AlN AE sensor.

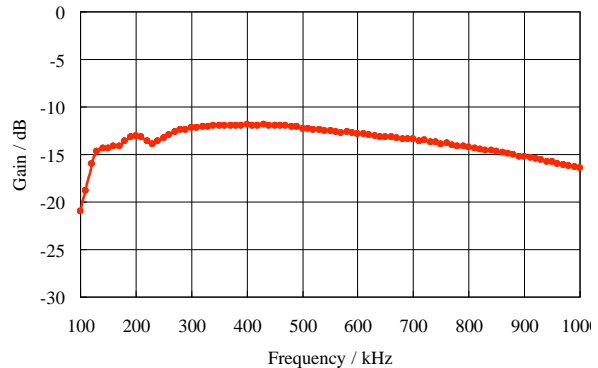


Fig. 2 Frequency responses of AlN AE sensor.

Evaluation of AlN AE Sensor at High-temperatures

Figure 3 shows a diagram of the experimental setup for AE sensor responses at elevated temperatures. A stainless steel rod (diameter: 20 mm, length 400 mm) was used as an AE waveguide, which transmitted elastic waves from the PZT sensor outside an electric furnace. The waveguide was cooled by water outside the furnace and the temperature of PZT sensor was maintained under 60°C. The responses of the AlN AE sensor were measured at ambient temperature, 200, 300, 400, 500, 600 and 700°C after keeping the AlN AE sensor at each temperature for more than 30 min. A tone-burst of 10 sine waves was generated and the output of AlN AE sensor was observed. A preamplifier was used for the AlN AE sensor.

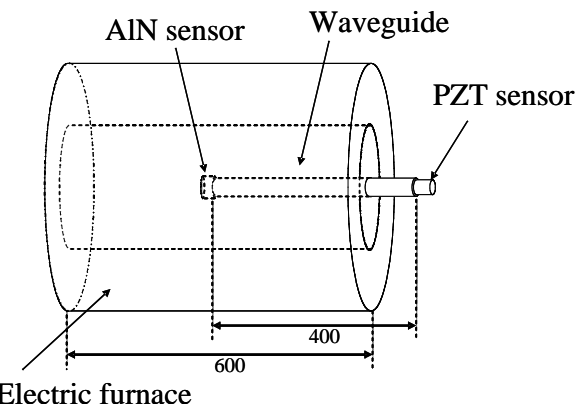


Fig. 3 Experimental setup for AE sensor responses at elevated temperatures.

The AlN AE sensor was coupled using an anti-seize paste (PBC® aka polybutylcuprysil, <http://www.kspaul.de/TDB-engl/MP-PBC-engl.pdf>). This is semi-synthetic grease with metallic powders and inorganic thickener. After high temperature exposure, it became powdery, but still functioned as a couplant during cooling. The sensor was mechanically held with a ceramic spring.

Figure 4 shows a generated envelope of a tone-burst wave with 10-cycle sine waves of 200 kHz, and the response signals of the AlN AE sensor at 300, 500 and 700°C. It is confirmed that the sensitivity of the AlN AE sensor is maintained from ambient temperature up to 700°C.

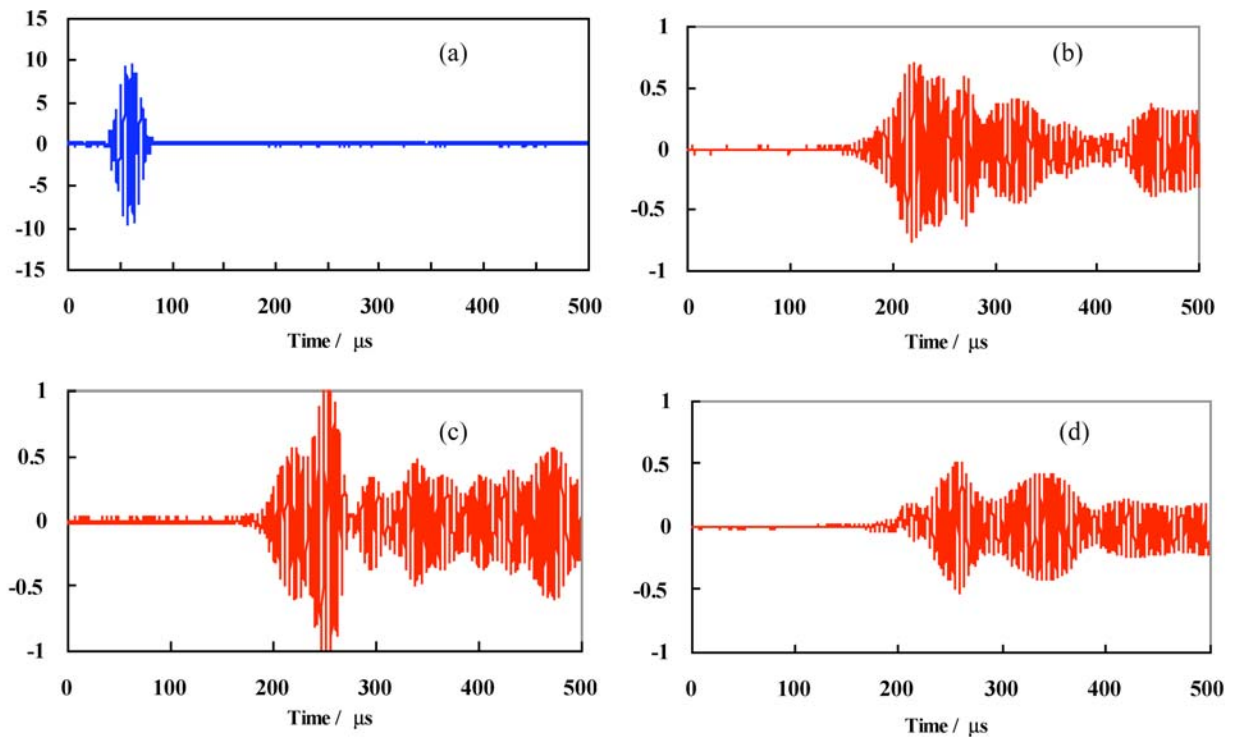


Fig. 4 Generated tone-burst wave (a) with 10 sine waves of 200 kHz and the response signals of AlN AE sensor at (b) 300°, (c) 500° and (d) 700°C.

AE Monitoring of Molten Salt Attack by AlN AE Sensor

Accelerated oxidation of heat-resistant alloys by molten salt is well known as the most dangerous damage, and often called as catastrophic oxidation. We measured AE signals by molten-salt attack (85 mol% $V_2O_5 + Na_2SO_4$) by using the AlN AE sensor. We used a similar experimental setup reported previously [8]. Figure 5 shows an experimental setup for molten-salt attack and AE monitoring method of a hot stainless steel pipe

(type-304) of 34-mm diameter, 3.0-mm thickness and 1200-mm length. The PZT sensor (AE-900S-WB) was also mounted as a reference on the pipe end, where the temperature was lower than 40°C. Preamplifiers (2/4/6, PAC) with 40-dB gain were used for the AlN AE and PZT sensor. We used an AE monitoring system (PAC, DSP PCI-2). We placed 0.1 g of a mixed salt (85 mol% $V_2O_5 + Na_2SO_4$) on the upper portion of the pipe at the center of the furnace and then heated the pipe.

Figure 6 shows cumulative AE hits of the AlN sensor and temperature of the pipe in the furnace. The pipe was heated to 700°C and kept for 3 hours, then the power of the furnace was turned off and the pipe was allowed to cool. The threshold for AE hits of the AlN AE sensor was set at 10 mV. We detected few AE hits during heating and holding, but monitored frequent AE hits during cooling. The similar AE during cooling was observed in a previous study using optical fiber sensors [8]. Therefore, the AE hits must be caused by frequent cracking of the oxide

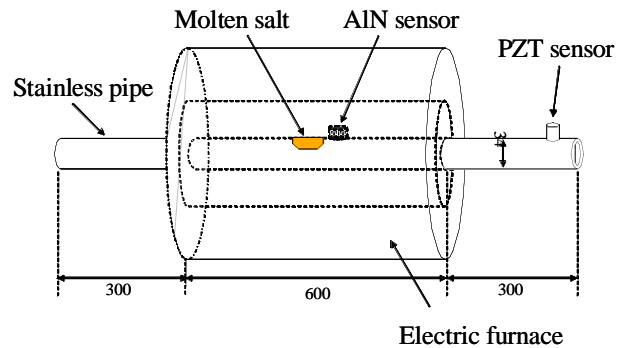


Fig. 5 Experimental setup for AE monitoring of molten salt attack.

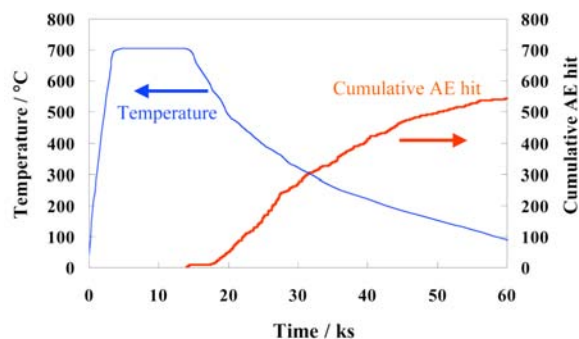


Fig. 6 Cumulative AE counts detected by the AlN AE sensor with temperature after molten-salt attack.

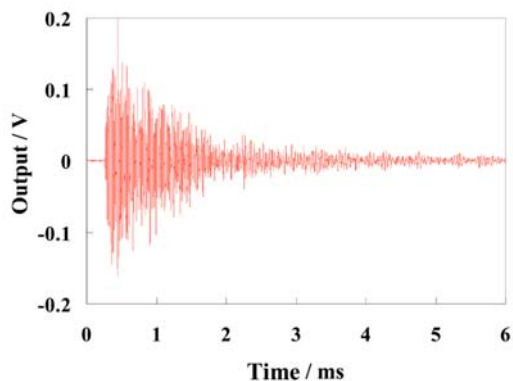


Fig. 7 Waveform of AE detected by AlN AE sensor.

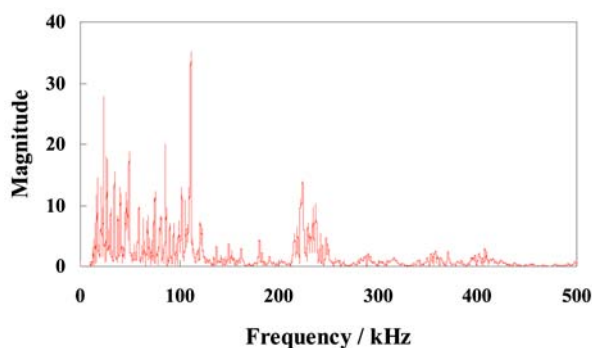


Fig. 8 FFT of waveform in Fig. 7.

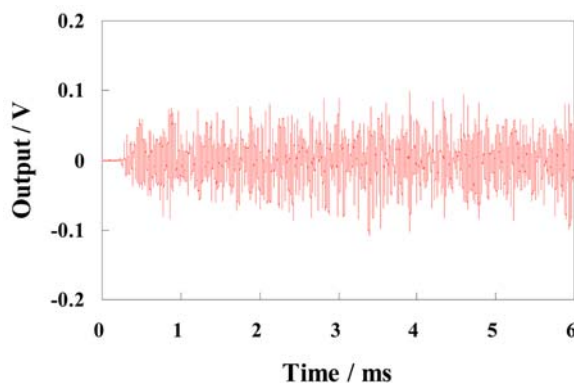


Fig. 9 Same signal as Fig. 7 by PZT sensor.

scales (and possibly salt cracks at lower temperatures) produced by the molten-salt attack during cooling of the pipe. A typical AE waveform is shown in Fig. 7. The power spectra of the AE (Fig. 8) showed many peaks below 100 kHz and a few peaks around 110, 240 and 360 kHz. The latter two appear to be due to F(1,2) and F(2,2) cylindrical waves from the cracking sources propagating on the pipe [9]. When the same signal (Fig. 7) was detected by the PZT sensor outside the furnace, the dispersion of cylindrical waves stretched the signal by several times, as shown in Fig. 9.

We have not tested for the durability on this AlN AE sensor, but it worked at 700°C for at least several hours for these experiments. The high-temperature couplant remained effective. It is confirmed that the AlN AE sensor detected AE signals from the fracture of the oxide scales produced by the molten-salt attack at 700°C during cooling of the pipe.

Summary

We developed a heat-resistant AE sensor using AlN thin films and detected AE signals from molten-salt attack of Type 304 stainless steel pipe. Aluminum nitride (AlN) is a promising acoustic emission (AE) sensor element for high-temperature environments such as gas turbines and other plants because AlN maintains its piezoelectricity up to 1200°C. Highly *c*-axis-oriented AlN thin-film sensor elements were prepared on silicon single crystals by rf magnetron sputtering. The heat-resistant AE sensors were developed using AlN elements with high d_{33} values and thickness of 9 μm . The sensor showed a constant sensitivity across a wide band of frequencies in the range of 100 kHz to 1 MHz at an ambient temperature. The sensor characteristics were

evaluated at elevated temperatures up to 700°C. It was confirmed that the AE sensor works well up to 700°C and does not deteriorate for at least several hours. The AE sensor detected AE signals from frequent fractures of the oxide scales produced by the molten salt attack (85% V₂O₅ + Na₂SO₄) at 700°C during the cooling of the pipe.

Acknowledgment: A part of this study was supported by Industrial Technology Research Grant Program in 2004 from New Energy and Industrial Technology Development Organization (NEDO) of Japan.

References

1. A. Chichibu, K. Jo, M. Nakamura, T. Goto and M. Kamata, *Proc. 9th International Acoustic Emission Symposium*, Kobe, Japan, 1988, pp. 92-97.
2. I.L. Guy, S. Muensit and E.M. Goldys, *Applied Physics Letters*, **75**, 1999, 4133-4135.
3. R.C. Turner, P.A. Fuierer, R.E. Newnham and T.R. Shrout, *Applied Acoustics*, 1994, **41**, 299-324.
4. M. Akiyama, C. N. Xu, K. Nonaka and T. Watanabe, *Thin Solid Films*, **315**, 1998, 62-65.
5. H. Noma, K. Kishi, N. Ueno, M. Akiyama and S. Takahashi, *The Society of Instrument and Control Engineers (SICE) 21st Sensing Forum*, 2004, pp. 51-54.
6. E. Ushijima, H. Noma, K. Kishi, N. Ueno and M. Akiyama, *The 3rd U.S.-Japan Symposium on Advancing Applications and Capabilities in NDE*, Hawaii, 2005, pp. 139-142.
7. H. Noma, E. Ushijima, Y. Ooishi, M. Akiyama, N. Miyoshi, K. Kishi, T. Tabaru, I. Ohshima, A. Kakami and T. Kamohara, *Proc. 27th European Conference on Acoustic Emission Testing (EWGAE 2006)*, Cardiff, 2006, pp. 111-116.
8. T. Hayano, T. Matsuo, H. Cho and M. Takemoto, *Progress in Acoustic Emission XIII*, 2006, JSNDI, pp. 205-211.
9. H. Nishino, K. Yoshida, H. Cho and M. Takemoto, *J. Acoust. Soc. Jpn.*, **63**, 2007, 13-20.

RECENT ADVANCES IN THE MECHANICS OF MEMS ACOUSTIC EMISSION SENSORS

DAVID W. GREVE, IRVING J. OPPENHEIM*, AMELIA P. WRIGHT* and WEI WU

*Dept. of Civil & Environmental Eng., Carnegie Mellon University, Pittsburgh, PA 15213 USA;
Dept. of Electrical and Computer Eng., Carnegie Mellon University, Pittsburgh, PA 15213 USA

Abstract

Resonant sensors for acoustic emission detection have been designed and fabricated as MEMS capacitive transducers with resonant frequencies between 100 and 500 kHz. We report four recent advances in our understanding of their mechanics and in the implications of those advances for improved sensitivity. One advance involves a successful laboratory method to seal and evacuate the MEMS device within its ceramic package, thereby operating in a coarse vacuum and reducing or eliminating squeeze film and radiation damping effects; we present characterization measurements showing an approximate fourfold increase in quality factor Q . A second advance is a summary of our theoretical analysis of noise sources for a resonant, capacitive MEMS transducer; we report that Brownian noise associated with the impact of air molecules is the major source. A third advance is the use of a grillage of beams, rather than a perforated plate, as the moving plate in the spring-mass system; we present characterization measurements showing a significant reduction in damping and therefore a higher Q . The fourth advance is a finger-type mechanism to sense in-plane motion; we show characterization measurements confirming the resonant behavior of that device and showing that the in-plane device has a much higher Q than comparable out-of-plane devices.

Keywords: Damping; in-plane motion; MEMS; sensor innovation.

Introduction

Our research group has developed a series of MEMS devices to function as resonant transducers sensitive to out-of-plane motion. Their mechanics and their use as acoustic emission sensors are most completely described in a paper by Ozevin *et al.* [1]. The transducers are fabricated in the PolyMUMPS surface micromachining process as spring-mass systems to form capacitors in which the moving plate is an elastic structure in polysilicon with a thickness of 2 μm . We typically place on each chip a suite of transducers at different frequencies in the range up to 500 kHz, placing four transducers on a 5 x 5 mm chip or a larger number of transducers on a 10 x 10 mm chip.

Figure 1a shows a completed four-channel AE sensor system [2, 3]. It consists of a MEMS chip, nominally 5 x 5 mm, containing four independent transducers with resonant frequencies in the range between 126 and 500 kHz. The chip is mounted in a Spectrum Semiconductor Materials CPG06856 pin-grid array ceramic package, 26 x 26 mm, chosen because it provides a smooth bottom surface for coupling to structural plates. The ceramic package engages a bottom PC board and Sullins 2.0 mm connectors engage a bottom PC board containing four amplifier circuits, as shown in Fig. 1a, each with a nominal gain of 100 V/V (40 dB). The whole system (apart from the cable connector) is contained in a volume of 35 x 35 x 30 mm.

Vacuum Sealing of a Perforated Plate Transducer

Among various mechanisms limiting the sensitivity of such transducers, the damping effect of air is very significant. Damping occurs both from acoustic radiation into the air and from squeeze-film damping as air is forced through the gap between the moving plate and stationary plate. The effectiveness of a resonant transducer is related to its sharpness of resonance, or (equivalently) to its dynamic magnification, and is commonly calculated as the quality factor Q . Operation in coarse vacuum would reduce the damping effects and increase Q , and we report a practical laboratory method for sealing and evacuating the chip in its ceramic package.

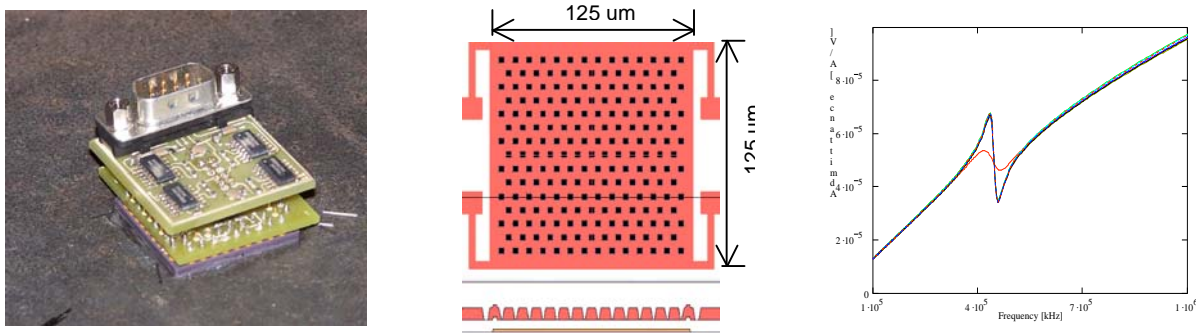


Fig. 1a. Four-channel AE sensor system in 35 x 35 x 30 mm volume (Left); 1b. CAD layout and section of one unit (Center); 1c. Admittance at resonance, $f \sim 443$ kHz, $Q \sim 5.5$ (atmospheric), $Q \sim 19.7$ (evacuated) (Right).

Figure 1b is the CAD layout and section of a single unit, showing a perforated square plate (125 μm on a side, with 3.5 μm square etch holes on a triangular grid with 8 μm between holes) suspended by four flexural springs, with a gap of 1.25 μm between the plate and the underlying stationary electrode. FEM simulation was used in selecting the flexural spring length to achieve target design frequencies between 126 and 500 kHz. Each transducer consists of 144 units (a 12 x 12 array) to obtain a target design capacitance near 13 pF. Figure 1c shows the admittance plot for the transducer with nominal design frequency of 500 kHz, and resonance is observed near 443 kHz. The admittance plot depicts the sharpness of resonance before and after the process of sealing and evacuation. The broader resonance in Figure 1c is the admittance plot at atmospheric pressure, corresponding to a Q of 5.5.

For the different transducers (different resonant frequencies) the admittance measurements at atmospheric pressure showed Q factors ranging from 2.4 to 5.5, and the measured Q generally increased with transducer frequency, as predicted. In an attempt to make the transducers more sensitive, we next developed a laboratory method to seal and evacuate the device within its package. The CPG06856 ceramic package product has an accompanying lid, plated with nickel and gold. In our method, a hole is drilled in the solder seal lid, the perimeter of the lid is soldered to the CPG06856 package, and a small amount of solder is dropped around the hole. The package is then moved to a vacuum chamber, within which a soldering iron can translate on a vertical axis. After the chamber is evacuated, the soldering iron is energized and the solder around the hole is melted, sealing the hole in the lid. After the solder cools, the package is removed from the vacuum chamber. This method has proven reliable and the resulting seal appears to be durable.

The sharper resonance in Figure 1c is a coincident set of numerous admittance plots repeated over a period of 28 days, showing no loss of vacuum, and corresponding to a Q of 19.7. The increase observed in Q , approximately fourfold, is helpful in increasing the expected sensitivity of the transducer. However, it immediately raises the question, what factor is limiting the Q ?

Internal damping in polysilicon is too low to explain the observed Q , which would correspond to 2.5% of critical damping. In our opinion, the observed Q is limited by other influences, such as imperfect coherence in the response of the 144 units that comprise the transducer. The 12 x 12 array occupies an area less than 2 mm square, which is small compared to the ultrasonic wavelength in steel at the frequencies (below 500 kHz) of our transducers, and therefore it is reasonable to expect that an arriving mechanical excitation will uniformly drive the units in the array. It is more likely that the 144 units do not have identical resonant frequencies. For example, the stiffness of the anchors, assumed to be rigid, will differ from the perimeter of the array to the interior, creating one source for slight deviations in the resonant frequencies. The effect of imperfect coherence would be a “spreading” of the aggregated peak, which is equivalent (in terms of our admittance test) to higher damping.

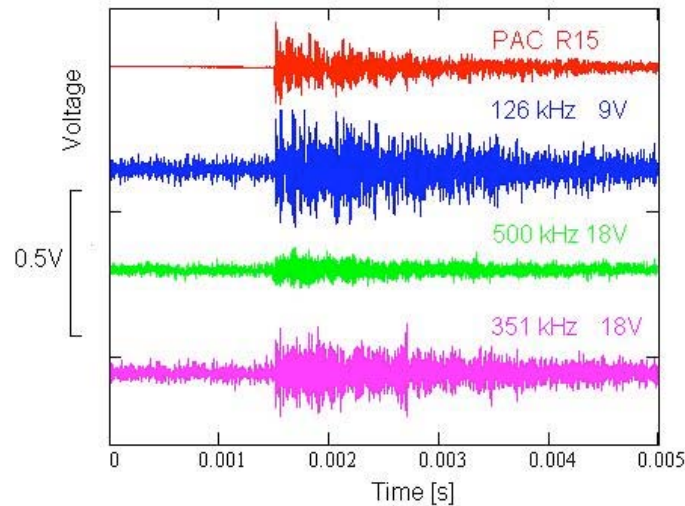


Fig. 2. Pencil-lead break response, comparing three MEMS sensors to PAC R15 sensor.

We applied pencil-lead breaks at the center of a large steel plate, 9.5-mm thick, with the MEMS system (Fig. 1a) and a PAC R15 sensor mounted symmetrically 20 mm from that source. Figure 2 shows the response of three sensor channels on the MEMS device, after onboard amplification, and the raw response of the PAC R15 sensor; for each MEMS channel, we indicate in Fig. 2 its design frequency and its bias voltage. Signal strength from the sensor channels on the MEMS device is comparable to that from the PAC R15 sensor, although the SNR is not as favorable.

Noise Analysis

We recently developed a theoretical analysis of noise sources [4] in the electromechanical behavior of a resonant, capacitive-type transducer. We determine that Brownian noise from impact excitation of the moving plate by air molecules, as examined by Gabrielson [5], is the mechanism of primary interest. Summarizing those findings here, we report the RMS amplitude of the current resulting from such agitation to be

$$i_{RMS} = \frac{V_{DC}C_0}{g} \sqrt{4k_B T} \cdot \left[\sqrt{m\omega_0} \int f(\omega, Q) d\omega \right],$$

where V_{DC} is the DC bias voltage, g is the gap between the capacitor plates, C_0 is the capacitance at rest, k_B is the Boltzmann constant, T is the temperature ($^{\circ}\text{K}$), ω_0 is the circular resonant frequency, and m is the mass of the spring-supported plate. The term in square brackets, with its

integral, captures the dynamic response of the resonator to air molecule impact, and therefore depends upon the quality factor Q , together with the influence of amplifier bandwidth; see [4] for the derivation and details. For a strongly peaked resonator, with suitable amplifier bandwidth, the term in square brackets tends to a result that is independent of Q . Recent measurements over a wide range of design resonant frequencies (from 126 to 500 kHz) show reasonable comparison between the predicted and measured noise level [4].

Grillage Transducer for Out-of-Plane Motions

We report on a new transducer mechanism, fabricated in 2007, an out-of-plane sensor with a design frequency of 250 kHz. The design features a moving plate constructed as a grillage rather than as a perforated plate with periodically spaced etch holes. We show characterization measurements suggesting two advantages to the grillage geometry. Capacitance measurements and FEM simulations show the grillage to approximate a whole plate in its electrical behavior, and admittance measurements show the grillage to have higher Q (lower damping) than a comparable perforated plate.

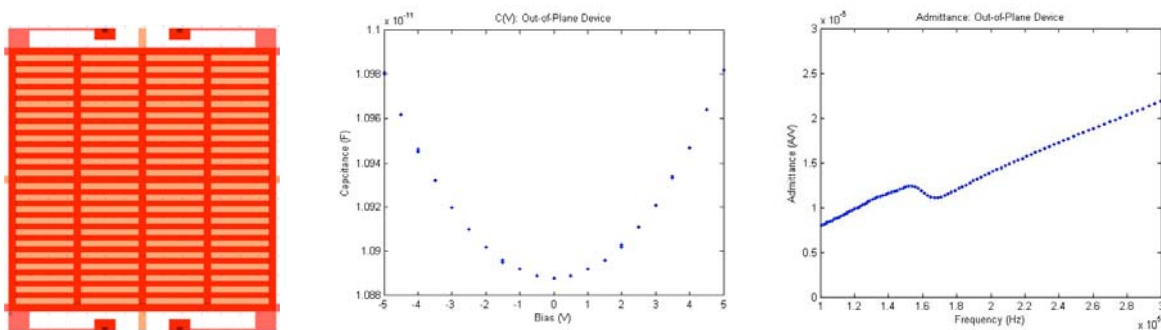


Fig. 3a. CAD layout of grillage unit for out-of-plane sensing (Left); 3b. C-V plot, $C_0 \sim 10.9$ pF (Center); 3c. Admittance at resonance, $f \sim 160$ kHz, $Q \sim 6.7$ (Right).

Figure 3a is the CAD layout of a single unit, showing a grillage (outside dimensions $138 \times 140 \mu\text{m}$) supported by four flexural springs; the beams forming the grillage are $3 \mu\text{m}$ in width, with a clear spacing of $3 \mu\text{m}$ between beams, and a gap of $1.25 \mu\text{m}$ between the grillage and the underlying stationary electrode. FEM simulation was used in selecting the flexural spring length to achieve the target design frequency of 250 kHz. The transducer consists of 72 units (a 9×8 array) to obtain a target design capacitance, C_0 , of 5.8 pF, calculated based upon the net area of the grillage. Figure 3b shows the C-V plot, referring to the capacitance as a function of applied DC voltage. A capacitive spring-mass system should show an increase in capacitance with applied DC voltage, because the electrostatic attraction force will deflect the system, reduce the gap, and thereby increase the capacitance. The C-V plot confirms the expected behavior of the transducer, but it indicates a C_0 near 10.9 pF. Subsequent FEM simulations show that the capacitance closely approximates that of the gross area of a whole plate rather than the net area of a grillage; in other words, the “cutouts” between grillage beams do not diminish the capacitance. Figure 3c shows the admittance plot in the vicinity of resonance, which is observed to occur near 160 kHz. (The difference between predicted and observed frequency is not of great concern, and is attributed to support flexibility and to fabrication deviations in the spring thickness.) Figure 3c depicts the sharpness of resonance, from which a Q near 6.7 is extracted. A comparable perforated plate transducer (as depicted in Figure 1b) with a resonant frequency of 182 kHz displayed a Q near 2.0, and the grillage geometry represents substantial improvement. (Considering

squeeze-film and radiation damping in air, by theory, Q will increase with frequency, and comparisons must be taken between transducers at comparable resonant frequencies.) Compared to a perforated plate, we predicted that the grillage geometry would decrease damping by permitting freer venting of the air beneath the grillage, reducing squeeze-film damping; we interpret these results as evidence qualitatively confirming that prediction.

Finger Transducer for In-Plane Motions

Finally, we report on another new 2007 transducer, designed to sense in-plane motion. It is a finger-type (comb-type) capacitive transducer with a design frequency of 250 kHz. The predicted Q is much higher (predicted damping is much lower) than for out-of-plane sensors, because in-plane motion mostly produces only a direct shearing of air in the gap, rather than a squeeze-film or radiation actuation of the air. At the same time, squeeze-film damping in the out-of-plane direction is used beneficially to isolate the desired in-plane mechanical response from the unwanted out-of-plane response.

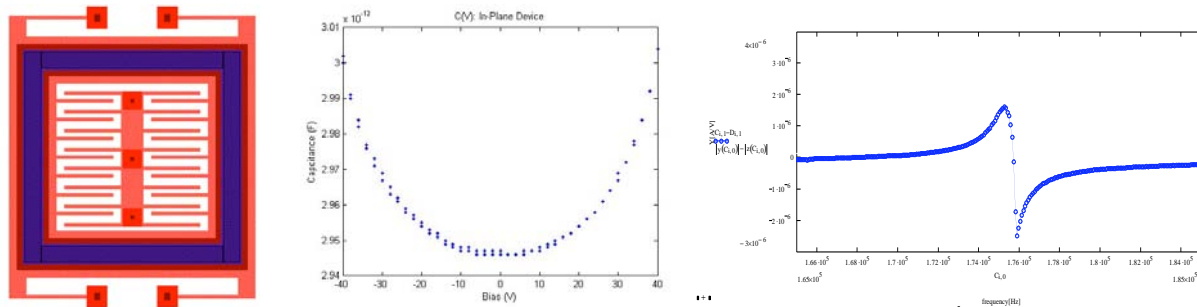


Fig. 4a. CAD layout of finger-type transducer to sense in-plane motion in the y -direction (Left); 4b. C-V plot, $C_0 \sim 2.95$ pF (Center); 4c. Admittance at resonance, $f \sim 176$ kHz, $Q \sim 197$ (Right).

Figure 4a is the CAD layout of a single unit ($128 \times 132 \mu\text{m}$) showing a stationary central spine with projecting fingers, which form capacitors in relation to fingers that project from a frame supported by four flexural springs and oriented to sense motion in the y -direction; the pitch between fingers is unsymmetrical in order to effect a change in capacitance during motion. Again, FEM simulation was used in selecting the flexural spring length to achieve the target design frequency of 250 kHz, and to calculate the predicted capacitance C_0 , which is significantly and beneficially influenced by the effects of fringe capacitance. The transducer consists of 532 units (a 19×28 array) to obtain a target design capacitance, C_0 , of 3.1 pF. Figure 4b shows the C-V plot, confirming the expected behavior of the transducer with a measured C_0 near 2.95 pF. Figure 4c shows the admittance plot in the vicinity of resonance, which is observed to occur near 176 kHz, and the sharp resonance corresponds to a Q near 197. The characterization measurements confirm the design characteristics outlined above, and suggest that the transducer may provide a practical approach to sensing in-plane particle displacements. In principle, the transducer can be fabricated on one MEMS chip together with a similar transducer orthogonal to it, along with a third transducer sensitive to out-of-plane motion, creating a sensor system responding to the three-dimensional components of particle motion.

Summary

We have described four recent advances in our understanding of the mechanics of capacitive MEMS transducers resonant in the range between 100 and 500 kHz. We seek to improve the

sensitivity of these transducers as acoustic emission sensors, and the advances provide insights for those improvements. Among other factors, damping and noise limit transducer sensitivity, and all four advances guide us to better sensitivity. We have shown an effective laboratory approach for sealing and evacuating a device, thereby reducing the squeeze film and radiation damping effects of air. Characterization experiments show an approximate fourfold increase in quality factor Q , and response of the sensor in pencil lead break testing, after onboard amplification, is compared to the response of a commercial transducer. We have also summarized our recent theoretical analysis of noise, identifying the effective floor to result from Brownian motion and the impact of air molecules with the resonator, confirmed by our measurements. We have reported a significant reduction in squeeze-film damping, in air, when using a grillage of beams as the moving plate rather than a perforated plate with periodically spaced etch holes. Finally, we have reported our first characterization measurements of a new transducer designed to sense in-plane motion. Those results confirm its design characteristics, and show it to be minimally damped (in air) because the in-plane motion mostly produces a shearing of an air volume rather than a squeeze film or radiation excitation of the air volume.

Acknowledgements: This work is supported by the National Science Foundation, Grant CMS-0329880 entitled SENSORS: Collaborative Research: MEMS for Multi-Mode Civil Infrastructure Sensing, and by the Pennsylvania Infrastructure Technology Alliance. We gratefully acknowledge contributions of our research collaborators at Lehigh University, Professor S. P. Pessiki and Dr. D. Ozevin, who is now a research Scientist with Physical Acoustics Corporation. The opinions, findings, conclusions, and recommendations expressed in this material are those of the current authors and do not necessarily reflect the views of the sponsors or of our collaborators.

References

1. D. Ozevin, D. W. Greve, I. J. Oppenheim, and S. P. Pessiki, Resonant capacitive MEMS acoustic emission transducer, *Smart Mater. Struct.*, **15**, 2006, 1863-1871.
2. D. W. Greve, I. J. Oppenheim, and W. Wu, Modes and Damping in Cmut Transducers for Acoustic Emission, *IEEE Ultrasonics Conf.*, 2006.
3. D. W. Greve, I. J. Oppenheim, W. Wu, and A. P. Wright, Development of a MEMS Acoustic Emission Sensor System, *SPIE Smart Structures/NDE Joint Conf.*, 2007.
4. W. Wu, D. W. Greve, and I. J. Oppenheim, Characterization and Noise Analysis of Capacitive MEMS Acoustic Emission Transducers, *IEEE Sensors Conf.*, 2007.
5. T. B. Gabrielson, Mechanical-thermal noise in micromachined acoustic and vibration sensors, *IEEE Trans. Electron. Devices*, **40**, 903-909.

FILM-TYPE PZT SENSOR AS AE SENSOR AND ACTIVE GUIDED WAVE TRANSDUCER -Application for detecting wall reduction and corrosion of pipes-

HIDEO CHO and MIKIO TAKEMOTO

Faculty of Engineering, Aoyama Gakuin University,
5-10-1 Fuchinobe, Sagamihara, Kanagawa 229-8558, Japan

Abstract

Film-type PZT sensor, called as MFC (Micro-Fiber Composite) or AFC (Active-Fiber Composite), is made from PZT fibers embedded between integrated electrodes. We utilized the MFC for monitoring of both the progression of atmospheric corrosion (rust fracture) and wall reduction of pipe by corrosion simultaneously. The former was achieved by AE monitoring using the MFC as AE sensor and the latter using it as transmitter and receiver of cylinder waves. This type of utilization can contribute to reduce the cost of integrity loss evaluation. We first studied the detection capability of wall reduction of the pipe (slit-shaped and circumferential notch) by the cylinder waves produced by the MFC. It detected the wall reduction of 1.1%. Though the sensitivity of the MFC to the AE produced by rust fracture was lower than that by conventional PZT-type AE sensor, the MFC is found to be useful in detecting both the corrosion zone and wall reduction, and reduce the inspection cost significantly.

Keywords: Film-type PZT sensor, corrosion, rust fracture, wall reduction, acousto-ultrasonic testing,

Introduction

Corrosion damage of pipes in industrial plants is becoming serious problems. Inspection of the pipe corrosion under thermal insulations is time-consuming and is one of most troublesome problems in industrialized countries. Guided waves are expected to measure cross-sectional loss of the pipe damage [1]. It requires special transducer/receiver system and monitoring equipment. The system is massive and expensive. Inspection by the guided waves is generally possible during shutdown maintenance period, but it cannot monitor the progression of corrosion during plant operation. On the other hand, acoustic emission (AE) method can monitor the progression of corrosion of the pipes in service, since the fracture of growing rust emits the AE [2]. AE method, however, cannot measure the residual wall thickness of the pipe or the cross-sectional loss. When we can monitor both AE and active guided waves simultaneously using small and inexpensive sensors, we can estimate both the location of corrosion and wall reduction of pipes in service. For this purpose, we need an advanced sensing system, which serves as both AE sensor and transmitter/receiver of the guide waves.

In this study, we utilized film-type PZT element as the transducer and AE sensor. This element is called as micro-fiber composite (MFC), which was originally developed by Bent and Hagood as an adaptive actuator for FRP [3]. Brunner et al. reported the utility of another element called the AFC (active-fiber composite), which they fabricated. The AFC was used as the sensor for AE monitoring and the transducers for active Lamb waves [4]. They measured damage accumulation in FRP using the AFC. We attempted to measure both the active guided waves and AE from pipe corrosion, using the MFC elements. Here, the flexible MFC was wound

on a pipe. We first measured cylinder waves reflected by an artificial dish-shape defect in the pipe and then monitored AE from accelerated corrosion of the steel pipe. The wall reduction by the corrosion was detected by the active Lamb waves.

Experimental setup and results

Film-type PZT sensors

We used commercially available MFC elements. The MFC was fabricated by inserting PZT fibers between two electrodes and embedded in a polymer sheet as shown in Fig. 1. There are two types of MFC elements with different vibration mode, functionalized by both polarization and configuration of the electrodes. The MFC with vibration mode in the direction parallel to the film is called as Type-33, while that with vibration perpendicular to the film as Type-31. The former measures the in-plane motion of the wave and the later the out-of-plane motion. We first studied functionality of these elements.

Figure 2 shows an experimental setup. The cylinder waves were excited and detected by the two types of MFC elements. The MFC (10 mm^w x 110 mm^L) was wrapped with a metallic band using silicon grease couplant on the whole surface of an aluminum pipe of 35-mm outside diameter, 3-mm thickness and 2000-mm length. Propagation distance of the cylinder waves was set as 600 mm. The MFC as a transmitter (right one of Fig. 2) was excited by a tone-burst of 3 cycles with 60 V_{pp} amplitude utilizing a function generator and a power amplifier. Frequency of the burst signal was selected so that the MFC generates strong cylinder waves. Transmitted waves were detected by the left MFC and amplified 40 dB by a pre-amplifier and fed to a personal computer via a digital oscilloscope. We used 3 combinations of Type-33 and Type-31 MFC elements.

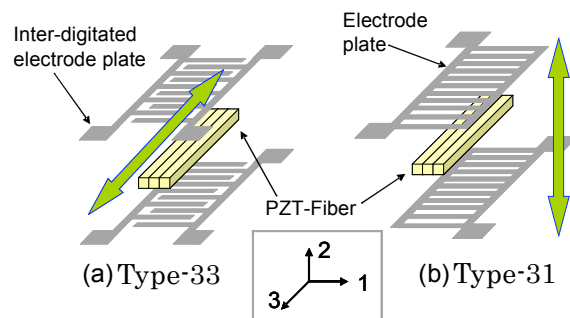


Fig. 1 Internal structure of MFC element of Type-33 and -31.

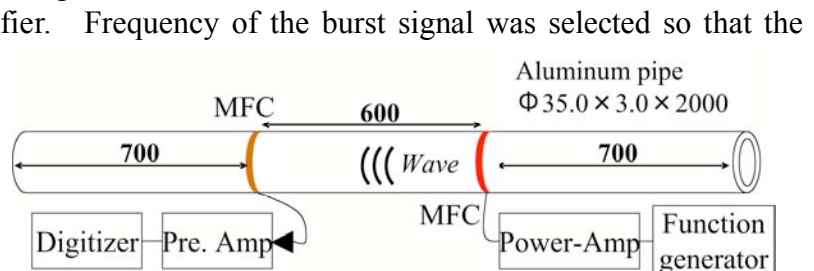


Fig. 2 Experimental setup for excitation and detection of cylinder waves by MFC.

Figure 3 compares the waveforms detected by the three combinations of the MFCs. Here, the wave (a) was excited and detected by two Type-31 MFCs at 190 kHz, the wave (b) by two Type-33 MFCs at 300 kHz, and the wave (c) was excited by the Type-31 and detected by the Type-33 MFC at 220 kHz. There observed three wave packets in waveforms. First arrival wave packet at approximately 120 μs was identified as the L(0,2) mode or the breathing mode, which vibrates in the radial direction. Second packet at approximately 200 μs corresponds to the L(0,1) mode. Third packet at 400 μs was identified as the L(0,2) mode reflected by right edge of the pipe. It was found that the wrapped MFC strongly excites the L-mode waves but cannot produce the F-mode. This is because the motion in the radial direction by the L-mode and Type-31 element coincides. Coupling of the MFC sensor via silicon grease couplant is another reason for weak F-mode.

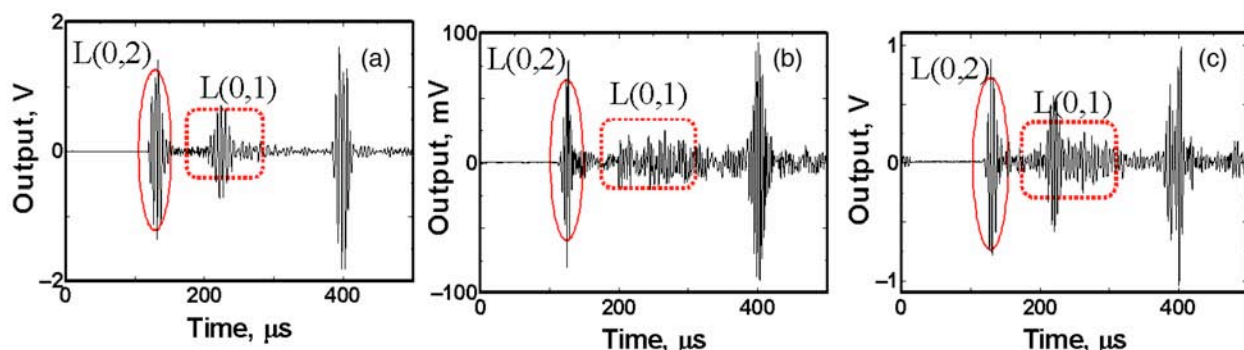


Fig. 3 Cylinder waves detected by various combinations of MFC elements. (a) Excited and detected by Type-31; freq: 190 kHz. (b) Excited and detected by Type-33; freq: 300 kHz. (c) Excited by Type-31, detected by Type-33; freq: 220 kHz.

We next detected the AE generated by the Hsu-Nielsen source. Figure 4 compares waveforms of AE signals detected by Type-31 and Type-33 MFC sensors. Here, the distance from the source to the sensor was 300 mm. Type-31 MFC detected the signal with S/N ratio of 24 dB and Type-31 at 32 dB. Waveform detected by Type-33 MFC contains both the L- (dotted ellipse) and F- (solid ellipse) modes, while the wave detected by the Type-31 sensor only the L-mode. Wave amplitude by Type-33 MFC was larger than that by Type-31. This is because the Hsu-Nielsen source excites the flexural vibration due to its step-wise force on upper point of the pipe. Thus, we decided to use Type-31 MFC element for the guided wave inspection and Type-33 for the AE monitoring.

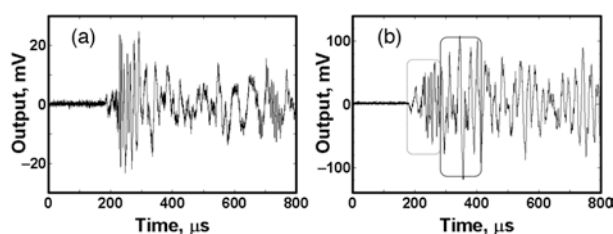


Fig. 4 Waveforms excited by Hsu-Nielsen source detected by (a) Type-31 and (b) Type-33 MFC.

Wall reduction inspection by the Type-31 MFC

In order to study the detection limit of wall reduction by the active guided waves, we prepared three carbon-steel pipes (35-mm outside diameter, 3-mm thickness and 3000-mm length) with flat defects with three depths (A, B and C). The defects were induced by end-milling at 200 mm from the edge, and the depths are 0.58 mm for A, 1.0 mm for B and 1.2 mm for C as shown in Fig. 6. Dimension of these defects are 6 x 8 mm for A, 20.5 x 11.5 mm for B and 20 x 12.5 mm for C. Loss of the cross-sectional area is 1.1 % for A, 2.4 % for B and 3.2 % for C. As shown in Fig. 5, two Type-31 MFCs were wrapped over the whole circumferences at the center portion of the pipe with 50 mm separation.

The right MFC was used as the transmitter to excite the cylinder waves and the left as the receiver to detect the waves reflected by the defect. The transmitter was excited by a tone-burst with 3

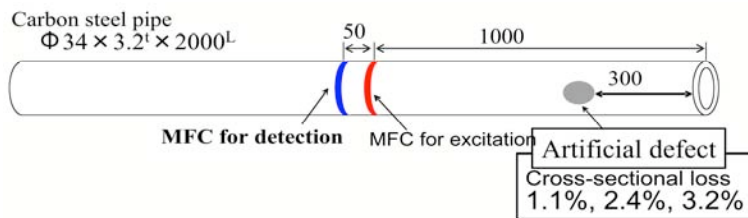


Fig. 5 Experimental setup for measuring an artificial defect utilizing cylinder waves utilizing MFC elements.

cycles at frequency of 300 kHz. This combination effectively excites and detects the L(0,2)-mode waves. Figure 7 shows the detected waveforms and their time transients of wavelet coefficient at frequency of 300 kHz for the three flaws. We can clearly detect the reflected waves at approximately 270 μs . It is noted that the sensor arrangement in Fig. 5 can detect the reflected waves from the defect with cross-sectional loss of 1.1%. Amplitude of the reflected waves was roughly proportional to cross-sectional area loss up to 4.5% loss. The present method possesses the detection capability similar to that of the commercial system reported as 1%.

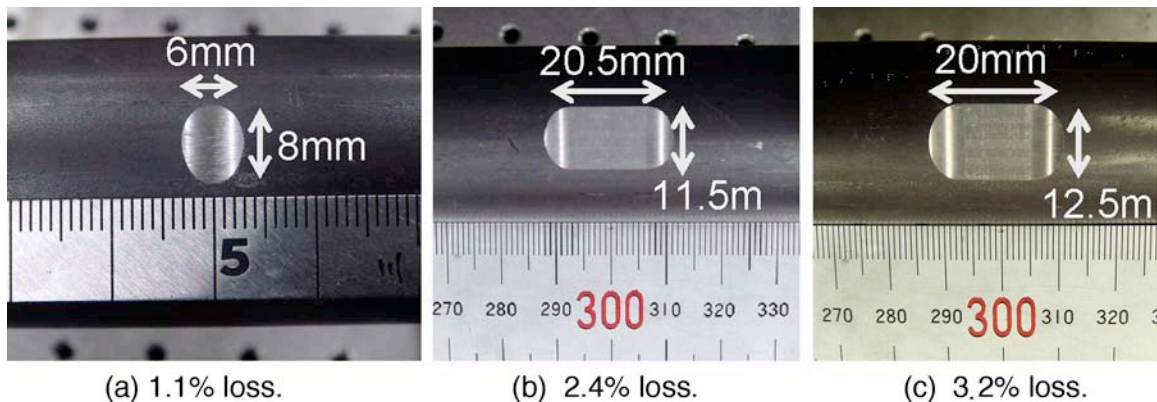


Fig. 6 Photograph of artificial defects with various cross sectional area loss.

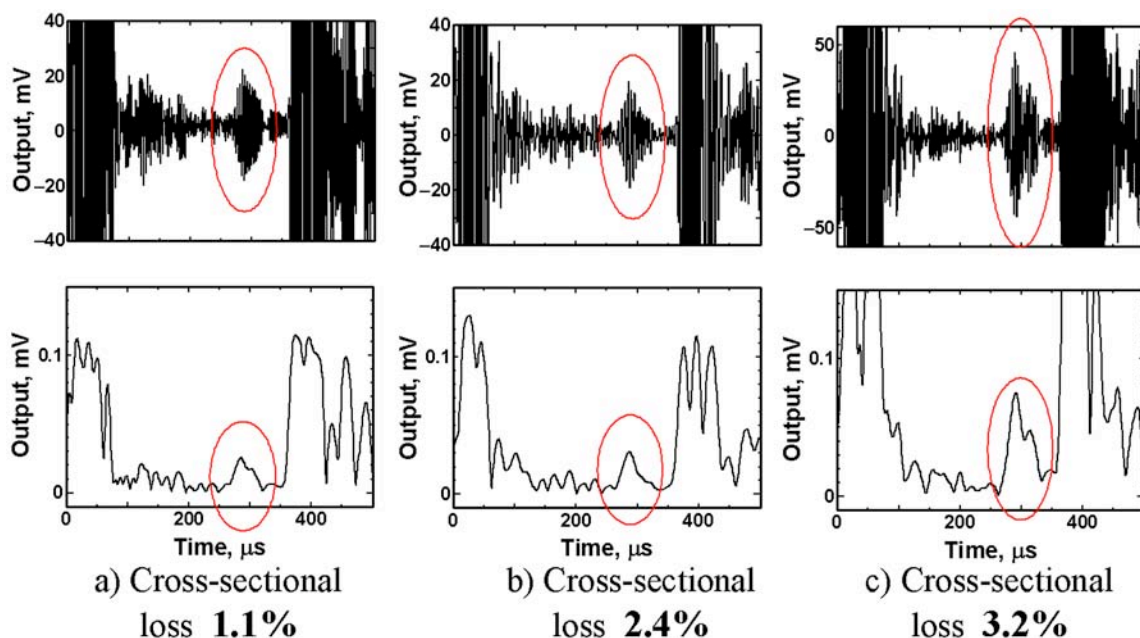


Fig. 7 Waveforms detected for samples with different cross-sectional loss and their wavelet coefficients at 300 kHz.

Simultaneous detection of AE and defect depth by external corrosion utilizing MFC

Next, we monitored AE from external corrosion of the pipe and detected the progression of the wall reduction. Figure 8 shows the experimental setup. We made a flat defect with 1.5-mm depth and 14.5-mm square on a carbon-steel pipe at 300 mm from an edge. The cross-sectional area loss of this defect is 4.5% to the pipe of 34 mm diameter and 3.2-mm thickness. Next, we produced accelerated corrosion damage by thermal cycling and mist-spraying of

1% $MgCl_2$ solution for 25 days. Temperature changes at corrosion site were monitored by thermocouples.

For AE monitoring, we used two Type-33 MFC sensors mounted on both sides of the corrosion area. One is at 100 mm (ch. 2) from the right edge of

the pipe and another at 800 mm (ch. 1). For comparison, we mounted two PZT-type sensors (PAC, Type-PICO). Outputs of all these sensors were amplified 40 dB by preamplifiers and fed to a personal computer with an A/D converter boards. Sampling interval was set as 200 ns.

Wall reduction was detected by using two Type-31 MFCs, wrapped at the center portion of the pipe by the same manner as Fig. 5. Figure 9 showed changes of cumulative AE events by both MFC and PZT sensors with temperature history. Event counts increased with progression of corrosion, and reached 143 by the MFC sensor.

Total event counts by the PZT sensor reached 325. Sensitivity of the Type-31 MFC sensor is less than that of the PZT sensor. The MFC sensor, however, detected important strong AE from the fracture of the rust. It is noted that the emission rate is higher at high temperatures and low at lower temperatures. Figure 10 compares waveforms of AE signals detected by the PZT and MFC sensors. The maximum amplitude of the PZT sensor is three times that of the MFC sensor. This is because the PZT sensor monitors the strong out-of-plane motion by the F-mode waves, while the Type-33 MFC sensor the weak in-plane motion.

In order to estimate the corrosion progression and corrosion location, we need not monitor weak AE and noise, but should rather detect strong signals from corrosion without being disturbed by noise. Source locations of AE signals detected by the MFC sensors were mostly in the corrosion zone.

Wall reduction by corrosion was monitored using active guided waves. Figure 11 shows cylinder waves and its time transient of wavelet coefficients after 25 days. We detected clear waves reflected by fractal surface of corrosion damage. Wall reduction by corrosion is, however, as low as 0.1 mm with the 25-day exposure and could not be detected.

Conclusions

We developed a unique method for monitoring the damage progression of pipes by corrosion. This method utilizes two types of macro fiber composite (MFC) sensors (Types-31 and -33), and

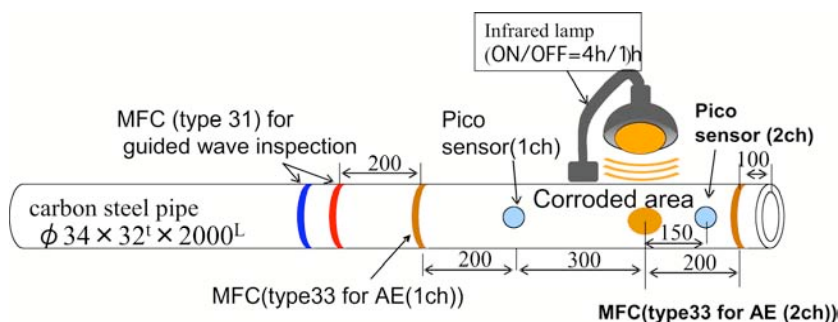


Fig. 8 Experimental setup for AE monitoring and guided wave inspection for corroded carbon steel pipe.

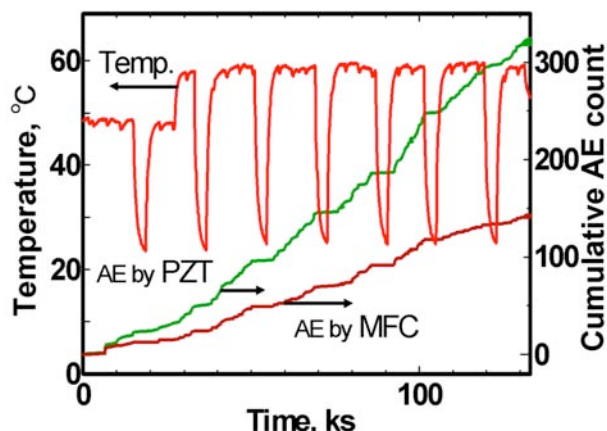


Fig. 9 Cumulative AE count detected by MFC and PZT AE sensor and temperature.

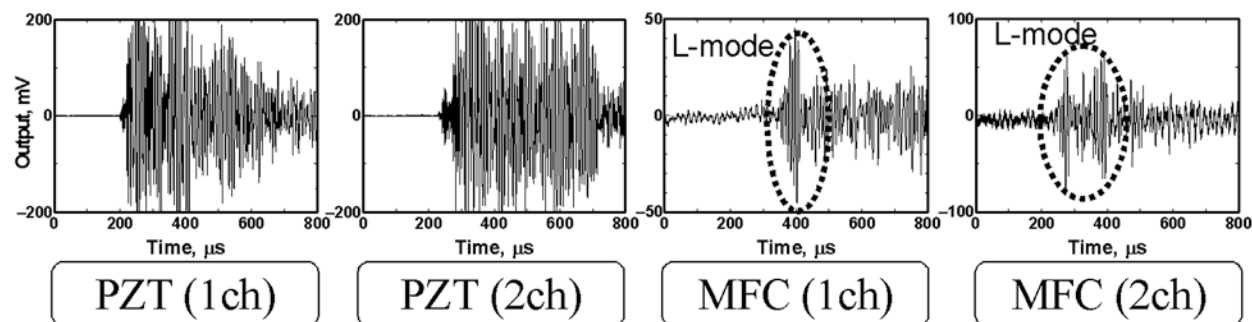


Fig. 10 Typical waveforms detected by PZT and MFC sensors from corrosion.

detected both AE signals from corrosion and wall reduction. Results obtained are summarized below.

- 1) The MFC was found to generate strong L-mode waves when it was wrapped around pipes. Type-31 MFC is better for guided wave inspection and Type-33 for AE monitoring.
- 2) Using the active cylinder waves excited by Type-31 MFC, we detected flat defects of cross-sectional area loss of 1.1%. Amplitude of the L-mode waves reflected by the defects increased with the loss of cross-sectional area.
- 3) We monitored corrosion progression by detecting AE signals from rust fractures, using Type-33 MFC as AE sensor. We also estimated the fractal wall reduction by corrosion, using the active cylinder wave excited by Type-31 MFCs.

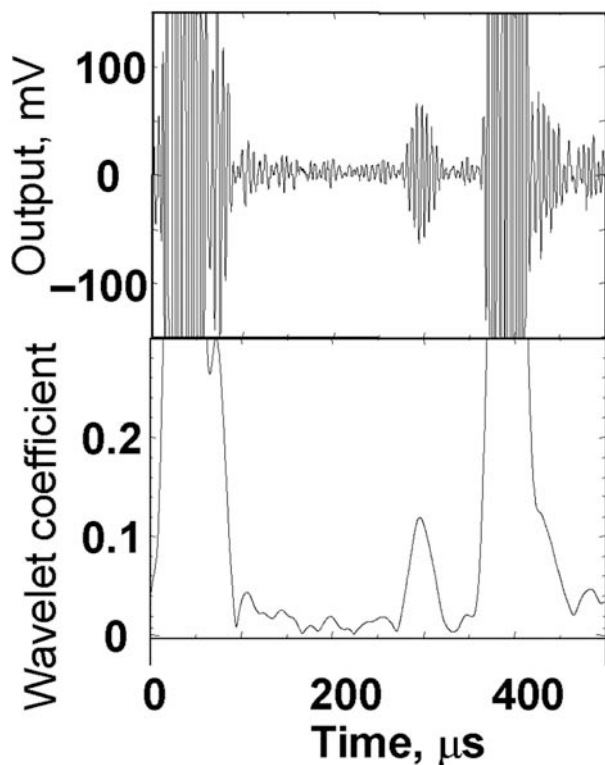


Fig. 11 Reflected cylinder waves from corroded area.

References

- [1] Cawley, P., Lowe, M. J. S., Alleyne, D. N., Pavlakovic, B., and Wilcox, P., *Material Evaluation*, **61** (2003) 67-74.
- [2] Takemoto, M., Cho, H., and Suzuki, H., *Progress in acoustic emission XIII* (2006), JSNDI pp. 373-380.
- [3] Bent, A. A., Hagood, N.W. and Rodgers, J.P., *Journal of intelligent material systems and structures*, **6** (1995) 338-349.
- [4] Brunner, A. J., Barbezat, M., Huber, Ch. and Flueller, P. H., *Journal of Materials and Structures*, **38**, (2005) 561-567.
- [5] <http://www.imperial.ac.uk/ndt/public/productservice/disperse.htm>

HEAT RESISTANT OPTICAL FIBER SYSTEM FOR MONITORING AE IN HIGH TEMPERATURE VACUUM CHAMBER

TOMO HARU HAYANO, TAKUMA MATSUO, HIDEO CHO and MIKIO TAKEMOTO

College of Science and Engineering, Aoyama Gakuin University,
5-10-1, Fuchinobe, Sagamihara, Kanagawa 229-8558, Japan.

Abstract

With the aim of characterizing the oxide scales produced by high temperature oxidation at low oxygen pressure, we developed an advanced heat-resistant optical fiber AE monitoring system, which can measure the AE signals from fracture of oxide scale in vacuum chamber. The system is a Mach-Zender-type laser interferometer with a copper-coated silica fiber. The sensing fiber inside the vacuum chamber was connected to outside monitoring system by a special high-vacuum seal connector installed in the chamber wall, and monitored AE from oxide scales of iron pipes heated to 440°C at three different oxygen pressures. Here, the optical fiber sensor was wound on the iron pipes and measured the AE signals as a function of vacuum. We detected frequent strong signals from the thicker oxide scale of Fe₃O₄ and Fe₂O₃ produced at higher oxygen pressure and very few weak signals from thin FeO scale. AE technique is useful as a characterization tool of mechanical and thermal properties of growing oxide scales.

Keywords: Heat-resistant optical fiber, vacuum chamber, growing oxide scale, Ellingham diagram

Introduction

AE monitoring of hot equipment has been an important problem for a long time. In order to accomplish both the source location and source wave analyses, we must measure AE of the hot members using a heat-resistant AE sensor mounted on them. Development of the heat-resistant AE sensor is an important research project. Another problems are 1) heat-resistant sensors on the market were massive and could not be used in tight spaces such as autoclave and vacuum chamber, 2) pressure proofing and chemical resistance of the sensors were poor and sensitive to noise.

We are developing an optical fiber AE system [1]. In this system, 1) a sensor is small and pressure proof, and 2) the system is environment adaptive and can reduce the noise from environment. We reported that the heat resistance of sensing fiber was improved by using a copper-coated fiber [2]. The copper, however, suffered oxidation in air and tended to produce noise and break the silica core.

There are needs to use AE technique in analysis instrument such as a differential thermal analyzer (DTA). As the oxide scale changes its nature quickly depending on the environments and time, an in-vivo characterization method of growing oxides is needed. When we use the copper-coated fiber in hot vacuum chamber, we can significantly reduce the oxidation of the copper, and prepare an advanced AE system free from noise. Low-frequency noise from evacuating machines such as a rotary pump can be easily eliminated by the feedback controlling system developed in the laboratory.

Another purpose of this research is to study the feasibility of the optical fiber AE monitoring system as an analysis instrument. Characterization of adhesion strength and fracture toughness of oxide scales is one of our interests. If we can determine the location of the fine cracks in the scale, this makes a significant contribution to a detail analysis of crack sources. As the optical-fiber sensor is easily mounted on the hot samples or sample holders, we can monitor AE behavior from the oxide scales at controlled pressure and temperature.

In this research, we studied the nature of oxide scales produced on iron pipes at 440°C as a function of pressures by monitoring AE signals during cooling. Relationships between the AE parameters, cooling rate, structure and thickness of the oxide scales were studied in detail. Though we have to accumulate reliable AE data for various types of oxide scales in future, AE was found to be a useful characterizing method of the growing oxides.

Optical fiber AE monitoring system

The AE system used is a homodyne Mach-Zender-type laser interferometer as shown in Fig. 1. Laser beam from a laser diode is split into the sensing and reference fibers. We used copper-coated fiber as the sensing fiber. The system contains a feedback control system to reduce the low frequency noise from environment, and is an environment adaptive system [1].

We reported heat resistance of the copper-coated fiber in air [2]. The resistance was studied again in the vacuum chamber. Figure 2 shows change of S/N ratio with time at 7 Pa (0.53 torr). The S/N ratio was found to be slightly improved at low oxygen pressure. We did not observe serious oxidation on the sensing fiber after 100 hours at 600°C. At much lower oxygen pressures, heat resistance will be improved. Thus, the sensing fiber can monitor the AE signals from oxide scales during heating (growth) and/or cooling at selected oxygen pressure, and characterize the nature of the scales.

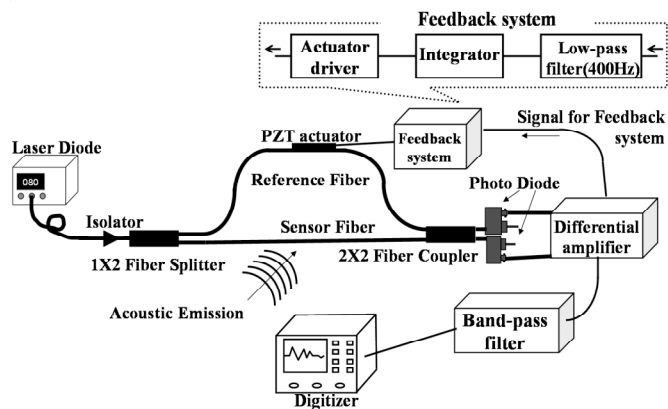


Fig. 1 Mach-Zender-type optical fiber AE monitoring system with feedback system.

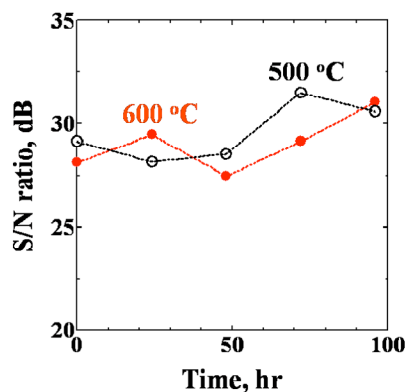


Fig. 2 Change of S/N ratio of AE signals by copper-coated fiber sensor at 7 Pa vs. t.

AE activities at different oxygen pressures

Experimental setup

Figure 3 shows an experimental setup for AE monitoring in vacuum chamber. The sensing fiber in the chamber was connected to the fiber of the monitoring system via a special connector installed in the chamber wall. Pressure proofing was enough for the lowest pressure achieved by a rotary pump. Polished iron pipes of 30-mm diameter and 50-mm length were heated to 440°C by an infrared heater through a quartz rod. In this experiment, the light diameter was controlled as 20 mm. The pipes were oxidized at 440°C for 24 hours and

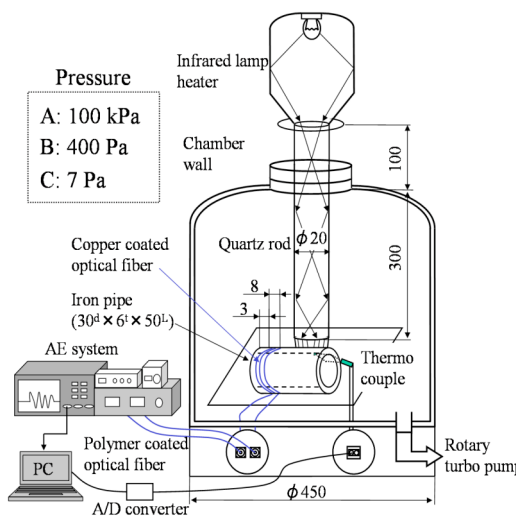


Fig. 3 Experimental setup for AE monitoring in vacuum chamber.

cooled in the chamber. Temperature was monitored by a thermocouple welded on the inner surface of the pipe. Both the AE and temperature data were digitized and fed to a personal computer. We changed the pressure at three levels, i.e., 100 kPa, 400 Pa and 7 Pa. It is noted that the temperature of 440°C is slightly higher than the temperature (250 to 400°C), which causes the blue brittleness of the steel [3]. Thus the chemical composition of the oxide film changes from FeO to Fe₂O₃ via Fe₃O₄, depending on the oxygen partial pressure. These films have different mechanical and thermal properties and show different fracture characteristics. We can prepare various types of oxides by changing the temperature and pressure according to the Ellingham diagram and study the nature of these oxides [4].

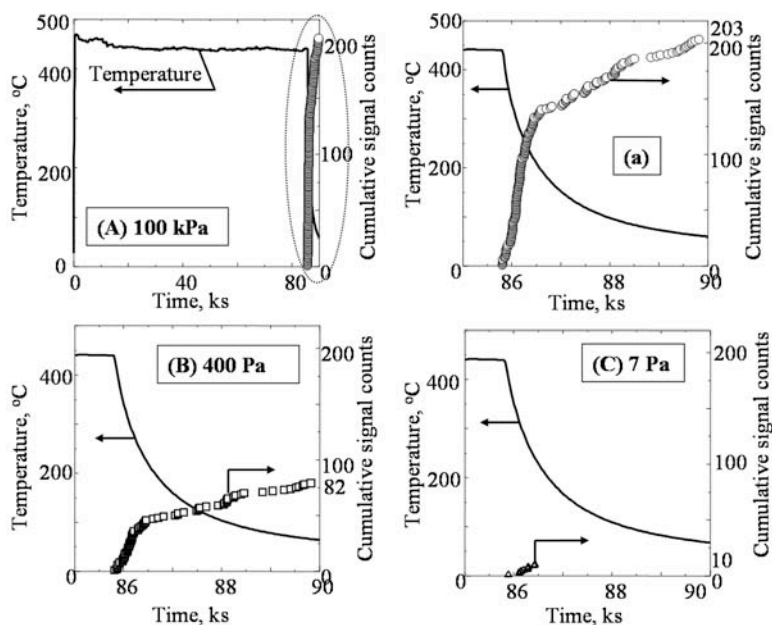


Fig. 4 Changes of cumulative AE signal counts with test time at three pressures.

Results and Discussion

Figure 4 compares changes of cumulative AE counts with test time at three pressures. We did not detect any signals during heating as shown in (A), but detected signals during cooling period as shown in (a). Figure 4(a) shows the magnified portion of the cooling process of (A). This tendency was the same for other two pipes oxidized at 400 (B) and 7 Pa (C).

According to the Ellingham diagram of Fig. 5, the iron produces three kinds of iron oxides, i.e., FeO (inner layer), Fe₃O₄ and Fe₂O₃ (outer layer) at pressure of 100 kPa (atmosphere pressure as indicated by A) and 400 Pa (B). At pressure of 7 Pa (C), the iron produces both the FeO and Fe₃O₄. We observed thick, black and spotted oxide scales in the heated zone at 100 kPa. The spotted scale indicates partial exfoliations of the thick Fe₃O₄ scale. The iron oxidized at 400 Pa showed a thin and brown color. The brown color is considered to be produced by interference of a light by two thin layers of FeO and Fe₃O₄. On the surface of the iron oxidized at 7 Pa, we observed a bright

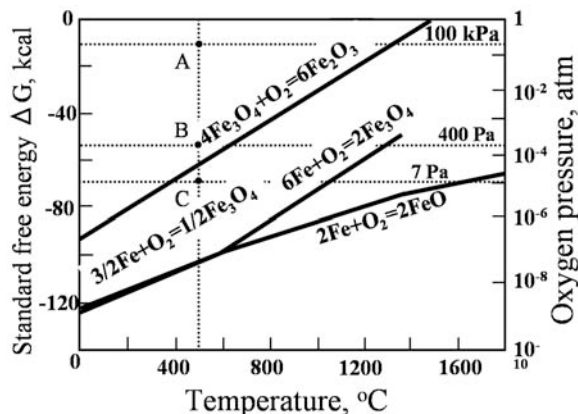


Fig. 5 Ellingham diagram of iron (A, B and C represent the experimental conditions).

blue film, suggesting thin layer of FeO and trace of Fe₃O₄. At oxygen pressures higher than the equilibrium oxygen pressure, the sub-oxides (Fe⁺²) are likely to be converted to the stable oxide (Fe^{+2.6} and Fe⁺³). Thus the oxide scale is often a multi-layer composite structure of sub-oxides and stable oxides.

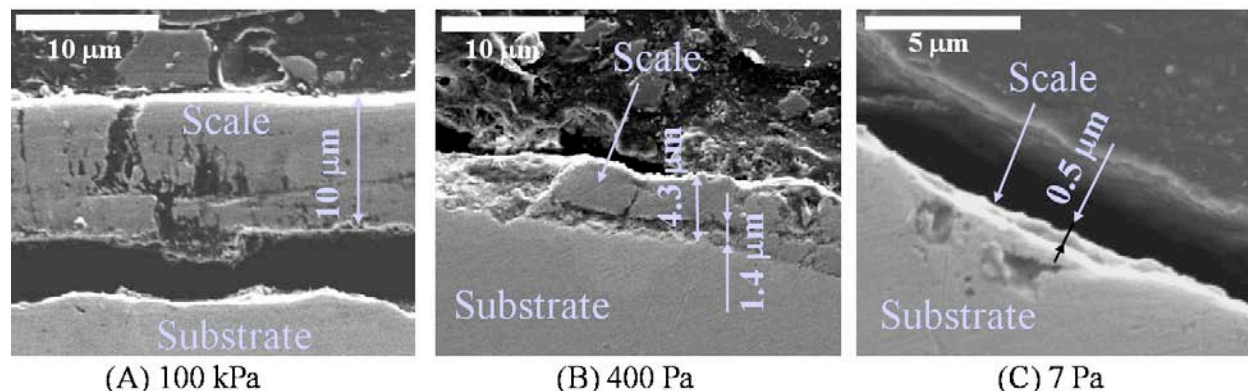


Fig. 6 Cross-sectional SEM of three oxide scales.

Figure 6 shows transverse SEM of three scales. We observed very thin oxide scale (0.5 μm) on the iron oxidized at 7 Pa. In contrast, the oxidation at 100 kPa and 400 Pa produced the oxide scales with average thickness of 10 μm and 4 μm, respectively. We observed both exfoliation with large opening and vertical fine cracks for the oxides produced at 100 kPa and 400 Pa. The scale produced at 400 Pa shows a two-layer structure with soft inner layer. Thus, the strong AE signals were supposed to be produced by the large exfoliation and weak signals by partial exfoliation and/or fine cracks. We analyzed the oxides by X-ray diffraction method, but it did not supply us with reliable data. Characterization of the oxides by advanced analysis equipment is needed.

Next, we studied how AE generation is affected by the nature of the oxides. The cumulative signal counts of Fig.4 appear to be approximated by parabolic curves. The parabolic curves are commonly observed in the weight change of metals by high temperature oxidation. However, it must be noted that the AE signals in this experiment were produced during the cooling, and the parabolic curves do not represent the growth behavior of the film during the oxidation. Nevertheless, the parabolic curves are considered to present the nature of the oxide scales. If we can find some reliable relationships between the nature of the oxide scales and AE behavior, we can use the AE technique as an analyzing tool of the oxides. Then we studied relationships between the parameters of the parabolic curves and nature of the oxide scale.

We approximated the cumulative signal counts N by equation: $N = a \log(t - t_0) + N_0$. Both a and N_0 are constants and t is the test time (ks). The parameter t_0 designates the time when the infrared lamp heater was stopped and is the same (85.8 ks) for three oxide scales. Figure 7 compares the change of cumulative signal counts with $(t - t_0)$ and the fitted curves. The parameter a , or the slope of the curve, at 100 kPa is 45 and largest among the three scales. It was 5 at 7 Pa and the smallest. The parameter N_0 means the cumulative signal counts at 1 ks and is close to the total counts detected during the first period of rapid emission. Thus the larger N_0 and a indicate the non-protective and brittle nature of the scale. There observed a few step-wise increases for the thick scales produced at 100 kPa. These steps are supposed to be due to the successive fractures of the oxide scale. Driving forces of these fractures are the stress caused by temperature decrease and/or cooling rate.

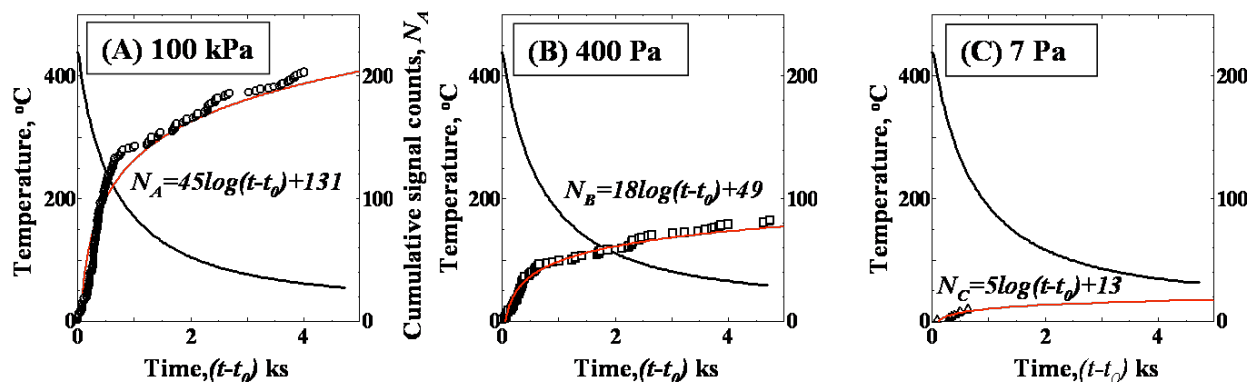


Fig. 7 Changes of cumulative signal counts with $(t-t_0)$ and the fitted parabolic curves.

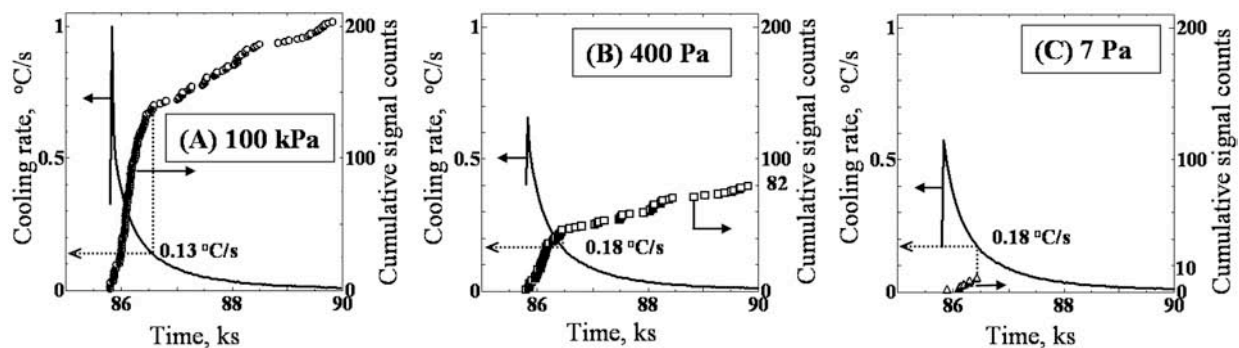


Fig. 8 Relation between the cooling rate and cumulative AE signal counts.

Figure 8 shows relation between the cooling rate ($^{\circ}\text{C/s}$) and cumulative signal counts. It is noted that the cooling rate changes depending on the pressure, i.e, lower at a lower pressure. We detected rapid increases of signals at higher cooling rates. We here define the critical cooling rate as the rate, above which AE signals were rapidly produced. The critical cooling rates were 0.13°C/s , 0.18°C/s and 0.18°C/s for the scales produced at 100 kPa, 400 Pa and at 7 Pa, respectively. Interesting is that the critical cooling rate is almost the same, independent of the pressure and film composition. This suggests that the rapid increase of AE is caused by the exfoliation along the interface between the substrate and FeO. The suboxide FeO is supposed to be an inner layer of the three scales.

A relationship between the cumulative signal counts and temperature differential ΔT from 440°C is shown in Fig. 9. This figure means that the cumulative signal counts increase from zero at 440°C with ΔT . Three straight lines appear to represent the magnitude of thermal stresses induced in oxide scales. Larger slope for the thicker scales suggests frequent cracking due to higher thermal stresses.

We also found interesting relations between the signal amplitude and oxide scales. Figure 10 shows the distribution of event counts as a function of signal amplitude. The oxide scale produced at 100 kPa emitted numerous strong signals. Strong signals seem to be produced by large-scale exfoliation, while weak signals at 7 Pa by vertical cracks in thin films. Thus, the amplitude distribution can also represent the nature of the oxide scale.

Above data suggests that we can use the AE for studying the nature of oxide scales. When we accumulate reliable and reproducible AE data for various types of oxide scales based on the Ellingham diagram, we can analyze the mechanical and thermal properties of the scale. Accumulation of the data requires further work.

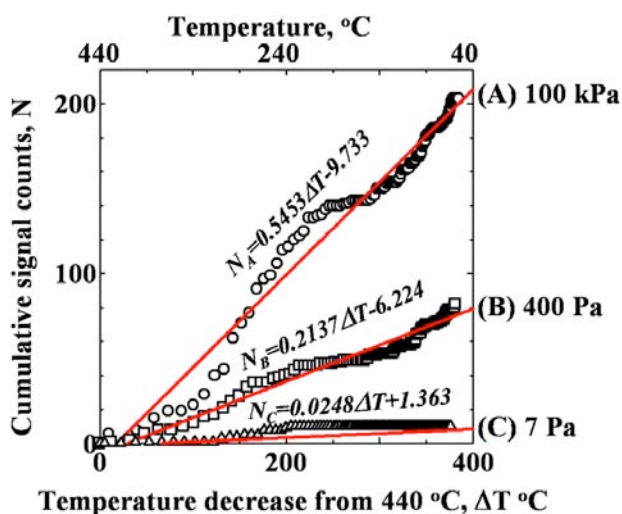


Fig. 9 Relationships between the cumulative signal counts and temperature decrease.

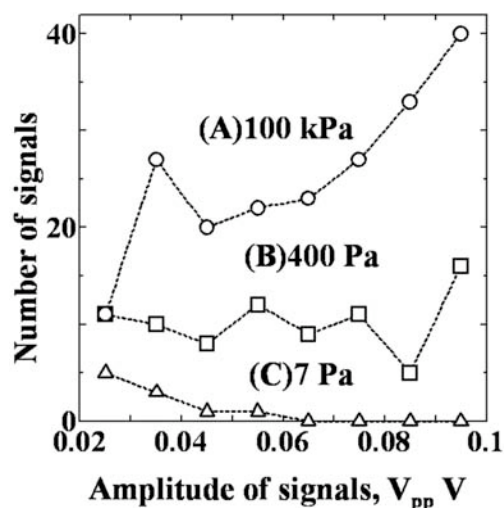


Fig. 10 Distribution of event counts as a function of signal amplitude.

Conclusion

We monitored AE signals from oxides produced at different oxygen pressures using an optical-fiber AE system and studied the feasibility of the AE technique as in-situ analysis method of mechanical and thermal properties of the growing oxide scales. Results obtained are summarized below.

- 1) Utilization of copper-coated optical fiber makes the in-vivo monitoring of AE from growing oxide scales possible.
- 2) We obtained some useful relationships between the AE parameters and nature of the oxide scales. Thicker oxide produced a number of strong AE, suggesting weak adhesion and fragile nature.
- 3) Accumulation of reliable and reproducible AE data from various types of oxide scales at different pressures and temperatures makes the in-vivo characterization of the oxide possible.

References

1. H. Cho, R. Arai, H. Suzuki and M. Takemoto, *Non-destructive Inspection*, **53** (11), 709-714 (2004). (In Japanese)
2. T. Hayano, T. Matsuo, H. Cho and M. Takemoto, *J. Acoustic Emission*, **24**, 67-75 (2006).
3. Daniel H. Herring, *Industrial Heating*, **73** (10), 16-18 (2006).
4. F. D. Richardson and J. H. E. Jeffes, *J. Iron Steel Inst.*, **160**, 261 (1948).

IMMERSION-TYPE QUADRIDIRECTIONAL OPTICAL FIBER AE SENSOR FOR LIQUID-BORNE AE

TAKUMA MATSUO, HIDEO CHO, TAKESHI OGAWA
and MIKIO TAKEMOTO

Department of Mechanical Engineering, Aoyama Gakuin University,
5-10-1, Fuchinobe Sagamihara, Kanagawa 229-8558, Japan

Abstract

Immersion-type AE sensor is needed for corrosion monitoring of underground fuel tanks. We have developed a multi-directional optical fiber AE sensor to monitor the longitudinal AE signal through liquid (liquid-borne AE). The developed AE system is an optical-fiber-based Mach-Zender-type laser interferometer using a weak laser and is intrinsically safe. Multi-sensing function was facilitated by winding an optical fiber on four small-size short hollow pipes with different diameters, which were installed on the inside walls of a box of 22.5-mm square and 230-mm height. Each sensor element was screwed on a different sidewall. The four fiber sensors were cascaded in series on a single fiber and monitored the liquid-borne AE signals from quadridirection simultaneously via frequency discrimination. As the each fiber-wound sensor element monitors at the resonant frequency of the pipe, we can estimate the direction of AE signals using their frequency spectra and wavelet transform. The functionality of the sensor was demonstrated by 50-day monitoring of liquid-borne AE signals from rust fractures on four corroded carbon-steel sidewalls of a water tank. The immersion-type quadridirectional sensor successfully monitored liquid-borne AE signals from the four corroded plates.

Keywords: Optical fiber AE sensor, intrinsically safe sensor, immersion-type sensor, quadridirectional sensor, rust fracture, parabolic law

Introduction

Integrity loss of underground fuel tanks by localized soil corrosion is becoming serious problems in Japan. Fire and Disaster Management Agency (FDMA) reports leak accidents of 344 tanks in 2001. Localized corrosion was the cause of leaks in 30% of the tanks [1].

AE technique is expected to be a useful tool for monitoring corrosion damages of the tank, however we cannot use the conventional AE system using the piezo-sensors, since the system is not intrinsically safe.

We are developing an optical fiber laser interferometer to monitor AE signals [2]. This system is composed a homodyne Mach-Zender-type laser interferometer with a phase compensation feedback circuit. The sensor of this system uses a telecommunication single-mode optical fiber. This system is intrinsically safe, immune from corrosion and electromagnetic noise. It was previously used to monitor liquid borne P-waves by immersing the sensing fiber into the liquid [3]. We have improved this sensor so it can monitor the corrosion zone or the direction of the P-waves over a long time. Here, a single sensing fiber was spirally wound on four pipes, and detected AE signals quadridirectionally.

We first introduce our new quadridirectional AE sensor and next AE monitoring from four plates with rust (corroded steel plate samples) for 50 days. We discuss relationship between the AE activity and corrosion of the steel with rust.

Immersion-Type Optical Fiber Sensor

A sensing box developed is shown in Fig. 1. The box was designed for underground gasoline tanks and contains four AE sensors. Box size is 22.5-mm square and 230-mm height. The top and bottom plug-plates were thick enough so that four aluminum sidewalls were screwed on with special polymer sheet as gasket. This structure can prevent the vibration interference of neighboring walls and gasoline leakage into the box. A hollow long pipe of 16-mm diameter was screwed into the top plug-plate. This pipe is used to insert the sensing box in the tank through a 32-mm diameter nozzle, and to connect the optical fiber to the monitoring system.

Sensing fiber was wound on four cap-shaped aluminum cylinders of 20-mm height (called sensor elements) each with a different diameter (8, 10, 15 or 19 mm). These elements were screwed on the side walls with a polymer sheet. The sensing fiber was wound on the holders multiple times. This structure improves the sensor sensitivity significantly. Four sensors were connected by a single fiber in series and connected to the monitoring system via fiber connectors. The four sensors detect the wall vibration excited by liquid-borne P-waves. Here the different resonance frequencies of four sensors are utilized to identify the direction of the P-waves. We call the sensor with 15-mm diameter element as “D15 sensor” and the entire system as ITQS (Immersion-Type Quadridirectional System), hereafter.

Directionality of ITQS was studied using a rectangular water container of 1220 x 700 x 250 mm. Water-borne P-wave was produced using a PZT transmitter (DE, S140B) immersed in water at 1000 mm from the ITQS. We fixed the transmitter and rotated the position of the ITQS counter-clock-wise. Here $\theta = 0^\circ$ designates that the normal of the sidewall with the D19 sensor orients to the transmitter; D10 faces the transmitter at 90° , D15 at 180° and D8 at 270° .

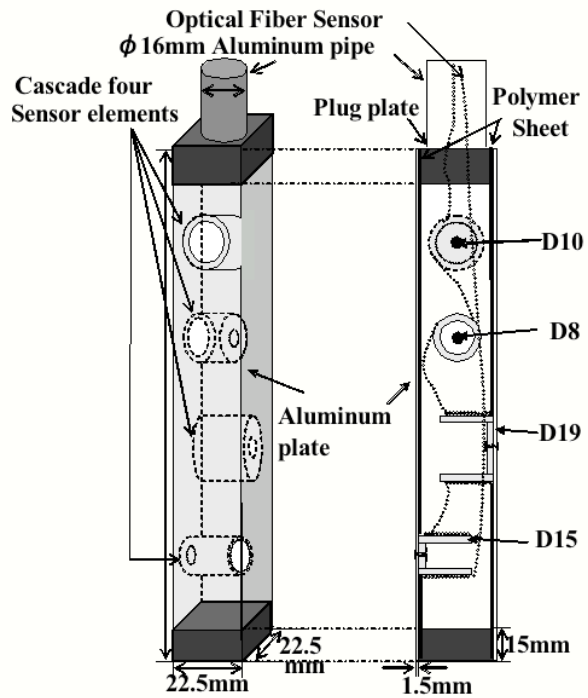


Fig. 1 Immersion-type quadridirectional AE sensor using optical fiber.

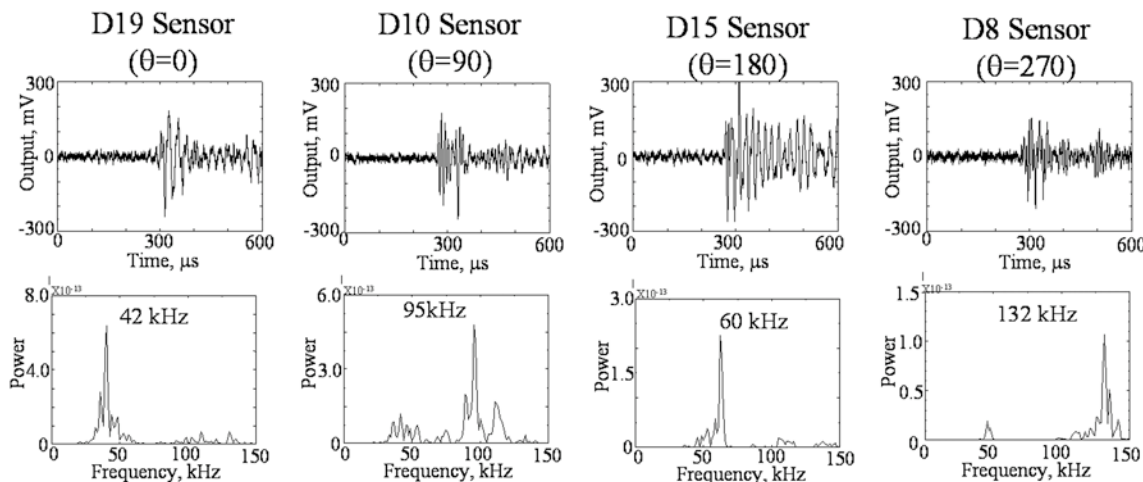


Fig. 2 Waveforms and frequency spectra of AE signals at $\theta = 0^\circ, 90^\circ, 180^\circ$ and 270° .

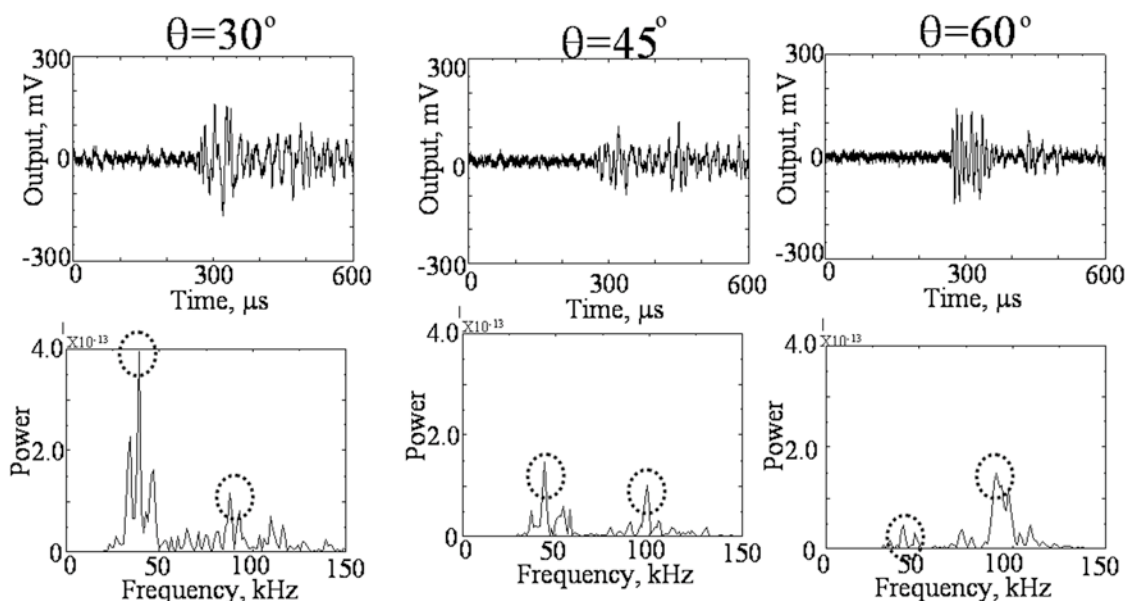


Fig. 3 Waveforms and frequency spectra of AE signals detected by ITQS at $\theta = 30^\circ, 45^\circ$ and 60° .

Figure 2 show examples of the waveforms and power spectra at $\theta=0^\circ, 90^\circ, 180^\circ$ and 270° . These are waveforms detected by the sensor, whose sidewall faces the transmitter. Resonance frequencies of the sensors were separated with frequency separation of more than 15 kHz.

We next studied relationship between angle θ and wave amplitude. Figure 3 shows examples for the P-waves from $30^\circ, 45^\circ$ and 60° . These angles are between the D19 sensor and D10 sensor. We observed two or three wave packets. Power spectra show two higher peaks at around 42 and 95 kHz. Using the normalized amplitude profiles of two peaks of Fig. 4, we can estimate the directivity of the P-wave sensing as $\pm 30^\circ$.

Table 1 Specimen size, area of rust and corrosion test method.

Sample	Size (mm)	Area of rust (cm ²)	Thickness of rust (mm)	Corrosion element
A	380 ^w x370 ^h x10 ^t	247	0.30	Mist spray(5% NaCl)+ Thermal Cycle
B	100 ^w x240 ^h x4 ^t	240	0.18	Mist spray(5% NaCl)
C	80 ^w x290 ^h x6 ^t	232	0.06	Thermal Cycle
D	80 ^w x280 ^h x6 ^t	224	0.04	Room atmosphere

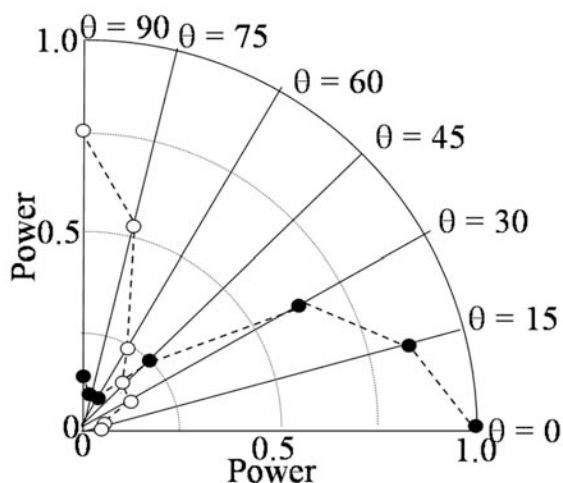


Fig. 4 Amplitude profile as a function of rotating angle of ITQS.

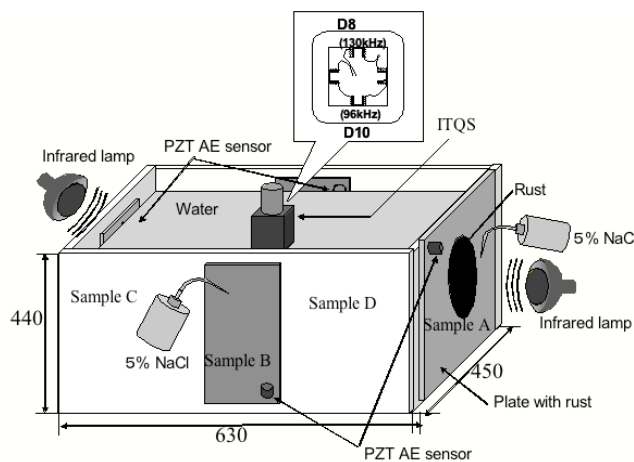


Fig. 5 Experimental setup for monitoring AE from rust fracture of corroded four plates.

Monitoring of Water Borne P-wave From Rust Fracture

Experimental Setup

We monitored AE signals from rust fracture using the ITQS for 50 days. Experimental setup is shown in Fig. 5. We inserted four steel plates in the four side walls of a rectangular water container, 630 x 450 x 440 mm. Four steel plates with natural rust produced by atmospheric corrosion were taken from a tank yard in a sea coast area. As these samples have rusts on one side, the samples were placed on the sidewalls using silicone rubber sealant such that the rusted surfaces face outward. Sample size, area of rust, rust thickness and corrosion method are shown in Table 1. Rust area is different among the samples, but we used them in as-received condition, since the rust tended to separate during cutting.

These samples were further corroded in a room without air conditioning using different methods in Table 1. Sample A with the thickest rust was exposed to both thermal cycles (heating to 23°C and natural cooling to room temperature) and mist spraying of 5% NaCl solution to the rust. By coating silicone grease, other parts were not corroded. Sample B was mist sprayed with 5% NaCl solution without thermal cycles. Sample C was exposed to the thermal cycles. Thermal cycling and mist spray were not given to sample D. Here, the thermal cycles were given by turning on-off of an infrared lamp at 6-hours intervals. The mist was sprayed for 60 minutes (total spray amount 66 ml for sample A, 24 ml for sample B) at 8-hour intervals. Sample A was exposed to the severest corrosion environment and sample D to the least. These combinations were selected to simulate the corrosion condition, which each sample was supposed to be exposed.

The container was filled with water. A trace of corrosion inhibitor was added to prevent wet corrosion of the inner surfaces of the samples. The boxed AE sensor was immersed with its bottom at 200-mm height. Experimental setup is shown in Fig. 5. We also mounted PZT-type AE sensors (PAC, Type PICO) on sanded parts of the samples to examine the timing and amplitude of water-borne P-waves and Lamb waves. Outputs of the PZT sensors were amplified 40 dB, while those of the ITQS were not amplified but used a 20-150 kHz bandpass-filter. AE monitoring was started on February 27, 2007 and continued to April 19 for 51 days. We simultaneously measured room temperature and temperatures of samples A and B.

AE activities

The left of Fig. 6 shows change of room temperature and cumulative AE events counts of the ITQS. Here one cycle of the temperature corresponds to one day, and the cumulative event counts mean all events from four samples, since the four sensors were connected on a single fiber in series. We had two cold days on March 25 and April 9. We observed four fairly large step-wise increases, as marked by four ellipses. Step-wise increases of number 2 and 3 coincide with large temperature changes, but two others (1 and 4) were at higher temperatures. It is noteworthy that less AE signals were emitted for about ten days from 38 to 47th days.

We believe that the rust fracture will be accelerated by temperature changes of the member. Thus, we studied relations between the temperature change of the samples A and B and event counts, since AE signals were supposed to be mostly generated by these samples. As shown in the right of Fig. 6, we observed a fairly good relation between the plate temperature and event counts. Stepwise increases of AE events tend to occur when the plate temperature is at high or low. Stepwise increases of No. 1, 3 and 4 occurred at higher temperatures and that of No. 2 at a low temperature. However, very few AE signals were emitted at 3.7 Ms (42nd day) in spite of low temperature. This appears to be due to capricious nature of living rust, which often makes corrosion monitoring of tanks difficult. It is also noted that the corrosion rate cannot be estimated from AE data monitored for one or two hours.

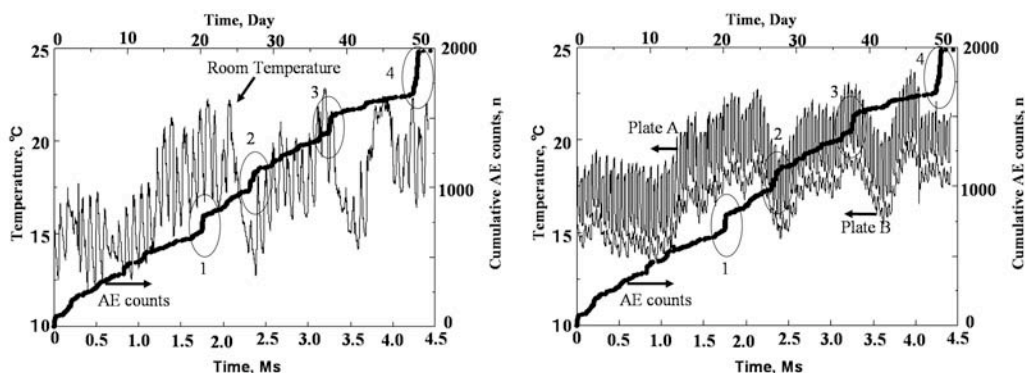


Fig. 6 Change of room temperature (left) and plate A, B (right) and cumulative AE counts by optical fiber AE system.

Direction of the P-wave

We next estimated the direction of the P-wave. Figure 7 shows typical examples of AE signals. Event I was classified as the AE from the sample A due to its strong frequency component at 45 kHz (D19 sensor). It counted 936 events. In the same manner, event II was from the sample B (by D10 sensor). We observe two or three wave packets in events III (D15 sensor) and IV (D8 sensor). Two peaks at 40 kHz and 60 kHz of event III suggest simultaneous emission from the sample C and A, respectively. Two packets of the event IV suggest two AE signals from the sample D due to frequency component at around 130 kHz.

The left of Fig. 8 shows changes of classified events with time. Sample A with large thick rust produced many AE signals when exposed to severe corrosion, but sample D, exposed to mild environment, less AE signals. These are expected result, and nothing new. However, it is noted that the event count of sample C, exposed to the thermal cycles, is large.

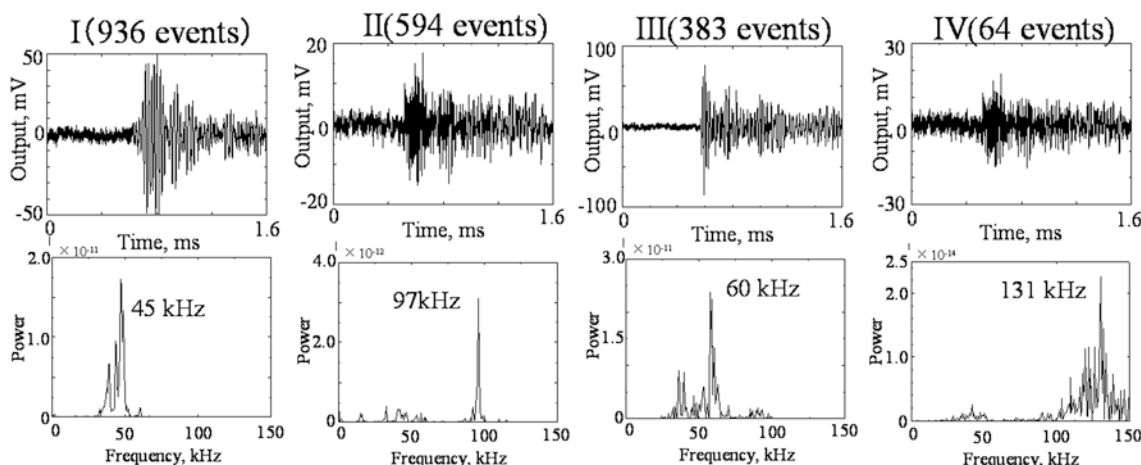


Fig. 7 Waveforms and their frequency spectra detected by four optical fiber sensors.

We next compared the event counts per unit rust area. The right of Fig. 8 shows change of classified event counts per 100 cm² from the samples A, B, C and D. There are some interesting findings. These are:

- 1) Cumulative event counts, N , increase with time, t , according to the parabolic law, i.e., $N=N_o(t-t_o)^n$, where $n < 1$. This law is common to high temperature oxidation of metals covered by protective oxide films. Small N_o and n indicate a protective film. Steps in a parabolic oxidation curve indicate the rapid oxidation due to partial breakdown of the film. These correspond to the stepwise increase of AE signals due to fractures of the rust.

- 2) Incubation time, t_o , becomes longer for the samples exposed to mild corrosion environment.
- 3) There are slight time lags in the timing of steps for samples A, B and C, suggesting that the AE activity changes depending on the rust history and corrosion environment. Step height of samples A and B with thicker rust are larger than that of sample C.
- 4) In spite of non corrosive environment, sample C shows higher emission rate.

Next we determined two parameters: N_o and n by curve fitting of the time-shifted data. Here the parameters were decided so that the parabolic curves pass through the bottom of the steps, as shown in the right of Fig. 8. Due to the limited data for only 50 days, correct determination was impossible, but tentative values were estimated. The parameter N_o increases in the order of samples $D \rightarrow C \rightarrow B \rightarrow A$, indicating corrosiveness and rust nature. The parameter n presents the role of rust on the corrosion rate. Here, it is noted that the rust plays two roles. One is protection of the base metal as a diffusion barrier of water and oxygen. Another is acceleration effect of corrosion by lowering the acidity of impregnated water. The latter is enhanced by chloride ions. It is noted the sample A, with thicker rust and exposed to severe corrosion environment, shows $n = 0.68$, and almost the same values for the samples B (0.685) and C (0.7). This suggests the rust on sample A is playing a protection role.

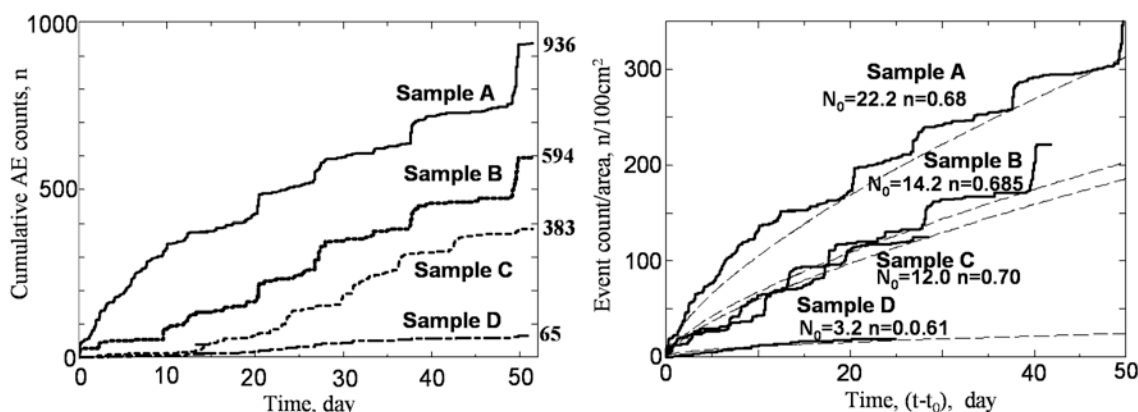


Fig. 8 Cumulative AE counts (left) and changes of classified event counts per 100 cm^2 from four samples (right).

Conclusion

We developed a quadridirectional AE system and monitored liquid-borne AE signals from four corroded plates which were exposed to different corrosion environment.

- 1) Immersion-type quadridirectional sensor was developed. Direction of AE can be identified by the frequency characteristics of four sensor elements with the directivity of $\pm 30^\circ$.
- 2) The sensor monitored the water-borne P-wave from rust fracture.
- 3) We observed good relations between AE activity and rusted plate temperature. Stepwise increases of AE events tend to occur when the plate temperature is at higher or lower.
- 4) AE events increased with time according to a parabolic law: $N = N_o(t - t_o)^n$, suggesting protective nature of the rust.

References

1. *Corrosion Center News*, 29, Japan Society of Corrosion Engineering, 2004.
2. H. Cho, R. Arai and M. Takemoto, *J. Acoustic Emission*, **23**, 2005, 72-80.
3. T. Matsuo, H. Cho and M. Takemoto, *Progress in Acoustic Emission XIII*, IAES-18, 2006, 311-318.

OPTICAL FIBER AE SENSOR FOR BLOCKAGE MONITORING OF WATER PIPES OF POWER GENERATION PLANT

TAKUMA MATSUO, HIDEO CHO, TAKESHI OGAWA
and MIKIO TAKEMOTO

Faculty of Science and Engineering, Aoyama Gakuin University,
5-10-1, Fuchinobe Sagamihara, Kanagawa 229-8558, Japan.

Abstract

Blockage of water pipes by barnacle or bivalve shells is a serious marine pest problem for safe operation of power plants. We recently have non-native bivalve shells from another Asian country. The shells invade fresh-water pipes seriously block them in summer season. This study aims to monitor the blockage of pipes at an early stage using an optical fiber AE sensor mounted on the pipe surface. We first studied the utility of the optical-fiber AE system for a model-PMMA pipe blocked by various shapes of materials. We used small shells and broken pieces of magnet for modeling shells. AE signals were monitored by winding an optical fiber multiple times using a Michelson-type laser interferometer. AE sources were classified into four types: Type-1: flow turbulence by rigidly fixed irregular blocks, Type-2: weak vibration and flow turbulence of and by a plate inserted in the pipe, Type-3: collision of bivalve shells to wall and Type-4: collision and collapse of air bubbles. Four types of sources generated characteristic AE signals. Amplitudes of AE signals from Types-3 and -4 sources were stronger than those from Types-1 and -2. Amplitude of AE signals from Types-1 and -2 changed depending on the flow velocity of water.

Keywords: Blockage, water pipe line, crust, cylinder wave, optical fiber AE sensor

Introduction

Blockage of cooling-water pipes and water in-take pipes for hydraulic power plant by shells is an important problem for safe operation. Blockage is caused by two types of shells. One is acorn barnacles, which attach on the wall tightly. Another new problem in Japan is caused by non-native bivalve shells, which came from another Asian country. It is called as *Limnoperna fortunei* (called as new bivalves in this paper). Figure 1 shows colonies of acorn barnacles and *Mytilus edulis*. Here, the *Mytilus edulis* is a native shell. New bivalves come into the pipe as larva and quickly grow to shell size of 20 mm during a summer season. Longevity is reported to be from one to several years [1]. The new bivalves grow by making colonies, and tend to block the pipe. Dead bivalves also block the filter during autumn and winter. Another characteristic feature of the new bivalve is that the shells attach on the pipe wall by its threads as shown in an ellipse of Fig. 1. Then, the shell hits the pipe wall and each other. We cannot use live bivalves due to the environmental regulations [2] and have to simulate these shells by another material. Flow turbulence caused by shells is a possible AE source and can be used to detect early stage

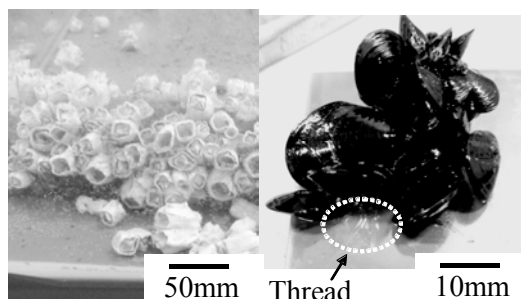


Fig. 1 Photos of acorn barnacle (left) and native *Mytilus edulis* (right).

of shell invasion. Plant owners need information on which pipe is invaded and blocked by the new bivalves without opening the pipes.

AE has been used to study the cavitation in xylem conduits of plants [3, 4]. The cavitation produces strong AE signals. Owner of the power plant, however, has to know early stage of pipe blockage before the pipe suffers the cavitation. We developed an optical fiber AE monitoring system (OFS). This system is a kind of laser interferometer and especially useful in health monitoring of the pipes [5-7], due to its easy handling and high sensitivity. The high sensitivity is achieved by multiple winding of the sensing fiber on the pipe. Waterproofing is also unnecessary.

In this paper, we report our fundamental research results of AE monitoring of the model pipes, blocked by four types of materials attached to the wall rigidly or flexibly.

Michelson type optical fiber AE system

Our original optical fiber AE system was a Mach-Zender-type interferometer, in which the laser beam was transmitted in one direction. Both ends of the sensing and reference fibers were connected to photodiodes. Thus, setting of the sensing fiber for long parallel pipes was difficult. In order to overcome this problem, we developed a Michelson-type optical fiber AE system as shown in Fig. 2. This system is a laser interferometer using the lasers reflected by the mirrors coated on the end surfaces of the fibers. AE signals were detected as the phase shifts of interfered lasers via sensing and reference fibers. Advantage of the Michelson-type system is the free-end fibers, which make the mounting of the sensing fiber on pipes easy, especially on the parallel pipes in a closed space [6]. Sensitivity of the sensor can be improved by multiple winding of the fiber on the pipe. We reported that the amplitudes of L- and F-modes of the cylinder wave increased in proportional to the turn numbers of the sensing fiber [7]. Sensitivity of the Michelson-type interferometer is approximately the same that of the Mach-Zender-type interferometer [6].

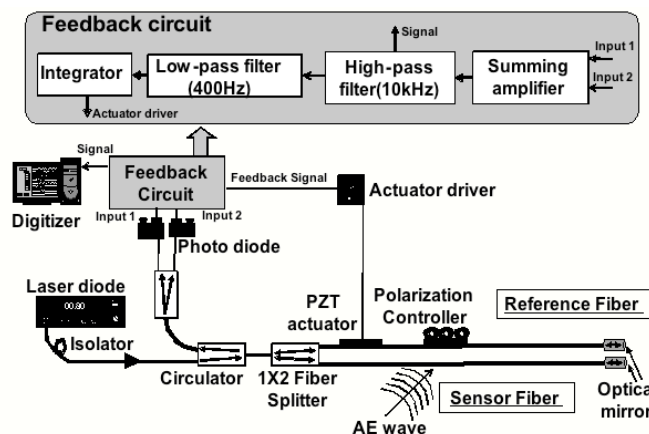


Fig. 2 Michelson-type optical fiber AE system.

Modeling of Four Types of AE Sources

In this basic experiment, we monitored AE signals from four types of artificial sources, as shown in Fig. 3. Type-1 source simulates AE signals from vortex behind irregular obstacles, rigidly fixed on the pipe wall by glue. Type-2 simulates the vibration of shells, but not hitting the pipe wall, by PMMA plate into the pipe sealed by soft silicone rubber. Type-3 simulates collision of shell to the wall. These new bivalves attach on the wall by thread and hit the pipe wall and other shells at higher flow velocities. We used native bivalve shells attached to the pipe wall by small Velcrotape. The tape was adhered to the wall by cyano-acrylate glue. Type-4 simulates collision and collapse of air bubbles at shell.

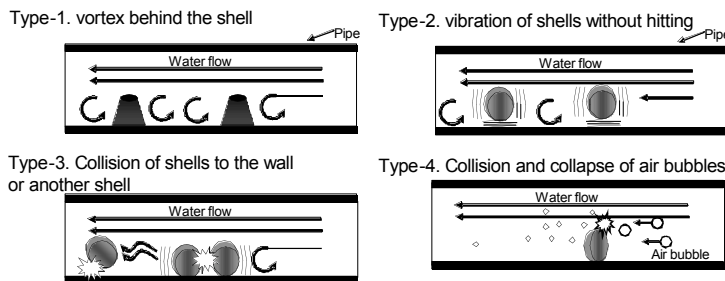


Fig. 3 Four types of artificial AE sources.

AE signals from Type-1 source or the vortex

Figure 4 shows experimental setup for AE monitoring from Type-1 source. We used a transparent PMMA pipe with inner diameter of 11 mm, to observe the inside of the pipe. Fragmented irregular magnet pieces of approximately 5 mm width, 5 mm thickness and 1.5 mm height, was rigidly fixed by the cyanoacrylate glue at 250 mm from the right end. Flow velocities are changed from 0.9 to 3.1 m/s. Reynolds numbers are from 9,900 to 34,000, indicating the turbulent flow.

Cylinder-wave AE signals were monitored by the optical fiber wound on the pipe by 52 turns (total length of 4.2 m) at 250 mm downstream from the obstacle. A PZT-type AE sensor (PAC, Type-R6 with center frequency of 60 kHz) was also mounted near the optical fiber. Outputs of the optical fiber and PZT sensors were amplified by 10 and 40 dB, respectively. Figure 5 show examples of waveforms detected at the flow velocities of 0.9 and 3.1 m/s, with noise at no flow. AE signals are continuous type. Amplitude increased with the flow velocities as shown in Fig. 6. However, the frequency components (7 to 27 kHz) are independent from the flow velocity. Sensitive fiber sensor can detect AE signals from flow turbulence induced by irregular obstacles.

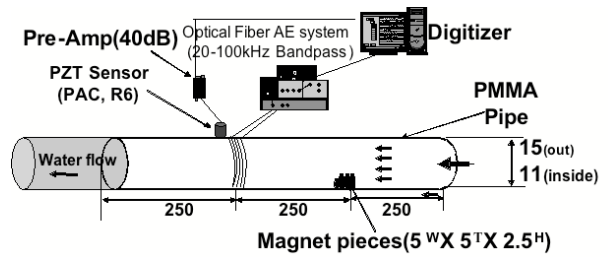


Fig. 4 Experimental setup for AE monitoring from Type-1 source.

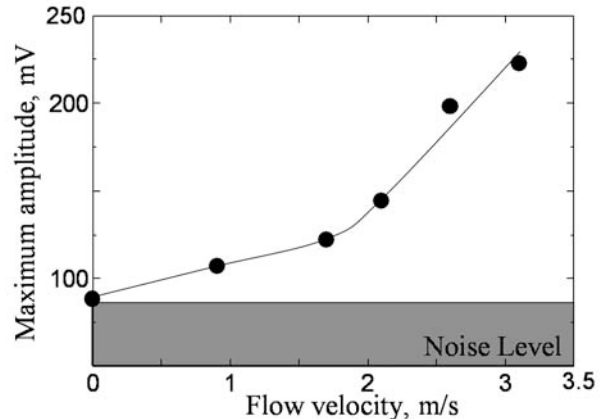


Fig. 6 Relationship between flow velocity and amplitude of optical fiber sensor.

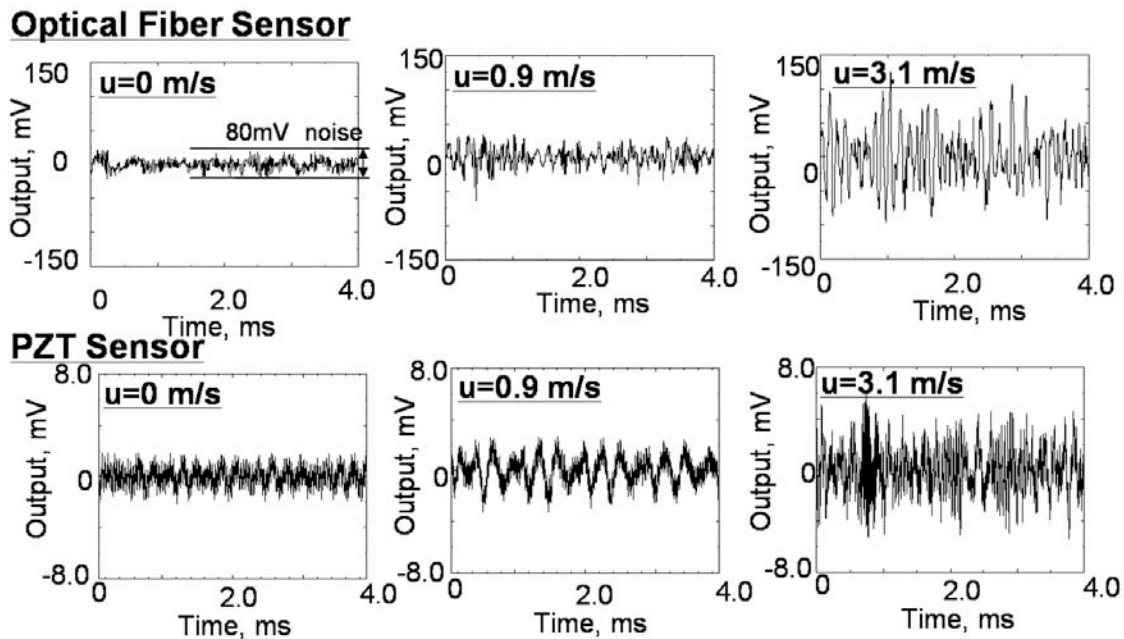


Fig. 5 Waveforms detected at flow velocity of 0, 0.9 and 3.1 m/s by optical fiber sensor (Upper) and PZT sensor (Lower).

AE signals from Type-2 source or shell vibration and vortex

Type-2 source simulates the vortex and weak vibration of the obstacle. A PMMA pipe of 11-mm inside diameter was used. We inserted a PMMA plate of 1-mm thickness into the pipe through a slit so that the maximum heights are from 2 mm to 10 mm. Thus the obstacle is a crescent shape. The plate was sealed by a soft silicone rubber at the end of 250 mm from the right end of pipe. AE signals were detected by the wound optical fiber of 4.2-m long and the PZT sensor. Location of both the sensor and obstacle are the same as these of Fig. 4. We changed band-pass filter from 20-100 kHz to 5-300 kHz. Flow velocities were changed from 0.9 to 3 m/s. Corresponding Reynolds numbers are from 9,900 to 33,000.

Figure 7 shows AE waveforms by the optical fiber sensor as a function of plate height: H at 3.0 m/s. Both the amplitude and frequency increased with plate height. The left of Fig. 8 shows change of the maximum amplitude (V_{pp}) and peak frequency with plate height at 3.0 m/s. These data were obtained from 10 events. The maximum amplitude increases with the plate height, while the peak frequency increased above 9-mm height. The right of Fig. 8 shows change of the maximum amplitude and peak frequency with flow velocity at plate height of 8 mm. The maximum amplitude increased rapidly around the flow velocity of 1.5 m/s, but the peak frequency remained around 10 kHz.

There are two mechanisms in this source, i.e., plate vibration and vortex. The former is likely to be low-frequency AE source and the latter the higher frequency. Resonance frequency of the plates was measured as 2.9 kHz independent from the flow velocities. Thus, the frequency of AE signals excited by the vibrating plate stayed near 9 kHz. AE signals with higher frequency components are supposed to be produced by vortex.

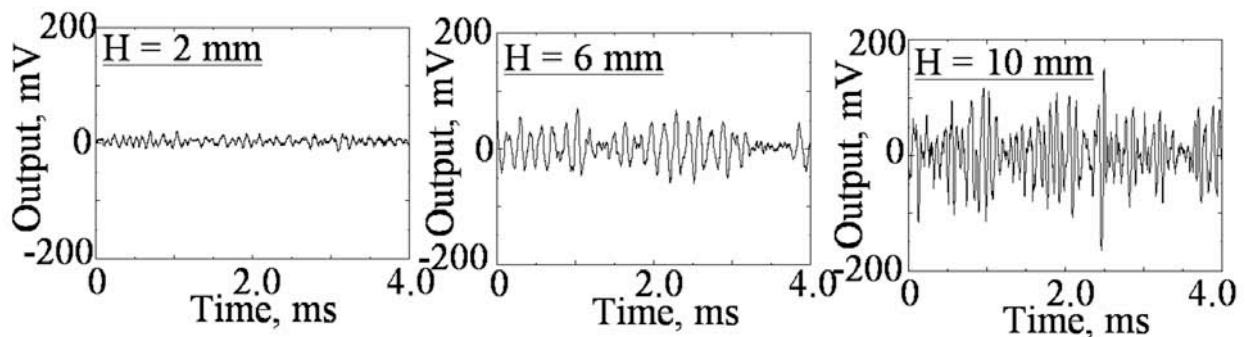


Fig. 7 Waveforms of AE signals detected by optical fiber AE system at plate height: H of 2, 6 and 10 mm at flow velocity of 3 m/s.

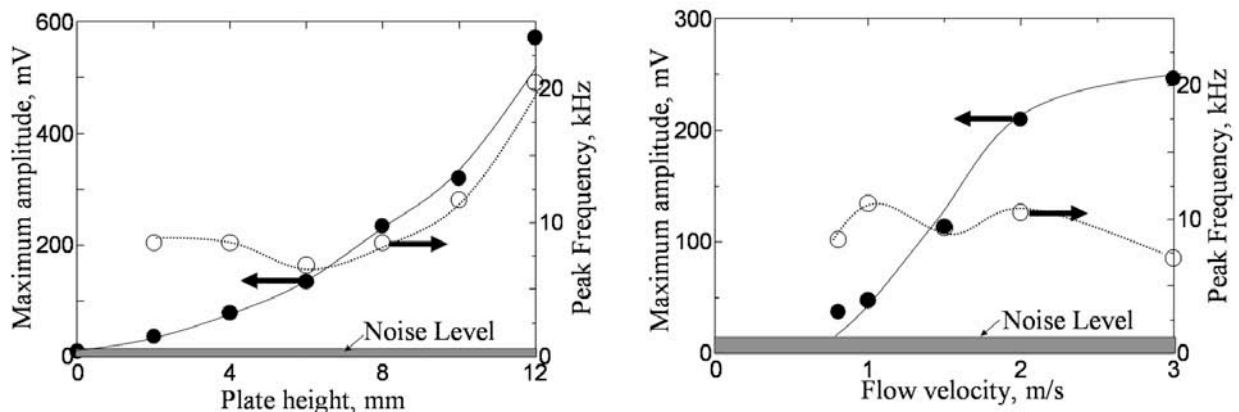


Fig. 8 Change of maximum amplitude and peak frequency with plate height at flow velocity of 3.0 m/s (left) and with flow velocity at plate height of 8 mm (right).

AE signals from Type-3 Source or collision of the shell to the wall

Type-3 source simulates the collision of the shell to the pipe wall and is a peculiar phenomenon caused by bivalve shells. We simulated this source using a dead native bivalve, which was attached to a small Velcro-tape by acryl-cyanate glue. The Velcro-tape was then fixed to inside the pipe. Figure 9 shows experimental setup. We monitored AE signals using the same fiber sensor, but changed the PZT sensor to another sensor (PAC, Type-R3, with center frequency of 30 kHz). These sensors were mounted at 500 mm from a pipe edge. We observed the shell vibration at flow velocities above 0.6 m/s. Reynolds number is 12,500 when flow velocity reached 0.6 m/s.

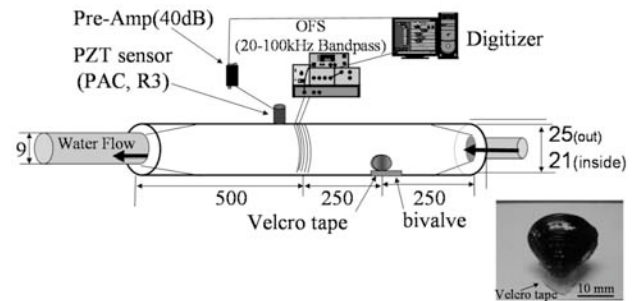


Fig. 9 Experimental setup for AE monitoring from Type-3 source.

Figure 10 shows waveforms as a function of the flow velocity. We detected strong burst-type AE signals at flow velocities above 0.6 m/s. Maximum amplitude of optical fiber sensor often exceeded 300 mV. Waveforms, however, significantly change depending on the vibration behavior of the shell. We observed no clear relationship between the amplitude, frequency and flow velocity, but frequent emission of AE signals at higher flow velocities above 0.8 m/s ($Re: 17,000$). This velocity, however, changes depending on the shell size and the density of bivalves in the colony, but we can monitor whether the bivalves are growing in the pipe. Wave amplitude is expected to increase with shell size and colony density.

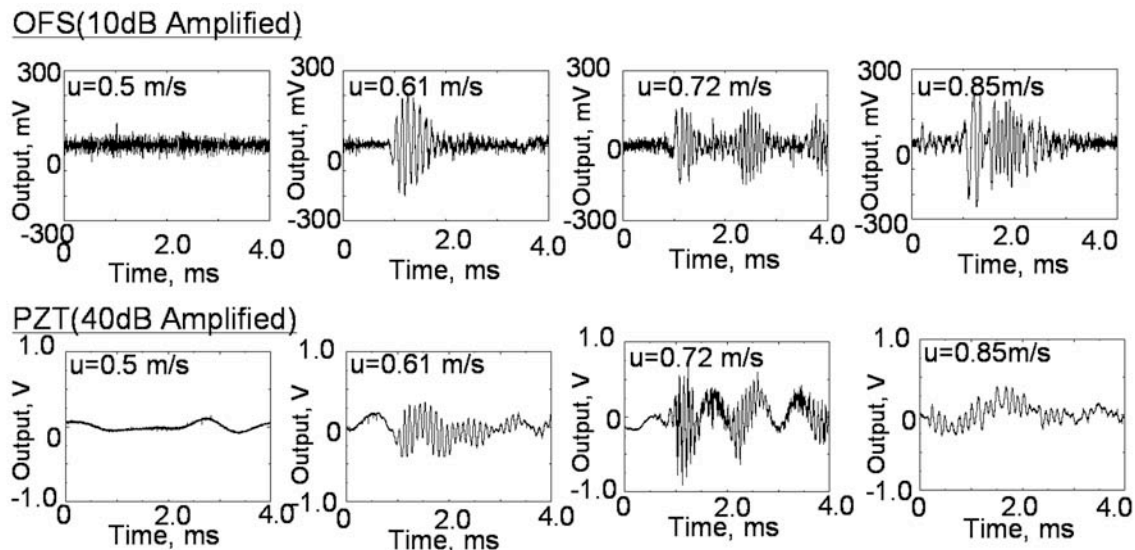


Fig. 10 Waveforms of Type-3 AE signals as a function of the flow velocity.

AE signals from the Type-4 source or gas bubble collision and collapse

A dead bivalve shell (14 mm^L , 12 mm^W and 9 mm^h) was rigidly glued to the pipe wall. Air bubbles of 2 to 3 mm diameters were injected in the flowing water using a bubble generator. Bubble injection corresponds to the location of bivalve of Fig. 9. Flow velocities were changed from 0.24 m/s ($Re=5,000$) to 0.85 m/s ($Re=18,000$).

AE signals were monitored by the wound optical fiber of 4.2-m length at 500 mm from a pipe edge and PZT-type AE sensor (PAC, type-R6) was also near the optical fiber.

Figure 11 shows examples of the cylinder waves produced by collision and collapse of air bubbles at flow velocity of 0.5 m/s. The optical fiber sensor detected strong and dispersive cylinder waves even at 10 dB amplification. The PZT sensor also detected the AE signals of 100 mV at 40 dB gain. Two types of AE signals, with only lower frequency (15 - 27 kHz) components (Type-A, top row) and with both of higher (48 kHz) and lower frequencies (Type-B), were detected. Waveforms, however, changed case by case, possibly due to bubble size, collision angle and so on. Though these AE signals were always detected at flow velocities higher than 0.3 m/s, they cannot be quantitatively correlated to the flow velocity.

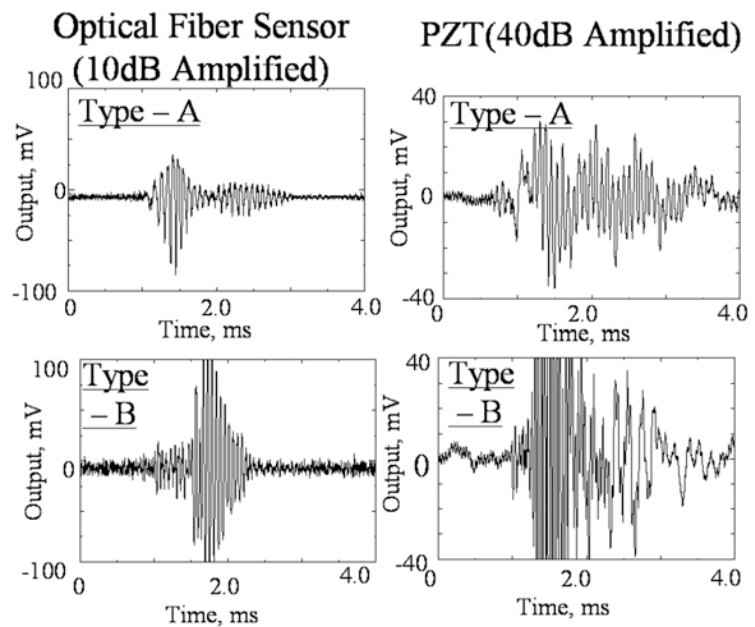


Fig. 11 Waveform of AE signals produced by collision and collapse of air bubbles.

Conclusion

We monitored AE from four kinds of blockages using the Michelson-type optical fiber AE system. Relations between AE signals and blockages are summarized below.

- 1) AE signals from vortex behind obstacles (Type-1 and -2 sources) were detected by the optical fiber sensor. Signal amplitude increased with increasing flow velocity.
- 2) AE signals from collision of shell to the wall (Type-3) were stronger than those from Type-1 and -2 sources. There observed no relations between the amplitude and frequency vs. flow velocity, but frequent emissions at higher velocities.
- 3) Strong cylinder waves were produced by collision and collapse of air bubbles (Type-4 source). Two types of AE signals, with lower frequency (15 - 27 kHz) components and with both of higher (48 kHz) and lower frequencies, were detected. Waveforms, however, changed case by case, possibly due to bubble size, collision angle and so on.

References

1. T. Kaziwara (ed.), *Attaching Organisms and Aquaculture*, Kosei-sha, 1987, p. 87. (in Japanese)
2. *The Invasive Alien Species Act*, Ministry of the Environment, Government of Japan, 2004.
3. G.Y. Que, L. Okushima, S. Sase and I.B. Lee, *J. Japan Agricultural Research Quarterly*, **36**, 2002, 103-109.
4. K. Kageyama and H. Kato, *Progress in Acoustic Emission XIII*, JSNDI, 2006, pp. 359-366.
5. H. Cho, R. Arai and M. Takemoto, *J. Acoustic Emission*, **23**, 2005, 72-80.
6. T. Matsuo, N. Yokoi, H. Cho and M. Takemoto, *Materials Transactions*, **48**, 2007, 1208-1214.
7. T. Matsuo, H. Cho and M. Takemoto, *Science and Technology of Advanced Materials*, **7**, 2006, 104-110.

DAMAGE IDENTIFICATION OF A CONCRETE WATER-CHANNEL IN SERVICE BY ACOUSTIC EMISSION

TETSUYA SUZUKI, MASAYASU OHTSU*, MASAO AOKI and RYOTA NAKAMURA

Nihon University, 1866 Kameino, Fujisawa, Kanagawa, Japan;

* Kumamoto University, 2-39-1 Kurokami, Kumamoto, Japan

Abstract

The durability of concrete structures decreases easily due to such physical and chemical environmental effects. The degree of damage in concrete is, in most cases, evaluated by mechanical tests. For effective maintenance of concrete structures, it is necessary to evaluate the damage degree of concrete explicitly. In this study, an existing water-channel structure was investigated. Quantitative damage evaluation of concrete is proposed by applying acoustic emission (AE) method and damage mechanics. The procedure is named DeCAT (Damage Estimation of Concrete by Acoustic Emission Technique). The damage was evaluated as a relative value by DeCAT in core tests. Core-samples were collected from a water channel of reinforced concrete that had been used for 46 years. After estimating the mechanical properties of concrete, damaged areas were surveyed. In situ observation was conducted in the channel, over which the railway traffic was passing. Damaged areas in the channel walls were located from vibrations recorded and AE activities measured. It is demonstrated that damages estimated by the DeCAT analysis from core samples are clearly correlated with the damaged areas identified.

Keywords: AE monitoring, rate process theory, damage mechanics, DeCAT, concrete

Introduction

The durability of concrete structures decreases due to physical and chemical effects. The degree of damage in concrete is, in most cases, evaluated from mechanical properties. However, mechanical properties obtained from, for example, the compression test are not directly associated with concrete damage. Accordingly, it is necessary to develop a quantitative damage evaluation technique for concrete structures.

To inspect existing structures for maintenance, acoustic emission (AE) technique is known to be useful. This is because crack nucleation and extension are readily detected and monitored. In this respect, measurement of AE activity in the uniaxial compression test of core samples was proposed [1]. AE behavior under compression is formulated by the rate-process theory. Quantitative evaluation of damage has been performed by AE rate-process analysis and damage mechanics [2]. The damage of concrete samples drilled out from structures were attempted to be estimated. By calculating Young's modulus of intact concrete E^* from the AE database, the degree of damage in a road bridge was successfully estimated [3]. Thus, a procedure to estimate the relative damage E_0/E^* of concrete is implemented as DeCAT (Damage estimation of Concrete by Acoustic emission Technique).

In this study, damage estimation of a water-channel structure is investigated by AE method. This structure has been deteriorated for 46 years due to wearing by water flow and impact load by a railroad. In situ observation was conducted at the channel, over which the railway traffic was passing. The resonant frequency and AE activity are evaluated on the channel wall. Concrete damage is evaluated from core samples by DeCAT in the compression test. Core-samples were collected from a wall structure.

Analytical Procedure

Damage Evaluation Method by DeCAT

The DeCAT system is applicable to evaluate concrete damage based on estimation of an intact modulus of elasticity from AE database. AE database consists of 120 samples tested in the Kumamoto University from 1988 to 2006. Analytical process is shown in Fig. 1.

AE Rate-Process Analysis

AE behavior of a concrete sample under compression is associated with generation of micro-cracks. These micro-cracks gradually are accumulated until final failure. The number of AE events, which correspond to the generation of these cracks, increases accelerated by the accumulation of micro-cracks. It appears that the process is dependent on the number of cracks at a certain stress level and subjected to a stochastic process. Therefore, the rate process theory is introduced to quantify AE behavior under compression. The following equation of the rate process is formulated to represent the number of AE hits dN due to the increment of stress from V to $V+dV$,

$$f(V)dV = \frac{dN}{N}, \quad (1)$$

Where N is the total number of AE events and $f(V)$ is the probability function of AE at stress level $V(\%)$. For $f(V)$ in Eq. 1, the following hyperbolic function is assumed,

$$f(V) = \frac{a}{V} + b, \quad (2)$$

where a and b are empirical constants. Here in after, the value 'a' is called the rate.

*Estimation of Intact Young's Modulus E^**

A damage parameter Ω in damage mechanics can be defined from a relative ratio in modulus of elasticity [4],

$$\Omega = 1 - \frac{E}{E^*}, \quad (3)$$

where E is Young's modulus of concrete and E^* is Young's modulus of concrete which is assumed to be intact or undamaged. Assigning Ω_0 is the initial damage at the onset of the compression test. The following equation is derived,

$$E_0 = E^*(1 - \Omega_0). \quad (4)$$

According to Eq. 3, the initial Young's modulus E_0 is associated with the current degree of damage Ω_0 . Corresponding to the damage Ω_c at the ultimate static ϵ_c , scant Young's modulus, E_c , is defined. In this study, Young's modulus, E_0 , was estimated as a tangential modulus.

As given in Eq. 4, the initial damage Ω_0 is an index of damage. It is fundamental to know Young's modulus of intact concrete E^* . Since it is not easy to obtain E^* from an existing structure, it is attempted to estimate E^* from

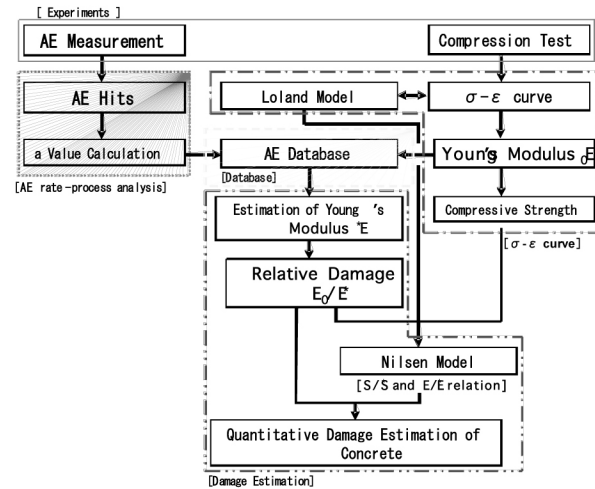


Fig.1 Calculate flow of DeCAT.

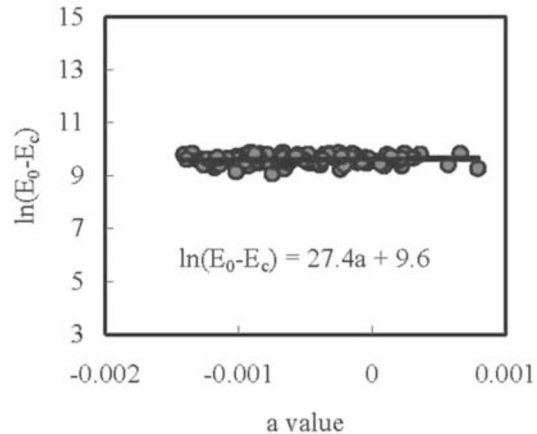


Fig. 2 Relations between $\ln(E_0 - E_c)$ and a value.

AE measurement. A correlation between the decrease of Young's modulus, $\log_e(E_0 - E_c)$, and the rate 'a' derived from AE database is shown in Fig. 2. Results of all samples damaged due to the freeze-thaw process are plotted by red circles. A linear correlation between $\log_e(E_0 - E_c)$ and the rate 'a' value is reasonably assumed. The decrease of Young's modulus $E_0 - E_c$ is expressed,

$$E_0 - E_c = E^* (1 - \Omega_0) - E^* (1 - \Omega_c) = E^* (\Omega_c - \Omega_0) \tag{5}$$

Based on a linear correlation in Fig. 2,

$$\log_e (E_0 - E_c) = \log_e [E^* (\Omega_c - \Omega_0)] = xa + c \tag{6}$$

Here, it is assumed that $E_0 = E^*$ when $a = 0$. This allows us to estimate Young's modulus of intact concrete E^* from AE rate-process analysis as,

$$E^* = E_c + e^c. \tag{7}$$

Experimental Procedure

AE Monitoring during an Impact Load of a Concrete Water-Channel Structure

In situ monitoring of vibration and AE activity was conducted on a concrete water-channel wall, of which was of dimensions (H: 1000 mm × W: 3100 mm). The channel was constructed in 1961 at Kanagawa prefecture, Japan. The data was measured when the railway traffic was passing. The monitoring wall is shown in Figs. 3 and 4. The vibration property was evaluated from the resonant frequency. The vibrations were measured by a laser vibrometer LK-G150 (KEYENCE) inside the channel. The sampling frequency was set at 200 μs. The monitored wall was divided into 15 sections and the resonant frequency was evaluated at each section. For AE monitoring, the wall surface was divided into 3 sections and 4 AE sensors (resonance frequency: 150 kHz) were placed at 1 m intervals to determine AE locations (Fig. 4). The threshold level was set to 45 dB with a 40 dB gain in a pre-amplifier and 20 dB gain in a main amplifier. For event counting, the dead time was set as 2 ms. AE events were located when 3 or more sensors detect the first motions clearly.

Damage Evaluation of Core-Concrete by DeCAT

Core samples of 10 cm in diameter and 20 cm in height were drilled from the concrete water-channel wall. AE measurement was conducted in the compression test. Silicone grease was pasted on the top and the bottom of the specimen, and a teflon sheet was inserted to reduce AE events generated due to friction. SAMOS-AE system (PAC) was employed to count AE hits. AE hits were detected by using an AE sensor UT-1000 (resonance frequency: ~1 MHz). The frequency range was from 60 kHz to 1 MHz.

The longitudinal wave velocity was measured to estimate dynamic Young's modulus, E_d , which was determined from

$$E_d = \frac{(1 + \nu)(1 - 2\nu)\rho}{1 - \nu} V_p^2. \tag{8}$$

Here, ρ is the density of concrete specimen and ν is Poisson's ratio. V_p is the longitudinal wave velocity.

Table 1 Mechanical properties of core samples.

Sample Name	Sample Number	f_c (N/mm ²)	E_c (GPa)	E_d (GPa)	V_p (km/s)	Carbonation (mm)
SAGAMI 1961	10	25.7~40.7 (30.5)	16.0~30.6 (23.4)	12.8~32.7 (24.2)	2.6~4.2 (3.5)	2~14 (7)

*values determined show "Minimum - Maximum (Average)"



Fig. 3 Overview of monitoring site.

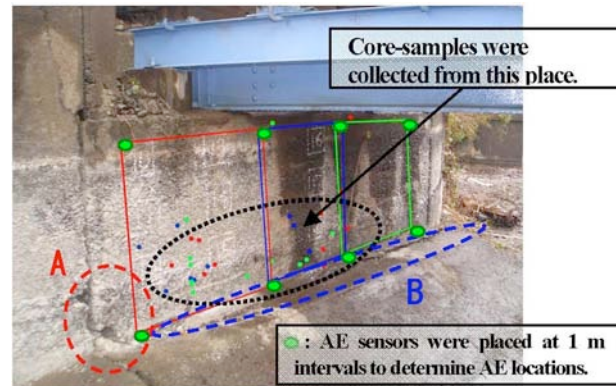


Fig. 4 Core sampling and AE monitoring wall.
(●: Detected AE events)

Results and Discussion

Properties of Vibration and AE in Damaged Concrete Wall

The maximum amplitude of the vibrations was detected in the range from 0.4 to 2.4 mm. The resonant frequency was estimated in the range from 0.86 to 1.63 Hz. Near particular wall portions (A and B in Fig. 4), the decrease of the resonance was observed. In the figure, AE source locations were found at the middle of the wall. At these portions, high AE activity was observed. Thus, in this study, concrete damage is evaluated using core-samples, which were drilled out from high AE activity portions.

Mechanical Properties of Concrete

Mechanical properties of core samples are summarized in Table 1. Compressive strengths are 30.5 N/mm² on the average, 40.7 N/mm² at the maximum, and 25.7 N/mm² at the minimum. Young's moduli (E_c) are 23.4 GPa on the average, 30.6 GPa at the maximum, and 16.0 GPa at the minimum. Dynamic Young's moduli (E_d) are calculated from Eq. 8. The longitudinal velocity of concrete V_p are 3.5 km/s on the average, 4.2 km/s at the maximum, and 2.6 km/s at the minimum. Young's moduli E_d are 24.2 GPa on average, 32.7 GPa at the maximum, and 12.8 GPa at the minimum. Carbonation depth is 7 mm on the average, 14 mm at the maximum, and 2 mm at the minimum.

AE Generation Behavior under Compression

AE generating behavior in each core sample was evaluated by AE rate-process analysis. Typical relations between the probability function of $f(v)$ and the stress level is shown in Figs. 5 and 6. For sound concrete, AE activity gradually increases (Fig. 5), while damaged concrete exhibits higher activities from the early loading stages (Fig. 6). AE rate process analysis was conducted at stress level in the range from 30% to 80%. This is because AE events occurring at initial loading below 30% strength due to contact with the loading plate and at an accelerated stage above 80% has little to do with the damage.

AE activity of a sound concrete specimen (with 28-day moisture curing) showed a negative 'a' value in AE rate-process analysis; $a = -0.0013$. In the case of negative rate, the probability $f(v)$ is low at a low stress level, because concrete is in a stable condition. With stress, $f(v)$ increases as seen in Fig. 5. AE activity of core specimens showed negative 'a' values in AE rate-process analysis. That is, the damage is not severe (giving positive "a" values). Compared to the value for normal concrete, the value obtained for the specimen affected by impact load (Fig. 6) was -0.0005 . [The "a" values of other core samples were between -0.0010 to -0.0005 .] This increasing trend of 'a' value correlates to the increase in damage.

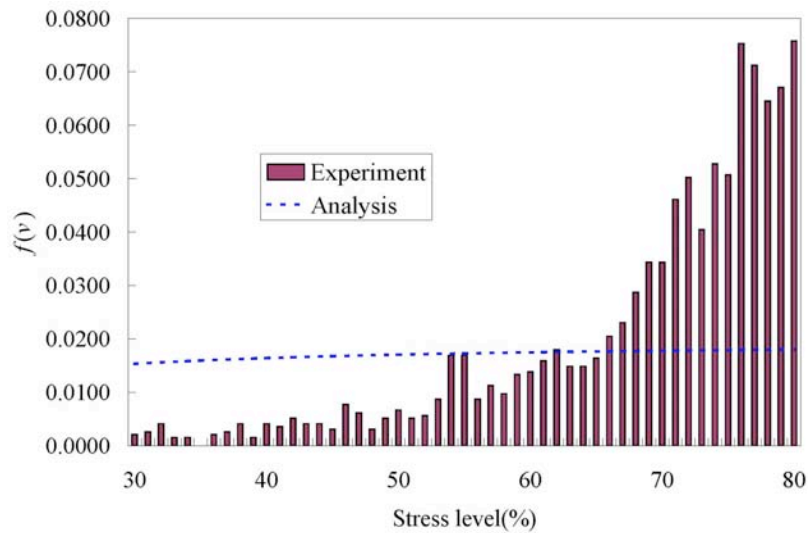


Fig. 5 AE generating behavior of sound concrete, moisture-cured 28 days.

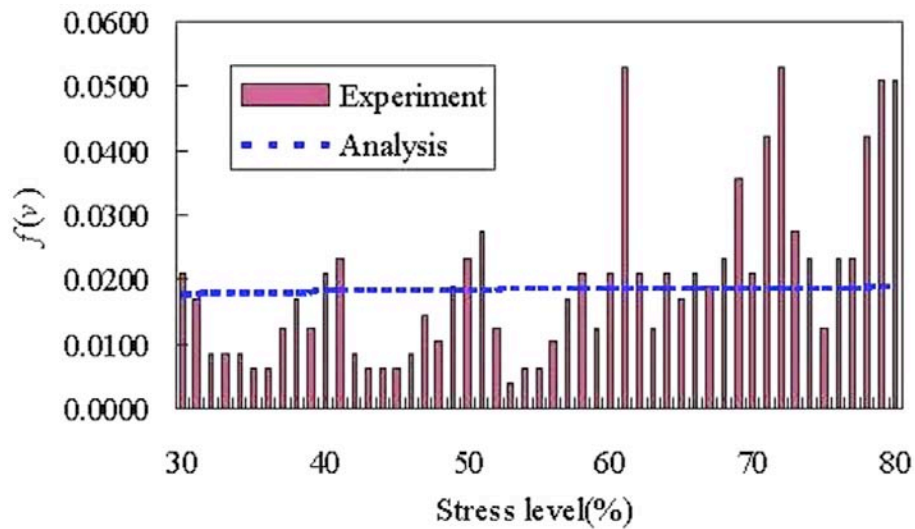


Fig. 6 AE generating behavior of a core concrete sample. Compressive strength = 25.7 MPa.

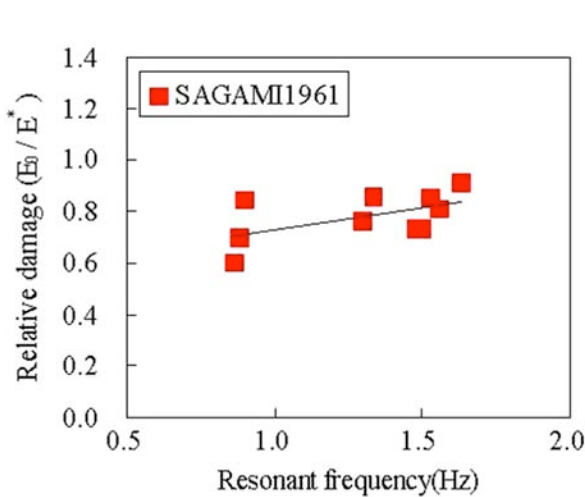


Fig. 7 Relation between relative damage and resonant frequency.

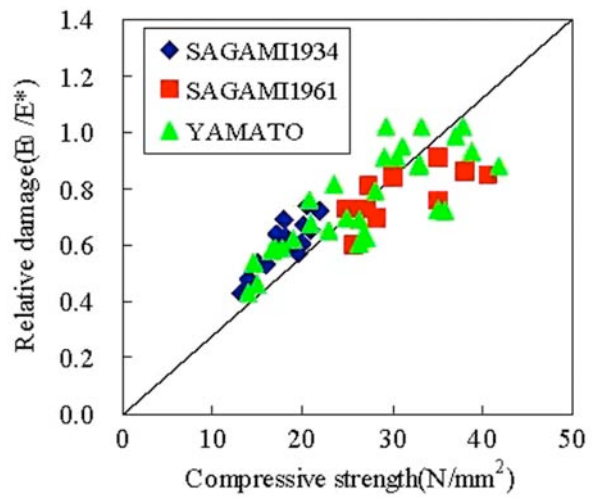


Fig. 8 Relation between relative damage and compressive strength.

Relative Damage Evaluation of Concrete by DeCAT

Relative damages of specimens were estimated from the ratios of initial Young's moduli E_0 to intact E^* . Relative damage (E_0/E^*) is compared with resonant frequency in Fig. 7. Relative damages are almost positively correlated with resonant frequency.

Relation between relative damage and compressive strengths (f^c) is shown in Fig. 8. This figure also shows previous results of SAGAMI1934 and YAMATO in addition to present results "SAGAMI1961". Those samples were collected from other concrete water-channel structures [6]. The SAGAMI1934 samples were collected from a cast-in-place concrete constructed in 1934 at Ebina city, Japan. The YAMATO samples were taken from the same type of structure constructed in 1984 at Nara city, Japan. It is clearly observed that relative damages E_0/E^* are positively correlated with the compressive strengths. Because the relative damages of specimens are lower than 1.0, they are considered to be damaged. A similar trend was confirmed in current research [3, 7, 8]. This result shows that the damage of concrete is quantitatively estimated as the relative values by DeCAT.

Conclusion

For quantitative evaluation of concrete damage in a water-channel structure, AE method was applied to the in situ monitoring and the uniaxial compression test of core samples. In situ observation was conducted in the channel wall, over which the railway traffic was passing. The resonant frequency is found to decrease in damaged portion. High AE activity is also detected near the portions of decreased resonance. AE generation behavior in core test is closely associated with the damage, which can be quantitatively evaluated by DeCAT. Core-samples were taken out of AE monitoring site. It is confirmed that an increasing trend of the rate 'a' with the increase in damage. The relative damages E_0/E^* estimated show reasonable agreement with the compression strengths.

References

1. M. Ohtsu, *Proc. of JSCE*, No. 442/V-16, 1992, pp. 211-217.
2. H. Watanabe, M. Ichinose, Y. Tomoda and M. Ohtsu, *Proc. of the Japan Concrete Institute (JCI)*, **23** (1), 2001, pp.493-498.
3. T. Suzuki, M. Ohtsu and M. Shigeishi, *Materials and Structures*, **40**, 2007, 221-227.
4. Suredra P. Shah, Stuart E. Swartz and Chengsheng Ouyang, *Fracture Mechanics of Concrete*, John Wiley & Sons Inc., 1995, pp. 452-459
5. T. Suzuki, G. Komeno G., Y. Ikeda and M. Ohtsu, *Proc. of JSCE*, No. 809/V-70, 2006, pp. 29-40.
6. T. Suzuki and M. Ohtsu, *Journal of Applied Mechanics*, 2007, accepted.
7. M. Ohtsu and T. Suzuki, *Journal of Acoustic Emission*, **22**, 2004, 30-38.
8. T. Suzuki and M. Ohtsu, *Construction and Building Materials*, **18**, 2004, 197-202.

TEMPORAL EVOLUTION AND 3D LOCATIONS OF ACOUSTIC EMISSIONS PRODUCED FROM THE DRYING SHRINKAGE OF CONCRETE

GREGORY C. MCLASKEY and STEVEN D. GLASER

Department of Civil and Environmental Engineering, University of California, Berkeley, USA

Abstract

Acoustic emission activity produced by unrestrained drying shrinkage of an early age normal strength concrete specimen was measured with an array of fourteen broad-band high-fidelity acoustic emission sensors. The specimen was continuously monitored for 17 days, and full waveforms of the acoustic emissions were recorded throughout this time period. We present the source locations in three dimensions, the evolution of these events over time. Additionally, we discuss the reliability of source location estimates and consider uncertainty and bias introduced by array geometry effects, choice of velocity models, and poor picking of arrival times. We report on experimental procedures and tools created for fully quantitative, signal-based acoustic emission analysis.

Keywords: High fidelity, sensors, concrete, wave propagation, source location

Introduction

Drying shrinkage of concrete is a known cause of micro and macro cracking. Because the presence of cracks can have many detrimental effects on the durability of a concrete structure, it is important to understand the development of the cracks as the concrete ages. It is generally expected that shrinkage will commence almost immediately after exposure to a low relative humidity. Though aggregates complicate the stress state of a shrinking concrete specimen, cracking is expected to occur in the region of tensile stresses near the outside surface of the specimen [1].

Current research on drying shrinkage cracking in concrete relies on observations via optical microscopy [2]. These studies have confirmed that the location of drying shrinkage cracking is near the surface and around aggregates, and occurs during the first few days of drying. The disadvantage of these optical methods is that the specimen must be cut open. The method of acoustic emission allows cracks to be identified continuously and non-invasively.

In this paper, the cracking of concrete due to drying shrinkage without external restraint is studied through the method of acoustic emission. Similar experiments have been reported [3, 4] but for the first time the events are located in three dimensions and over a 17-day drying period. Additionally, the sources of error in the localization schemes are identified and quantified and error ellipsoids are calculated for each of the source location estimates.

Experimental Setup

A prismatic specimen (175 x 175 x 250 mm) of normal strength concrete with a water/cement ratio of 0.46, design strength of 27.5 MPa, and largest sized coarse aggregate of 15 mm diameter (pea gravel) was tested for drying shrinkage cracking using the method of acoustic emissions. The specimen was cast into a wooden mold with PMMA inserts for improved surface smoothness. The specimen was cured for 28 hours and then demoulded and instrumented with an array of NIST-Glaser-type high fidelity broadband transducers modeled after the NBS conical transducer [5]. The sensing element is PZT-5a (lead-zirconate-titanate) truncated cone with an

aperture diameter of 1.5 mm. The sensors have a very flat frequency response from 12 kHz to 960 kHz and with unidirectional sensitivity to particle displacement. Further details on the sensors can be found in [6, 7].

The prismatic specimen was instrumented with an array of fourteen sensors located on the North, East, South, and West sides of the specimen. (Sensor locations are shown in Fig. 2.) The top side of the specimen was exposed to ambient humidity (30±5% relative humidity) and the rest of the specimen was partially sealed with cellophane. Before digitization, all signals went through a DigitalWave™ FM-1 signal conditioner/preamplifier where they were subject to a gain of 36 dB and a 20 kHz high pass filter to remove low frequency background noise. The signals were sampled at 5 MHz using a 12-bit High-Techniques™ Digitizer. The specimen was continuously monitored for 17 days. During this time period if the voltage from any one of four pre-selected trigger sensors exceeded 31 mV (corresponding to displacements on the order of 3 pm), the digitizer was triggered and 800 μs of the displacement time history from each sensor was recorded and saved starting 250 μs before the time of triggering and ending 550 μs after the time of triggering. Each one of these triggered ‘hits’ was saved for offline analysis and was later classified either as an ‘event’ or as ‘noise’.

Estimating the Location of Acoustic Emissions

Source location is perhaps the single most important analysis procedure in the method of acoustic emission because many other analyses—such as energy and magnitude estimates and source kinematics—rely on the accurate determination of the source location. There are a number of methods for determining a source location, but this paper will only discuss methods which use the observed arrival time of a specific wave phase at a number of sensor locations to calculate the coordinates of the source in space and time. (We refer to the wave phase as the P-wave because it is most commonly used. The same schemes could be implemented for S waves.)

Because the absolute source time is not known, finding source coordinates based on the differences in arrival times recorded from an array of n sensors requires the solution of a series of $n-1$ nonlinear equations. A solution (in the least squares or least error sense) can be found by calculating the minimum of a suitable cost function (usually iteratively). By subtracting one equation from the rest, the nonlinear equations can be manipulated into $n-2$ linear equations from which source coordinates can be solved directly; or, if more than five sensors are used, a method of ‘quasi least squares’ may be used [8, 9]. When errors are included in the arrival times, this method can produce wildly inaccurate results, thus it has been suggested that the ‘quasi least squares’ method be used only a starting point for an iterative scheme [10].

In our tests, the locations of the hypocenters of the acoustic emissions recorded were found using the minimization of the cost function

$$\text{cost} = \sum_{i=1}^n \left| \sqrt{(x - x_i)^2 + (y - y_i)^2 + (z - z_i)^2} - c(t_i - t_0) \right| \quad (1)$$

where t_i , x_i , y_i , and z_i are the observed P-wave arrival times, and the known spatial coordinates for the i^{th} sensor, c is the assumed wave velocity, n is the number of sensors used for the determination of the source location, and x , y , z , and t_0 are the unknown source location in three spatial dimensions and time. This method assumes (1) that the hypocenter and sensors can be modeled as points, (2) that the ray path from source to receiver is a straight line, and (3) that P waves travel at some known and constant velocity c .

Once an estimate of the source location is found, the quantification of uncertainty and bias in the source location estimate must be considered. In this study, the sources of errors were divided into four main categories: picking errors, array geometry-induced errors, velocity model errors,

and minimization errors. Note that all results presented here, both synthetic and real, are for the array and specimen geometry shown in Fig. 2.

Picking Errors

Picking errors are those which can be modeled by an inaccurate selection of the arrival time of the P-wave. Slow rise times or low signal to noise ratios can cause picking errors, but even if the arrival times are unambiguous, the observed arrival time may deviate from the ideal case. Equivalent picking errors may be calculated and quantified for these sources of error.

The majority of the events recorded from the drying shrinkage test have P-wave rise times of 1-3 μs which allow the arrivals to be picked to within an accuracy of about 500 ns. This provides a baseline from which other sources of picking error can be quantitatively compared. For example, the 1.5-mm aperture of the sensor would produce the equivalence of at most 170 ns of error for the P wave velocities found in concrete. (In contrast, an 8-mm diameter sensor aperture can produce up to 800 ns of equivalent picking error.) The increase in travel path due to a crack or void 3 mm in diameter would produce at most 80 ns of equivalent picking error under the geometry of our test setup. Alternatively, under the same geometry, if the average P-wave velocity deviates (due to inhomogeneities in the material, for example) from the assumed value by only 5% (200 m/s) it would produce 500 ns of equivalent error.

In order to model picking errors and gain an estimate of the uncertainty associated with each source location estimate, a random error term was added to each picked arrival time. This error term was assumed to be a normally distributed random variable with a mean of zero and a standard deviation of 500 ns. The source location was then calculated fifty different times, drawing upon fifty different realizations of the error terms. Error ellipsoids and confidence intervals were then calculated from the cluster of fifty source locations generated via this procedure.

Array Geometry Errors

While the array geometry does not introduce new errors, for certain source locations relative to the sensor array the picking errors can be amplified by array effects [10, 11]. This is similar to the concept of a blind spot in the sensor array. Figure 1(a) shows the effect of the sensor array and specimen geometry used for the drying shrinkage test setup. In the figure, the 95% confidence error ellipsoids are shown relative to the true location of simulated sources located on the top surface of the concrete specimen. The error ellipsoids are based on normally distributed random picking error with a mean of zero and a standard deviation of 500 ns. It was found that array geometry-induced errors are greatest near the corners of the specimen, especially the Southwest corner.

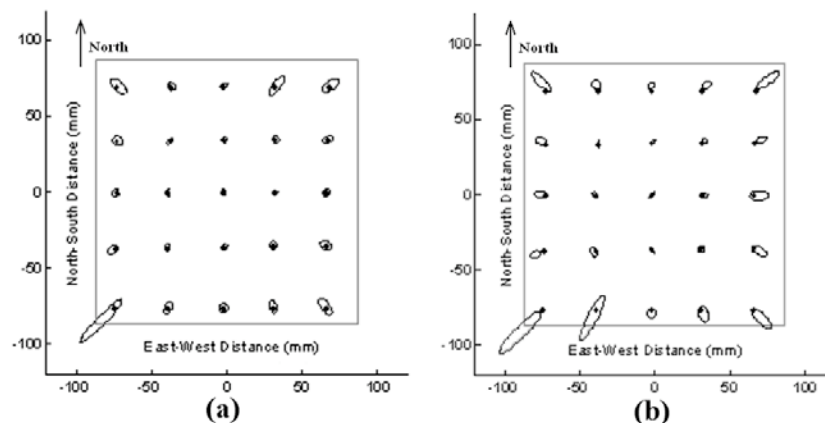


Fig. 1. Error ellipsoids for simulated sources located on the top surface of a specimen with identical array geometry to the drying shrinkage test setup demonstrate the amplification of picking errors due to (a) array geometry alone, and (b) bias induced by an inaccurate velocity model.

Velocity Model Errors

The cost function (1) used for localization assumes that the P-wave velocity is known and constant over every ray path in the concrete specimen, but in reality the P-wave velocity is unknown, difficult to measure, inhomogeneous, and is changing over time as the concrete cures and dries and cracks [12]. An incorrect velocity model will surely yield biased estimates of source location.

For example, if the assumed velocity is only off by 100 m/s (about 3%) the source location estimate will be biased by 1-4 mm depending on the true source location relative to the sensor array. Figure 1(b) shows the combined effect of picking errors (same as described above), array geometry, and velocity model errors (the assumed velocity is 100 m/s faster than the true velocity). This figure shows that this velocity model error will introduce uncertainty and will bias location estimates by pushing them further from the center of the sensor array.

Minimization Errors

Array geometry-induced errors, picking errors, and velocity model errors can yield cost functions which lack a well defined minima. Thus, a fourth category of errors can arise due to the imprecision and bias introduced by the algorithm which computes the minimization of the cost function. In the absence of errors, the cost function will vary smoothly over four dimensional space (three spatial dimensions and source time), but when deviations between observed and expected travel times are introduced, this function often becomes highly nonlinear. Iterative solution schemes often fail to find the global minimum and instead pick local minima or satisfy their convergence criteria on a very flat portion of their path, far from the true minimum. For this study, an iterative scheme which incorporates random jumps into the search path was used for the minimization of the cost function. While this solution strategy was computationally expensive, it was very robust and often performed better than conventional algorithms. By comparing different types of minimization schemes, imprecision was estimated to be on the order of 0.25-0.5 mm within the spatial region of interest.

Results and Discussion

Over two thousand acoustic emissions were recorded in the prismatic specimen over the 17-day monitoring period. About 800 events were deemed large enough to be located. Reasonably accurate (± 10 mm) source locations were found for about 80% of those events. Figure 2 shows the principle axes of error ellipsoids for only those events which were found to be located near the center of the specimen (within the dashed lines) and with 95% confidence error ellipsoids less than 20 mm in all directions. (Error ellipsoids were found from the method described above.) Of these 340 events, most were located a few centimeters below the drying surface. A smaller number of events were found to be much deeper (8-10 cm) in the interior of the specimen.

The evolution of depth over the 17-day monitoring period (for the same 340 events shown in Fig. 2) is shown in Fig. 3. The bars represent 95% confidence intervals calculated via the same method as those shown in Fig. 2. The upper graph shows the locations found using a constant velocity model while the lower graph shows the results using a time varying velocity model. To estimate the change in P-wave velocity over time, pencil leads were broken at two different locations on the surface of the specimen on a daily basis, and from the evolution of pencil lead sources at known locations a velocity model was created which assumes that the P wave velocity is initially increasing and then leveling off over the 17-day period.

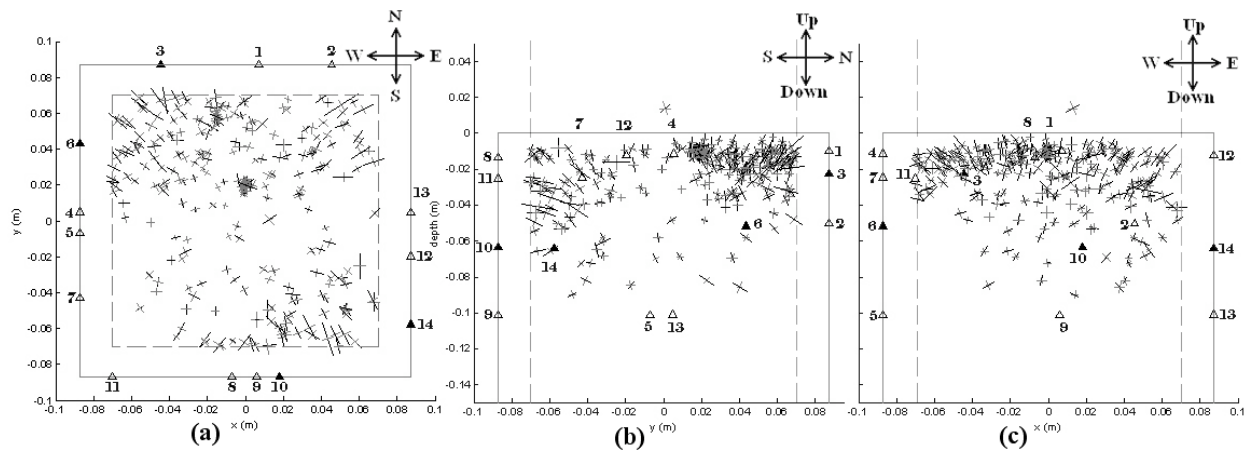


Fig. 2. Spatial distribution of estimated source locations in (a) top and (b, c) side views.

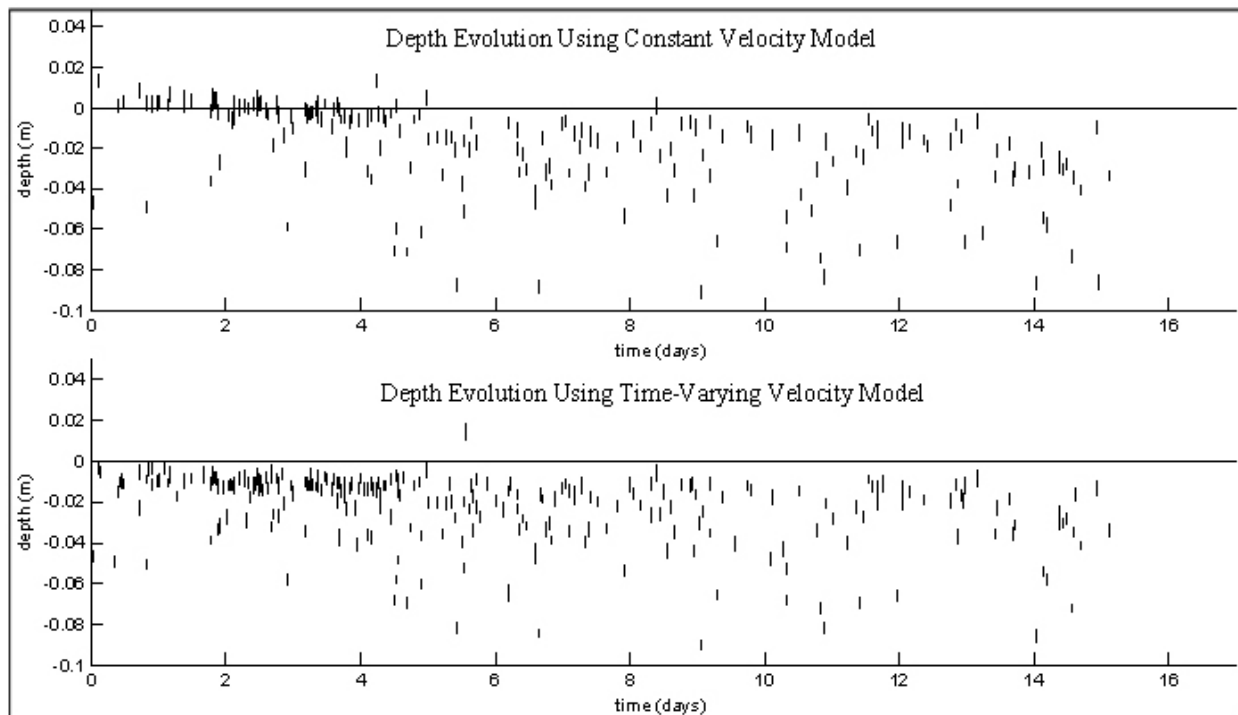


Fig. 3. Evolution of depth over time using (a) constant velocity model (b) time varying velocity model.

A very clear trend from surface to interior events can be seen from estimates using the constant velocity model, but the apparent increase in depth was due, in part, to bias induced by an inaccurate velocity model. For example, if the estimated velocity is higher than the true velocity, as is the case for the first few days of the monitoring period under the constant velocity model, the location will be pushed further from the center of the sensor array. In this case the inaccurate choice of velocity causes the events to locate above the surface of the specimen. From this analysis it is clear that the choice of velocity model can have a large effect on source location estimates, yet even with the time-varying velocity model a trend toward increasing depth is apparent.

One would expect that the emissions due to drying shrinkage would be spread evenly over the entire drying surface in plan view (Fig. 2(a)) and be located within a few centimeters of the surface in side view (Fig. 2(b) and (c)). The relatively small number of events found in the SW

corner of the specimen may be due to the large amount of array-induced localization errors in this location. The larger numbers of events in the NW and SE corners of the specimen may be due in part to a triggering bias (i.e. smaller events closer to trigger sensors are recorded while similar events further from trigger sensors will be undetected). The four trigger sensors (#3, 6, 10, 14) are shown as filled triangles in Fig. 2. Finally, while drying shrinkage cracking is expected to be located on or near the surface of the specimen, even under the time varying velocity model most events were estimated to be well beneath the surface of the specimen. This may be bias due to the inaccurate assumption of a homogeneous velocity model.

Despite the fact that inaccurate velocity assumptions make the absolute accuracy of source locations difficult to calculate, the relative uncertainty of the source locations is relatively well known, and the error bars shown in Figs. 2 and 3 provide a good measure of precision.

Conclusion

The 3D locations of hundreds of acoustic emissions recorded over a 17-day drying period have been estimated. Imprecision in P wave picking and the inhomogeneous nature of P wave velocity of concrete seem to be leading sources of picking errors. These picking errors may be amplified by the array geometry and minimization errors. By making use of equivalent picking errors, uncertainty was modeled, and the propagation of this uncertainty via array geometry effects and minimization errors can be accurately tracked. Alternatively, an inaccurate velocity model is a large source of error, and it is one that is very difficult to quantify. Consequently, the absolute accuracy of a source location is difficult to measure. Despite this, the relative precision of the estimates can be quantified and a clear trend from surface to interior events can be seen over the 17-day period in the drying concrete specimen.

References

1. Bisschop, J., *Drying Shrinkage Microcracking in Cement-Based Materials*, Delft University Press, 2002.
2. Bisschop, J., and van Mier, J. G. M., *Materials and Structures*, **35**, 2002, 453-461.
3. Shiotani, T., Bisschop, J., and van Mier, J. G. M. *Engineering Fracture Mechanics*, **70**, 2003, pp. 1509-1525.
4. Uomoto, T., Kato, H., *Progress in Acoustic Emission V*, eds. Yamaguchi, K., Takahashi, H., and Niitsuma, H., The Japanese Society for NDI, Sendai, Japan, 1990, pp. 325-330.
5. Proctor, T. M. *Journal of Acoustic Society of America*, **71**, 1982, 1163-1168.
6. Glaser, S., Weiss, G., and Johnson, L., *Journal of Acoustic Society of America*, **104**, 1998, 1404-1412.
7. McLaskey, G., Glaser, S., Grosse, C., *Proc. of SPIE Vol. 6529*, San Diego, Mar. 18-20, 2007.
8. Mahajan, A., and Walworth, M., *IEEE Transactions on Robotics and Automation*, **17**, 2001, 91-94.
9. Ohtsu, M., and Ono, K., *NDT International*, **21**, 1988, 143-150.
10. Salamon, M. D. G., and Wiebols, G. A., *Rock Mechanics*, **6**, 1974, 141-166.
11. Ge, M., and Hardy, H.R., *Fifth Conference on Acoustic Emission/Microseismic Activity in Geologic Structures and Materials*, Pennsylvania State University, June 11-13 1991.
12. Boyd, A. and Ferraro, C., *ASCE J. of Materials in Civil Engineering*, **17**, 2005, 153-158.

DEMAND ON FLEXURAL TENSION STEEL REINFORCEMENT ANCHORAGE ZONES IN FULL-SCALE BRIDGE BENT CAPS QUANTIFIED BY MEANS OF ACOUSTIC EMISSION

THOMAS SCHUMACHER, CHRISTOPHER HIGGINS,
STEVEN GLASER* and CHRISTIAN GROSSE[†]

School of Civil and Construction Eng., Oregon State University, Portland, OR, USA;

*Dept. of Civil and Environmental Engineering, University of California, Berkeley, CA, USA;

[†]Non-Destructive Testing and Monitoring Techniques, Univ. of Stuttgart, Stuttgart, Germany

Abstract

This paper documents the development of an AE technique for monitoring and quantifying the demand on anchorage zones of the flexural-tension steel reinforcement in full-scale bridge bent caps. Bent caps are deep transverse bridge beams that support the longitudinal girders and transfer loads into the columns. The horizontal flexural-tension reinforcement at the bottom of the bent cap is anchored into the columns and acts as a crucial structural element. Pull-out or anchorage failure could lead to system collapse since this member is non-redundant. A new approach to monitor the column anchorage zone and to quantify the maximum demand of rebar pull-outs by means of quantitative AE is presented and applied to test data on full-size bent column anchorage sub-assemblages.

Keywords: Reinforced concrete, bridge bent caps, column anchorage zone, structural health monitoring

Introduction

Large numbers of conventionally reinforced concrete deck-girder (RCDG) bridges were constructed during the federal highway system expansion of the 1950s. During this time period, research developments on anchorage of reinforcing bars resulted in rapid changes to design specifications and practice. Specifically, the geometric standardization of deformed reinforcing bars in ASTM A305-50 resulted in higher allowable stresses with reduced detailing requirements. Failures later in the decade revealed that the contemporary design practice was inadequate. By the early 1960s, design specifications were amended and at the same time, pre-stressed concrete began to supersede conventionally reinforced concrete for bridge construction.

One concern of the design found in existing bent caps is the detailing of the anchorage zones in bent caps. The flexural-tension reinforcement at the bottom of a bent cap is anchored into the bent column. For many bridges, these rebars are straight (not hooked) and terminated so that minimum concrete cover (c_c) is provided at the tail. This is normally around $c_c = 38$ mm. The typical anchorage length provided in a 610-mm-square column is only around $l_d = 572$ mm. The development length (l_d) required by the current AASHTO-LRFD (2004) specification for a bar with a diameter of $d_b = 36$ mm (#11) is:

$$l_d = 1.25 \cdot A_b \cdot f_y / \sqrt{f_c'}, \text{ but not less than } 0.4 \cdot d_b \cdot f_y \quad (1)$$

which results in $l_d = 1490$ mm assuming Grade 60 ($f_y = 414$ MPa) rebar steel and concrete compressive strength of $f_c' = 28$ MPa. This required development length is more than 2.5 times greater than the available anchorage length (although Grade 40 ($f_y = 276$ MPa) rebars were generally used in mid-20th century bridge construction).

Experimental Setup and Load Protocol

To better understand the behavior and structural mechanics during a rebar pull-out, reduced bent column sections were designed, constructed, and loaded until failure [1]. Figure 1 illustrates a test specimen with applied force P and the support reactions $P/2$. The force was applied with hydraulic cylinders supplied by a manually activated pump. Load cells measured the applied force.

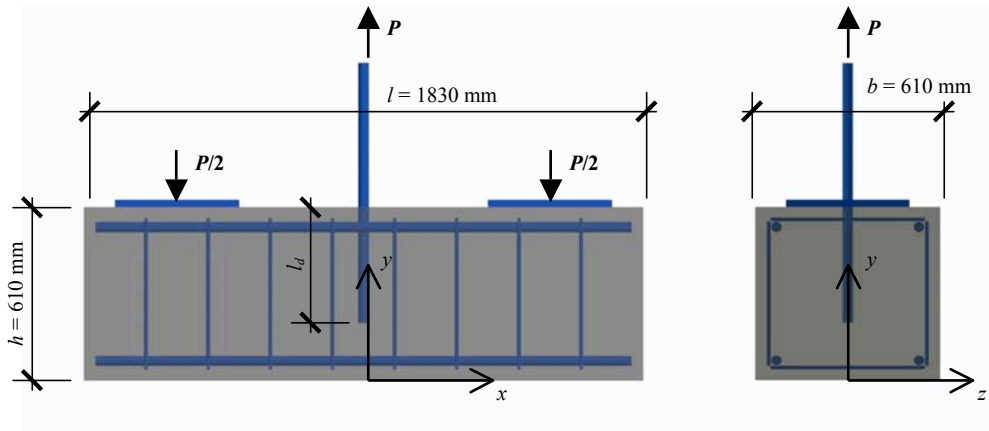


Fig. 1 Elevation and side view of a test specimen for rebar pull-out tests.

The overall dimensions of the tested bent column sub-assemblages were $l \times b \times h = 1830 \times 610 \times 610$ mm. Each specimen had four Grade 60 steel reinforcing bars with diameter $d_b = 36$ mm in the corners as well as one in the center for the actual pull-out. The embedment length for the pull-out rebars were chosen as $l_d = 533$ mm and $l_d = 305$ mm for specimen 1A and 1C, respectively. Ties were Grade 60 $d_b = 13$ mm (#4), spaced at $s = 203$ mm.

Both specimens were loaded using load steps (LS) with increasing amplitude followed by unloading until failure was reached. A Vallen AMSY-5 system with eight channels was used to monitor AE activity. For specimen 1A, eight broadband DECI SE1000-H sensors were used and for specimen 1C eight resonant Vallen SE150-M sensors. According to the calibration sheets, the variation of frequency response was 4 dB and 20 dB for the broadband and resonant sensors, respectively (for a frequency range between 40 and 250 kHz). For non-AE data acquisition, the software DASYLab 8 was utilized. The deformation of the pull-out rebar at the top and bottom ends was monitored during the experiment as well as support movements.

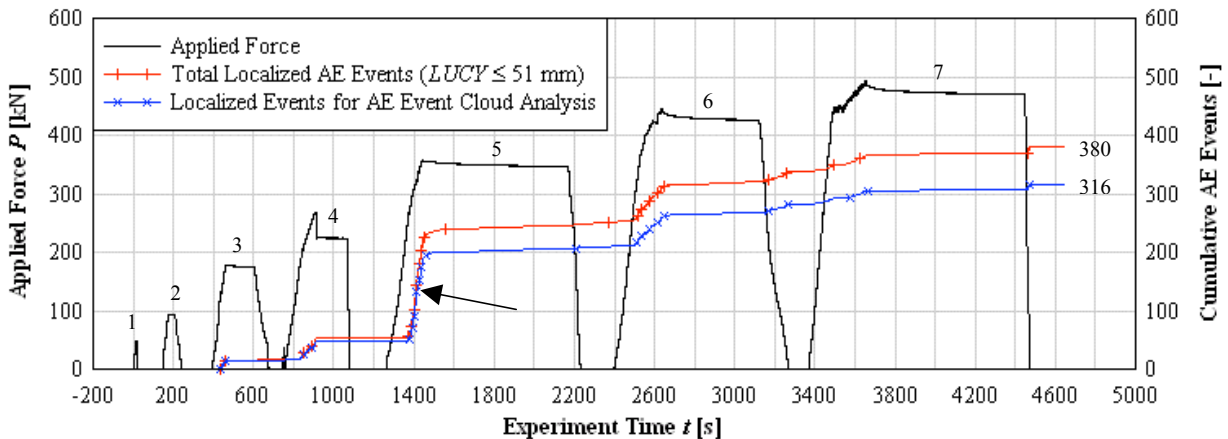


Fig. 2 Applied force vs. localized AE events for specimen 1A.

Figure 2 shows the applied force on the pull-out rebar and localized AE events for specimen 1A. Note that a filter (*LUCY*) was set to exclude inaccurate localization results (see next section for description). The experiment ended after reaching a force of $P_{max} = 492$ kN when the rebar started to enter strain hardening. Most of the AE events were produced in load step five (indicated by arrow) when the first visible surface crack formed on the specimen.

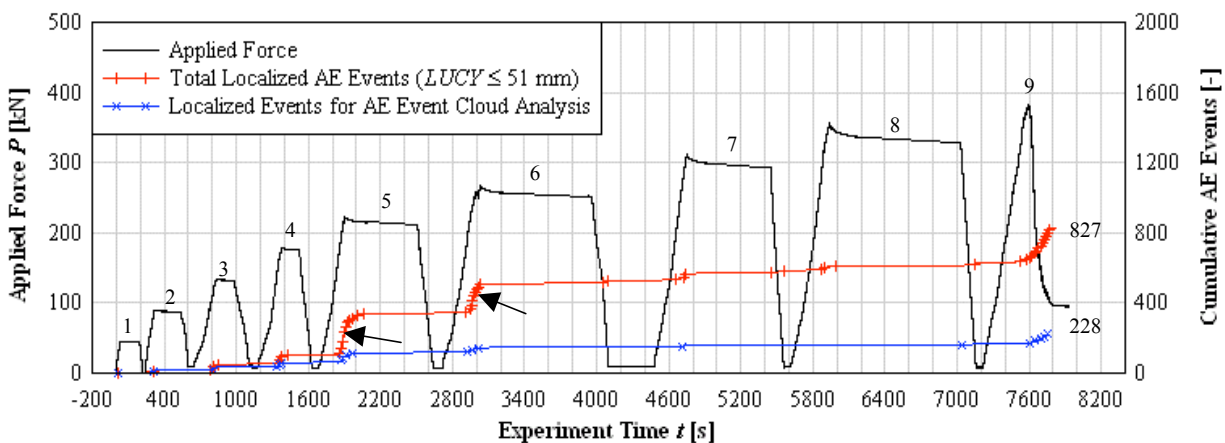


Fig. 3 Applied force vs. localized AE events for specimen 1C.

In Fig. 3, the applied force on the pull-out rebar and recorded AE events for specimen 1C are shown. The experiment was discontinued after reaching a force of $P_{max} = 382$ kN when the rebar pulled out of the concrete. In load steps five and six, the majority of AE events were generated (indicated by arrows). Again, this corresponded well with the occurrence of major cracks on the specimen surface.

3-D AE Event Localization

In a first step, 3-D AE event localization was performed. The arrival-time picking was improved by introducing a floating threshold dependent on the recorded background noise. A factor, sometimes called crest factor, is multiplied by the background noise voltage to determine the threshold. This crest factor was set to 8.0 and 13.0 for the broadband and the resonant sensors, respectively. The threshold updating interval was set to 1.0 second. Pencil-lead breaks were performed on the surface of one of the specimens to quantify localization errors and variability in results. It was found that including five to seven signals in the computation leads to the most accurate localization results. For this study, only the first five arrival times within an AE event were included to maximize the number of localized AE events. This turned out to be helpful in later stages of the experiment where developed cracks distorted stress wave paths and increased localization errors. A comparison with 26 real AE events recorded from one load step was performed using PolarAE, a program developed at the University of Stuttgart, Germany. The average spatial difference of the results over all events was found to be $\Delta_{xyz} = 16$ mm between the two programs. It was concluded that the developed picking and localization options available with the commercial product used for this study was sufficiently accurate for this experiment and the specimen size. A filter setting to eliminate inaccurate localization results was set to $LUCY \leq 51$ mm. *LUCY* stands for *location uncertainty* and is the root-mean-square of the difference between calculated and observed distances between source and sensor that is calculable when at least five arrival times are available. It describes how well a calculated source position explains the observed arrival time differences. Unfortunately, *LUCY* does not contain any directional information. A better representation of the uncertainty would be the principal standard deviations of the numerical least-squares solution.

The first author of this paper has implemented a localization algorithm in MatLab based on Geiger’s method that plots 3-D error ellipsoids with principal standard deviations as axes for each localization result. In future analyses, this algorithm will be used to enhance interpretation of localization results.

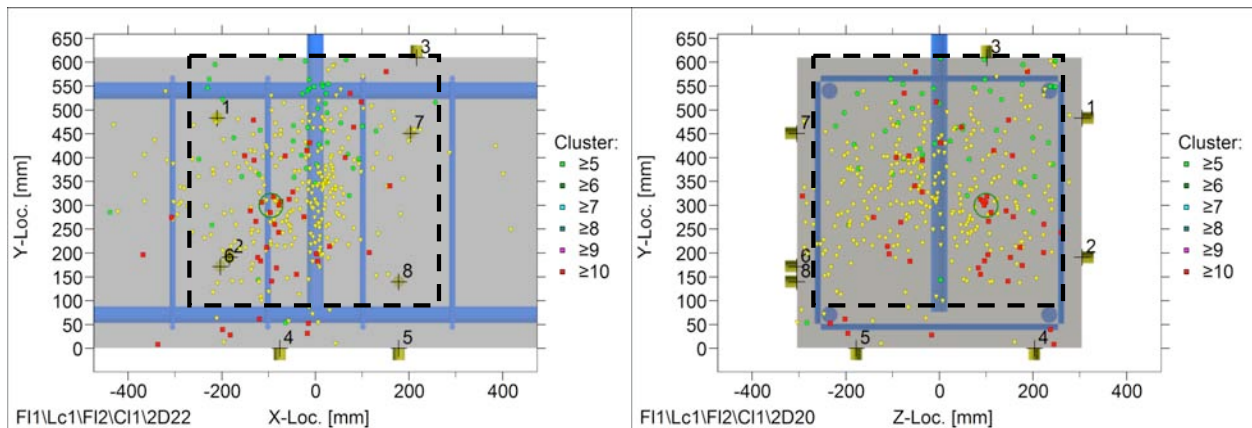


Fig. 4 AE event localization results for specimen 1A.

Figures 4 and 5 illustrate all localized AE events during the experiment. The green circles (●) represent AE events that occurred during the load steps before the major failure (macro-) crack formed, the yellow triangles (▼) the AE events between that observation and the failure load step, and the red squares (■) the AE events during the final load step when the experiment was terminated due to rebar strain hardening and pull-out for specimen 1A and 1C, respectively. The circles represent spatial clusters of AE events that occurred within a sphere with a diameter of 51 mm, which indicates localized activity in a certain area. The numbered yellow cylinders illustrate the AE sensors mounted on the surface of the specimen.

It can be observed that there were fewer localized AE events for specimen 1A than 1C. The reason was that one of the sensors for specimen 1A did not work properly and the utilized broadband sensors are less sensitive than the resonant ones.

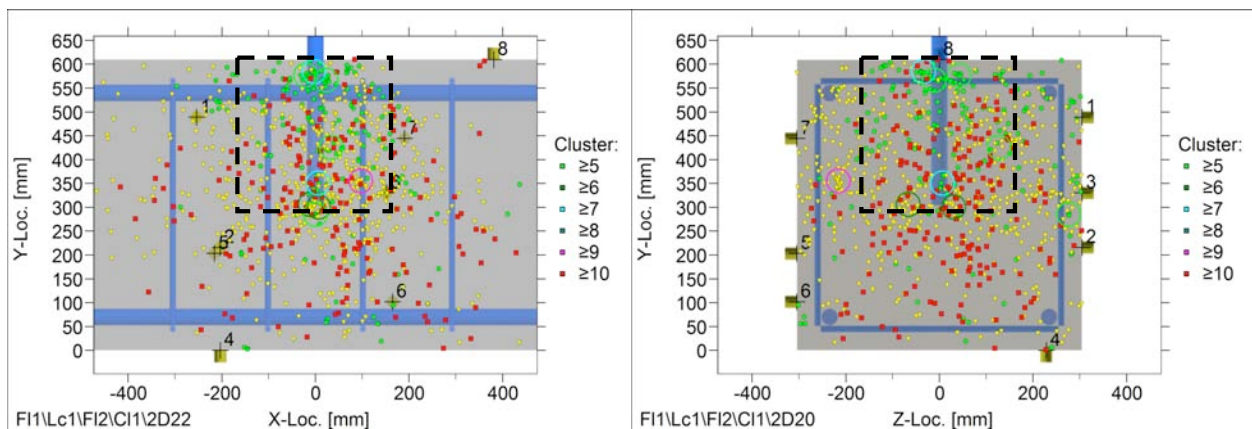


Fig. 5 AE event localization results for specimen 1C.

Indicated with a dashed line in Figs. 4 and 5 are the spatial filter settings used for the analysis of AE event cloud front, to be described subsequently. Only AE events that were identified inside the cube were taken for further analysis. This volume was chosen as a cube with a side length equal to the embedment length of the pull-out rebar, i.e. $l_d = 533$ mm and $l_d = 305$ mm for specimen 1A and 1C, respectively and centered about the rebar.

AE Event Cloud Front Analysis

Many experiments on monitoring of AE activity during rebar pull-out experiments can be found in the literature [2-5] and both qualitative as well as quantitative AE evaluation methods have been applied to the test data. This study intends to use AE event localization as a quantitative means to describe the demand on the pull-out rebar during a load test. The central idea is that there should be an evolution of the location of the captured AE events while going to higher load levels.

Bond stresses are assumed as uniform and their integration leads to a linearly increasing rebar stress over the embedment length. Based on this idealized bond stress distribution, it was expected that AE events are created when a certain stress threshold is crossed along the embedment length (l_d). As higher forces are applied to the pull-out rebar, the higher the stress gradient becomes, and AE events should therefore progress along the embedment length away from the free surface of the specimen. The *AE event cloud front* was identified as the location of the upper quartile (75%) of all localized AE events within one complete load step. A normal distribution of AE events was assumed for statistical evaluation. The depth of progression for this cloud front was then expressed as a percentage of the embedment length and given the variable name q .

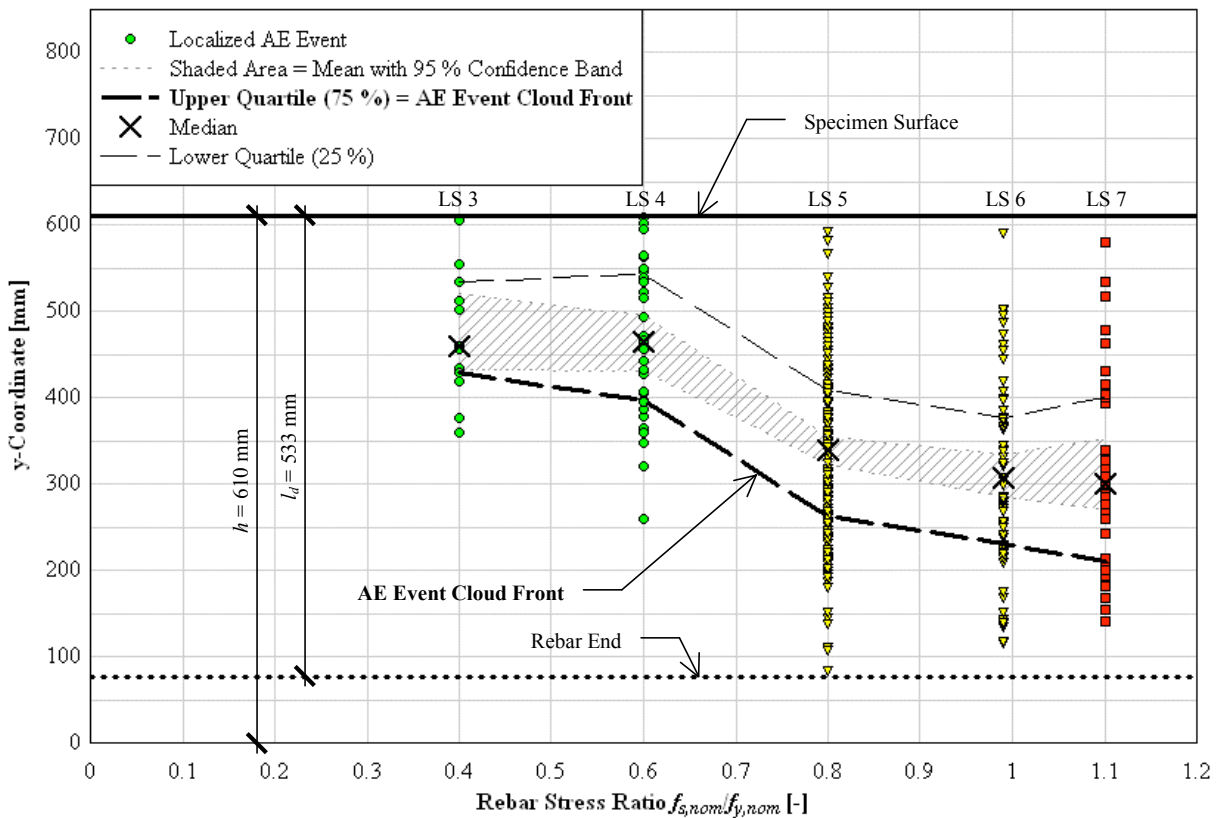


Fig. 6 AE event cloud analysis for load steps 3 through 7 of specimen 1A.

Figures 5 and 6 illustrate the progression of the *AE event cloud front* for all load steps of the two specimens. The y-coordinate corresponds with the longitudinal orientation of the pull-out rebar. Statistical values such as median and mean with 95 % confidence bands for localized AE events are given as well as the *AE event cloud front* (thick dashed line). Some of the first load steps were not included in the analysis because too few AE events occurred.

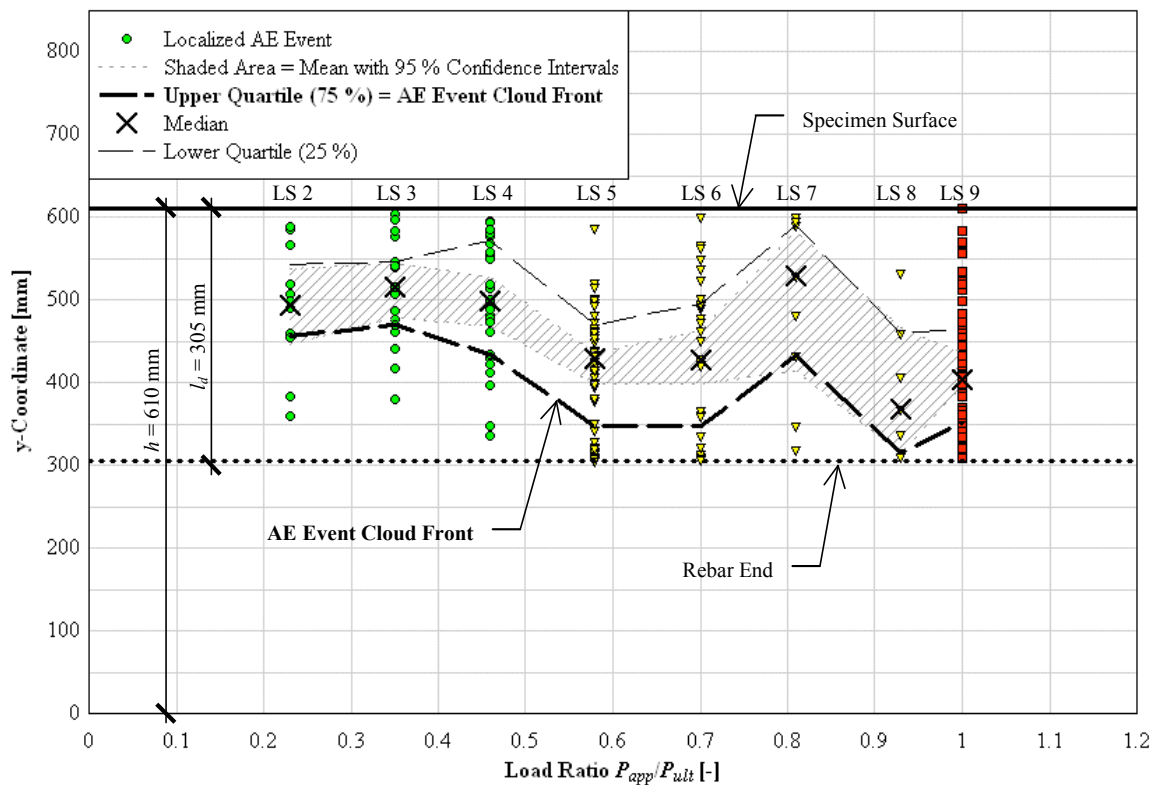


Fig. 7 AE event cloud analysis for load steps 2 through 9 of specimen 1C.

Conclusions and Future Work

A clear trend of progression of the *AE event cloud front* from one load step to the next can be found for specimen 1A, which supports the proposed hypothesis. For specimen 1C, the trend is less clear. This could be due to the fact that only few localized AE events were created. Generally, after big cracks form, localization of AE events becomes more difficult due to distortion of the media. Stress waves travel longer and more convoluted paths, which lead to bigger errors in the computed source location. The maximum value for the progression of the AE cloud front was found to be $q = 75\%$ for specimen 1A where the rebar did not pull-out (experiment discontinued after rebar entered strain hardening) and $q = 96\%$ for specimen 1C where the rebar pulled out of the concrete. It appears that this maximum value could be taken as an indication of the maximum rebar demand.

In a next step, the behavior of other rebar configurations (two and four rebars) with applied normal forces (similar to a real bent cap) will be studied. The final goal will be to evaluate AE data collected from full-scale bent cap experiments and use AE event localization to quantify anchorage demands at overall member failure.

References

1. C. C. Koester, M.S. Thesis, Oregon State University, 2007.
2. G. L. Balazs et al., Magazine of Concrete Research, **177**, Dec. 1996, pp. 311-320.
3. A. S. Kobayashi et al., Experimental Mechanics, **9**, Sept. 1980, pp. 301-308.
4. St. Koeppel, Dissertation ETH Zurich, Technical Report Nr. 272, Feb. 2002.
5. S. Weihe et al., Characterization of damage and failure during the pull-out of a reinforcement bar by acoustic emission and numerical simulation, *1st International Conference on Damage and Failure of Interfaces*, Vienna 1997.

DAMAGE EVALUATION OF POST-TENSIONED CONCRETE VIADUCT BY AE DURING PROOF LOADING

EDOARDO PROVERBIO, GIUSEPPE CAMPANELLA and VINCENZO VENTURI*

Dept. Industrial Chemistry and Materials Engineering, University of Messina, 98166 Messina, Italy. *Sidercem srl, 95045 Misterbianco (CT), Italy.

Abstract

Recent collapses of civil structures (reinforced concrete, prestressed concrete or mixed steel structures, i.e. buildings, bridges, dams, and so on) have demonstrated once again the need for reliable tools for an early monitoring of damage progression. Damages due to deterioration processes, overload, bad design, poor material quality, can grow subcritically until final collapse. Acoustic emission has been successfully used for more than 20 years in industry for monitoring metal equipments (pipelines, pressure vessels, gas tanks, etc.) and the technology is quite mature. The application of the AE technique in the civil engineering requires however the overcoming of several problems related to structural complexity, material inhomogeneity and the high attenuation factor for high-frequency acoustic waves in concrete, and environmental noise. A great effort yet has to be done on data handling and data interpretation.

We have used AE technique for damage evaluation of two severely deteriorated viaducts during proof loading. The viaducts, made at the end of the 1950's along the national road 114 in Sicily (Italy), consist of several spans. Each span was built in a post-tensioned concrete girder configuration. The load test consisted basically of 5 loading steps and 5 unloading steps. For each load test step, it has been possible to evaluate the displacements in the middle, in the border and in the center of the span. It was observed that, during loading phase, the mean AE hits rate, corresponding to a minimum in the mean amplitude, reached a maximum at an intermediate load, while at higher loads a reduced number of AE hits characterized by high mean energy was recorded. AE behavior was asymmetric with respect to the loading sequence (relaxation dominant), indicating the advanced degradation status of the viaducts.

Keywords: Concrete structures, bridge, proof loading, corrosion

Introduction

Segmental cast-in-place post-tensioned structures were extensively used in Italy during the reconstruction processes soon after the Second World War, as innovative design solutions adopted for a rapid and economical building of bridges. After 50 years, most of those structures have formally concluded their design service life, but social and economic reasons frequently force their owners toward rehabilitative solutions instead of undertaking demolition and rebuilding. The rehabilitation project and the evaluation of the residual load-carrying capacity involves the solution of unusual problems arising during the degradation assessment step linked to the peculiar geometry and to the structural weakness of such constructions. For such structures, the main concern is the status of prestressing or post-tensioning cables.

The evaluation of corrosion of the post-tensioning cables (usually grouted in ducts placed in box girder walls) required the use of new, but not yet well established, techniques such as those based on magnetic induction, while indirect techniques such as impact echo could locate grouting defects, but not give any information about cable conditions.

Since the difficulties in accessing to cable anchorage and the impossibilities to re-tensioning

cables themselves the evaluation of mechanical characteristics and performance of the viaducts could be estimated on the basis of a dynamic behavior analysis, whose main limit is however the definition of the right theoretical model. AE technique seems to be very promising in this field since it is not invasive, allows a volume evaluation and at the same time has the possibility to locate discrete defects. AE was however introduced very recently in the field of health assessment of reinforced concrete structures notwithstanding some difficulties to be overcome in the field of data handling and analysis. Relationship between AE signal parameters and failure processes that produce these signals have in fact to be properly defined for example by means of the development of pattern recognition techniques. With the same aim, several health indices as well as “Load ratio”, “Calm ratio”, “Felicity ratio” or “Historical index” have been defined [1-2].

Experimental

The Agrò and Fiumedinisi viaducts, on the national road number 114 on the eastern coast of the Sicily Island were designed in 1954 by Riccardo Morandi and built during 1955-56. They are 13- and 8-spans viaducts, respectively, with the span length of ~22 m. The viaducts are segmental cast-in-place post-tensioned prestressed concrete box girder type, characterized by a five-cell longitudinal trapezoidal void section box girder. Four cast-in-place diaphragms were provided at each end and along each span of the bridge. An 11-cm-thick top concrete slab was monolithically cast-in-place. The post-tensioning ducts of 40-mm diameter were drilled in-place and the post-tensioning internal tendons consisted of 5-mm wires bundle. Following detailed visual and instrumental inspection, which showed a critical degradation status due to seaside vicinity and to the “advanced” age [3], it was decided to evaluate damage effects on structural behavior by means of proof-loading test and a simultaneous AE monitoring.

The set-up of the AE system involved a long series of calibration tests on concrete samples at rest, carrying out the scratching and breaking of pencil-leads of different hardness and dimensions on the surface of samples; these tests have been carried out in different environments to test the effectiveness of filter system and to calibrate the “trigger threshold” suitable to extract the significant components of AE signals.

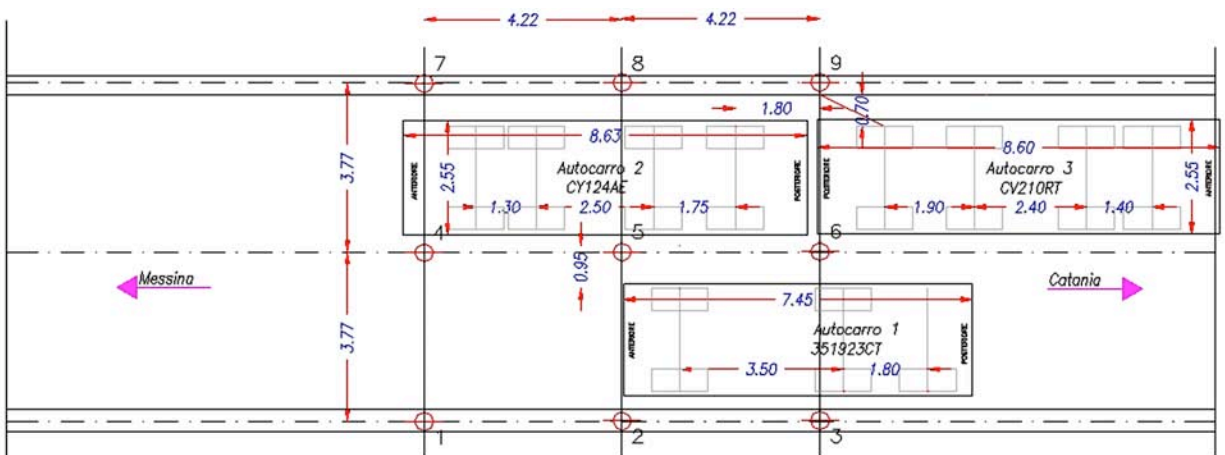


Fig. 1. Scheme of the static loading condition during the fourth loading step.

The proof loading test consisted basically of 5 load steps:

I° load test step: the load was produced by a 30 tons (0.3 MN) truck set in the middle of the span;

II° load test step: the load is produced by a 30 tons truck set in the middle and by a 20 tons

(0.2 MN) truck set on the parallel lane; Total = 0.5 MN

III° load test step: the load is produced by two 30 tons trucks set on the same lane; 0.6 MN

IV° load test step: the load is produced by two 30 tons trucks set on the same lane and a 20 tons truck set on the parallel lane; 0.8 MN

V° load test step: the load is produced by two 30 tons (0.3 MN) trucks set on the same lane and a 20 tons (0.2 MN) truck plus 30 tons (0.3 MN) truck set on the parallel lane; 1.1 MN.

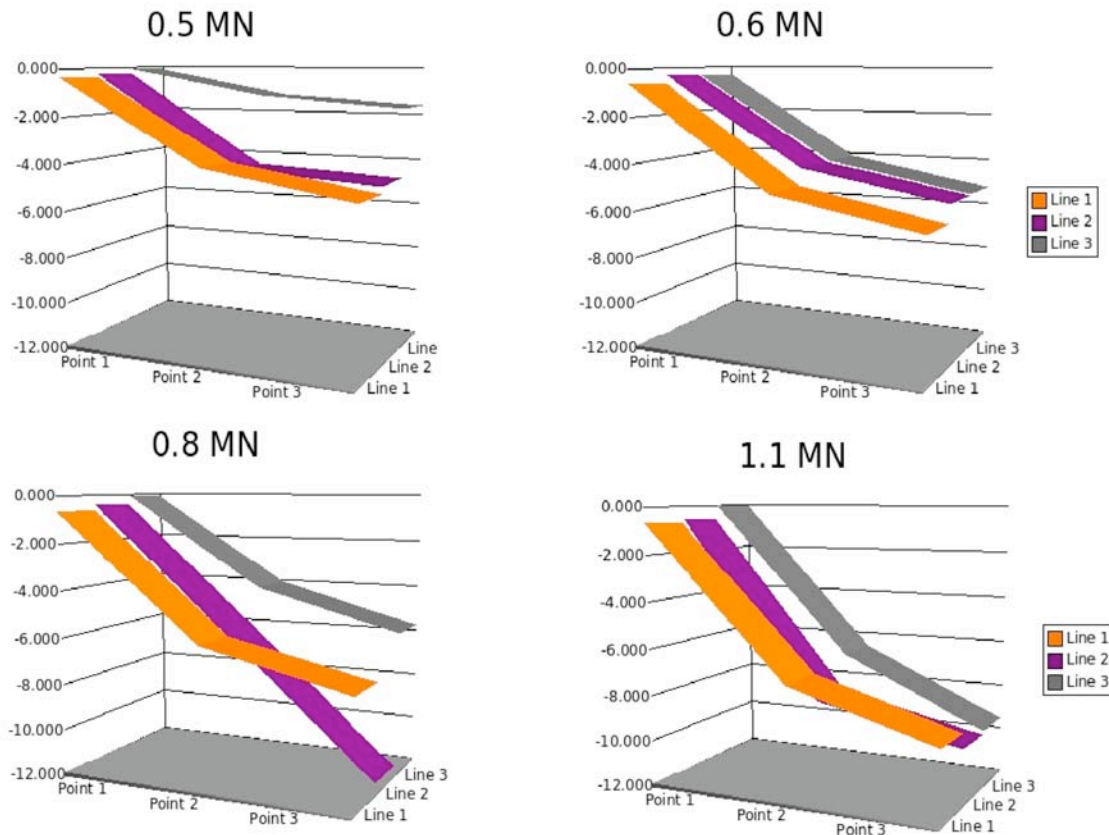


Fig. 2. Displacement of the measuring point (Fig. 1) on the viaduct span during proof loading.

A scheme of the 4th load test step with the indication of displacement measurement points is reported in Fig. 1. For each load test step, it has been possible to evaluate the displacements in the middle of the span in the border and in the center (Fig. 2). AE sensors adopted were VS30-V flat response type (23-80 kHz bandwidth, 140 pF capacitance), a total of ten sensors were used and positioned on the lateral side of different segments of box girders as shown in Fig. 3.

Results

The AE application has proven effective to detect vibration phenomena produced by trucks crossing on the structure, and the intense AE activity recorded was connected to the residual stress in the structure induced by the post-tensioning system, while the events recorded during the first phase seems to be connected with the phenomena of internal rearrangement of pre-existing defects.

Considering the huge amount of data recorded, only a limited amount of available results are reported here and related to span No. 12 of the Agrò viaduct. Hits, energy and amplitude of AE events have been reported as mean values of the total amount of events recorded during a specific loading step (i.e., within a specific time interval).

An example is reported in Fig. 4 and refers to the second load step. One of the main aspect that must be highlighted is that the great amount of hits have been recorded during transient phases (loading and unloading), while, at the maximum load, the structures remained almost silent (Fig. 4A). On the contrary, the energy of the AE events reached the maximum value at the intermediate loading (0.3 MN) as reported in Fig. 4B. It is important to keep in mind that by considering the specific loading procedure, which considered the presence of asymmetric loads, the maximum displacements of all the measuring points of the side beams do not correspond to the maximum load applied (Fig. 2). In Fig. 5, relationship between AE parameters for sensors 7 and displacements measured at the nearest measurement points (3 and 6) are reported.



Fig. 3. AE sensors positioning on box girders.

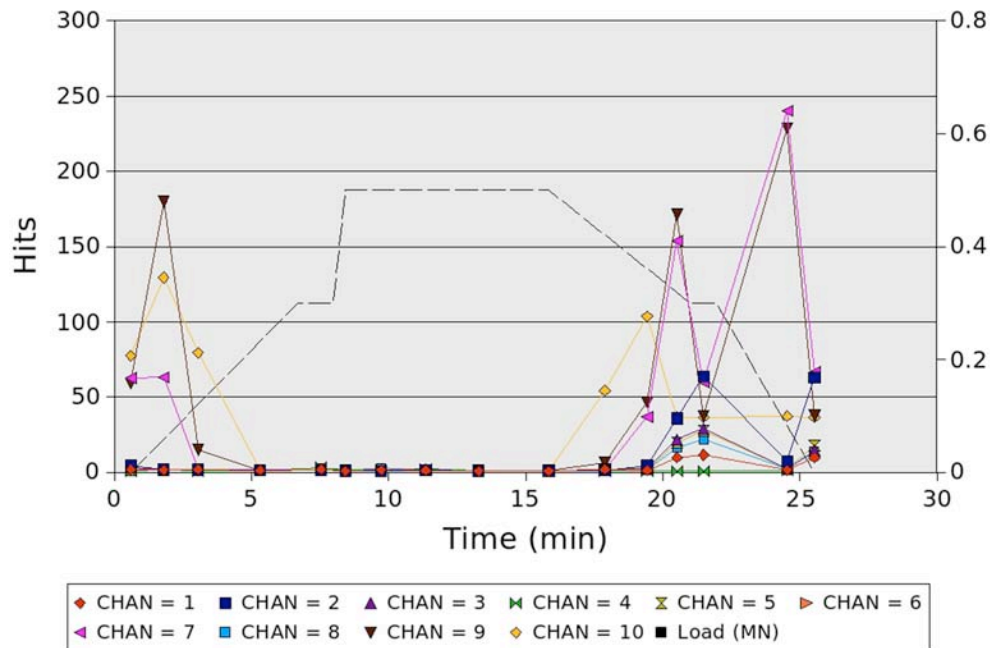


Fig. 4A. Mean numbers of hits for all channels vs. time for the second load step (load: dashed line; load scale on the right side in MN).

As a further evaluation of the degradation status of the viaduct, we carried out a relaxation ratio analysis [4]. Relaxation ratio is defined as the ratio of the average energy during unloading phase to the average energy during loading phase. Considering that AE activity during the unloading process is generally an indication of structural instability [5], a relaxation ratio greater than one (relaxation dominant) implies a defective structure.

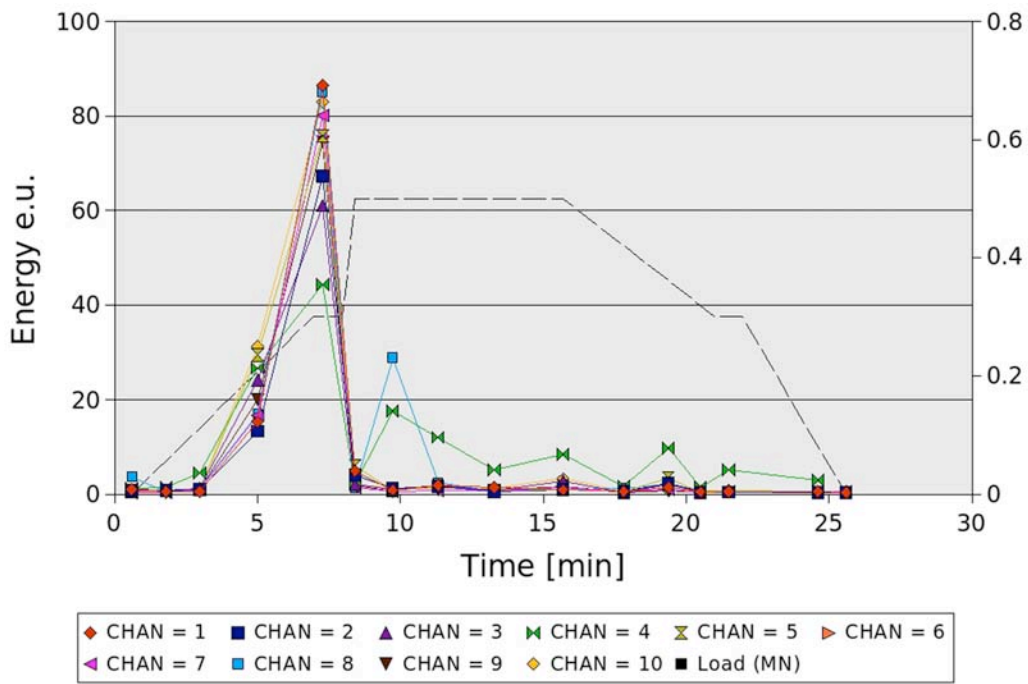


Fig. 4B. Mean energy for all channels vs. time for the second load step ($1 \text{ eu} = 10^{-14} \text{ V}^2 \text{ s}$; load: dashed line; load scale on the right side in MN).

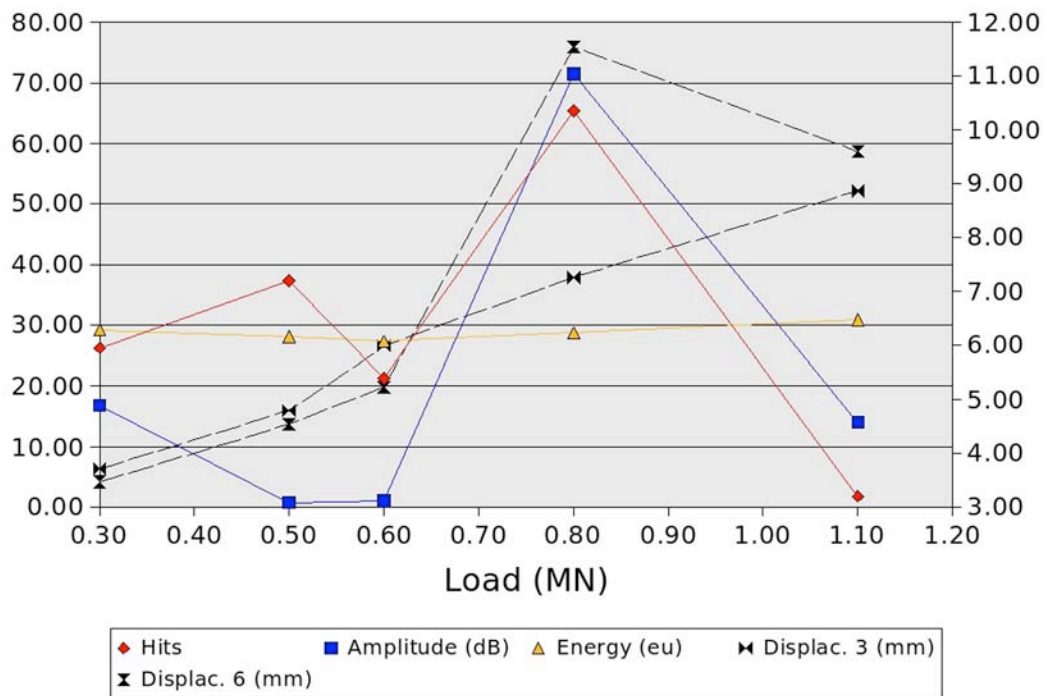


Fig. 5. Mean hits, amplitude and energy for channel 7 during loading steps matched with effective displacement measured at points 3 and 6 (Displacement scale on right side).

In Fig. 6, results obtained on the second box girder are reported. A strong peak in the relaxation ratio during the third loading condition is evident for channels 3, 8 and 9 (on the same box girder side), while at higher load condition (0.8 MN) the peak was recorded on channel 4 (on the opposite side of the box girder).

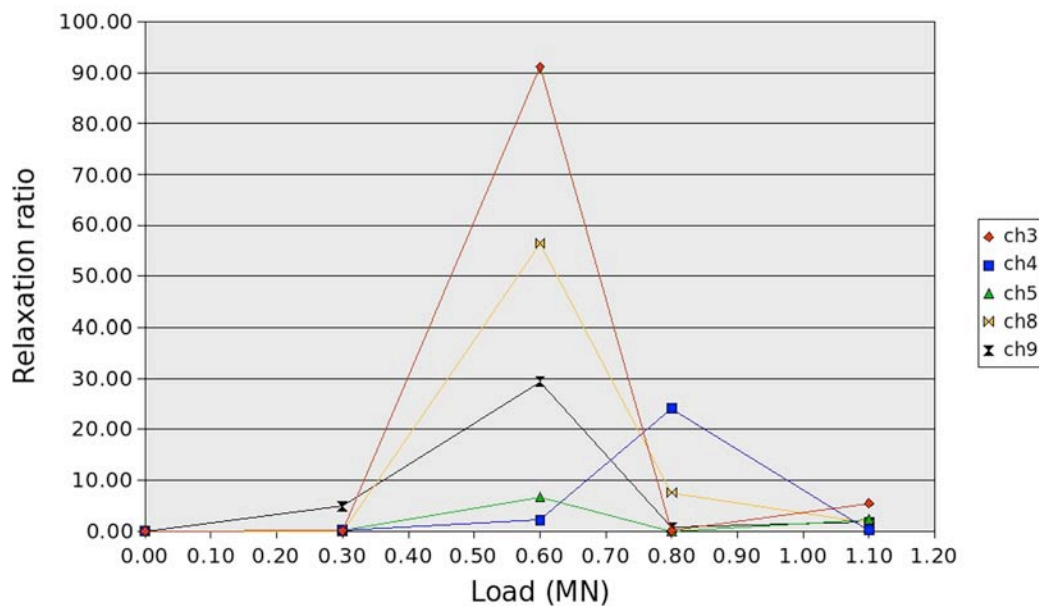


Fig. 6. Relaxation ratio for channels 3-4-5 and 8-9 on box girder No. 2.

Conclusions

We used AE technique for damage evaluation of two severely deteriorated viaducts during proof loading. The viaducts, made at the end of the 1950s along the national road 114 in Sicily (Italy), consist of several spans. Each span was built in a post-tensioned concrete girder configuration. It was observed that during loading phase, the maximum mean AE hits rate, corresponding to a minimum in the mean amplitude, was reached at an intermediate load, while at higher load a reduced number of AE hits characterized by high mean energy was recorded.

The application of the relaxation ratio analysis indicated the structural instability (relaxation dominant) of the two viaducts.

Acknowledgment: The present research was carried out with the financial support of the Ministry of University and Scientific Research in the frame of the research project n°12278 “New technologies for the evaluation of deterioration and the control of prestressed reinforced concrete structures”.

References

1. L. Golaski, P. Gebiski and K. Ono, *J. Acoustic Emission*, **20**, 2002, 83-98.
2. Recommended Practice for In-Situ Monitoring of Concrete Structures by Acoustic Emission, NDIS 2421, Japanese Society for Non-Destructive Inspection, 2000.
3. E. Proverbio, G. Laganà, V. Venturi, *Integrated Lifetime Engineering of Buildings and Civil Infrastructures Proc. 2nd Int. Symp. ILCDES 2003*, pp.239-244
4. S. Colombo, M.C. Forde, I.G. Main, J. Halliday and M. Shigeishi, *Materials and Structures*, **38** (11), 2005, 851-856.
5. M. Ohtsu, M. Uchida, T. Okamoto and S. Yuyama, *ACI Structural Journal*, **99** (4), 2002, 411-417.

ASSESSING DAMAGE EVOLUTION IN CORRODED REINFORCED CONCRETE BY ACOUSTIC EMISSION

EDOARDO PROVERBIO, LESZEK GOLASKI¹ and ROBERTO BONFIGLIO²

Dept. Industrial Chemistry and Materials Engineering, University of Messina, Salita Sperone 31, 98166 Messina, Italy. ¹Dept. Civil Engineering, Kielce University of Technology, 25-314 Kielce, Poland. ²National Firefighter Corp, I.S.A. (Fire Higher Institute), 00154 Rome, Italy.

Abstract

The influence of damage due to reinforcement corrosion on AE behavior under mechanical load was evaluated on reinforced concrete beams. Corrosion of reinforcement was accelerated by applying electrical current of 100 or 200 $\mu\text{A}/\text{cm}^2$ in a salt bath. Samples were continuously monitored by means of 5 AE sensors. After two weeks of accelerated corrosion condition the samples were tested by AE without current. Each sample was then gradually loaded under AE monitoring with three-point bending machine in order to evaluate its mechanical behavior in comparison with the beams without corrosion damage.

AE data were subjected to calm ratio analysis. We found that the low strength concrete samples treated with electric current showed the highest calm ratio values in the first and intermediate loading steps. We defined and used "load-hold" calm ratio in lieu of "unload" calm ratio. NOESIS classification of the AE signals was also performed by supervised method.

Keywords: Concrete, corrosion, damage evaluation, pattern recognition, load-hold calm ratio

Introduction

The application of the AE technique in the civil engineering still requires the overcoming of several problems related to structural complexity, material inhomogeneity and the high attenuation factor for high frequency acoustic waves in concrete, and environmental noise. Relationship between AE signal parameters and failure processes that produce these signals have to be properly defined by means of signal analysis procedures, but these need a database of reference AE signals. The reference signals have to be identified in laboratory tests on samples, for which the dominant failure mechanism was under control.

Different approach in AE in signal analysis could be used. AE signal depends on different transfer functions: that one related to the source (H_s), to the transmitting media (H_m) and finally to the transducer (H_t), so in the frequency domain AE signal can be expressed by the following equation in terms of convolution integral (*)

$$H_{AE} = H_s * H_m * H_t \quad (1)$$

The AE waveform in the time domain could be obtained by means of an inverse Fourier transform of H_{AE} . However, the use of deconvolution analysis for AE hardly developed in the last twenty years mainly because this technique is unstable and sensitive to noise. Other factors also affected depending on the AE source and on the possible propagation path of the acoustic waves, so it was difficult to obtain outcomes whose validity could be confirmed. Difficulties in defining H_m for different sample geometries reduce furthermore the applicability of this analysis approach.

At the end of the 1980s, Ohtsu and Ono [1] developed an AE generalized theory on the basis of the elastodynamics theory and on dislocation models. AE sources are represented as dislocation movements including discontinuities and displacements. Ohtsu and Ono [2] extended

then source representation in the generalized theory relating cracks to moment tensor. Main vectors and values of the moment tensors identify crack orientation and displacement (or displacement area). On the basis of this theory, it was demonstrated [3] that the distribution of arrival time amplitude renders the source characteristics and the moment-tensor components. Such results allowed the differentiation of tensile from shear sources and was at the basis of the SiGMA analysis that was successfully applied to reinforced concrete [4]. Takemoto and Hayashi [5] starting from such results by mean of a computerized system developed a simulation analysis that included a procedure for the optimization of the correspondence between observed and simulated waveforms. Further models were developed by Suzuki et al. [6-8].

In this paper, the preliminary results of an experimental research aimed to evaluate the feasibility to distinguish different AE sources are reported. AE signals were recorded from reinforced concrete samples during accelerated corrosion tests and during loading test of the pre-damaged samples. Waveform analysis allowed to distinguish three different types of AE sources plausibly being linked to: rebar corrosion, concrete micro-cracking at the steel/concrete interface and concrete macro-cracking.

Experimental

Six concrete beams (150 x 25 x 25 cm) were made using two different concrete mix designs (Table 1). Three samples were made using the mix design 1 and three with mix design 2. In four samples (two for each type), calcium chloride (3% by cement weight) was added to the concrete mix. Five internal stirrups were used. The stirrups at the beam extremities had been welded to four longitudinal reinforcing bars (12-mm diameter), and the remaining ones had been fixed to the longitudinal reinforcing bars by means of steel wire but electrically insulated with rubber tubing (Fig. 1). Such configuration was adopted in order to promote concrete spalling at the beam edges.

Table 1. Concrete mix designs

Component	Dosage (kg/m ³)	
	Mix design 1	Mix design 2
Water	120	124
Cement	355	430
Basalt aggregate 1	590	637
Sand	707	717
Basalt aggregate 2	668	637
Additive 1	1.41	1.92
Additive 2	1.06	1.29
W/C	0.34	0.29
R _{ck} (MPa)	35	45

Three vertical steel bars emerging from concrete beam and used as electrical connections were welded to one longitudinal bar. After curing, concrete beams were immersed in a bath with a 3mass% sodium-chloride solution, and a copper plate was used as counter electrode.

Accelerate corrosion was obtained by an anodic current flow of 100 $\mu\text{A}/\text{cm}^2$ for 170 hours and 200 $\mu\text{A}/\text{cm}^2$ for 170 hours more. During accelerated corrosion test, AE was monitored by means of three sensors (sensors n°1-3) placed on concrete surface and two sensors (sensors n°4-5) connected to vertical steel bars.

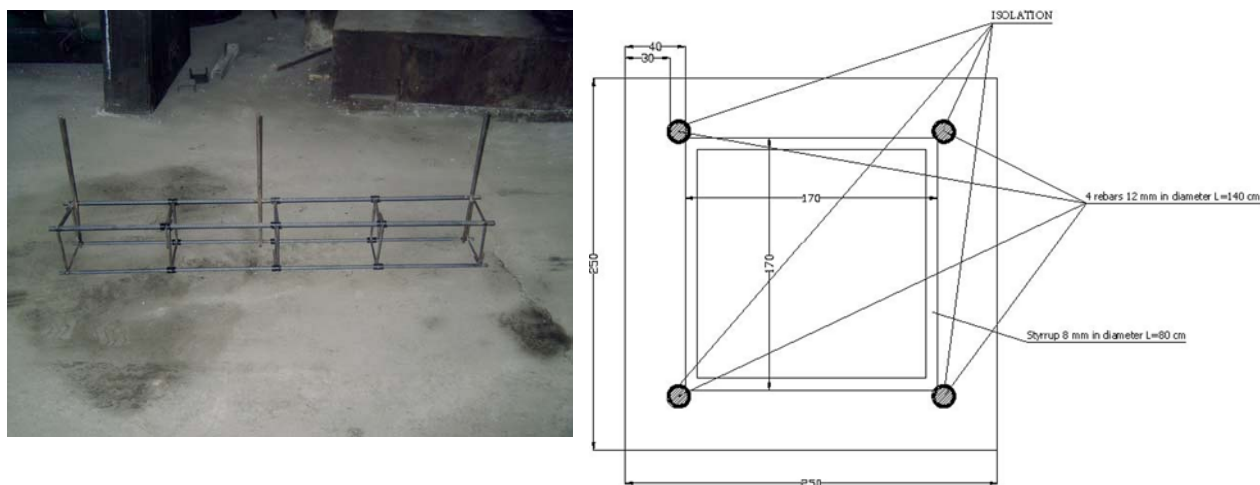


Fig. 1. Reinforcing bars and stirrups position in concrete beams.

Sensors on concrete surface were positioned at equal distance to each other. Sensors used were broadband type Vallen VS30-V, with bandwidth 23–80 kHz. Threshold level was set at 40 dB. Following a test, acoustic wave attenuation for concrete beam was set to 15 dB/m. AE monitoring was performed without current flow.

After accelerated corrosion, test beams were subjected to three-point bending with increasing load up to the incipient failure according to the sequence reported below.

- 1) 0 kN a 50 kN, loading rate 0.05 kN/sec;
- 2) 5 minutes at constant displacement starting from a load of 50 kN;
- 3) 50 kN a 75 kN, loading rate 0.05 kN/sec;
- 4) 5 minutes at constant displacement starting from a load of 75 kN;
- 5) 75 kN to 87.5 kN, loading rate 0.05 kN/sec;
- 6) 5 minutes at constant displacement starting from a load of 87.5 kN;
- 7) 87.5 kN to 100 kN, loading rate 0.05 kN/sec;
- 8) 5 minutes at constant displacement starting from a load of 100 kN;
- 9) Unloading step from 100 kN to 0 kN in 30 sec;

Table 2. Type of samples used and accelerated corrosion testing set-up.

Beam n°	R _{ck} (MPa)	Chloride	Accelerated corrosion
1	350	3%	Yes
2	350	3%	No
3	350	No	No
4	450	3%	Yes
5	450	3%	No
6	450	No	No



During loading test a different configuration of the AE acquisition system was adopted. Six sensors positioned on concrete surface were used (coordinates of sensor position are indicated in brackets, coordinates origin was located at the lower left corner of the beam, Fig. 2):

- Sensor n°1 (52.5; 12.5; 25) broadband type VS30-V; sensor n°2 (92.5; 12.5; 25) 55-kHz resonant sensor; sensor n°3 (92.5; 12.5; 0) broadband; sensor n°4 (52.5; 12.5; 0) 55-kHz;

sensor n°5 (0; 12.5; 12.5) broadband; sensor n°6 (145; 12.5; 12.5) 55-kHz.

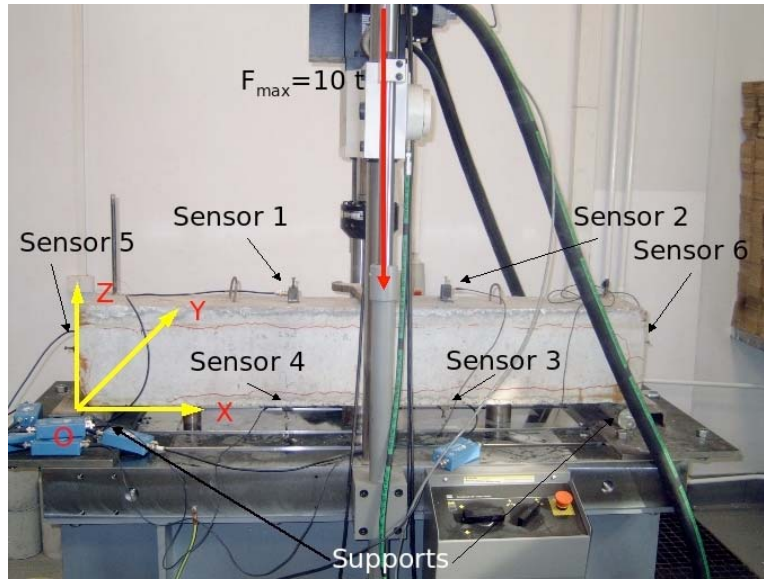


Fig. 2 Load test set-up.

Results

Corrosion phenomena had been clearly identified by AE technique, in particular when corrosion promoted concrete cracking at the steel/concrete interface. For low-strength concrete, it was observed that the number of recorded events grew after current application and stabilized after some days (a slight increase in the AE activity was noted after the application of the 200- $\mu\text{A}/\text{cm}^2$ current density), whilst for high-strength concrete the number of hits reduced with time (Fig. 3). The number of hits recorded on steel bars was from one to two orders of magnitude higher than that recorded from sensors located on concrete surface.

At the end of the accelerated corrosion test, AE events have been analyzed by mean of the Vallen VisualClass software. Three different classes of events were evident for signals collected from steel bars: AE events included in Class 1 showed the higher duration (1100 μs), the main frequency component was at 30 kHz with minor components at 26 and 22 kHz. Class 2 signals were characterized by the duration of about 900 μs and the main frequency component at 28 kHz. Class 3 signals were characterized by the duration of about 800 μs and the main frequency component at 100 kHz. Signal classified in Class 3 showed low rise times and reduced amplitude and were associated to corrosion processes on steel surface. Concerning sensors located on concrete surface, all three signal classes were characterized by the main frequency component at about 18 kHz.

As far as the step-loading test was concerned, the use of calm ratio analysis highlighted interesting aspects. The calm ratio is the number of cumulative AE activities during the unloading process/total AE activities during the last loading cycle up to the maximum [9]. In our case, there was no proper unloading step, because it was decided to keep the sample loaded at constant displacement. Calm ratio was therefore calculated as the ratio between the total AE events during the constant displacement step to the number of total AE hits during the previous loading step. This is “load-hold” calm ratio, to be distinguished from “unload” calm ratio [9].

The load-hold calm ratio analysis (Table 3) showed that the sample No. 1 (damaged during the accelerated corrosion test) showed the higher values during first steps (a calm ratio bigger

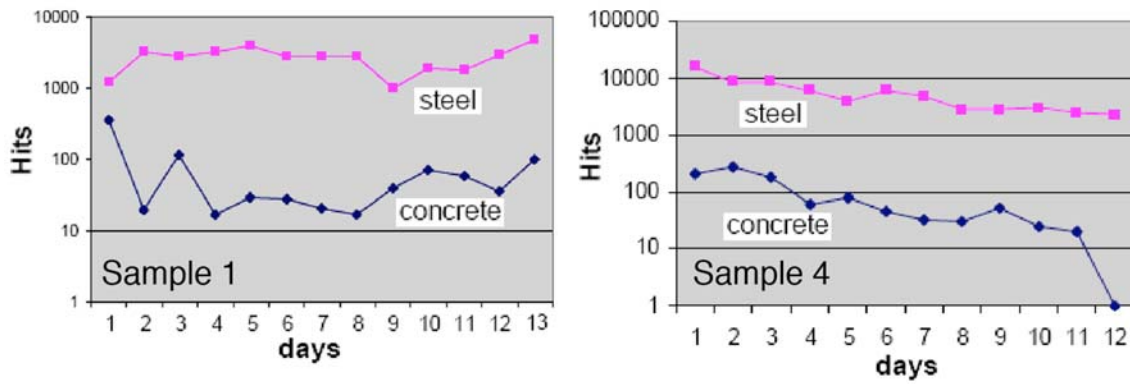


Fig. 3. Hits vs. time during accelerated corrosion tests.

than 1 is related to a damaged structure). In the third stage (steps 5-6) the sample No. 6 showed the maximum value of calm ratio (1.53).

A structurally serious damage condition should in fact result in a relaxation phase being dominant and thus a calm ratio greater than one. Some of the results showed, however, a disagreement with such assumption, which was thought to be due to concrete property variations from different aging conditions and to different corrosion/degradation conditions.

Table 3. Calm ratio analysis results

Beam n°	Calm ratio sensors 1 – 3 - 5	Calm ratio sensors 2 – 4 - 6	DF/F
Steps 1-2			
1	0	1.04	0.21
4	0.07	0.24	0.04
5	0.38	0.44	0.06
6	0.35	0.13	0.08
Steps 3-4			
1	0.52	0.76	0.10
4	0.08	0.32	0.05
5	0.33	0.24	0.05
6	0.84	0.18	0.06
Steps 5-6			
1	1.24	0.65	0.09
4	0.07	2.52	0.06
5	0.90	1.67	0.06
6	1.39	0.61	0.07

The application of NOESIS classification by supervised method to the signals allowed the identification of different AE sources during load test as shown in Fig. 4. Further experiments

are needed to evaluate in which specific conditions the analysis may be successful and to establish the limit of its application. It will also be necessary to make other loading tests, with unloading cycles, and a load factor analysis to evaluate the damage state of the concrete beams.

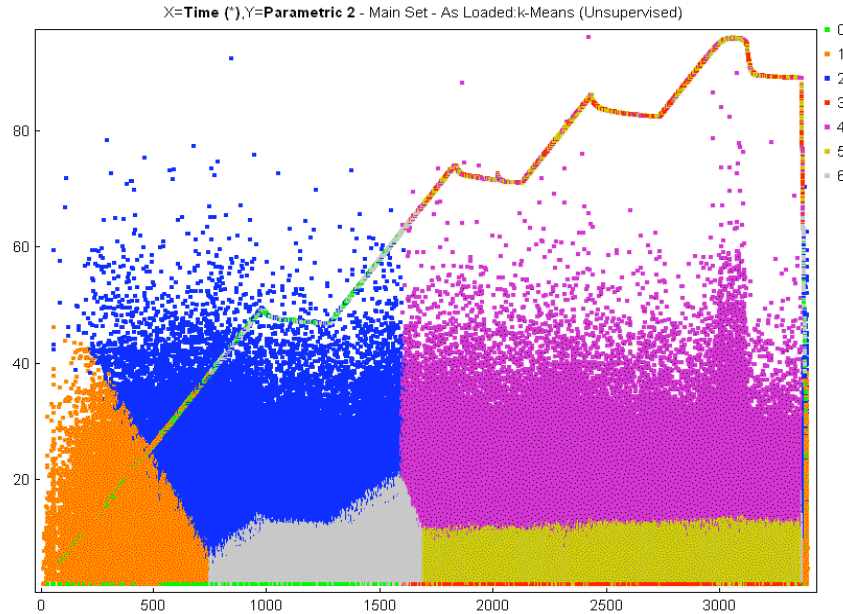


Fig. 4. Rise time values vs. time (loading phases identified by step curve) and AE classification following NOESIS procedure.

Conclusions

AE technique provides a suitable instrument for the identification of corrosion phenomena and corrosion-related damage in reinforced concrete samples. However, relationship between AE signal parameters and failure processes that produce these signals have to be properly defined by means of an improvement of pattern recognition techniques. In this work, AE data were treated by means of calm ratio analysis. We defined and utilized a new parameter, “load-hold” calm ratio. From this analysis, we found that the low-strength concrete samples treated with electric current showed the highest calm ratio values in the first and intermediate loading steps. NOESIS classification of the AE signals was also performed allowing the identification of five classes of AE sources.

References

1. M. Ohtsu and K. Ono, *J. Acoustic Emission*, **3**, 1984, 27-40.
2. M. Ohtsu and K. Ono, *J. Acoustic Emission*, **5**, 1986, 124-133.
3. M. Ohtsu and K. Ono, *NDT Intl.*, **21**, 1988, 143-152.
4. M. Shigeishi and M. Ohtsu, *Acoustic Emission*, **6**, 1992, 211-217.
5. M. Takemoto and Y. Hayashi, *J. Acoustic Emission*, **7**, 1988, 185-192.
6. H. Suzuki, M. Takemoto, K. Ono, *J. Acoustic Emission*, **11**, 1993, 117-128.
7. H. Suzuki, T. Kinjo, Y. Hayashi, M. Takemoto and K. Ono, *J. Acoustic Emission*, **14**, 1996, 69-84.
8. H. Suzuki, M. Takemoto and K. Ono, *J. Acoustic Emission*, **14**, 1996, 35-50.
9. M. Ohtsu, M. Uchida, T. Okamoto, S. Yuyama, *ACI Structural Journal*, **99**(4), 2002, 411-417.

IMPACT IMAGING METHOD TO MAP DAMAGE IN CONCRETE BRIDGE DECK SLABS

STEPHEN D. BUTT, VIDYADHAR LIMAYE¹ and JOHN P. NEWHOOK²

Faculty of Engineering, Memorial University, St. John's, Newfoundland and Labrador, Canada;

¹MacDonnell Consulting Group Limited., Halifax, Nova Scotia, Canada;

²Dept. of Civil & Resource Engineering, Dalhousie University, Halifax, Nova Scotia, Canada

Abstract

An acoustic impact imaging method was developed to map damage in concrete bridge deck slabs and was evaluated by conducting a survey on a damaged full-scale bridge deck model. The imaging system consisted of a mechanical hammer source, two acoustic sensors and a digital waveform recorder. Imaging surveys were conducted along transverse lines that resulted in acoustic measurements on a 30-x-30-cm grid covering the entire upper surface of the slab. Acoustic measurements were processed to determine relative attenuation and then displayed using spatial imaging software. The resulting images showed increased levels of attenuation around punch-out failure zones and coinciding with many of the cracks mapped on the upper deck surface. Overall, the imaging technology showed good potential as a means of rapidly and nondestructively mapping damage in concrete bridge deck slabs.

Keywords: Impact imaging method, damage survey, concrete bridge deck inspection, structural health monitoring, acoustic transmission technique, acoustic attenuation.

Introduction

A simple and robust acoustic impact method was developed to identify damage in concrete bridge deck slabs by measuring the relative signal attenuation between two acoustic sensors [1]. This technique was applied to monitor progressive damage during fatigue testing of a full-sized model of a bridge deck slab at the Heavy Structures Laboratory at Dalhousie University, Halifax, Canada. Testing ended with punch-through failure of the deck and details of the pre-failure acoustic monitoring are presented in related publications [1-3]. This paper is focused on the related Impact Imaging Method (IIM) which was developed for post-failure mapping of damage in the bridge deck model. The IIM is an improvement over many existing acoustic impact methods, which have been used for several decades to map damage in engineering structures [e.g., 4], since it incorporates image generation to enhance damage resolution. The objective of this work was to evaluate the potential of the IIM to provide reliable mapping of bridge deck slab damage to aid inspection of bridges in-service.

The bridge deck slab model measured 12.2 m x 3.0 m on plan and was divided internally into four 3.05 m long panels along its length, each with varying internal reinforcement. Panel A was the control panel with no internal reinforcement while Panel B was similar to Panel A, but with a 75-mm high crack trainer midway along its length. Panel C had a bottom mesh of GFRP crack control reinforcement, and Panel D had a bottom mesh of steel crack control reinforcement. Each panel was tested under step-wise increasing fatigue loading to simulate wheel loading in-service until punch-through failure of the panel by the formation of a punch shear cone beneath the loading pad. Throughout testing, internal and external measurements of load, displacement and strain were made, and detailed mapping of visible cracks were made at regular intervals (Fig. 1). After all 4 deck slab panels had failed, the IIM was used to map damage over the full area of the deck

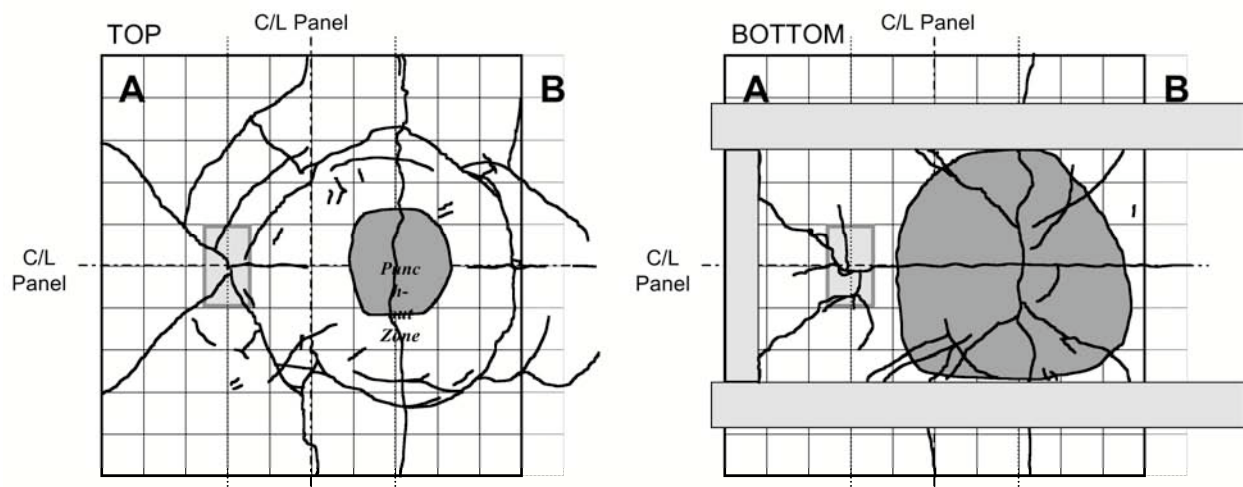


Fig. 1. Crack patterns mapped on the top and bottom surfaces of Panel A after punch-through failure. The punched-out conical slab is shaded in gray.

using the methodology described in the next section. Further details regarding the deck slab model fabrication, configuration, instrumentation and testing procedures are provided in related publications [5, 6].

Acoustic Survey Method

Acoustic System and Survey Procedure

The acoustic system consisted of a mechanical acoustic source, two acoustic sensors, a PC-based acoustic signal digitizing and recording system, and custom data processing software [1]. For the damage survey, the acoustic source was a ball-peen hammer that was struck onto thin steel plates, measuring approximately 7.5 x 7.5 cm, that were mounted on the side of the deck model at mid-height using quick-setting epoxy. The acoustic sensors were Physical Acoustics Corp. R6I acoustic transducers with a frequency range of 25 to 110 kHz, and were mounted on the upper deck utilizing vacuum grease as an acoustic couplant.

Survey Procedure

The acoustic survey was conducted over the top surface of the deck on survey lines oriented along the transverse direction, i.e., along the short dimension of the deck slab. The first survey line was situated 30 cm from the transverse edge of Panel D and adjacent lines were spaced at 30 cm along the longitudinal direction. Details of the survey procedures along each transverse line are given in Fig. 2. Along each survey line:

- a) One acoustic sensor (reference sensor) was fixed at a position 30 cm from the edge of the panel.
- b) The second sensor (active sensor) was positioned at a position 30 cm further along the survey line from the reference sensor.
- c) The hammer source was struck on the steel plate, resulting in the recording of the same waveform as it propagated past the reference and active sensors. Multiple hammer strikes were made and later averaged during data processing.
- d) The active sensor was moved to a new position 30 cm further along the survey line and Step c) was repeated.
- e) Step d) was repeated until the active sensor was positioned in its final location at the longitudinal centerline of the deck slab.

Steps a) through e) were then repeated for the next transverse survey line. When the survey was completed along one side of the deck, the survey was repeated on the other side of the deck with the final active sensor positions also ending at the longitudinal centerline of the deck. At the completion of this procedure a reference or active sensor had been positioned at every point of a 30-x-30 cm grid pattern covering the entire upper surface of the deck.

Acoustic Data Processing

The acoustic waveform magnitude measured by each sensor for the hammer strikes was computed by summing the positive area under the recorded full waveform to get the integrated amplitude I_{Amp} . The normalized magnitude M of each recorded waveform was then determined by:

$$M = \frac{I_{Amp}_a}{I_{Amp}_r} \tag{1}$$

where the subscripts a and r denote the active and reference sensors, respectively. The dataset of M values was then analyzed to evaluate the standard fall-off of acoustic signal magnitude F_s during propagation from one sensor position to the next in undamaged regions of the deck:

$$F_s = \frac{M_{n+1}}{M_n} \tag{2}$$

where the M_n and M_{n+1} are the normalized waveform magnitudes at two sensor positions spaced 30 cm apart along the same transverse survey line with little or no damage between them. Figure 3 shows the standard fall-off values resulting from this analysis. Note the anomalous fall-off values from 0.6 m to 1.2 m are what are attributed to the focusing of the acoustic waveform when propagating from the thickened haunches to the thinner deck slab. The relative attenuation $Atten_{rel}$ of the waveform when propagating through the deck slab was then computed as:

$$Atten_{rel} = \frac{F_s - (M_{n+1}/M_n)}{F_s} \tag{3}$$

where the M_n and M_{n+1} are defined above and F_s given as Eq. (2). Thus, the relative attenuation represents the decimal percentage that the actual signal fall-off is less than the standard fall-off i.e. when there is no damage along the wave travel path.

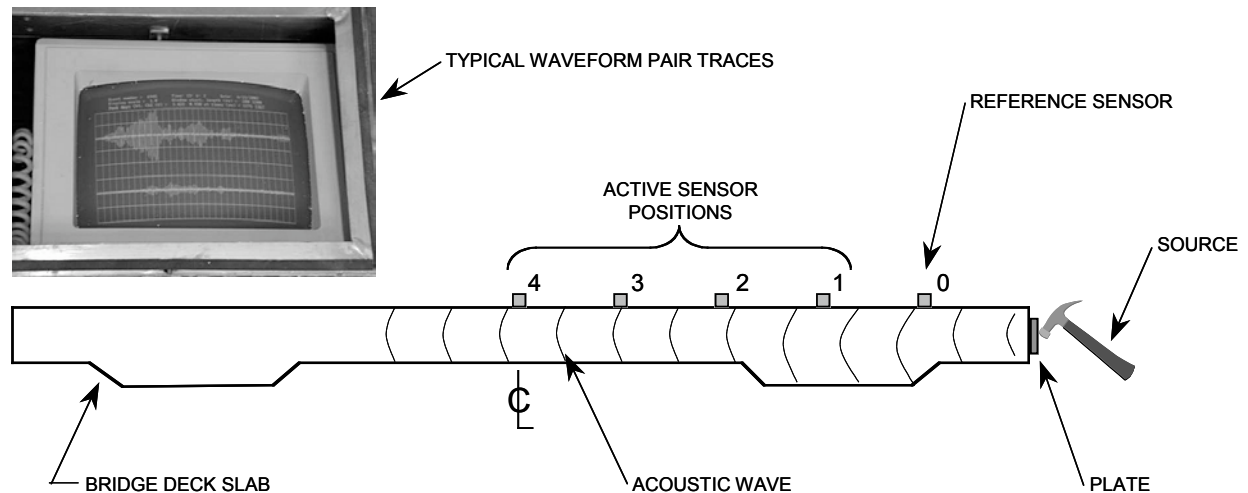


Fig. 2. Schematic of acoutsic survey procedure along a single transverse survey line.

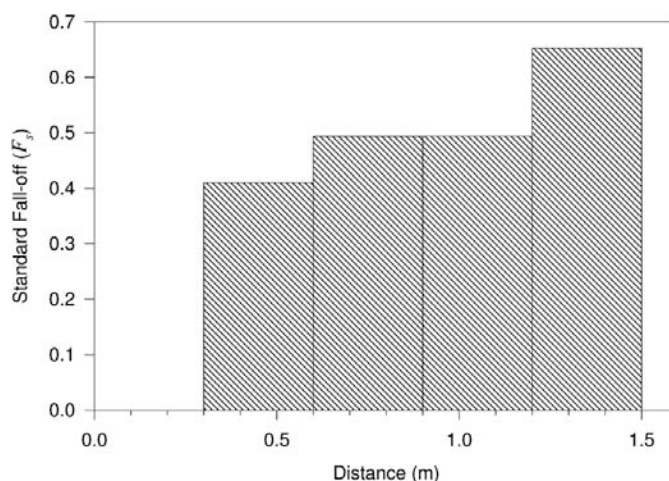


Fig. 3. Values of standard fall-off used to determine relative attenuation. The distance shown is with respect to the edge of the deck model.

Image Generation

Image generation was based on the presentation of the relative attenuation values as a 2-D plan image of the deck slab. The relative attenuation values were assigned 2-D coordinates, which were 15 cm from the active sensor position along the transverse survey line in the direction of the reference sensor. Global variogram analysis was conducted to generate a suitable semi-variogram model for the relative attenuation data and standard point estimation methods using ordinary kriging [7] were used to estimate the relative attenuation values on a 15-x-15 cm grid covering the full plan of the deck model. Industry-standard geostatistical modeling software was then used to generate the contoured relative attenuation images.

Figure 4 presents a plan composite photograph of the deck model showing the cracks mapped on the upper surface of the slab and the upper trace of the punch-through failure zone for each panel. For comparison, the relative attenuation image is given in Fig. 5. Note the good correlation between damaged and cracked regions of the deck and the regions of highest attenuation.

Discussion

As stated above, there is good correlation between the regions of highest acoustic attenuation shown in Fig. 5 and many of the cracked and damaged regions visible on the upper deck surface shown in Fig. 4. For example, each of the four punch-through failure zones is surrounded by a region of greater than 16% relative attenuation, which increases to up to 40% relative attenuation immediately adjacent to the failure zone. As well, most of the longitudinal cracks and other cracks oriented at less than 45° to the transverse survey direction are imaged as zones of greater than 16% relative attenuation. The cracks that are not imaged well include the discontinuous low-aperture longitudinal crack running from Panel A to Panel D on the upper side of Fig. 4 and most of the transverse oriented cracks. This makes sense since the transverse cracks are in a direction parallel to the survey direction and thus are not generally crossed by the acoustic wave raypath between the sensors during the survey.

A final observation from these imaging results is that there are no regions with high levels of relative attenuation that do not have corresponding damage. In other words, the acoustic imaging technique does not generate false positives indicating damage where there is none. From a structural health point of view, this feature of the technique is as significant as its ability to correctly identify locations where damage is present.

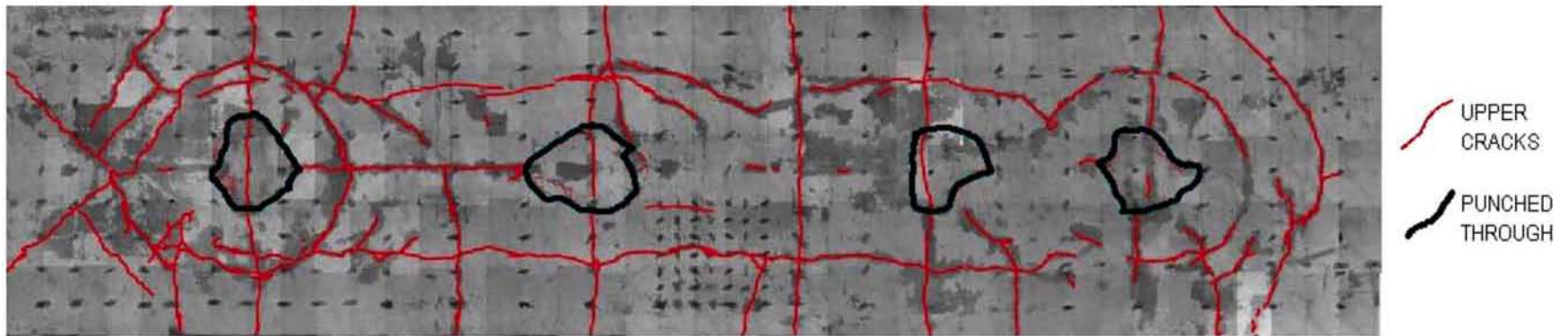


Fig. 4. Composite photograph looking down onto the upper surface of the deck model after punch-through failure of all four panels. The regular pattern of sensor positions can be partially seen as the regular grid pattern of dark spots. The legend is to the right.

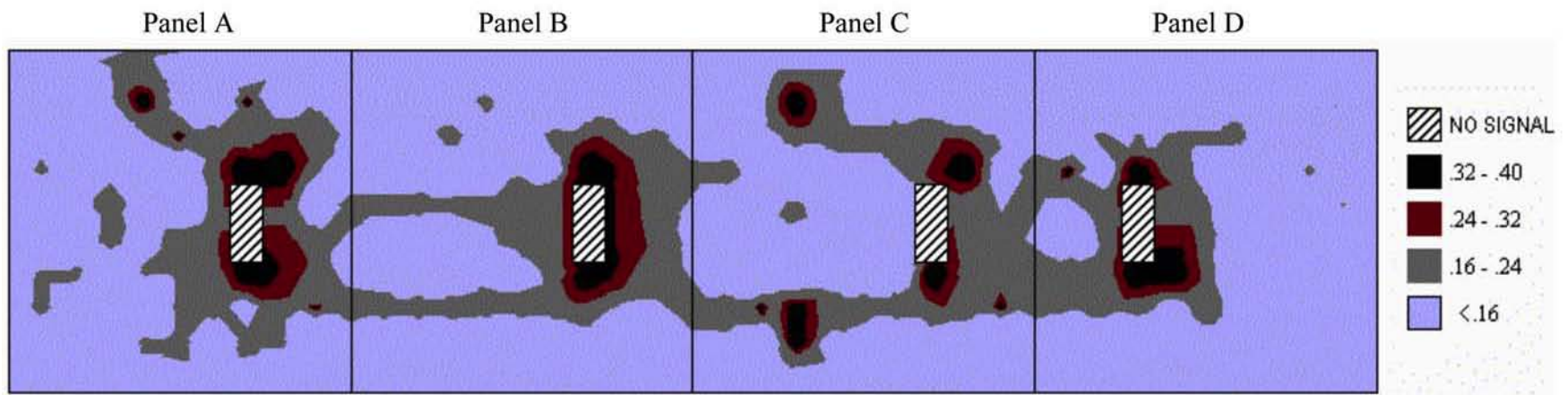


Fig. 5. Acoustic attenuation image of the bridge deck model. The image is oriented the same as Fig. 4 and the legend is to the right.

Conclusions and Recommendations

Overall, the Impact Imaging Method has demonstrated good potential to image damage due to cracks in concrete bridge deck slabs. Cracks are imaged best when they are oriented perpendicular to the direction of the acoustic survey and worst when they are oriented parallel. Equally important, the imaging technique does not falsely identify damage when there is none. Both of these factors highlight the robustness of the imaging technique and its potential to contribute to the non-destructive evaluation and structural health monitoring of concrete bridge deck slabs. Based on these promising results, several recommendations can be made for further research and development with respect to this technology. From an operational point of view, recommendations for future work include:

- Acoustic surveys should be run in multiple directions to ensure that all cracks are imaged and, at a minimum, each area should be covered by two perpendicular survey orientations.
- Investigate the use of rolling acoustic sensors and sources to enable surveys to be done more rapidly than the method described in the paper.
- Investigate the impact of asphalt layers on imaging the underlying concrete slab.

Acknowledgements: This investigation was funded by Intelligent Sensing of Innovative Structures (ISIS) Canada and the National Science and Engineering Research Council (NSERC).

References

1. S.D. Butt, V. Limaye, A.A. Mufti and B. Bakht. Acoustic Transmission Technique for Evaluating Fatigue Damage in Concrete Bridge Deck Slabs, *ACI Structural Journal*. **101**, 1, 2004, 3-10.
2. S.D. Butt and V. Limaye. Damage Detection in Concrete Bridge Deck Slabs using Acoustic Attenuation, in *Proc. 1st Int. Conf. on Structural Health Monitoring of Innovative Civil Engineering Structures*, Winnipeg, Sept. 2002.
3. S.D. Butt, V. Limaye and D. Connors. Imaging damage in concrete bridge deck slabs using acoustic attenuation, in *Proc. 31st CSCE Conference*, ed. N.B. Moncton, June, 2003, 1406-1414.
4. R. Schroerer, Acoustic Impact Technique, *Non-destruct Test*, **3**(3), June, 1970, 194-6.
5. V. Limaye, A.A. Mufti, B. Bakht and S.D. Butt. Steel-free Deck Slabs under Cyclic Loading, in *Proc. 6th Int. Conf. on Short and Medium Span Bridges*, Vancouver, July/Aug, 2002.
6. V. Limaye, *Steel-free bridge decks under cyclic loading: a study of crack propagation and strength degradation*, Unpub. Ph.D. dissertation, Dalhousie University, 2004.
7. A.G. Journel and C.J. Huijbregts, *Mining Geostatistics*, Academic Press, New York, (1978).

HIGH PERFORMANCE USER CODE PROCESSING WITHIN STANDARD AE SOFTWARE ENVIRONMENTS

JOCHEN VALLEN, HARTMUT VALLEN, JENS FORKER
and TOMOKI SHIOTANI*

Vallen-Systeme GmbH, D-82057 Icking, Germany;

* Tobishima Corporation, Noda, Chiba 270-0222, Japan

Abstract

Acoustic emission is successfully used in more and more different applications. The complexity and power of available instrumentation allows one to perform AE testing on materials and structures one would not have expected a few years ago. With a growing market of certain applications the market demands on specialized instrumentation and data evaluation grow. Adequate standard components fulfilling the requirements of nearly all generic AE testing needs are commercially available. There are high-speed systems capable to acquire AE data with or without waveforms. Any kind of frequency filter combination is available to perfectly focus on the frequency range of interest. Powerful software analysis processors are available to separate interesting information from disturbing noises. Source location and automatic cluster detection algorithms process AE data in real time and provide graphical indications on a virtual display of the real structure right after the AE occurred.

Even if AE tells you when it happened and where, however, often the most interesting question is still left open: The question about what actually has happened.

The interpretation of AE data to identify an AE source still needs expert knowledge about the material, shape and structure under test. However for many applications it is possible to define rules to successfully distinguish different sources of interest. Even if it might take some time and experience to create specially adapted algorithms to interpret AE, the need for application-specific analysis algorithms grows, especially where large numbers of similar or identical objects shall be tested. Obviously, specialized data analysis procedures save time for data analysis and interpretation, but also reduce the requirements on operator qualification, which is an important issue for industrial applications.

Standard software consists of standard modules, however. If you have a need for a specific algorithm not already built in, then one has to either interface with the plain ASCII data output from standard software or read the raw data and code all data analysis from scratch. Reading ASCII data does not allow for online processing. Reading the raw input data and programming user written code to perform all data analysis from scratch is definitely not efficient.

This paper summarizes the structure and limitations of standard software and the intentions and possibilities of an already realized Embedded Code Processor (ECP). The ECP provides an interface that the user can develop code, running within the standard analysis data stream in real time. With such an ECP complex algorithms can quickly be implemented to perform any type of data analysis. Like a subroutine, any AE feature is passed from the standard software to the user algorithm. On return, the user algorithm passes its results back to the standard software in order to present the results in the existing graphs and listings. There is no need for the user to care about anything but the algorithm itself when incorporating application-specific code.

Finally, an example for the determination of a well-known parameter, the "improved b -value" is presented.

Keywords: AE-Data analysis, embedded code processor, user processor, VisualAE

Introduction

Figure 1 shows the data flow principle for the analysis of acoustic emission (AE) data in form of a structure tree: Data from a source, usually an AE data file, are passed, data set by data set, to a number of processing stages. A processing stage might be, e.g., a filter processor rejecting data according to user-defined filter criteria, or a location processor determining results concerning the position of the AE source, or, a Visual, which visualizes user-selected results, etc.

The user may add and combine any number and kind of processing stages. In that way, one can realize a very powerful, flexible and sophisticated analysis procedure. Figure 2 shows the screen dump of a structure tree.

The following summarizes some analysis tools from basic to advanced functionality.

Visuals: Visualize analysis results graphically or numerically. The following Visuals are often used:

Correlation diagram: Shows value pairs or triples as dots or symbols in 2D or 3D-space, any result versus any other result, e.g. y-location vs. x-location, or, amplitude vs. time.

Line diagram: Similar to correlations but the dots are connected by a line in the sequence of occurrence, e.g. cumulative hits versus load.

Statistical distribution: Usually a bar graph whereby the position of the bar indicates an interval of a result and the length of the bar the number of events grouped to that interval. Simplest case: Number of hits vs. channel number, or vs. amplitude. Cumulative distributions show an increasing line from left to right or from right to left, representing the sum of the numbers in all intervals.

History: Usually a line graph that shows a parameter vs. time.

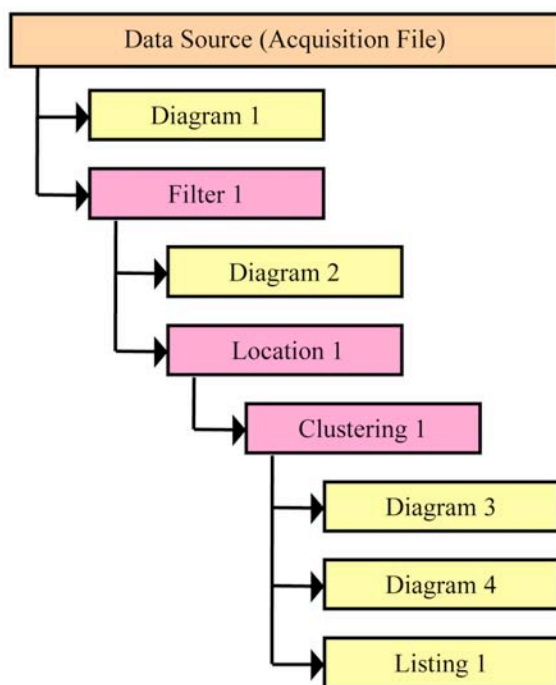


Fig. 1: Example of a data flow scheme in VisualAE. Processors and Visuals are arranged by the user according to the application's needs

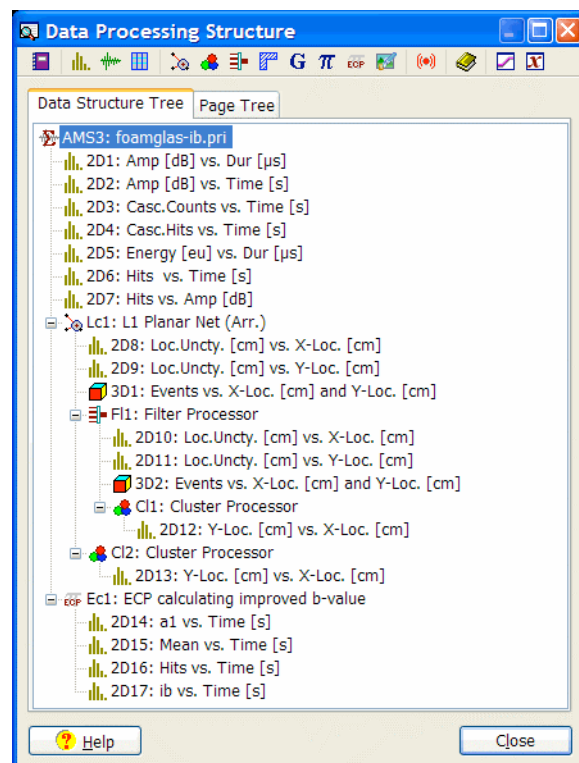


Fig. 2: Example of a VisualAE data processing structure arranged by the user by drag and drop. Last branch includes an ECP.

Numerical listing: Shows a table with one line per hit or event and one column per user-selected result.

Waveform diagram: Shows any selected part of a waveform in time and / or frequency domain.

Data Processors: These get data sets from file or from another processor and usually add new results to the currently processed dataset which is then passed to the next processing stage.

Filter Processor: Compares the current data set against user defined criteria and either rejects it or lets it pass to the next processing stage.

Location Processor: Uses known sensor positions and measured arrival-time differences to calculate the source location and other location results.

Cluster Processor: Determines the spatial event density within a 2- or 3-dimensional spatial element of a user-defined size.

Polygon Processor: Marks data whether they fall inside or outside user-defined polygons in a 2D-correlation diagram.

Alarm Processor: Allows the user to define warning and alarm criteria. If these criteria are met or exceeded user-selected warning and alarm actions are carried out respectively.

Grading Processor: Calculates Severity Index and Historic Index using equations by Fowler [6].

User Processor: Offers a number of statistic and arithmetic functions as well as amplitude distance correction and three different rate evaluations. The user can define the inputs (e.g. events, locations, etc.), which function shall be executed and how the outputs shall be named for use in subsequent processors or visuals.

Embedded Code Processor (ECP) New: An ECP executes user-programmed code of any complexity on user-selected input data in order to create new output results for use in subsequent processors or visuals. ECP can process hit-driven or time-driven data and results of any other processor.

Potential applications of Embedded Code Processing

There are almost no limits for the use of embedded code in an AE analysis program. However, the following applications have primarily driven the development of ECP:

- Implementation of publicly available new analysis procedures, e.g. the French AFIAP guide, as well as proprietary analysis procedures, e.g. the Cluster Evaluation Factor (CEF) algorithm of TÜV Austria for small LPG vessels.
- Determination of proprietary or publicly available key features, such as Felicity ratio [1], Load ratio [2], Calm ratio [2], improved b-value [3-5], etc.
- Automatic determination of test-stop-criteria.
- Automatic determination of the load-, hold-, or unload status of a test.
- Intelligent background noise surveillance and alarm activation.
- Cluster- or Polygon-specific data evaluations.
- Smoothing of parametric data.
- Analysis of time-series of events.
- Channel specific delta-t correction (e.g. for installations of waveguides of different lengths).
- User-developed location algorithms.
- Use of arrival-time corrections from transient recorder data for improvements of location accuracy.

ECP Programming Language

ECP uses a high-level programming language that combines simple procedural syntax (similar to Pascal) with data description constructs. The ECP stored in the VisualAE setup is compiled to an operation code when the setup is loaded. The operation code is interpreted during ECP execution. ECP-execution is slightly slower than the normal code in VisualAE, but this is usually negligible in practice.

Application example: “Improved b-Value” (*Ib*-value)

Principle and use of the *Ib*-value is described e.g. in [3-5]. In short, the *Ib*-value is the slope of the cumulative log-log amplitude distribution from high to low amplitudes between two corner amplitudes (a_1 , a_2). The corner amplitudes are dynamically determined from the mean value “Mean“ and the standard deviation “StdDev“ over the most recent „Beta“ amplitudes in dB as follows:

$$a_1 = \text{Mean} - \text{StdDev} * \text{Alpha1}$$

$$a_2 = \text{Mean} + \text{StdDev} * \text{Alpha2}$$

Alpha1, Alpha2 and the window length Beta are user-parameters that allow for optimizations depending on the tested material.

This example requires the definition of three user-parameters (Alpha1, Alpha2, Beta), the feeding of the amplitude A, and the calculation and output of *Ib*-value, a_1 , a_2 , Mean, und StdDev.

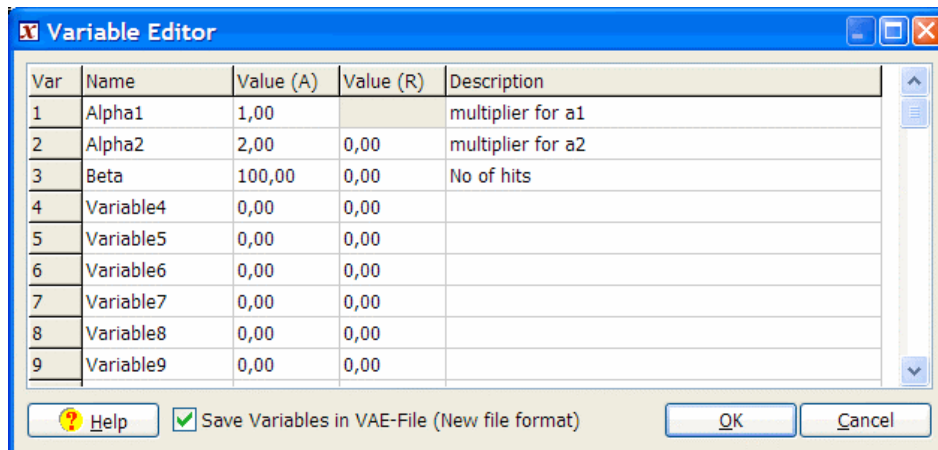


Fig. 3 Variable Editor used to enter and show parameter designators and values.

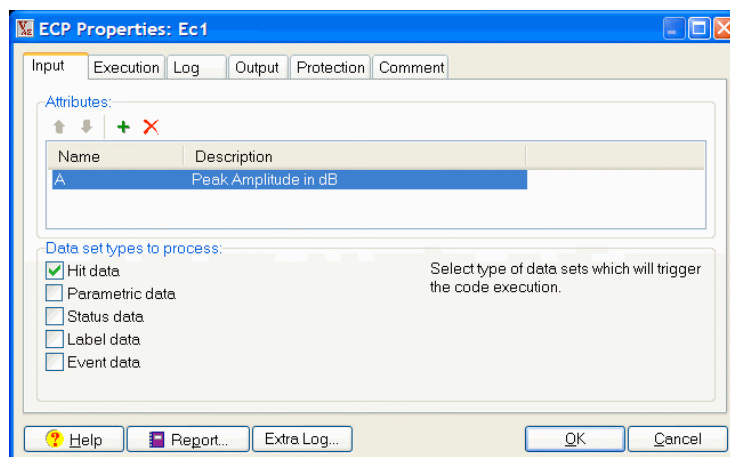


Fig. 4 Menu for ECP-input definitions.

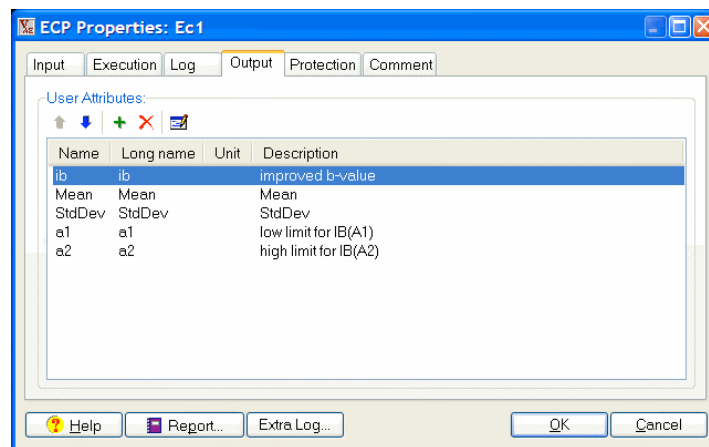


Fig. 5 Menu for ECP-output definitions.

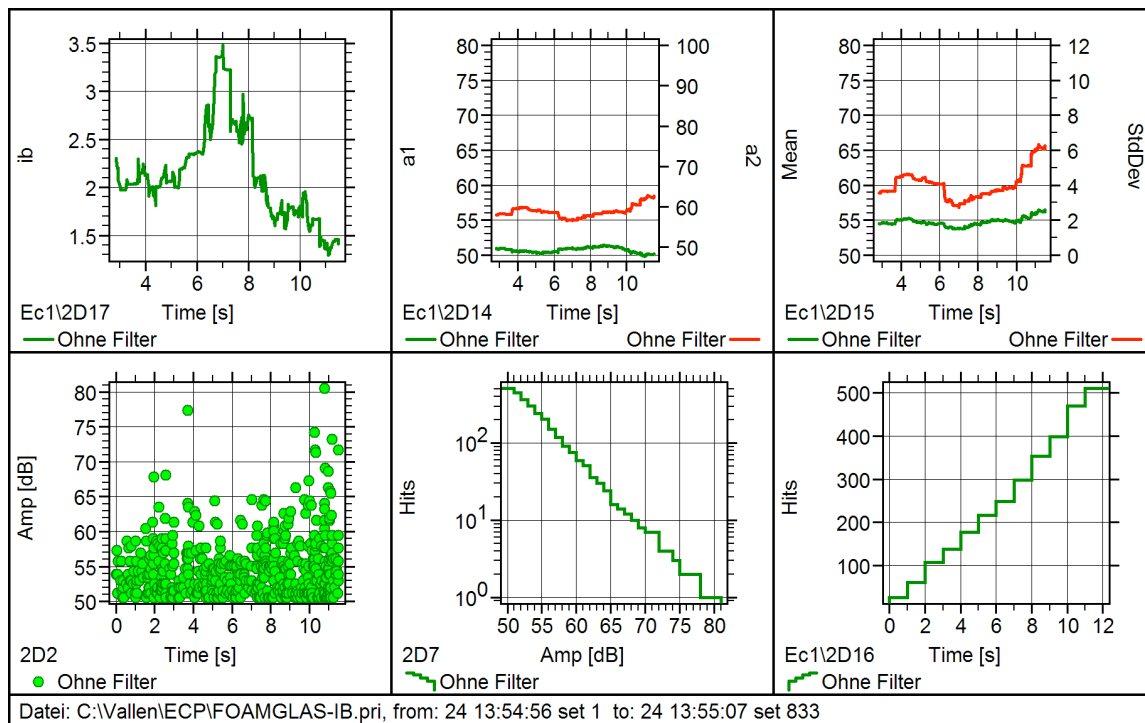


Fig. 6 Example of a VisualAE graphic showing a combination of normal (lower diagrams) and ECP-results (upper diagrams; Ib-value, a1(green), a2 (red), Mean (g), StdDev (r)).

Interfacing parameter values: The Variable Editor in VisualAE (Fig. 3) allows for entering global variables that can be used by different filter processors anywhere in the data analysis structure, and also for the ECP. One can give any variable a unique designation, e.g. “Alpha1” and the ECP takes that variable value by a simple statement like:

“Alpha1 = VAEVariables.Alpha1”.

Interfacing inputs and outputs: The menu in Fig. 4 supports the selection of input results, very similar like adding results to a listing. Here the programmer also defines what kind of data sets (e.g. event driven or time driven) shall be considered. Figure 5 shows how the programmer informs VisualAE about the designations of new results. These designations can be used by processing stages behind the ECP. Figure 6 is an example of a VisualAE-result graphic with

```

ECP Properties: Ec 1
Input Execution Log Output Protection Comment
ECP-Code:
100 function ProcessIB()
101   mean  = SumAmp / HitCnt;
102   stddev = math.sqrt( (SumSquare - (SumAmp * SumAmp) / HitCnt) / HitCnt);
103   a1 = mean - Alpha1 * stddev;
104   a2 = mean + Alpha2 * stddev;
105   local i, a;
106   local n1, n2 = 0, 0;
107
108   --count hits, N(w1) and N(w2)
109   for i = 1, HitCnt do
110     a = Hits[i]
111     if a >= a1 then
112       n1 = n1 + 1;
113       if a >= a2 then n2 = n2 + 1 end;
114     end;
115   end
116
117   if n2 == 0 then
118     print('a2 is too high, check Alpha2 value');
119     n2 = 1;
120     --set the upper amplitude to maximum found
121     --otherwise the ib value would be lower
122     a2 = a1;
123     for i = 1, HitCnt do
124       if Hits[i] > a2 then a2 = a1 end;
125     end;
126   end;
  
```

diagrams showing ECP-results (see axis legends in upper diagrams from left: Ib-value, a1, a2, Mean, StdDev), and conventional results (lower diagrams). Figure 7 is a large part of the code that calculates the Ib-value.

Conclusion

Embedded Code Processing (ECP) extends the functionality of standard AE analysis software by virtually unlimited possibilities for online and off-line use. Results from the measurement can be combined in any complexity to new results and further processed by VisualAE as the user desires. The ECP programmer can add such functionality fully independent of the manufacturer of VisualAE.

Fig. 7 Part of ECP-code for Ib-value calculation.

References

- [1] T.J. Fowler, Experience with acoustic emission monitoring of chemical process industry vessels. *Progress in Acoustic Emission III*, Japanese Society for Non-Destructive Inspection, 1986, pp. 150-162,
- [2] *Recommended practice for in situ monitoring of concrete structures by acoustic emission*, NDIS2421, Japanese Society for Non-Destructive Inspection, 2000.
- [3] T. Shiotani, K. Fujii, T. Aoki, K. Amou, Evaluation of progressive Failure using AE Sources and Improved b-value on Slope Model Test, *Progress in Acoustic Emission VII*, Japanese Society for Non-Destructive Inspection, 1994, pp. 529-534.
- [4] T. Shiotani, S. Yuyama, Z.W. Li, M. Ohtsu, Application of an improved b-value to quantitative evaluation of fracture process in concrete material, *Journal of Acoustic Emission* **19**, 2001, 118-133.
- [5] T. Shiotani, Y. Nakanishi, X. Luo, H. Haya; Damage Assessment in railway sub-structures deteriorated using AE technique. *Proceedings EWGAE 2004*, DGZfP, Berlin, lecture 21 (CD), Vol. I, pp. 255-266 (print).
- [6] *Recommended Practice for Acoustic Emission Evaluation of Fibre Reinforced Plastic (FRP) Tanks and Pressure Vessels, Draft I*, CARP, 1999, XII-8~XII-12.

REASSIGNED SPECTROGRAM AND SPARSE NON-NEGATIVE TENSOR FACTORIZATION FOR ACOUSTIC EMISSION TRANSIENT ANALYSIS

E. POMPONI, G. ROMITI* and F. PIAZZA

DEIT Department, Università Politecnica delle Marche, 60121 Ancona, Italy;

* R&D Department, Loccioni Group, 60030 Angeli di Rosora (AN), Italy

Abstract

Acoustic emission clustering algorithms based on transient analysis have to overcome an intrinsic difficulty due to the structure complexity of signals. In order to reach good AE clustering performance, a representation emphasizing the latent element features that allow the discrimination of similarities and differences, needs to be found. In this article a novel approach based on the reassigned spectrogram energy distribution (RSP) in conjunction with tensor decomposition is proposed. The algorithms have been developed in MatLab and tested on AE signals obtained using a Vallen-Systeme GmbH multi-channel AE system in a real test on different pressure vessels. As shown by the preliminary experimental results, the principal strength of the proposed method is that it allows correctly aggregating of different events as function of their spectral representation properties.

Keywords: AE transient analysis, reassigned spectrogram, non-negative tensor factorization, sparseness constraint, clustering, lamb wave.

Introduction

As known from the literature, in many applications Lamb waves are present due to plate-like test specimens and observations of AE signals in far field. Various works have shown that, by identifying Lamb waves modes from some representation of the measured signals (e.g., wavelet transform, spectrogram) and extracting some features (e.g., maxima of the wavelet transform coefficients) from the detected mode trajectories, it is possible to locate and characterize [1-3] the source of the hit, although with some limitations. In this paper a novel approach based on the reassigned spectrogram energy distribution (RSP) in conjunction with tensor decomposition is proposed for AE events clustering. Potential differences in signal structures due to propagation path (i.e. from source to sensor) has been almost eliminated selecting hits that come from a narrow area of the test specimens (i.e. localized using VisualAE software by Vallen-Systeme GmbH [4]). Reassigned spectrogram (RSP) is a sharply localized time-frequency energy distribution that has the same performance in describing multimode Lamb waves as the reassigned smoothed pseudo Wigner-Ville distribution [5], but with lower computational cost. Moreover, it has been demonstrated [6] that RSP better describes multimode Lamb waves in comparison with reassigned scalogram or Hilbert spectrum. Tensor decompositions are widely used in signal processing, psychometrics, chemometrics and image analysis [7] for their ability in disclosing the latent relation within multi-dimensional data. In this paper, non-negative tensor factorization (NTF) with sparseness constraint (also named non-negative multi way factorization with sparseness constraint - NMWF) [8-10] has been taken into consideration: third order tensor (i.e. a cube) with dimensions *time x frequency x hitNumber* can be constructed putting together RSP hits. Each dimension (i.e. mode) is decomposed in n factors that can be reassembled to reconstruct the

data. Non-negativity means that factor contributions sum to the others without cancellation (i.e. no cancellation is possible reassembling the factors that decompose each dimension) and, therefore, factors can be easily connected to clusters. This does not happen using other tensor decompositions like HOSVD (high order singular value decomposition) [11] where cancellation between contributions of decomposition elements in reconstructing the data makes this task more difficult. Force sparseness constraint is necessary to reduce (almost eliminate, as highlighted by experimental results) the non-uniqueness of the solution [12].

Brief Theory Review

A brief introduction on reassigned spectrogram and sparse non-negative tensor factorization follows. For a detailed treatment, we suggest to refer to the given references.

Reassigned Spectrogram

Special attentions in the AE research community have been given to the class of energy time-frequency distribution. Spectrogram, scalogram and pseudo Wigner-Ville belong to this class and are extensively used by AE practitioners. In contrast with linear time-frequency representations, which decompose the signal on elementary components (the atoms), the purpose of the energy distributions is to distribute the energy of the signal over two description variables: time and frequency. As energy is a quadratic function of the signal, the time-frequency energy distributions will be in general quadratic representations. Spectrogram is defined as the squared modulus of the STFT (i.e. Eq. 1). Since the window h of the STFT is assumed of unit energy, the spectrogram satisfies the global energy distribution property [5]. A critical point in applying this method is its readability, which means both a good concentration of the signal components and no misleading interference terms. Some efforts have been made in that direction, in particular a general methodology referred to as reassignment has been proposed [13]. Spectrogram as a 2D-convolution of the Wigner-Ville distribution (WVD) of the signal and the WVD of the analysis window is expressed as reported in Eq. 2.

$$S_x(t, \nu) = \left| \int_{-\infty}^{+\infty} x(u) h^*(u-t) e^{-j2\pi\nu u} du \right|^2 \quad (1)$$

$$S_x(t, \nu; h) = \int_{-\infty}^{+\infty} \int_{-\infty}^{+\infty} W_x(s, \xi) W_h(t-s, \nu-\xi) ds d\xi \quad (2)$$

A closer look at Eq. 2 shows that $W_h(t-s, \nu-\xi)$ delimits a time-frequency domain at the vicinity of the (t, ν) point inside which a weighted average of the signal WVD values is performed. The key point of the reassignment principle is that these values have no reason to be symmetrically distributed around (t, ν) , which is the geometrical center of this domain. Therefore, their average should not be assigned at this point, but rather at the center of gravity of this domain, which is much more representative of the local energy distribution of the signal. Auger and Flandrin [14] provide a computationally efficient way to compute the reassigned values for the spectrogram:

$$\hat{t}(x; t, \nu) = t - \Re \left(\frac{S_x(t, \nu; T_h) S_x^*(t, \nu; h)}{|S_x(t, \nu; h)|^2} \right) \quad (3)$$

$$\hat{\nu}(x; t, \nu) = \nu - \Im \left(\frac{S_x(t, \nu; D_h) S_x^*(t, \nu; h)}{|S_x(t, \nu; h)|^2} \right) \quad (4)$$

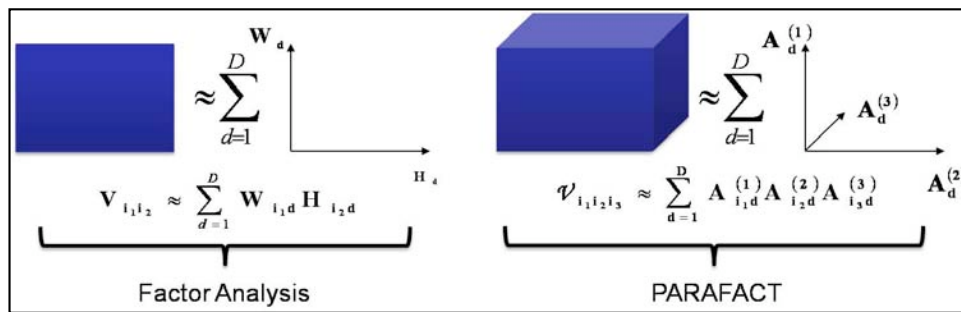


Fig. 1 Factor Analysis (2-D array) and PARAFACT (3-D array case).

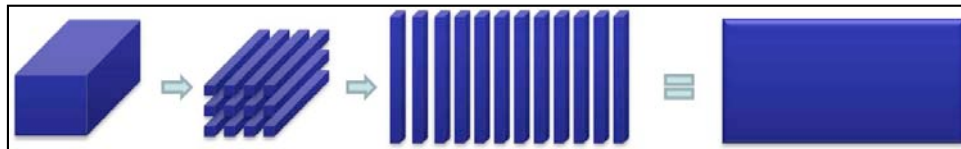


Fig. 2 Matricizing operation.

$$S_x^{(r)}(t', v'; h) = \int_{-\infty}^{+\infty} \int_{-\infty}^{+\infty} S_x(t, v; h) \delta(t' - \hat{t}(x; t, v)) \delta(v' - \hat{v}(x; t, v)) dt dv \quad (5)$$

where (\hat{t}, \hat{v}) is the reassigned coordinates, $h(t)$ is the STFT window function, $\delta(t)$ is the Dirac impulse, $T_h(t) = t \times h(t)$ and $D_h(t) = \frac{dh}{dt}(t)$. The reassigned spectrogram $S_x^{(r)}(t', v'; h)$ (i.e. Eq. 5), is therefore easy to implement, and does not require a drastic increase in computational complexity. Another interesting property of reassignment method is that it can be applied to any time-frequency shift invariant distribution of Cohen's class [5].

Sparse Non-Negative Tensor Factorization

Factor analysis for 2-D array was introduced by Spearman in the early 1900 and has been object of much development. This approach suffers on the non-uniqueness of the solution. To overcome this problem, it is necessary to impose some kind of constraint like orthogonality or mutual independence among factors. Researchers have developed different approach to factor analysis like PCA, ICA, SVD and NMF. If we move our attention to higher order data starting from 3-D arrays, the natural extension of factor analysis is parallel factor analysis also known as PARAFACT (see Fig. 1). It was independently proposed by Harshman [15] and by Carroll and Chang [16], the latter naming it canonical decomposition (i.e. CANDECOMP). In this case the uniqueness of the solution has theoretically been proved under mild conditions [17]. NMWF is an extension of well-known NMF algorithm to higher-order data and adopts the PARAFACT decomposition model. NMF was introduced by Lee and Seung [9, 10]. What makes non-negative decomposition attractive, also with higher-order data, is that it is known to give a part-based representation that often is easier to interpret than other forms of decompositions such as PCA/SVD or ICA. Although non-negativity improves uniqueness of the decomposition by constraining the solution space to the positive octant, non-negative decompositions are not in general unique [18]. No theoretical uniqueness property has been given under non-negativity constraint for PARAFACT model as well. Consequently, to get uniqueness of the decompositions, constraints in the form of sparsity can be imposed. This can be done using the L-1 norm as suggested by Eggert and Körner [12] for NMF and extended to NMWF and high-order non-negative matrix factorization by Mørup et al., see [8, 19] for details. Having explained the role of sparseness in the decomposition of high-order data, we now describe the original algorithms NMWF to highlight the properties that make this method suitable for our clustering problem. Lee and Seung have developed two different variants of their method both based on gradient descent: one minimizing the

squared error (LS), the other minimizing the Kullback-Leibler divergence (KL) [10]. In our approach, we have used the multi-way LS variant of NMF. Both algorithms are easily adapted to the PARAFAC model with non-negativity on all modalities. Formulation of the cost function and update rule can be easily obtained through the matricizing operation and Khatri-Rao product. The first for the n -mode of multi-way array $X^{I_1 \times I_2 \times \dots \times I_N}$ defines the matrix $X_{(n)}^{I_n \times I_1 I_2 I_3 \dots I_{n-1} I_{n+1} \dots I_N}$ (see Fig. 2). The latter is expressed as $A|\otimes|S = [a_1 \otimes s_1 \ a_2 \otimes s_2 \ \dots \ a_F \otimes s_F]$. In the following, the matrix $\mathbf{A}_d^{(1)}$, $\mathbf{A}_d^{(2)}$ and $\mathbf{A}_d^{(3)}$ will be defined as shown in Fig.1. For the update rule, refer to [10].

$$\mathbf{V}_{(1)} = \mathbf{A}_d^{(1)} \mathbf{Z}^{(1)} \quad \mathbf{Z}^{(1)} = (\mathbf{A}_d^{(3)} |\otimes| \mathbf{A}_d^{(2)})^T \quad (6)$$

$$\mathbf{V}_{(2)} = \mathbf{A}_d^{(2)} \mathbf{Z}^{(2)} \quad \mathbf{Z}^{(2)} = (\mathbf{A}_d^{(3)} |\otimes| \mathbf{A}_d^{(1)})^T \quad (7)$$

$$\mathbf{V}_{(3)} = \mathbf{A}_d^{(3)} \mathbf{Z}^{(3)} \quad \mathbf{Z}^{(3)} = (\mathbf{A}_d^{(2)} |\otimes| \mathbf{A}_d^{(1)})^T \quad (8)$$

$$\text{Const. Func.} = \|\mathbf{V}_{(1)} - \mathbf{A}_d^{(1)} \mathbf{Z}^{(1)}\| = \|\mathbf{V}_{(2)} - \mathbf{A}_d^{(2)} \mathbf{Z}^{(2)}\| = \|\mathbf{V}_{(3)} - \mathbf{A}_d^{(3)} \mathbf{Z}^{(3)}\| \quad (9)$$

We can take advantage of the NMF property that produces part-based representation and defines a clustering procedure as described in the following. To simplify the exposition we shall refer to 2-D array factorization that has been shown formerly is a special case of PARAFAC decomposition. Once we have a non-negative decomposition of matrix $\mathbf{X} \in \mathbb{R}^{m \times n}$ where, e.g. \mathbf{X} is composed by RSP hits with m time-point and n frequency-point, $\mathbf{f} < \min(m, n)$ is the number of factors ($\mathbf{X} \approx \mathbf{W}\mathbf{H}^T$ s.t. $\mathbf{W}, \mathbf{H} \geq 0$), we can use the basis matrix $\mathbf{W} \in \mathbb{R}^{m \times \mathbf{f}}$ to divide the m time-point to \mathbf{f} time-cluster and the coefficient matrix $\mathbf{H} \in \mathbb{R}^{\mathbf{f} \times n}$ to divide the n frequency-point to \mathbf{f} frequency-cluster. Typically, time-point i is assigned to time-cluster q if the $\mathbf{W}(i, q)$ is the largest element in $\mathbf{W}(i, :)$ and frequency point j is assigned to frequency-cluster q if the $\mathbf{H}(q, j)$ is the largest element in $\mathbf{H}(:, j)$. This procedure can be easily adopted for higher-order case and is cleanly simple due to the NMF property.

Application to AE Event Clustering

We have tested the proposed approach with different setup. Here, we report an example with hits conveniently selected. Specimen under test: type 2 steel/E-glass cylinder with diameter 360 mm, length 1630 mm and 160 l capacity.

Event selection

We have chosen, within the available tests, groups of events that have been localized in a narrow area of the specimens using commercial software VisualAE by Vallen-Systeme GmbH [4]. This choice has been done because it is necessary to reduce as much as possible the difference between signals due to propagation path from source to sensor.

Experimental setup

Common signal properties: max amplitude $A \geq 60$ dB, energy $E \geq 10^3$ eu and sample rate $fs = 5$ MHz. All the signals were filtered with a 40-kHz high-pass four-pole Butterworth filter. Hit positions on specimens and experimental details are shown in Fig. 3. NMWF max iterations have been set to 5000 to guarantee convergence. The number of factors accepted was purely based on visual inspection of the results. Each decomposition was performed several times to avoid local minima. Without loss of generality, we report the HitNumber as was assigned by the Vallen software.

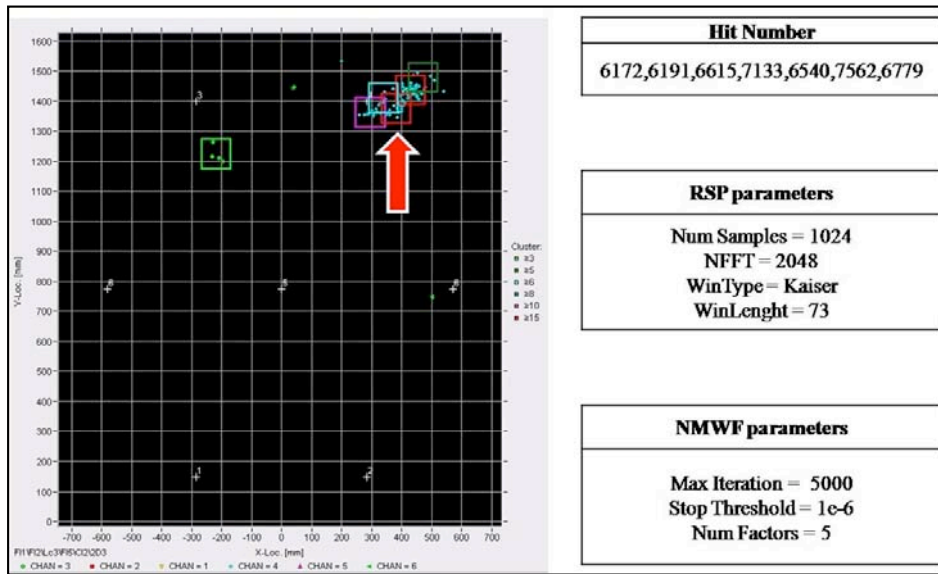


Fig. 3 On the left, Hits positions on specimens shown by VisualAE software [4] (red arrow). On the right three tables with HitNumer and RSP/NMWF parameters.

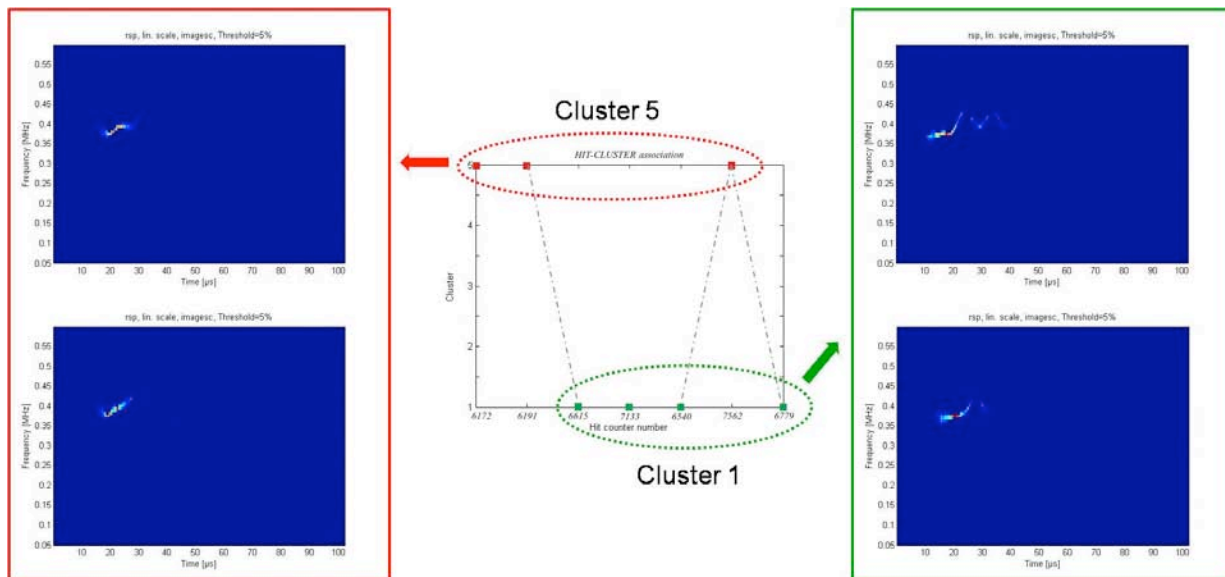


Fig. 4 Experimental results: The central plot is the Hit-Cluster association. On the left (red line) two examples of hit RSP belonging to cluster 5. On the right (green line) two examples of hit RSP belonging to cluster 1.

Results

The obtained experimental results are shown on Fig. 4. The Hit-Cluster association is reported in the center plot. On the right, there are two examples of RSP hits that come from cluster 1, while on the left there are two examples of RSP hits that come from cluster 5. It is possible to appreciate the algorithm's ability to discriminate different events due to their time-frequency property. However in few cases, we have observed some convergence problems of the NMWF. These problems arise from the difficult to disclose hits similarity where only few points in the RSPs are non-zero.

Conclusion

We have proposed a novel approach to AE events clustering based on RSP and NMWF. As highlighted by the preliminary experimental results, the procedure is suitable to reach the goal of good AE event clustering and it is capable of disclosing time-frequency similarity on RSP hits. As stated above, different improvements can be done, especially in the cluster procedure that we have expressly chosen as simpler as possible to emphasize the non-negative factorization properties. Moreover, method to determine the correct number of factors other than visual inspection of the results should be developed (e.g. based on Bayesian Information Criterion). Other experiments on synthetic signals created by a 3D finite element code are scheduled in order to fully validate the method and to study, in a well-defined test environment, how source properties are mapped in the proposed data representation/decomposition.

Acknowledgment: This work was partially supported by the Loccioni Group.

Reference

1. M. A. Hamstad, A. O'Gallagher and J. Gary, *J. Acoustic Emission*, **20**, 2002, 39-61.
2. M. A. Hamstad, A. O'Gallagher and J. Gary, *J. Acoustic Emission*, **20**, 2002, 62-82.
3. J. Jiao, C. He, B. Wu, R. Fei and X. Wang, *I. J. Pres. Ves. Piping*, **81**, 2004, 427-431.
4. Vallen-Systeme GmbH. www.vallen.de.
5. L. Cohen, *J. Math Phys*, **7**, 1966, 781-786.
6. M. Niethammer, L. J. Jacobs, J. Qu and J. Jarzynski, *J. Acou. Soc. of America*, **107**, 2000, L19-L24.
7. T. G. Kolda, *Multilinear operators for higher-order decompositions*. Sandia National Laboratories. 2006. Technical Report. SAND2006-2081.
8. M. Mørup, L. K. Hansen, J. Parnas and S. M. Arnfred, *Decomposing the time-frequency representation of EEG using non-negative matrix and multi-way factorization*. Intelligent Signal Processing, Technical University of Denmark. 2006. Technical report.
9. D. D. Lee and H. S. Seung, *Nature*, **401**, 1999, 788-791.
10. D. D. Lee and H. S. Seung, Algorithms for non-negative matrix factorization, *Adv. Neural Information Processing Systems*, **13**, 2001, pp. 556-562.
11. L. De Lathauwer, B. De Moor and J. Vandewalle, *SIAM J. Matrix Analysis and Applications*, **21**, 2000, 1253-1278.
12. J. Eggert and E. Körner, *Sparse coding and NMF*, *IEEE Int. Joint Conf. on N. N.*, 2004, pp. 2529-2533.
13. K. Kodera, R. Gendrin and C. de Villedary, Analysis of time-varying signals with small BT values, *IEEE Trans. on Acoustic, Speech and Sig. Proc.*, **26**, 1978, pp. 64-76.
14. F. Auger and P. Flandrin, *Improving the readability of time-frequency and time-scale representations*, *IEEE Trans. on Sig. Proc.*, **43**, 1995, pp. 1068-1089.
15. R. A. Harshman, *Foundations of the PARAFAC procedure: Models and conditions for an 'explanatory' multi-modal factor analysis*, *UCLA working papers in phonetics*, **16**, 1970, pp.1-84.
16. J. D. Carrol and J. Chang, *Psychometrika*, **35**, 1970, 283-319.
17. J. B. Kruskal, *Linear Algebra Appl.*, **18**, 1977, 95-138.
18. D. Donoho and V. Stodden, *Adv. in Neural Inf. Proc. Sys.*, **16**, 2004.
19. M. Mørup, L. K. Hansen and S. M. Arnfred, *Algorithms for Sparse Higher Order Non-negative Matrix Factorization (HONMF)*, Intelligent Signal Processing, Technical University of Denmark. 2006. Technical report.

REAL-TIME DENOISING OF AE SIGNALS BY SHORT TIME FOURIER TRANSFORM AND WAVELET TRANSFORM

KAITA ITO and MANABU ENOKI

Department of Materials Engineering, The University of Tokyo,
7-3-1 Hongo, Bunkyo, Tokyo 113-8656, Japan

Abstract

Laser AE method is a non-contact AE detection technique, which utilizes laser interferometer as sensor. This method is less subjected to environmental difficulties and can be adaptive for wider target than conventional PZT sensors. However, laser AE method has to improve its sensitivity because the noise level of laser interferometer is higher than PZT sensors. In this study, a method to reduce the noise component of output signal of laser interferometer is investigated. Output signals from laser interferometer were recorded continuously with 10-MHz sampling frequency and transformed into spectrogram (time-frequency-magnitude data) by time-frequency analysis method. After noise component in this spectrogram is cut, inverse transform is applied to obtain clear AE signals in time domain. Whole signal processing can be done in real time. Simulated AE detection test was conducted to confirm the effectiveness of this noise reduction scheme. In the result, weak AE signals buried in noise could be recovered and the improvement of sensitivity of laser AE system was demonstrated. Current real-time processing can extract about 100 events/s.

Keywords: Noise reduction, continuous waveform recording, short-time Fourier transform, wavelet transform

Introduction

Conventional PZT AE sensors are difficult to use under some of severe environments. For example, conventional AE sensor needs waveguide or some of heat avoidance mechanism if the testing temperature is higher than the Curie temperature of PZT. In another case, PZT sensors often cannot be attached to the target material during manufacturing process. Therefore, laser AE method [1] has been developed to realize a direct AE measurement under such severe environments by non-contact detection of AE with laser interferometer [2, 3]. However, laser AE method has to improve the sensitivity because the noise component of output signals from a laser interferometer is larger than the conventional PZT sensors. Frequency filtering is one of the most important techniques to improve the sensitivity. However, conventional analog filter is not so effective for the output waveform of laser interferometer because the noise component is closed to the frequency range of effective signal component. Digital signal processing (DSP) system can do more powerful and flexible noise reduction than analog system. In this study, a high performance method for noise reduction of the output signal from laser interferometer was investigated. The waveform from laser interferometer was continuously sampled and once transformed into spectrogram by time-frequency analysis methods. Effective noise reduction process was examined using this spectrogram.

Analytical Method

Time-Frequency Analysis

Time-frequency analysis is a method to convert a waveform (time-voltage data) into a spectrogram (time-frequency-magnitude data). In this study, short time Fourier transform (STFT) and wavelet transform (WT) were used as time-frequency analysis techniques. In STFT method, a long waveform is split into short sections and each section is processed by Fourier transform using the following formula:

$$F(\tau, f) = \int_{-\infty}^{+\infty} s(t)w(t - \tau)e^{-2\pi if} dt, \quad (1)$$

where $s(t)$ is the sectioned waveform, $w(t - \tau)$ is window function, f is frequency and $F(\tau, f)$ is the result of STFT. Meanwhile, in wavelet transform method, the original signal is expressed as summation of scaling and shift of certain short waveform called “mother wavelet” as

$$W(a, b) = \int_{-\infty}^{+\infty} s(t)h_{a,b}^*(t)dt, \quad (2)$$

where $h(t)$ is mother wavelet, a is the scaling factor, b is the shifting factor and $W(a, b)$ is the result of WT. Fourier transform loses the time information in the transform section because it supposes ordinary wave. Then, if the section length becomes shorter, the time resolution of STFT improves, but the frequency resolution degrades. Thus, the overall resolution of STFT cannot be so high by this trade-off relationship. Meanwhile, wavelet transform can get high resolution, but the calculation amount is larger than STFT, so wavelet transform of very long continuous waveform is not realistic. Thus, less-intensive calculation and low-resolution STFT is better for rough estimation of long waveform, and intensive calculation and high-resolution wavelet transform is better for strict estimation of short waveform. Tactful use of both methods is important.

Noise reduction

Figure 1 shows a spectrogram of output waveform of laser interferometer and contains two main components as discrete AE signal component and continuous noise component. The noise appeared in a broad frequency range between about 200 kHz and 500 kHz, and this range partially overlaps with the effective signal component. Furthermore, often the noise component is larger than the effective signal component in laser AE methods. In such a waveform, conventional frequency filter which utilizes moving average or pulse reaction is ineffective. In this study, pruning method and soft-thresholding methods are adopted as noise reduction process. This combination of the two processes was already reported in voice processing and ultrasonic testing area [4]. At first the spectrogram of recorded waveform is filtered by pruning method:

$$W_2(f, t) = \begin{cases} 0 & \text{for } f < f_1, f > f_2 \\ W_1(f, t) & \text{for } f_1 < f < f_2 \end{cases}, \quad (3)$$

where W_1 is waveform before processing, W_2 is waveform after the processing, f is frequency, t is time, f_1 and f_2 is cut-off frequency. Pruning method works as frequency filter and cuts off sharply. After that, remained white noise component was cut by soft-thresholding method:

$$W_2(f, t) = \begin{cases} 0 & \text{for } |W_1(f, t)| < \lambda \\ |W_1(f, t) - \lambda| & \text{for } |W_1(f, t)| \geq \lambda \end{cases}, \quad (4)$$

where λ is the threshold of noise and signal. Originally, these methods are used for wavelet transform result; however, it can be used for STFT result too. After these noise reduction processes, the spectrogram was reconverted into waveform by inverse STFT or inverse WT.

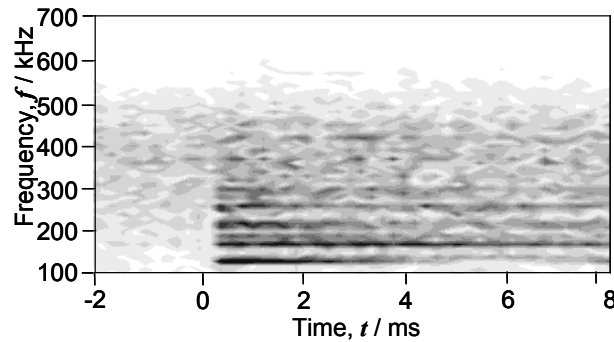


Fig. 1 Sample spectrogram of output signal of laser interferometer.

Real time signal processing

The CWM system basically can do a real-time noise reduction process based on the above theories by a combination of high-speed STFT and high-resolution WT. At first, the whole recorded waveform is converted into spectrogram by STFT. The noise component in the spectrogram is reduced by pruning method and soft-thresholding method. Then, the processed spectrogram is reverted by inverse-STFT with Hanning window function to connect smoothly at the connection points of inverse-STFT period. After that, AE events are extracted from the noise reduced time domain data. However, the time resolution of this waveform may not be enough because this waveform is processed by STFT-based method. Therefore, a waveform with a few milliseconds length is clipped out from as-recorded waveform around AE event and processed again by WT-based method to get precise time information. The WT-based method is the same manner as the STFT-based method.

In particular, the current CWM system with two 2.2 GHz processor (Athlon64 X2 Processor, AMD Inc.) can process 2-channel AE waveforms of 10-MHz sampling in real time by STFT-based method and can extract about 100 events/s by WT-based method.

Experimental Procedures

Simulated AE detection test was conducted to confirm the above noise reduction method. Figure 2 shows the experimental equipment. Specimen was SUS304 disk of 30 mm in diameter and 5 mm in thickness. Simulated AE was generated by thermal stress of pulse YAG laser system (Tempest-20, New Wave Research, Inc.), measured by He-Ne laser heterodyne interferometer (AT3600S and AT0022, Graphtec Corp.) and analyzed by our CWM system [5]. The output power of YAG laser was 40 mJ/pulse or 20 mJ/pulse and pulse length was about 4 ns. The maximum detectable frequency of the laser interferometer was about 400 kHz. CWM sampled the output signal of AT3600S continuously during the whole test with 10-MHz frequency and 12-bit resolution. The noise level was about 30 mV in RMS.

Results and Discussion

Figure 3 shows the result of 40-mJ pulse. The pulse was strong enough to register as an AE event from as-recorded waveform (Fig. 3(a)). The spectrogram (Fig. 3(c)) of this waveform also contained strong signal component and weak noise component between 200 kHz and 500 kHz. In order to reduce this noise component, only a frequency range between 100 kHz and 250 kHz remained after applying pruning method. The white noise was reduced by soft-thresholding

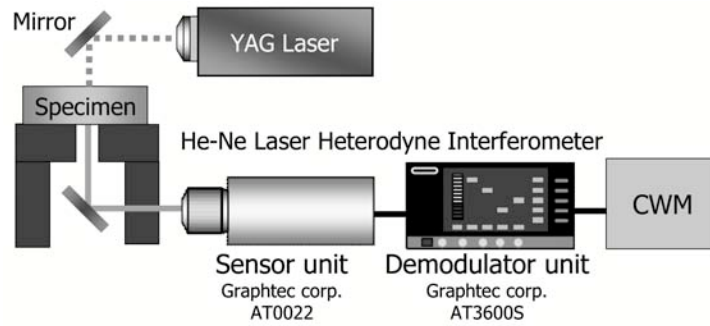


Fig. 2 Experimental equipments of simulated AE signal detection.

method with 6% of maximum magnitude as the threshold value (Fig. 3(d)). A clear waveform (Fig. 3(b)) was obtained by inverse STFT in comparison to the original waveform.

Figure 4 shows the result of 20-mJ pulse. Pulse was very weak and AE event was not visible in as-recorded waveform (Fig. 4(a)). However, a weak signal component was discernible in the STFT result (Fig. 4(b)). Therefore, only a frequency range between 75 kHz and 175 kHz was remained by pruning method, and the white noise was reduced by soft-thresholding method with 6% of maximum magnitude as the threshold value. The processed waveform (Fig. 4(c)) could be detected as AE event.

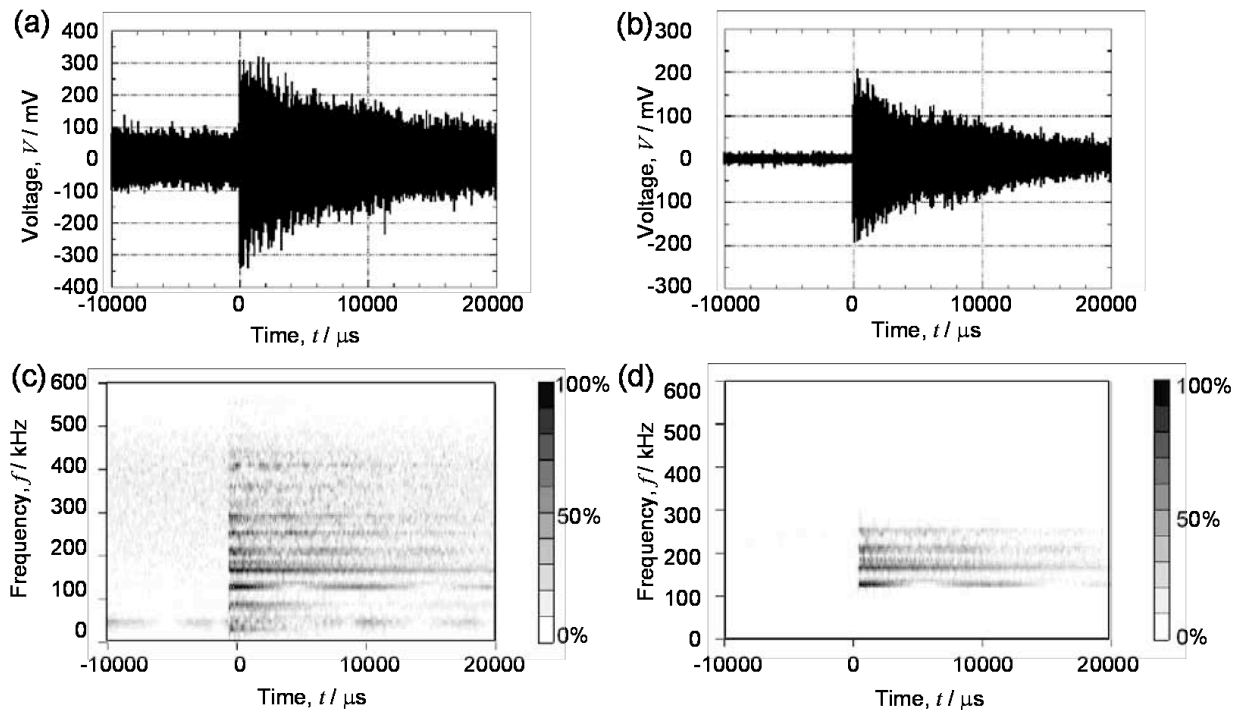


Fig. 3 Noise reduction of simulated AE signal by 40mJ pulse; (a) recorded waveform, (b) processed waveform, (c) STFT result of recorded waveform, (d) spectrogram after noise reduction.

The noise-reduction processing was also conducted with WT. Figures 5 and 6 show the waveform and spectrogram of the same AE event in Fig. 3. The noise component below 100 kHz was relatively strong in the spectrogram of the as-recorded waveform, but this noise can be cut by pruning method (Fig. 5(d)). The noise-reduced waveform (Fig. 5(b)) is clear in the time domain and the major characteristics of waveform are kept as the original waveform. Figure 6

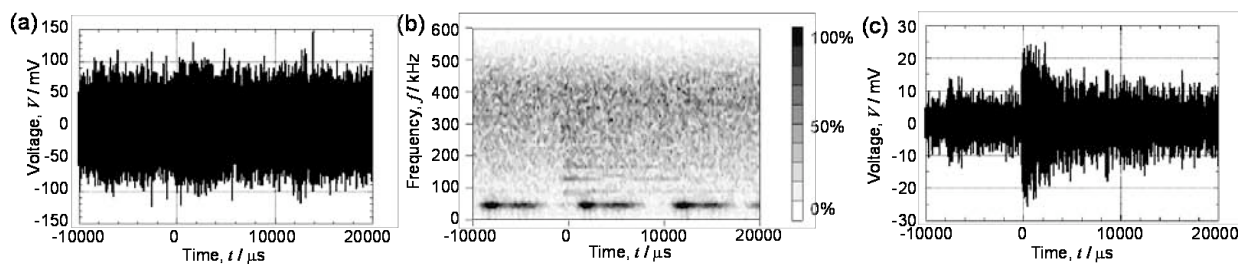


Fig. 4 Noise reduction of simulated AE signal by 20mJ pulse; (a) recorded waveform, (b) STFT result of recorded waveform, (c) noise reduced waveform.

shows the comparison of rising waveform by the STFT-based and WT-based noise-reduction processes. WT shows sharper rising waveform than STFT. This good time resolution of WT is effective for the location of AE events.

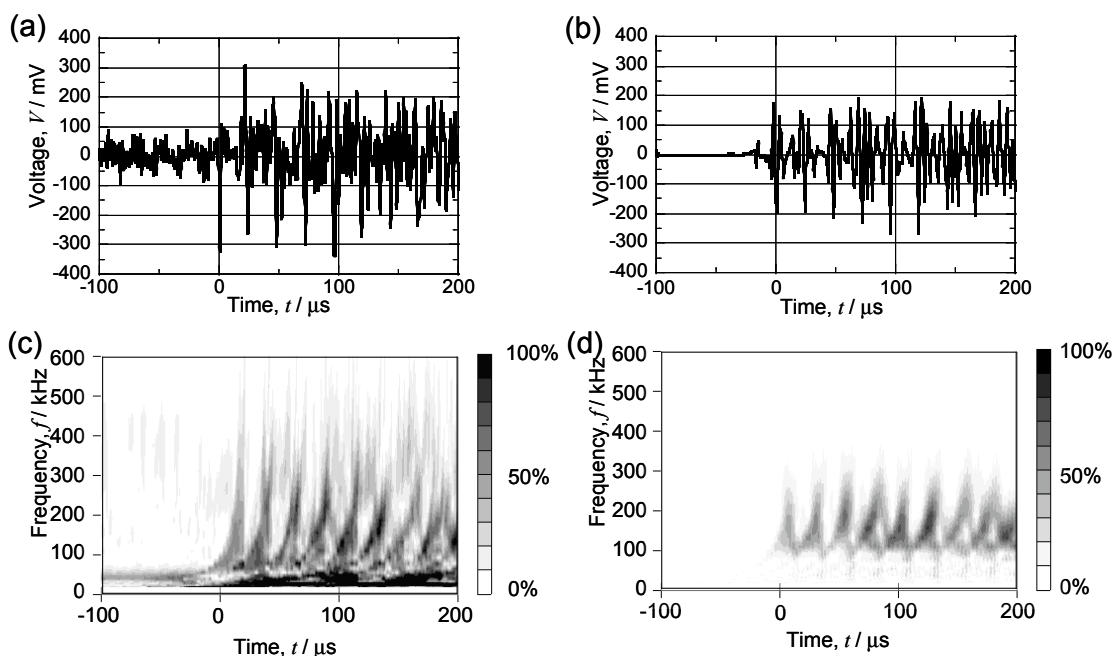


Fig. 5 Noise reduction of simulated AE signal by 40-mJ pulse; (a) recorded waveform, (b) noise reduced waveform, (c) WT result of recorded waveform, (d) spectrogram after noise reduction.

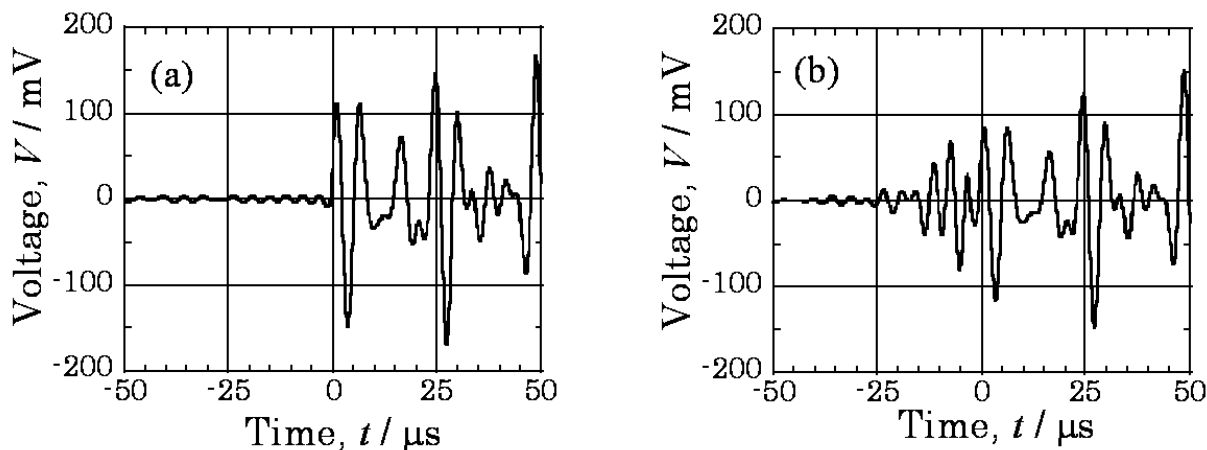


Fig. 6 Results of (a) STFT-based and (b) WT-based noise reduction process.

Conclusion

A noise-reduction process to improve the sensitivity of laser AE method was investigated. The output signal of laser interferometer was continuously recorded and the recorded waveform was processed to reduce noise component by time-frequency analysis and combination of pruning method and soft-thresholding method. Simulated AE detection test was conducted to confirm the effectiveness of the noise reduction process. Weak AE signals buried in noise can be recovered and the improvement of sensitivity of laser AE system was demonstrated. Current CWM system can process 2-channel AE waveforms of 10-MHz sampling in real time, extracting about 100 events/s.

References

1. M. Enoki, M. Watanabe, P. Chivavibul and T.Kishi, *Sci. Technol. Adv. Mater.*, **1**, 2000, 157-165.
2. M. Watanabe, M. Enoki and T. Kishi, *Mater. Sci. Eng. A*, **359**, 2003, 368-374.
3. S. Nishinoiri, M. Enoki, T. Mochizuki and H. Asanuma, *Mater. Trans.*, **45**, 2004, 257-263.
4. A. Abbate, S. C. Schroeder and P. Das, *IEEE Trans. on Ultrasonics, Ferroelectrics, and Frequency Control*, **44**, 1997, 14-26.
5. K. Ito and M. Enoki, *Mater. Trans.*, **48**, 2007, 1221-1226.

ACOUSTIC EMISSION SOURCE LOCATION ON AN ARBITRARY SURFACE BY GEODESIC CURVE EVOLUTION

G. PRASANNA, M. R. BHAT and C. R. L. MURTHY

Department of Aerospace Engineering, Indian Institute of Science, Bangalore 560 012, India

Abstract

Location of an acoustic emission (AE) source is generally obtained by assuming simplified velocity models on surfaces and solids, for which a definite parametric representation exists. These attempts employ triangulation to form distance equations using time-differences obtained from experimental data, which are solved analytically or numerically to get to the location of source. This approach may not be suitable for complex geometry components. Also, the problem gets compounded if the material of the structure is anisotropic warranting complex analytical velocity models. Hence, there has been a need to obtain a practicable source location solution in a more general setup on any arbitrary surface containing finite discontinuities. The approach suggested here is based on the fact that the wave takes minimum energy path to travel from a source to any other point in the connected domain. An AE signal takes this path from the source to an AE sensor array. By propagating the waves in reverse virtually from these sensors along the minimum energy path and by locating the first intersection point of these waves, one can get the source location.

Keywords: Source location, geodesics, geodesic evolution

Introduction

One of the major advantages of AE technique as an on-line monitoring tool is its capability to locate active defects in larger structural components without having to physically scan them. Different methods used for source location include zonal location, computed location, and continuous location. These approaches are affected by the signal attenuation and dispersion due to inhomogeneity and geometry of the material [1]. An alternative location technique uses the concept of 'the first sensor hit by an AE event' to identify a more generalized region around each sensor, from which the AE signal likely originated. In this case, one can determine which one of the several sensor regions on the test specimen has more concentrated AE activity [2]. Some AE systems determine signal arrival times using fixed threshold techniques [3] and because of the aforementioned complications, such AE systems measure arrival times for signals using various portions of the AE signal, which travel at different velocities.

The approach suggested here is based on the fact that the wave takes minimum energy path to travel from a source to any other point in the connected domain. In isotropic media, minimum energy path gets reduced to shortest distance path, which can be seen mathematically as shortest geodesics. Hence, by allowing geodesic waves to propagate from multiple sensors and identifying their point of meet, one can obtain the source location. In an object with complex geometry, a graph-theory based concept can be employed to determine the shortest path using Dijkstra's algorithm [4] for finding discrete geodesics, which are propagated from each sensor location till the source is reached.

Our approach

This conceptual view can be visualized as in Fig. 1, which shows waves propagating in all possible directions from a defect location, along the minimum energy path. With imposed material limitations, this path is generated by geodesics. Once the geodesic paths are extracted in a given geometry, the defect location is reached by back-propagating along those paths, from the sensor locations, as shown in Fig. 2. To start with, it can be assumed that AE sensors detect only Rayleigh waves, which in turn means that the study is restricted to 2-D surfaces.

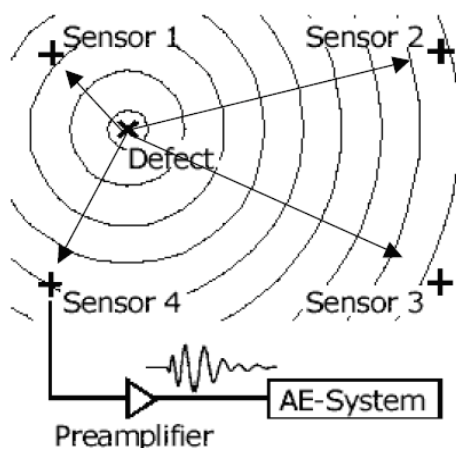


Fig. 1: Wave front propagation – from defect location.

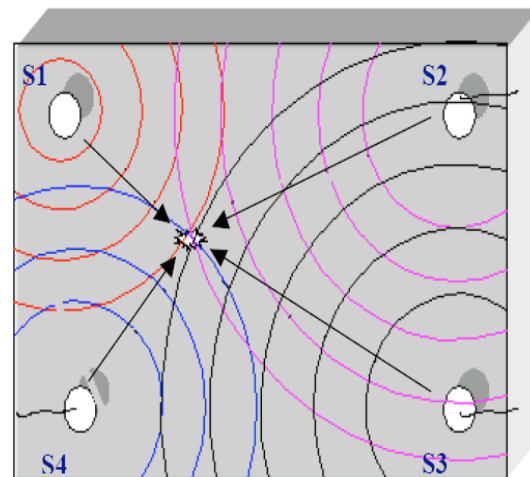


Fig. 2: Conceptual view – back-propagation to defect location.

It is to be noted that even the triangulation method utilizes the same approach, only that it has an inherent assumption that the geometry is a 3-D continuum resulting in simple distance equation based on Pythagorean theorem, which is solved analytically or numerically.

Since our approach builds on the fact that a wave takes minimum energy path, when the assumption of isotropy in the media is imposed, the shortest energy path reduces to shortest distance path, which is provided by the evaluating the geodesics. Mathematically, the energy along a path is seen as weighing function defined along the path. Hence, the minimum energy path is given by

$$\text{Energy along path, } L = \int w(x)dx ,$$

$$\text{Min. Energy, } \min(L) = \min\left(\int w(x) dx \right)$$

$$\text{If isotropic, Min Energy path, } \min(L) = w \cdot \min\left(\int dx \right)$$

where, $\min(\int dx)$ is the required geodesic.

So, the minimum-energy-path problem is equivalent to shortest-distance-path problem. The intersection of geodesic wave fronts from multiple sources gives the location of the source.

Formulation - Wave Propagation Approach:

This approach involves discretizing the domain as curved or planar simplicial complex chains, followed by finding local geodesics in each of the simplex and finally gluing them together to get the required global geodesic. There are many suggested methods to calculate

discrete geodesics and it is still an active area of research investigation [5-7]. Dijkstra [4] proposed an algorithm for the same and most of the present techniques is built over it.

The source location formulation proceeds as follows:

$$D(S1 - S) - D(S2 - S) = V \cdot dt$$

which is recast into the implicit form,

$$\Phi(D, V, dt) = 0$$

The geodesics 'D' in above formulation is arrived from 'wave-propagation' perspective using graph-theory based Dijkstra algorithm.

The governing equation is subsequently further recast as

$$D(S1 - S) \pm V \cdot dt = D(S2 - S)$$

leading to the view that the solution lies in the boundary of the Voronoi diagram and the exact location is the intersection of two more boundaries.

With above observation and understanding, the algorithm was implemented and tested for shortest path extraction over some simple cases and also over Stanford Bunny (Fig. 3), proving convincingly the wave-propagation based construction.

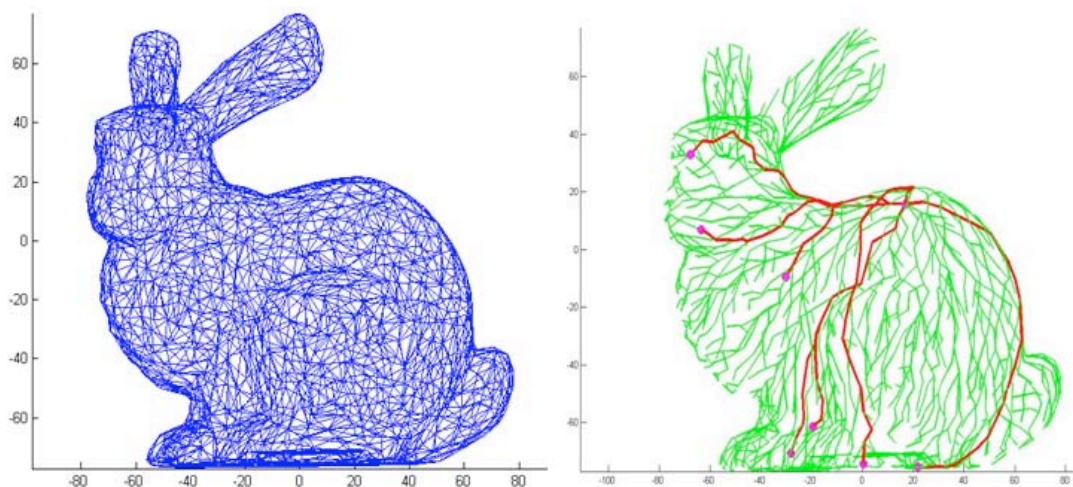


Fig. 3: (a) Surface model.

(b) Generated by geodesic propagation.

The bunny in Fig. 3(b) was generated by flow of wave along the shortest cost path from an arbitrary vertex in the mesh. The thick lines in the figure are samples of shortest paths between two points on the bunny surface (which are the required 'geodesics').

This proves the ability to extract discrete geodesics on arbitrary surface, which is the first part of geodesic evolution approach. The second part of solution is the construction of Voronoi-like diagram to locate the intersection of wavefronts, which is discussed in the following section.

Voronoi Construction:

Taking a case of 3-sensor setup provides 3 sets of time-difference equations. Using the recast formulation, all the points that are equidistant from sensor locations are found (using distance map calculated based on Dijkstra algorithm along with $V \cdot dt$ corrections).

When information from only two sensors is available, then only one equation is formulated and hence there exist multiple solutions meeting the distance criteria. This is depicted in Fig. 4(a) with the jagged thick line passing between sensors S1 and S2 indicating all points that are equidistant (which is the Voronoi diagram). An important observation is that this line passes through

the defect location (AE source) and hence we need to search only along this line for getting to the source.

When information from one more sensor (S3) is considered, then 3 equations are formulated, from which the other lines in Voronoi diagram are constructed. All these lines intersect exactly at the AE source, as in Fig. 4(b). The geodesic lines joining the 3 sensors give the Delaunay triangle, which is the dual of conventional Voronoi diagram.

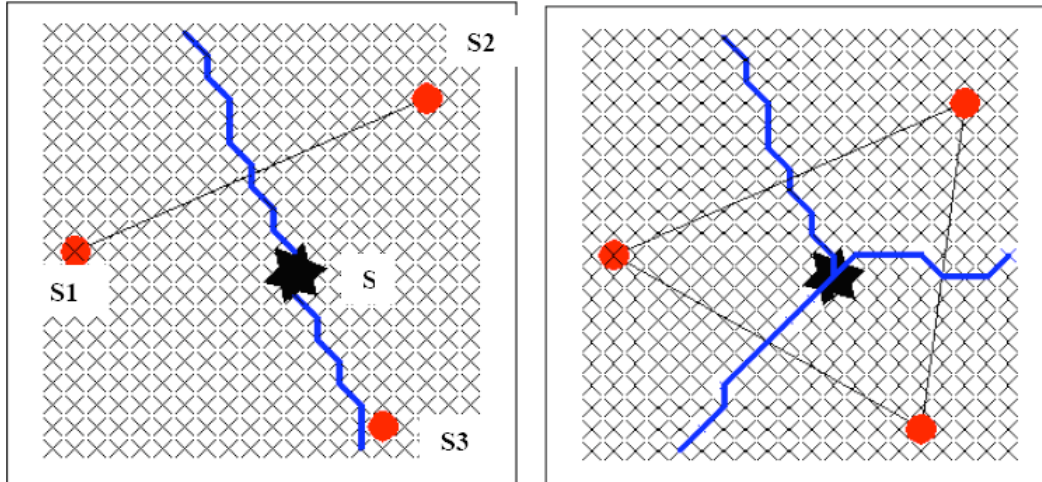


Fig. 4: Voronoi diagram considering (a) 2 sensors; (b) 3 sensors.

Above construction is trivial to implement in form of set operations. For a given mesh,

- Let n_k be the k th node in the mesh and
- $D(n_k S_i)$ be the distance between k th node and i th sensor and
- $D_k(S_{ij})$ be the difference in distances of a node k from sensors S_i and S_j ,

i.e., $D_k(S_{ij}) = D(n_k S_i) - D(n_k S_j)$, then

- the Voronoi line between any two sensors S_i and S_j is formed by nodes which satisfy the condition that $D_k(S_{ij}) = V dt_{ij}$

where, dt_{ij} is the hit arrival-time difference between the sensor S_i and S_j and D 's are geodesic distances and the corresponding line can be seen as set of these nodes which is given by

$$L_{ij} = \{ n_k \mid D_k(S_{ij}) = V dt_{ij} \}$$

- Hence for 3 sensors we get, L_{12} , L_{13} & L_{23} as shown in Fig. 4. The intersection point is the intersection node in the set L_{ij} given by

$$\text{Source, } S = \{ n \mid (L_{12} \cap L_{23} \cap L_{13}) \}$$

- For surfaces, which are intrinsically 2-dimensional in parametric space, only two of the above sets are to be included for getting the source node.

Experimental Evaluation

The trial is initially made for a curved planar structure. Source location was attempted using both numerical-continuous and numerical-discrete (wave-propagation approach). It was followed by experimentation on an odd geometry component containing sharp changes and discontinuities. The AE setup that is used (MISTRAS) has an auto-sensor-test (AST) mode where each sensor acts as source and emits an AE pulse, which is received by other sensors. With known sensor

locations, time-difference equations are formed and solved to get the velocity of the AE in the test component. AE sources were also simulated by pencil-lead breaks at known locations and the AE data was continuously recorded. The extracted data is sent to source location algorithm (coded in MATLAB) for evaluation.

Cylindrical Geometry:

The setup is shown in Fig. 5(a). Based on the dimensions, a sector of the object was meshed using ANSYS (Fig. 5b) and mesh information was imported to MATLAB. Wave propagation algorithm was applied over the mesh to find the location of artificially created sources. The program output shows a deviation of approximately 7.5% from the actual, as shown in Table I.

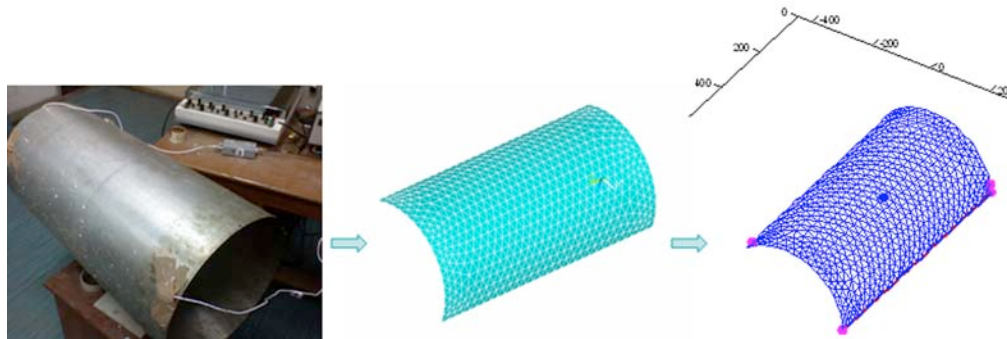


Fig 5 (a) Cylinder - AE setup (b) ANSYS mesh of a sector.

Table I: Source location in cylindrical geometry.

Sensor Location	Measured Value			Program output		
	X	Y	Z	X	Y	Z
S-1	105	0	0	105	0	0
S-2	-80.43	0	-67.49	-80.43	27.69	-67.49
S-3	-80.43	360	-67.49	-80.43	332.31	-67.49

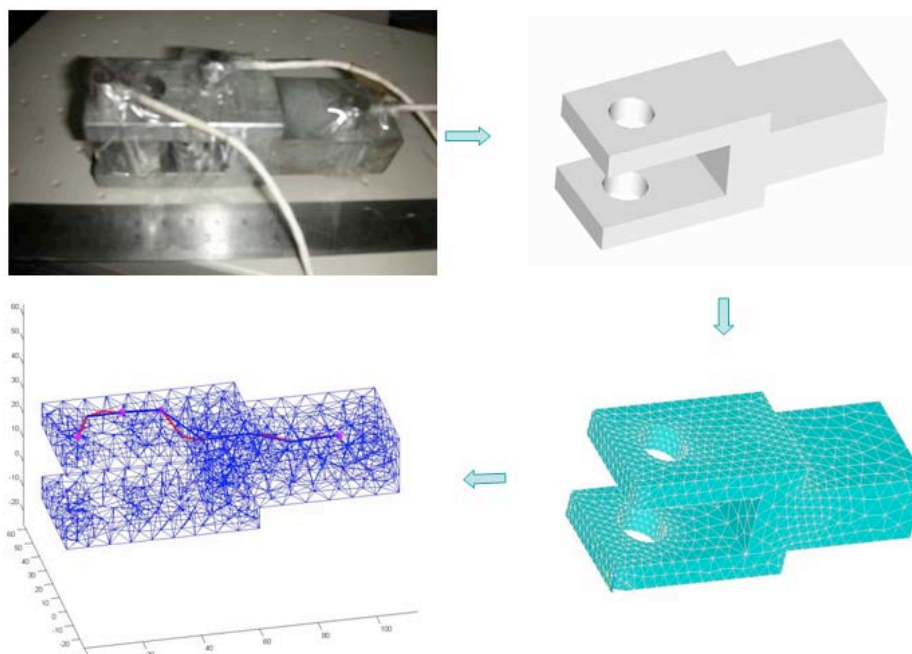


Fig. 6: Source location on a clamp with holes and sharp discontinuities.

Figure 6 shows the geometry as 3D model, the test setup, the ANSYS mesh and the MATLAB output (with a thick line showing the path from sensor location to the source). See Table II for the results. Error in this case is less than 10%.

Table II: Source location in clamp.

Location	Measured Value			Program output			% Error (Euclidean)
	X	Y	Z	X	Y	Z	
L-1	31	25	39	24.5	24.5	39.0	6.4
L-2	45	8	39	50	14.8	39.0	8.4
L-3	73	33	31.5	66	34	30.5	6.8
L-4	114	30	28	106	37	30.5	4.0
L-5	55	0	30	50	0	30	6.9

Conclusion

The approach presented in the study used a property of wave by which it tends to take minimum-energy path to travel between points on domain. This minimum-energy path was proved to be equivalent to shortest-distance path marking the birth of geodesics. The relation of geodesics to source location problem was established by proving that location of source is the first intersection point of multiple geodesics. This was implemented and proved by using Voronoi like diagram construction. The approach was experimentally validated on curved planar and odd geometry component. The solution based on two methods – conventional Numerical method and Geodesic Evolution method was presented. It can be asserted that the geodesic curve-evolution method hold great promise for versatile implementation catering to non-conventional geometries. By the very nature of approach, extension of it to inhomogeneous and anisotropic geometry appears feasible.

References

1. M. Ohtsu. AE Theory for Moment Tensor Analysis, *Res. Nondestructive Evaluation*, vol. 6: 1995. pp. 169-184.
2. M.A. Hamstad and K.S. Downs, On Characterization and Location of AE Sources in Real Size Composite Structures - A Waveform Study, *J of Acoustic Emission*, **13** (1-2), 1995, 31-41.
3. Bernard Castagnede et al., Location of Pointlike AE Sources in Anisotropic Plates, *J. Acoust. Soc. Am.*, **86** (3), 1989, 1161-1171.
4. E. Dijkstra, A note on two problems in connection with graphs. *Numerical Math.* **1**, 1959. 269-271.
5. K. Polthier et al., Straightest Geodesics on Polyhedral Surfaces, *International Conference on Computer Graphics and Interactive Techniques, ACM-SIGGRAPH courses*, pp. 30-38, 2006.
6. G.V.V. RaviKumar et al., Geodesic Curve Computations on Surfaces. *Computer Aided Graphics Design*, Elsevier, 2003, pp. 119-133.
7. Vitaly Surazhsky et al., Fast Exact and Approximate Geodesics on Meshes, *Proceedings of International Conference on Computer Graphics and Interactive Techniques, ACM SIGGRAPH 2005 Papers*, pp. 553-560, 2005.

THIRTY YEARS EXPERIENCE OF INDUSTRIAL APPLICATIONS OF ACOUSTIC EMISSION TESTING AT TÜV AUSTRIA

PETER TSCHELIESNIG

Institute for Technical Physics, TÜV Austria Services, Deutschstr. 10, A-1230 Vienna, Austria

Abstract

Since 1977 the TÜV Austria (till 1990 TÜV Vienna) has tested different pressure equipment with acoustic emission. The aims for these tests have been different for various applications such as: first hydrotests, requalification tests of pressure containments, leak detection and the detection and evaluation of corrosion. The different equipment technologies shall be mentioned and their influence on the test results shall be pointed out. As examples for successful applications the following test objects shall be mentioned:

- Gas storage spheres,
- Flat bottomed storage tanks (leakage and/or corrosion testing),
- Steam drums (dryers) in paper mills,
- Leak detection with an acoustic pig,
- Automatic testing of receptacles during the filling procedure,
- Corrosion tests of oil tankers.

The importance of standardization beginning within the EWGAE, and now with CEN/TC138 WG7 "Non-destructive testing - Acoustic Emission Testing" as an accepted method in Europe will be pointed out. At the end the rules for the training and certification according to the EN473 and their implementation within the three NDT societies from Germany, Austria and Switzerland will be presented. The three societies give common training courses and certification examinations.

An outlook in the future of the on-coming application, based on EC funded project, shall be provided. This outlook will show that AE testing will become in the years ahead more and more important for the competitiveness of the European industry to make the inspection of pressure equipment cost-effective and safe.

Keywords: Pressure equipment, integrity test, leak detection, training and certification

Introduction

Since 1977 the TÜV Austria has tested different structures, especially pressure equipment, storage tanks and pipelines with acoustic emission. Till today more than 30.000 different structures were tested and although the methodology has changed tremendously over the time I will review some typical applications, which were performed in the last 30 years. During this survey, I will point out the different technology and equipment used. Especially the rapid development of the electronic data acquisition and treatment has changed the possibilities and application of AE testing tremendously.

Our first contacts with AE were in 1975, when TÜV was nominated from the Austrian government to supervise the AE testing of Exxon Nuclear (with Dwight Parry) of the pressure vessel of the Austrian nuclear power plant at Zwentendorf. Two years later, we started our first own measurements with an Exxon Nuclear 2-channel equipment on different small structures even in the above-mentioned nuclear power plants. Our main tasks were pumps, penetrations through the

pressure containment, valves and other installations. Although this equipment had no real-time data storage and mainly engaged to collect AE hits, it provided a Δt -measurement for linear location. With this tool, we were able to detect and also roughly locate different defects, leaks and non-reported repairs in the tested structures. Even then, perhaps more so, it was very important to combine the AE results with other information of materials science and conventional NDT applications. Based on the meaningful results, we decide to buy a 24-channel equipment from AE International (Richland, Washington, USA) in 1979. With this system, we were able to acquire and process data coming from 4-channel arrays. The analog information was stored on a multi-channel tape recorder with a dynamic range of 26 dB at 100 kHz, which was at that time remarkable [1], although this would for some of colleagues sound like a tale from the Stone Age. With this equipment we reached a complete new stage in the application of AE.

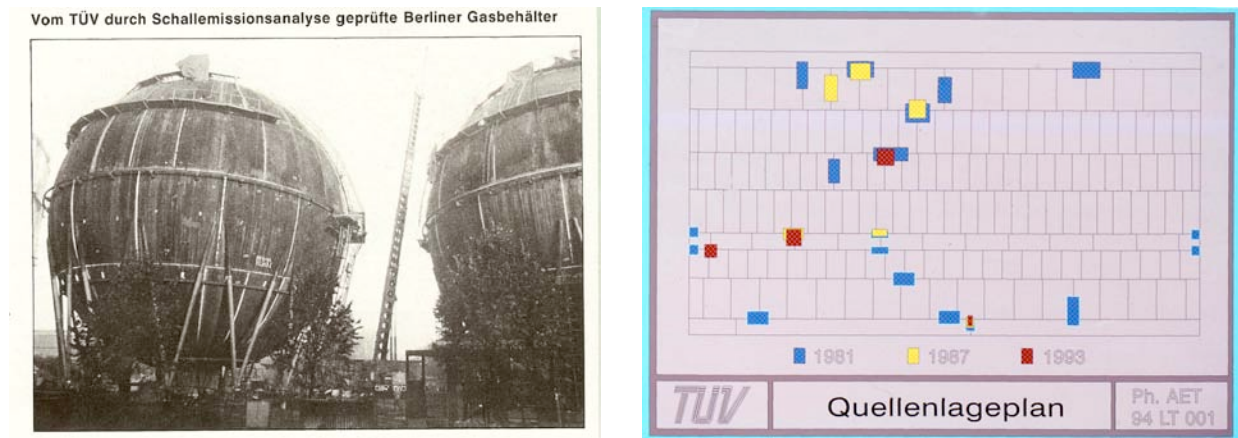


Fig. 1: Storage sphere (left) tested with acoustic emission; location map of acoustic emission test with active areas indicated by colored rectangles (right) at weld seams of the sphere.

Examples over the years

Gas storage spheres

In 1979/80 the Viennese gas supplier built 2 natural gas storage spheres with a diameter of 32 m and a service pressure of 1 MPa [2]. The hydrotests before service were monitored with AE, where we found stress concentrations based on improper welding, because parts of the sphere with different wall thickness were not welded according the neutral phases. Both spheres have had small inside-surface cracks, mainly caused by the bending over the support during filling. Although all welds had to undergo an NDT before the hydrotest, one big slag-inclusion was detected and located and has to be repaired.

It was remarkable, that we found many problems in the spheres, although the contemporary AE equipment had only a few features. This shows, that the normal hydrotest with its binary information (pass or not) is not a sufficient acceptance test for pressure equipments. The repetition tests every 6 years with different AE technology verified the results.

We have monitored during pneumatic loading two gas storage spheres of 33-m diameter at West Berlin in 1982, and in 1991 a natural gas storage sphere with 39-m diameter at service pressure of 1.2 MPa (the biggest storage capacity for natural gas within Europe). The AE tests were performed mainly for safety reasons (early alarm tool) as the structures were situated within a residential area, but also its NDT ability was used [3].

Leakage testing of flat bottomed storage tanks

In 1981, we started, after laboratory tests and on-site trial tests, AE monitoring of the flat bot-

toms of storage tanks for leaks [4-6]. This testing method uses the turbulences of the fluid media in the gap and some secondary effects between the bottom and the basement. Over the time, we tested more than 300 tanks and were able to improve the method, especially for the discrimination between leak source and background noise and also developed special location software. In those days, every test was a combination (comparison) of a low-liquid level (1–2 m) and high-liquid level (nearly full) test.

A good example for the successful application of the method was the leak within the bottom of a product tank. This was not detected even by vacuum boxes and could only be verified by penetrant testing (PT) of the weld between the sump and the bottom. Further development of the method led to the application of the cross-correlation method, which also gave us the opportunity to use the continuous AE for the detection and location of leaks. Some changes in the Austrian legislation and the demands of the customer to get more information about the status of the bottom led to the development of the corrosion testing, within an European Commission (EC) funded project in the second half of the 1990's.

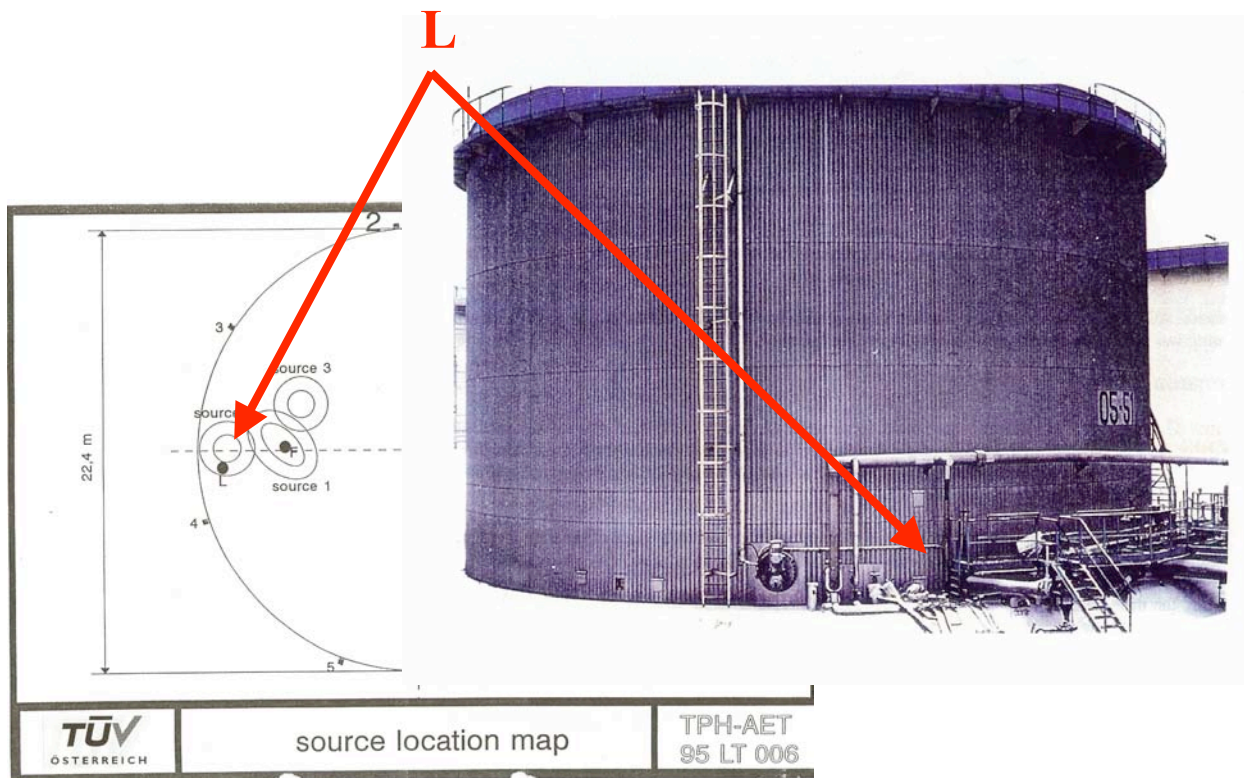


Fig. 2: Leakage testing of storage tanks; AE sources indicate position of leakage.

Corrosion testing of flat bottomed storage tanks

Beside the prevention of leaks, the corrosion problem was a pressing problem for the petroleum and petrochemical industry. Because it seems to be possible, but not proven, that corrosion can be detected with AE, the TÜV Austria together with a consortium of Vallen Systeme, (AE equipment manufacturer), CISE (AE testing company) and Shell Global Solution and Dow Germany (Tank user) proposed in 1995 a research and development project to the EC, which was accepted in 1997.

By extensive research works during laboratory tests and real tank tests, the consortium was able to prove, that corrosion and leakage can be detected but it is also possible to distinguish both types of AE sources. To make the distinction, the normal AE parameters were inadequate, and,

Therefore, we applied a frequency-domain pattern recognition system (VisualClass®) on the complete transient time signal. Based on the different physical events, the system was able to distinguish the different signals on a statistical basis. Of course, beside the pattern recognition additional filter criteria have to be applied on the whole data set.

Within the EC-funded project, which was completed 2000, we could develop and validate this testing method. But the results showed that the AE testing has changed from a method, which was only counting hits, events or threshold crossings to a sophisticated method, where the data processing replaced more and more the experience and “feeling” of the test operator [7].

From now on, the flat-bottomed storage tanks in some refineries, tank farms and chemical plants will be tested regularly for corrosion and leaks. By testing several hundreds of tanks the necessary database will be enlarged permanently and testing method will be accepted by more and more authorities [8, 9].

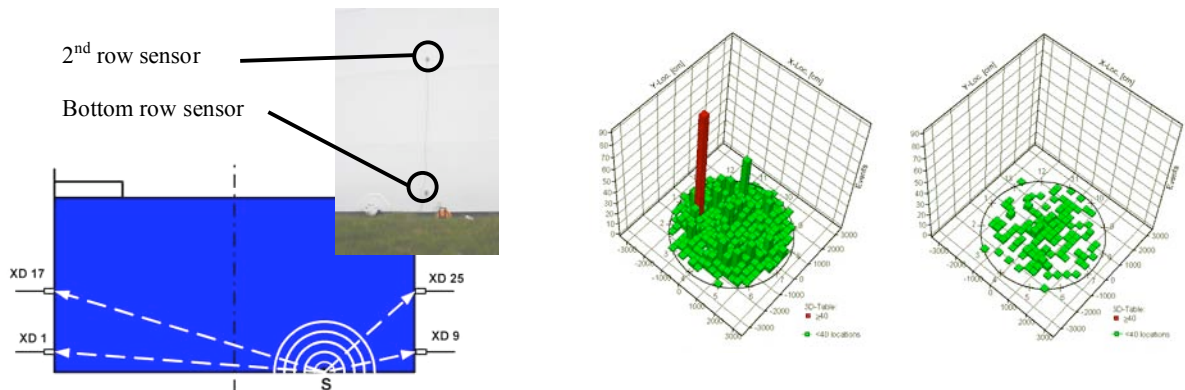


Fig. 3: Sensor layout for storage tank testing (left) and results obtained with only bottom row (red column, right) and with two rows of sensors (no indication, far right). With the arrangement in two rows it is possible to prevent the test result for the tank bottom from being flawed by corrosion of the floating roof.

AE testing of dryers (steam drums) in paper mills

For a long time, the paper mills have had the repetition of problems with their dryers tested by hydrotest and inside inspection. Problems increased more and more due to the enlarged production output. The higher rotation speed and higher temperature led also to a smaller wall thickness and resulted in damages to bearings, un-roundness and balance of the dryers during the hydrotests. If the cylinders have to be removed for the test, these resulted in shut-down periods of several weeks, which was unacceptable for the production. We started to develop a more sophisticated testing method than the hydrotest by the application of AE during a pneumatic loading of the drums in their normal service position [10, 11]. The AE testing was inserted as a pre-warning system for the pneumatic loading and also as a powerful NDT method, with a rough location based on a linear location. This became necessary due to the restricted accessibility of the surface of the drums.

During a shut-down period of 24 hours with AE testing, 6 to 8 cylinders can be tested. This brought not only big advantages for the performance of the paper industry, but a substantial gain for the safety was achieved. Defects, which were not detected during the conventional testing method, are now detected by the AE testing. Beside cracks, cavitations and corrosion attacks, we found also cracks in the balance weights. If these defects remain undetected during the shut-down period, these weights could destroy several cylinders during the subsequent service periods with further incalculable consequences.



Fig. 4: Testing of steam drum with AE sensor installation (left); Erosion found after entering into the steam drum due to indications obtained by AE measurement (right).

Leak detection Pig (ALARM)

In the early 1990's, we started with the OMV to develop a leak detection pig for diameters of 100 mm and up. This development was done for the connection lines between the refinery and tank farm of OMV. A pig has always the advantage, because it carries the sensor close to the AE source (leak) and gives the opportunity to check the pipeline in-service. After pre-tests in the laboratory and on a test rig, test runs on real pipelines with artificial leaks were done. The worst-case leak (drilled hole) sensitivity of the pig is 5 l/h at a minimum pressure of 300 kPa. Since 1994, the pigs (different modules for different diameters) run regularly on the OMV pipelines [12]. At a service for the Pinghu Oil & Gas field, near Shanghai (China), on a transmission line between on-shore and an off-shore loading platform over a length of 360 km, we detected 2 leaks and located them with an uncertainty of less than 1‰. This allowed the customer to repair these defects in welds.

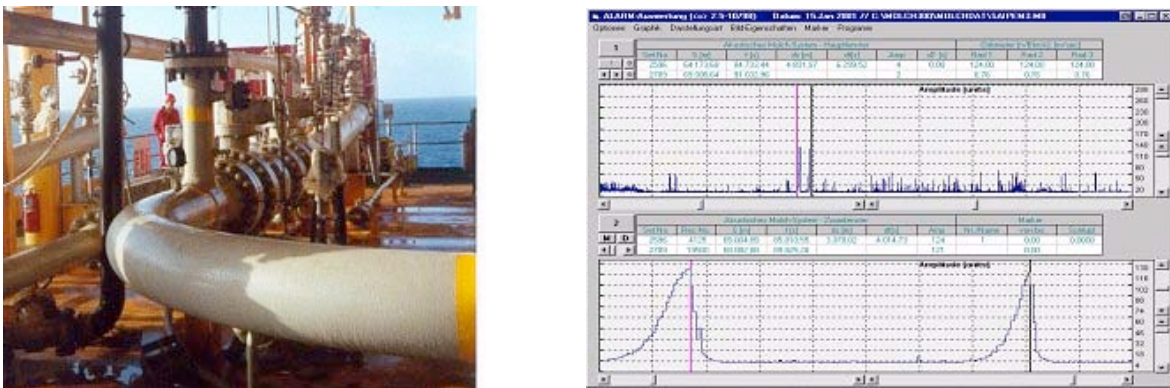


Fig. 5: Receiving pig trap off the coast of China (left) and indications of two leaks obtained by one pig run (right).

Automatic testing of receptacles during filling

Together with the gas distribution company Messer Austria, we developed a brand new test- and filling bench. Instead of testing the receptacles by a hydrotest, the tests will be performed automatically during the filling operation. The test rig allows overfilling the bottles up to 1.4 times of the service pressure. The whole period of this action will be monitored with 2 sensors each and the evaluation and stop criteria will be checked automatically from the computer according a pre-defined procedure. The criteria, which are established during lab-tests, are locked and can be changed only with our password. All rejected receptacles will be re-tested manually to identify the reason for the test-stop and undergoes a follow-up [13-15].



Fig. 6: AE testing on gas cylinders, 12 cylinders are tested simultaneously by pressurization with gaseous product (left), laboratory tests of fatigue cracks till burst with hydraulic pressurization for establishing a set of testing parameters (right top and bottom).

Detection and localization of corrosion attack on ship tankers

Based upon the application of AE testing for flat-bottomed storage tanks and horrible ship disasters in the last several years, e.g., Erika, Prestige, Napoli, which devastated hundreds of kilometers of the coast of Brittany, Galicia etc., we launched together with Vallen Systeme (Germany, equipment manufacturer) and four Polish companies, Gdansk University of Technology, Polish Registration society, Institute for Applied Sciences and Maritime Institute of Gdansk, an R&D project funded by the European Commission for detection and localization of corrosion attack on ship tankers.

The aims of the project were

- a permanent testing with an installed system, which will acquire the data during the shipping conditions and measure on-line the status of the structure and
- a spot-testing, which can be applied on ships in the harbor or on the anchor place before discharge.

Both systems have had to overcome the problems with the rough sea environment. Based on laboratory tests and background measurements on real ships (naval and commercial tankers), we found out that it is possible to distinguish the AE coming from corrosion and AE produced from shipping actions with different filter steps - frequency, localization and pattern recognition [16]. We demonstrated that we are able to detect “real corrosion sources” within ship tankers under normal shipping conditions. For these measurements, it was necessary to develop intrinsically safe, explosion-proof sensors, which were certified for zone 0 according the European directive and approved from a shipping classification society [17].

The spot testing was solved with a new multi-element sensor (holder with 4 sensing elements), which was able to detect but also locate the direction from the incoming AE wave. This

was a further advantage of this project and the application of this sensor type shall also be used for tank testing on-shore.

The project was finished in July 2006 [18]. Nevertheless, further investigations for ship corrosion become necessary, because the current technique acquires only those corrosion signals, which are in contact with liquid. A very important part for the integrity of a vessel is the deck, which at the moment cannot be checked.



Fig. 7: Oil tanker towed to the mooring buoy at an oil field off the coast of Poland (left), cargo tanks have been tested with a multi-element sensor (right) which was lowered down through deck opening and then immersed into the crude oil.

Standardization

Over the decades, the application of AE testing as an NDT method changed completely. At the beginning, it was an exotic method, which was applied only for very specific problems, and also the confidence on the results was limited, although AE testing has often demonstrated their ability and reliability. Now based on all further developments, AE testing became more and more an accepted and regular NDT method. But such a method needs beside the technical excellence

- standardization of the method and their application and
- trained and certified personnel, which has to be demonstrated against a commonly accepted standard.

Based on these demands, the test method made a big step forward, when the CEN/TC 138 “Non-destructive Testing” established the Working Group 7 “Acoustic Emission” [19] for the development of basic standards for the method (terminology, control of the used equipments and general principles of the different possibilities of applications). Since then, the WG7 developed many standards, which sometimes are now under review.

The finalized standards are:

- EN 1330 – 9 “Terminology used in AE testing”,
 - EN 13477 -1/-2 “AE testing-equipment characterization and control of their abilities”,
 - EN 14584 “AE testing of metallic pressure equipment – planar location”,
 - EN 15495 “AE testing of metallic pressure equipment – zone location”
- and the following work items are under preparation;
- WI 00138140 “Corrosion detection on flat-bottomed storage tanks”
 - WG7 NWI 607 “AE testing of fiber-reinforced plastics”.

As important as these standards were, it was crucial that AE testing was included in the EN 473, which regulates the qualification and certification of the test personnel, and establish the

abilities and allowances of the different 3 levels of AE testing personnel. The new EN 473:2007 or 2008 requires also a common training content all over Europe in TR 25107 “Guidelines for NDT training syllabi”. Although training and certification do not guarantee producing excellent AE testing personnel, it is an important basis for the further training on-the-job, which has to be performed in the respective testing organization [20].

Beside these bundle of standards of the methodology AE testing has been introduced to different product standards in normative and informative annexes, like

- EN 13445 – 5 “Unfired pressure vessels, Testing and Inspection”,
- EN 12817/18 “Inspection and re-qualification of LPG tanks up to 13 m³” and
- EN 14334 “LPG road tankers”.

All these standards give, beside the guidance for the application and the test performance, criteria and rules for evaluation, real-time control and source-severity grading. Nevertheless this is the weakest point of these standards, because the specific numbers and other qualitative threshold are based on the experience of the test organization and/or have to be defined in the product standards. It is obvious, that these test organization, which has a large database for many different test objects will not give them just for free to other competitors. This is a problem, which has to be solved hopefully in the years ahead.

Conclusion

The test history over the last 30 years showed, that acoustic emission was and is still a very prospective testing method. Although it is not a classical non-destructive test method, I think we shall require from it the same rules, which are taken into account for all other NDT methods.

- AE testing shall be only applied by qualified and certified test personnel, and has to be implemented in a test organization with a quality management system in accordance with EN/ISO 17025 and EN 473.
- AE testing shall be performed according to specific EN standards (process and/or product oriented), if available, or the method including the evaluation criteria have to be validated according to the specific EN or other international standards.
- AE testing has to be used only by well equipped and well experienced test organizations, which have available the specific database for the respective test object or has performed the necessary number of pre-tests on specific test samples. This is one very important requirement, because according to our experience every test object is unique in its AE behavior.

If these requirements are fulfilled AE testing will be and become much more in the future a real-time NDT, which will not only more time saving and cheaper than other testing method, but it will increase the safety of the structure and will be an excellent tool for the fitness for purpose for the structures.

References

1. Tscheliesnig P., Theiretzbacher H. (1981) “Praktische Erfahrungen mit Hilfe der Schallemissionsanalyse”, 2nd ECNDT 1981, pp. 221-223.
2. Tscheliesnig P., Theiretzbacher H. (1982) “Practical experiences with Acoustic Emission on large storage pressure vessels”, 10th WCNDT 1982.
3. Tscheliesnig P., Theiretzbacher H. (1984) “Schallemissionsprüfung bei Druckaufbringung mit gasförmigen im Vergleich mit flüssigen Medien”, 3rd ECNDT 1984.

4. Tscheliesnig P., Theiretzbacher H. (1985) "Leakage test by Acoustic Emission Testing (AET) on flat bottom tanks", 11th WCNDT 1985 pp. 40-45.
5. Tscheliesnig P., Theiretzbacher H. (1989) "New results from the detection of micro-leakages in the petrochemical industry", 12th WCNDT 1989, pp. 905-911.
6. Tscheliesnig P., Krenn G., Schauritsch G. (1990) "Dichtheitsprüfung mittels akustischer Korrelationstechnik in der petrochemischen Industrie", ÖGfZP-Jahrestagung 1990, pp. 51-59.
7. TÜV Österreich, CESI Spa, Vallen System. Shell Global Solutions. DOW Deutschland (2000), "Inspection of Flat Bottomed Storage Tanks by Acoustical Methods", Synthesis report of SMT4-CT97-2177 (EC).
8. Marino A., Tscheliesnig P. (2002) "A comparison between AE and MFL for tank floor inspection", 8th ECNDT 2002, p. 116, CD.
9. Tscheliesnig P. (2002), "Acoustic Emission Testing (AE) of bulk liquid storage tanks – Basics, case studies and future perspectives", 8th ECNDT 2002, pp. 119, CD.
10. Strunz K., Heck G., Tscheliesnig P. (1995) "Moderne ZFP-Verfahren zur Prüfung von Trockenzyklindern in Papiermaschinen", ÖGfZP-Jahrestagung 1995, pp. 65-73
11. Tscheliesnig P. (1998) "New inspection method of steam drums in paper mills", 7th ECNDT 1998, pp. 2288-2294.
12. Lackner G., Tscheliesnig P. (2004) "Field testing of flat bottomed storage tanks with acoustic emission – a review on the gained experience", 15th EUROCORR 2004, CD.
13. Tscheliesnig P., Krenn G., Schauritsch G., Edinger H. (1995) "An Acoustic Leak Detection Pig", 2nd International Pipeline Technology Conference 1995, pp. 205-210.
14. Tscheliesnig P., Lackner G., Hermeling W. "The automatic performance of the repetition tests of pressure bottles with AE" 15th WCNDT 2000, CD.
15. Lackner G., Tscheliesnig P. (2001) "Automatisierte Durchführung von Wiederholungsprüfungen an Gasflaschen mit Schallemission", 13. DGZfP-Kolloquium Schallemission 2001, pp. 193-201.
16. Tscheliesnig P. (2004) "Detection of Corrosion Attack on ships, especially oil tankers, with acoustic emission (AE)", 16th WCNDT 2004, CD.
17. Tscheliesnig P. (2005) "Entwicklung einer Schallemissionsprüftechnik zur Prüfung von Korrosionen an Öltankern", DGZfP Jahrestagung 2005, CD.
18. TÜV Austria et al., Final Report of the EC-funded project „Detection and Discrimination of corrosion attack on ships (crude oil tankers) with Acoustic Emission (AE)“ project No. EVG1-CT-2002-00067.
19. Tscheliesnig P., Fontana E. (1998) "European standardisation in CEN TC138 WG7", EWGAE 1998, pp. 287-290.
20. Tscheliesnig P. (2004) "Training and certification on field of acoustic emission testing (AT) according the European standardisation (EN 473)", EWGAE, pp. 235-237.

APPLICATION OF ACOUSTIC EMISSION TECHNOLOGY TO MONITOR THE LUBRICATION CONDITION OF A DIESEL ENGINE OF AN ARMORED FIRE SUPPORTING VEHICLE

N. JAMALUDDIN, M.J. MOHD NOR, O. INAYATULLAH¹ and B.I. SURAYA MURAT²
Dept. of Mechanical and Material Engineering, Universiti Kebangsaan Malaysia, Bangi, Selangor, Malaysia; ¹Royal Malaysian Corps, Malaysian Ministry of Defense, Kuala Lumpur, Malaysia; ²School of Mechatronics Engineering, Universiti Perlis Malaysia, Perlis, Malaysia

Abstract

This paper presents an investigation of the capability of acoustic emission (AE) technology to monitoring and detecting the variation of engine-oil viscosity in a diesel engine. The investigations were conducted on a 320-hp diesel engine of an armored fire-supporting vehicle of Malaysian Army. Two lubrication conditions were tested; namely, using new and old engine oil. The lubrication condition in the diesel engine was successfully monitored based on the AE signatures generated by the interaction of the engine components. The generated AE signatures were captured using an AE measurement system. The captured waveform signatures were then analyzed using MatLab software. The results of the experimental works show that the statistical analysis parameters including root-mean-square, maximum amplitude and energy values are capable of distinguishing between the new and old engine oil in the diesel engine. The AE technology can assist the Malaysian Army in determining the correct time to change the engine oil of the armored fire-supporting vehicle.

Keywords: Lubrication condition, stress wave signatures and statistical analysis

Introduction

Acoustic emission (AE) technology has been utilized as an effective condition-monitoring and diagnosis technique for many types of rotating machinery [1-4]. AE technology was also utilized to monitor and identify the efficient classifiers for the detection of two different failure modes in a marine diesel engine using AE. The investigated failure modes were the exhaust valve leakage during the compression and also the defective injection during the firing process. The root-mean-square (RMS) of the captured AE signals was identified as an efficient classifier capable of discriminating between leak sizes in the exhaust valve and detecting the misfire phenomena [5].

AE technique was also found to be capable of determining the strength of the air-fuel mixture in a 30.56-liter Perkins 4-stroke, 8-cylinder turbocharged gas engine [6]. The results also revealed that the AE signatures could be used to identify the strength of the gaseous fuel mixture. The RMS values of the AE signatures were correlated with the pressure in the time and frequency domains. El-Ghamry also developed generic techniques for diagnosing faults in reciprocating machines [7]. The generic pattern was based on the time-domain RMS signals, which correlated to the AE responses to specific events in the engines.

Steel et al. have investigated the ability of AE signatures to monitor and diagnose the actual operation and degrading processes in the engine [8]. The analysis on AE data could be enhanced with a detailed knowledge of the operating conditions of the engines, such as the injector timing, running speed and valve movement. Furthermore, AE technique was used to monitor and

diagnose the wear of piston ring while in operation [9]. The AE signals were analyzed using typical signal parameters such as the ring-down count and RMS voltage. The particular value of the RMS voltage and ring-down count indicate that the ring wear remains relatively constant for various engine load conditions.

Engine Oil Monitoring Using AE Technique

It appears AE technique has not been utilized to monitor and diagnose the engine oil condition. Joyce has used direct measurement technique to identify the engine-oil film thickness in the piston-liner contact [10]. The technique involved the capturing and analyzing the reflection of an ultrasonic pulse at the oil film. The proportion of the reflected wave amplitude was then related to the thickness of the oil film. The study was conducted using a single cylinder, 4 stroke engine on a dynamometer test platform and a piezoelectric transducer was bonded to the outside of the cylinder liner to emit high frequency with short duration pulses.

Experiment Setup

This experiment was carried out on a 320-hp at 1900 rpm, 4 strokes MAN D 2566 MK 6 cylinder in-line water-cooled turbocharged diesel fit in the vehicle as shown in Fig. 1. The engine used in Sibmas armored fire supporting vehicle was shown in Fig. 2. The engine oil used in this study was Shell Rimula X oil. The engine oil data is shown in Table 1. The experiment was conducted on a single cylinder operating at 1900 rpm. The experiment involved old engine oil (had been used for 24 months) and new engine oil.

The standard AE instrumentation, a 2-channel system from PAC was utilized along with a broadband sensor, WD35. The sensor was bonded to the outside of the engine block as shown in Fig. 3. For each signal, the waveform data was captured and recorded. The waveform signatures were then analyzed using MatLab software for further analysis. Finally, the old engine oil was sent to laboratory to undergo simple physical test to determine the viscosity and contamination.



Fig. 1: Malaysian Army Sibmas AFSV used in the study.



Fig. 2: Top view of the Malaysian Army Sibmas engine MAN D 2566 MK 6 cylinder.

Results and Discussion

Typical AE time-domain signature for the engine oil monitoring is shown in Fig. 4. 25 time signals for each condition of the engine oil were selected for further analysis.

The AE time domain signatures were analyzed using simple statistical analysis parameters including maximum peak amplitude, root mean square (RMS) and energy. The results of the

Table 1: Specification data for Shell Rimula X Oil SAE.

Product Name :	SHELL RIMULA X OIL SAE 40
Product Type :	High speed diesel engine oil
K. Viscosity at 100 °C	14.5 mm ² /s
Density at 15 °C	895 kg/m ³
Pour Point	-15 °C
Flash Point	250 °C
K. Viscosity Limit at 100 °C	Max - 18.0 mm ² /s Min - 11.5 mm ² /s

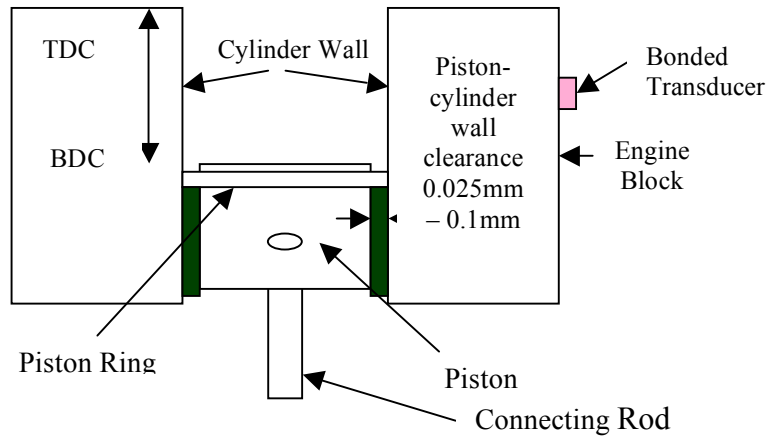


Fig. 3: Location of the AE transducer on the diesel engine.

statistical analysis for the new and old engine oil are shown in Table 2. The results show that the statistical parameters of the new engine oil are higher than the old engine oil.

Viscosity Test

The measured values of the kinematics viscosity using the simple viscosity test for the new engine oil and old engine oil at 100°C are equal to 14.37 mm²/s and 13.15 mm²/s, respectively.

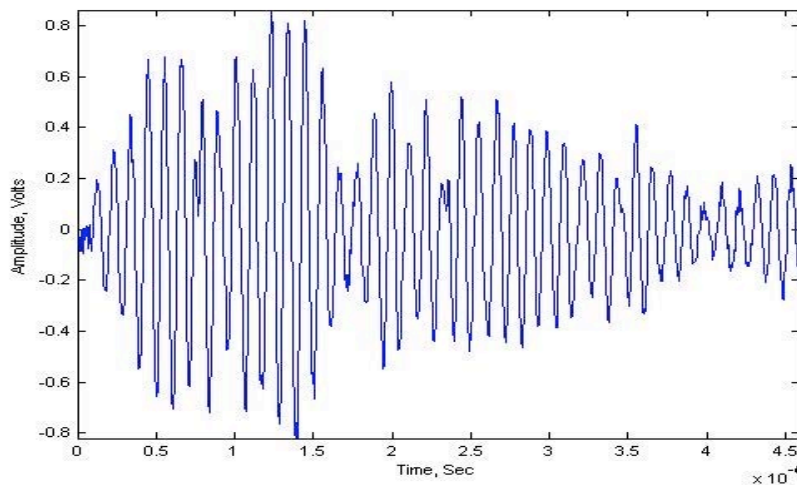


Fig. 4: Typical AE time wave form for the engine oil monitoring.

Discussion

It is expected that the interaction between the piston and cylinder generates AE signatures. The operating speed of the engine during the test was equal to 1900 rpm or 31.67 Hz. The results of the investigation demonstrate that the transmutability of AE signatures generated by the interaction of the piston and cylinder wall is dependent on the viscosity of the engine oil. The higher the viscosity of the oil, the more AE energy can be transferred through the cylinder block. The same phenomenon has been discovered by Jamaludin et al. [11, 12], who utilized AE technology to monitor lubrication condition in a low-speed bearing.

The statistical analysis show that the averaged peak amplitude, RMS and energy levels can be utilized as a measurement criteria to monitor the viscosity variation in a diesel engine of an armored fire supporting vehicle. The authors suggest that the energy level should be used as an indicator, since there are significant changes in the energy level when the viscosity of engine changed from 14.37 mm²/s to 13.15 mm²/s. Energy level can easily be used to alert the maintenance team regarding the deterioration of the viscosity of the engine oil. Therefore, a trending technique is suggested to monitor the variation of the engine oil viscosity over a period of time. This parameter has been used to monitor the lubricant condition, i.e., deterioration in viscosity.

In order to utilize the energy analysis to determine the viscosity of engine oil inside a diesel engine, baseline signatures for new engine oil is required as a reference signal. The baseline data will then be used to trend the energy level to identify any significant change in the viscosity of the engine oil.

After a period of time, the viscosity of engine oil will reduce due to ageing and contamination. Consequently, it is expected that the transmissibility capability of the engine oil will also reduce accordingly. This phenomenon is detectable with the AE monitoring technique since the reduction in transmissibility will result in the reduction of energy levels.

Table 2: Time series analysis of the resultant PIT signal with different amounts of grease inside.

Statistical Parameter	Engine Oil Condition	
	New	Old
Averaged RMS (volts)	0.3200	0.1300
Averaged Peak (volts)	0.7433	0.3466
Averaged Energy (Volts.msec) $\times 10^{-6}$	9.4301	5.2110

Conclusion

Based on the results of this study, the AE monitoring technique has demonstrated its capability in assessing the variation of engine oil viscosity within a diesel engine, which is closely associated with the lubrication condition in the bearing. This method is found to be effective due to the fact that the acoustic emission propagation is sensitive to the transmission path, which in turn is affected significantly by the viscosity value of the engine oil. Also, allowing AE signatures to travel over longer distances, after transmission across an interface, will result in a more pronounced effect on the signature shape. To the author's knowledge, this particular technique has never been used before to monitor the variation of engine oil viscosity in a diesel engine.

References

1. I. Sato, Electrical Eng Japan, **110** (2), 1990, pp 115-127.
2. T. J. Holroyd and N. Randall, British Journal of Non-Destructive Testing, **35** (2), 1992, 75.
3. D. Mba and R. H. Bannister, Proc Inst Mech Engrs, **213** Part E, 1999, 153-185.
4. A. Choudhury and N. Tandon, Tribology International, **33** (1), 2000, 39-45.
5. A. Friis-Hausen and T. L. Fog, COMADEM, 2001, pp. 641-648.
6. M. H. El-Ghamry, R. L. Reuben, J.A. Steel and T. L. Fog, Mech. System and Signal Processing, **19** (4), 2005, 751-765.
7. M. H. El-Ghamry, R. L. Reuben and J. A. Steel, Mech. System and Signal Processing, **17** (4), 2003, 805-823.
8. R. L. Reuben and J. A. Steel, J. Strain Analysis for Eng. Design, **40** (1), 2005, 45-57.
9. A. N. Haq and T. Tamizharasan, Int J Adv Manuf Tech. **31** (2007), 2006, 1148-1155.
10. R. S. D. Joyce, D. Green, S. Balakrishnan, P. Harper, R. Lewis, P. King and H. Rahnejat, SAE Technical Papers, 2006.
11. N. Jamaludin and D. Mba, NDT and E International, **35**, 6, 2002, 349-358.
12. N. Jamaludin, D. Mba, and R.H. Bannister, J. of Process Mech. Eng., **215E**, E4, 2001, 245-271.

PLASTIC-REGION TIGHTENING OF BOLTS CONTROLLED BY ACOUSTIC EMISSION METHOD

YOSHIHIRO MIZUTANI, TADASHI ONISHI and MASAMI MAYUZUMI

Dept. of Mech. Sci. & Eng., Tokyo Institute of Tech., Meguro, Tokyo 152-8552, Japan

Abstract

We have proposed a control method for plastic-region tightening of bolts using AE method. In this paper, in order to investigate the validity of the tightening control by AE method, the tightening test in an actual condition was conducted and both tightening accuracy and variations were compared with those by conventional control methods. The results show that AE method is more effective for plastic-region bolt tightening control than the conventional methods. Finally, a new system using a Maharanobis distance for controlling plastic-region bolt tightening by AE method was developed.

Keywords: Plastic-region bolt tightening, tightening control, Maharanobis distance

Introduction

A plastic-region tightening method used in the automotive industries is known as a good method for preventing fatigue of bolts. However, the most common tightening-control method by using a torque wrench (called torque-control bolt tightening method) cannot apply to a plastic-region tightening [1]. Both an angle control method and a torque-gradient control method are regulated in JIS (Japanese Industrial Standards) [2] for a plastic-region tightening control, although the method requires a special torque wrench and complicated procedures. We have proposed a new control scheme using AE method, but the accuracy and validity were not examined. In this paper, in order to investigate the accuracy and validity of the tightening-control in field, the tightening test was conducted. The tightening-accuracy and variation by AE method were found superior to those controlled by conventional methods.

Experimental Setup and Method

When a tightening is performed in field, noise due to friction on bearing surfaces was monitored with AE. In order to confirm whether AE method can be utilized in an industrial condition, tightening test in simulated factory environment was performed. Moreover, accuracy and variation of the tightening control by AE method were compared to those by conventional methods (angle control method and torque-gradient control method). Figure 1 shows photograph and schematic illustration of experimental setup used for the test. The axial load of a bolt was measured by a load cell (TEAC, TU-NR-C50kN), which was placed between two steel plates (SKS93, thickness: 10 mm). We prepared two sets of steel plates, of which surface roughness (arithmetical mean surface roughness) were less than 3.1 μm (plate 1) and 25 μm (plate 2). A torque was measured with a digital torque wrench (Nakamura, DTC-N1000EX). A potentiometer (Nidec Copal Electronics Corp., M-22E10-050 1k) was used for measuring the rotation angle. A socket of a torque wrench was equipped with a timing pulley, rotation angle of a bolt was transmitted to the potentiometer with the timing belt, and the rotation angle was measured. An AE sensor (PAC, Type: PICO) was attached to a bolt head.

AE signals were filtered by high-pass filter of 100 kHz and amplified 66 dB by AE analyzer (NF Electronic instruments, Type: 9501). By using this experimental setup, a torque, an axial load, a rotation angle and AE can be measured simultaneously during bolt tightening.

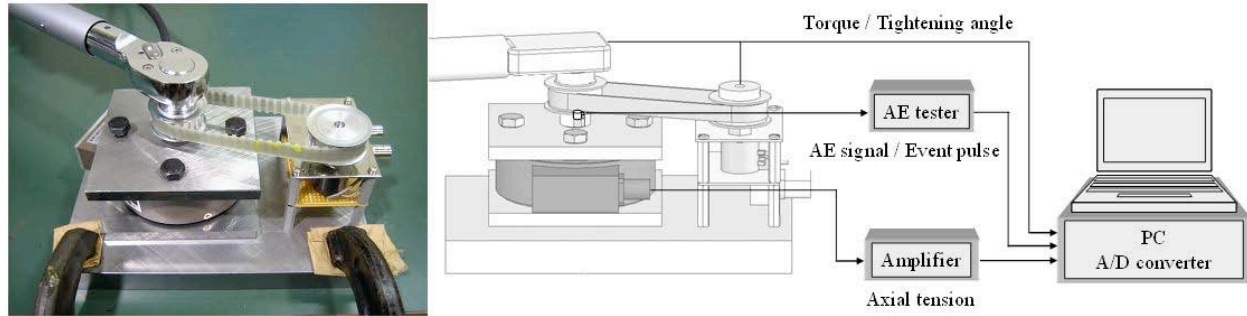


Fig. 1 Photograph and schematic illustration of tightening test

Conventional Control Methods

We first investigated tightening accuracy and variation of conventional methods. One of the plastic-region tightening control methods regulated in JIS B 1083 is an angle control method. According to the JIS, desired angle (θ_{fA}) for a plastic-region tightening is determined by a following equation.

$$\theta_{fy} \leq \theta_{fA} \leq \frac{1}{2}(\theta_{fy} + \theta_{fu}) \quad (1)$$

Here, θ_{fy} is rotation angle corresponding to the yield point of bolts, and θ_{fu} is that of the ultimate point. Angles of θ_{fy} and θ_{fu} are determined by load-rotation angle diagram as shown in Fig. 2. Desired angle-range for plastic-region tightening (Eq. (1)) and axial-load-range controlled by the method are shown in the figure as $\Delta\theta_f$ and ΔF_f , respectively.

Next, we conducted several experiments and the accuracy and variation of tightening control were examined. Since the axial loads of yield point and ultimate point varied with torque applied to bolts and the applied torque is changed by tightening conditions (even if bolts with same lot are used), it is needed to normalize axial load when the data of different experiments are compared. The following normalized axial-load F^* is introduced for this purpose

$$F^*_{\min} = \frac{F_{fA\min} - F_{fy}}{F_{fu} - F_{fy}} \quad F^*_{\max} = \frac{F_{fA\max} - F_{fy}}{F_{fu} - F_{fy}} \quad (2)$$

Here, F_{famin} and F_{famax} are axial loads correspond to minimum and maximum of desired angles by Eq. (1). F_{fu} and F_{fy} are the yield load and ultimate load determined by θ_f - F_f diagram for every experiment. Therefore, when a symbol F^* becomes 0, axial load of bolt reaches the yield point, and when a symbol F^* becomes 1, axial load reaches the ultimate point. Results of 8 experiments (1-5th experiments used plate 1, 6-8th experiments used plate 2) are shown in Fig. 3. When a desired tightening angle is set to a minimum in the range defined by the Eq. (1), the variation of axial loads for every examination becomes large, although, while a desired angle is set to a maximum, the variation becomes small and axial-loads are controlled at near the ultimate load. Axial tensions of each examination are always set in the range of 0 to 1, and it can be said that the angle control method is an accurate control method for plastic-region tightening. The other plastic-region tightening control method regulated in JIS B 1083 is a torque gradient control method. According to the JIS, desired torque gradient ($dT_f/d\theta_f$) for a plastic-region tightening is determined by the following equation.

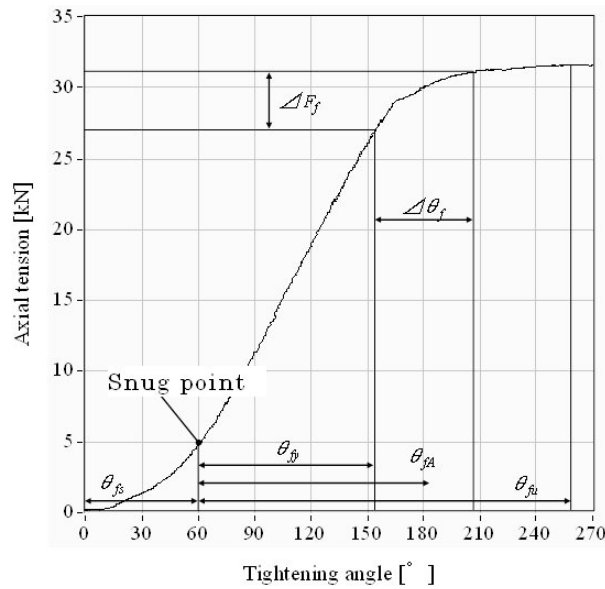


Fig. 2 Axial tension vs. tightening angle.

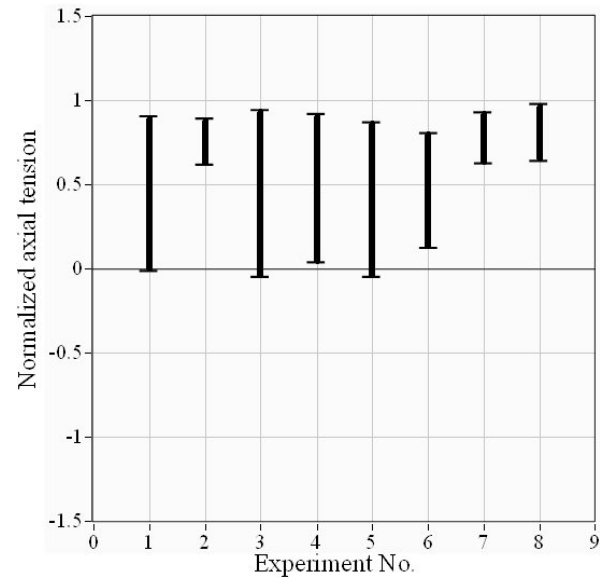


Fig. 3 Accuracy and variations of axial load.

$$\frac{1}{3} \left(\frac{dT_f}{d\theta_f} \right)_{\max} \leq \left(\frac{dT_f}{d\theta_f} \right) \leq \frac{1}{2} \left(\frac{dT_f}{d\theta_f} \right)_{\max} \quad (3)$$

Torque, torque gradient and axial tension with tightening angle monitored during 1st experiment are shown in Fig. 4. Desired range for plastic-region tightening (Eq. (3)) and axial-load range controlled by the method are also shown. In order to discuss tightening control accuracy for each experiment and variation for every experiment, the normalized axial load of eight experiments are investigated (see Fig. 5). Tightening variations were large compared to those by angle-control method (Fig. 3). Furthermore, the result shows that there is a possibility that the axial load will not be managed in a plastic region in some cases. Therefore, this control method is inaccurate.

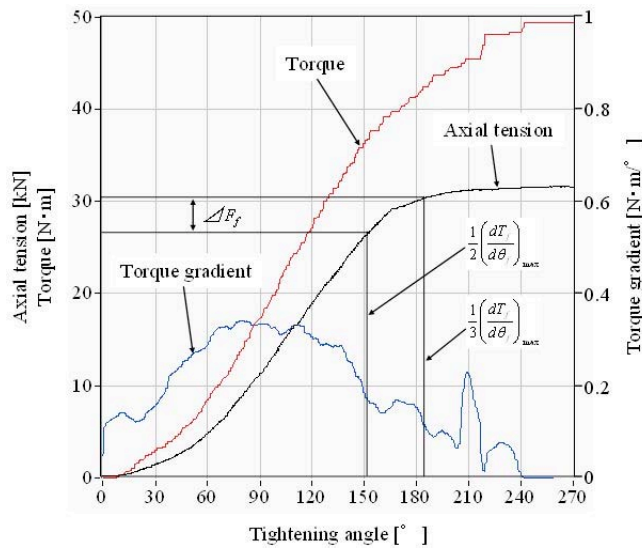


Fig. 4 Tightening range of torque-gradient load. method.

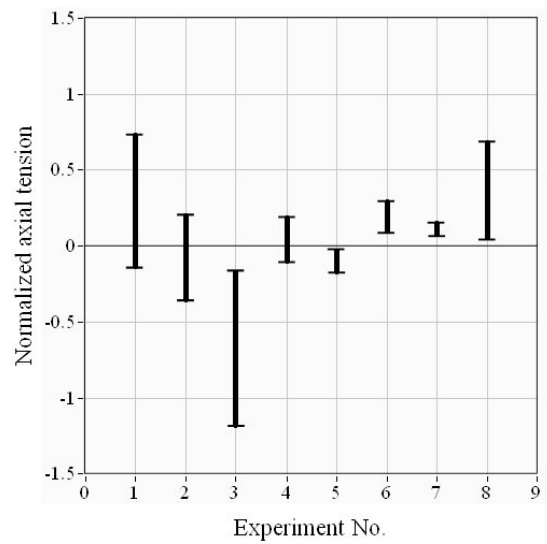


Fig. 5 Accuracy and variations of axial load.

Acoustic Emission Method

Variations of AE event count rates and Ib-values with tightening angle during tightening is shown in Fig. 6. Axial tension vs. tightening angle diagram is also shown.

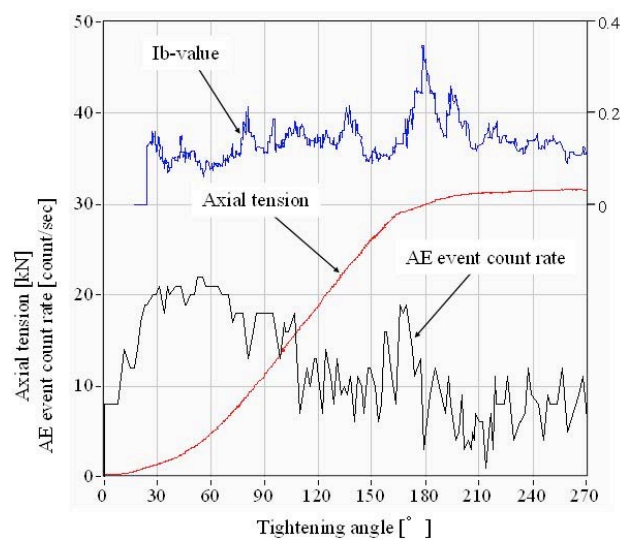


Fig. 6 AE activities during bolt tightening.

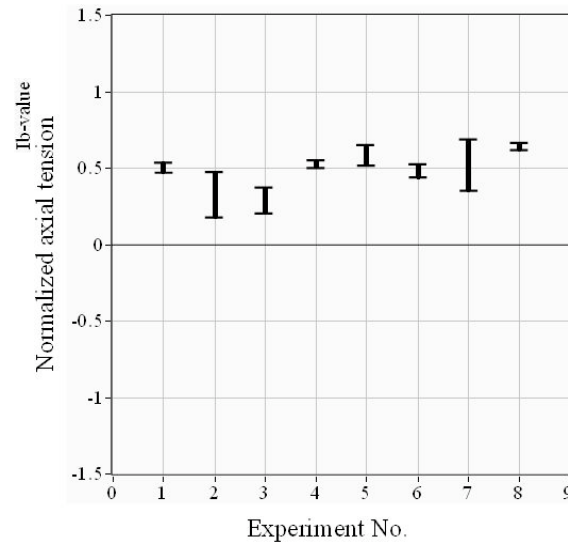


Fig. 7 Accuracy and variations of axial load.

We observed a large number of AE events in the initial stage of the test. These AE signals are noise due to friction on the bearing surfaces. In spite of having measured many noise events, this result clearly shows that AE event count rates have a peak near the yield point and Ib-values reach the peak just beyond the yield point. Therefore, AE signals due to plastic deformation can be monitored even in real tightening conditions as the indicator of yielding. Both AE event count rates and Ib-values will be useful parameters for controlling plastic-region tightening. Figure 7 shows normalized axial load controlled by AE method for eight experiments. Maximum position in each experiment is determined by the peak in Ib-values, and the minimum position by the AE event count rate peak. Variations for the experiments are similar to that of angle control method (when desired angle is set to the maximum value in Eq. (1)). The axial loads of experiments were controlled in the range of 0.2 to 0.7, and the average variation was ± 0.11 . This compares favorably with ± 0.16 and ± 0.30 for angle control and torque-gradient control methods, respectively. This demonstrates that AE method is the most accurate control method for plastic-region tightening among the three examined here. Although roughness of the bearing surfaces differs between the 1st-5th experiments and the 6th-8th experiments, AE method has controlled the axial load appropriately. The experimental results show that AE method is more effective in plastic-region bolt tightening control than the conventional methods.

Development of Plastic-region Bolt Tightening Control System

In the previous section, we showed a feasibility of controlling plastic-region tightening by AE method. However, it is difficult to judge the peak of AE parameters due to plastic deformation automatically by a computer system. Thus, we developed a method in lieu of the peak detection of AE event count rates and Ib-values. The new method relies on the Maharanobis distance and a new index for judgment is defined; i.e., the inverse of Maharanobis distance.

Here, Maharanobis distance of AE signals detected is defined as follows [3, 4]:

$$D = \sqrt{\frac{((x - \bar{x})/\sigma)^T \cdot R^{-1} \cdot ((x - \bar{x})/\sigma)}{p}} \tag{4}$$

Here, $x = [x_{rate}, x_{Ib}]$ is a two-dimensional vector consisting of the AE event count rate and the Ib value of the comparison data. $\bar{x} = [\bar{x}_{rate}, \bar{x}_{Ib}]$ is a two-dimensional vector, consisting of the averages of the reference AE parameters. We used the event count rate and the Ib-value that were detected at a yielding range of $\theta = 164^\circ$ - 180° in the 1st experiment for the angle-control method as the reference AE parameters. p is the number of the dimension and is two for this study. R^{-1} is an inverse matrix of a sample correlation matrix.

The inverse of Maharanobis distance during 4th and 6th experiment is shown in Fig. 8. The axial load-tightening angle diagram is also shown. The inverse of Maharanobis distance became large when the axial load reaches the yield point. This can be used to judge the yield point during tightening. Note that the conditions for 6th experiment tightening are not the same as those for the reference data (plate No. 2 was used); thus the absolute value of the inverse of the Mahalanobis distance is smaller than that of 4th experiment.

Based on the experimental results, the judging criteria of the plastic-region tightening was determined as follows;

- 1) The torque become larger than 20 [N·m].
- 2) Inverse of Maharanobis distance become larger than 5.

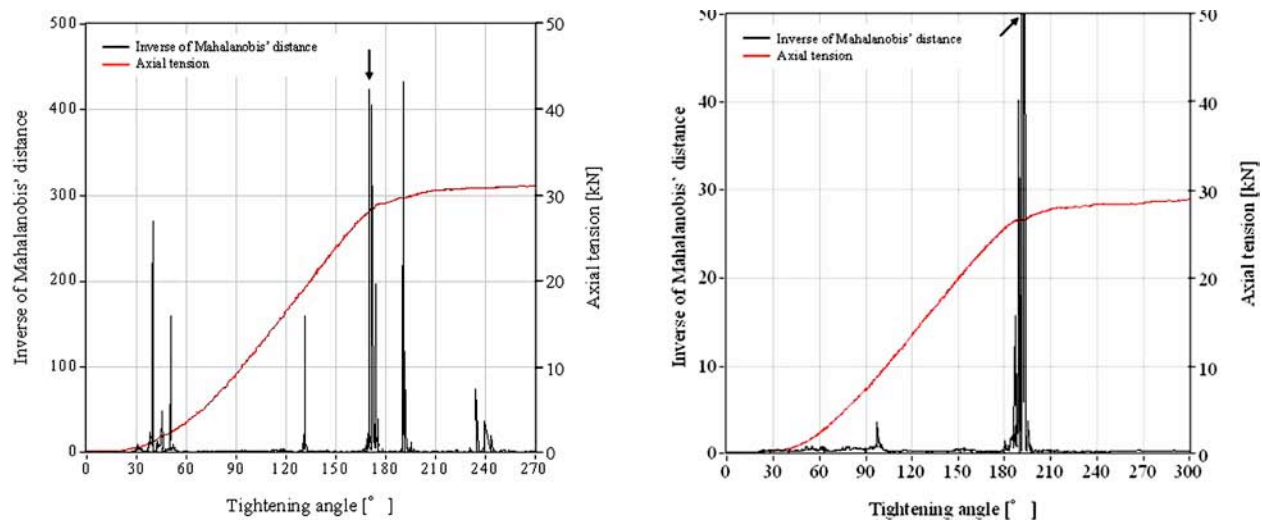


Fig. 8 Inverse of Maharanobis distance during the test (left: 4th experiment, right: 6th experiment).

We developed a control system for plastic-region tightening as shown in Fig. 9. The equipment consists of a digital torque wrench, an AE monitoring device, and an analysis system. AE sensor was attached to the head of a bolt. AE parameters and torque were monitored and analyzed by the developed software. When correct tightening conditions are reached, the LED in the software-screen is turn on. Figure 10 shows the axial load, torque and inverse of Maharanobis distance when tightening is conducted by the developed system. As we used plates in which the surface roughness was not regulated, tightening conditions differed from those of the reference data. The absolute values of the inverse of the Mahalanobis distances were smaller than those of Fig. 8. Although ratchet mechanism of wrench was used during tightening, appropriate judging was performed by the developed system.

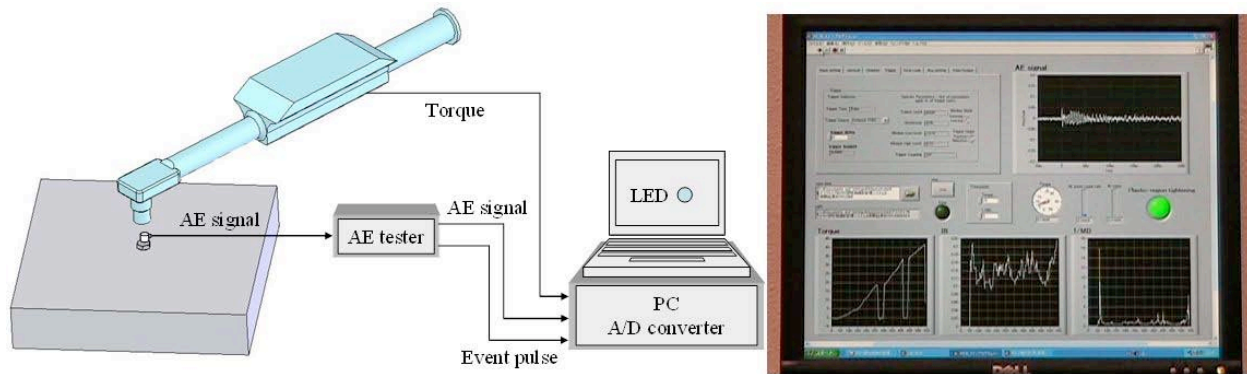


Fig. 9 Developed control system for plastic-region tightening.

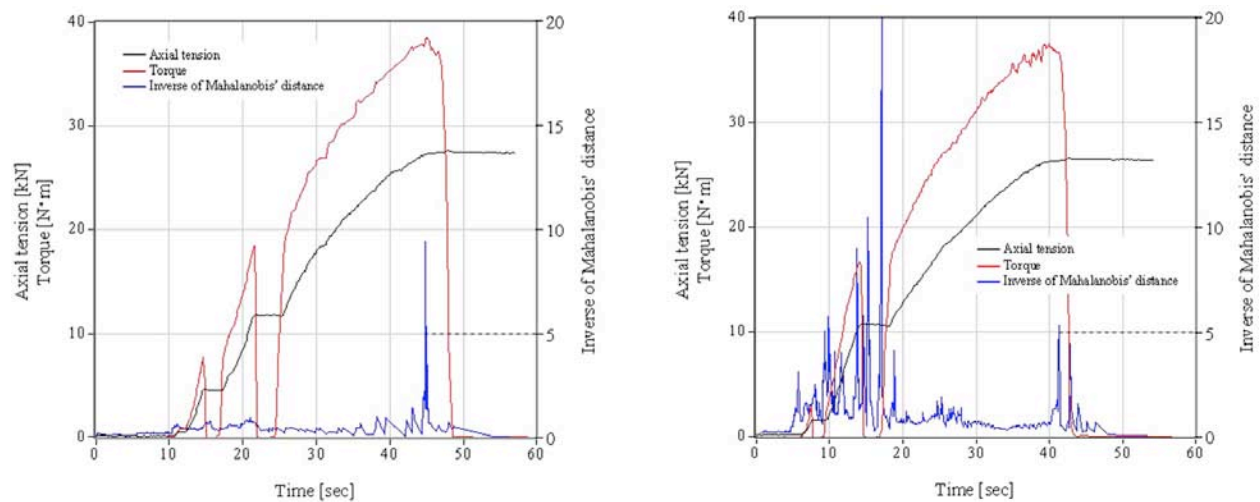


Fig. 10 Axial tension, torque and inverse of Maharanobis distance during the test.

Conclusion

Fundamental study of plastic-region bolt-tightening control by AE method was conducted. Results are summarized as follows,

- 1) Tightening test in a real condition was conducted and both the accuracy and variations of tightening were compared with those by conventional control methods. It was found that AE method is superior to conventional methods for plastic-region bolt-tightening control.
- 2) A new control system for plastic-region bolt tightening was developed. A new index for judging the yield point was implemented in the analysis system. The utility of the developed system was demonstrated by conducting tightening tests successfully.

References

1. T. Hattori, Failure analysis and prevention of mechanical, adhesive and welded joints, paper delivered at study group on the accident/failure analysis method of JSME (2002).
2. JIS B 1083-1990 General rules for tightening of threaded fastener.
3. Y. Tanaka and K. Wakimoto, *Methods of Multivariate Statistical Analysis*, 14th ed., Gendai-Sugakusha, (2004).
4. http://en.wikipedia.org/wiki/Mahalanobis_distance

MEASUREMENT OF MEMORIZED STRESS AFTER VARIOUS LOADING CONDITIONS BY AE

SHOICHI NAMBU, YOSHIHIKO FUJINO and MANABU ENOKI

Department of Materials Engineering, The University of Tokyo
7-3-1 Hongo, Bunkyo, Tokyo 113-8656, Japan

Abstract

A new sensing method called “smart stress memory patch” for structural health monitoring has been developed. It can estimate the maximum stress, the stress amplitude and the number of fatigue cycles of structure in principle. The stress amplitude and the number of fatigue cycles can be obtained by the crack growth behavior of this patch, and the maximum stress can be also estimated by the AE onset stress during the reloading using Kaiser effect of AE. In this study, the possibility of estimating the previous maximum stress of this patch was investigated. The electrodeposited-copper (ED-Cu) specimen with 40-mm length, 5-mm width and 0.1-mm thickness was prepared, and its microstructure was changed by heat-treatment. The stress of AE onset during tensile loading was investigated, and it was proportional to the yield stress of ED-Cu specimen. AE behavior was also measured after various fatigue loading conditions such as constant amplitude loading, over-loading and variable amplitude loading to estimate the applied maximum stress. The maximum stress under various fatigue loading conditions can be estimated by this heat-treated and notched ED-Cu specimen.

Keywords: Structural health monitoring, fatigue loading, Kaiser effect

Introduction

Structural health monitoring has become important to ensure the reliability of structures. In the case of infrastructures such as bridges and ships, the fracture due to fatigue damage is a huge problem. The strain gauge is usually used to monitor the fatigue damage of a structure, while the off-line monitoring method is also desired. Some fatigue sensors, which consist of sacrificial specimens with crack, have been developed to evaluate the fatigue damage of structures [1, 2]. Although the fatigue damage can be obtained by crack length after fatigue loading, there are several problems such as the needs for measuring applied stress or number of cycles by another system and for the same fatigue characteristics between the sensor and the structure.

A new sensing method called “smart stress memory patch” has been developed to evaluate the fatigue damage of structures [3]. This patch consists of the sacrificial specimen made of pure copper. The maximum stress, the stress amplitude and the number of fatigue cycles of structure can be obtained by this patch. The maximum stress can be estimated by the AE onset stress during the reloading using Kaiser effect of AE. The stress amplitude and the number of fatigue cycles can be also estimated by the fatigue crack growth behavior. In this study, the possibility of estimating the previous maximum stress of this patch was investigated. The effects of yield stress and notch length on the AE onset stress were evaluated. AE behavior was measured after various fatigue loading conditions such as constant amplitude loading, over-loading and variable amplitude loading to estimate the applied maximum stress.

Experimental Procedures

Materials and Geometry

ED Cu (99.8% purity) with thickness of 0.1 mm was prepared. A controlled heat-treatment procedure was applied in order to obtain a variety of grain sizes in the range from 2 to 40 μm . The mean grain size and the heat-treatment conditions are shown in Table 1. Samples were cut to 40-mm length and 5-mm width. Furthermore, a single edge notch was introduced into the center of a specimen to investigate the dependence on notch length (Table 1). The notch tip was round shaped with about 150- μm curvature.

AE measurement

AE behavior was investigated during tensile loading with the cross-head speed of 0.1 mm/min. AE sensor (M304, Fuji Ceramics Corp.) was attached to the surface of each specimen, and AE waveform was recorded by CWM (continuous wave memory) system [4]. In AE measurement, the sampling rate was 10 MHz and high-pass filter was 200 kHz. The monotonic loading pattern was conducted to obtain the AE onset stress of each sample. Various fatigue-loading patterns were also applied to estimate the maximum stress from the AE onset stress. The applied maximum stress and the number of cycles under the constant amplitude fatigue loading are shown in Table 2. We want to estimate these conditions by this patch. Furthermore, AE was measured in the case of the over-loading condition and the variable amplitude condition. In the over-loading condition, an over-load of 50 MPa was applied during the constant amplitude loading with 30 MPa. In the variable amplitude loading, a stress distribution of log-normal distribution with mean stress of 30 MPa, maximum stress of 55 MPa and 100,000 cycles was applied.

Table 1 Heat-treatment conditions and normalized notch length.

	Temperature, $T/^{\circ}\text{C}$	Time, t/min	Grain size, $d/\mu\text{m}$	Normalized notch length, α
as-rec.	-	-	1-2	0, 0.2, 0.4, 0.5, 0.6, 0.7
300-10	300	10	1-2	0, 0.2, 0.4, 0.5, 0.6, 0.7
300-30	300	30	2-3	0
300-60	300	60	4	0
400-30	400	30	4	0, 0.4, 0.5, 0.6, 0.7
400-60	400	60	8	0
450-60	450	60	15	0
500-45	500	45	10	0
600-30	600	30	25	0

Results and Discussion

AE onset stress

Effects of the heat-treatment conditions and notch length on the AE onset stress were explored. Figure 1 shows the relationship among stress, strain and RMS voltage of as-received ED-Cu specimen. The AE peak stress, which is the stress when the RMS voltage reaches the peak value, is smaller than the yield stress. In this study, the AE

Table 2 Applied maximum stress and cycles of fatigue loading.

Maximum stress [MPa]	Cycles
30	300,000
35	100,000
40	100,000
45	50,000
50	50,000

onset stress is determined by the stress at the cross point of the noise level and the increasing RMS voltage as shown in Fig. 1.

The effect of the AE peak stress on the AE onset stress was examined as shown in Fig. 2. The AE onset stress decreases with the AE peak stress linearly and it is almost zero when the AE peak stress is about 50 MPa. The relationship between the AE peak stress and the yield stress is also linear as shown in Fig. 3. Relative increase of the AE activity during tensile loading is large as the yield stress is low. It appears that this tendency is related to the mobility of the dislocation. According to Baram et al. [5, 6], AE activity increases with grain size in the range of grain size used in this study. Figure 4 shows the effect of the notch length on the AE onset stress and demonstrates that the AE onset stress decreases as the notch length increases. However, this decrease of the AE onset stress is caused by the decrease of the cross section area and the notch sensitivity is not observed as shown in Fig. 5.

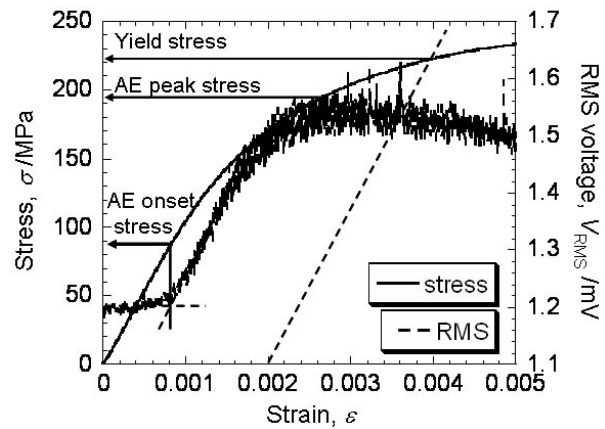


Fig. 1 AE behavior of as-received ED-Cu specimen with stress-strain curve.

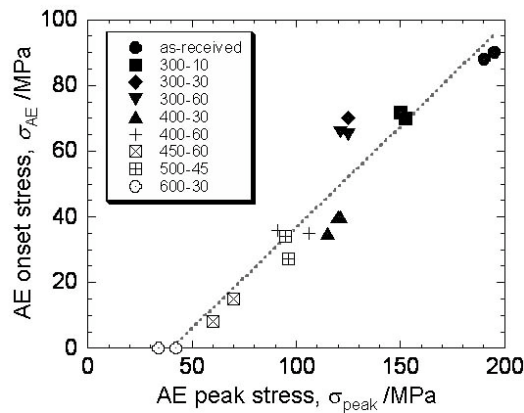


Fig. 2 Relationship between AE onset stress and AE peak stress of smooth specimen.

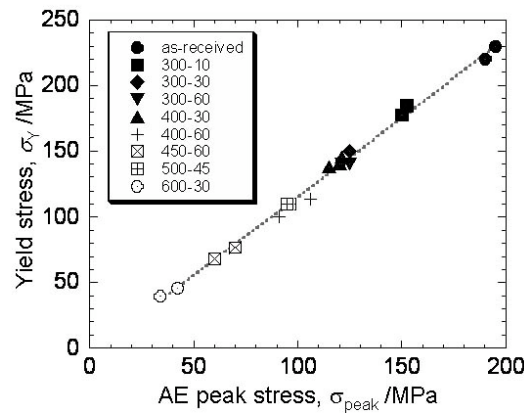


Fig. 3 Relationship between yield stress and AE peak stress of smooth specimen.

Estimation of the maximum stress

The fatigue loading was conducted on the ED-Cu specimens (400°C, 30 min, $\alpha = 0.4$ and 0.5). AE behaviors were measured to estimate the applied maximum stress during the fatigue loading. Figure 6 shows the AE behavior under the fatigue condition of the maximum stress of 30 MPa and 300,000 cycles. This result demonstrates that the applied maximum stress of 30 MPa can be estimated by the AE onset stress. The relationship between the applied maximum stress and the AE onset stress is plotted in Fig. 7. The applied maximum stress between 30 and 50 MPa can be estimated by the ED-Cu specimen with $\alpha = 0.4$.

In the case of the specimen with $\alpha = 0.5$, the maximum stress of 45 and 50 MPa cannot be estimated. This is because the yield stress of this specimen is small and Kaiser effect cannot be observed as in the case of rolled Cu specimen with large grain size [3]. On the other hand, the applied maximum stress of 45 and 50 MPa can be estimated by the ED-Cu specimen with $\alpha = 0.4$ normalized notch length. Therefore, it is found that the ED-Cu specimen with $\alpha = 0.4$ is

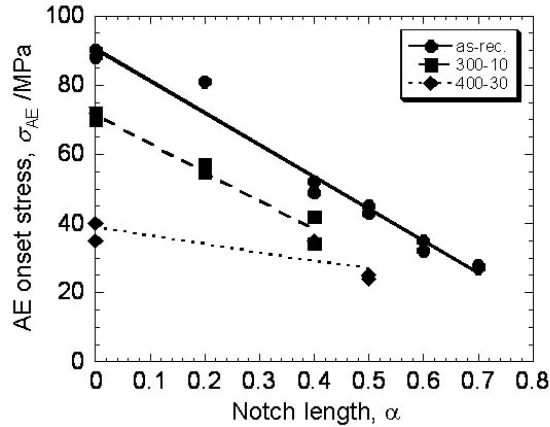


Fig. 4 Relationship between AE onset stress and notch length.

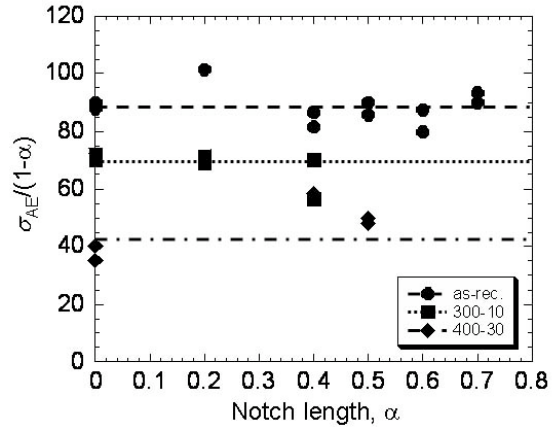


Fig. 5 Notch sensitivity of ED-Cu specimen.

appropriate as the sensor, which can estimate the maximum stress between 30 and 50 MPa under the constant amplitude loading.

The maximum stress under the over-loading and the variable amplitude loading conditions was also estimated. To apply the maximum stress of 50 MPa and 55 MPa, the smooth ED-Cu specimen (400°C, 30 min) was used. Figures 8 and 9 show the relationship between the AE onset stress and the applied maximum stress during over-loading and variable amplitude loading, respectively. These results demonstrate that the AE onset stresses of ED-Cu specimens after over-loading and variable amplitude loading conditions were in agreement with the applied maximum stresses. These results demonstrated that the maximum stress under various fatigue loading conditions can be estimated by this heat-treated and notched specimen.

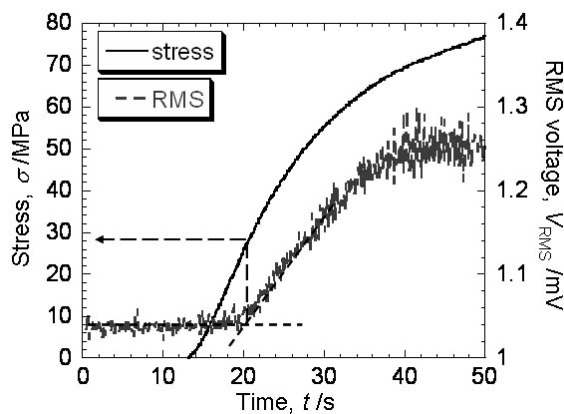


Fig. 6 AE behavior of ED-Cu specimen (400°C, 30 min, α=0.4) after fatigue loading with σ_{max}=30 MPa and 300,000 cycles.

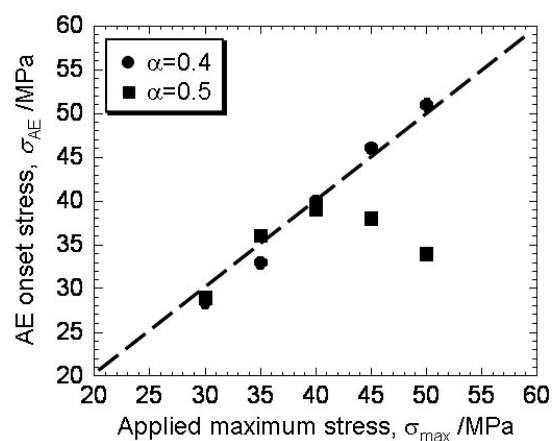


Fig. 7 Relationship between AE onset stress and applied maximum stress of ED-Cu specimen after fatigue loading.

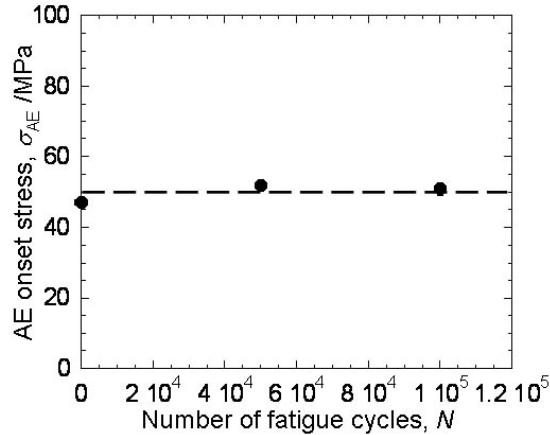


Fig. 8 AE onset stress after over-loading of 50 MPa at 1, 50,000 and 100,000 cycles.

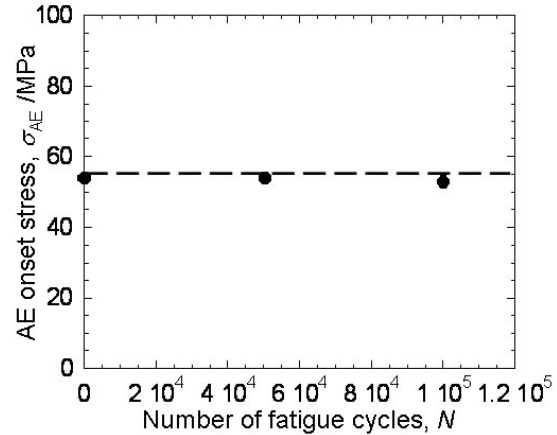


Fig. 9 AE onset stress after variable amplitude loading with the maximum stress of 55 MPa, which was applied at 1, 50,000 and 100,000 cycles.

Conclusions

- (1) The AE onset stress of pure copper specimen used for smart stress memory patch was proportional to yield stress and it is almost zero when the AE peak stress is about 50 MPa, while the notch sensitivity was not observed.
- (2) The maximum stress under various fatigue loading conditions, such as constant amplitude loading, over loading and variable amplitude loading, can be estimated by this heat-treated and notched specimen.

References

1. T. Kobayashi, O. Muragishi and K. Nihei, *Key Eng. Mater.*, **261-263**, 2004, 1313-1318.
2. Y. Fujimoto, G. Pirker, H. Ito, E. Shintaku and S. Shono, *Ship Tech. Res.*, **49**, 2002, 33-44.
3. S. Nambu and M. Enoki, *Mater. Trans.*, **48**, 2007, 1244-1248.
4. K. Ito and M. Enoki, *Mater. Trans.*, **48**, 2007, 1221-1226.
5. J. Baram and M. Rosen, *Mater. Sci. Eng.*, **45**, 1980, 255-262.
6. J. Baram and M. Rosen, *Mater. Sci. Eng.*, **47**, 1981, 243-246.

DAMAGE ASSESSMENT OF GEARBOX OPERATING IN HIGH NOISY ENVIRONMENT USING WAVEFORM STREAMING APPROACH

DIDEM OZEVIN, JASON DONG, VALERY GODINEZ and MARK CARLOS

Physical Acoustics Corporation, 195 Clarksville Road, Princeton Junction, NJ 08550, USA

Abstract

Threshold and timing parameters are two fundamental factors that control arrival times and waveform signatures collected in an acoustic emission test. While this approach works successfully in many applications, recording the complete, continuous waveforms emitted from an AE test independently of threshold value is more appropriate for some specific applications. Applications such as those with high background noise or complex structures with numerous boundaries and interfaces are better served by continuously streaming with duration in the order of hundreds of milliseconds instead of the traditional hundreds-of-microseconds-long AE waveforms. State-of-the-art AE data acquisition hardware enables the user to take this "AE waveform-streaming" approach at high sampling rates throughout a traditional AE test. Then, these waveforms can be analyzed in real time to extract traditional AE features in the time and frequency domains.

In this paper, the application of waveform streaming will be shown on detecting corrosion pitting on gear teeth under a high background-noise environment. The tests were performed using an FZG machine to generate pitting corrosion on gear teeth under fatigue. In these tests, a recently designed "integrated" AE-and-vibration sensor was used for collecting high and low frequency data while monitoring the condition of the gears. Recording the complete, continuous waveforms provided tremendous flexibility during post-processing data analysis, which can be implemented in real time during consecutive tests. The paper also presents the impact of the waveform-streaming approach in terms of understanding threshold effects on waveform signatures, in the ability to set and analyze different digital filters, and in the extraction of low-frequency vibration information.

Keyword: Waveform streaming, threshold independent, gearbox, frequency analysis, real time analysis

Introduction

Threshold-based data acquisition has been used and operated successfully in many acoustic emission (AE) applications. Threshold is a key factor for AE technology as the technology is mostly based on arrival times for source location and time- and frequency-domain feature extraction for pattern recognition [1, 2]. However, the threshold-based approach creates a detection reliability problem for high noise, high hit-rate applications, such as the monitoring of highly dynamic systems or process monitoring. Additionally, threshold and timing settings may perturb the direct AE wave signature, which is substantial for a quantitative analysis and source discrimination [3]. In this paper, we will discuss the new data acquisition tool of waveform streaming in addition to threshold-based data acquisition. The advantages of the streaming-waveform approach are discussed using the gearbox testing application.

Approach

The high sampling rates required together with the high hit rates of AE signals are two constraints for the continuous recording of waveforms. State-of-the-art data acquisition hardware allows recording waveforms continuously with high sampling rates throughout an AE test. The data acquisition system can record long duration waveforms with a high sampling rate continuously or at predefined time intervals. The waveform shown in Fig. 1 has 2-s duration sampled with 500-kHz rate at 5-s interval. The waveform presents several transient signals during the 2-s period as shown in the zoomed view. These transient signals have typical AE signal characteristics, i.e. short duration, rise time and decay time. The waveform-streaming approach allows the identification of the transient-signal characteristics without being affected by threshold and timing parameters.

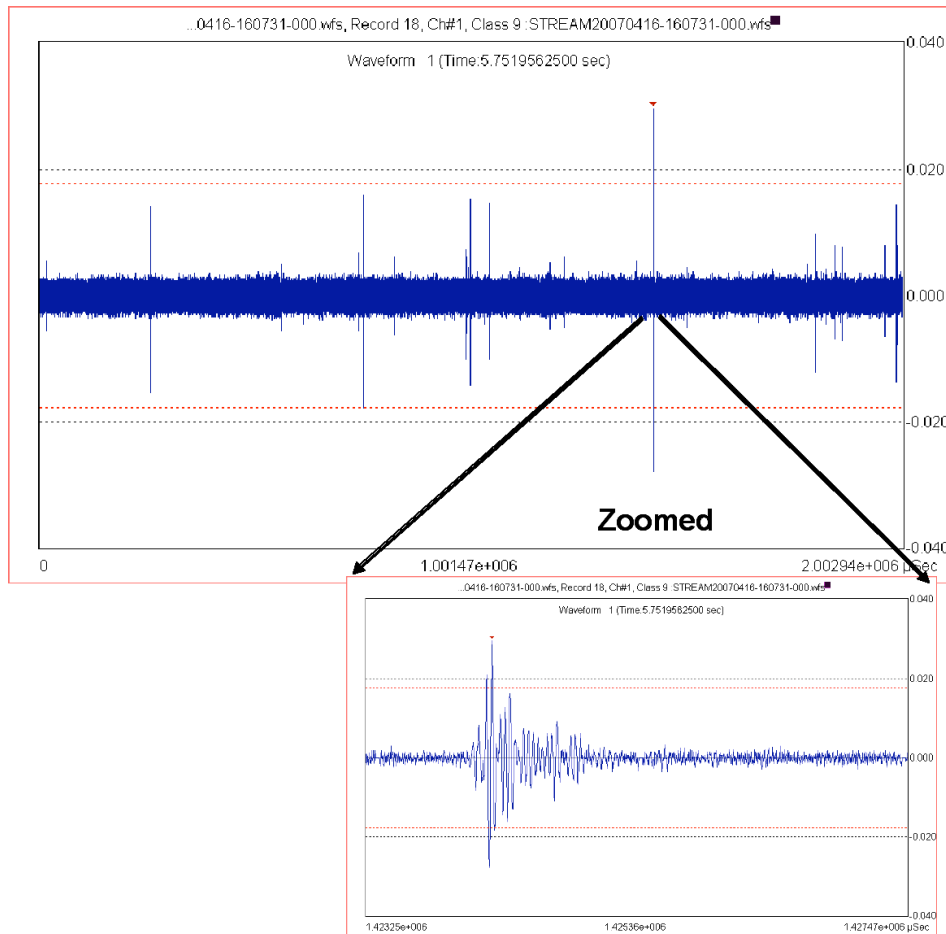


Fig. 1. An example of 2-s-long waveform sampled at 500 kHz.

Recording complete, continuous waveforms provides flexibility during post-processing data analysis, which can be implemented real time in consecutive tests, for example:

- Understanding the effect of threshold and timing settings on waveform-feature extraction that can be used to optimize the settings of threshold-based acquisition for consecutive tests.
- Extracting time-domain features using post-process digital filters and different threshold setting.
- Optimizing frequency segments for spectral feature configuration.
- Extracting low-frequency vibration information if AE waveform length is sufficiently long to capture multiple revolutions.

Additionally, although the arrival-time information of transient signals is not registered in real time, single or multiple AE hits in a streamed waveform can be separated with their actual arrival times using the NOESIS™ software. The NOESIS™ software has an option to extract features and arrival times of multiple transient signals in a streamed waveform based on threshold or length. Furthermore, streamed waveforms of multiple channels can be synchronized so that the relative arrival times of transient signals of different channels can be extracted. The waveform streaming can be acquired using PCI-2 (2-channel) or PCI-8 (4-channel AE, 4-channel Vibration) board developed by Physical Acoustics Corporation [PAC]. It is important to note that the boards have the capability to record threshold-based data and waveform streaming concurrently.

Gearbox Application

As an example of the flexibility offered by the waveform-streaming approach for practical AE monitoring, a series of tests were performed at the Ohio State University Gearbox Laboratory using an FZG machine to generate micro-pitting or spalling in spur gears at elevated temperature (90°C) as shown in Fig. 2a. The rotation speed of the input gear was 1440 RPM with 1944 lb-inch torque. The gear pitting formation under fatigue was monitored using two recently developed integrated AE/vibration [AE/VIB] sensors by PAC. The detailed information about the integrated AE/VIB sensor was presented elsewhere [4]. The sensors were mounted on the front and side panel of the FZG machine (shown in Fig. 2b). AE/VIB 1 was mounted below the lubricant level of the machine and AE/VIB 2 was mounted at the same level as the lubricant. The PCI-8 board was used to record the data from two AE/VIB sensors. The board has 16-bit A/D conversion capability and 1 Msample/s waveform-streaming rate to hard disk. The board was installed inside a PAC μ -Samos chassis manufactured, and the system was controlled by a laptop as shown in Fig. 2c. See [4] for the detailed analysis results of the gearbox tests. In this paper, we will present the outcomes of recording long-duration waveforms.

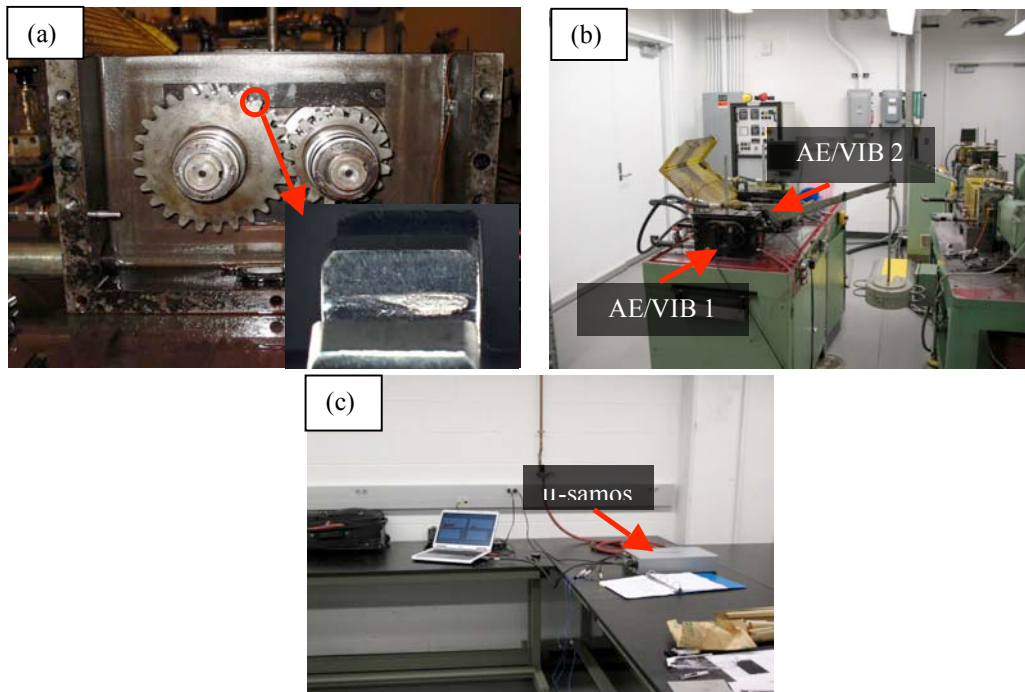


Fig. 2. Photographs of (a) input and output gears, (b) AE/VIB sensors, (c) DAQ system

Extracting features using different sets of digital filters and spectral divisions

Test 1 included a gear with no damage at the beginning and end of 1-hr duration testing. Test 2 included a gear with a minor damage at the beginning of the testing and the damage grew over the 1-hr test duration. The same gear but opposite teeth was used at Test 1 and Test 2. Figure 3 shows the energy trends of two tests recorded by the AE/VIB 1. The fluctuation was because of water pump operation to cool the lubricant inside the gearbox. While the same gear was used during the tests, the time-domain signal level changed just because the gearbox was opened and the opposite side of the gear teeth, which had a tooth with minor damage, was mounted. Variation of time-domain feature due to mechanical feature indicates the difficulty of comparing one test to another if the mechanical structure has any slight modification. Spectral features gain significance as descriptors to differentiate damage emissions and background noise emissions.

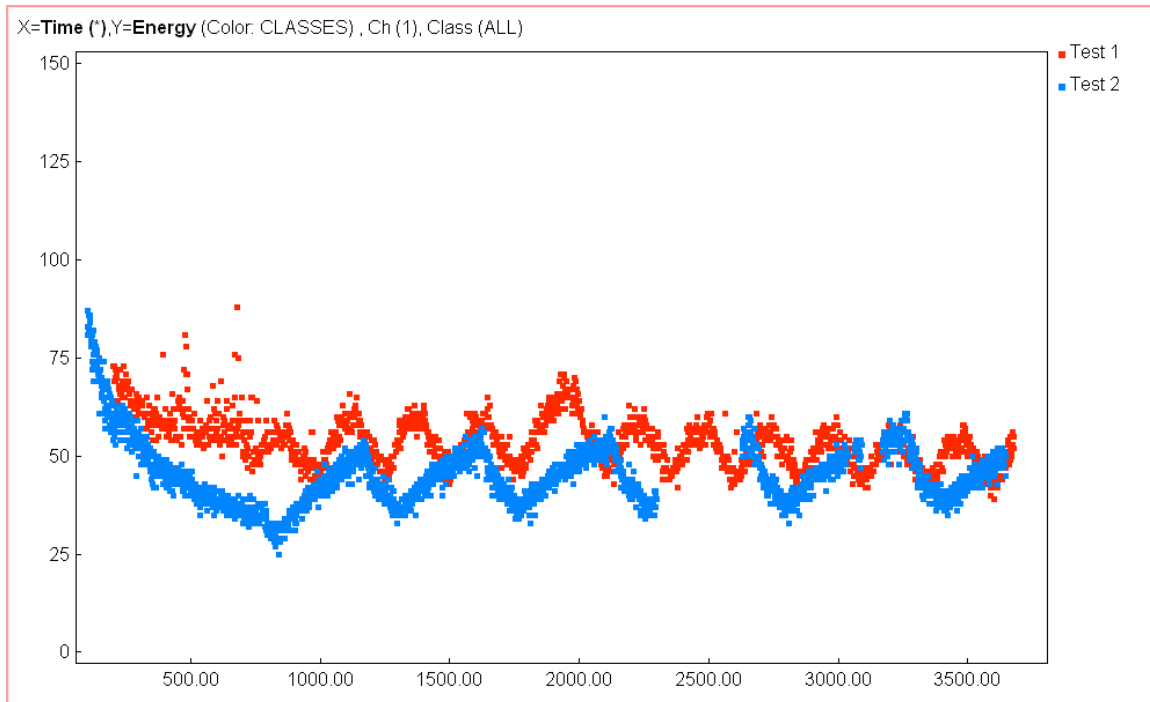


Fig. 3. Time-domain feature, energy (e.c.), trends for two tests recorded for 3600 s. The fluctuations were generated due to the operation of water pump inside the gearbox.

Figure 4a and b show examples of a raw, streamed waveform and its frequency spectrum. The frequency spectrum of the raw waveform, Fig. 4b, shows the dominant frequency components due to mechanical noise are 22 and 33 kHz. If frequency centroid or peak frequency was calculated directly using a raw waveform, the mechanical noise frequencies would mask the result. When a waveform is streamed from an AE sensor, it is expected that low-frequency mechanical noise and high-frequency damage growth emission would be summed. Extracting high-frequency, relatively low-amplitude (as compared to mechanical noise), damage-growth emission requires filtering background noise frequencies. Figure 4c shows the same waveform with 80 kHz high-pass filter using a 10th-order Butterworth filter. The software allows segmenting (green lines) the time-domain waveform for frequency spectrum calculation. Spectral features, such as peak frequency, partial powers (partial powers indicate how the energy distribution at defined frequency segments changes as compared to the full defined spectrum band) can be extracted using digital filters.

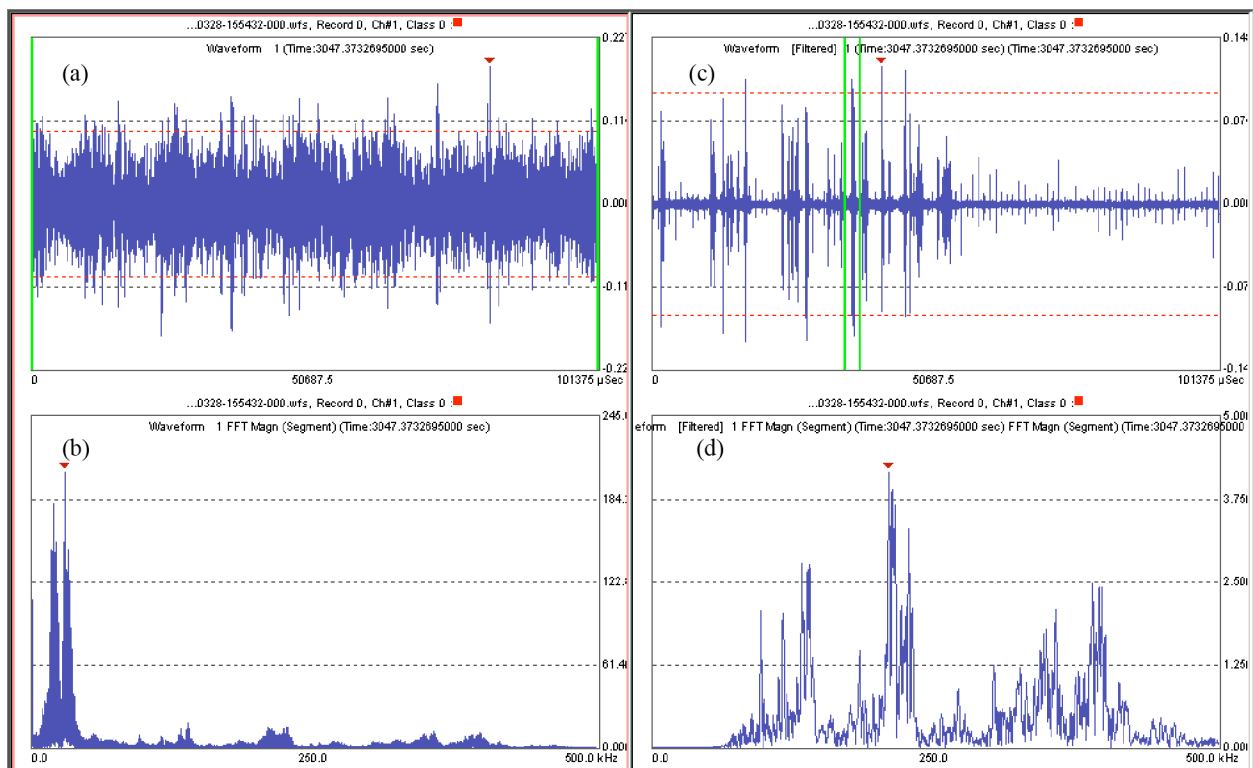


Fig. 4. A streamed waveform of Test 2 (a) raw waveform and (b) its frequency spectrum, (c) filtered waveform having 80 kHz high-pass and (d) its segmented (green lines) frequency spectrum. Horizontal scales: (a), (c) 0-101.4 ms; (b), (d) 0-500 kHz.

Extracting gear-mesh frequency

Vibration monitoring detects coupling failure by comparing two different states (undamaged versus damaged) of structural components. The most fundamental challenge for the detection of cracking is that it is typically a local phenomenon and may not significantly influence the lower-frequency global response of a structure that is typically measured during vibration tests [5]. However, vibration monitoring provides additional information to the findings of AE method. It is advantageous to extract vibration information using long-duration AE waveforms.

The gear-mesh frequency is the combined effect of all gear inertia. In these tests, the input-gear rotation speed was 1440 RPM, which corresponds to 24-Hz frequency. The input gear has 26 teeth, which correspond to 624-Hz gear-mesh frequency. Figure 5a shows a long-duration AE waveform acquired in Test 2. The time-variant average-signal level (ASL) is extracted from this streamed waveform so that high frequency noise is filtered out as shown in Fig. 5b. ASL spectral energy is further calculated based on the time-variant ASL and its maximum spectral energy that just lies in the gear-mesh frequency as shown in Fig. 5c. ASL spectral-energy plot indicates that the streamed AE waveform can be effectively used to extract a gear-mesh related feature that is not available with the conventional AE signal-processing technique.

Summary

Recording complete, continuous waveforms provides flexibility during post-processing data analysis. We can deduce signal characteristics without being influenced by threshold and timing parameters, and identify damage-emission frequency information. Additionally, governing vibration frequencies can be extracted using AE sensor if AE waveform length is sufficiently long to

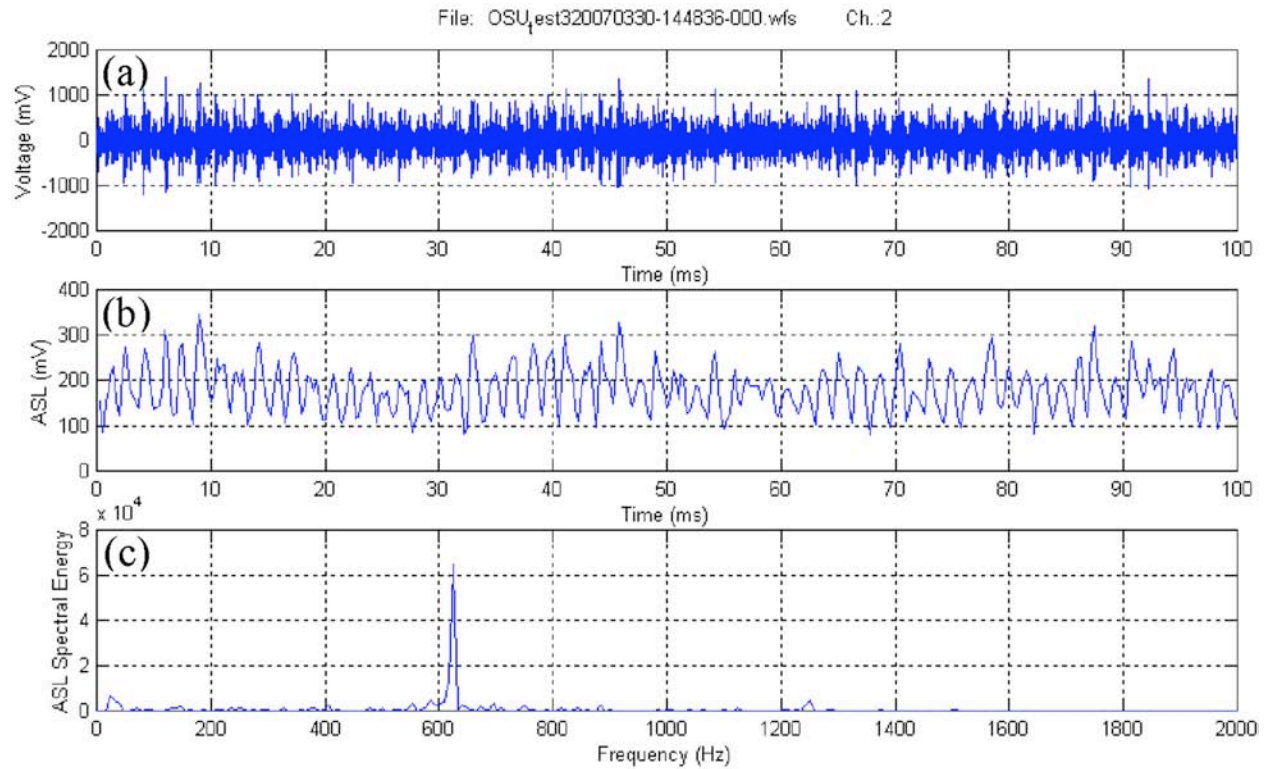


Fig. 5. Extracting gear-mesh frequency using a long duration AE waveform; (a) AE waveform, (b) Average signal level (ASL) trend, (c) ASL spectral energy.

capture multiple revolutions. Waveform streaming can also be used to optimize the settings of threshold based data acquisition.

Acknowledgements: This study was performed as a part of SBIR Phase II program sponsored by NAVAIR under contract number N68335-04-C-0202. We would also like to thank Professor Ahmet Kahraman and his graduate student Jeremy Bluestein for their help during testing in the Ohio State University Gearbox Laboratory.

References

1. V.F. Godinez, F. Shu, R. Finlayson, B. O'Donnell, Proceedings of SPIE, Vol. 5394, *Health Monitoring and Smart Nondestructive Evaluation of Structural and Biological Systems III*, 2004, pp. 428-437.
2. V.F. Godinez, F. Shu, R. Finlayson, B. O'Donnell, A. Anastopoulos, and A. Tsimogiannis, Canadian Institute for NDE (CINDE) Journal, **25**, 2004, 8-16.
3. M. Ohtsu and K. Ono, Journal of Acoustic Emission, **5**, 1986, 124-132.
4. V.F. Godínez-Azcuaga, D. Ozevin, A. Anastopoulos, A. Tsimogiannis, *Proc. Aging Aircraft Conference*, 2007, JCAA (to be published).
5. C.R. Farrar, S.W. Doebling, D.A. Nix, Philosophical Transactions of the Royal Society A: Mathematical, Physical and Engineering Sciences, **359**, 2001, 131-149.

ASSESSMENT OF THE SURFACE CONDITION AT THE REMOVAL OF COATINGS BY DRY ICE BLASTING USING THE ANALYSIS AND LOCATION OF ACOUSTIC EMISSION SIGNALS

**CHRISTIAN SCHEER, PASCAL BRUEGGEMANN, WILFRIED REIMCHE
and FRIEDRICH-WILHELM BACH**

Institute of Materials Science, Leibniz Universität Hannover
An der Universität 2, 30823 Garbsen, Germany

Abstract

Dry ice blasting is a rather new procedure for the cleaning and removing of coatings, with special features of the blasting medium characterizing the process. At temperature of -78.5°C , the used carbon dioxide is solid as well as ductile. It almost gains sonic speed and sublimates completely upon impact on the coating. Apart from cleaning tasks, the removal of coatings is the most common application of dry ice blasting. Particular advantages of the dry ice blasting procedure are the lack of blasting media residues as well as not damaging the substrate materials like metal. This is due to the fact that a dry ice blast does not have abrasive properties. Apart from the kinetic energy of the pellets, induced stress due to the high temperature differences between the structural material and the coating is the main mechanism of coating removal. These special characteristics and the advantages associated with them have led to the acceptance of this process in several applications [1-3].

To date, the lack of knowledge about the interaction of material properties and removal mechanisms has been the limiting factor hindering the widespread use of this technology. Thus, the field of application is being widened and the process efficiency being improved in the context of a research project supported by the DFG (German Research Foundation).

For process control, acoustic emission analysis is being applied for the evaluation of the surface's condition and the quality of the coating removal, respectively. The different impact properties of the coating and the substrate enable the controlled removal of the coating and directed reworking. Due to the very high data acquisition rates of several megahertz, location of the acoustic emissions is possible by runtime analysis using several sensors, and thus the progress in removal of the coating can be correlated with the surface of the substrate [4-8].

Keywords: Dry ice blasting, removal of coatings, location

Introduction

Using acoustic emission (AE) analysis different types of process control are possible. A sensor, which is placed at the jet, allows the detection of collisions of pellets with the inner surface of the blasting jet. This enables to supervise the mass flow of the dry ice, which is quite important for an automated operation of the system. Additionally, it is possible to evaluate the geometric quality of the jet since many collisions inside the jet reduce the amount of kinetic energy of the pellets and the efficiency of the removal decreases.

Another possibility for process supervision is the location of AE signals by run time analysis. Using four sensors on the test sample, it is possible to locate the impacts of pellets and use some of their properties, e.g. their intensity, their count and their energy, to evaluate the surface condi-

tion. Is the coating removed or not? Where is the coating not removed to perform a specific post-treatment?

The principle of dry ice blasting

The dry ice blasting process uses particles of solid carbon dioxide at temperature of -78.5°C . The particles consist of compressed carbon dioxide snow with a diameter of 1 to 3.5 mm and a length between 2 and 10 mm. The dry ice pellets are accelerated in a compressed air stream to a velocity of about 300 m/s and forced to strike against the coated surface. Typical blasting pressures used are between 0.1 and 1.6 MPa. Depending on the application, tubular and flat nozzles with a removal width of up to 160 mm can be used.

The dry ice blasting process uses a combination of mechanical and thermal mechanisms to remove material as seen in Fig. 1. The kinetic energy of the blasting media generates cracks by the effect of a shock wave at the interface between the coating and the substrate as well as removing particles that are already cracked or that have low bond strength. During impact, part of the kinetic

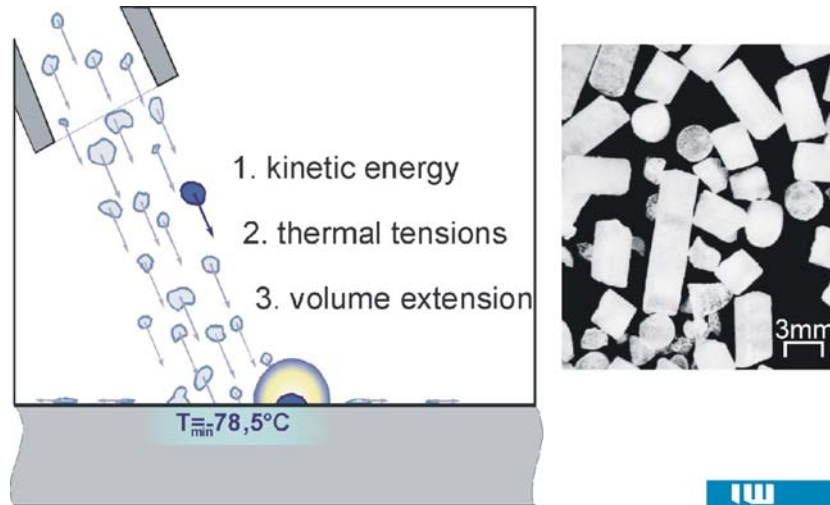


Fig. 1: Mechanical and thermal mechanisms at dry ice blasting.

and thermal energy is transformed into sublimation energy. The volume of the solid carbon dioxide increases by a factor of 700. This results in high-pressure gradients on the surface. Due to the short time of the impact only a small part of the dry ice sublimates on the surface directly, and most sublimates while spreading out. The gaseous carbon dioxide can be vacuumed together with the removed coating particles and the filtered gas stream may be discharged to ambient air, resulting in no secondary waste.

A very thin upper layer of the surface is cooled to a maximum of -50°C at a high cooling rate, thereby inducing thermal stresses. This occurs especially for high differences in thermal expansion coefficients between the substrate and the coating. The thermal stresses can result in cracks and can weaken some materials by making them brittle. In order to increase the removal rate, the dry ice blasting process can be combined with a laser. The heat that is induced by the laser beam increases the thermal shock.

Dry ice is quite soft, comparable to gypsum, so there is nearly no abrasive effect. Consequently, it is possible to remove coatings without damaging substrate materials like mild or stainless steel or even most aluminum alloys. It must be noted that the operative range of the dry ice blasting process is limited to coatings that do not exceed a process specific maximum hardness or bond strength [1-3].

Test assembly

The dry ice blasting jet is fixed to a 3-axis-handling-system. The pressure is set to the maximum value of 1.6 MPa. The arrangement of the sensors is displayed in Fig. 2. One sensor is directly placed at the blasting jet, and the other four sensors are placed on the metal sheet used for the tests. To avoid disturbances, the sheet is decoupled from the subsurface by rubber elements.

Since the impacts of the dry ice pellets cause very high amplitudes of the AE data, quite insensitive sensors are used without amplification. Their signals are additionally low-pass filtered at 600 kHz for damping and flattening the frequency response.

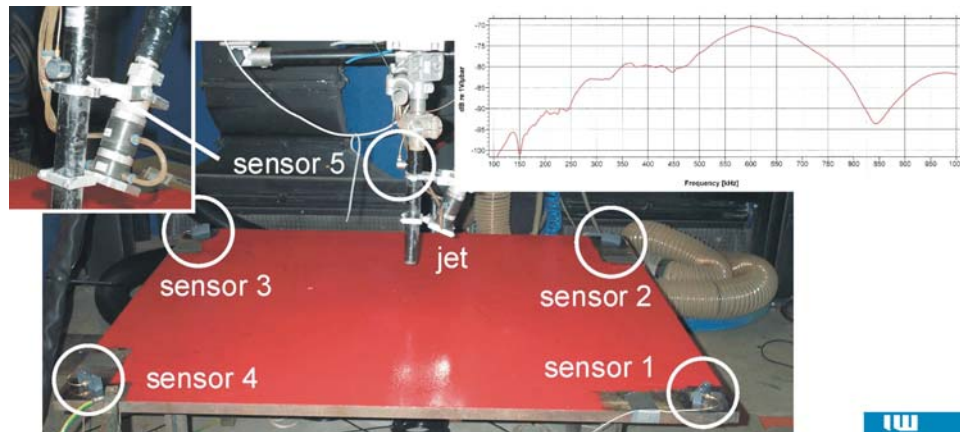


Fig. 2: Test assembly with sensors and dry ice blasting jet.

Analysis of the impact behavior of single pellets

To achieve high impact intensities during the dry ice blasting process, the pellets have to hit the coating of the substrate without pre-damages. If a damaged pellet splits into several parts before impact, the single fragments together possess less energy than before. The potential of removal decreases.

There are three possible reasons for a pre-damaging of the dry ice pellets. The first is related to the dry ice blasting system, especially the device which feeds the pellets into the stream of compressed air. The second is related to the hose between the compressor and the blasting jet. Its

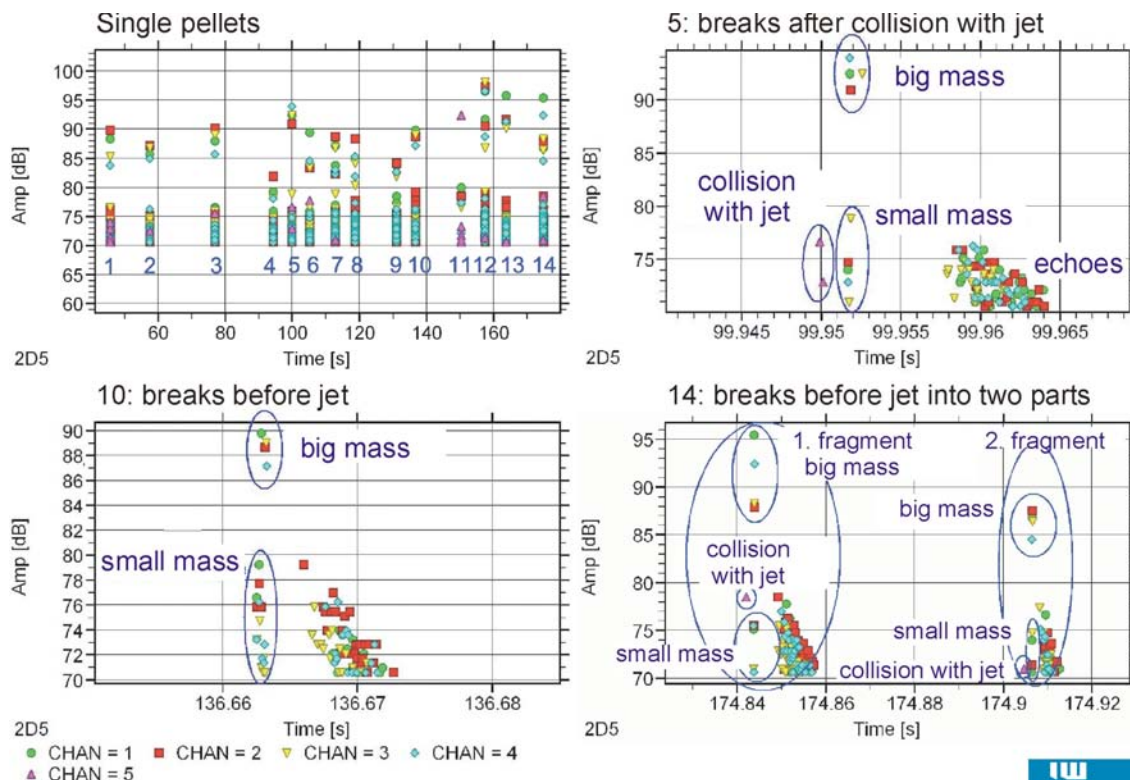


Fig. 3: Evaluation of pre-damages at single pellets.

length and several bends may cause the pellets to collide with the inner surface of the hose and receive damage. The third reason is the behavior of the blasting jet itself. If the dimensioning of the inner geometry of the jet is not optimal, collisions between pellet and inner surface or pellet to pellet may occur.

To avoid damage of the pellets, inside the blasting system and the hose, a single pellet feeder is used, which minimizes the possibility of damaging pellets. Thus, the damaging of pellets by the blasting jet is detectable. The single pellets are fed via an auxiliary port with lower air pressure into the main jet. The sensors are placed as shown in Fig. 2.

The AE data of 14 single pellets is shown in Fig. 3. The pellets are fed to the blasting jet with a time delay. For each of the pellets there are several hits at different sensors detected. The higher are the signal amplitudes of detected contacts with the inner surface of the jet (Channel 5), the higher is the stress of the pellets. This may lead to pellet breakage, which decreases the maximum energy at impact and therefore the efficiency.

A closer look at the hits for each pellet, especially the short time behavior, provides more information about the process of collision, breakage and impact. In the upper right corner of Fig. 3 a zoom of the impact of pellet no. 5 is shown. The pellet leaves the feeder without damage and collides with the inner surface of the jet. The pellet splits into a big mass and a small mass fragment, which can be divided by the different amplitudes on impact. The zoom of pellet no. 10 is displayed in the bottom left corner of Fig. 3. In this case the pellet already splits into different fragments in the feeder. There is no contact to the blasting jet and there are two impacts on the surface. Regarding pellet no. 14 there is also a damage, which occurred already in the feeder. Figure 3 bottom right shows two different pellet fragments, both of them showing a collision with the inner surface of the jet, splitting and causing different impact amplitudes dependent on their masses.

The damage or breakage of pellets inside the single pellet feeder may be caused by a collision in the feeder or by the air stream when the pellets get from the auxiliary port into the main jet. The huge amount of hits after the impact of the pellet fragments is caused by echoes because of the relative small test sheet.

Process control of dry ice blasting

The supervision of the dry ice blasting process avoids harm to system and personnel at hand-operated as well as automated service. The sensor at the blasting jet detects the pellets, which are fed through it to the point of impact on the coating to be removed. Combined with sensors on the coating it can be investigated if the pellets are hitting the desired object or

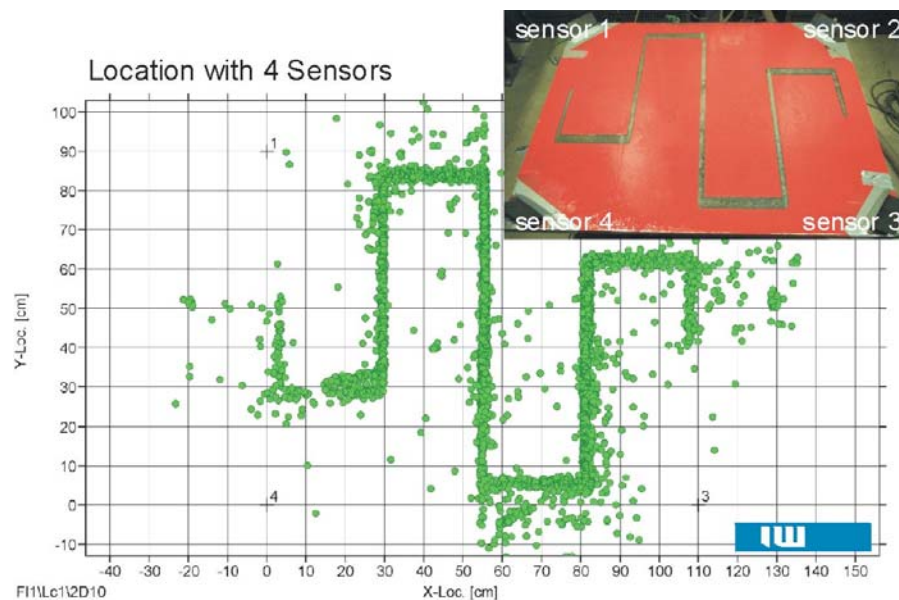


Fig. 4: Pellet location during dry ice blasting.

something else. Another point is the supervision of the mass flow of the dry ice. If there are no collisions inside the blasting jet anymore, there is a fault in the feeder system or the dry ice reservoir is empty. This is of great importance when using a combined dry-ice laser-beam process, which uses the laser to heat the area of removal first to get a greater temperature difference. When there is an interrupt in the dry ice mass flow the laser may damage the substrate because there is no cooling effect by the dry ice. Therefore, the laser must be shut down, which may be controlled by AE measurements. Additionally, the laser power can be controlled using AE data like amplitude or hit rate.

Controlled removal of coatings

The controlled removal of coatings on surfaces is another feature to use AE-measurement technique for process control. Locating the AE signals by run time analysis, it is possible to detect where the removal of the coating actually takes place. If there are any interrupts of the dry ice mass flow, it is possible to locate the area where a rework is necessary. Considering the amplitude, hits, counts and energy of the AE signals, it is possible to evaluate the condition of the coating to be removed and map this information back to the surface. Therefore, the process parameter may be adjusted to make the process more efficient. Figure 4 shows the location of the coating removal at a metal test sheet.

Evaluation of the surface condition during dry ice blasting

In addition to the controlled removal of coatings using the location of AE events, an evaluation of the actual surface condition while removing the coating is possible. For the removal of a rubber coating from a steel plate, four sensors were placed on the surface in the same manner as shown in Fig. 2. Before removal, some spots were applied to the rubber coating as shown in Fig. 5 to show the difference in the AE-data between coating and metal surface more clearly. To remove the coating four passes were performed. The values of the AE-data are shown in Fig. 5 as well as the photos of the different conditions of the coating.

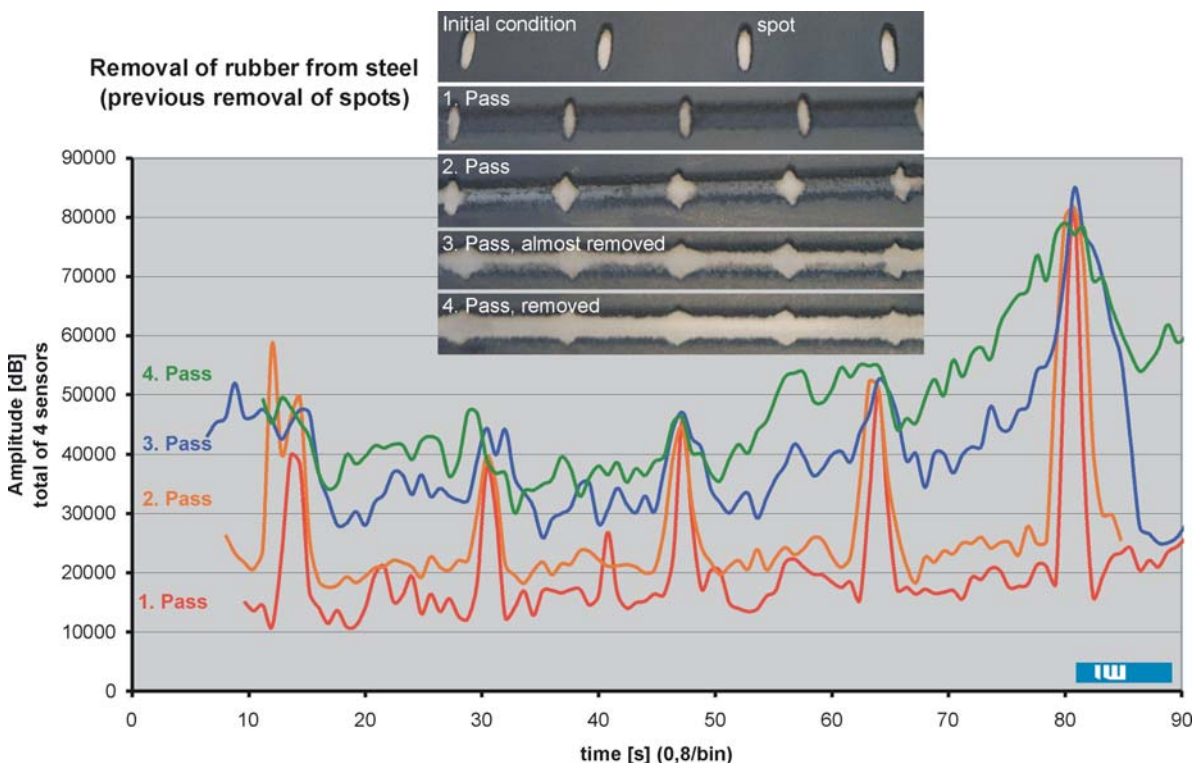


Fig. 5: Influence of the coating thickness on AE-data.

The most significant distinction is the amplitude of the AE events, which is shown summarized for the four sensors to minimize the influence of the different distances between the sensors and the actual dry ice blasting location. Regarding only single sensors, the amplitudes will decrease when the distance to the sensor increases. During pass 1 and pass 2, the difference between the removal of the coating, ca. 15000 dB, and passing the spots, ca. 40000 dB and more, is clearly visible. The 3rd and 4th pass visually do not differ essentially from the plain surface condition. But there are still differences in the amplitude values of the AE-signals between the spots. Comparing the different conditions of coating removal the coating can be regarded as “removed” when the amplitude total exceeds ca. 35000 dB. To evaluate the surface conditions when removing harder coatings additional tests are necessary.

Summary

This fundamental research work to the application of the AE analysis for the removal of coatings by dry ice blasting allows the development of a process control and supervision technique. The aim is to improve the industrial application of this method.

The basic influences of pellet impacts on AE signals, like size of the pellets, behavior at collisions in the main jet are proved. Additionally, a supervision of the dry ice mass flow is possible.

Using the location of AE events, a localized evaluation of the coating removal at the substrate is possible. Different amplitudes of the AE signals allow the distinction between the remaining coating and plain surface. Further research work shall improve the location and evaluation of the surface condition and therefore allows a process control and supervision on more complex parts.

Acknowledgements: We express our sincere thanks to the German Research Foundation (DFG) for the promotion of this work within the research project „Erstellung und Verifizierung eines Modells zur Beschreibung der Vorgänge beim Trockeneisstrahlen“.

References

1. Bach, Fr.-W.; Redeker, C.F.: Abtragen und Entschichten von thermisch gespritzten Schichten, in: *Handbuch der thermischen Spritztechnik*, E. Lugscheider [Ed.], p. 116-127, DVS-Verlag, Düsseldorf, 2002, ISBN 3-87155-186-4
2. Redeker, C.F.: Abtragen mit dem Trockeneisstrahl, Diss. University of Hanover, VDI-Verlag, Düsseldorf, 2003, ISBN 3-18-363902-5
3. Bach, Fr.-W.; Brüggemann, P.; Louis, H.; Schenk, A.; Versemann, R.; Dry ice blasting and water jet processes for the removal of thermal sprayed coatings; *Conf. Proceedings International Thermal Spray Conference '05 – ITSC '05*, May 2–4, 2005, Basel, Switzerland, S. 1549-1555
4. Vahaviolos, S.J. [Ed.]: *Acoustic Emission: Standards and Technology Update*, ASTM STP-1353, 1999.
5. Vallen, H.: Die Schallemissionsprüfung, Castell-Verlag, 2003
6. N.N.: Vallen-Systeme, About AE, www.vallen.de/ae, 2007
7. N.N.: Physical Acoustics Corporation, Acoustic Emission Measurement Technologies, www.pacndt.com, 2007
8. Scheer, C.; Reimche, W.; Peter, D.; Bach, Fr.-W., Südmersen U.: Qualitätssicherung und Produktivitätssteigerung in Produktionsanlagen am Beispiel Wasserabrasivstrahlschneiden, 15. Kolloquium Schallemission, *Statusberichte zur Entwicklung und Anwendung der Schallemissionsanalyse*, Berlin, November 2005

USING A SIMPLIFIED ACOUSTIC EMISSION EQUIPMENT TO RANK PAPER MATERIALS WITH RESPECT TO THEIR FRACTURE TOUGHNESS

HARTMUT VALLEN, JOCHEN VALLEN, PER A. GRADIN¹ and PER NYGÅRD²

Vallen-Systeme GmbH, D-82057 Icking, Germany;

¹ Mid-Sweden University, S-85170 Sundsvall, Sweden;

² Paper and Fibre Research Institute, NO-7491 Trondheim, Norway

Abstract

In the papermaking industry, standard tensile tests are performed routinely and deliver the tensile strength and the strain at break. By adding an acoustic emission (AE) sensor to such tests, AE can provide information regarding changes in a paper structure during mechanical loading. AE testing can be used to determine a parameter, the elastic strain-energy density, W_C , at the onset of AE. A correlation between W_C and a fracture toughness measure has been found in a study that considered nine different paper materials (with a large span regarding properties).

Wider uses of AE in the paper industry would need an easy to mount AE sensor and a simplified equipment that is easy to operate by a non-AE expert. Such an equipment has been developed in the frame of a European-funded project, "AE applied to mechanically loaded paper". It was used for the AE testing and determination of the parameter W_C in this study reported here.

Keywords: Fracture toughness, bond failure, signal conditioner

Introduction

In the papermaking industry, standard tensile tests are performed a number of times every day in order to determine the tensile index (in essence, the tensile strength) and the strain at break on a series of 5 to 10 specimens per test. Another important value for the characterization of paper is the fracture toughness. This value is a measure for the energy per unit mass needed to enlarge an existing crack. The determination of this value needs more efforts than the tensile test and requires additional specimens with a defined crack and additional working steps. The additional determination of the fracture toughness, or a parameter that correlates in sufficient accuracy with the fracture toughness, from the tensile test that has to be performed anyway, would be of great interest to the papermaking industry.

The use of acoustic emission (AE) monitoring of paper has been described in [1–6]. In a study described in [1], tensile tests on standard specimens were carried out at a strain rate of 1%/min and the following values sampled in a 200 μ s time interval and recorded: Force, elongation, and APK. APK stands for an analogue signal that represents the maximum amplitude during the most recent 400 μ s time window. After the test, APK is used to determine the optimum threshold for the post-analysis and then applied on the recorded data in order to obtain the cumulative number of AE events versus elongation and to correlate this with the force-elongation curve.

Performing a tensile test on paper and plotting stress and the cumulative number of AE events versus strain, one gets a $\sigma - \epsilon$ curve as shown in Fig. 1, where σ denotes stress and ϵ strain, respectively. It is shown in [3] that in situations where it can be assumed that the dominant damage mechanism is fiber/fiber bond failure, damage starts when the elastic energy density reaches a critical parameter W_C . The term „energy density” has the physical meaning of an energy per

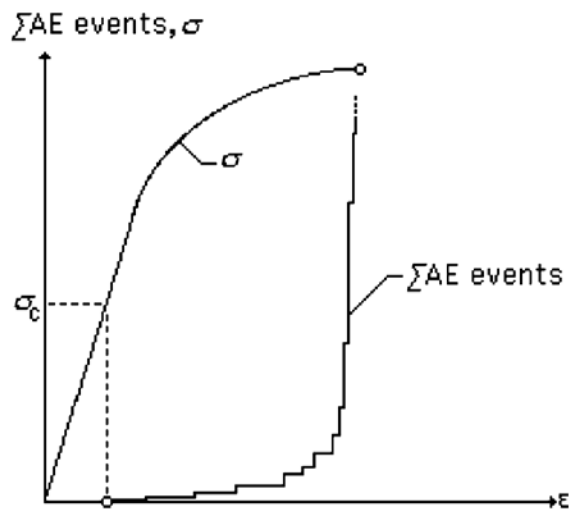


Fig. 1: Example for determination of σ_c

For uniaxial loading, W_C can be determined as follows:

$$W_C = \sigma_c^2 / (2E), \text{ and, } E = kL/Bt$$

$$W_C = F_c^2 / (2BtkL) \quad \text{in [J/m}^3\text{]} \quad (1)$$

It is customary in the paper industry to use the surface weight instead of the thickness. This results in:

$$W_C = F_c^2 / (2BGkL) \quad \text{in [J/kg]} \quad (2)$$

If the onset of AE is taken to be equivalent to the onset of damage, then for the force F_c in Eq. (2), one can use the force measured at the onset of AE.

AE Measurement

In the study [1], nine different, commercial paper grades were tested. The loading was in machine direction (MD), which is the travel direction of paper web through the paper machine during production. For each paper grade, 10 specimens were tested. The specimens had 100-mm grip length and 15-mm width. Figure 2 shows the experimental setup, Fig. 3 the used AE sensor VS700-D (Vallen-Systeme GmbH). This sensor is sufficient small and light (D6.3xH10.0 mm, 1.5 g) and was attached to the paper specimen with a magnet. No coupling agent was used.

Figure 4 shows the frequency response of the sensor used. It shows resonances at 300 kHz and 750 kHz. For data acquisition, an ASCO-DAQ2 [8] (Vallen-Systeme GmbH) was used. This is a combination of an AE-signal-conditioner ASCO-P (Variant ASCO-PH5, 90 to 1300 kHz) and a 4-channel data acquisition module for the USB bus, DAQ2. Both modules are housed in a small robust aluminum case, visible in Fig. 5 on the right of the notebook PC.

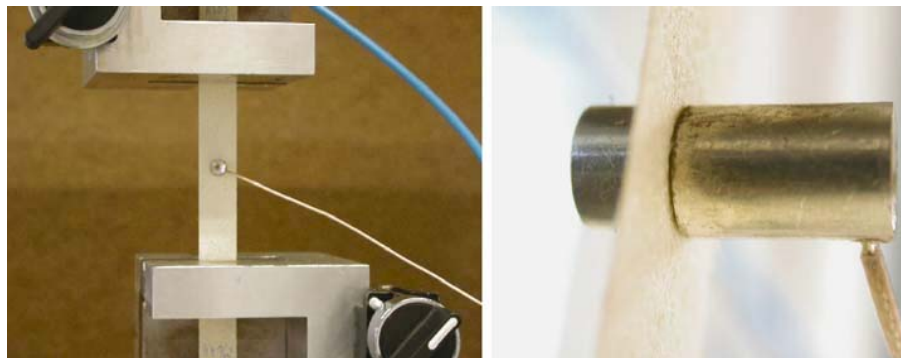


Fig. 2 Experimental setup. Fig. 3 AE sensor and magnet holder.

unit volume or unit mass. Accordingly, the unit of energy density is $[J/m^3]$ or $[J/kg]$. The meaning of the abbreviations used in the following formulas:

- E: Elastic modulus in N/m^2 ,
- σ_c : Stress at onset of damage in N/m^2 ,
- k: slope (linear part) of the stress-strain curve in N/m ,
- L: Grip length of specimen in m (0.1 m)
- B: Width of specimen in m (0.015 m)
- t: Thickness of specimen in m (use G)
- F_c : Force at onset of damage in N to be measured,
- G: Surface weight in kg/m (specimen specific)

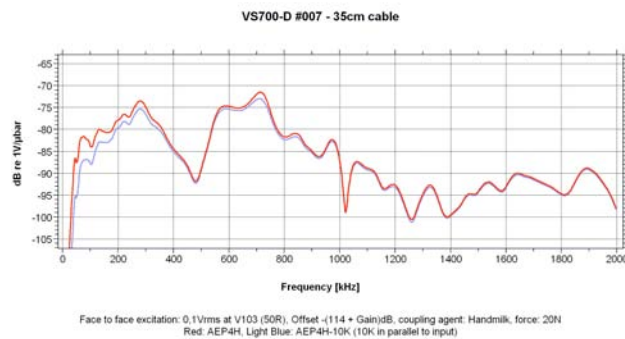


Fig. 4 Frequency response of sensor VS700-D.



Fig. 5 ASCO-DAQ2 at right of a PC.

Figure 6 shows the functional blocks of ASCO-DAQ2. A preamplifier is part of the signal conditioner ASCO-P and amplifies the AE-signal from the sensor and passes it over a 90-1300 kHz band-pass filter. Afterwards the absolute value is converted to a logarithmic representation.

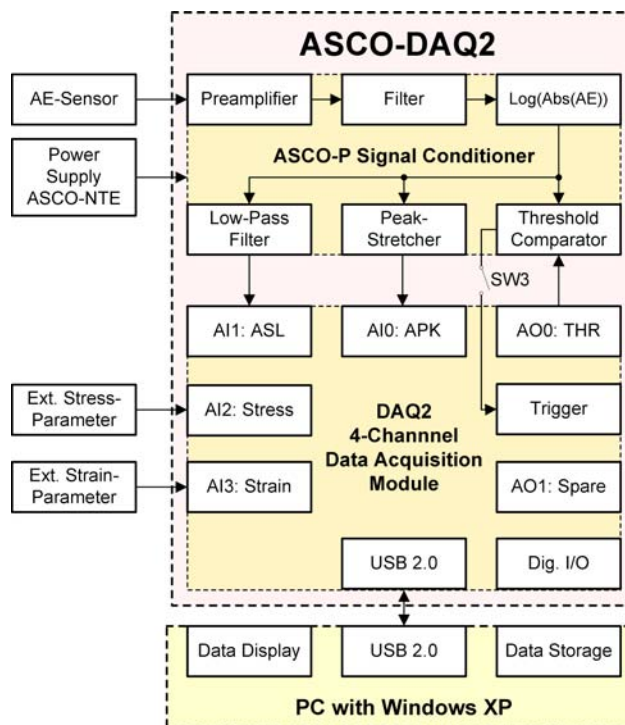


Fig. 6 ASCO-DAQ2 Functional blocks.

The peak stretcher prolongs shortest amplitude peaks to a pulse of about 400 μ s duration and an amplitude of 40 mV per dB input level, whereby 0 dB refers to 1- μ V sensor signal. A sampling interval of 200 μ s is fully sufficient to acquire even shortest peaks on the AE signal.

The peak stretcher output, signal APK, goes to input AI0 of the data acquisition module DAQ2. The 2nd output ASL and the threshold input of ASCO2 were not used in this study. An external force and an extensometer was measured by two other inputs (AI2 and AI3) of DAQ2. All DAQ2-inputs were continuously sampled and recorded in 200 μ s time interval. Figure 7 shows sample data of a tensile test.

The horizontal axis is scaled in seconds, the left vertical axis scales APK in dB_{AE} (re. 1 μ V), the right hand vertical axis scales force and elongation in N and 0.1mm steps, respectively. APK exhibits background noise of

about 40 dB_{AE}, since the frequency range is wide-banded (90-1300 kHz). Peaks above 40 dB_{AE} represent the events of interest. Around 60 s, the force reached the maximum, AE becomes very intense. At 63.5 s the final failure occurred, AE reached very high amplitudes and then the force went down. Figure 8 is a time zoom around the peak at 55 s in Fig. 7.

Now, the time scale shows ticks 1 ms apart. Two events about 25 ms apart can be identified in Fig. 8. It is easy to see that this simple equipment manages a high dynamic range as well as a high burst rate. Figure 9 shows a situation immediately before and after final failure. There, bursts overlap and cannot be separated and counted anymore

The concept of this threshold independent data acquisition allows for a determination of the optimum detection threshold from the recorded data. That makes operating much easier, compared to normal AE systems that demand a firm setting of the detection threshold before the test is started.

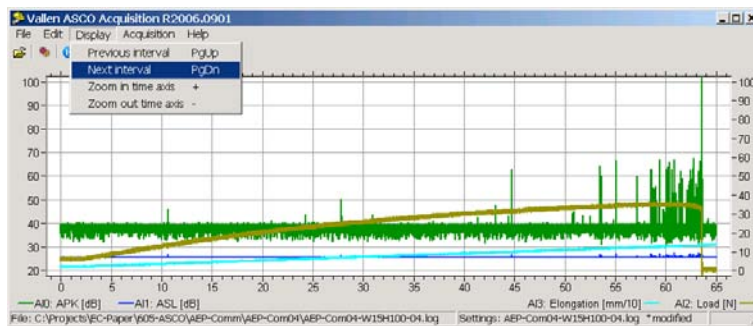


Fig. 7: Signal APK (green), force (brown) and elongation (blue) vs. time.

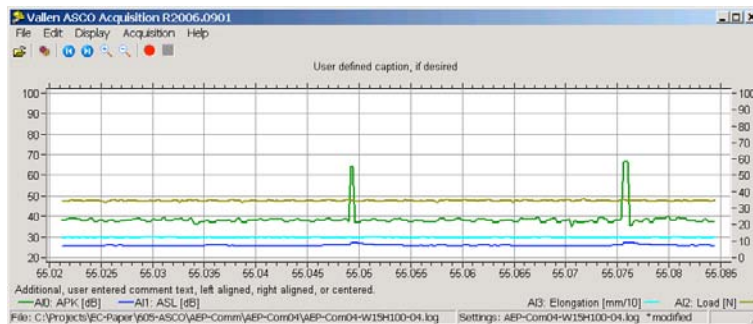


Fig. 8 Time zoom of Fig. 7 around the event at $t=55$ s.

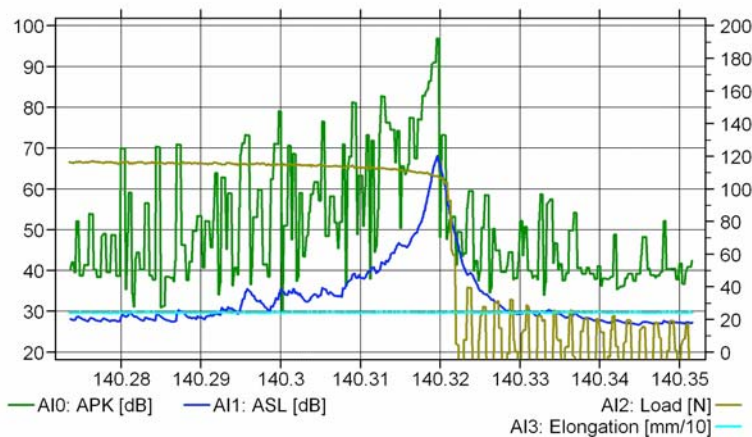


Fig. 9 Time zoom around final failure (different specimen than Fig. 8).

critical force F_c was therefore and quite arbitrarily defined as the force, at which the total number of AE events was equal to 10% of the total number of AE events at final failure. This arbitrarily chosen criterion may offer some optimization because as shown in Fig. 9, counting events near final failure may introduce some inconsistencies.

Determination of the fracture toughness parameter

Ten additional specimens of the same geometry for each of 9 paper grades were used to obtain the fracture toughness by means of a J-integral method as described in [7]. Loading was in MD with the crack being orthogonal to this direction. The values were given the notation J_{IC}^W . Paper thickness was again substituted by surface weight, resulting in the unit of [Jm/kg]. Surface weight and thickness were determined according to [9] and [10] respectively.

The detection threshold is per definition [11] „the voltage level, which has to be exceeded before an AE burst is detected and measured.“ If the detection threshold is set too low, electrical and other noise could be interpreted as an event and contaminate the data. If one selects too high a setting for the detection threshold, then events that generate low maximum values will not be detected.

Figure 10 clarifies the case „too low a detection threshold“: The diagram shows eight cumulative event curves of the same tensile test, whereby eight settings of the detection threshold between 40.0 and 40.7 were applied. The legend shows the corresponding threshold values for each curve.

Obviously the upper curve in orange (Thr = 40 dB) presents false events already at the beginning of the test, where no damage can happen. The higher the threshold the more plausible the curve. The two highest thresholds settings deliver plausible curves, since these almost equal each other. For all analysis work in this study a detection threshold of 41 dB was used.

Figure 11 shows for one paper grade the cumulative AE-events of all 10 specimens. We observed a large scatter in the force where the first AE event happened. The critical

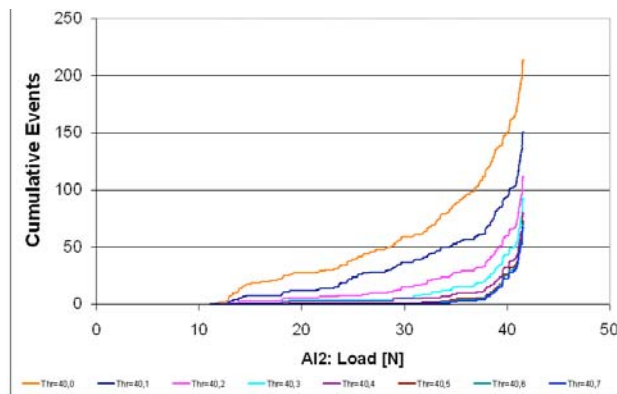


Fig. 10 Cumulative events vs. force for 8 values of threshold level, 40.0 to 40.7 dB.

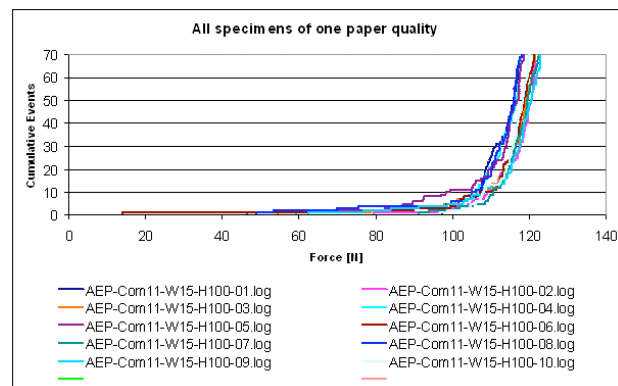


Fig. 11 Cumulative events vs. force, 10 specimens.

Results of tensile testing

The results are detailed and discussed in [1] and are summarized, since this contribution is more dedicated to the measurement and analysis method used.

The critical elastic strain energy density, W_C , determines the initiation of damage whilst the fracture toughness determines the growth of an existing crack. So far it was not sure whether the two parameters would correlate.

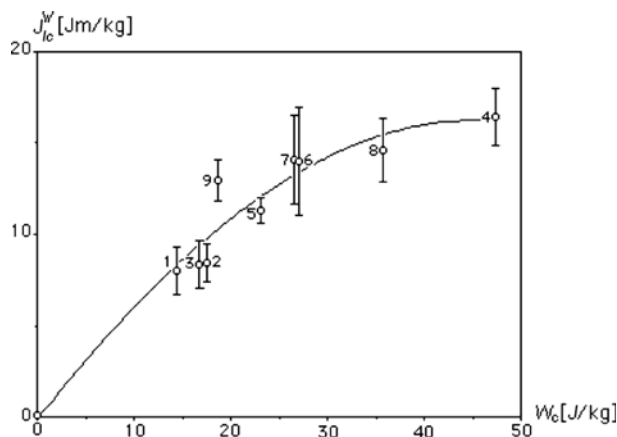


Fig. 12 Results with polynomial relation fitted to the average values.

Figure 12 presents the values of W_C and J_{Ic}^W and the standard deviation of J_{Ic}^W , the numbers identify the paper grade (see also Table 1 below). Quite arbitrarily, a third-order polynomial has been fitted to the average values and it should be noted that an extra point has been added since it is, for physical reasons, assumed that $W_C = 0$ when $J_{Ic}^W = 0$.

There seems to be a correlation between J_{Ic}^W and W_C even if it is not a linear correlation.

Table 1 Paper grades.

Mat.	Type of paper	Mat.	Type of paper
1	Newsprint	6	Sack paper
2	Improved Newsprint	7	Sack paper
3	Improved Newsprint	8	Abrasive raw paper
4	Linerboard	9	Office board
5	Coreboard		

Outlook

The AE method delivers information about processes within paper material under mechanical load that other measurement methods are unable to deliver. The determination of the parameter

W_C (the critical elastic strain energy density) by using a simplified AE equipment described here shall be seen as first trial to stress the potential of the AE method for the paper making industry. More investigations have to be performed in order to be certain of the correlation between the parameters of fracture toughness and W_C .

Acknowledgement: The financial support from the European Commission's 5th framework program under contract number, QLK5-CT-2002-00722, is greatly acknowledged.

References

- [1] P.A. Gradin D. Graham, P. Nygård, H. Vallen, The use of acoustic emission monitoring to rank paper materials with respect to their fracture toughness. *Exp. Mech.*, accepted: 25 April 2007.
- [2] P.A. Gradin, S. Nyström, P. Flink, S. Forsberg, F. Stollmaier, Acoustic emission monitoring of light weight coated paper, *J. Pulp Pap. Sci.* **23**: 3, March 1997.
- [3] P. Isaksson, P.A. Gradin, A. Kulachenko, The onset and progression of damage in isotropic paper sheets. *Int. J. Solids Struct.* **43**, 2006, 713–726.
- [4] T. Yamauchi, S. Okumura, M. Noguchi, *J. Pulp Pap. Sci.*, Jan. 1990, **16**:2.
- [5] T. Yamauchi, S. Okumura, K. Murakami, *J. Pulp Pap. Sci.*, Jan. 1989, **15**:1.
- [6] L.I. Salminen, A.I. Tolvanen, M.J. Alava, Acoustic emission from paper fracture. *Phys. Rev. Lett.* **89**, 2003, 185503.
- [7] P. Wellmar, C. Fellers, L. Delhage, Fracture toughness of paper - development of a test method, *Nordic Pulp Pap. Research J.* **12**(3), 1997, 189–195.
- [8] Vallen-Systeme GmbH, *User Manual ASCO-P, User Manual ASCODAQ2*.
<http://www.vallen.de>.
- [9] *Paper and board-determination of grammage*, ISO 536, 1988.
- [10] *Paper and board-determination of thickness and apparent bulk density or apparent sheet density*, ISO 534, 1988.
- [11] *Non-destructive testing – Terminology – Part 9: Terms used in acoustic emission testing*, CEN TC138, EN 1330-9, 2000.

ACOUSTIC EMISSION TESTING OF SEAM-WELDED HIGH ENERGY PIPING SYSTEMS IN FOSSIL POWER PLANTS

JOHN M. RODGERS

Acoustic Emission Consulting, Inc., Fair Oaks, CA 95628, USA

Abstract

The structural integrity of seam-welded fossil high-energy piping has remained a major safety and operations-maintenance issue for US utility companies. Several failures of seam-welded superheat and hot reheat piping segments have occurred since 1992, two of them catastrophic. Advanced methods of inspecting piping welds with ultrasonic testing (UT), such as time-of-flight diffraction and focused/phased arrays, are pushing back the envelope of detection to earlier stages of creep damage, but these are still very expensive, and involve considerable logistical planning and downtime to perform. The Electric Power Research Institute (EPRI) has sponsored development activities since 1986 to mature the utilization of a real-time online evaluation method for seam-welded piping: Acoustic emission (AE) testing guidelines were published by EPRI in 1995, and over 100 full-scale tests have been performed to develop a database and correlate results with other established evaluation methods. An effort was begun in 2002 to standardize the testing method within ASTM (AE Subcommittee of E07.04) utilizing the developed database. Tests to date have shown high sensitivity to early stage creep damage, which is evidenced by development of cavities around inclusions in the grain boundaries. Successful double-blind testing with advanced ultrasonic inspection methods has proven both the reliability and sensitivity of the AE technique. The economics of the method are highly favorable. Only small areas of insulation need to be removed every 4.6-6 m to weld waveguides to the piping surface. These form a linear location array along the length of piping, providing global coverage of the piping system. Testing is performed online with normal peak loading and load cycling. No outage schedule is required to perform the AE examination. Results will be presented showing that the AE method has become a reliable and economical field evaluation tool for seam-welded high energy piping.

Keywords: Seam-welded piping, fossil power plants, online monitoring, high temperature creep

Introduction

Ever since the catastrophic failures of seam-welded, hot reheat (HRH) piping at Southern California Edison's Mohave plant in 1985 and Detroit Edison's Monroe plant in 1986, utility companies have been carefully considering the need for periodic inspections of critical piping to guard against creep-induced failures. Figure 1 illustrates the creep-damage mechanisms associated with seam-welded, high-energy piping. A number of serious defects in seamed piping were removed after inspections in the late 1980's, and for a number of years there were no more catastrophic failures [3]. Beginning in 1992, however, there have been six known failures of seam-welded superheat (SH) link piping supplied with Combustion-Engineering boilers, as well as two failures in hot reheat long seamed bends. Two of these have been catastrophic: Virginia Power's Mt. Storm Unit 1 in June 1996, and Kansas City Power & Light's Hawthorne Unit 5 in August 1998. No loss of life occurred in either of those two failures, but the cost of repairs and loss of power generation is of critical concern to utility companies in this age of growing competition. All failures of SH link piping have occurred on units with accumulated service time of

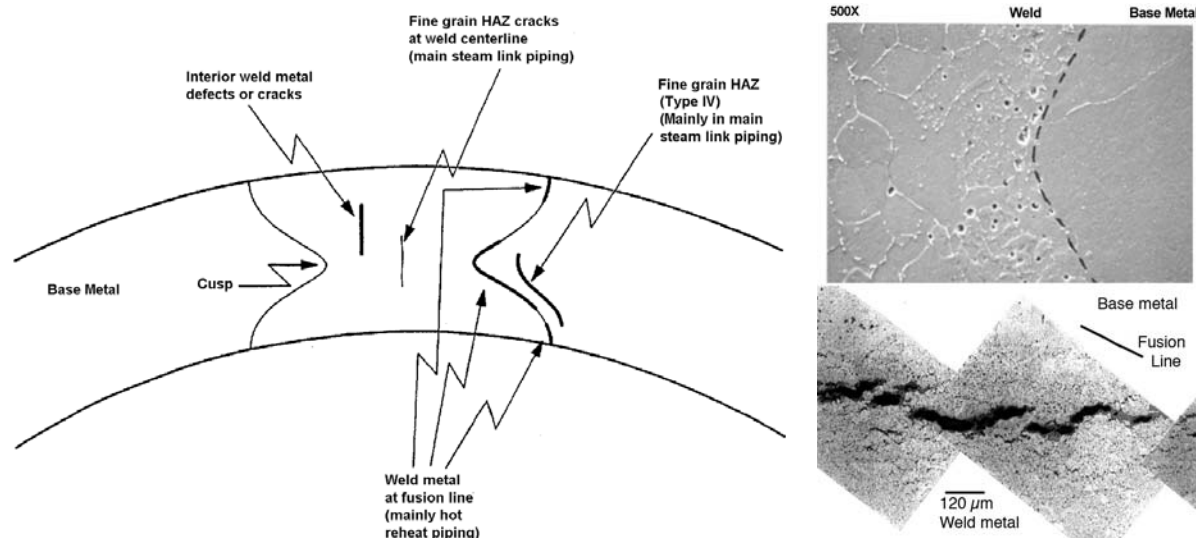


Fig. 1. Typical high-temperature creep damage occurring in seam-welded fossil piping systems constructed of P11 or P22 grade steels (left) [3]. Type IV damage in the fine-grained HAZ typically occurs in subcritically annealed welds, which is more typical of thick-section SH link piping and some HRH piping. Top right shows cavitation damage in the cusp region of an HRH double-V weld [4]. Bottom right shows advanced damage in the form of microcracks from a failed long seam bend [5].

125,000 to 225,000 hrs. Compounding the problem of inspection is the inaccuracy of supplied documentation, which may not reflect the true alloy content and method of fabrication. The Hawthorne SH link piping was not known to be seam-welded. The general aging of fossil plants will continue to raise concerns about the safety of operating seamed high-energy piping systems. Even seamless piping systems have had problems, including creep-related failures of circumferential welds, and the through-wall creep failure of a seamless SH bend that had been improperly fabricated. Current strategies for effectively managing the safety and life of seam-welded piping are based upon periodic inspection of the weld area for evidence of in service damage.

Equipment and AE Testing Set-up

The process of AE monitoring applied to piping systems starts with installation of AE transducers on welded waveguides (WG) along the length of the piping system. Spacing intervals for the WG are typically 4.6-6.1 m (15-20 ft), and installation of the sensors does not require full removal of piping insulation. There are several unique requirements for successful monitoring of high-energy piping with AE [1, 2]:

- The use of high-frequency sensors (300-400 kHz) and high frequency filtering (>200 kHz) to mitigate the effects of the steam-flow background noise. This noise is predominant below 300 kHz, and would obscure detection and accurate source location if lower-frequency, or broadband, sensors were used.
- The employment of a “floating” or automatic threshold that can control the sensitivity of detection by keeping the voltage threshold of detection above the average background noise.
- The use of active linear source location to determine the position of emitting sources on the line. The accuracy of location is dependent on the distance between sensor/waveguide positions, the pipe diameter, and the position of the emitting source. In the middle of the array between two sensors, accuracy has been demonstrated at ± 2.4 cm ($\pm 0.6''$). Near the sensors accuracy may degrade to ± 60 cm ($\pm 24''$). Still, this limits areas for follow-up inspection.

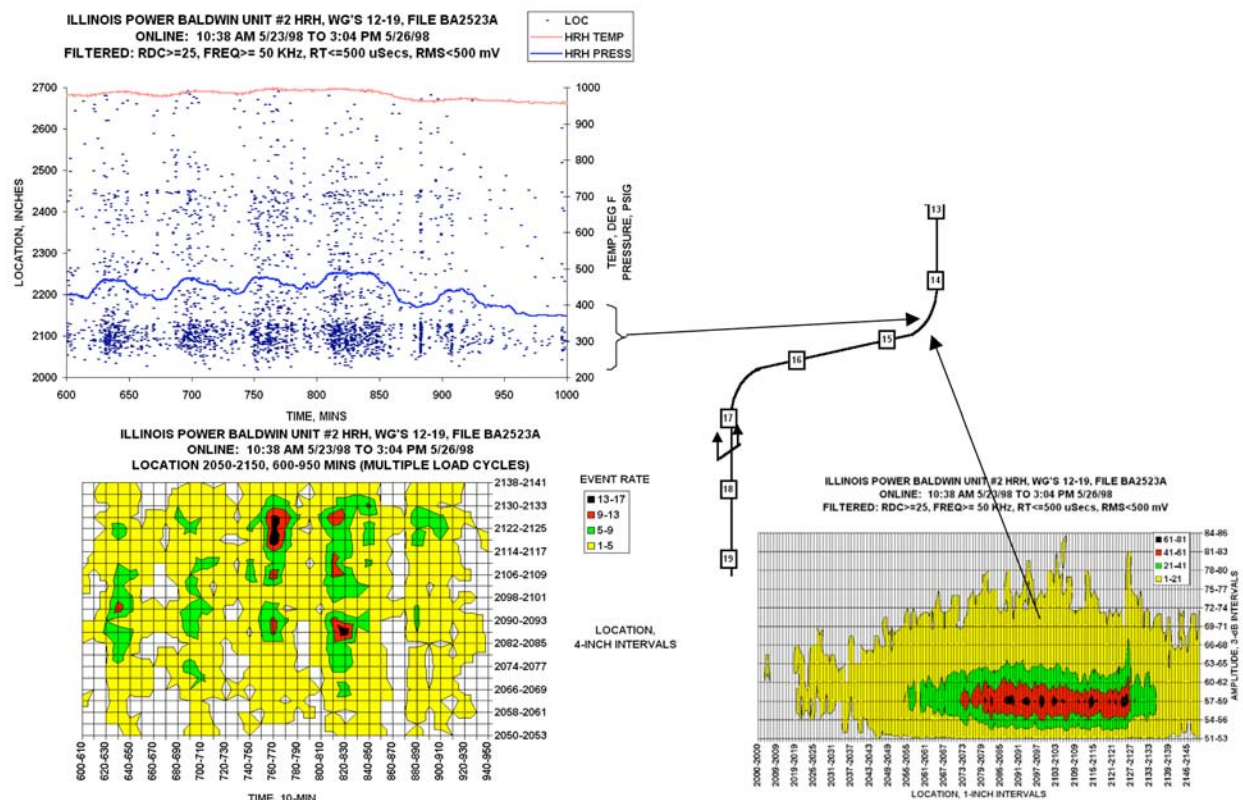


Fig. 2. A seam-welded clamshell elbow on Illinois Power’s Baldwin #2 HRH line shows typical creep-related AE behavior under cyclic pressure loading (upper left). The mechanism shows high sensitivity to load, and shows a distribution of activity along the elbow that varies with each load cycle (lower left). Bottom right shows the amplitude density feature map of this elbow location. Distributed higher activity sources are evident, and the amplitude dynamic range is larger in the high activity area. Defect growth at this early stage is probably related to decohesion of inclusions that are being affected by the creep process.

- The use of active AE-signal-feature filtering to further refine the data and eliminate obvious noise sources, such as flow turbulence. Rise time, duration, and average frequency have proven most valuable.
- Simultaneous recording of piping temperature and pressure are required to provide correlation between active AE sources and the likely source mechanisms.

Data Evaluation and Correlation

The primary characteristics of seam-weld creep-related sources are behavioral in nature—they respond to the pressure in the piping (hoop stress) and other mechanical sources of stress (geometry, hanger supports, etc.). During online conditions with normal peak load cycling, creep-related sources reveal themselves by repeated behavior with each peak load cycle [2]:

- The sources are sensitive to pressure, and may show a pronounced effect of emission rate with pressure (Figs. 2, 3).
- During load cycling, emission rates will typically peak near the start of the peak-load period.
- There is periodic emission activity during steady-state pressure and temperature conditions.
- The AE location profile is typically spread out over 1 m (40”) or more of piping length, and shows intermittent high-density locations of activity (Fig. 2).

- The amplitude range of emission sources broadens to higher values with higher activity rates (Fig. 2).
- Emission rates are much higher during startup conditions, even before substantial pressure loading. This demonstrates that the damaged area is responsive to stresses even when the piping is not in the creep regime (>510°C, 950°F).

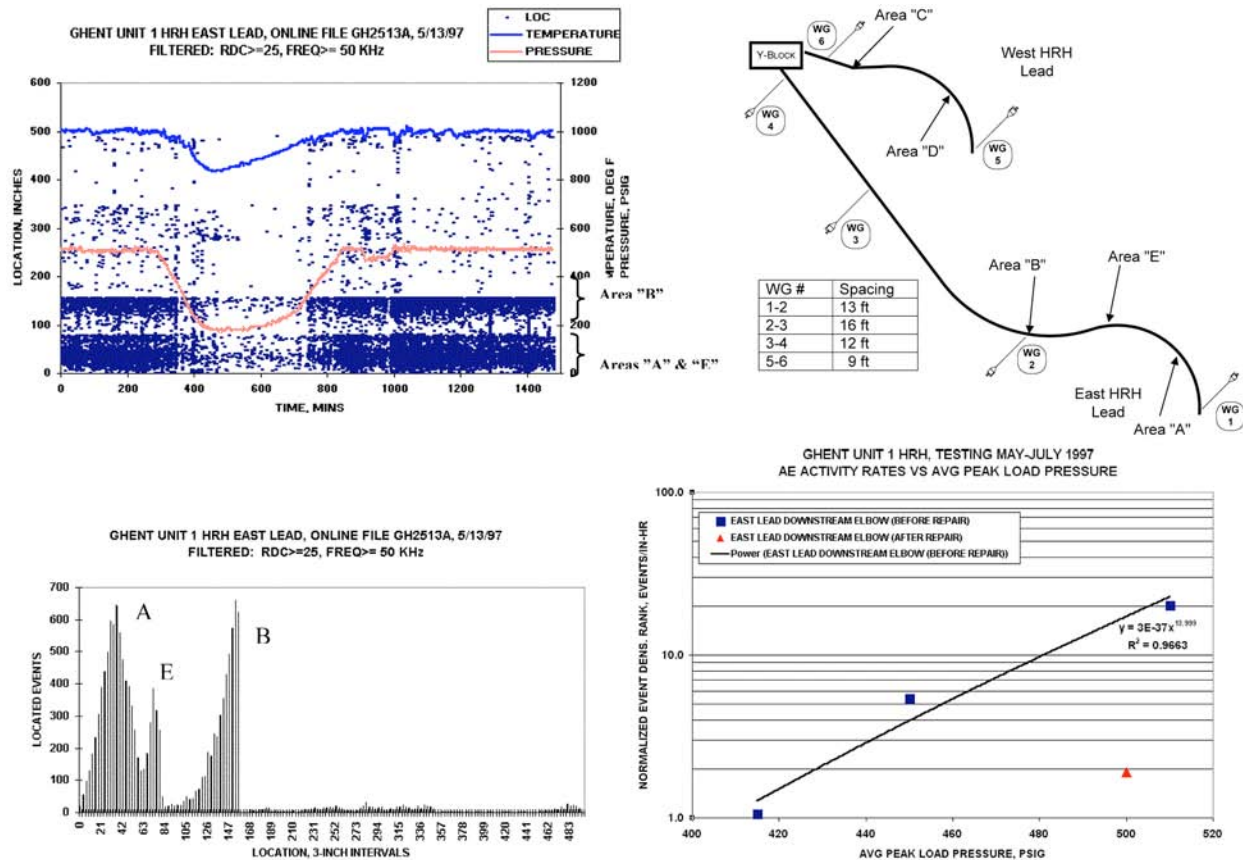


Fig. 3. Results of AE monitoring of the Ghent #1 East HRH link piping. Configuration is shown in top right. Three AE clusters were detected (A, E, B) as shown in the linear source location plot in lower left. Upper left shows a composite graph of plant parameters and AE source location vs. time for the three clusters detected. The pressure sensitivity of the sources is obvious, marking them as creep-related sources. Bottom right shows the relative activity in events/inch-hr at different pressures for Cluster “A” in the original monitoring program. After through-weld repair of the piping, the activity drops by >90% for this area, indicating that the original sources of emission have been removed.

The amount of emission generated by the creep mechanism, the repetitive nature with each peak load cycle, and the extensive dynamic range (45-90 dB amplitude) of signals, is extraordinarily different from normal ductile fracture mechanisms, such as fatigue crack growth in mild steels. Many thousands of locatable signals are sometimes accumulated over 1 m or so of weld length and several cycles (days) of steam line operation at peak load. The sheer numbers of the sources is inconsistent with a ductile crack growth mechanism, which produces infrequent emission of more limited dynamic range with repeated load cycles. The acknowledged mechanism of creep in seam welds is the development of cavities (cavitation) around nonmetallic inclusions and carbides on the grain boundaries in the fine-grained heat affected zone (HAZ) or fusion zone of the seam weld (Fig. 1). Isolated cavities soon give way to aligned cavitation along grain

boundaries, then coalescing into scattered microcracks. Final consolidation and linking into macrocracks along the seam-weld direction occurs in the last stage of growth, which can be very rapid depending on a host of factors (wall thickness, annealing state, inclusion densities, thermal and localized mechanical stresses, etc).

The early stage of this process involves the degradation of the bonding between particles and the metal matrix. These are load-carrying interfaces, and their eventual failure (decohesion) is the most plausible explanation for the amount and dynamic range of emission detected in the creep process. From the viewpoint of classifying AE behavior, this bears similarity to the experience of monitoring an organic-based composite material that has incurred extensive matrix damage. This also explains the emission that has been noted during the thermal excursion on startups, even without pressure in the system, when the piping is clearly not operating in the creep range. Damaged particle-to-matrix interfaces are prone to disbonding under high strain conditions, and startups are known to produce an even higher axial strain than at full load operation. Indeed, the results of the extensive EPRI field testing program to date has yielded detection of cavitation damaged seam welds that have not developed to the stage of micro- or macro-cracking.

A separate test program conducted in collaboration with a UK utility demonstrated that controlled creep-crack growth in small specimens produced increasing emission with increased crack growth rate. The emission rate was orders of magnitude higher for the increment of crack growth than would have been expected at lower temperatures and growth under fatigue conditions. The decohesion mechanism remains active throughout the creep regime, regardless of whether induced by directed stress at the tip of an active crack or in a volume of weld without visible cracking. This leads to high probability of detection of the creep-related failure process from very early stages, well before the damage represents a significant threat of structural failure.

Correlation of AE findings on seam-welded lines with other NDE methods and metallography were an important part of the EPRI studies and field tests from 1991 to 2001. Double blind testing was performed on Pacific Gas & Electric's Potrero #3 line in 1994, American Electric Power's Gavin #1 line in 1996, and Sierra Pacific Power's Valmy #2 line over 1997-1999. In these tests good correlation was established between conventional automated and manual multi-angle UT methods and AE cluster locations in seam and girth welds. But metallography was not used extensively in these tests to confirm the nature of the indications. Later testing would provide more extensive correlation between AE and advanced UT methods (TOFD, Phased Array, Focused Array), and more sensitive metallographic analysis (cryo-cracking with SEM examination). These included programs on Kentucky Utilities Ghent #1 HRH line and Brown #3 SH link piping (1997-98), Central Power & Light's Joslin #1 HRH line (1997), Illinois Power's Baldwin #1 HRH (1998), Salt River Project's Navajo #2 HRH line (1998), Southwestern Public Service Co's Harrington #2 HRH line (1999), and Portland General Electric's Boardman HRH line (2001).

By the late 1990's it was becoming better understood that creep damage in seam welds did not initiate as distinctive crack-like flaws, but rather as an accumulation of microstructural damage evidenced by "cavitation" development around inclusions and carbides along the grain boundaries in the heat affected zone or fusion zone of the seam weld (depending on whether the structure was normalized and tempered or subcritically annealed after welding). Several high profile failures of seam-welded piping after missed or misinterpreted UT findings (Sabine #2 HRH bend in 1992, Mt. Storm #1 SH link piping in 1996, Gaston #4 HRH bend in 2001) led to a greater sense of urgency in the fossil utility industry to find earlier stage damage more reliably in seam welds. The AE studies mentioned provided proof of early stage detection of creep damage at the cavitation stage, often well before UT methods could reliably indicate a developing problem. Only the advanced metallographic method involving the use of cryo-cracking and SEM

examination at 2000-5000X was able to confirm this damage that AE was detecting at an early stage.

The standardization of the EPRI AE methodology for seam-welded piping began in earnest in January 2002 at the ASTM E07.04 acoustic emission subcommittee meeting. EPRI gave approval to the use of its documents and database as a necessary background for the development of the standard. The proposed standard WK 658 "Standard Test Method for Acoustic Emission Examination of Seam-Welded High Energy Piping" is nearing final balloting, and is expected to be approved in 2008. It is one of the most comprehensive and specific ever undertaken by an ASTM committee on an AE application.

Conclusions

Acoustic emission has proven its worth in online testing programs. Approximately 30% of lines tested have shown no significant findings of creep damage, and most others have shown only minor activity at suspect locations. The majority of seam-weld findings has been in elbows and bends, followed by hanger locations on horizontal line segments. These are known to be higher stressed areas, and offer further validation of the AE methodology. The correlation with follow-on nondestructive inspection has been very good, but the lesser sensitivity of UT inspection methods will generally not confirm early stage creep damage at the isolated cavitation stage. The economics of inspection and relative certainty of detection at an early stage of creep damage should be increasingly attractive to companies attempting to manage their piping systems in a climate of reduced capital and operations-maintenance spending.

References

1. B. Morgan, C. Foster, *Acoustic Emission Monitoring of High-Energy Piping, Volume 1: Acoustic Emission Monitoring Guidelines for Hot Reheat Piping*, Electric Power Research Institute, TR-105265-V1. 1995.
2. J. Rodgers, R. Tilley, *Standardization of Acoustic Emission Testing of Fossil Power Plant Seam-Welded High Energy Piping*, ASME Pressure Vessels & Piping Conference, San Diego, July 25-29, 2004, PVP-Vol. 471, pp. 113-131.
3. J. Foulds, R. Viswanathan, J. Landrum, "*Guidelines for the Evaluation of Seam-Welded High Energy Piping*", Electric Power Research Institute, TR-104631, 1996.
4. R. Munson, J. Rodgers, R. Tilley, *The Utilization of Advanced Metallographic Techniques to Verify In-service Damage in Long-seam Welded, High Energy Piping*, EPRI Fossil Plant Inspection Conference, Atlanta, 1999.
5. J. Foulds, R. Carnahan, *Examination of Sabine 2 Hot Reheat Pipe Seam Weld Cracking*, Electric Power Research Institute, TR-107141, 1997.

APPLICATION OF ACOUSTIC EMISSION IN MONITORING OF FAILURE IN SLIDE BEARINGS

IRENEUSZ BARAN, MAREK NOWAK and WOJCIECH DARSKI*

Cracow University of Technology, Institute of Production Engineering M-6, Kraków, Poland;

*Gdańsk University of Technology, Ocean Eng. and Ship Technology, Gdańsk, Poland

Abstract

The article describes the laboratory tests, which make the first stage of the study concerning the use of the AE method to determine the technical state of the slide bearings in engines with self-ignition. The aim of the present tests was to compare the recorded signals in relation to the technical state of the material of the bearing bush and to check the possibility of using the AE method in determining the transition moment from the fluid friction into the semi-dry friction in the bearing and signaling the first micro-defects of the material of the bearing bush. The experiment has not solved the problem, but they are of a development character and will be continued in the nearest future.

Keywords: Frequency analysis, slide bearing, friction factor, bearing bush

Introduction

Ship combustion engines with self-ignition have fundamental influence on the profitability of ships and their safety at sea. Therefore, it is important to ensure the failure-free operation of these engines. In ship engines, the maintenance of the sliding abilities of the main bearings and connecting-rod bearings is of special importance because the failures of these bearings constitute almost 30% of the total number of failures in all parts of engines. Since the costs of failures of combustion engines caused by the failures of slide bearings are high, intensive theoretical and experimental tests of the slide bearings properties have been undertaken [1, 2].

The currently used methods of monitoring of the technical state of slide bearings indicate the state of failure only when a considerable degradation of the slide bearing material appears. In many cases, this is unsatisfactory in avoiding severe defects or failures. Testing by means of the AE method occurs in real time, and this method can be used as a system of the early warning to avoid damage in structural parts of combustion engines [3, 4].

The presented tests were carried out on the fully computer-controlled laboratory stand (PG-2 1L type) for the examination of slide bearings, as shown in Fig. 1. This stand enables one to simulate the real performance conditions of a bearing and to record all the essential parameters, such as: moment of friction, rotational speed, temperature of the bearing and of the lubricating oil.

Technical data of PG-2 1L laboratory stand:

- Power of engine: 11 kW,
- Range of rotation of shaft: 1-4000 RPM,
- Maximum transversal load: 150 kN,
- Diameter of shaft: 76.18 or 80.25 mm,
- Length of bush: 36.75 or 40.00 mm.

The tested bearing bush of MB10-type (Fig 2) is used in C-330-type diesel engine. This engine is generally used for drive auxiliary assembly on ships.



Fig. 1. The laboratory stand PG-2 1L for examination of slide bearing.

Technical data of MB10-type bush:

- Catalogue No.: 1006022010
and 1006021010,
- Length: 40.00 mm,
- Outside diameter: 86.00 mm,
- Thickness of wall: 2.905 mm,
- Thickness of steel part:
2.600 mm,
- Diameter of seating of frame:
86 mm.

Tests were made under different conditions of slide bearings:

- Constant transversal load and constant rotation:
1 or 2 kN, 1700 RPM,
- Constant transversal load and cyclic variable rotation:
1 or 2 kN, 1-1700 RPM,
- Step changing transversal load and cyclic variable rotation:
1, 2, 4 and 8 kN, 1-1700 RPM.



Fig. 2. The bearing bush MB10-type after several cycles.

The trials by the AE method were carried out with the use of the Vallen AMSY5 system with different types of sensors (VS150RIC-Vallen, WD-PAC and others) in order to cover the widest band of frequency measurements. At the same time, the AE system enabled us to record the test parameters (moment of friction, rotational speed, loading force, temperature) in order to correlate them later with the recorded AE.

Measurements of the acoustic background

The first stage of the tests concerned both the measurement of the acoustic background and the noise generated by the operation of the installations on the testing stand. That is why the first tests were carried out on a new bearing in different loading variants and rotational speeds with the recording of signals in a widest band of frequency. The frequency analysis of the recorded signals allowed us to determine the main band of noise and the selection of frequency high-pass and low-pass filters for subsequent measurements in order to minimize noise coming from the operation of the testing stand.

An example of the recorded bands of frequency on two wide-band PAC-WD sensors with constant transversal load and constant rotation is presented in Fig. 3. Two examples are given for narrow-band filtered signals (a) and wide-band signals with strong low-frequency activity (b).

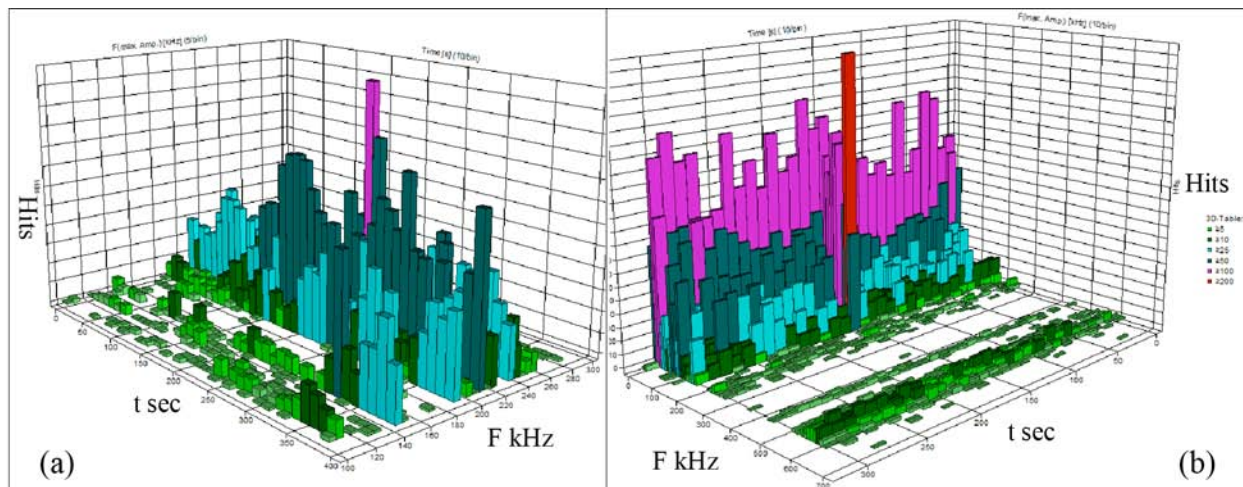


Fig. 3. The arrangement of the frequency bands of the signals recorded by 2 wide-band sensors. (a) narrow band, 100-300 kHz segment of 95-850 kHz filter output; (b) Wide band, 20-850 kHz.

Measurements of bearings in different technical state

The first stage of the tests using frequency filters was the measurement of a new bearing with the accepted conditions (loading and rotational speed) similar to the preliminary tests. We used the constant rotational speed of the shaft of 1700 RPM and two values of the bearing loadings, 1 and 2 kN. The AE parameters for these operating conditions for a new bearing established the basis of comparison in the remaining tests.

In order to compare the AE signals recorded during the testing of the new bearing with the signals coming from defected bearing, the measurements were taken of three sliding bearings made of the same material (simulated different bearing capability):

- The new bearing bush without defect – full bearing capability,
- The bearing bush with an opening, simulating a local defect in the material of the bush, which caused disturbances in the flow of lubricating oil – a small but apparent loss of bearing capability,
- The bearing bush with longitudinal and circumferential scratches simulating considerable wear of the bush material – large loss of bearing capability.

High activity of AE was recorded but clearly different for each kind of tested bearing bushes. General AE parameters such as: Hits, Counts, Duration, Energy and RMS showed differences between bushes. However, Amplitude of signals contained similar ranges for all the tested bearing bushes. To evaluate different activities of AE, uses of different threshold levels made

comparison difficult with these parameters. At this time, the best parameters for comparison are RMS and frequency distribution of signals. Recorded RMS for the new bearing and the bearing simulating the local loss in the bearing bush material are presented in Figs. 4, 5 and 6. There are data of RMS from different channels with different frequency ranges. Two types each of low- and high-frequency data (with or without *) and medium frequency data are shown. Note RMS for High Frequency (red line) is off-scale because overloading occurred on this channel.

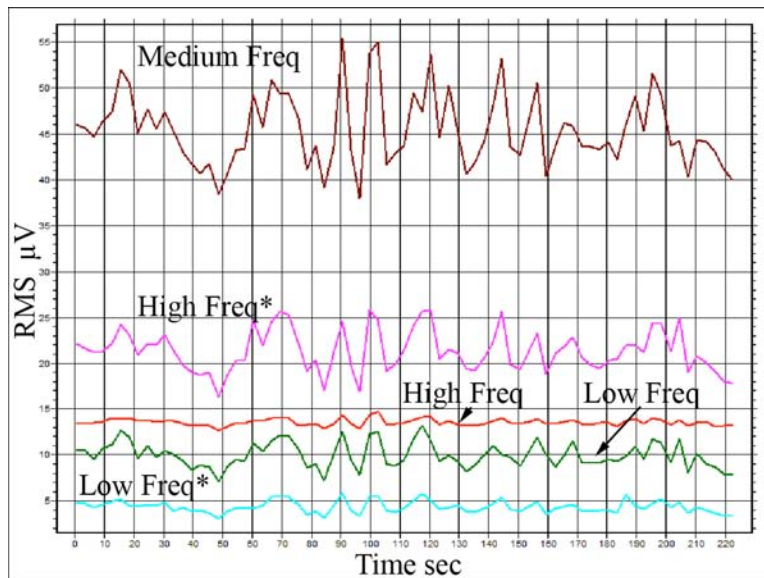


Fig. 4. RMS for different ranges of frequency filters – new bush with no defect.

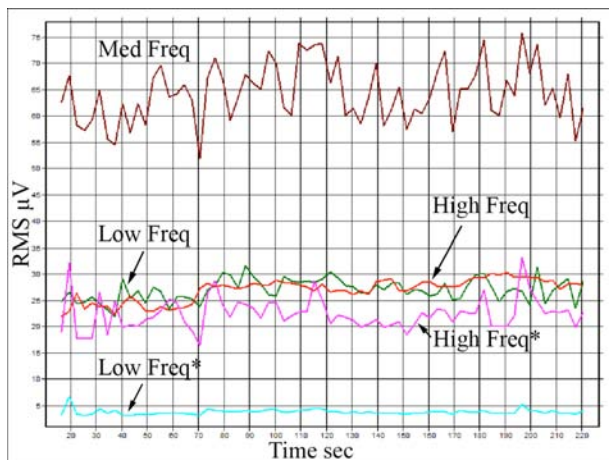


Fig. 5. RMS for different ranges of frequency filters – bush with an opening defect.

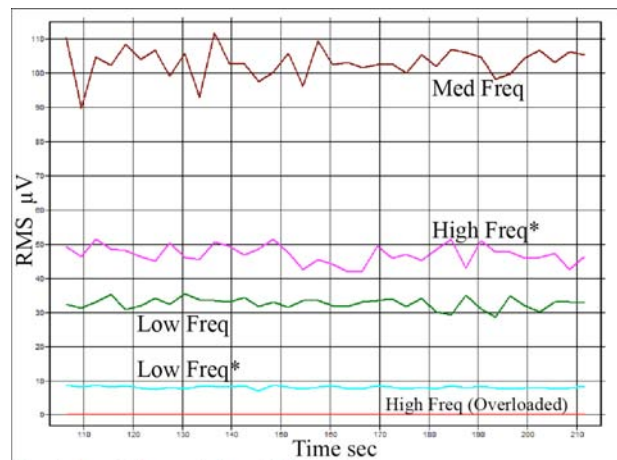


Fig. 6. RMS for different ranges of frequency filters – bush with scratches.

The observed data shows general increase of AE RMS levels (except Low* and High* channels between Figs. 4 and 5). Medium and High channels respond to bush damage states sensitively. The relative changes in the 5-channel data provide clear indication of the bush damage states.

The initial dimensions of the bearing and the bearing’s fit are of vital importance on the parameters of the recorded AE. For the bearings of the same dimensional group, different level of the AE activity was recorded. It is especially visible in the first stage of the bearing operation, when the initial wear of bearing bush surfaces to the shaft neck takes place. Therefore, it is vital

to enlarge the data library by taking a larger number of measurements for each of the accepted variant of the bearing states.

Considering the serious differences in the intensity of emission for the particular kinds of the state of bearings during the measurements, changes were being made in the arrangements of the acquisition parameters in order to record the measuring data, which could enable the subsequent analysis with the use of the waveform [5].

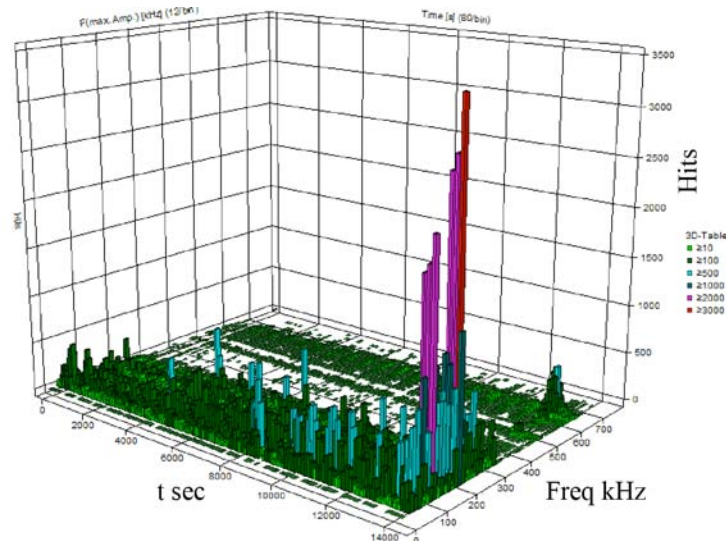


Fig. 7. The arrangement of the frequency bands of the signals during long-time tests with variable rotation and step changing of transverse load.

The measurement of the bearing with changeable parameters

During the testing of the new bearing, a measurement was also taken under the conditions of variable rotational speed and step changing of transverse load, which were to lead to a quicker wear of the bearing bush material. After the cyclic changes in rotational speed, the AE was recorded during the operation of the bearing under the established conditions. The recorded AE was to detect the appearance of the first damage in the material of the bearing. The sum of distribution of hits in frequency bands is presented in Fig. 7. The visible change in the activity of hits indicated a change in the operation of the bearing. The reason of the sudden increase in the AE activity was the wear of the surface layer of the bearing. These changes were invisible in the conventional bearing parameters (moment of friction, temperature, ...) recorded on the testing stand PG-2 1L. It was indicated that significantly changing inside slide bearing is detectable by AE. The example of one of the half bush after these tests is shown on Fig. 2, where surface wear can be seen. It should be noted that this research requires a larger number of the trial tests in order to record AE in different states of wear of the bearing material.

The measurement under the conditions of intermittent fluid friction

One of the essential aspects of the tests was the measurement of AE during the disappearance of the fluid friction and transition into the semi-dry friction; i.e., at the moment of the first contact of the pin with the bearing bush. To this end, the test methodology was modified and caused to decrease the friction factor till the start of the contact of the metal pin with the bearing bush. The AE recorded at this time signaled the decrease of the friction factor due to the disappearance of the activity of the AE signals. This was followed by the increase in the friction factor during the contact of the pin surface and the shaft, then a sudden increase in the activity of

AE was observed. Figure 8 shows the changes of the bearing parameters, the moment of friction (left) and RPM (right) in the new bearing test. The changes in the AE hit activities in various frequency bands are also presented in Fig. 8. Here, actual RPM reached zero when the friction was high. No AE was emitted in this period and until ~700 RPM was reached.

In this connection one should suppose that carrying out of a larger number of tests will allow the unequivocal identification of the moment of transition from the fluid friction into the semi-dry friction. The presented tests were carried out on the testing stand under the laboratory conditions. In the future, measurements of the bearings installed in combustion engines are planned.

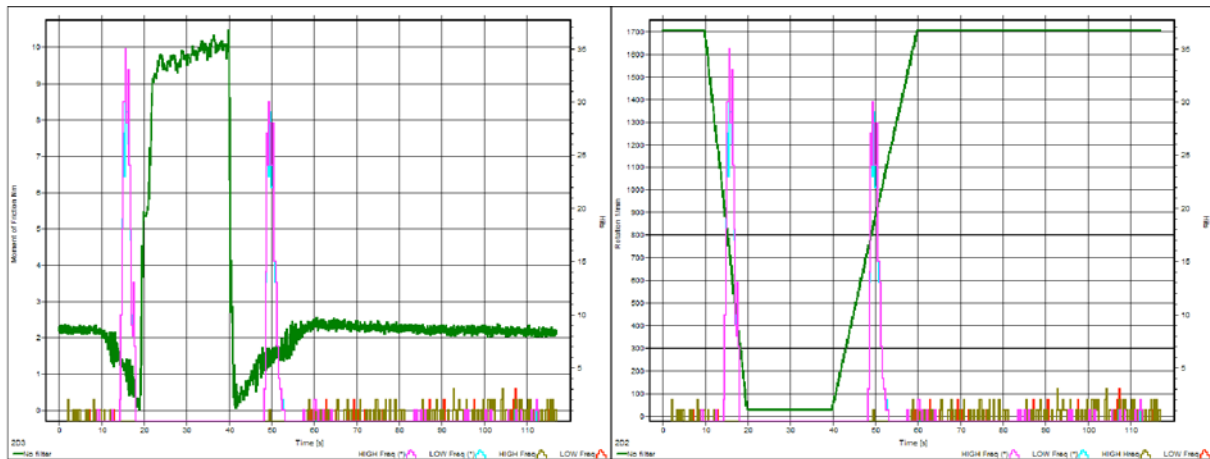


Fig. 8. The changes of the moment of friction (left) and RPM (right) parameters and the AE hit activities in the new bearing test.

Conclusions

The application of the frequency filters allowed to reduce the majority of noise for the testing stand, but in the future it will be necessary to determine noise on real engines. The presented examples illustrate that it is possible to apply the AE method in order to define the state of the bearing material. The sensitivity of the AE method allows one to record the signals, which indicate the transition from the fluid friction into the mixed friction. In the future, it will be advisable to use a pattern-recognition analysis software to identify the recorded signals.

References

- [1] Burger W., Albers A., Scavino R., Dickerhof M.: Proc. of WTC2005 World Tribology Congress III, Sept. 12–16, 2005, Washington DC, USA.
- [2] Scavino R., Burger W., Fritz M., Albers A.: Tribologie Fachtagung 2004, Hungary Academy of Sciences, Kozma: Veszprem.
- [3] Al-Ghambi, Zhechkov D., Mba D.: 26th European Conference on Acoustic Emission Testing, Berlin, 2004,
- [4] Yoshioka T., Fujiwara T.: *Wear*, **81** (1), 1994, 183-186.
- [5] Gołaski L., Gębski P., Baran I., Ono K.: *Journal of Acoustic Emission*, **17** (3-4), 1999, S37.

THRESHOLD INDEPENDENT ACOUSTIC EMISSION MONITORING OF A CRIMPING PROCESS IN SERIES PRODUCTION

JENS FORKER, HARTMUT VALLEN and KURT OBRIST*

Vallen-Systeme GmbH, 82057 Icking (Munich), Germany;

* Pfisterer Sefag AG, 6102 Malters, Switzerland

Abstract

End fittings of high-voltage insulators are connected to a fiber-reinforced rod by a crimping process. Depending on the process parameters, pressure and duration and some arbitrary parameters of the fitting and the rod, it might happen that the rod becomes damaged during the crimping process. A feasibility study showed that a damaging and a non-damaging crimping process can be distinguished by a factor of 100 to 1000 of the acoustic emission (AE) energy rate picked up by an AE sensor mounted on a crimping claw. Requirements for AE equipment suited to monitor series production of high-voltage insulators are identified. The realization of a rugged monitoring device is described.

Keywords: High-voltage insulators, high-voltage isolators, crimping monitoring, FRP, end fitting

Application

Figure 1 shows the crimping of an end fitting onto an FRP rod using a hydraulic press. Figure 2 shows two different types of end fitting already pressed to the FRP rod. Figure 3 shows a part of a completed high-voltage insulator.



Fig. 1 Crimping an end-fitting onto a rod.



Fig. 2 After crimping.



Fig. 3 Final product.

Such insulators may carry heavy high-voltage lines: they have to bear the weight and maintain electric isolation.

The end fitting to FRP rod joint needs to be very reliable. Failure of this joint may cause the high-voltage line to sag or even to fall down. This could cause injury or even death to humans and harm the environment. Further, the operation of the high-voltage line would be affected and/or interrupted.

If the crimping pressure is too high, the FRP rod inside the end fitting is damaged. This will cause failure of the FRP rod below the nominal tensile load. If the crimping pressure is too low, the FRP rod is pulled out of the end fitting before reaching the nominal tensile load. Hence the crimping process needs to be optimized to reach a crimping pressure as high as possible, but

must avoid a damaging over-pressing. A fundamental analysis of this topic can be found in [1, 2]. Both studies use AE measured during pull-out tests to verify theoretical analysis and numerical simulations.

High-voltage insulators are usually tested (by manufacturer and buyer) by destructive pull-out tests of random samples. This reduces the risk of using damaged FRP rods, but the risk still remains. Obviously, there is a need for monitoring the crimping process to identify ‘problematic’ joints or inadvertent changes of process parameters. Further, it could be used to determine the optimum values for crimping pressure and crimping duration. We found a first publication of an online-monitoring of the crimping process using AE in 2001 [3]. The authors suggested to evaluate the time evolution of the hit rate.

Realizing the Online Monitoring of the Crimping Process

1. Feasibility Study

In 2001 we made a first feasibility study, which came to the following results:

- In the frequency range 300-700 kHz we obtained a better signal-to-noise ratio than in 100-300 kHz („noise“ includes undesired background signals).
- The sensor can be mounted on the fix crimp claw. The energy transfer from the FRP rod into the claw is reproducible and sufficient for testing (see Fig. 4).
- A 40 dB threshold provides enough sensitivity
- Noise signals can be neglected. This was shown e.g. by crimping an end fitting to a steel rod where no damage can be introduced by over-pressing. Over-pressing causes a rise of the AE energy rate by factor of 10-1000.



Fig. 4 Sensor bonded to the fixed crimping claw.

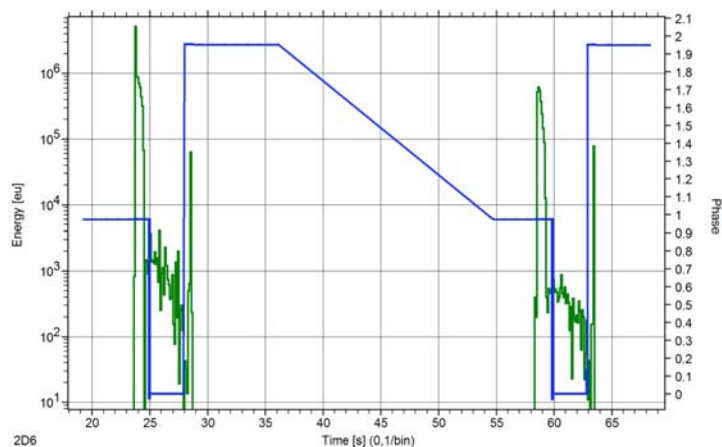


Fig. 5 Energy rate during steel-rod-crimping.

Figure 5 and 6 show data of the first feasibility study. Figure 5 shows in green the energy rate (left axis) per 0.1 s vs. time for two crimping processes on a steel rod. The blue line (right axis) shows the processes steps: Value = 1: Closing claws (e.g. 19-25s); Value = 0: Pressure increase and hold (e.g. 25-28s); Value = 2: Pressure release and opening the claws (e.g. 28s).

This test allows us to rate the AE caused by the hydraulic press itself, because no FRP could contribute to the measured AE. One can see a brief increase in the energy rate where the crimping starts and ends. This can be explained by the touching and lift-off of the crimping claws.

Figure 6 shows initially (starting at 175s) the crimping of an FRP rod with an extend pressure-hold period causing a damage to the rod. From 183s the energy rate increases by a factor of 100-1000, indicating damage. From 228s, ‘good’ crimping started next where the energy rate is comparable with the steel rod crimping. Figure 6 provides an additional, important hint: while

damaging the FRP rod (from 183-189s), the energy rate decreased only few times, but the hit rate (not shown) fluctuates very strongly. This means: for this application, the hit rate is less distinctive than the energy rate. For an industrial device, this raises the requirement for a threshold independent measurement of an amplitude or energy parameter.

AE equipment used for this feasibility study: sensor VS900-M, sensor cable SEC (1.2 m), preamplifier AEP4 (34 dB), AE signal processor ASIPP with filter 300-850 kHz, threshold 40 dB, DDT: 0.4 ms, RAT: 1.6 ms, AE-System: AMSY4 (Vallen-Systeme GmbH).

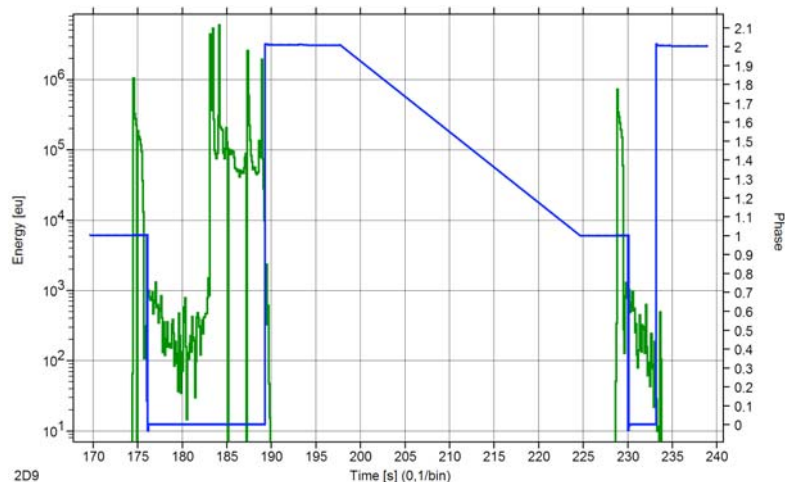


Fig. 6 Energy rate for a damaging (left) and a good crimping of an FRP rod.

2. Demands on a device for monitoring a series production

- Installation and operation of the device needs to be very simple and straightforward. Series production is done by trained workers where the time for instructing frequently changing staff is very limited. AE know-how cannot be expected and time-consuming operation won't be accepted at all.
- Maintaining the inspection equipment, *AE device* must not be more complicated than a simple voltmeter.
- Directly after crimping, the AE device needs to visually and acoustically indicate one of three possible results: a) good crimping; b) questionable crimping; c) damaging crimping.
- Nothing more than noticing the results shall be required from the crimping staff. Hence the AE device needs to detect start and end of the crimping process itself, e.g. from the crimping pressure, and to evaluate the data accordingly.
- Correct operation of the AE device needs to be easily verified.
- The AE device needs to be rugged and connectors must differ from each other to avoid wrong connection.
- The AE device needs to determine at least one energy or amplitude parameter without the need for setting a threshold (threshold independent).

These demands show clearly that an AE system developed for well-trained AE service providers and researchers cannot be the best solution. Meeting these demands requires a different concept.

3. Market Situation

Between 2001 and 2006, we received about 10 inquiries for a turn-key AE device to monitor crimping of end fittings to FRP rods. This did not justify a market research or a self-funded development of such AE device. At the beginning of 2006, Pfisterer Sefag AG indicated their interest in a cooperative development of such a device. At this time, a prototype of the ASCO-DAQ1 existed and the effort to adapt this to the requirements was manageable and justified.

4. ASCO-DAQ2 for Monitoring the Crimping Process

ASCO-DAQ2 is a combination of AE signal conditioner ASCO-P (for this application the derivative ASCO-PH3, 300-750 kHz) and the 4-channel USB data acquisition module DAQ2. Both modules are integrated in a small, rugged case connected to the PC via a USB cable. Windows 2000 or XP is recommended as PC operating system.



Fig. 7 ASCO-DAQ2 mounted to hydraulic press.

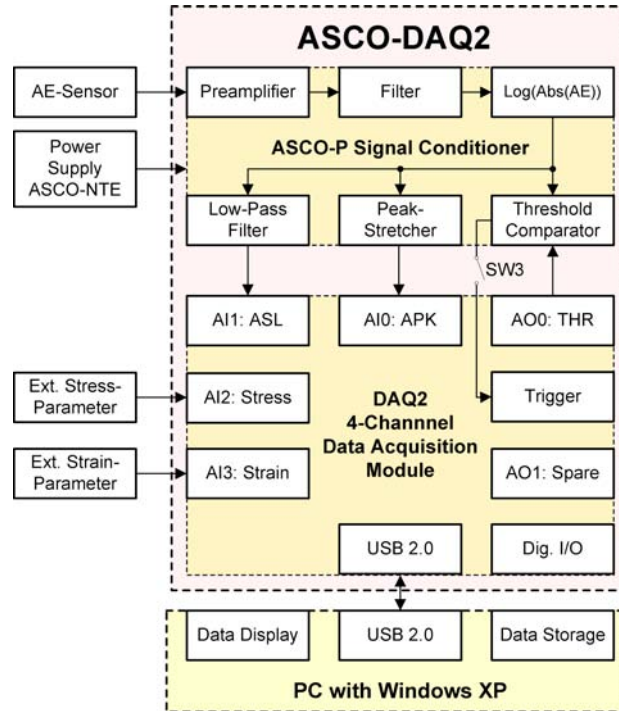


Fig. 8 ASCO-DAQ2 hardware schematic.

ASCO-P amplifies and filters the AE-signal from the AE sensor and determines the logarithm of the absolute value. This logarithmic signal is scaled to 40 mV/dB_{AE} and then passed to the peak stretcher and the low-pass filter. The low-pass filter averages the signal and provides it as ASL (average signal level). The peak stretcher elongates shortest peak amplitudes to approximately 50-ms duration. With this, even a 40-ms sampling interval (25 Hz) is sufficient to detect shortest peak amplitudes as APK (amplitude peak) signal. The signals ASL, APK and the crimping pressure are recorded by the data acquisition system at 10-ms interval (100 Hz).

5. Examples

Figure 9 shows an example for a good crimping. The colors indicate:

- Brown: pressure (right axis, in bar),
- Blue: ASL Signal (left axis, in dB_{AE})
- Green: APK Signal (left axis, in dB_{AE})
- Yellow: limit for *Warning*
- Red: limit for *Bad*

The limit lines are bi-colored: the first color indicates if the limit is for *Warning* (yellow) or *Alarm* (red); the second color indicates whether the limit is for the signal ASL (blue) or APK (green). ASL stayed below 42 dB_{AE}, and APK below 73 dB_{AE}. The peak of 71 dB at 6.5 s was verified to be meaningless.

Figure 10 shows an example for a bad crimping: ASL exceeded 85 dB_{AE}, APK was even above 103 dB_{AE}. (measurement range is up to 106 dB_{AE}). The electronic noise can be seen at the

very left, before the pressure increase. It is about 23 dB_{AE} for ASL and 33 dB_{AE} for APK.

If only the *warning limit* but not the *bad limit* is exceeded, a yellow *warning* field is shown instead of the red *bad* field. The text in these fields can be defined by the user. Simultaneously with showing the *green/yellow/red* field, one of 3 wav files can be played for the acoustic indication.

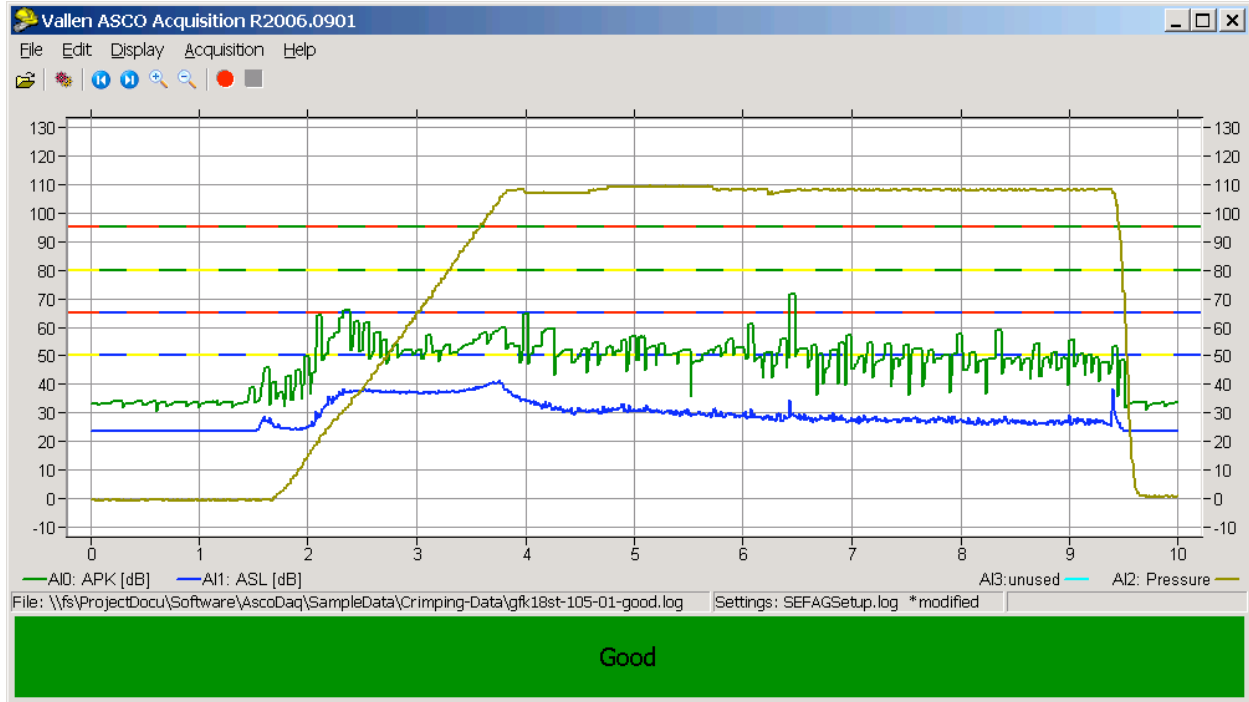


Fig. 9 An example for a good crimping screen.



Fig. 10 A screen after a damaging crimping.

6. Control by Pressure

Only at the first start-up, the settings (e.g., limit and texts to be shown) need to be defined. For practical use, one needs to start the software and switch the acquisition mode on. Data evaluation starts as soon as the pressure exceeds a certain value and data evaluation ends when pressure falls below a certain value. After data evaluation is completed, the result is shown graphically and indicated acoustically. The operator needs not to care about the AE device: he starts the crimping process as before and waits until crimping is completed. He just needs instructions how to proceed in case of questionable or bad crimpings.

Pressure control can be deactivated to allow for manual operation of the AE device. Further details; e.g., how data is stored, post-test analysis possibilities and more can be found in [4].

Conclusion

An AE device to monitor series production of crimping end fittings onto FRP rods of high-voltage insulators was developed. Detecting over-pressing, which would cause catastrophic failure of the part, is reliable. The AE device is threshold independent and does not require intervention from the hydraulic-press operator as the crimping pressure controls data analysis. The result (good/questionable/bad) is indicated visually and acoustically immediately after crimping. The good cooperation between manufacturer of the high-voltage insulators and manufacturer of the AE device was important for the success of the project. Since the beginning of 2007, the AE device monitors the crimping in series production and prevents further processing of pre-damaged high-voltage insulators.

Potential for improvements

Fan et al. [3] suggested to also detect under-pressing (too low a crimping pressure) using AE. Whether this can be realized could be estimated if data from a sufficient number of good and under-pressed crimpings would be collected.

Discrimination between good and damaging crimping could be improved by numerical inversion of the analogue logarithm, subtracting a base line (background noise), and integrating the positive remainder. This was not implemented in order to keep the mode of operation, especially the setting of the limits, as simple as possible. An additional parameter *base line* would have increased complexity.

References

- [1] M. Kumosa, Y. Han, L. Kumosa, Analysis of composite insulators with crimped end-fittings, Part II - Suitable crimping conditions, *Composite Sci. Tech.*, **62** (9), 2002, 1209-1221.
- [2] A. Preneloup, T. Gmür, J. Botsis, K.O. Papailu, Acoustic emission study and strength analysis of crimped steel-composite joints under traction. *Composit Structures* **74**, 2006, 370-378.
- [3] Fan Ju, Liang Xidong, Yin Yu, Wang Chengsheng, Chen Ling, Application of acoustic emission technology on structure design and quality control of composite insulators, *Proceedings of 6th ICPADM*, June 2000, pp. 358-361.
- [4] *ASCO-P User Manual, ASCO-DAQ2 User Manual*, www.vallen.de

PROBABILITY OF DETECTION FOR ACOUSTIC EMISSION

ADRIAN POLLOCK

Physical Acoustics Corporation, Princeton Junction, NJ 08550, USA

Abstract

Probability of detection (POD) is a discipline within the field of nondestructive testing, that bears on the reliability of the inspection and has been of great value for selecting and validating NDT procedures, qualifying NDT personnel, and even establishing the acceptability of structural designs. This paper shows a way to bring the POD concept to AE technology. It reports the development of a model, which quantifies each step in the classic AE process – stress stimulus, flaw growth, wave release, wave propagation, sensing and detection. In its first implementation, the model treats fatigue crack growth in pressurized cylinders. A small percentage of the fracture surface is assumed to be formed by cleavage, the source of the AE. With the help of the Paris law for fatigue crack growth, the source theory of Wadley and Scruby, the power-law amplitude distribution and other relevant theory, it is possible to determine the probability of detecting AE from a flaw of given initial size, in a given vessel subjected to a given pressurization schedule. Because of attenuation the POD depends on the source position, so the findings are presented with POD encoded as color on a map of the vessel. Use of this POD concept will open the way to engineered AE inspections, better quality AE tests, and better integration of AE with other NDT methods to meet industrial needs for structural integrity.

Keywords: Probability of detection

Introduction: Probability of Detection (POD) in the NDT Industry

"Probability of detection" (POD) is a quantitative discipline with the field on nondestructive testing, addressing the topic of inspection reliability. In the late 1960's and early 1970's, it was common knowledge in the NDT industry that many inspections were producing incorrect results and that some inspection teams were more reliable than others. POD methodology was developed to address these facts and to furnish tools for securing adequate reliability of NDT on high-visibility, high-cost structures, such as the space shuttle [1]. Continuing to develop during the last 30 years, the POD discipline has delivered value in many activities especially selecting and validating NDT procedures, qualifying NDT personnel, and even establishing the acceptability of structural designs.

POD is the probability of actually detecting a given flaw that is assumed to be present in a given nondestructive inspection. POD is of obvious significance to structural integrity and safety. POD is a statistical quantity. The probability of detecting a given flaw depends on many factors including flaw characteristics (e.g. type, size, shape and orientation), test method and procedure, and personnel proficiency. In the early years of POD development, the approach was to collect together a large number of test objects with flaws and a substantial number of inspectors (sometimes teams of inspectors); to have the inspectors perform NDT; and to analyze the results in terms of how many flaws were detected. The outcome of this kind of analysis is conventionally presented as a graph showing POD as a function of flaw size. Work of this kind has provided valuable support to many programs, especially in the aerospace industry where the POD concept has been a good partner to the concepts of damage tolerance that were being developed at the same time. The main setback to the empirical approach to POD (multiple test

specimens, multiple inspection teams) is that it is laborious and costly. As the use of POD increased, techniques for modeling the NDT processes were brought in to supplement the empirical approach. By using models to handle some of the variables, the numbers of test specimens and inspectors needed to estimate POD could be reduced, resulting in a less costly and more efficient analysis.

Model Developed for Estimating POD for AE

A model for the probability of detecting flaws by means of AE was developed in the context of a project for monitoring a set of high-pressure gas cylinders during a planned 30-year service life. AE was under consideration both for the pre-service hydrotest and for in-service monitoring of these vessels. Availability of POD numbers for AE would support the project through the design approval process and lead to a more economical design. The model was developed first for the in-service monitoring scenario. The POD model is essentially a quantification of the classic path from AE source to processed data. All the variables along the path are quantified – stress stimulus, source behavior, wave propagation, sensor sensitivity, instrumentation gain and detection threshold. Figure 1 is a block diagram of the model, in which the variables are arranged in a way that facilitates the desired calculation.

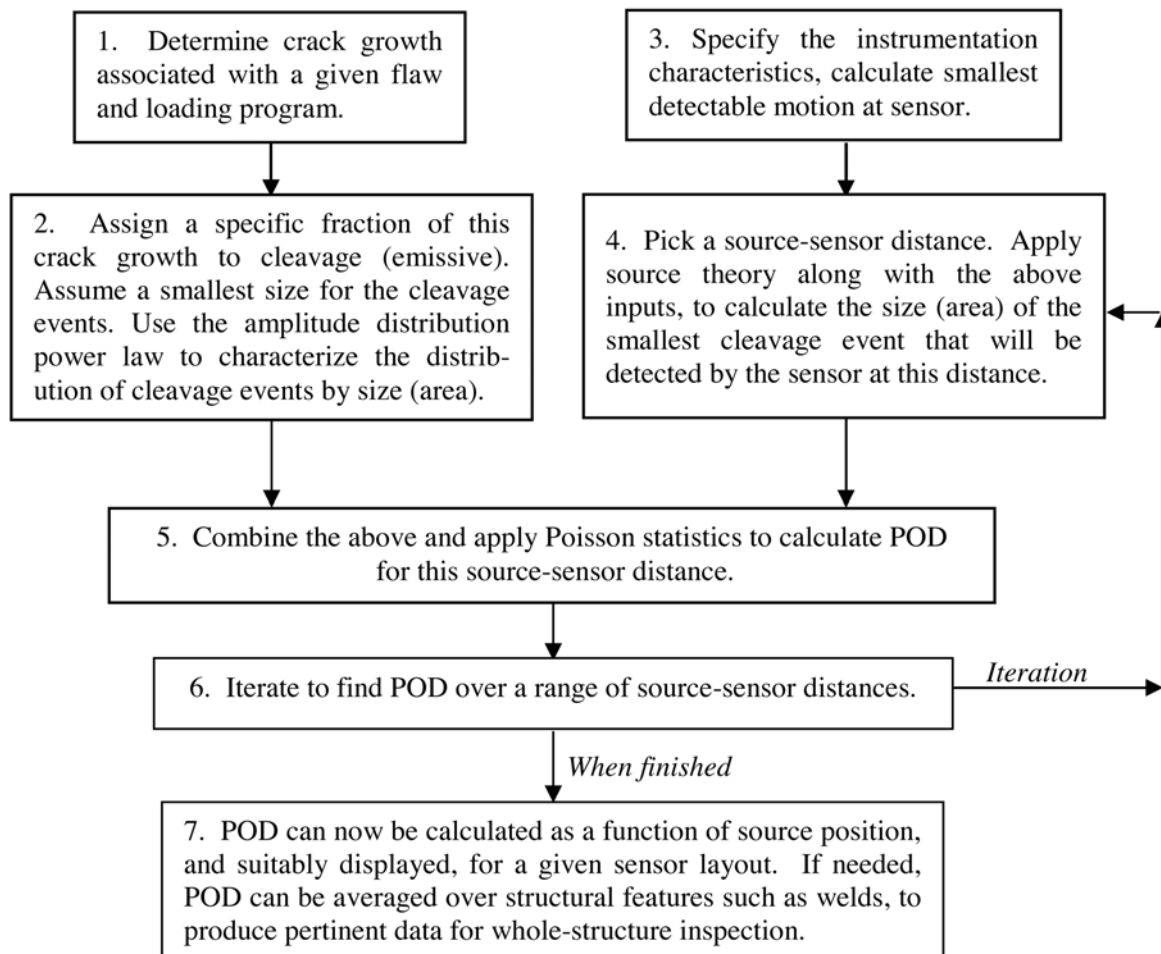


Fig. 1 Method for determining the probability of detecting a flaw with AE.

POD is determined at the convergence of two lines of inquiry, related to AE generation and AE propagation/detection respectively. The operative questions are:

1. "How many cleavage-crack events will take place at the specified flaw under the loading program under consideration, and what is their size distribution?"
2. "How big is the smallest cleavage-crack event that will be detected by the AE equipment, at the distance under consideration?"

Given the answers to these two lines of inquiry, it is not hard to find the probability of detecting the flaw during execution of the specified loading program, using the specified equipment setup. Because of attenuation, the probability of detection is naturally a function of source position. It is assumed that the AE is produced by "cleavage-crack events" that form a definite percentage of the fracture surface area. This assumption is a key feature of this particular case; i.e., fatigue crack growth in these metal cylinders. However, it is not essential to this POD methodology in general. Other cases could be based on different assumptions about AE source mechanisms. Indeed, this is a major area for the future growth of this POD methodology. To show how the process works, the less obvious steps of Fig. 1 will be discussed in turn.

1. *Determine crack growth associated with a given flaw and loading program.*

The loading program is a key part of any AE test [2]. For the case of fatigue crack growth in the high-pressure gas cylinder, the assumption was made that a flaw was growing according to the Paris law. A computer program and graphic user interface were developed to calculate the amount of flaw growth with user-entered initial flaw sizes and loading programs. The graphic user interface is shown in Fig. 2. The upper part shows the vessel dimensions, the pressures applied and the cycling process to be monitored. From the dimensions and pressures, the hoop and axial stresses and stress intensity factors are calculated by conventional techniques. Then, the program calculates the flaw growth cycle by cycle, finally arriving at the total new crack area opened up during the entire specified loading program.

2. *Characterize the cleavage increments (AE events) that will make up this crack growth.*

The model used here for fatigue crack growth is a synthesis of insights from several sources. The pioneering work of Pelloux [3] showed that in Stage II fatigue, the new surface is created mainly by slip-like dislocation movements; but, occasionally, this process is punctuated by abrupt transgranular cleavage events that can even be seen on fractographs. The studies of Wadley and Scruby on emission amplitudes from various source mechanisms, summarized in [4], indicate that such cleavage events would give useful AE signals while the dislocation movement would not. The early observation of Harris and Dunegan [5], that peak load emission does not occur on every cycle until the crack is growing relatively fast towards the end of its life, also fits our story that just a certain fraction or percentage of the fracture surface area is formed by cleavage, and that this is the source of the AE. This fraction or percentage is an input parameter to the POD model.

This gives us a total cleavage area resulting from the loading program under consideration. The next step is to break up this total area into discrete increments – AE events. This is done with the help of the amplitude distribution power law [6], whose exponent b is an input parameter to the POD model. It is assumed that the smallest event is single-grain cleavage, while large events correspond to cleavage extending over multiple grains simultaneously. Using the power law, the number of AE events $F(A)$ is calculated as a function of A , the cleavage area of the individual event. This completes the first line of inquiry, *Steps 1 and 2* in Fig. 1.

It is generally agreed that different flaw types have different AE characteristics. Therefore, the above argument is only a specific, limited prototype of this generic step in the POD model. Fresh thought will be needed when the scope of the methodology is extended to cover flaw types other than cracks, and/or loading regimes other than Stage II fatigue.

3. Specify instrumentation characteristics, sensor layout, attenuation.

The specified instrumentation characteristics include the sensitivity of sensor and preamplifier, the preamplifier gain and the detection threshold. These obviously influence whether a wave of given strength will be detected by the instrument. Another instrumentation characteristic that comes into the model is a characteristic frequency of the sensor. This is used to convert the stated sensor sensitivity from $V/(m/s)$ to V/m . This approach does not consider the full complexity of sensor spectral responses or directional effects, but it does allow a calculation of the smallest displacement at the sensor that will be detected at the characteristic frequency.

4. Source theory and wave attenuation.

The focus of this step is to determine the smallest cleavage increment detectable by the sensor. First, this requires some source theory, which is drawn from reference [2]. This source theory relates the cleavage event area to the resulting AE motion (displacement) as a function of distance in an infinite medium. We apply this source theory at a reference distance of one plate thickness from the source. Then, the measured attenuation from that distance outwards is used to infer the smallest detectable cleavage event area at any arbitrary distance.

5. Apply Poisson statistics to calculate POD for a given source-sensor distance.

This is an interesting step in the model. Here the stochastic nature of the AE phenomenon leads naturally to a stochastic (probabilistic) outcome for the detection process. Here also, evaluation criteria are considered. For now, detecting a single AE event is considered equivalent to detecting the flaw. Other evaluation criteria can be found in industrial practice. In tube trailer testing, for example, the evaluation criterion is framed in terms of a cluster of several events, located close together. The POD concept described here can be readily extended to such cases.

To conclude the present analysis: we have a probability distribution of cleavage event areas and we know the smallest cleavage event area that will be detected. The expected number of detectable events λ is immediately found. Then, this expected number λ can be used as the "rate" parameter of the Poisson distribution. This distribution (a function of λ) tells about the probability of actually detecting 0, 1, 2, ... events in a given test when the expectation number is λ . The probability of detecting no (zero) AE events is $e^{-\lambda}$. So the probability of detecting at least one AE event, is $(1 - e^{-\lambda})$. This is the probability of detecting the flaw; a good simple result to close out the POD model calculations.

Illustrative Results

The screenshot shows the 'POD-POL Setup' dialog box with the following parameters:

Category	Parameter	Value	Units
Cylinder Geometry	Outer Diameter	32	(in)
	Height	100	(in)
	Thickness	0.6	(in)
	Head Effective Radius	50	(in)
	Head Thickness	0.72	(in)
Instrumentation	Threshold	50	(dBae)
	Sensitivity of Sensor + Preamp (dB ref 1v/(m/s))	69	
	Sensor Characteristic Frequency	100	(kHz)
	Preamplifier Gain	40	
Loading	Hydrotest Pressure (HP)	1650	(psi)
	Max Working Pressure	1100	(psi)
	Min Working Pressure	50	(psi)
	Number Initial Cycles at Hydrotest Pressure	0	
	Number Cycles in a block at Working Pressure	2000	
	% Overload Margin	5	
Material	Poisson Constant (C)	4.0	(10e-13)
	Poisson Constant (m)	3.0	
	Grain Size	4.0	(micrometer)
	% Cleavage	2.0	
Flaw Characteristics	Flaw Type	Crack-Like	
	Crack Depth (a)	1.0	(mm)
	Crack Length (c)	10	(mm)
	Crack Length Correction Factor	1	
	Membrane Correction Factor	1	
	Crack Orientation Opened by	Hoop Stress	
Source Factors	Source Bandwidth Factor	1	
	Source Speed Factor	0.5	

Fig. 2: Setup for illustrative runs of the POD-POL software.

Figure 2 shows input data used to generate the POD results in a typical run of the POD software. The structure being modeled is a cylindrical pressure vessel being subjected to 2000 pressure cycles. The flaw being modeled is a crack, initially 1.0-mm deep. AE is monitored using a 50-dB threshold setting. There are many adjustable parameters but to illustrate the functioning of the model, just these three will be varied while the others are held constant.

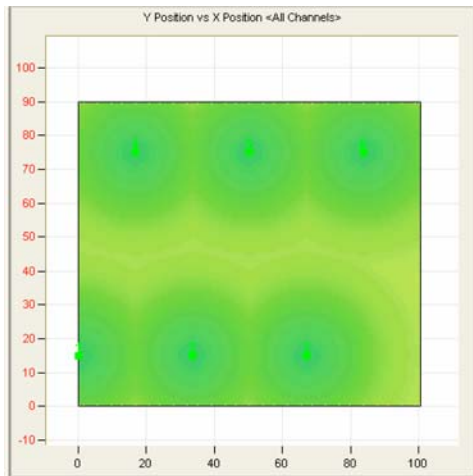


Fig. 3: 1-mm flaw, 2000 cycles, 50-dB threshold.

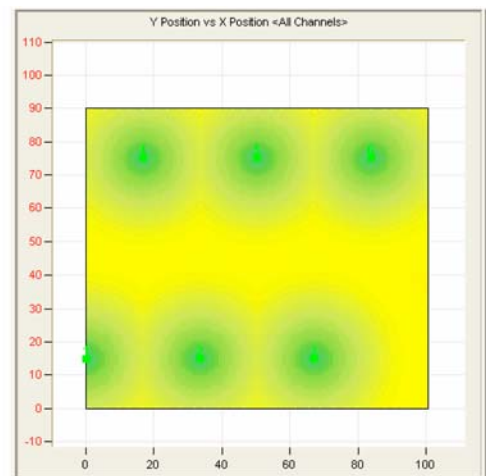


Fig. 4: 1-mm flaw, 1000 cycles, 50-Threshold.

Figure 3 is map of calculated POD for the test setup detailed in Fig. 2. Six sensors are placed on the vessel, two rings of three sensors each. The POD values are encoded in color as shown in the key beside the map. The color is mostly green, indicating high POD (80-100%) for flaws almost anywhere on the vessel surface. Midway between the sensor rows, the POD is lower (60-80%). The model also displays some statistics of the flaw growth - the number of AE events occurring at the crack, the total area of cleavage, and the number of grains cleaved – but these cannot be shown here for the lack of space.

Figure 4 shows the result of only monitoring 1000 cycles instead of 2000, with the same initial flaw size. The POD drops to 40-60% over most of the vessel surface. The POD is only high if the flaw is close to a sensor. This kind of result can be useful in engineering an AE test, because it shows how the reliability of the test will depend on the duration of the monitoring.

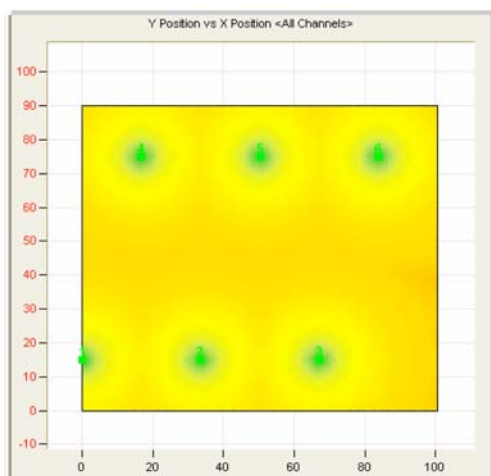


Fig. 5: 0.4-mm flaw, 2000 cycles, 50-dB threshold.

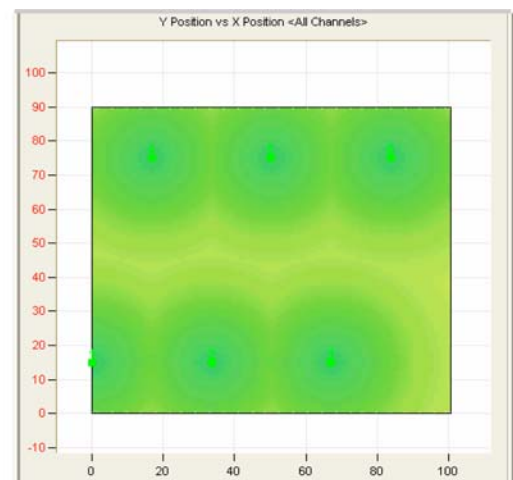


Fig. 6: 0.4-mm flaw, 2000 cycles, 40-dB threshold.

Figure 5 reverts to 2000 cycles of loading, but the initial flaw is only 0.4-mm deep instead of 1.0-mm. Now, the POD is only 30-55%, over most of the surface area. The flaw has to be very close to a sensor if it is to be detected with high reliability. This kind of result is useful because it shows how the AE test results will depend on the initial flaw size.

In Fig. 6, the detection threshold is lowered to 40 dB. This renders the 0.4-mm flaw detectable with much higher probability, 70-80% and better, over most of the vessel surface. In a real test, of course, lowering the threshold would also increase the likelihood of picking up noise sources.

Finally, Fig. 7 shows a logical extension of the POD concept: Probability of location (POL). This is readily incorporated in the model. Figure 6 shows how the POL is greatest when the source is in the open space surrounded by sensors. POD, in contrast, is greatest when the source is close to the sensors. POD and POL can both be considered when planning the strategy for an AE test or test series.

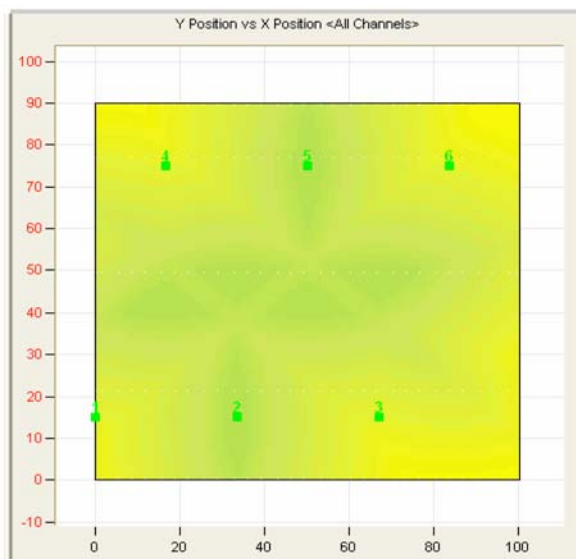


Fig. 7: Probability of location (POL).

Discussion and Conclusions

These results illustrate how POD depends on the many variable parameters involved in the AE test. With this model, the effects of changing sensor layouts, sensitivities and test parameters in general can be assessed quickly, easily and quantitatively. AE test planning often involves tradeoffs around cost, technical difficulty and so forth. With this model, quantitative expectations about test results can now be included in this planning process. This quantitative planning capability will also make AE more viable in the eyes of reliability engineers, who are considering its use in their structural integrity assurance programs.

References

1. W.D. Rummel, Probability of Detection as a Quantitative Measure of Nondestructive Testing End-to-End Process Capabilities, *Materials Evaluation*, **56**, 1, 1998, 29-35.
2. A.A. Pollock, Loading and Stress in Acoustic Emission Testing, *Materials Evaluation*, **62**, 3, 2004, 326-333.
3. R.M.D. Pelloux, *The Analysis of Fracture Surfaces by Electron Microscopy*, Boeing Scientific Research Laboratories, Report Z254824 (available from Storming Reports), 1963.
4. R.K. Miller and P. McIntire (eds.), *Acoustic Emission Testing, Nondestructive Testing Handbook*, 2nd ed., Vol. 5, American Society for Nondestructive Testing, 1987, pp. 77-78.
5. D.O. Harris and H.L. Dunegan, Continuous Monitoring of Fatigue Crack Growth by Acoustic Emission Techniques, *Experimental Mechanics*, EXMCA, **14**, 2, 1974, 71-81.
6. A.A. Pollock, Acoustic Emission Amplitude Distributions, *International Advances in Nondestructive Testing* (ed.: Warren J. McGonnagle), Vol. 7, 1981, pp. 215-240.

ACOUSTIC EMISSION WAVEFORM ANALYSIS OF GAS LEAKAGE ON PIPE WITH VARIOUS TYPES OF ARTIFICIAL DEFECTS

LAODENO REM NUNEZ, HIDEO NISHINO and KENICHI YOSHIDA

Faculty of Engineering, The University of Tokushima,
2-1 Minamijosanjima, Tokushima, 770-8506 Japan

Abstract

In actual pipeline installations, difficulty is encountered in identifying the leak when it is buried underground. This paper helps develop AE method to facilitate the analysis and characterization of pipeline defects. The results describe a common behavior of AE waveforms for each type of pinhole using FFT analysis. The pinhole diameter varies from 0.3 to 0.5-mm and from 0.5 to 1.85-mm depth for straight-type and stepwise-type, respectively. The stepwise pinhole is considered as converging-diverging nozzle, in which high-pressure air ranging from 100 kPa to 500 kPa flows over the sonic velocity. When air flows through the pinhole, instability of AE signals occurred above the critical value due to the burst pressure at the throat. We recorded the highest value of AE magnitude as 153 mV at 280 kPa for straight pinhole with 0.5-mm diameter and as high as 37 mV at 290 kPa for 0.3-mm diameter. Here, the pressure shock occurred for all types of pinhole and the screech tone was generated specifically for straight-type and slit-type defects because of the large-scale instability of waves from airflow, in which the peak frequency decreases with increasing pressure. The critical pressure at 0.22 MPa was calculated based on the assumption that the flow velocity reached to its sound velocity. In the case of stepwise-type pinhole, different characteristics of AE waveforms were observed. Apparently, this was due to the inflow of air through the pinhole at various depths as well as the bursting of signal and unusual noise occurred beyond its critical pressure. Also, before reaching the critical value, a monotonic increase of amplitude took place since unsteady flow occurred at the onset along with the self-excited vibration of the generated AE. For stepwise pinhole with 1.0-mm depth, a disturbed flow was detected having a noticeable drop of AE amplitude from 13.2 mV to 8.9 mV over the critical pressure. Furthermore, experiment was conducted for slit-type pinhole, which shows that the rapid fluctuation of the waveforms was caused by stronger energy released so its amplitude became higher in magnitude. Clearly, the unstable AE signals above the critical pressure were due to effect of varied pinhole diameter since the greater the pinhole the larger the volume of air released while the pressure increases.

Keywords: FFT, gas leak, pipes

Introduction

Acoustic emission (AE) technique has been established for the monitoring and inspection of flaws specifically on gas leakage from pipeline installations through research in the field and laboratory. However, in actual pipeline installations identifying the leak is the common problem that usually happens specifically when it is buried underground. Several research works have been continuously carried out using AE technique to monitor and inspect leakage from pipeline installations. This method is a well-established non-destructive testing technique for flaws specifically on gas leakage detection as well as other material defects. It is efficient and cost-effective process among other applications. Such method could also be used to locate the

leak source and could effectively characterize the development of defects such as deformation, corrosion, cracks, etc. According to the report which shows that it is desirable to study small leak rates so that we could characterize them in the laboratory and reproduces as well in the field since the leakage rate is important in the context of environmental protection regulation [1]. It is also reported that the characteristic frequency of acoustic emission due to gas leakage is 10 kHz [2]. Despite of scholarly works, there is still a consistent need to improve and develop techniques and procedures that could further enhance in the analysis of AE waveforms detected during gas leakage. Acoustic emission studies on the attenuation of elastic waves in pipelines and the acoustic noise environment associated with leak detection have been conducted which states that the AE amplitude is proportional to the leak energy as mentioned [3-5]. In the previous study, it was observed that when the pressure reached to about 0.11 MPa for stepwise pinholes, the amplitude tended to go up and down at which the peak frequency of 150 kHz was dominant [3]. It was also discussed that it is easy to detect gas leakage from the stepwise pinholes compared to straight-forward pinholes. Until now, the process of evaluation on gas leakage has been continuously undergoing to perfectly determine the defects in pipeline and specifically the source location since it seems a lot of complexities come across during monitoring and inspection.

In this study, the main purpose is to analyze as well as characterize the AE waveforms detected during gas leakage. It is essential to follow certain procedures and especially the signal filtration process and of choosing the threshold level. A pressurized cylinder filled with air has been used in order to eliminate the associated noise from the surrounding environment dissipated by the moving parts and the mechanical equipment. Several types of artificial defects have been prepared and used for data gathering such as straight-type, stepwise-type, and slit-type pinholes. The valve controlled the flow of gas and pressure varies from 100 kPa to 500 kPa continuously. The critical pressure at 0.22 MPa was calculated based on the assumption that the flow velocity reached to its sound velocity [6]. So as to avoid complexity in the analysis of AE waveforms, various types of pinhole dimensions were considered for experiment to find out signals in the time domain and frequency domain. In this case, the acoustic emission waveform is analyzed using MISTRAS2001. It has been observed that the result describes a common behavior for each type of pinhole with different dimensions. The stepwise pinhole is considered as converging-diverging nozzle in which high pressure air flows over the sonic velocity. Furthermore, other experimental measurements of wave attenuation and propagation in time domain have been completed as well. Consequently, the analysis and characterization of AE waveforms detected during the leakage were investigated.

Materials and Experimental Methods

In this experiment, the same methods have been adopted [6], however, a pressurized gas-filled tank has been utilized to force the air into a conventional pipe (SGP20A designated by JIS as Carbon Steel pipe for ordinary piping). The outside diameter is 20 mm and corresponding length is 150 mm. In order to properly attach the AE sensor (M5W, Fuji Ceramics), a flat surface of pipe was prepared with a reduced pipe thickness of 2.0 mm and it was mechanically polished with #1000 grain sander where pinhole was formed using electric discharge machining. Various artificial defects have been considered a pinhole with diameters (ϕ) of 0.3 mm and 0.5 mm and a depth (d) from 0.5 to 1.85mm for straight-type and stepwise-type, respectively. Other is slit-type pinhole with different dimensions as $w = 0.2$ mm, $l = 5.0$ mm and $w = 0.5$ mm, $l = 5.0$ mm. The schematic view of the experiment is shown in Fig. 1.

To further isolate the generated signals from any unwanted noise emitted from the surrounding environment, a heuristic threshold level was set to 45 dB. The gain has a total of 60 dB and a

band-pass filter ranging from 100 to 1200 kHz are used. The AE signals were detected at varying pressures from 100 kPa to 500 kPa continuously for the entire experiment. The sensor location was fixed at a distance of 10.0 mm from the simulated defect. The flow of air coming from the gas cylinder was controlled by regulating the pressure valve. It is assumed to be at normal operating condition all throughout the test run.

At this instance, there was no great influence on AE signal by other wave of motion since other moving mechanical parts were eliminated. As a result, the detected AE waveforms were certainly relative to the energy released commencing from air leakage. At the frequency domain clearly shows the behavior of AE which is analyzed using MISTRAS2001.

Figure 2 illustrates the data analysis which we mainly adopted the FFT processes in the entire study.

Results and Discussions

After taking necessary preparations in the conduct of the experiment, the following results were obtained and subsequently were analyzed using the FFT. A threshold level of 45 dB was configured to eliminate the unwanted signals caused by the surrounding environment and noise coming from the electronics parts in order to find out consistent results of AE generated signals during leakage. It was generally shown that AE waveforms differ from each other with respect to pressure values and nature of simulated defects. The peak frequency was generally decreasing for all types of leakage while pressure was continuously increased, as was mentioned in previous study. It was also observed in this study that upon reaching the critical pressure of 0.22 MPa, the expansion wall apparently developed at high pressure, in which the screech tone simultaneously occurred [3, 6, 7]. In this case, the characteristic of screech tone as reported [8] for converging nozzle is generated because of the large-scale instability of waves from airflow. The higher the pressure the greater the volume of air flows through the pinhole so its ratio between the flow velocity and sound velocity reaches unity, the value of Mach number [9] at steady flow condition. The continuous surging of air leakage pressure appears at turbulent stage for all types of artificial defects.

Amplitude variations analysis relative to air pressure

The generated AE signals have its distinct characteristics as observed in all types of artificial defects such as straight-type, stepwise-type and slit-type pinholes. As shown in Fig. 3, the

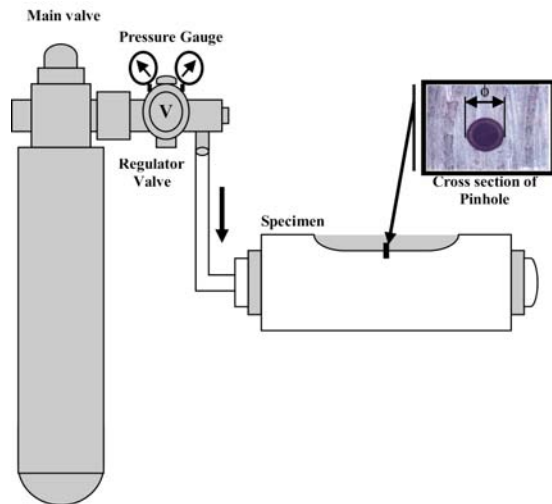


Fig. 1. Schematic view of the experiment and the specimen.

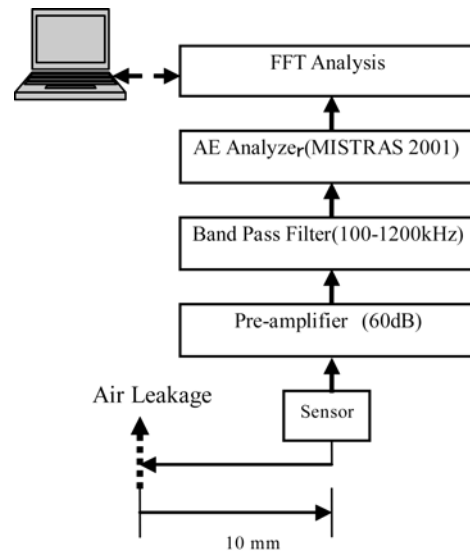


Fig. 2. Flow of data analysis.

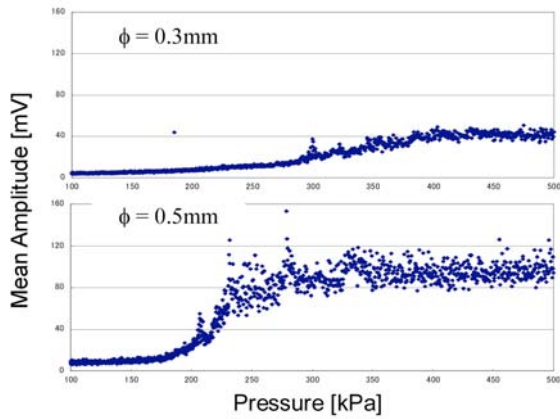


Fig. 3. Mean amplitude in relation to air pressure for straight-type pinhole.

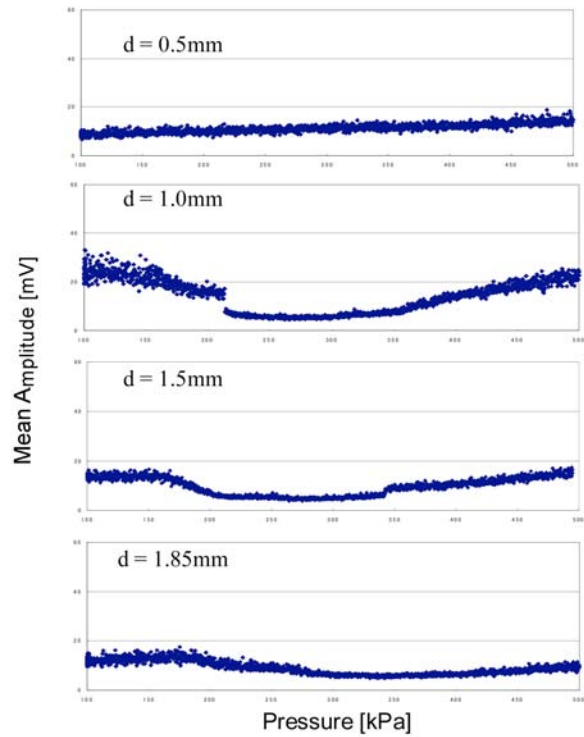


Fig. 4. Mean amplitude in relation to air pressure for stepwise-type pinhole.

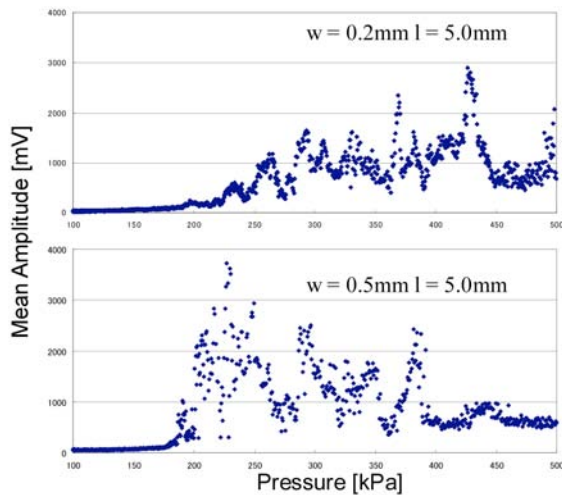


Fig. 5. Mean amplitude in relation to air pressure for slit-type pinhole.

amplitudes of signals are steadily increasing below its critical pressure and suddenly scattered until it reaches 500 kPa for a straight-type pinhole with 0.5-mm diameter. The highest mean amplitude was recorded as 153 mV at 280 kPa. The pressure shock occurred above critical value due to the effect large-scale instability of airflow. In the pinhole with 0.3-mm diameter, lengthy stability of AE signals was observed and the mean amplitude increases gradually while pressure continuously increases and its highest amplitude value is only about 37 mV at 290 kPa. On the other hand, the instability of flow was caused by the burst pressure at the throat of the pinhole. For stepwise-type, the AE waveform reflects for its own characteristics. As shown in Fig. 4, a noticeable drop of magnitude from 13.2 mV to 8.9 mV occurred over critical pressure due to the inflow of air through the pinhole with 1.0 mm depth. Apparently, the abrupt increase of its amplitude at the onset was due to the self-excited vibration of the generated AE. But eventually it decreases when it reached the critical value and then follows a monotonic increase while pressure increases. However, for stepwise-type with depth of 0.5 mm, this effect seems not to occur since it was smoothly increasing and constantly while pressure goes higher from 100 kPa to 500 kPa. It seems that in other depths such as 1.5 mm and 1.85 mm the AE waveforms characteristics have similar pattern with that of 1.0-mm depth. As the depth increases the amplitude tends to decrease while reaching 500 kPa pressure. It appears that the AE signals decreases as it approaches the critical pressure and then following a constant pattern but suddenly increased when pressure

is about 340 kPa up to 500 kPa. The sudden attenuation of amplitude was also seen since the flow velocity was reduced abruptly due to its diverging nozzle.

In the case of slit-type defect, scattered AE signals have been recorded (Fig. 5) over the critical pressure due to the effect of flow instability caused by a large amount of energy released while pressure goes higher up to 500 kPa. The tendency of rapid fluctuation of amplitude showed that the airflow was affected due to the wide dimension of the defect. We traced out the highest amplitudes as 2900 mV at 427 kPa and 3730 mV at 227 kPa for $w=0.2$ mm and $w=0.5$ mm at the same length of 5.0 mm, respectively. Although they have dissimilar pattern, the occurrence of disturbed flow was noticed beyond its critical pressure and apparently decreases over 450 kPa.

Frequency spectral analysis relative to air pressure

Figure 6 is the peak frequency variations for straight-type pinhole. The highest value of the peak frequency was 612 kHz occurring at 215 kPa and 478 kHz at 197 kPa for diameter of 0.3 mm and 0.5 mm, respectively. It was shown that the peak frequency decreases with an increasing pressure and the turbulent flow is also observable because of unstable generation of AE signals. The frequency spectra seem to be at the same pattern but above the critical pressure instability of flow was observed and its magnitude tends to go up and down. In the case of step-wise-type pinhole shown in Fig. 7, it was observed that the instability of flow became obvious with increasing depth. The peak frequency registered as 137 kHz at critical pressure for 1.0 mm depth. The burst signals were predominantly seen from 100 kPa to 500 kPa. Also, looking at the amplitude it is evident that for stepwise pinhole with 0.5-mm depth, the AE signals tend to be stable but when the depth increases disturbed flow suddenly takes place. In Fig. 8, for two slit-type defects, looking at the frequency spectra, the AE signals below 180 kPa were more stable with little disturbance

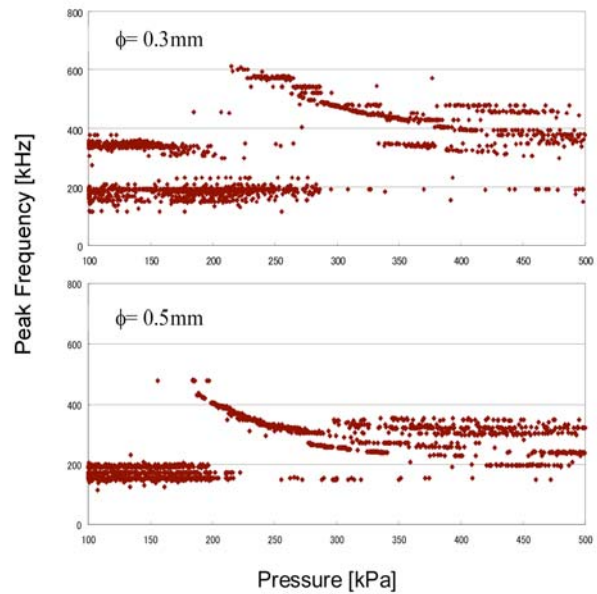


Fig. 6. Peak frequency vs. pressure.

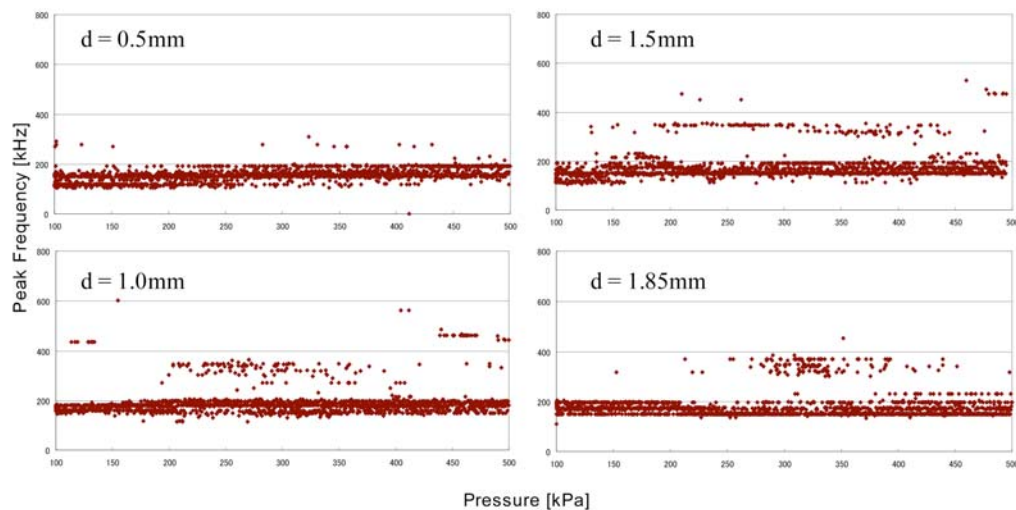


Fig. 7. Peak frequency in relation to air pressure for stepwise-type pinhole.

compared to decreasing values over the critical pressure. The peak frequency for slit-type with $w=0.2$ mm, $l=5.0$ mm and $w=0.5$ mm, $l=5.0$ mm were 502 kHz and 471 kHz, respectively. The emerging noise level at this point appeared to be the attributes of the screech tones, which show that the peak frequency decreases with an increasing pressure.

Conclusions

The characteristics of AE waveforms have to be carefully analyzed in order to effectively identify the leakage on pipeline installations especially when it is buried underground. This study shows the experimental results to enhance the method of leak detection relative to the generation of AE signals emanated from gas leak. It was concluded that the common behavior of AE waveform differs only from varied types of pipe defects. The peak frequency of various types of dimensions whether it is straight-type or slit-type was decreasing when the pressure surging from 100 kPa to 500 kPa and the AE amplitude rapidly fluctuating for all types of defects as pressure goes higher. In the meantime, the occurrence of unusual noise as observed during the experiment attributed to be the characteristics of screech tone, which could be determined using the peak frequency analysis of the AE waveforms as mentioned in the previous study [6, 7].

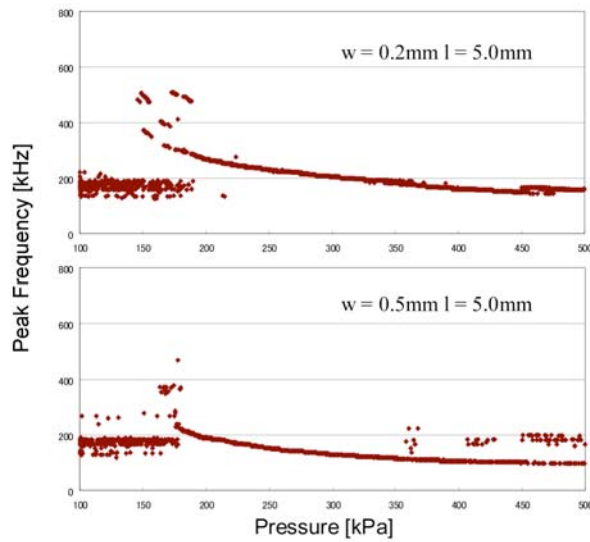


Fig. 8. Peak frequency vs. air pressure.

References

1. R. K. Miller, A. A. Pollock, D. J. Watts, J. M. Carlyle, A. N. Tafuri, and J. J. Yezzi Jr, *Journal of NDT&E International*, Elsevier, **32** (1999) 1-8.
2. M. Kotani, H. Hirano and K. Akazawa, *Acoustic Characteristic of Leakage Sound and Detection of the Sound under Noisy Environment*, SICE, **35**, 4(1999), pp. 554-559.
3. Kenichi Yoshida, Hidero Kawano, Yoshiaki Akematsu and Hideo Nishino, *Frequency Characteristics of Acoustic Emission Waveforms during Gas Leak*, *Proceedings of EWGAE*, 2004.
4. A. E. Lord, Jr., J. N. Diesher and R. M. Koerner, *Attenuation of Elastic Waves in Pipelines as Applied to Acoustic Emission Leak Detection*, *Materials Evaluation*, 1977, pp. 49-54.
5. E. G. Eckert, M. R. Fierro and J. W. Maresca, Jr., *The Acoustic Noise Environment Associated with Leak Detection in Aboveground Storage Tanks*, 1994, pp. 954-958.
6. Kenichi Yoshida, Y. Akematsu, K. Sakamaki and H. Horikawa, *Effect of Pinhole Shape with Divergent Exit on AE Characteristics during Gas Leak*, *J. Acoustic Emission*, **21** (2003), 223-229.
7. Y. Akematsu, K. Yoshida, K. Sakamaki and K. Horikawa, *Progress in Acoustic Emission XI*, The Japanese Society for NDI, 2002, pp. 319-324.
8. Young-Kill Yu, et.al, *Screech Tone Noise and Mode Switching in Super Swirling Jets*, *AIAA Journal*, **36**, 11 (1998), 1968-1974.
9. T. Ichikawa, *Hydrodynamics*, *Fluid Mechanics*, Corona Publishing Co., 1987, p. 127.

ACOUSTIC EMISSION EVALUATION OF RETROFITS ON THE I-80 BRYTE BEND BRIDGE, SACRAMENTO, CALIFORNIA

DAVID E. KOSNIK and DANIEL R. MARRON

Infrastructure Technology Institute, Northwestern University, Evanston, Illinois 60208, USA

Abstract

Fatigue-prone details on highway bridges present a challenge to engineers as structures age and face increased traffic loads. The Bryte Bend Bridge (Caltrans Bridge B-22-26 R/L), a steel trapezoidal box girder structure, which carries I-80 over the Sacramento River at Sacramento, California, contained fatigue-prone connections between the unusually thin girder walls and the internal diaphragms. These details were slated for retrofit when very active cracking was discovered nearby. Engineers at Northwestern University's Infrastructure Technology Institute performed acoustic emission (AE) tests before the retrofit, during evaluation of several retrofit designs, and after the final retrofit. Evaluation of the retrofit designs was particularly useful as it was discovered that some of the proposed retrofit designs actually exacerbated crack activity. AE testing of the final design revealed that the retrofit was effective in reducing crack activity.

Keywords: Steel box girder, fatigue-prone detail, retrofit evaluation

Introduction

The Bryte Bend Bridge (Caltrans Bridge B-22-26 R/L), opened in 1971, carries Interstate 80 over the Sacramento River at Sacramento, California. I-80 is a truck route of national importance; regionally, it is particularly important to agricultural trucking. Many of these agricultural trucks are especially heavy, as produce such as tomatoes are shipped in water. According to a 2005 California Department of Transportation (Caltrans) report, the average annual daily traffic for I-80 near the bridge is 84,000 vehicles per day, 9.57% of which is trucks; 45.89% of trucks on the route consist of five or more axles [1]. An overall view of the bridge is shown in Fig. 1.

The bridge consists of twin 1235-m (4,050') welded trapezoidal steel boxes with composite concrete decks. Inside the box girder are K-shaped vertical stiffener cross frames. The box girder walls are 9.5-mm (3/8") thick [2]. Fig. 2 shows the cross frames in the interior of the box girder. The twin bridges carry three lanes of traffic each.

An in-depth visual inspection by Caltrans personnel revealed cracking in the webs of the trapezoidal box at the cross frame connections. Cracks typically initiated at the toe of the weld connecting cross frame to the web. The cracking was attributed to out-of-plane bending at the connection. Several cracks, which had turned into the flange, were later drilled [2].

Crack sites on the bridge are identified by span number, cross frame (XF) number, and girder number, where girder G1 is the left sloped web, G2 is the center vertical web, and G3 is the right sloped web. Work described in this paper was carried out on spans 18 and 19.

Crack Characterization

Engineers from the Infrastructure Technology Institute (ITI) at Northwestern University first performed AE tests at crack sites selected by Caltrans in 1993 and 1994. Data were acquired using a Vallen Systeme AMS-3 acoustic emission (AE) monitoring system and 375-kHz piezoelectric transducers. An AE transducer was placed at the visible crack tip and guard transducers

were placed in an array around the crack tip. AE first-hit channel analysis showed that the cracks were actively driven by live stresses in the structure [2].



Fig. 1: I-80 Bryte Bend Bridge overall view.



Fig. 2: Box girder (north half) interior showing cross frames.

AE Evaluation of Retrofit Prototypes

Because of the complex nature of the structure, Caltrans engineers opted to test prototypes of two proposed retrofits on selected cross frames in span 19 of the Bryte Bend Bridge. Shoe plates and knee braces were added to the outside corners and both sides of the center web of cross frame 3. Shoe plates and knee braces were also added to cross frame 4; additionally, the diagonal braces on frame 4 were cut from their attachment points at the deck and reattached to a new horizontal cross member.

In 1996, ITI engineers assisted in the evaluation of these retrofit designs through AE and strain gauge testing. First-hit channel (FHC) analysis was employed to distinguish crack-related events from events originating elsewhere on the structure. The activity level for each crack is given as the ratio (expressed as a percentage) of crack-related AE hits to total recorded AE hits [2]. The activity level at each crack is shown in Table 1 and Fig. 3.

Table 1: Crack activity at prototype retrofit sites on span 19 (modified from [2]).

Crack Site	% Crack Activity Before Modification	% Crack Activity After Modification
XF3-G1	17.8	4.8
XF3-G2	29.6	3.0
XF3-G3	25.5	4.3
XF4-G1	4.8	3.4
XF4-G2	5.3	6.4
XF4-G3	26.0	25.3

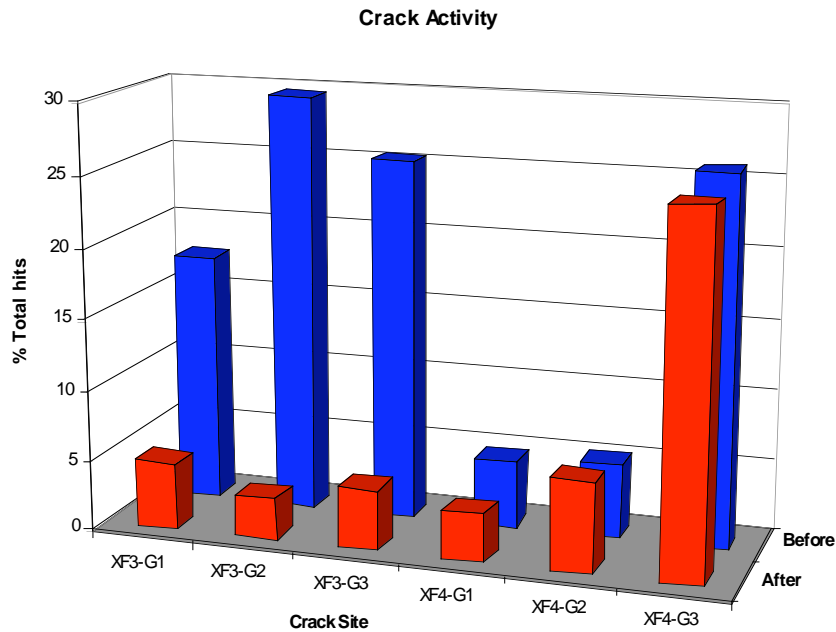


Fig. 3: Crack activity at prototype retrofit sites (modified from [2]).

The retrofit prototype installed at cross frame 3 was clearly shown to be superior to the prototype installed at cross frame 4. In fact, the retrofit at cross frame 4 seemed to make the crack activity level slightly worse on the center web connection.

The value of AE testing is clearly illustrated in this prototype evaluation experience. On a complex structure, it is often difficult to accurately predict the performance of a retrofit. AE analysis, however, provides repeatable quantitative data on crack activity levels before and after a fatigue-mitigation retrofit.

AE Evaluation of Full Retrofit

In 2004, Caltrans let contracts to retrofit all active and potential crack sites with the design tested on cross frame 3 as noted above. The retrofit is shown in Fig. 4.

ITI engineers were engaged to perform AE tests on five selected sites along span 18 of the bridge in September 2004, before the retrofit, and again in September 2005, after the retrofit. A six-channel Vallen Systeme AMSY5 AE monitoring system was used for both tests. The six 375-kHz piezoelectric transducers (with internal preamplifiers) were deployed as in an array for FHC analysis as shown in Fig. 5, with transducer 1 as close as possible to the crack tip, transduc

ers 2-5 forming a guard array around the crack tip, and transducer 6 mounted on the diagonal brace to intercept any noise transmitted through the cross frame itself.

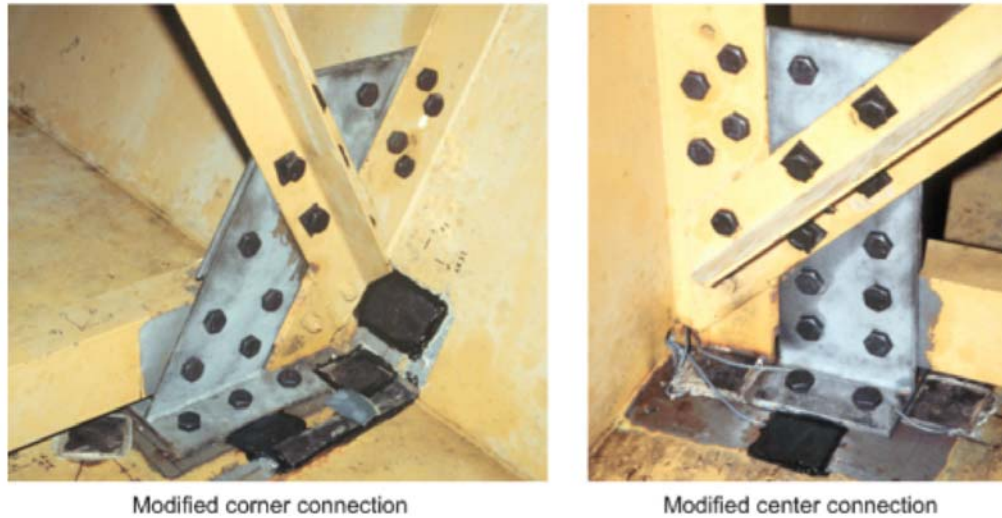


Fig. 4: Final retrofit design (modified from [3]).

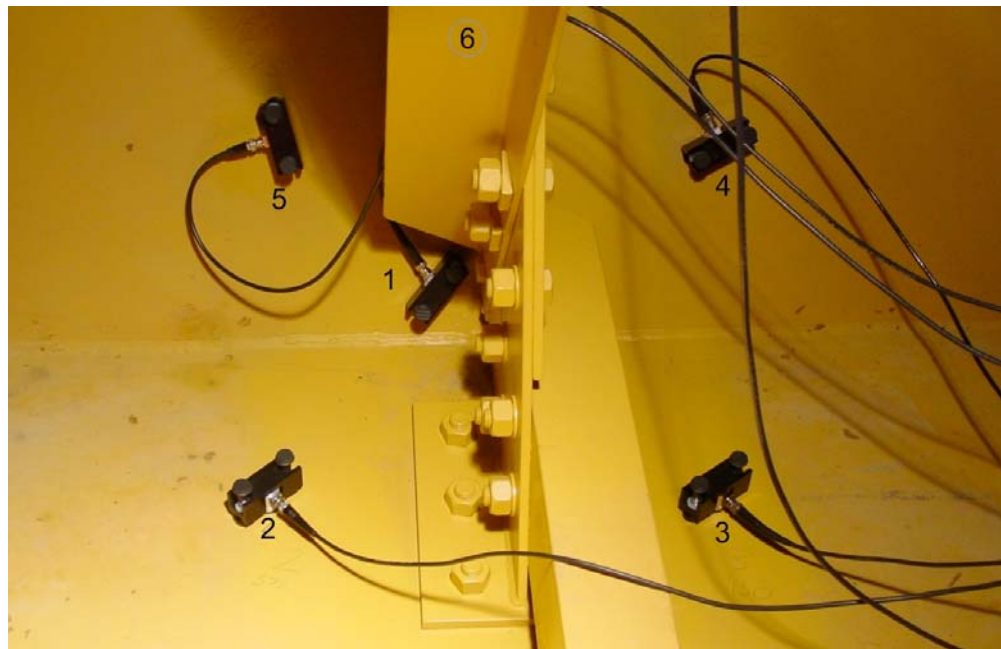


Fig. 5: AE transducer array for first-hit channel analysis.

The transducers were acoustically coupled to the structure with silicone grease and were held in place with magnetic clamps. At each site, system integrity was verified using internal calibration and pencil-lead breaks; then, AE data were acquired for 30-60 minutes using a laptop computer. Data were recorded in both statistical and digitized waveform formats.

FHC analysis of the data taken before and after the full retrofit suggests that the retrofit was quite effective in reducing fatigue crack growth. Each site showed a dramatic decrease in crack activity as measured in number of AE hits per hour from the crack with peak amplitude above 55 dB, as shown in Fig. 6.

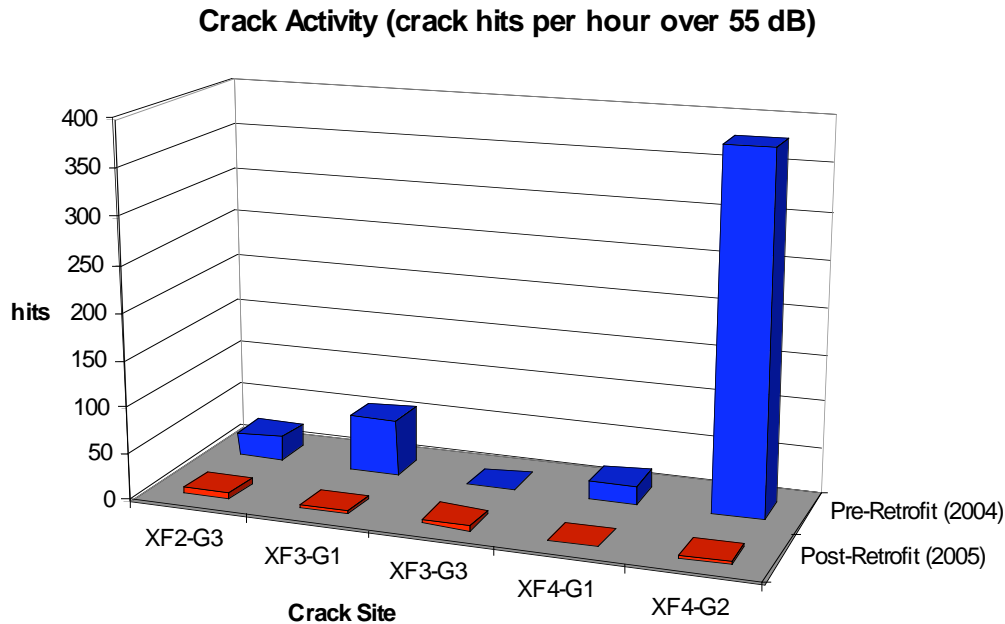


Fig. 6: Crack activity before and after full retrofit.

Conclusions

Acoustic emission testing with first-hit analysis techniques can be extremely useful in providing quantitative data for evaluation of fatigue crack mitigation techniques. In the case of the Bryte Bend Bridge, AE was successfully employed several times to aid in the characterization of cracks, development of an effective retrofit design, and finally in the evaluation of a complete fatigue retrofit of the structure. Without the feedback provided by AE testing, much time and effort could have been wasted on ineffective retrofit designs.

References

1. *2005 Annual Average Daily Truck Traffic on the California State Highway System*, California Department of Transportation, 2006.
2. D. Prine and D. Marron, *Acoustic Emission and Strain Gage Monitoring of Prototype Retrofit for Caltrans Structure B-22-26 R/L, I-80 Sacramento River (Bryte Bend)*, Sacramento, California, Northwestern University Infrastructure Technology Institute report, 1997.
3. D. Prine, "Acoustic Emission Monitoring of Bridges and Other Large Civil Structures," presented at AEWG-48, 2005.

ACOUSTIC EMISSIONS OF DEHYDRATING WOOD RELATED TO SHRINKAGE PROCESSES

SABINE ROSNER

Institute of Botany, Department of Integrative Biology; University of Natural Resources and Applied Life Sciences, Vienna (BOKU); Gregor Mendel Str. 33, 1180 Vienna, Austria

Abstract

Cavitation events in water conducting elements of wood and dehydration cracks caused by wood shrinkage processes induce acoustic emissions (AEs) in the high-frequency range. The aim of this study was to relate spectrum features of AEs from dehydrating Norway spruce (*Picea abies* (L.) Karst.) trunkwood to shrinkage processes. Wood shrinkage in the radial direction was assessed by load cells. Either resonant 150-kHz, 60-kHz or broadband transducers (operating range 50-200 kHz, 35-100 kHz and 100-1000 kHz, respectively) were used to detect AEs at the same time on standard size samples (5 or 10 cm (length) x 6 mm (radial) x 6 mm (tangential)). Two different shrinkage processes were detected, where the first shrinkage period was termed "tension shrinkage". Shrinkage caused by high tensions is a phenomenon observed also in field measurements and is practically used for drought stress measurements of living trees. The final shrinkage process started at relative water contents around the "fiber saturation point", where most of the cell lumina contain no water, but walls are fully saturated with liquid. The AE-rate showed three peaks. The first peak corresponded to the start of the tension shrinkage process ($r = 0.99$). The valley between the second and the third AE peak was located at the onset of the final shrinkage process. Characteristic for AEs during the tension shrinkage period were higher proportions of AEs with very high amplitudes (> 60 dB) and lower frequency components. Therefore, the highest relative AE energies (pVs) were measured during this stage. AEs during the final shrinkage period showed lower amplitudes, lower energy values and higher frequency components.

Keywords: Lumber drying, wood shrinkage, peak amplitude, frequency, AE transducers

Introduction

Norway spruce wood consists to 90 % of small water conducting elements with a diameter of about 10-40 μm and a length of 1-4 mm (tracheids). Water in tracheids exists in three states, first, as vapor and second, as "free" liquid water within the tracheids, and third, as chemically "bound" water in the cell wall matrix [1]. „Free" water in the tracheids of the sapwood is transported under tension, requiring high mechanical strength of the cell walls in order to avoid implosion, and hydraulic safety against breakage of the water column (cavitation). During periods of drought stress decreases in the stem diameter of living trees can be observed [2-3]. These shrinkage processes are supposed to induce internal checking in living trees [4]. Stem diameter changes are caused by hydrostatic tension forces resulting in a decrease in diameter of the conducting elements, which still contain "free" water. The breakage of the water column is induced when the tension stress increases above a certain threshold. Once cavitated, the conduit does not conduct water any longer and the hydraulic conductivity of the plant is reduced, leading to impairment of water supply of the crown [5]. Cavitations induce AEs with the highest amplitudes in the range of 100-300 kHz, which are used to detect periods of drought stress

non-destructively [2]. AE testing is also an established method for optimizing lumber drying conditions, where the analysis of the amplitude or energy distribution of AE signals has been successfully used to pinpoint wood checking [6-7]. Most of these tests are not performed on fully saturated wood, where still all conducting elements contain “free” water, but on “green” wood at varying moisture contents. When cell lumina contain no water, but cell walls are fully saturated with liquid (“fiber saturation point”), further dehydration leads to a shrinkage process, which can induce drying checks. Drying checks develop because the fiber saturation point is reached far earlier in the shell than in the core of a specimen and because wood is an anisotropic material concerning shrinkage (radial = in direction of the annual rings: tangential = 1 : 1.5) [7-8]. Nevertheless, combined shrinkage- and AE tests are rare in AE literature on wood [9] and plant physiologists stop observations of stem diameter changes and AE-rates long before most of the tracheids reach the fiber saturation point [2]. The aim of this study was to relate AEs of dehydrating Norway spruce (*Picea abies* (L.) Karst.) sapwood to radial wood shrinkage processes from the totally saturated “green” state till the cessation of all shrinkage processes.

AE testing procedure and data analysis

AE signals were monitored with the μ DiSP™ Digital AE system from Physical Acoustics Corporation (PAC, Princeton Jct, NJ USA). Preamplifiers (40 dB) were used in connection with 150-kHz R15 resonant transducers, R6 and WD broadband transducers (operating frequency range 50-200 kHz, 35-100 kHz and 100-1000 kHz, respectively). AE signals were recorded with a detection threshold of 35 dB (0 dB = 1 μ V input). The detection threshold was chosen as the peak amplitude of signals produced by waving the AE transducer in air, plus 15 dB. Extraction of features such as the number of counts, the peak amplitude (dB), the AE duration (μ s), the relative AE energy (pVs) and the average frequency (kHz) of each AE signal was carried out with AE Win® software (PAC). AE energy (also referred to as “PAC-Energy”) is defined as the area of the rectified voltage signal over the duration of the AE signal.

AE transducers were positioned on the tangential face of fully saturated Norway spruce standard beams (cambial age = 20 - 25) using an acrylic resin clamp [9]. Preparation of fully saturated sapwood beams (0.6 cm tangential, 0.6 cm radial, and 5.0 or 10.0 cm longitudinal) is described in [10]. Silicone paste (Wacker, Burghausen, Germany) served as a coupling agent. The samples were positioned on an acrylic resin sample holder fixed upon a compression spring. Coupling pressure during the dehydration process was recorded with a DMS load cell (Type 8416-5500, range 0 - 500 N; amplification with an inline amplifier for DMS, Type 9235; Burster, Gernsbach, Germany) between the AE transducer and the screw of the acrylic resin clamp. The coupling pressure was set to 30 N. The acrylic resin clamp was then kept so deep in water that the wood sample was totally covered till the applied pressure reached a constant value. After quickly removing superficial water from the clamp and the wood, recording of AEs and coupling pressure was started. AE testing was done at ambient temperatures (25°C, 30 % r.h.) until coupling pressure reached a constant value, which was the case after about 20 h. The coupling pressure decrease during dehydration induced by shrinkage (about 3 N in total) was related to the total radial shrinkage (digital gauge, accuracy 1 μ m). AE data filtering and presentation was done with Vallen VisualAE™ software (Vallen Systeme GmbH, Munich, Germany).

Values are given as mean values \pm standard error. Differences between mean values were tested for significance with One-Way ANOVA and subsequent Scheffe-test. Associations between two variables were examined using linear regression analysis.

Results and Discussion

Shrinkage processes and total AE-rate

Two different radial shrinkage processes were observed (Figs. 1-3). First, a shrinkage period at moderate water losses, which was termed “tension shrinkage”, and second, the final shrinkage period, leading to $3.86 \pm 0.11 \%$ ($n = 71$) shrinkage. The onset of the tension shrinkage coincided with the decrease of the rapid rise of the total AE-rate ($r = 0.99$, $n = 22$). Tension shrinkage is caused by a decrease in diameter of tracheids, which still contain “free” water. Hydrostatic tension forces acting perpendicular to the cell walls try to draw the walls inwards. When the stress becomes too high cavitation occurs [8]. In accordance, tension shrinkage was to some extent a reversible process, because the tension was released after cavitation. After this relaxation period, the final shrinkage process started when most of the cell lumina contained no free water but cell walls were still fully saturated with liquid. The start of the final shrinkage process coincided with a rapid rise in the AE-rate. Towards the end of AE detection, two peaks in the AE rate could be found in most of the samples. The first peak occurred after $72.76 \pm 0.72 \%$, the second after $85.38 \pm 0.45 \%$ ($n = 42$, respectively) of the AE detection time, which was defined as the time between the start of AE testing and when the last AEs were detected. No AEs were detected after no more than 25 % of the total radial shrinkage had taken place (Figs. 1-3).

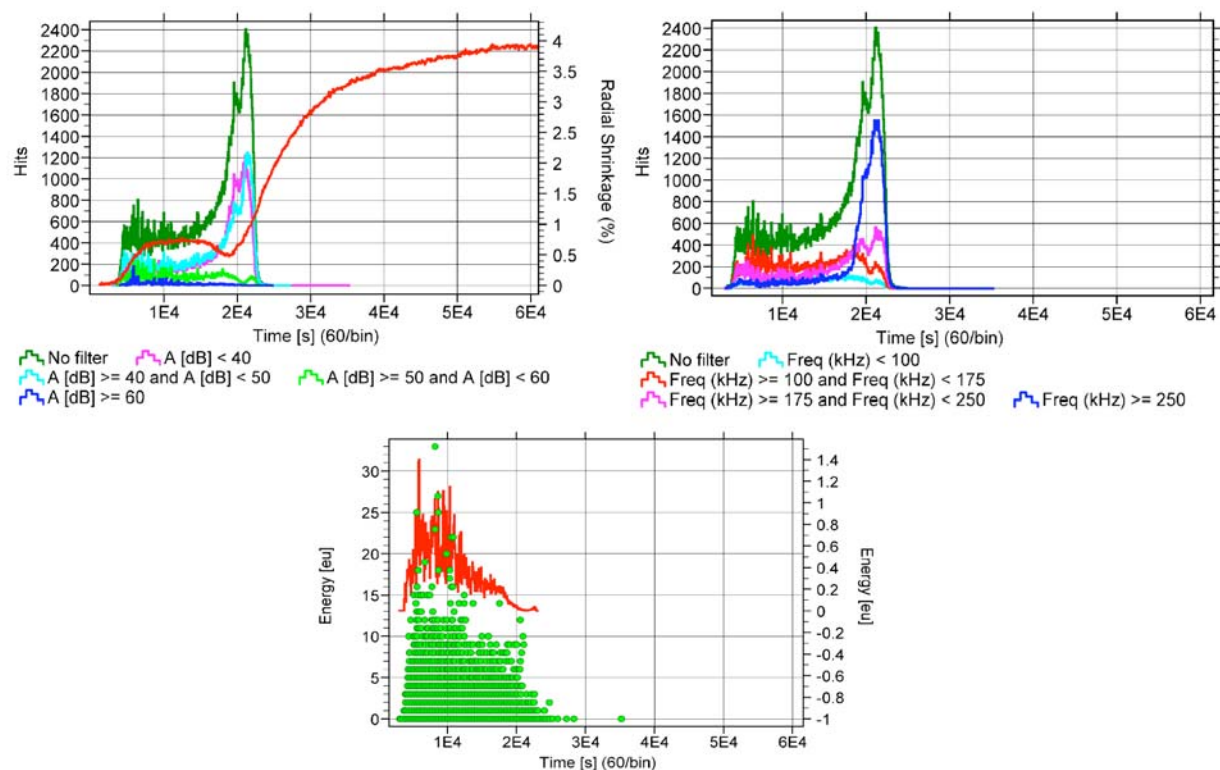


Fig. 1 AE activity (rate/min) and radial wood shrinkage during dehydration detected by WD transducer and load cell, respectively. AE rates were clustered in peak amplitude steps (left side) and average frequency steps (right side). Mean AE energy (1 eu = 1 pVs) was calculated for 1-min steps (below, red line, right y-axis).

AE characteristics during shrinkage processes

Highest mean peak amplitudes and energies were measured during the tension shrinkage period at moderate water losses (Figs. 1-3). The relative time occurrence of the maximum mean peak amplitudes/min showed no significant differences between the transducer types (WD, R6, R15). Highest mean amplitude values were reached after $27.77 \pm 0.90\%$ of the AE detection time ($n = 42$). The cumulated AE energy rate can be used to characterize the hydraulic vulnerability of sapwood. It is supposed that mean high energy AEs represent cavitations of more vulnerable, larger tracheids, because more elastic energy is stored in larger conduits when under tension [10]. Tension shrinkage processes can be observed in living trees and are used to pinpoint periods of drought stress out in the field [2-3]. In accordance, the maximum AE-rate > 60 dB and the maximum AE energy rate/min was detected in the middle of the tension shrinkage period (R6, R15, $r = 0.88$, $n = 14$). At this time, significant lower AE rates/min were measured by WD transducers (573.14 ± 55.69) than by R6 (1271.43 ± 59.44) or R15 (1003.71 ± 179.44) transducers ($P < 0.001$, sample length = 10 cm, $n = 7$, respectively). The lower number of AEs recorded by WD transducers might be explained by the frequency operating range (100-1000 kHz). In highly attenuating materials, such as wood, the usable upper frequency level is supposed to be 100-200 kHz [6]. Analysis of average frequencies showed, that the number of signals < 175 kHz was 1.56 ± 0.13 times higher than those of signals > 175 kHz when the mean AE energy rate/min reached maximum values (WD, $n = 14$). At the same time, the number of AE signals with average frequencies between 30 and 50 kHz was 1.73 ± 0.18 times higher than the number of AE signals with average frequencies between 50 and 70 kHz (R6, $n = 14$). The rate/min of signals between 30 and 50 kHz, related to the corresponding total AE rate/min, reached highest values during the tension shrinkage period (R6, $49.13 \pm 2.50 \%$).

AE signals within the frequency range from 30 to 50 kHz reached highest absolute rates shortly before the final shrinkage process started (Fig.2). Their relative rates (related to the corresponding total AE rate) were however much lower than during the tension shrinkage period, when maximum mean energies/min were measured ($25.85 \pm 2.78 \%$, $P < 0.001$). The number of signals with average frequencies from 30 to 50 kHz was equal to the number of signals between 50 and 70 kHz at the next to the last AE rate/min peak (R6, factor 1.08 ± 0.18 x, $n = 14$). Shortly before the final shrinkage took place, WD transducers detected a quite similar number of signals < 175 kHz and > 175 kHz (factor 1.02 ± 0.09 x, $n = 14$). The AE rate/min measured by WD transducers (1228.14 ± 194.99) was significantly lower than measured by R15 (2214.29 ± 275.33) or by R6 (3026.43 ± 298.48) transducers ($P < 0.001$, sample length = 10 cm, $n = 7$, respectively).

The final shrinkage process was characterized by a very high proportion of signals with high average frequencies (> 250 kHz (WD), > 100 kHz (R6)), low amplitude and energies (Figs. 1-2). These signals may come from cavitation events in tracheids which contribute less to axial water transport than to other wood functions such as radial water transport, mechanical support and storage of water, or from cavitations in ray tracheids [10]. At the last AE peak, the number of signals < 175 kHz reached only 0.18 ± 0.01 times the number of AEs > 175 kHz (WD, $n = 14$). R6 transducers measured a much more lower number of AEs with average frequencies between 30 and 50 kHz in relation to signals between 50 and 70 kHz (R6, factor 0.51 ± 0.03 x, $n = 14$). The relative amount of signals in the frequency range between 30 and 50 kHz made up only $3.79 \pm 0.45 \%$ of the total AE rate ($n = 14$). The AE rate/min measured by WD (2002.14 ± 229.30), R6 (2286.14 ± 278.26) and R15 transducers (2338.80 ± 206.56) showed no significant differences (sample length = 10 cm, $n = 7$, respectively).

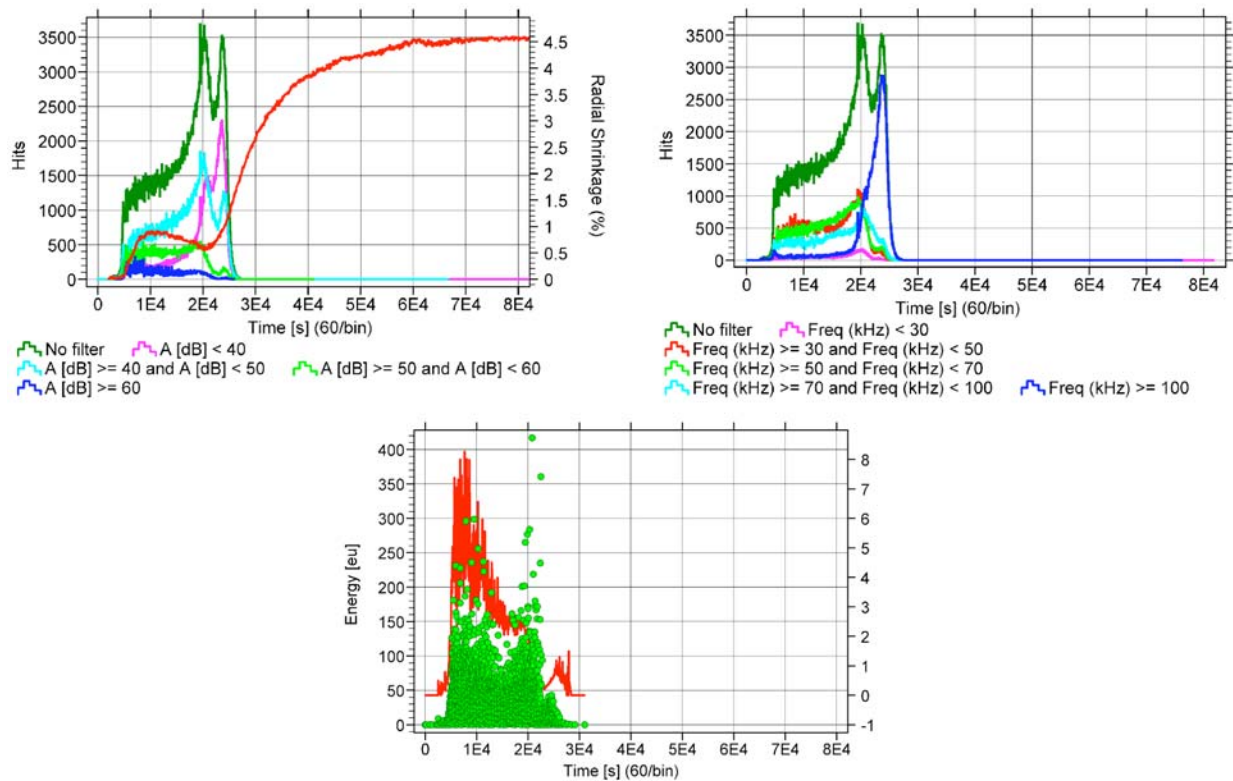


Fig. 2 AE activity (rate/min) and radial wood shrinkage during dehydration detected by R6 transducer and load cell, respectively. AE rates were clustered in peak amplitude steps (left side) and average frequency steps (right side). Mean AE energy (1 eu = 1 pVs) was calculated for 1-min steps (below, red line, right y-axis).

The bulk of AE signals during lumber drying resemble cavitation events of water conducting elements [7]. Extremely high-energy AE signals, which were detected during the tension shrinkage period as well as at the onset of the final shrinkage process may have been induced by mechanical failure [11]. References [12] and [13] could distinguish two phases during Norway spruce lumber drying by analyzing AE burst rates. The first peak in the AE hit rate was interpreted as checking caused by surface tension stress, and the second peak (at high water loss) as checking caused by tensile stresses inside the samples. Reference [8] supposes that sapwood within-ring internal checking is caused by water tension and not by differential shrinkage, because checking occurred long before most of the cells reached the fiber saturation point. Internal checks caused by high tensions may also occur in low density earlywood of living trees during periods of summer drought, and are a severe problem of short rotation forests [4].

The method presented might help to understand the mechanisms that cause internal checking in living trees. Knowledge about the relationship between shrinkage processes, AE-rates and AE features, such as the average frequency, the peak amplitude and energy (especially single high energy events), could be also helpful for analyzing checking processes during lumber drying stages. Both WD and R6 transducers were suitable to characterize the different stages of shrinkage by analyzing the average frequency composition of the AE signals. R6 transducers reacted, however, very sensitively to background noise and can only be recommended for acoustic labs.

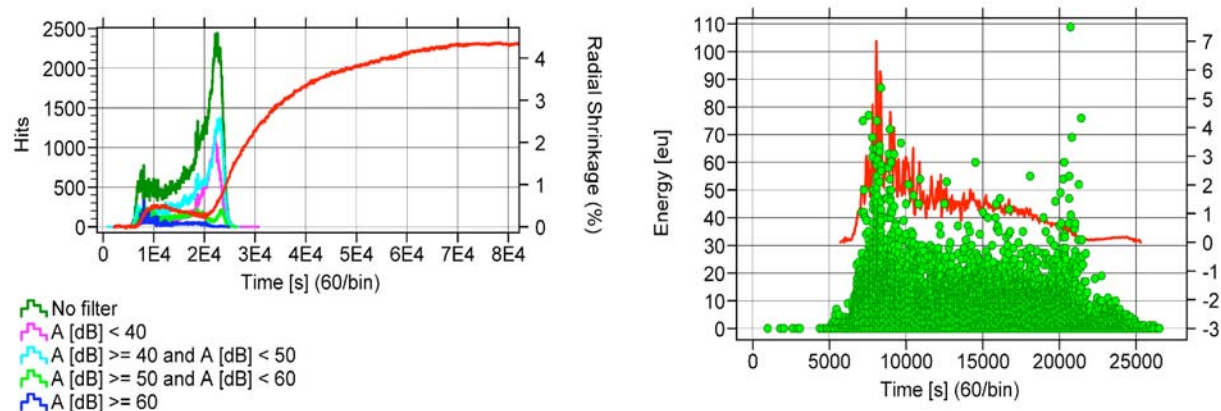


Fig. 3 AE activity (rate/min) and radial wood shrinkage during dehydration detected by R15 transducer and load cell, respectively. AE rates were clustered in peak amplitude steps (left side). Mean AE energy (1 eu = 1 pVs) was calculated for 1-min steps (right side, red line, right y-axis).

Acknowledgements: This study was financed by the Austrian Science Fund FWF (Project T304-B16). Raphael Klumpp and Peter Kritsch are thanked for providing Norway spruce sample material.

References

1. C. Skaar, *Wood-Water Relations*, Springer-Verlag, 1988, 283 p.
2. T. Hölttä, T. Vesala, E. Nikinmaa, M. Perämäki, E. Siivola, M. Mencuccini, *Tree Physiology* **25**, 2005, 237-243.
3. I. Offenthaler, P. Hietz, H. Richter, *Trees*, **15**, 2001, 215-221.
4. M. Grabner, P. Cherubini, P. Rozenberg, B. Hannrup, *Scandinavian Journal of Forest Research*, **21**, 2006, 151-157.
5. M.T. Tyree, M.H. Zimmermann, *Xylem structure and the ascent of sap*, Springer, 2002, 283 p.
6. F.C. Beall, *Wood Science and Technology*, **36**, 2002, 197-212.
7. S. Kawamoto, R.S. Williams, *Acoustic emission and acousto-ultrasonic techniques for wood and wood-based composites A Review*, U.S. Department of Agriculture, Forest Service, Forest Products Laboratory, Gen. Techn. Rep. FPL-GTR-134, 2002, 16 p.
8. R.E. Booker, *Proceedings of the 4th IUFRO Wood Drying Conference: Improving Wood Drying Technology*, 1994, pp. 133-140.
9. S. Rosner and R. Wimmer. *14th International Symposium on Nondestructive Testing of Wood*, Shaker Verlag, 2005, pp. 123-134.
10. S. Rosner, A. Klein, R. Wimmer, B. Karlsson, *New Phytologist* **171**, 2006, 105-116.
11. S.L. Quarles, *Wood and Fiber Science* **24**, 1992, 2-12.
12. P. Niemz, R. Emmeler, E. Pridöhl, J. Fröhlich, A. Lühmann, *Holz als Roh- und Werkstoff*, **52**, 1994, 162-168.
13. I. Cunderlik, W. Molinski, J. Raczkowski, *Holzforschung* **50**, 1996, 258-262.

USE OF ACOUSTO-ULTRASONIC TECHNIQUES TO DETERMINE PROPERTIES OF REMANUFACTURED PARTICLEBOARD MADE SOLELY FROM RECYCLED PARTICLES

SUMIRE KAWAMOTO, JAMES H. MUEHL* and R. SAM WILLIAMS*

Department of Wood-Based Materials, Forestry and Forest Products Research Institute, Ibaraki 305-8687, Japan; * USDA Forest Products Laboratory, Madison, WI53726, USA

Abstract

Properties of particleboard manufactured entirely from recycled particleboard were determined and a method for processing three-layer particleboard from all-recycled particles was described. Dynamic MOE (modulus of elasticity) before and after re-manufacturing was tested by a longitudinal stress-wave technique and compared with other stress-wave techniques. Nondestructive AU (acousto-ultrasonic) techniques were used to evaluate static, dynamic, and dimensional properties of re-manufactured boards. The results showed a large decrease in mechanical and physical properties for remanufactured boards, particularly for those made from high-density boards. AU parameters corresponded with density in the volume between the surfaces of transducers. Correlation between static MOE and dynamic MOE was improved by using the AU calculated density. Water absorption and thickness swell corresponded with the AU calculated density.

Keywords: Particleboard, AU (acousto-ultrasonics), recycle, remanufacture, dynamic MOE (modulus of elasticity), MOR (modulus of rupture), density, water absorption

Introduction

For the sake of the environment, raw materials for manufacturing wood-based materials could be derived from unprocessed forest products such as wood material from thinning operations [1, 2], industrial waste from veneer manufacture or sawmills, and slabs produced by industrial operations on dry wood. In addition to such wet and dry wood wastes, fibrous agricultural lignocellulosic natural resources such as flax or kenaf can be used as raw materials [3, 4]. Generally, wood-based composites manufactured from recycled materials use a combination of recycled and unused new materials. It is necessary to add new fiber, particles, or strands to compensate for the decrease in strength resulting from the reuse of materials. Although new products made from waste wood have been developed in many projects [1, 5], only one previous work focused solely on recycling particleboard [6].

The objectives of this study are (1) to provide fundamental data regarding the decrease in mechanical properties resulting from the use of recycled materials (2) to compare dynamic MOE values of longitudinal stress-wave techniques, and (3) to evaluate the mechanical and physical properties of particleboard using acousto-ultrasonic (AU) technique. A long-term goal of this study includes developing better methods for adding new constituents to increase the strength of a recycled structural composite panel.

Properties of particleboard before and after remanufacturing were compared nondestructively by both an AU method and a conventional stress-wave technique. The AU technique, a combination of acoustic emission (AE) signal analysis with an ultrasonic characterization method [7], was used to detect and assess damage conditions and variation in mechanical properties of a test material [8]. Vary used AU evaluation to determine the mechanical properties of composite

materials [9]. In regard to wood composite research using AU technique, Beall et al. obtained a patent for bond strength measurement of composite panel products using rotary transducers [10]. Green [11] and Rodgers et al. [12] reported that AU parameters corresponded with IB (internal strength). These reports described the correlation of AU to IB and were reviewed by Beall in 1993 [13]. Reis investigated AU behavior concerning the dimensional stability of medium-density fiberboard (MDF) [14]. Unlike solid wood, few studies have used AU technique to evaluate wood composites, probably because of the difficulty of measuring properties because of attenuation of AU waves traveling through wood-based composites [15].

This study provides fundamental data on a processing technique and on the mechanical properties of boards made with recycled particles from industrial recycled waste wood. Some new AU techniques are suggested for evaluating the mechanical and dimensional properties of particleboard.

Experimental

Original Materials

Raw materials were commercial three-layered particleboard (Tokyo Board Co. Ltd.). Dimensions were 0.9 m in width, 1.8 m in length, and 20 mm in thickness. Boards were manufactured from industrial waste wood such as plywood or slabs that were discarded as a waste in the same company. Species used in the original particleboard were identified as western hemlock (*Tsuga heterophylla*), Douglas-fir (*Pseudotsuga menziesii*), and a mixture of tropical species. Three boards, 150 mm in width, were sawn from the edge of the commercial particleboards for remanufacture into three 3-layered particleboards. These three original boards were selected from 50 boards, based on dynamic MOE (modulus of elasticity) values that were measured non-destructively. The dynamic MOE was calculated by a longitudinal stress-wave technique using a PVDF (polyvinylidene fluoride) transducer [16]. Density of original boards was 0.675, 0.754, and 0.806 (g/cm^3), and dynamic MOE tested by Metrigard equipment was 2.98, 4.09, and 4.60 GPa, respectively.

Remanufacturing Method

The original particleboards were cut into 50 by 50 mm square pieces on a table saw, then hammer milled. Particles were classified by size using the screen after drying to 3% moisture content. Particles were then separated using a 16-mesh screen. The core layer used particles of 16-mesh-on. For the surface layers, particles of 16-mesh-off were used. Weight loss from size reduction process by table saw was 12% to 13% and by hammer mill 3% to 4%, respectively.

Phenolic resin binder (10% of total weight of mat) was sprayed in a rotating drum blender. Forming (spreading particles in 305 by 305 mm square mat former) was conducted by hand. The weight ratio of the surface layer and core layer was 1.5:7:1.5. Planned densities and thickness were the same as values of the original particleboards (0.675, 0.754, and 0.806 (g/cm^3)). Hot pressing temperature was 180°C. Pressing time was 20 min. Boards were trimmed to 280 by 280 mm and stored in a conditioning room at 20°C and 65% relative humidity, before and during the property test. For the control, a single-layered particleboard was manufactured using industry sawdust. The species was identified as a mixture of yellow pine and spruce (636 kg/m^3).

Testing Properties of Remanufactured Particleboard

Properties of the remanufactured particleboard were measured both by dynamic and static methods. Figure 1 shows locations of each specimen for property tests, which included dynamic and static MOE and modulus of rupture (MOR), density, internal bond strength (IB), thickness swelling (TS), and water absorption (WA). The test was basically performed in accordance with

JIS A 5908 [17]. To avoid the effect of water repellent added to original materials, specimens cut from control board were used.

AU Measurements

AU equipment included a pulse generator, transmitting and receiving transducer, and AE equipment. Resonant 1.5-MHz, in 20-mm diameter, and 150-kHz, 20-mm diameter, AE transducers were used. The pulse generator generated a square wave, which excited a transmitting transducer. The output signal was amplified 40 dB. The maximum amplitude (up to 50 μ s from start of signal) and time differential, observed by oscilloscope, were taken as AU parameters.

For determination of density and dimensional properties of whole specimen using AU technique, 25-by-25-mm specimens were used so that a face of the 1.5-MHz transducer covered most of the surface area of the specimens. AU waves that propagated through the thickness of specimens were observed. Preliminary tests confirmed that AU parameters detected using a specimen having conventional test size (50 by 50 mm) did not correspond to actual density and dimensional properties.

For measurement of AU transmission time traveling in the through longitudinal direction, 150-kHz AE transducers, 9-mm diameter, were used. For determination of dynamic MOE by AU transmission time, the impact source was pencil-lead breaks at the edge of the specimen. The lead length was always about 10 mm. This stress-wave signal was very similar to the AE signal and was thus called the artificial AE. Transmission of the longitudinal direction was observed. AU transmission time (the time it took for the signal to travel between the two 150-kHz transducers), was observed by using an oscilloscope. For this AU technique, refer to author's original report [18].

Determination of Dynamic MOE by Longitudinal Stress-Wave Technique

1) Stress-Wave Technique by Transmission Time

Stress-wave transmission time was measured two different ways (AE and PVDF transducers). With AE transducers, pencil-lead breaks were used. That is, this artificial AE wave method used a mechanical pencil as an AU source and is included as an AU technique. Using PVDF transducers, an impact was induced by tapping an end of each specimen.

2) Stress-Wave Technique by Resonant Frequency of Longitudinal Vibration

Tapping the end of each specimen generated a stress wave. The signal detected by a PVDF transducer was processed through an FFT (fast Fourier transform) analyzer, and the resonant frequency of the first resonance mode was observed.

Result and Discussions

Decrease of Properties of Remanufactured Particleboard

Table 1 shows the properties of the original and remanufactured boards. The original particleboard with the highest density (0.806 g/cm³) showed a larger decrease of properties than boards made from the lower densities. Property decrease was the largest for the particleboard (III) that had the largest density and dynamic MOE in original boards. The remanufactured boards were intended to have the same density as the original boards, but their density decreased to 94, 87, and 84% (Table 1, density). This is because larger density raw materials are subjected to larger deformation by pressure and heat during the processing.

Decrease of dynamic MOE obtained by resonant frequency of longitudinal vibration was 40%-65%. Compared to representative values of similar samples from the company that provided original specimens, static MOE of remanufactured board decreased to 53% to 40%. MOR decreased to 44 % to 26%. MOR values showed larger decrease than MOE.

Comparison of Stress-Wave Techniques

Generally, dynamic MOE values obtained by vibration of resonant frequency are smaller than dynamic MOE values obtained by stress-wave transmission time propagating in solid wood. However, in the case of particleboard, that relationship is reversed. Comparing the stress-wave technique by using PVDF, dynamic MOE values by stress-wave transmission time (Table 1, (c)) were smaller than values by longitudinal vibration technique calculated by resonant frequency (Table 1, (b)). This is probably because the transmission time would be extended by attenuation of waves reaching the further transducer. Attenuation of stress waves in particleboard is much larger than in solid wood. Observing wave signals by oscilloscope, larger attenuation caused difficulty identifying starting points of signal waves. If it attenuated below the noise level, the actual initiation point would be missed. Several cycles of waves would be hidden under the noise level. Thus, the initiation point would be extended and longer wave transmission time was observed in particleboard.

The stress-wave method by artificial AE (Table 1, (a)), showed larger dynamic MOE values than the static MOE values, which was the same as the trend for solid wood and unlike using PVDA transducers. The sudden break of a pencil lead generated a sharp gradient at the start of artificial AE waves. Compared to output signal by PVDF, the artificial AE signal was easy to identify at the starting point.

Comparing three techniques (a), (b) and (c) in Table 1, dynamic MOE values obtained by resonant frequency (b) corresponded with static MOE the best. MOE values (a) obtained by artificial AE transmission time also showed the same trend and corresponded with static MOE as much as the conventional method (b). Advantage of the artificial AE transmission method is that the measurement is simple. Specimens need not be cut, and can be measured just using a mechanical pencil without using large equipment to induce a pulse.

Table 1. Physical and mechanical properties of original and remanufactured particleboards.

Specimen Number	Density (kg/m ³)		Dynamic MOE (GPa)				Static MOE* ⁵ (GPa)	MOR* ⁵ (MPa)	IB* ⁶ (MPa)
	Original* ¹	Re-manufactured* ²	Original* ³	Remanufactured (a)* ⁴ (b)* ⁵ (c)* ⁵					
I	675	640	2.98	1.59	1.62	1.25	1.36	7.68	0.39
II	754	656	4.09	1.46	1.45	1.35	1.25	6.09	0.22
III	806	677	4.60	1.95	1.90	1.44	1.48	6.98	0.56
Control		664		1.96	1.89	1.52	1.84	11.2	0.27

Notes: Stress-wave techniques: (a) artificial AE wave transmission time, (b) resonant frequency of longitudinal vibration, detected by PVDF, and (c) stress wave transmission time by PVDF transducers. ¹ Specimen: 150 x 20 mm x 1.8 m. ² Specimen: 280 mm x 280 mm x 20 mm. ³ Specimen: 150 x 20 mm x 1.8 m. Measured by longitudinal stress-wave technique using PVDF transducer [16]. ⁴ Pencil-lead breaks on 280 x 280 mm remanufactured particleboards before MOR specimens were cut. ⁵ Specimen: 345 x 50 x 20 mm. ⁶ Specimen: 50 x 50 x 20 mm.

AU and IB Strength

AU amplitudes and AU transmission time of AU signals that propagated through the thickness of IB specimens were observed at five locations on IB specimens. Unlike other properties, AU result did not correlate with IB strength. This was because AU values corresponded with density in the volume between the surfaces of transducers (20 mm in diameter), whereas IB strength values were measured in specimens, 50 by 50 (mm). This result also indicates that AU measurement should be taken with considerable care to ensure using the right AE transducers.

signals that propagated through the thickness of particleboards can provide density value nondestructively, thus properties that correspond with density can be estimated by this AU techniques. (7) For the specimens that did not contain water repellent, water absorption correlated with calculated density determined by AU techniques.

Acknowledgments: The authors wish to thank Mr. Saito, Tokyo Board Co. Ltd. for providing commercial particleboard, Mr. Yasuto Chiba, Japan Fiberboard and Particleboard Manufacturers Association, for conducting the internal bond strength test, Dr. Regis Miller, USDA Forest Service, Forest Products Laboratory, for identifying species of particles. First author thanks Dr. Robert Ross, Forest Products Laboratory, for the opportunity to visit the Forest Products Laboratory in 1997 and 1998, and for nondestructive testing of Japanese commercial particleboard.

This research project at the USDA Forest Products Laboratory, Madison, Wisconsin, was funded by former Science Technology Agency, Government of Japan.

References

1. T. Shibusawa, S. Kawamoto, H. Korai, and T. Fujii. US Patent No. 5814170.1998.
2. H. Spelter, R. Wang, and P. Ince. FPL-GTR-92. Madison, WI: US Department of Agriculture, Forest Service, Forest Products Laboratory. May 1996, 17 p.
3. R. M. Rowell. Composites from Agri-Based Resources. In: R. Falk, ed., Proceeding No. 7286. Madison, WI: Forest Products Society, 1996, pp. 217-222.
4. S. Kawai, Mokuzai Gakkaishi. **43**(8) 1997, 617-622. (in Japanese).
5. Forest Products Laboratory. FPL-GTR-110. Madison, WI: US Department of Agriculture, Forest Service, Forest Products Laboratory. May 2000, 31 p.
6. T. Shibusawa, Y. Hatano, S. Kawamoto, M. Zhang, Y. Okuno and Y. Chiba. 50th Annual Meeting of Japan Wood Research Society, 2000, p. 286. (in Japanese)
7. ASTM E 1316-99. Annual Book of ASTM Standards. Philadelphia, PA: ASTM. 1999.
8. ASTM E 1495-97. Annual Book of ASTM Standards. Philadelphia, PA: ASTM. 1997.
9. A. Vary, NASA Technical Memorandum 79180. 1979.
10. D.M. Shearer, R.C. Beetham and F.C. Beall.. Patent No. 4,750,368. 1988, 7 p
11. A. T. Green, J. Acoustic Emission. **8**(1/2), 1989, S306-S310.
12. J. M. Rodgers, A. T. Green and S.W. Borup, Materials Evaluation, May 1991, 566-571.
13. F. C. Beall, Proceedings, Second International Conference on Acousto-Ultrasonics. Atlanta. The American Society for Nondestructive Testing, Inc. 1993, pp. 153-161.
14. H. L. Reis and D. M. McFarland, J. Acoustic Emission. **5**(2) 1986, 67-70.
15. S. Kawamoto and R.S.Williams, FPL-GTR-134. Madison, WI: US Department of Agriculture, Forest Service, Forest Products Laboratory. May 2002, 16 p.
16. R.J. Ross and R.F. Pellerin, General Technical Report. FPL-GTR-70. Madison, WI: US Department of Agriculture, Forest Service, Forest Products Laboratory. May 1994, 40 p.
17. Particle boards. Japanese Industrial Standard. JIS A 5908. Tokyo, Japan. 1994.
18. S. Okumura, S. Kawamoto and M. Toyada and M. Noguchi, Bulletin of the Kyoto University Forest. **60** 1988, 299-309. (in Japanese)

This paper is a contribution of the USDA Forest Products Laboratory, Madison, Wisconsin and not subject to copyright in the United States.

INSPECTION OF WOODEN POLES IN BRAZIL USING ACOUSTO-ULTRASONICS PARAMETERS

RAQUEL GONÇALVES, ROBERTO SOUZA JÚNIOR¹ and SUZIE HERRERA²

Faculty of Agricultural Engineering (FEAGRI), State University of Campinas (UNICAMP), Brazil; ¹Department of Mechanical Engineering, University Methodist of Piracicaba (UNIMEP), Brazil; ²São Paulo Electricity Company (CPFL), Campinas, Brazil

Abstract

The goal of this research project was to evaluate which parameters of the acousto-ultrasonics are important in the evaluation of the residual strength of poles in service. These parameters (amplification, rates, filters, spectral analysis, maximum and minimum, rms, statistical analysis, graphs, curve storage, etc.) are used in the development of equipment specifically designed for in-field wood pole inspection. Although frequency response analyses are not common among the Brazilian researchers' works on ultrasonics applied to woods, tests using the prototype indicated that this analysis brings important information on some aspects of the structure of that material, which are not identified when the time of ultrasonic propagation is the only measured parameter.

Keywords: Pole inspection, eucalyptus, wooden poles

Introduction

The safety of electric power distribution lines depends, essentially, on the quality of its support structures. Those structures are in Brazil, regularly, of reinforced concrete, wood or steel. In the case of the wood and reinforced concrete, several are the factors that will influence on the type and speed of its deterioration. The wood, being a biological and hygroscopic material, has its deterioration accelerated mainly by the humidity and the attack of microorganisms. The presence of the mentioned problems will be retarded or accelerated as function of the initial quality of the pole. In Brazil, the electricity companies, mainly the ones in the State of São Paulo, are in phase of substitution of the wooden poles by concrete poles. That process is due, largely, to the lack of knowledge of the mechanical properties of the material, as well as to the process used for the pole inspection. This is causing improper pole substitutions, burdening the system. In the specific case of poles, the most critical zone is the zone between the lines that separates the buried part to the aerial part up to approximately 0.5 m above ground. In that zone occurs the largest bending stress; besides, it is also in that zone that moisture accumulations occur. This provides the ideal conditions for fungus to grow in the wooden pole. Today, the initial quality of new wooden or concrete poles, acquired by the electric power utilities for the distribution net, is unknown. For both materials, normalized tests with few samples are done [1, 2], but the quality of the material is not evaluated properly, and this leads to economical losses and to the lack of safety, since the durability of the pole in service is directly related to its initial condition. The standards based on the new concepts of structures security use the mean and the frequency distribution of the initial strength to establish the minimum value of the residual strength of the pole to remain on service [2]. After the establishment of the minimum value of the residual strength it is necessary to determine which parameters are necessary to use on inspections of the wooden poles on service. These parameters must be adequate to indicate the stage of degradation of the wood and consequently the residual strength of the pole. Moreover, the evaluation of the properties of the wood by ultrasound is affected by many different parameters, such as moisture content,

frequency of the transducer, direction of the measurement [3]. The objective of this research was to evaluate which parameters of the acousto-ultrasonics are important on the evaluation of the residual strength of poles in service. These parameters are used in the design of equipment specifically for in-field wood-pole inspection.

Experimental Procedures and Results

A system to measure the time of ultrasonic wave propagation through a wooden pole (radial direction) was developed. Beside the time of wave propagation, which is normally the only parameter used on the NDT application for wood in Brazil, the system also analyzes other parameters of the signal. The system operate with an NI PCI-6110 of National Instruments data-acquisition card and includes amplification, rates, filters, spectral analysis, maximum and minimum, rms, statistical analysis, graphs, curve storage, etc. In that way, it was possible to configure the system to carry out the functions needed in the prototype, the signal conditioning and manipulation functions as well as the interface functions with the user. With that prototype, it was possible to evaluate different parameters of wave propagation to allow the establishment of which parameters should be present in the final product. Figure 1 shows part of the signal acquired after filtering. The first maximum positive peak, which indicates the time of the wave propagation through the transducer, is determined. This time is used by the system calibration. In lower part of the figure, ten data acquisitions are shown. The results have a good repeatability (18.25 μ s).

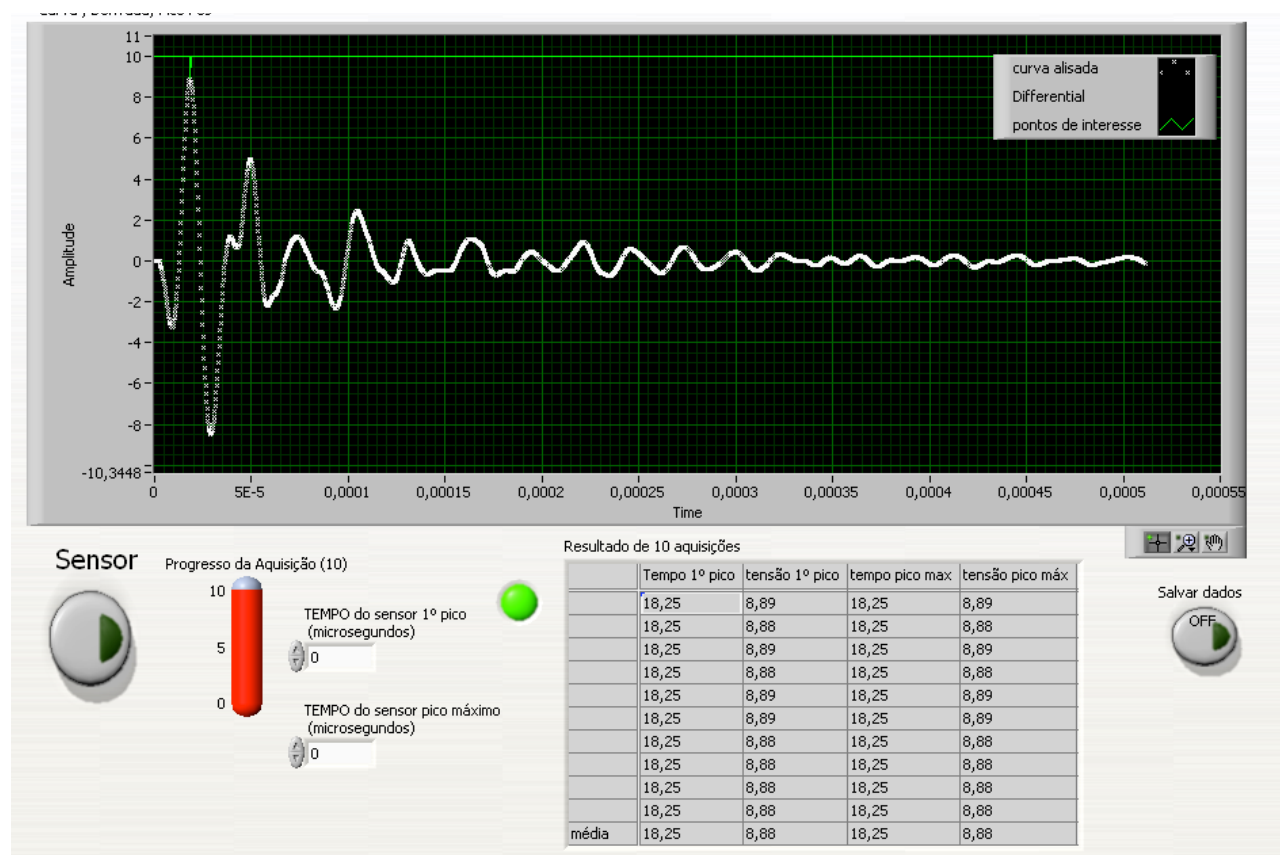


Fig. 1 – Screen of the system. On the upper part the signal acquired after filtering and on the lower part the results of 10 acquired signals used for transducer calibration.

The frequency spectrum response of the acquired signal is shown in Fig. 2. In this figure, it is observed that although the frequency of the transducer was 45 kHz, the component with larger amplitude occurs between 35 kHz and 35.5 kHz.

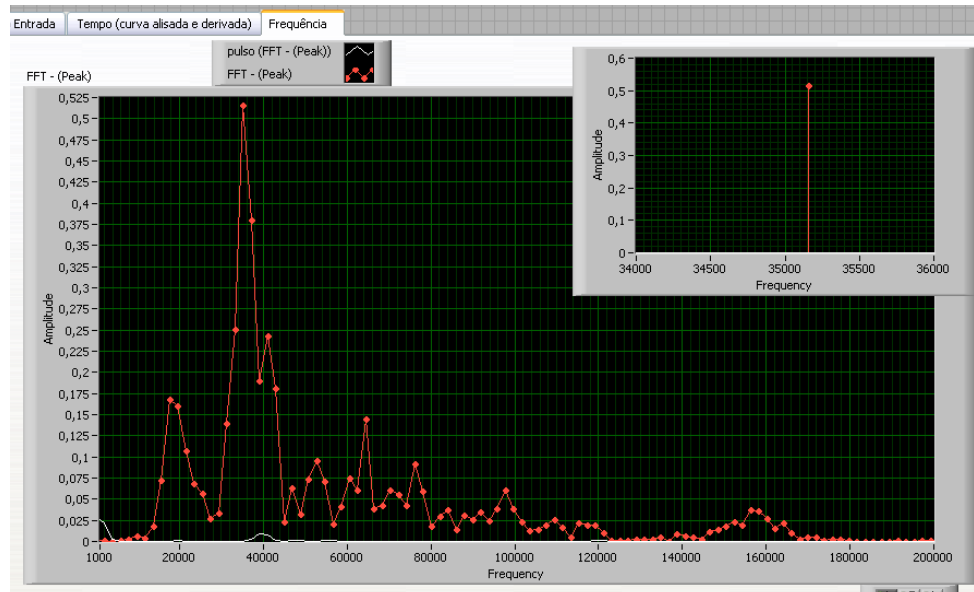


Fig. 2 – System screen with presentation of the frequency signal in the transducer.

The experimental arrangement for testing the poles is presented in Fig. 3. The same procedure of signal analysis was used (time of the first peak) to determine the time of wave propagation through the pole (Fig. 4). The measurements also have a good repeatability as it can be observed by the values on the table of the Fig. 4, which represents the ten results acquired with the wave propagation through the wooden pole on the radial direction. The time of wave propagation presented is obtained with automatic correction, deducting the transducer calibration time (18.25 μ s). Note that, in Fig. 4, there are the first peak and maximum positive peak. With the maximum positive peak, it is possible, using additional mathematical treatments, to determine the duration of the signal, which also was linked with the wood properties.

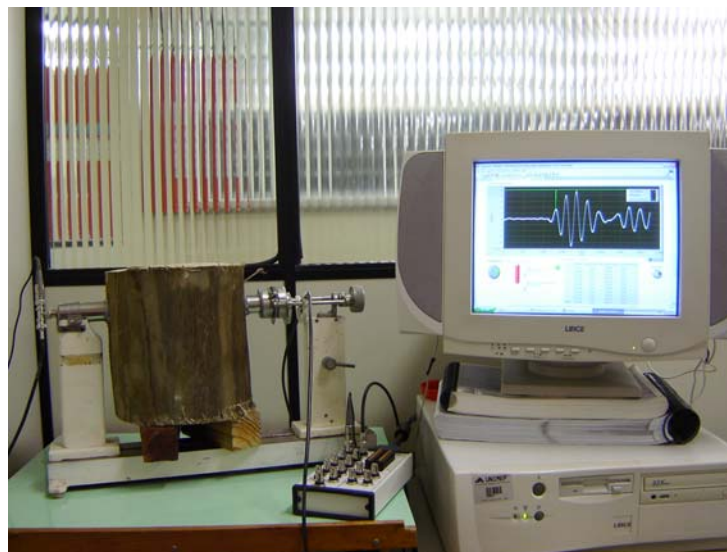


Fig. 3 – Simulation of the system using a test with a section of a eucalyptus pole.

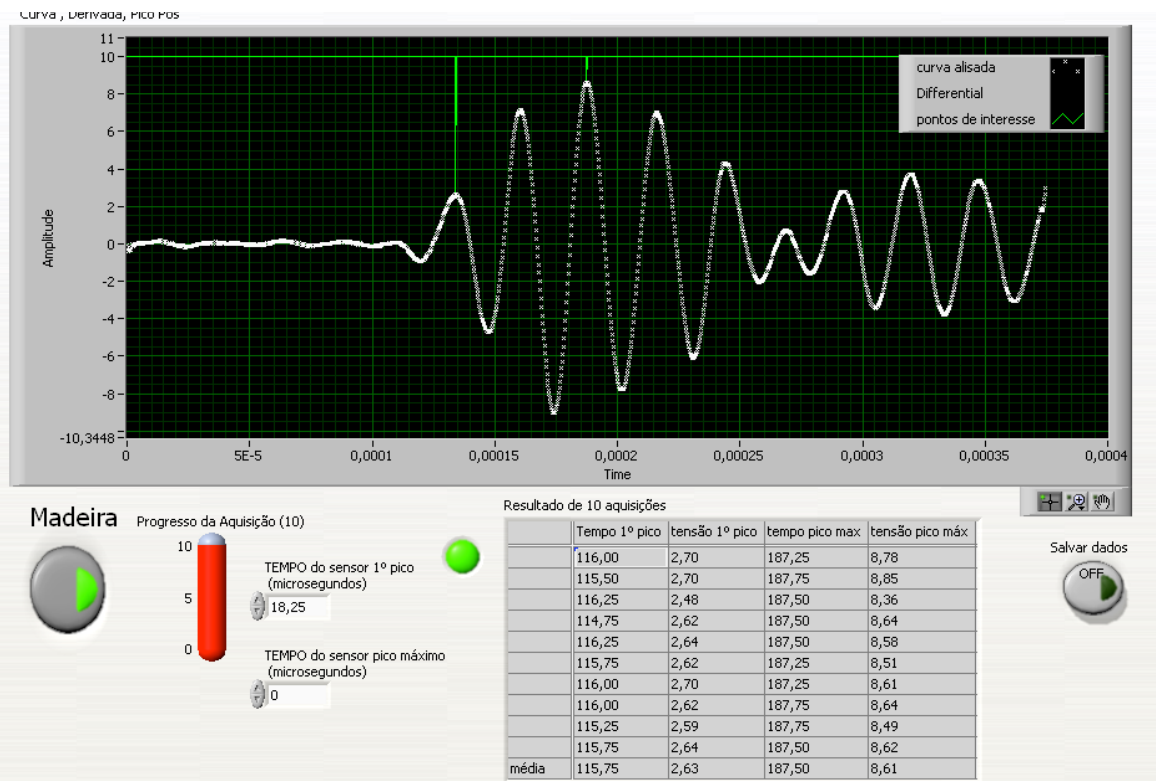


Fig. 4 - System screen. On the upper part, the signal acquired after filtering and on the lower part the results of 10 measurements of the wave propagation through the wooden pole.

Figure 5 represents the frequency response of the wave propagation through a wooden pole. It is possible to observe that, there are some alterations in the frequency spectrum. This alteration can be also related with the wood properties. The component with greater amplitude reduces its values in relation to signal on the transducer (see detail on the small picture of Fig. 5 and compared with Fig. 2).

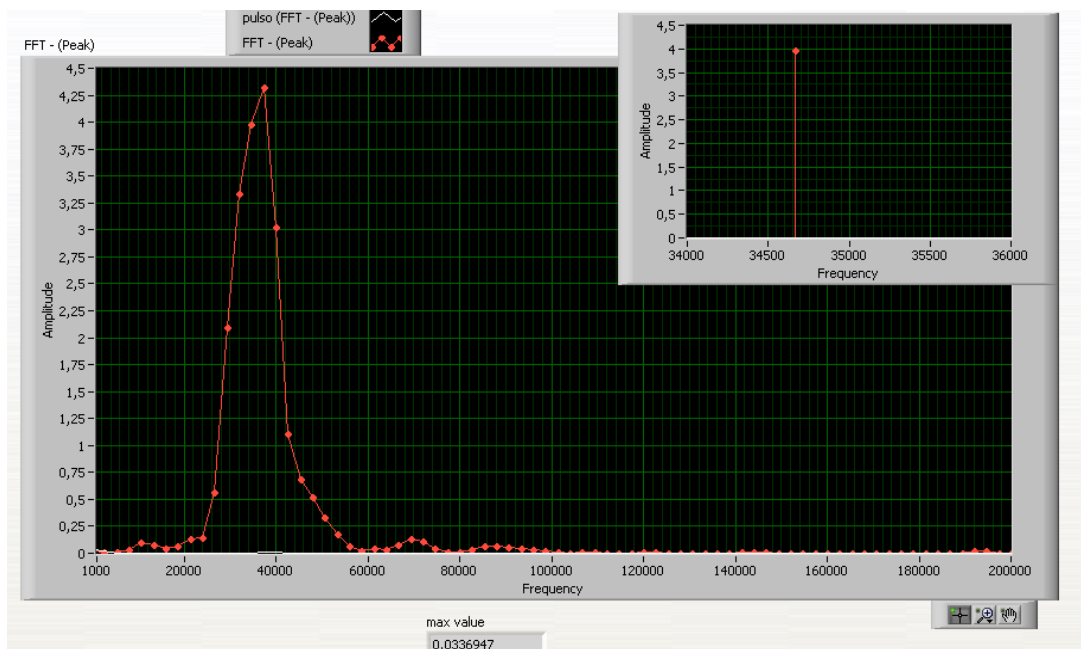


Fig. 5 – Measurements of the frequency during test with eucalyptus pole.

To analyze the sensitivity of the system, a test with a section of a pole, with the same diameter tested previously (Figs. 4 and 5) but with a small hole in the center, was carried out. The results are presented in Figs. 6 to 8. In Fig. 6, it is possible to observe that there are a signal with a smaller amplitude and greater noise component than those presented in Fig. 4. So, although most parts of noise can be eliminated by the applied filter, it is necessary to increase the gain to obtain a better signal.

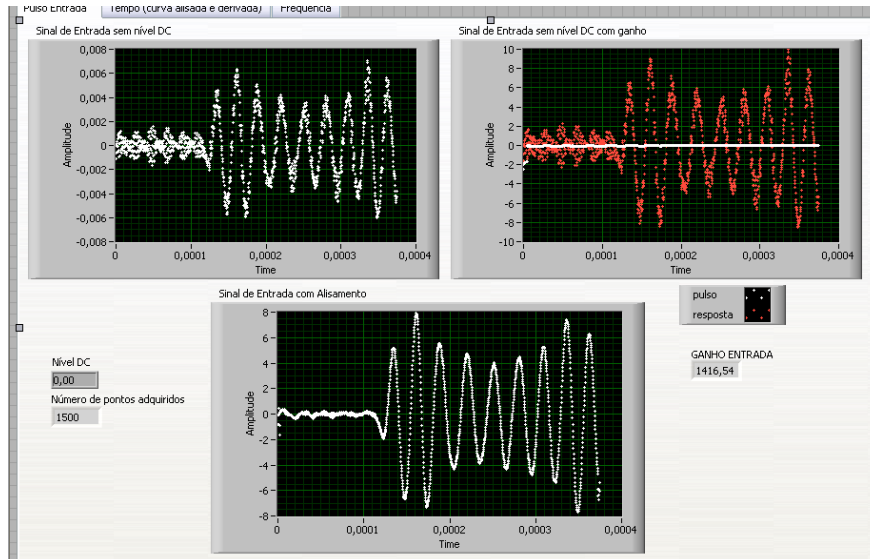


Fig. 6 – System screen during test with wooden pole with a hole.

The second screen (shown in Fig. 7) presents the results of the time of wave propagation. We observed that the time of the wave propagation measured using the first peak on the pole with a hole is quite similar to that measured on the wooden pole without a hole. This result is probably consequence of the size of the hole (very small to affect the time of propagation). The hole has more effect on the attenuation of the signal, which can be better explained by the time of the maximum peak. It was observed that this maximum peak, which was on the third peak (Fig. 4), now is in the second peak (Fig. 7). This change is also linked with the properties of the wood.

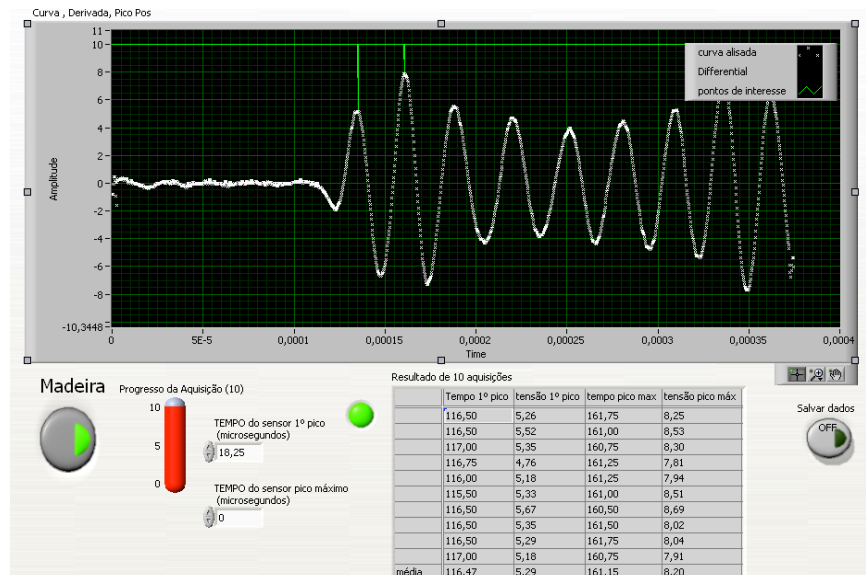


Fig. 7 – Results obtained with the wood pole with the hole.

Figure 8 presents the result in frequency of the wooden pole with the hole. In this figure it can be observed that the component with lower level is the same that the other test (with the pole without hole), but the other components do not have the same pattern. This behavior is directly related with the properties of the wood.

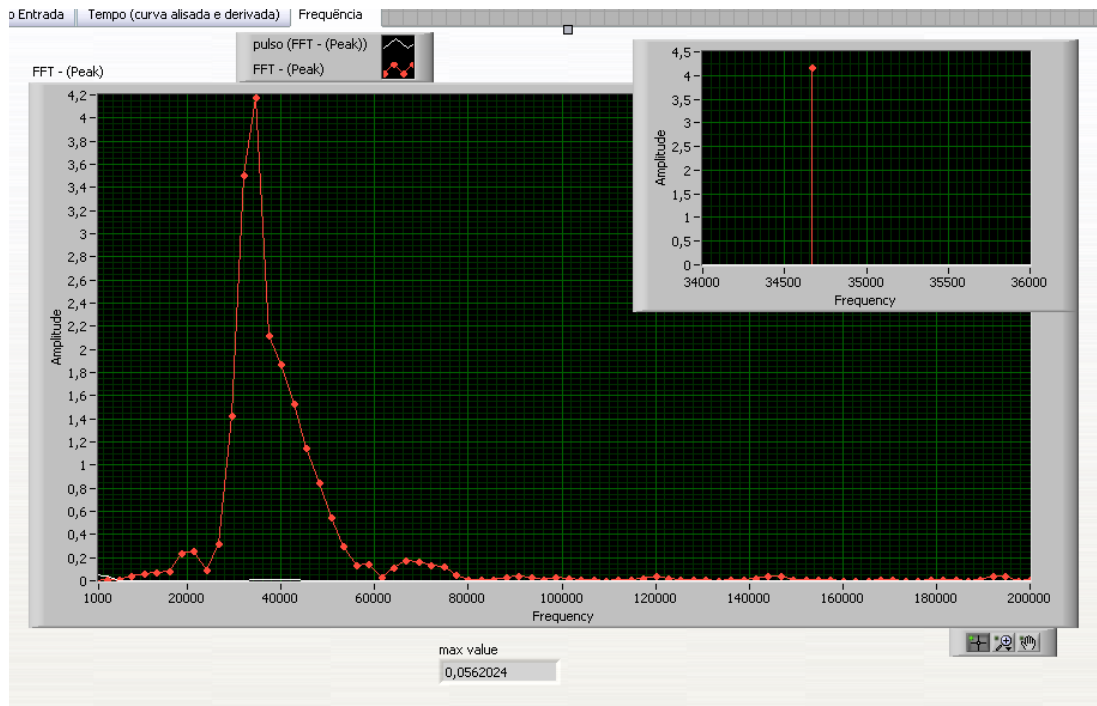


Fig. 8 – System screen; Frequency signal for the pole with a hole.

Conclusions

The use of the time of wave propagation (or velocity of wave propagation), based on the first peak, as an only parameter of analysis of a wood pole can be useful when there is a great decay. When it is important to evaluate small defects on the wood structures, it is also necessary to include other evaluation parameters such as the time of maximum peak and the response in frequency.

Acknowledgement: This research was carried on as part of a research project developed in partnership with the São Paulo Electricity Company (CPFL), College of Agricultural Engineering - UNICAMP (Campinas State University) and two engineering enterprises - MOLISE and AG-RICEF.

References

1. *Standard Test Methods of Static Tests of Wood Poles*, D1036 , American Society of Timber Methodology, 1999.
2. *Postes de Madeira – Resistência à Flexão.*, NBR 6231, Associação Brasileira de Normas Técnicas, 1980.
3. Benoit, Y. *Vieillessement et fiabilité des parcs de poteaux bois des réseaux de ligner aériennes : l'intérêt du contrôle non destructif*. Thèse 1997, 2004. 243 p.
4. Bucur, V. *Acoustics of Wood*. Springer-Verlag, 2006, 393 p.

ANALYSIS OF RACKING OF STRUCTURAL ASSEMBLIES USING ACOUSTIC EMISSION

JIAN LI, FRANK C. BEALL and TOM A. BREINER

College of Natural Resources, University of California-Berkeley, Richmond, CA, USA

Abstract

Monotonic testing is performed as the initial step for cyclic loading to evaluate potential seismic performance of shear walls. The AE analysis was a follow-up on a study to assess the use of small assemblies (1.2 x 1.2 m) using plywood and oriented strandboard (OSB) panels with variations in stud spacing, nailing, panel thickness, orientation, and addition of gypsum board. In this work, AE was studied for complimentary information on damage assessment and as a potential means of adaptive control in cyclic testing.

To provide an additional input of damage development, we attached four AE transducers, a pair at each upper corner, on both the frames and panels. AE outputs were obtained from both racking and load-unload (Felicity) tests. The pattern of AE was quite different for both framing and panels (plywood and OSB) and for materials in tension and compression. The AE showed a definite change in the Felicity ratio with load, providing an independent measure of damage. Based on this information, we feel that the AE technique can be a useful complimentary measure for either open- or closed-loop control in both monotonic and cyclic testing of shear wall assemblies.

Keywords: Shear wall, OSB, plywood, damage, small scale, Felicity ratio, lateral load

Introduction

The conventional approach in simulated cyclic seismic testing is to run monotonic tests to obtain the load-deformation curve and obtain a reference deflection that is used to establish a baseline deformation (Fig. 1). From the maximum load (P_{max}), the deformation at $0.8P_{max}$ (deformation capacity) is obtained (the point of maximum deformation can also be determined by consensus). The reference deformation (D_{ref}) is calculated as $0.6D_{fail}$. Both factors (0.8 and 0.6) are completely arbitrary, being largely based on seismic testing of other materials, such as concrete. Typically, the shape of the curves for matched assemblies can be similar up to P_{max} , and then very divergent beyond that point. Where damage occurs and how it develops in the assembly is unclear.

One means of assessing damage development in materials is to monitor acoustic emission (AE), which has been used with wood-based materials since the 1960s. The application of AE to wood-based materials has been substantially aided by developments in assessing the integrity of fiber-reinforced plastics (FRP), which have many characteristics similar to those of wood. Composite materials, including wood, typically exhibit the Felicity effect [1], which can be expressed by the Felicity ratio, the fraction of the applied load, at which the AE reappears during the next application of loading.

Experimental Approach

The assemblies included plywood (nominal 12 mm Structural-1 Douglas-fir) and OSB (nominal 12 mm Exposure-1 sheathing grade). Each assembly had 400-mm stud separation, and

150-mm edge-nail (8d coated) and 300-mm field-nail (8d coated) spacing. The framing material was 2x4 kiln-dried Douglas-fir Select Structural grade to minimize interference from defects and moisture content changes. Single framing members were used for all edges with 16d bright framing nails.

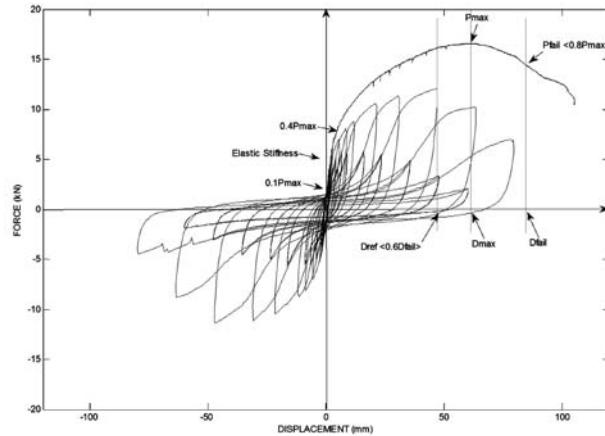


Fig. 1 Nominal output for monotonic testing and key variables for analysis.

The assemblies were tested using an MTS 407 controller with a 25-kN actuator mounted on a 0.9- x 3.6-m 10-t table (Fig. 2a). The test system was designed to be self-reacting since the floor at the Forest Products Laboratory was inadequately reinforced. The actuator drives an upper loading head that is stabilized laterally with guide rollers, and has a special fixture that permits horizontal and vertical movement, but prevents rotation in the plane of the assembly. The system is programmed for both monotonic and dynamic testing, and for automatic data acquisition. Monotonic and Felicity tests were run under deformation control at 0.5 mm/s, the standard rate used for previous tests on these assemblies [2].

Two panel transducers were attached with 27 N springs at a point 150 mm diagonally from each upper corner using a special spring holder. For the OSB, the panels were oriented to permit attachment to the smooth side. Two framing transducers were mounted similarly on the vertical framing member at 25 mm from the upper frame end. High-viscosity grease was used as a couplant. An AET5500 AE system was operated at 0.5-V automatic threshold and 80 dB total gain, which included 60 dB preamplification, and a preamplifier filter of 125-250 kHz. The transducers were 175 kHz resonance-type. The AET5500 data file was synchronized with the load output from the MTS controller. AE events with only one count were discarded as noise, according to accepted practice. Figure 2 shows the position of wood-to-frame nail connections, the main sources of AE in the tests.

Monotonic runs were performed without interruption to obtain overall AE data. All of the runs were ended when the load fell to $0.8P_{max}$, which has been the operating criterion for previous monotonic runs. After this point (and often prior to this), the load-displacement behavior becomes erratic from cumulative damage. A series of three monotonic tests were done (in duplicate) with both plywood and OSB, using a semi-rigid hold-down [1], and an essentially pinned hold-down, which was a modified version of that reported by Herbert and King [3]. Since the rigid hold-down caused some bending of the vertical studs, it was believed that the pinned hold-down would cause a more uniform distribution of stresses in both the frames and panels. In addition, the surface roughness was reduced by coating the transducer contact area of the panels with a wood filler (DAP cellulose fiber filler) and sanding it to provide a surface without voids. In both coupling types, viscous grease was used for coupling together with a 27-N spring.

Felicity runs were made by choosing nominal load fractions of previous monotonic runs for the plywood and OSB assemblies, beginning at about 35% of P_{max} . For each cycle, the load was

reduced to about 0 to 10% of the previous peak value before increasing the load at the same rate. The actuator yoke attachment was disconnected to permit the assembly to recover deformation without the actuator pulling it back.

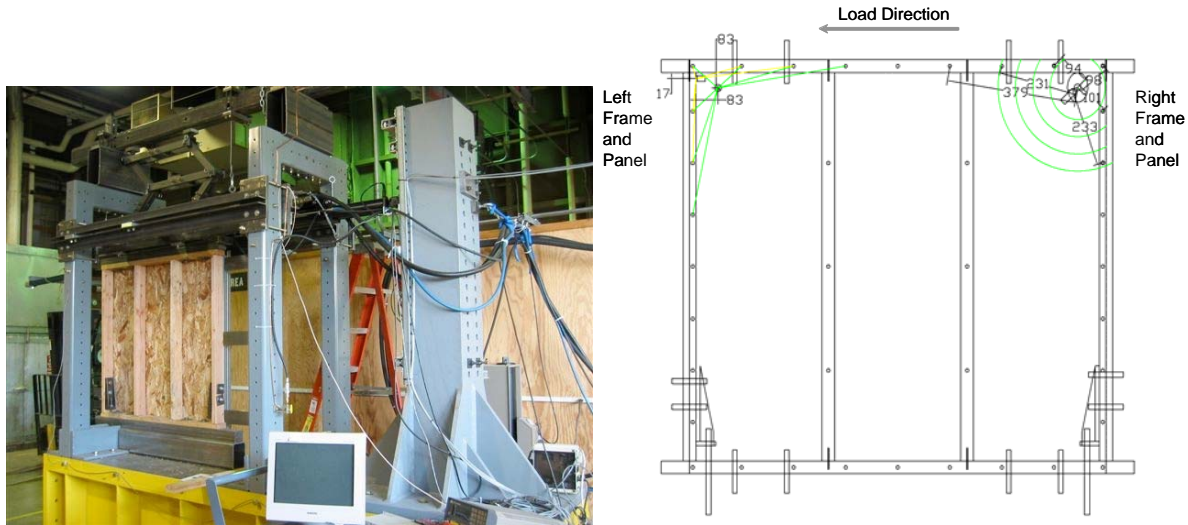


Fig. 2 Test setup for monotonic testing of 1.2 x 1.2 m assemblies.

Table 1 Testing matrix

	Loading	Anchor System	Surface Treatment
OSB(AE0)	Monotonic	Semi-rigid holddown	/
OSB(AES)	Monotonic	Pinned connection	Wood filler and sanding
OSB(AEN)	Monotonic	Pinned connection	/
OSB(AEF)	Non-reversed cyclic	Semi-rigid holddown	/
PW (AE0)	Monotonic	Semi-rigid holddown	/
PW(AES)	Monotonic	Pinned connection	Wood filler and sanding
PW(AEN)	Monotonic	Pinned connection	/
PW(AEF)	Non-reversed cyclic	Semi-rigid holddown	/

Table 2 Summary of performance of AE testing specimens

	P _{max}	D _{max}	P _{fail}	D _{fail}	D _{ref}	Ini _{stiff}
	kN	mm	kN	mm	mm	MN/m
OSB(AE0)	15.8(6)	47.4(4)	/	/	/	2.3(28)
OSB(AES)	13.8(3)	42(17)	11(3)	75(1)	45(1)	2.3(8)
OSB(AEN)	14.1(1)	43.3(3)	11.2(1)	76(5)	46(5)	1.99(8)
OSB(AEF)	15.4(4)	42.1(8)	/	/	/	2.1(9)
PW (AE0)	18.2(5)	53.5(29)	/	/	/	2.5(14)
PW(AES)	17.3(5)	43(1)	13.8(5)	91(3)	54.6(3)	2.1 (30)
PW(AEN)	16.4(5)	39.5(3)	13.1(6)	99(19)	59.3(9)	2.41(4)
PW(AEF)	16.1(12)	43.3(4)	/	/	/	2.1(18)

Results and Discussion

Table 2 summarizes the load performance of all test specimens. It shows that the plywood shear wall assemblies have consistently better performance than the OSB with the same

configuration. OSB is 20% lower in P_{max} , 10% lower in D_{max} than that of PW with same configuration. It was not possible to determine the effect of pinned vs. rigid hold-downs because of the large variations.

Monotonic tests

Figure 3 shows the AE events and cumulative AE as the load was applied monotonically without interruption; 3a: the output of a semi-rigid hold-down plywood assembly PW(AE0) with no surface treatment of the panel, 3b: a similar assembly, OSB (AE0). 3c: plywood assembly PW(AES) with a pinned hold-down and cellulosic fiber surface filling.

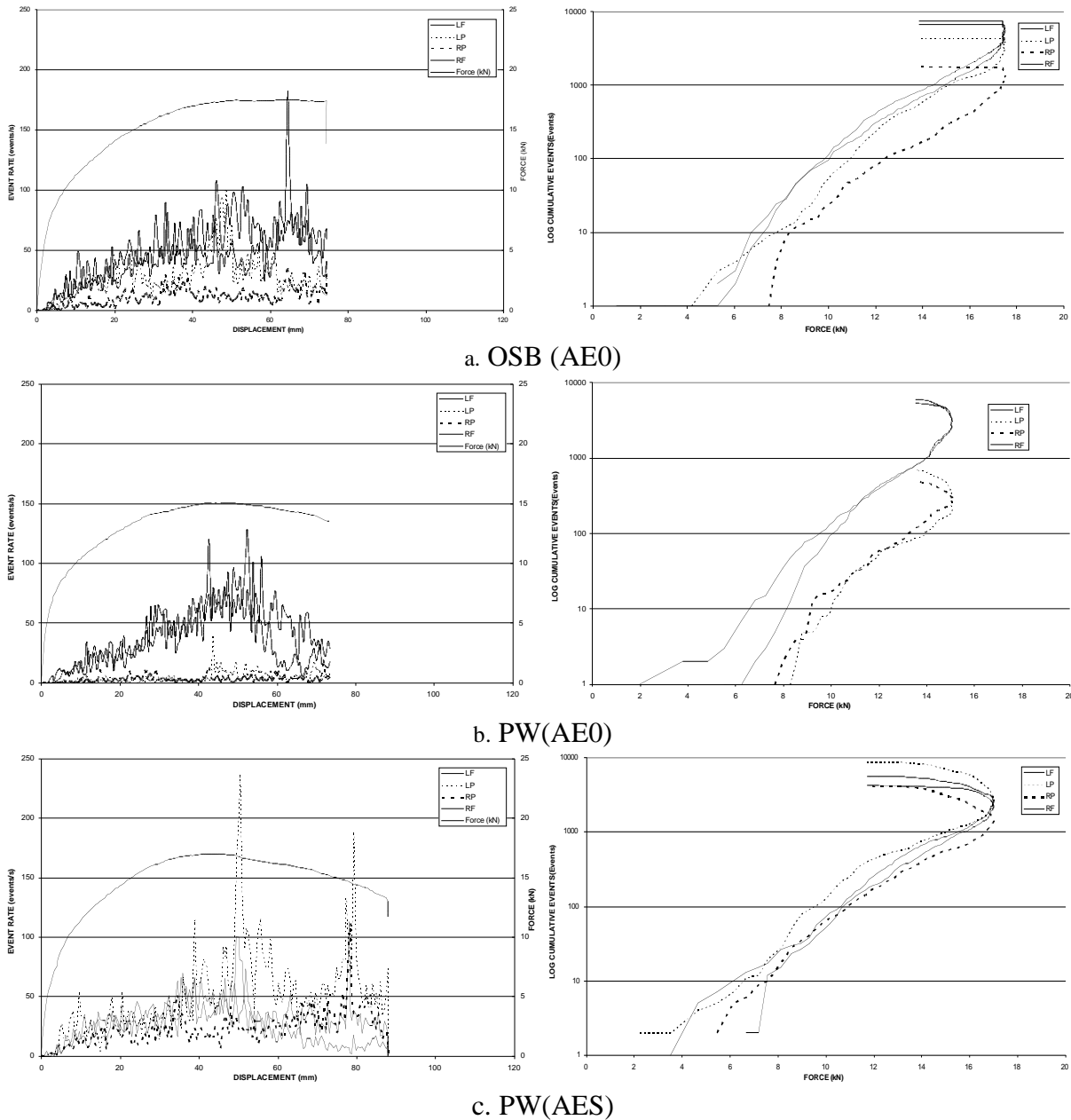


Fig. 3 AE outputs and log cumulative distribution for monotonic testing.

The large AE peak in Fig. 3a was a result of a split in the upper portion of the left frame member, which is a common occurrence in such testing. Since this was near P_{max} , it did not greatly affect the usefulness of the AE data. The OSB matched specimen (Fig. 3b), had relatively similar behavior of AE from each of the vertical frames, but substantially lower AE from the

panels. This latter effect was unexpected since OSB was anticipated to be a much "noisier" material based on its structure and creep testing results [4]. Also, it was found that the right frame (tension member) was consistently higher in AE output. The assembly with the pinned hold-down and surface filling (Fig. 3c) showed a higher AE output from the panel transducers and more clustering of panel and frame outputs. The reasons for the differences between plywood and OSB could not be determined from these tests, but OSB is less stiff than plywood and is much more susceptible to creep. OSB panel creep could be assessed by using different rates of deformation.

There were several consistent features: in all runs, there were few or no AE events up to 0.4 P_{max} , which is regarded as the endpoint for determining initial stiffness in the monotonic tests. Although this portion of the curve is not truly linear, the absence of AE indicates that the deformation is reversible and therefore can be considered to validate this range for stiffness determination. Up to about P_{max} , the shape of the AE event curves was the reverse of the load-deflection curve (concave vs convex). The net effect is that about one-half of the AE events occurred up to P_{max} . The right frame transducer (at the load application corner) in general had the highest level of AE events, and the right panel transducer the lowest level. This was unexpected, since it was anticipated that there would be more damage associated with the fractures in panels from movement of the nails. However, it is possible that the nails acted as waveguides to couple the AE events into the framing, which would have had lower attenuation than the panels. OSB panels typically had lower AE events than plywood. This was attributed to the much rougher surface of OSB compared with plywood, but it could have also been caused by greater scattering of waves in the OSB or more brittleness of the plywood. The most consistent observation is that the AE event rates increase rather uniformly up to P_{max} , and then become fairly erratic as damage develops in the assemblies. One feature that did not occur in the AE outputs was an exponential increase in AE as the system approached failure, which is characteristic of much AE testing.

Felicity tests

Based on the monotonic results, the decision was made to use the right frame transducer output for determining the Felicity ratios for the Felicity effect tests. Figure 4a and 4b show the outputs for a typical plywood panel assembly. Although it is difficult to see in the figures, the right frame transducer was typically the first to detect AE in the load reapplication. This was visually determined by expanding the time scale for the load reapplication periods.

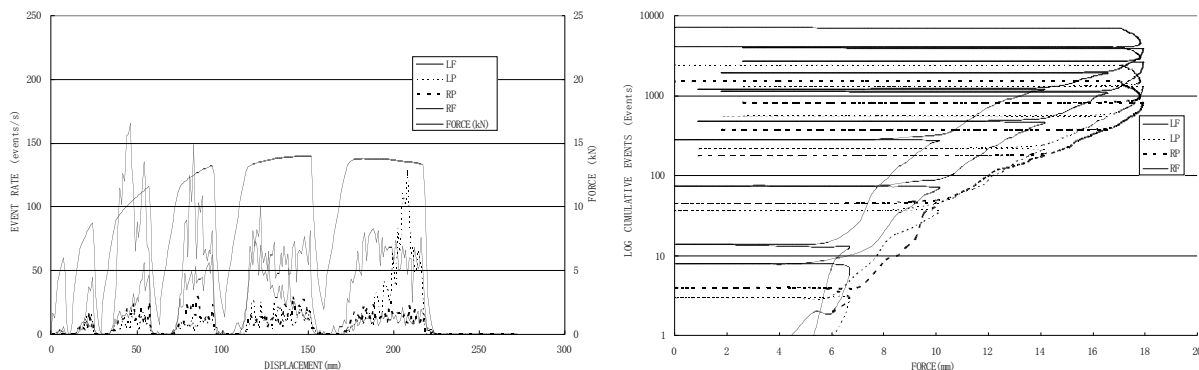


Fig. 4 a) AE outputs for felicity testing of a semi-rigid hold-down plywood assembly with no surface treatment of the panel (left). b) AE Log cumulative distribution in Felicity testing (right).

Figure 5 is a plot of the calculated Felicity ratios (FR) for the 6 runs. There were two general patterns, somewhat linear decreases for assemblies with higher P_{max} , and very abrupt decreases

for those with lower P_{max} . The patterns of FR values over the first three cycles were not good predictors of the subsequent FR values or P_{max} . However, the three higher P_{max} assemblies (16.1 to 18.0 kN) were consistently above FR of 0.7 over the complete deformation cycle, whereas the lower three (14.0 to 15.4 kN) had terminal FR values below 0.6. For these two groups, the terminal FR averaged 0.77 and 0.50, respectively. These values were obtained from the "tension" frame member prior to the improvement of coupling with wood filler on the surface of the panels. It is possible that better information could be obtained with the improved coupling, and that the choice of the specific point for obtaining Felicity information could be affected.

A number of these plots show increases in FR after the initial decreases, which occur largely in the middle range of the load application. This was not expected, since typically FR values show a down-trend from the extension of fractures that occur earlier. However, the increases could reflect the influence of fractures that terminate and no longer produce AE, at least within that particular cycle of load-unload.

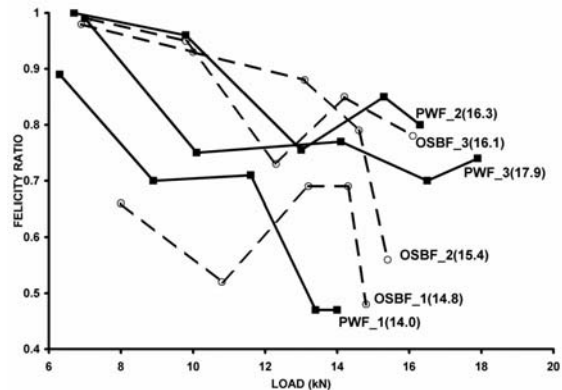


Fig 5. Felicity ratios for six tests of plywood and OSB assemblies.

Conclusions and Recommendations

1. The Felicity ratio was a useful complimentary technique to assess cumulative damage occurring in shear wall assemblies during monotonic testing.
2. Cellulosic fiber filler somewhat improved the coupling for both plywood and oriented strandboard.
3. Log cumulative events vs. force was the most useful means of data presentation to separate the outputs of the four transducers.
4. Testing is needed on single fastener connections to determine the sources and nature of AE. Location techniques could also be used to enhance the understanding of the damage development.

References

1. Beall F C, 1986, Effect of resin content and density on acoustic emission from particleboard during internal bond testing. *Forest Prod. J.*, **36**(7/8): 29-33.
2. Beall F C, Li J, Breiner T A, Wai J, Machado C, Oberdorfer G, Mosalam K., 2006. Small Scale Rack Testing of Wood-Frame Shear Walls. *Wood Fiber Sci.*, **38**(2): 300-313.
3. Herbert P D, King A B, 1998, Racking resistance of bracing walls in low-rise buildings subject to earthquake attack. *Building Res Assoc of New Zealand Study Report 78*. Judgeford, New Zealand.
4. Beall F C, 1996, The use of acoustic emission to assess duration of load behavior in oriented strandboard. *Proceedings, Tenth International Symposium on Nondestructive Testing of Wood*. Lausanne, Switzerland. pp. 33-41.

ISPESL EXPERIENCE FOR REQUALIFICATION OF SMALL LPG UNDERGROUND VESSELS USING AN ACOUSTIC EMISSION-BASED PROCEDURE AND STATISTICS

CARLO DE PETRIS, PAOLO QUARESIMA, ANGELO FARAGNOLI,
VITTORIO MAZZOCCHI and PAOLO LENZUNI*

Department of Technology of Safety, Italian National Institute for Occupational Prevention and Safety (ISPESL), Via Fontana Candida 1, 00040 Monte Porzio Catone (RM), Italy;

*Florence Division, ISPESL, Via G. La Pira 17, 50121 Florence, Italy

Abstract

About 500,000 small underground LPG vessels are to be inspected for requalification in the next few years, as mandated by the Italian national legislation. Traditional methods of inspection are exceedingly slow and expensive, so that their implementation is very impractical on such a large scale and has to be ruled out. AE-based tests represent a very attractive alternative. On-site AE tests of small underground vessels have been carried out in several countries for decades, and experimental techniques have reached a stage of high reliability. In order to customize the method to the specific Italian situation, the Italian National Institute for Occupational Prevention and Safety (ISPESL) has developed a data analysis procedure where data collected during AE tests carried out on individual vessels are used to establish compliance of homogeneous batches with existing criteria for continued operation, by means of statistical inference methods. This has eventually resulted in a very efficient inspection tool, which is much faster and much more cost-effective than its traditional counterpart. More than 10,000 vessels have been tested with this method by the end of July 2007.

This paper's aim is threefold: a) providing an outline of the ISPESL AE testing procedure; b) presenting some of the test results collected for individual LPG vessels; c) discussing the statistical methods which have been developed to establish compliance of homogeneous batches with existing regulations.

Keywords: LPG, underground vessel, procedure, statistics

Introduction

LPG is a relatively "clean" form of energy, widely used for industrial applications, domestic heating and transport. Several hundred thousand small LPG vessels have been set into operation in Italy during the last decade, mostly underground.

Inspection is mandated by Italian national legislation after ten years of operation, leading, if successful, to the tank requalification. Traditional methods of inspection require that the vessel is unearthed, which means that they are cumbersome, slow and expensive, i.e. not cost-effective. A viable and attractive alternative is represented by AE-based techniques. On site AE-based examination of underground LPG vessels has been common practice in Austria and France for at least two decades, with a good record of reliability established over many 10000's of tests. However, some peculiarities of Italian LPG vessels (mostly vertical geometrical configuration – see Fig. 1 – no internal visual testing possible) and the legal obligation to perform requalification according to a statistical approach based on sampling of homogeneous manufacturing batches, have created the need for a specific data analysis procedure.

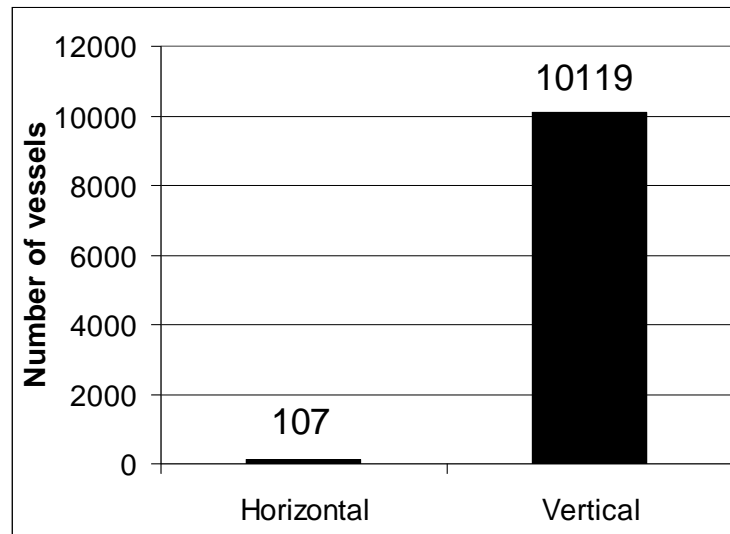


Fig. 1 Topology of vessels in Italy as determined by tests.

The Italian National Institute for Occupational Prevention and Safety (ISPESL) has developed such a tool. Its most attractive feature is that it allows one to determine both the structural integrity of individual small underground LPG storage vessels and the compliance with existing regulations of homogeneous batches. It is based on the European standard EN 12818, which has been supplemented with original information on all those issues, on which the standard does not go into details.

Determination of Homogeneous Batches and Associated Samples

The European standard EN 12818 allows the examination of vessels to be performed not only on an individual basis, but also through the sampling of homogeneous manufacturing batches. Its annex I specifies that the fractional sampled population is a steeply decreasing function of the batch size. It also includes a lengthy list of parameters that can be used to better discriminate strongly homogeneous batches.

Concerns were expressed that very low sampling fractions could lead to large uncertainties in the final result, possibly undermining the method’s credibility. The use of many discriminating parameters also proved untenable, as it tended to produce a huge number of very small, or even individual batches, the final result being unacceptably close to individual testing.

Homogeneous batches were accordingly assembled by using just a few simple manufacturing and specification parameters; that is, the producer, manufacturing year, vessel coating, geometrical topology and capacity. The sampling fraction was held constant at 33% for batches with a size M greater than 20 vessels, with larger fractions for smaller batches, reaching 100% for a size $M \leq 7$. Table 1 summarizes the resulting picture. Figure 2 shows how the vast majority of batches is of very small size, with only 1/5 of them gathering more than 20 vessels.

Table 1 Vessels operating since 1994 or 1995.

Total number of vessels in the field	34260
Homogeneous batches	1060
Average number of vessels per batch	32
Vessels to be sampled	13221
Sampling fraction	38.59%

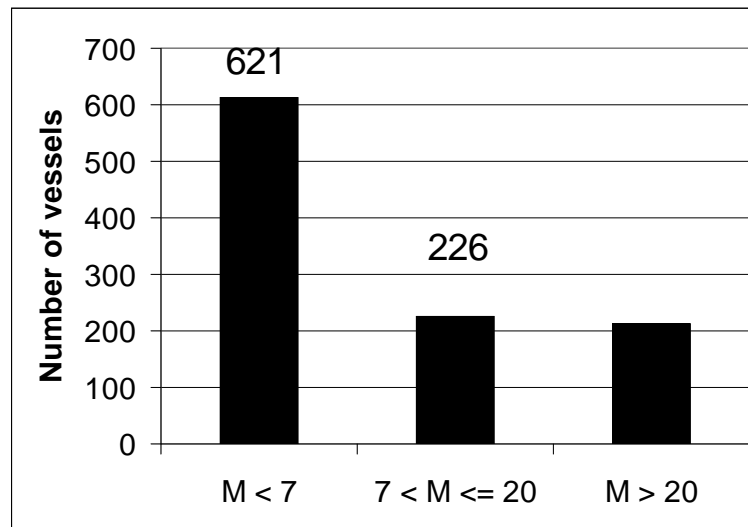


Fig. 2 Distribution of homogeneous batches according to their size.

AE Test Method

On site activity is performed using a mobile laboratory (Fig. 3), equipped with dedicated instrumentation for AE testing (Fig. 4). Pressurization takes place through a closed loop system that vaporizes LPG and injects it back into the vessel (Fig. 5).



Fig. 3 The mobile laboratory for AE tests.



Fig. 4 A view of the inside.

AE testing of an LPG underground tank is strongly constrained by the limited accessible area, and by the presence of its settings such as valves, connecting pipes, accessories and devices for protection, safety and control (see Fig. 6). Only two sensors could be therefore positioned on the tank surface, with a mutual distance of 400 mm. Attenuation of AE signals over short spatial scales, has suggested that the method be limited to vessels with capacity below 3 m^3 . An extension of this limit to 13 m^3 is currently under way.

The following is a short synopsis of the main features of this AE test:

- Pressurization begins at a pressure $P_{\text{start}} \leq 9 \text{ bar}$, and stops at a pressure $P_{\text{stop}} \geq 15 \text{ bar}$;
- The required pressurization gradient is 0.2 bar/minute ;
- Hits with duration $D \leq 30 \mu\text{s}$ are rejected, as that are known to be largely due to mechanisms having nothing to do with the vessel's structural integrity;

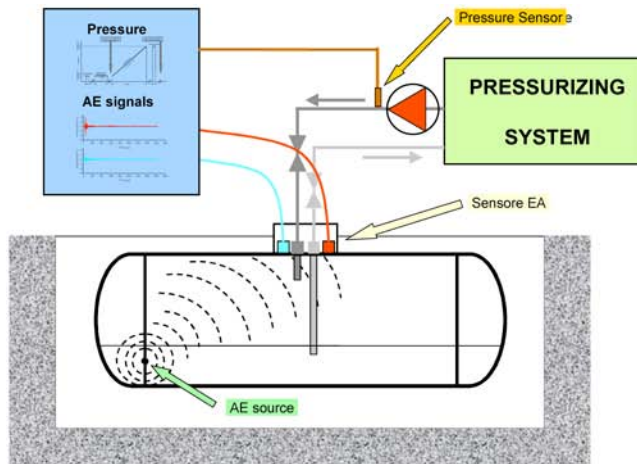


Fig. 5 A layout of the technique based on AE method.



Fig. 6 A view of the area of the accessible area of the underground vessel.

Evaluation Quality Index and Evaluation Factor γ for Classification

Classification of vessels requires relies on a four quantities:

1. The number N_1 of AE bursts (within the range of Δt – values used to identify AE events from the vessel), above a high specified peak amplitude value A_1 ;
2. The number N_2 of AE bursts (within the range of Δt – values used to identify AE events from the vessel), above a low specified peak amplitude value A_2 ;
3. Calculation of a *synthetic quality index* ICSE. Very general arguments, based on the mechanisms leading to energy release in AE tests, indicate that the ideal synthetic quality index should include elements related to:
 - The AE activity (e.g. number of significant AE bursts, their energy and/or amplitude);
 - The time evolution of the AE activity;
 - The homogeneity of AE activity in space.

The former two are needed to explicit the link between structural integrity and overall activity (i.e. more hits and more energy imply a higher chance of structural damage). The latter should be used to incorporate the relation between sudden energy bursts and/or strongly localized clusters of AE sources on one side, and the hazardous potential of existing defects on the other.

Careful investigation of AE test outcomes has been finalized to understanding the role and significance of various quantities, which are measured or calculated. This has led to the definition of a *synthetic quality index* ICSE with the general form:

$$ICSE = f \left(HC, K, \frac{EC}{\Delta p} AC \right) \quad (1)$$

The four quantities that appear in equation (1) are:

- The total number of AE bursts (HC), whose Δt between the two detectors is consistent with the vessel geometry;
- The pressure-specific total energy, i.e. the ratio of the AE cumulative energy (EC) to the pressure range (Δp) spanned during the test; energy units are $[(mV)^2s]$, pressure units are bar;
- The number of the most energetic events (K) needed to account for 50% of the cumulative energy released. This quantity has a very similar meaning to the parameter known as “severity” in some AE procedures;

- “Area factor” (AC), calculated as the (sign-independent) departure of the Normalized Cumulative Hits-Energy (NCHE) area from the “ideal” value of 0.5. The NCHE area is the area under the curve of normalized cumulative energy vs. normalized cumulative hit number (see Fig. 7). An area of 0.5 would result from a time-independent average energy per hit, a situation usually associated with minor structural damage. Deviations from 0.5 (typically created by a strong release of energy in the latest test stages), would give a lower value of the NCHE area, and a correspondingly large value of AC. It is seen therefore that this quantity is a good indicator of a non-ordinary time evolution of the energy released during AE tests.

Equation (1) lacks sensitivity to the spatial density of AE sources, which would be expected to correlate to the probability of structural damage. Furthermore, amplitudes and energies should be corrected to take into account the signal attenuation between source and detector. This in turn requires that a reliable location algorithm is available. Unfortunately, the task of precisely locating the AE source with just two very closely spaced detectors has proven extremely problematic, much more so for vertical vessels. This has prevented the development of a more complex index based on Δt clustering analysis or any other quantity linked to the maximum surface density of events.

The *synthetic quality index* ICSE is usually characterized by moderate fluctuations associated with the acquisition of low-energy hits. The occasional flaring of a very strong hit determines a sudden drop of the number K of relevant hits, as well as shrinkage of the AC area. Both features contribute to a quick increase in γ .

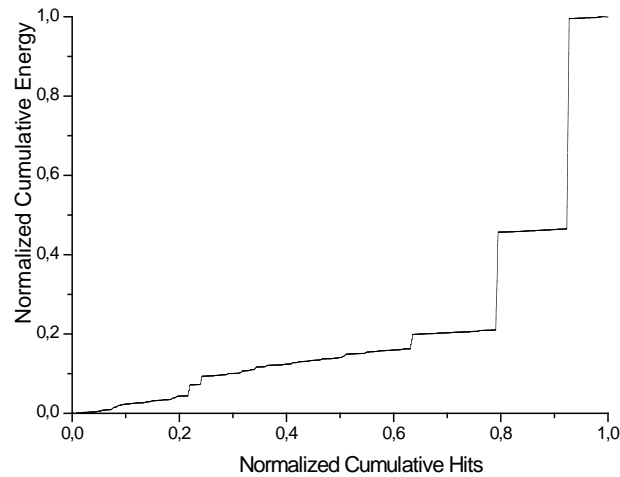


Fig. 7 An example of a typical curve of normalized cumulative hit energy vs. normalized cumulative hit number.

The calculation of a *time-history index* ISRE is given by

$$\text{ISRE} = \frac{\sum_1 E_j}{\sum_2 E_j} \quad (2)$$

where sum #1 is over the recent most 0.8 bar-wide pressure interval, and sum #2 is over the recent most 1.6 bar-wide pressure interval. A large value of ISRE implies that most of the energy has been released very recently, which in turn is an indicator of possible structural damage. Large and erratic fluctuations are the rule for ISRE. Again, energetic AE events can be assumed to be responsible for observed sudden variations, as they push this index to values of order 1

when they are recorded. ISRE then drops to almost zero if no significant event is recorded in the ensuing 0.8 bar-wide pressure interval.

Equations (1) and (2) is solved by the AE data processing system every time an AE burst is detected.

Classification of individual vessels

The classification of individual vessel is carried out using the largest value (γ_{\max}), reached by a specific evaluation factor γ during the test. The evaluation factor γ is computed by the AE data processing system every time a burst is detected as well as ICSE and ISRE solving a function with a general form:

$$\gamma = f(\text{ICSE, ISRE}) \quad (3)$$

The identification of one or more action thresholds is an essential step in building up a reliable assessment procedure. This task is complicated the dearth of objective independent criteria which could be employed to calibrate the AE-based method illustrated in this paper. The Italian national legislation on LPG vessels currently relies only on subjective expert judgment to declare compliance or non-compliance.

Classification of vessels takes place as follows:

CLASS 3: Vessels for which $\gamma_{\max} \geq 0,95$ – These vessels can no longer be operated. They must be unearthed and disposed.

CLASS 2: Vessels for which we get either

1. more than $N_1 = 30$ hits with amplitude above $A_1 = 75$ dB, or
2. more than $N_2 = 15$ hits with amplitude above $A_2 = 85$ dB.

These criteria have been deduced from similar criteria, which appear in several international standard that deal with AE testing.

Vessels in CLASS 2 are subjected to careful scrutiny (post-analysis), which takes into account the actual number of hits with amplitudes above A_1 and A_2 , and the pressure interval, in which they have primarily shown up. The post-analysis eventually produces either a negative (CLASS 3, dismissal), or a positive outcome (CLASS 1, approval).

CLASS 1: Vessels, for which none of these conditions apply. These vessels are allowed to continue operation for a period determined in accordance with existing Italian legislation (usually 10 years).

Compliance of homogeneous batches

Because requalification is mandated to be performed adopting a sampling approach, the final judgment on the structural integrity of vessels requires that some kind of global descriptor for the entire homogeneous batch is developed. The compliance of all vessels in a homogeneous batch is assessed through a single value γ_{batch} . The calculation of γ_{batch} is carried out assuming that the values of γ for individual vessels in the batch follow a Gaussian distribution. More in detail, γ_{batch} represents an estimate of a size-dependent percentile of the distribution. Because this implies the existence of a fraction of vessels with $\gamma \geq \gamma_{\text{batch}}$, it is vital to have an accurate estimate of this fraction, which in its turn requires that the distribution of γ values in the batch is well known.

Table 2 Results of classification of vessels according to the criteria of ISPEL procedure.

	Number	Percentage
Total number of tested vessels	10,226	
CLASS 1	9,739	95.3
CLASS 3	378	3.7
Rejected tests	109	1.0

Results

Classification of vessels

Table 2 summarizes the results available as of the end of July 2007. The two most outstanding elements are:

- The very small fraction of tests, which must be rejected (1%). This confirms that the test procedure is well suited to be carried out in the field with only occasional mishaps preventing its regular completion;
- The small, but not negligible, fraction of CLASS 3 vessels (3.7%). This figure may be expected to be larger than similar figures provided by different test methods. This discrepancy may be originated both by differences in the tested vessels, in terms of coating (bitumen coating vs. epoxy resin coating) or geometry (horizontal vs. vertical). It may also be due to the different testing strategies (individual vs. sampling), which has forced a more conservative threshold in Italy in order to account for the large fraction (about 2/3) of vessels not subjected to tests.

Distribution of γ of individual vessels

The probability density function of γ for all 10117 vessels with a valid test is shown in Fig. 8. Bins 0.05 wide have been used. Figure 9 shows that a Gaussian distribution provides an excellent approximation to the experimental probability function. The best Gaussian curve has a mean of 0.66, and a standard deviation of 0.16. The small positive *skewness* (0.46) indicates a slight asymmetry in favor of the high- γ tail of the distribution.

Compliance of homogeneous batches

The fact that a Gaussian distribution is an excellent approximation to the experimental distribution of the global distribution of γ values provides strong support to the hypothesis that this is also the case inside each and every homogeneous batch. As previously discussed, the precise knowledge of the fraction of vessels with γ above γ_{batch} corresponds to have an accurate estimate of the residual risk in the procedure. In this perspective, the result shown in Fig. 9 represents a powerful contribution to the overall reliability of the method from the assessment of compliance.

The departure from a Gaussian distribution, which shows up in the extreme high- γ tail is statistically significant for individual bins. Because of the minimal size of these bins, this is however inconsequential with respect to the estimate of the fraction of vessels with $\gamma \geq \gamma_{\text{lim}}$. The integral of the experimental distribution for any $\gamma \geq 0.95$ is within 5% of the corresponding value calculated assuming a Gaussian distribution.

Given the large number of tests, which have been taken to completion (more than 10,000), it is expected that future tests will not introduce any significant change. Major deviations will only be possible if associated to significant structural changes of vessels, possibly unveiled as test proceeds through samples drawn from younger and younger populations. Therefore, despite the

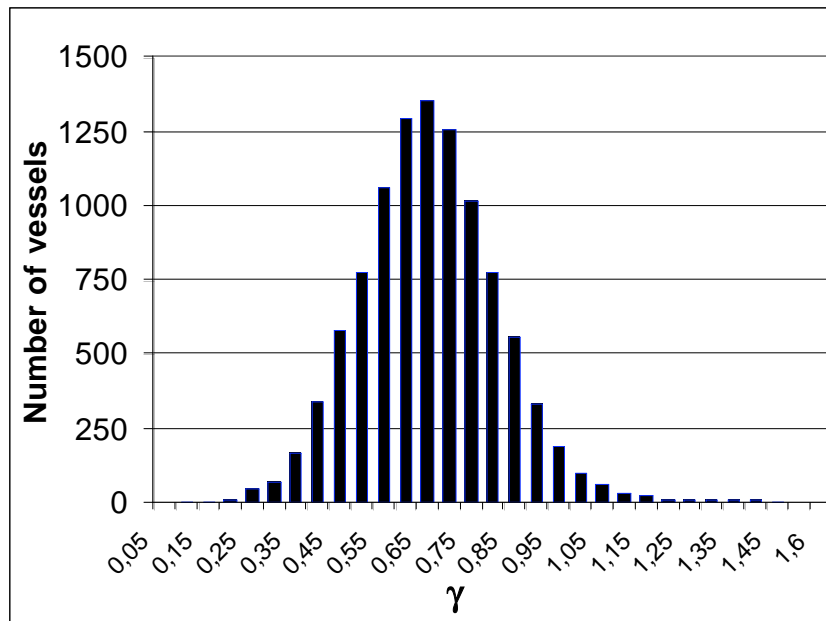


Fig. 8 Distribution function of γ for all tested vessels.

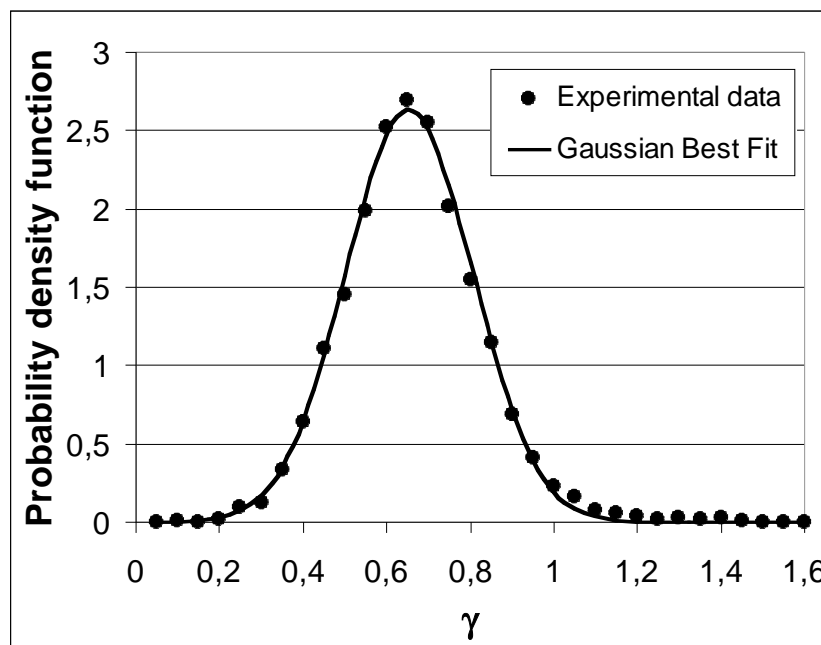


Fig. 9 Experimental and best-fitting Gaussian probability density functions.

limited fraction of vessels, which have been tested (10,000 out of a total of about 400,000, that is 2.5%), quantitative conclusions are firm.

Conclusions

An AE-based test procedure for requalification has been developed to perform a quick and cost-effective inspection of small underground LPG tanks. The limited and crowded accessible area on the tank severely constrains the size of any reasonable experimental set up. Despite the adoption of a very basic, two-sensors configuration, this method still provides enough information to allow a reliable assessment of the vessel's structural integrity. As such, it represents an

excellent alternative to traditional inspection methods, which are a lengthy and costly affair, and whose internal consistency is often very low.

Because of the stringent limitations on the experimental set-up, special emphasis has been placed on waveform analysis. The resultant evaluation factor γ has been shown to provide a solid tool for the assessment of structural integrity of tanks. In combination with two additional alert criteria based on the number of detected AE bursts with a high specified peak amplitude, it can be used to reliably assign individual vessels in one of three different quality classes, which make up the adopted classification scheme.

References

1. EN 12818 – 2002 *Inspection and requalification of LPG tanks up to and including 13 m³ underground.*

PERIODICAL TESTING OF LPG VESSELS (ABOVE- AND UNDERGROUND) BASED ON A VALIDATED ACOUSTIC EMISSION PROCEDURE WITHIN CENTRAL EUROPE

PETER TSCHELIESNIG

Institute for Technical Physics, TÜV Austria Services, Deutschstr. 10, A-1230 Vienna, Austria

Abstract

In Austria, the required main inspection (hydrotest and visual inside inspection) can be replaced by a pneumatic test monitored with acoustic emission since 1992. By the end of 2006, more than 30,000 aboveground and buried vessels have been tested with this method. The gained experience was incorporated into the new European Standard for LPG vessels, where a normative annex lays down the minimum requirements to perform an AE test. We can validate the integrity of the vessels not only qualitatively but also quantitatively by the application of a complex evaluation factor (or cluster evaluation factor, CEF) and its automatic calculation for conspicuous regions (Δt -clustering). CEF was evaluated on laboratory tests and will be improved continuously on basis of the test results. The AE TESTING and the evaluation procedure can also be applied to LPG vessels above 5 m³ with almost no limitation. With detected faults (e.g. cracks in juggle joints), the feasibilities and limits of the testing method shall be demonstrated. In particular, unstable critical crack propagation emits only few AE events and therefore the evaluation has to be very strict.

Outside Austria, the method is applied under different licenses in Germany, Czech Republic, Slovakia, Hungary as well as Slovenia and as an additional safety method partly in Italy. New European standards will extend this method also to trucks and railroad cars, which would increase the competitiveness of the European industry.

Keywords: LPG-vessels, periodical test, cluster evaluation factor (CEF), CEN-standard

Introduction

Until we started to test LPG vessels in 1992 the normal periodical tests, which were required every 6 years, were done by a hydro-test up to 1.3 times the service pressure (setting of the safety valve) and an inside-inspection. Every 2 years an additional outside inspection has to be performed. This procedure was time-consuming, expensive and did not give us a real answer about the status of the vessel. This is not a solitary problem for LPG vessels, because every hydro-test gives us only a binary answer: good or burst. A further problem, which was introduced by the hydro-test, was the residual humidity causing corrosion problem within the vessels and blocking of the valves during the winter season by ice.

After extensive laboratory test and further tests on real LPG vessels, we started with the acoustic emission testing of LPG vessels [1]. At the beginning, we investigated the maximum working pressure of above- and underground LPG vessels in Austria, which resulted in test-pressure for the LPG vessels of 1.25 and 1.1 MPa (at minimum 10% above the highest working pressure during the last year of service). One of the biggest advantages of the testing method was that the pressurization could be performed with the stock product (LPG) itself. Although the vessels were small enough to cover 100% of the vessel's surface under load with only a single

sensor, we decided to work with location software (which requires two or more sensors) for different reasons:

- 1) The application of 2 sensors gave us a further filter criterion to distinguish random background noise from useful AE signals.
- 2) The linear location for above ground vessels gives us the opportunity to re-calculate the amplitude of the AE wave to the point of origin, which gave us the possibility to weigh the energy of the emitted wave.
- 3) For underground vessels, where a normal linear location is impossible, we decided to make a Δt -discrimination to combine the AE signals, which are coming from one point and then delete those AE signals, which come scattered from all over the vessel.

This last paragraph is important, because it is obvious that a vessel fails because of defects coming from one or several AE sources (points of origin) and does not collapse in total. Therefore, it is important to look at the different clusters of the vessel, because we all know very well, that it is a big difference if we get e.g. 10 AE signals from 1 point or scattered over the complete wall of the vessel.

Another problem for the AE testing of underground vessels is that we are unable to re-calculate the acquired amplitude back to its origin. This leads to fact that we cannot measure only the amplitude or energy, but on the contrary we have to assess also these AE parameters, which would not be affected so much from the attenuation [2].



Fig. 1: Acoustic emission testing of LPG tanks. The sensor positions for aboveground application are near to circumferential welds (left) and for underground application the sensors are mounted at the man-way nozzle (right).

History

Over the years, numerous different problems specific for the LPG vessels occurred all over Europe. In 1994, we adapted the test method for France, where they found cracks in the juggle joints because of stress corrosion cracking. This method is now adopted in the French AFIAP guide and can be applied today [3]. During the development of this method, we introduced our first issue of the cluster evaluation factor (CEF), which combines different AE parameters to one number. A CEF value indicates the status based on the most dangerous cluster, which was detected and evaluated on the specific vessel. This CEF not only minimizes the influence of the distance between the AE source and the sensor but also reduces the reaction time of the pre-warning system in case of the critical crack growth. We improved the system continuously based on improvements of the AE equipment, which became more powerful and on further investiga-

tions of cracks, which occurred in Germany due to improper drying procedure in combination with bad weld production of the juggle joints [4,5].

The AE testing with the application of the CEF has been licensed to other countries (Czech Republic, Germany and Italy). At present, we are able to perform the CEF calculation automatically, increasing our capability of pre-warning and systems validation tremendously.

Cluster Evaluation Factor (CEF)

The application of the CEF is based on the EN 13554 “NDT – AE testing – General principles”, where it is ascertained in §9.2 “Data analysis, Grading”: A dedicated software, based on an extensive database can be used to provide an automatic evaluation of the identified zones [6].

The idea behind this factor was to combine different AE parameters, e.g. maximum amplitude, energy, duration, and activity in such manner that on one hand the combination minimizes the influence of the distance between the AE source and the point of detection (sensor) and on the other hand that critical situations (growing cracks) will be identified on time. The database, which led to this CEF included several thousands of AE tests and will be improved continuously. For the CEF calculation, the different AE parameters will be combined in a matrix, where the different values of the parameters will be related to numerical values. The combination of these values leads to a final number, which indicates the criticality of the cluster. The cluster with the highest value, because this is the most dangerous part of the structure, will be used for the classification of the LPG vessel.

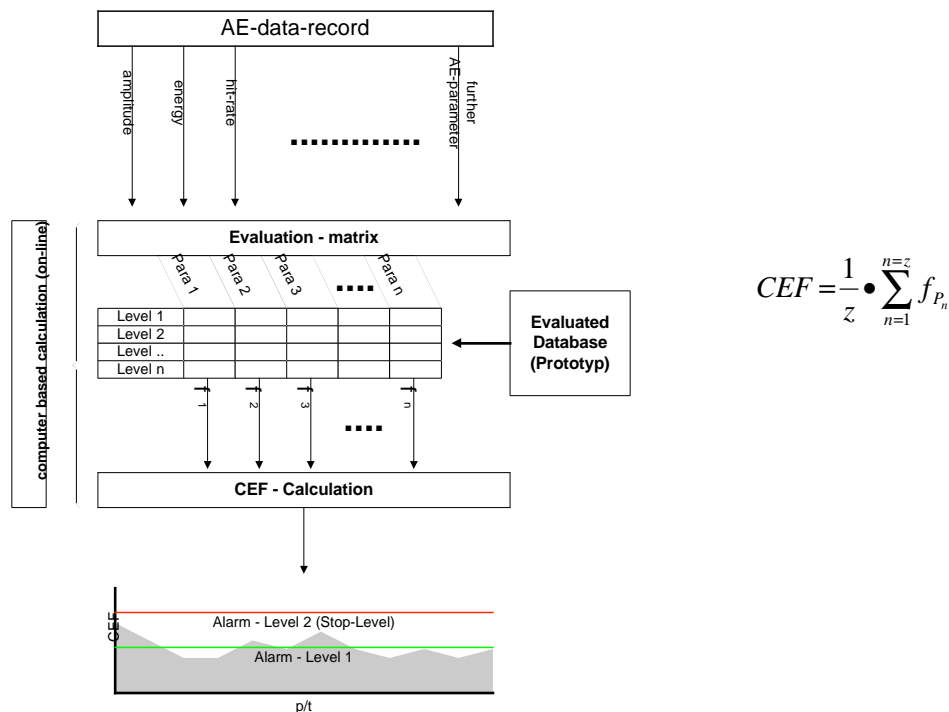


Fig. 2: The structure of CEF (left) and its calculation (right).

In the beginning this CEF was calculated from the AE testing inspector manually during the AE testing, which reduced his reaction for in expectable sometime critical situations. Based on the introduction of the “Embedded Code Processor” in the AE equipments of Vallen Systeme, we are able to calculate the CEF automatically. This calculation and all the numbers (matrix)

behind it is introduced in a sub-program, which was produced by TÜV Austria and will be licensed to other companies under cooperation contract for the further improvement of the CEF.

This automatic calculation of the CEF has the following advantages:

- 1) The result (grading) is available on-line. Critical situations can be prevented much easier.
- 2) In combination with a written test instruction, according EN473, an AT1 test inspector is able to perform the AE testing independently.
- 3) For the application of several thousands of these tests in several countries of Europe, the results are equal, independently of the country or the specific test crew.

According the new annex of EN 12817 and EN 12818, where the minimum requirements for an Acoustic Emission Test on LPG vessels up to a volume of 13 m³ are defined and evaluation factor "C" is for the on-line evaluation recommended as stop criteria and for the post analysis it is required [7].

Besides the more common requirements of how such a test has to be performed, the evaluation and stop criteria for a pneumatic loading (mainly by evaporation of LPG) are very strict in this European standard and rely on the EN 13584 under the specific situation of a nearly inaccessible structure and the problems for AE testing caused by juggle joints. The values for stop, acceptance and rejection criteria shall be established by the test organization and after the agreement by the customer and/or a third party organization, depending on the national law, and included in the AE testing instruction. Clearly such values need an extensive database with a lot of experiences and follow-up tests over the years.

Examples

Experience gained by conducting several burst tests shows that on the one hand the test organization, based on the results of the automatic calculation of the CEF, can evaluate the AE testing continuously and on the other hand it can stop the tests on-time, which is for LPG in any case very important. In any case, it shows that the result depends clearly on the applied stress. Therefore, the annex requires that the vessel shall be pressurized to a minimum of 10% above the highest service pressure reached during the last service period and should not exceed 110% of the maximum allowable pressure.

Application of the Test Methodology

Although the method including the CEF calculation was developed for application on LPG vessels up to a volume of 13 m³ the method is much more powerful than for this limited application. Based on the fact that methodology determines the AE behavior of a defined cluster, whether it is a location cluster or it remains a Δt -cluster, it can be used for every structure as long as an evaluation matrix is available.

TÜV Austria and its licensees use this method for all underground LPG vessels up to 350 m³, where we apply the sensors according a quality management procedure with the help of pre-installed application tubes. The results show no significant difference as long as the procedure is used precisely and the changed marginal requirements are incorporated into the application. The method is proven and accepted according the Austrian law for all LPG vessels as long as the European standard and the validated and certified procedures are also observed. A further point is that, in our opinion, it is very important to re-test all vessels, vessel per vessel, how it is done in most European countries, because the batch testing can only check the production of the vessel, and we have no opportunity to check the influence of location of installation on the integrity

of the vessel. Therefore, any estimation about the integrity of non-tested vessels within a batch is more or less a well-meant anticipation and not the result of AE testing.

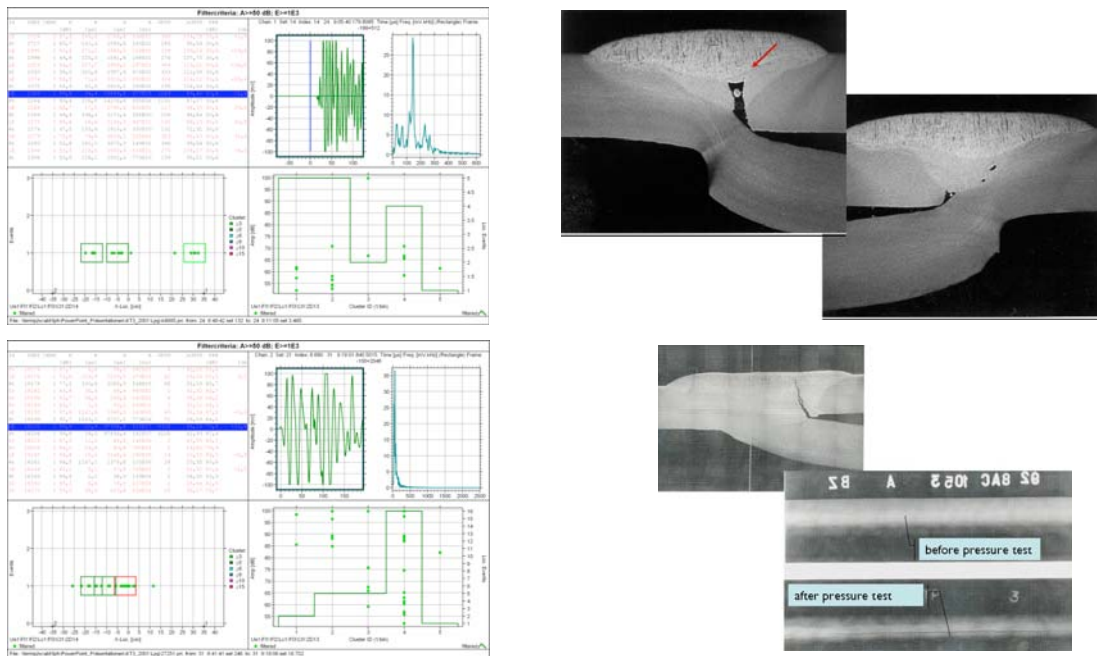


Fig. 3: Welding defect in juggle joint found with acoustic emission CEF = 2.7 (top left) and its verification with radiographic testing (top right), crack in juggle joint welding found with acoustic emission CEF = 3.2 (bottom left) and its verification (bottom right).



Fig. 4: Automatically calculated CEF = 2.8 obtained from the measured data (left) and corrosion damage found at the top of the underground vessel after clearing the indicated area (right).

The method using CEF for data evaluation and vessel classification can also be applied on other pressure equipment, if you are able to use a specific database for this kind of vessels. For aboveground structures you can also use the recalculated values of the different AE parameters and in this case the advantage of the technology is based on the fast response and a relief for the AE testing personnel. Based on the rapid development of the numbers of AE testing in Europe in the last year, a possibility to compare AE testing on the basis of quantitative values will become more and more important. Nevertheless, the application needs in any case an extensive database and a well-known validation procedure before its practical use.

References

1. Tscheliesnig P., Schauritsch G., Krenn G., Kragulj W. (1991) „Die wiederkehrende Untersuchung von Flüssiggasdruckbehälter durch Schallemissionsprüfung“, DACH – Jahrestagung, pp. 44; Luzern, Switzerland.
2. Schauritsch G., Tscheliesnig P. (2000) “Die Schallemissionsprüfung als integrales Prüfverfahren für die Beurteilung von Flüssiggaslagerbehältern – Erfahrungsbericht”, DACH-Jahrestagung, pp. 243-252; Innsbruck, Austria.
3. AFIAP (2004), “Annex 4 –Recommendations for Preparing a procedure applicable to small buried LPG tanks” Guide to good practice for Acoustic Emission (AE) Testing of pressure equipment of the Association Francaise des Ingénieurs en Appareils à Pression, pp. 48-59.
4. P. Tscheliesnig, G. Schauritsch (2007) „Applikation eines automatischen AT-Auswertesystems bei der Prüfung schwer zugänglicher Strukturen“ DGZfP - Jahrestagung; Fürth, Germany.
5. G. Schauritsch 2007 „Schallemissionsprüfung an betonummantelten erdvergrabenen Flüssiggaslagerbehälter – Wo herkömmliche Auswerteverfahren versagen“ DGZfP Seminar; Puchberg, Austria.
6. EN 13554:2004 „Non-destructive testing – Acoustic Emission – General principles“
7. prEN 12817/18:2007(8) Annex C „LPG equipment and accessories – Inspection and requalification of LPG tanks up to and including 13 m³ overground/underground“.

POTENTIALS OF AE APPLICATION IN TESTING INDUSTRIAL PIPELINES

MAREK NOWAK, IRENEUSZ BARAN, JERZY SCHMIDT and KANJI ONO*

Cracow University of Technology, Institute of Production Engineering M-6, Kraków, Poland;

* Department of Materials Science and Eng., University of California, Los Angeles, CA, USA

Abstract

This paper describes three cases of using acoustic emission method in testing pipelines in industrial high-pressure installations. In each, some defects had earlier been detected by other NDT methods and the AE method served to ensure safety operation till the time of next chance of repair. Additionally, in each of these cases, tests were carried out under various technical and different loading conditions; that is why the received testing results provided various level of knowledge of the monitored source.

Keywords: pipeline, defect monitoring

Introduction

The AE method is used in periodical testing with over-pressure tests as well as in continuous monitoring. The application of this method as continuous monitoring is expensive; therefore, it is only used in special cases. One of the reasons of using AE monitoring of pressure installations during their operation is the case when some defects were located in the material, and because of the economic or logistical reasons it was useful to continue the operation of the installations till the time of the possible repair. All the components can be monitored, but sometimes only the most dangerous zones of the installations are monitored.

The cases described in the paper deal both with the monitoring of the selected zones of pipelines as well as all technical pipelines since the aim was to ensure safe operation of the installations. The AE method was chosen because of its effectiveness in detecting and evaluating the growth of the defects and the possibility of testing large structures globally.

The article describes three kinds of the pipeline defects, for which some attempts were made to apply the AE method for tests under the operating conditions of the installations. Vallen AMSY5 system and the software of this firm were used for testing.

Discontinuities of the Wall Material in the Pipeline

Using the ultrasonic test (UT) method the occurrence of discontinuities was detected in one of the knees of a thick-walled technical pipeline of 760-mm diameter, operating under high pressure. To monitor the activity of the defect, the AE method was used. The tests were carried out during the pressure test using resonant sensors at 150 kHz. The testing detected the occurrence of a very active source of class 3 (according to the EN 14584) at the place of the UT-detected discontinuities. In Fig. 1, the location of the source on the pipeline jacket is shown.

This source was active during pressure increase and during pressure hold. The corrected amplitude of AE signals located at the defects exceeded 70 dB during the pressure increase and exceeded 60 dB during the load hold. The activity and corrected amplitude of the signals detected from the class-3 source during the load hold in pressure test are shown in Fig. 2. This source was identified as massive delamination after the pipe section was replaced.

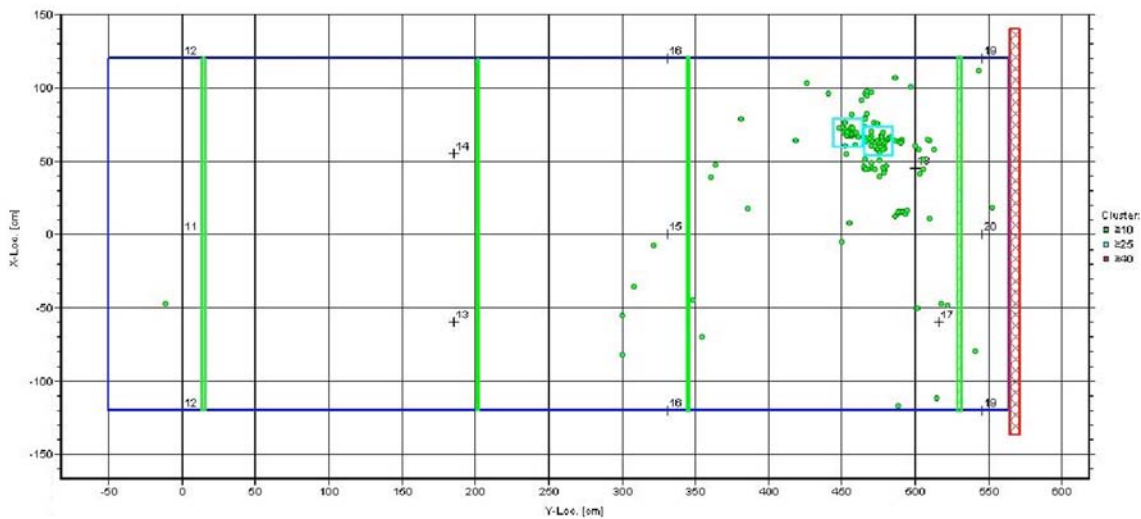


Fig. 1. Class-3 sources on the pipeline located under the conditions of the pressure test. The positions of the pipeline welds are marked with green color.

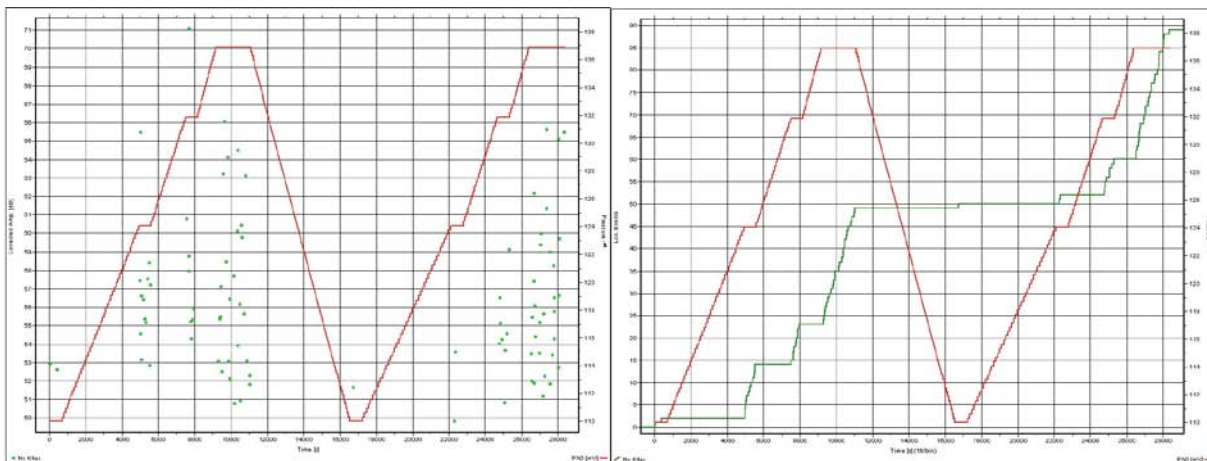


Fig. 2. The corrected amplitude of signals and the activity of the class-3 source during the pressure hold.

Considering the lack of the possibility of replacing this part of the pipeline immediately, an attempt was made at continual operation of the pipeline with on-line monitoring of the growth of the defect by different methods, including the AE method. Monitoring the pipeline during its operation by the AE method required eliminating and removing the signals, which were caused by the flow of the working medium through the pipeline and other operational noise. These need to be separated from the signals coming from the growth in the defect. The tests during its operation utilized different types of sensors in order to cover the widest band of frequency measurements. Figure 3 shows the frequency spectrum of signals for flows of medium through pipeline recorded with use the of 150-kHz sensors. Figure on left shows the distribution of the maximum frequency of spectrum, while the right shows the center of gravity of signal spectrum.

The frequency analysis of the signals recorded during the pressure test as well as during the operation allowed to select two values (180 kHz and 230 kHz) as the high-pass filter cut-offs for further monitoring. It was also found from the measurements taken during the operation it is useful to apply sensors with higher resonant frequency.

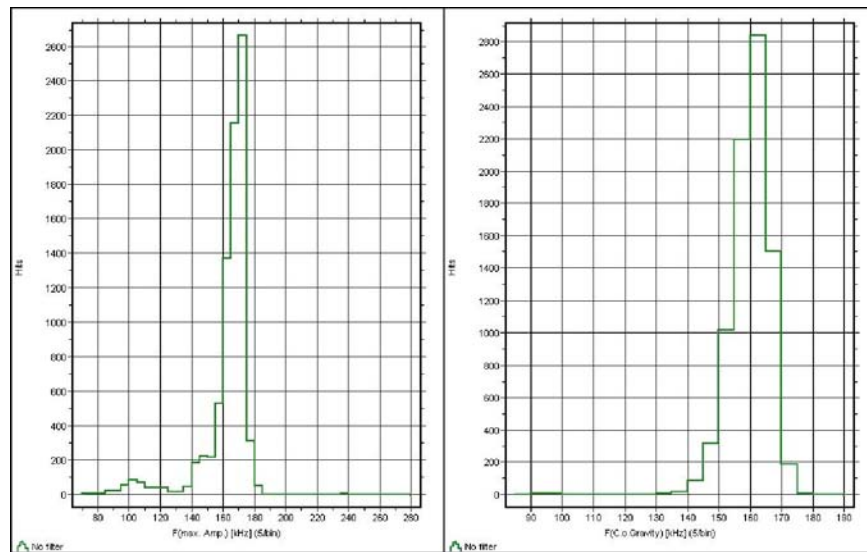


Fig. 3. The frequency of maximum of spectrum and the center of gravity of signal spectrum recorded with use of 150 kHz sensors.

Monitoring of the source during pipeline operation used with Vallen VS375-RIC sensors and the selected filters on the AE channels. Therefore, it was possible to decrease the threshold level in relation to the initial measurement. However, it was necessary to make another layout of the sensors on the pipeline by modifying the test layout used during the pressure tests. For on-line monitoring, six location sensors and six guard sensors were used. It allowed to locate the signals coming from the defect and to determine the activity of the source.

The periodical occurrence of the activity of the source with stable parameters (pressure, temperature) of the operation of the pipeline was detected. This source also became periodically active after decreasing the pressure of the operation of the pipeline. The activity of the monitored source from a 12-hr-measurement session is presented in Fig. 4.

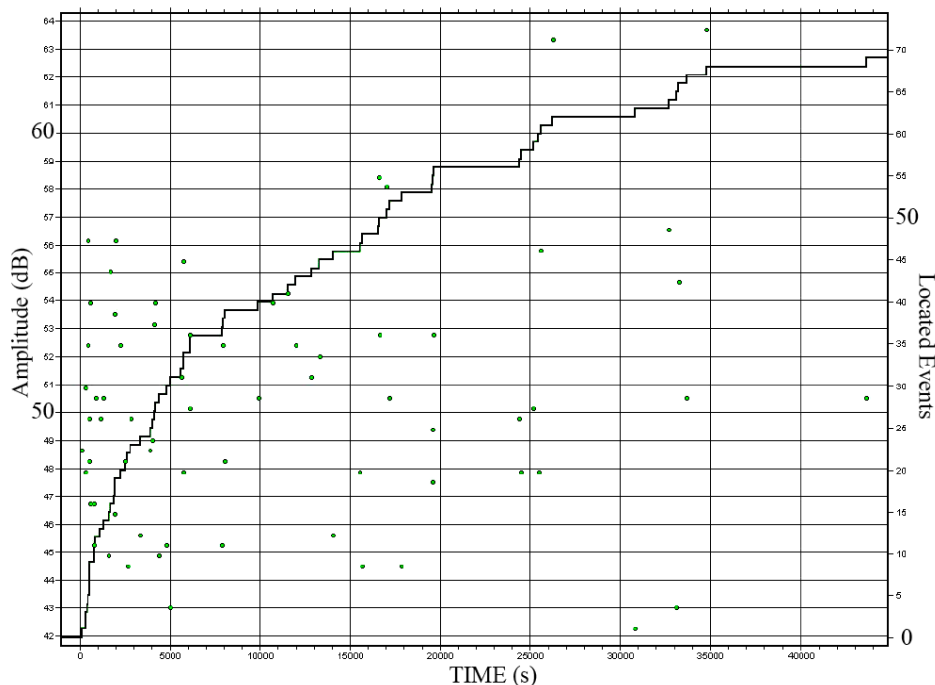


Fig. 4. The activity of the source during the 12-hr operation of the pipeline.

The well-prepared methodology of the measurements made it possible to locate the AE sources as well as to make an efficient evaluation of the growth of the defect. It allowed the installation operator to continue until the time of a shutdown for exchanging the defective element. The simultaneously used periodical UT monitoring and continuously monitoring by the resistance extensometer confirmed the results of AE test method.

Thinning of the Pipeline Walls

The second case concerns a technical pipeline, in which the thinning of walls was detected. This was a result of the flow of the working mixture in zones near the welds joining parts of the pipeline. It was suspected that the thinning occurred also in other zones of the pipeline. Therefore, the AE method was used to determine the activity of the located defect and to detect other places of thinning of walls.

During the operation of the pipeline, a comparative testing with standard filters was made between the defected zone and similar defect-free zones in order to determine the effect of the operation of the pipeline and the operational noise on the recorded AE. It allowed one to record the acoustic background coming from the working mixture flow through the pipeline. The AE activity of the zone with the thinning of walls was distinctly higher than the defect-free zones. The observed AE activities of the comparable zones are presented in Fig. 5.

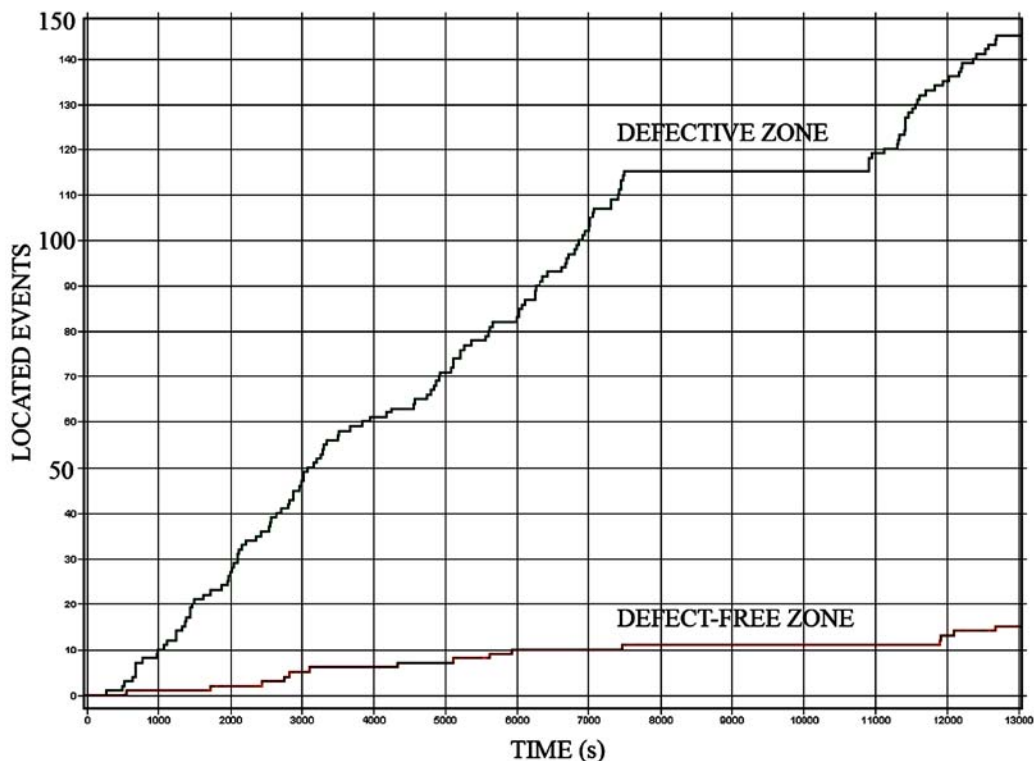


Fig. 5. The activity of the comparable zones of the pipeline over 13 ks.

Since the defect was of the character of thinning of walls and not cracking, the higher activity of the zone could result from the noise in the flow of the working mixture through the pipeline. That is why the result of such testing was burdened with a greater error and it was necessary to carry out the test under the conditions, which enabled to stop the flow through the pipeline. The successive test was made under the conditions of stopping the installation. This test with the use of 22 sensors included more elements of the pipeline in order to detect the occurrence of the

eventual defect in the other zones of the pipeline. Considering the technical reasons, it was possible to make only one loading cycle to the value equal to the working pressure.

For such loading conditions, an analysis was only possible, which was supported on the selected parameters of the recorded signals. This analysis revealed the zones with thinning of walls without the possibility of the precise location of the sources. For that reason, it was impossible to determine the classes of sources. The graph of RMS value indicating the thinning of wall in the zone with sensor No. 21 (along with defect-free zones with sensors Nos. 19 and 20) is presented in Fig. 6.

The examination confirmed the occurrence of thinning of walls in the places shown by other NDT methods, and additionally detected still another place of thinning of wall.

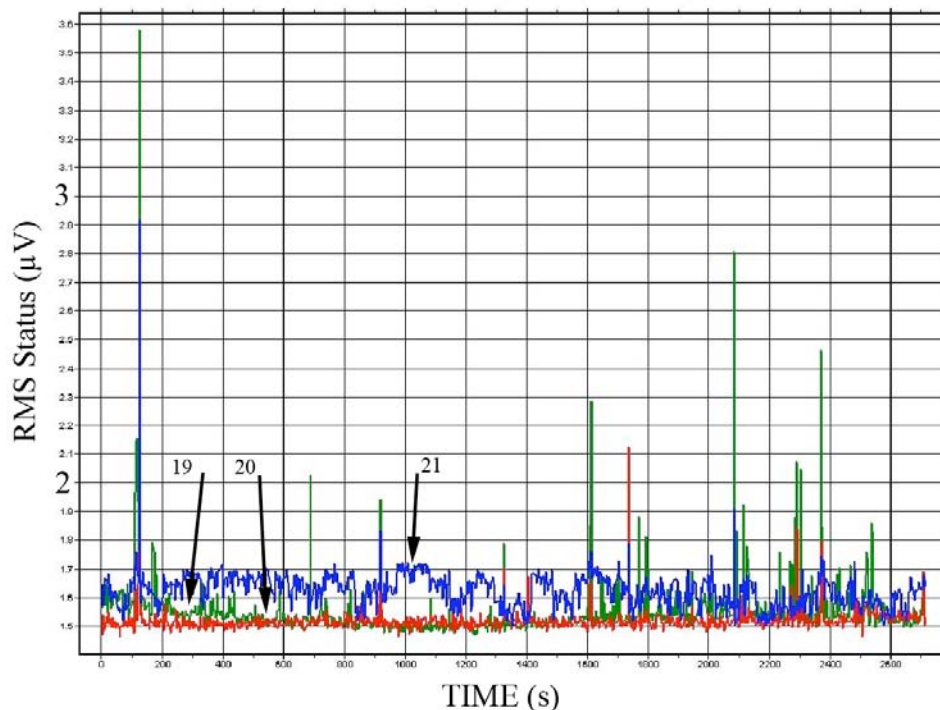


Fig. 6. The graph of RMS value indicating the thinning of wall

Crack in the Weld of the Pipeline

The third case concerns AE monitoring carried out periodically in the time intervals of the pipeline with the wall thickness of 55 mm operated under high pressure of the flowing gas at high temperatures. The aim of using the AE method was monitoring growth of the defect in the welds of the pipeline detected by other NDT methods.

The measurements were carried out under the operating conditions of the pipeline, with the use of waveguides. In order to minimize the noise coming from the flow of the working medium, the measurements were taken at different gas-flow rates in the pipeline. However, the complete stop of the gas flow was impossible. Considering technical reasons, the measurements were carried out at different pressure values.

It was possible to locate the defect despite the loading conditions, a great number and a degree of the operational noise together with the decreased sensitivity due to the use of the waveguides. However, the results of the measurements did not show the full view of the growth of the located defect in the welds. The application of periodical monitoring was not satisfactory enough to determine the time of the safe operation of the installation.

Conclusions

Three cases of using acoustic emission method in testing pipelines in industrial high-pressure installations are reported.

With the necessity of continued operation of an installation with the detected defect, it is useful to apply continuous on-line AE monitoring to detect the degree of the growth of the defect.

Examination under the pressure test preceding the continuous monitoring provides information concerning the character of AE signals and helps the further evaluation of the growth of the defect under the operating conditions.

AE examination under the loading conditions with the installation at normal working pressure is capable of detecting the zone with the thinning of walls.

Periodical monitoring carried out under the operational conditions at high degree of noise did not give sufficient information on the located defect necessary to assure safe operation of the installation.

References

1. M. Wevers, G. Van Dijck, W. Desadeleer, M. Winkelmanns, K. Van Den Abeele, Acoustic emission for on-line monitoring of damage in various application fields, Proc. EWGAE, DGZfP 2004.
2. P.T. Cole, Continuous Remote Monitoring Using AE, Proc. ECNDT 2006.
3. P.T. Cole, T. Bradshaw, AE signals from process monitoring, EWGAE 2004.
4. EN 14584: 2005 *Non-destructive testing – Acoustic emission – Examination of metallic pressure equipment during proof testing – Planar location of AE source.*

UNIQUE AE TESTING APPLICATIONS

CLAUDIO ALLEVATO

Stress Engineering Services, Inc., Houston, Texas, USA

Abstract

Commercial applications of conventional acoustic emission (AE) in the USA focus on assessing the structural integrity of pressure vessels and tanks. Even though there is a wide variety of newly developed advanced non-destructive techniques supporting these assessments as an alternative to AE, the variety of situations under which AE can be helpful continue to expand. This presentation aims at illustrating some new applications of AE on our historically pressure vessel oriented focus.

Keywords: Pressure vessels, conventional AE, alternative techniques

Introduction

Industrial applications of AE testing have, in the past, been concentrated on evaluating a pressure vessel, a piping section, a tank, etc., for the presence of active crack-like discontinuities. Some evaluations were based upon pressurizing the component to slightly higher than normal operating pressure levels. Other evaluations included monitoring during distinct types of loadings, such as liquid filling, and thermal gradients (cool-downs and/or heat-ups).

During the execution of these AE inspections, the aim was to correlate AE parameters with internal pressure and/or temperatures. Departure from a linear behavior would trigger closer scrutiny of the incoming data, as it is believed exponential behavior may be an indication of the presence of a “critically intense source” [1].

As industrial installations aged and damage mechanisms had time to develop, owners/operators faced the challenge of maintaining aging facilities, with known damage mechanisms, operating for longer than anticipated periods of time. Over the last two decades, special demand has been placed on the AE method. AE monitoring has been charged with monitoring existing damage in order to maintain a component in service, typically until a turnaround. This type of AE monitoring is focused at determining if existing indications and discontinuities are growing under certain circumstances.

A Historic Perspective

Traditional applications of AE testing aimed at determining if active discontinuities could be detected and located, under a certain loading condition. Conventional non-destructive examination (NDE), such as ultrasonic testing, magnetic particle, radiography, dye penetrant, etc. were applied as complementary NDE charged with identifying and sizing the active AE indications. In special cases, more “advanced” NDE methods such as automated ultrasonic testing (AUT) were brought in.

As NDE techniques evolved and new methodologies were developed and made available, many from aerospace and military applications, there is a wider range of advanced NDE techniques today. The list of available advanced NDE techniques include (but are not limited to), time-of-flight-tip diffraction (TOFD), phased array (PA), EMAT, alternating current field method (ACFM), long-range ultrasonics, real-time radiography, etc.

Owners/operators of pressure vessels, piping systems, or other components subjected to possible damaging mechanisms leading to catastrophic failure have a wider range of possible NDE methods at their disposal today, compared to 20, 10 or even 5 years ago.

New Challenges for AE Testing

It has become a common place for maintenance and reliability professionals to investigate which NDE techniques offers the best “cost benefit” ratio and delivers the expected results. Each NDE method still exhibits limitations, despite the fact that many are very powerful detection and sizing techniques.

In our experience over the last 10 years, AE has been charged with a new set of expectations. AE has been asked to execute a number of special monitoring, under certain conditions, which differ from the traditional, global screening for “crack-like detection and location” approach.

One of the most challenging applications being discussed is the on-line monitoring of existing through-wall crack-like flaws. These flaws are through-wall because there is a confirmed leak, visible by means of vapors/product emanating from a “weep hole” (tell-tale hole) in reinforcement plates (repads) around nozzles. The exact position and dimensions of the flaw is normally not known in detail. Reliability managers desire to use an NDE technique, which is capable of determining if the flaw is growing (primarily in length in this case) in order to manage the risk. The risk is related to the possibility of the flaw growing to a size, which could lead to loss of containment outside the “repad”. As an example, Fig. 1 illustrates a large diameter “manway” nozzle, which failed during a Vacuum Unit’s start-up for lack of a “tell-tale hole”. The failed repad was repaired, but a leak developed afterwards, which prompted an on-line AE monitoring of the region.



Fig. 1. View of a failed repad on a vacuum tower manway, prior to repair and AE monitoring.

In this case, AE is charged with a continuous monitoring of the “repad” area under normal operating conditions. The objective is to detect and locate AE signals, which are indicative of

possible “crack growth”. The difficulty is, obviously, to correlate the attributes of the AE signals with how much growth is being detected. One approach is to monitor certain AE parameters, and observe their behavior over time for exponential increases in some attributes. The frequency of occurrence of certain AE attributes is an indication of whether or not the existing flaw is growing at a stable rate, or if it is accelerating. The owner/operator is aware of the limitations of this type of AE monitoring, but their options are extremely limited, as far as other NDE methods.

AE’s capabilities of monitoring a remote location continuously and reporting departures from stable or accelerating “crack growth”, are of great value to the equipment’s owners faced with this situation. Figure 2 illustrates a typical remotely installed AE system, inside a purged box.

The challenges faced by AE in this type of application are many. Signal discrimination, background noise management, data transfer, long-term reliability of the hardware, weather, safety issues, and commercial issues are the most important, amongst others.



Fig. 2. Typical field installation of an AE system inside a purged box, with an Intranet connection for data transfer.

Monitoring repairs for existing through-wall cracks has produced a number of successful results, and many are under way today. Whether the existing crack(s) was(were) caused by an internally driven damage mechanism such as caustic stress-corrosion cracking, or caused by vibration-induced fatigue cracking, this type of AE monitoring deals with a known crack-like flaw in a specific region of the component.

A much more complex scenario develops when the owner/operator desires AE to monitor large components aiming at detecting a specific damage mechanism, without prior knowledge of where it could develop. This situation is typical of an operating unit, in which a significant flaw may have caused a loss of containment (leak). In some cases, the flaw may have been repaired and in other cases the situation may have been mitigated by using some sort of mechanical reinforcement or containment, designed to allow the through-wall crack to remain in place, even if it develops all the way around the circumference of the vessel. These reinforcing devices/plates are designed specially for this purpose, according to existing ASME procedures. Figure 3 illustrates a typical refining unit with an on-line monitoring of a flawed nozzle.

The damage mechanism, which caused the development of the flaw in the first place, is still present nevertheless. The charge for the AE monitoring is, therefore, to determine if there are indications of similar flaws developing at other locations in the component. In addition to the challenges listed in the previous application where a small region is being monitored by a relatively small number of AE channels, this type of AE application has to deal with a relatively large number of AE channels monitoring a large area/volume.



Fig. 3. Scaffolding access to a location in a process tower, where a flawed nozzle is being continuously monitored.

Most of these applications involve high temperature, thus welded stainless steel waveguides are used for coupling piezoelectric transducers to the part. Some of these applications are located thousands of miles from the service provider's head office, so reliable data transfer is very relevant.

Figure 4 illustrates two pressure vessels and piping headers, which are being monitored continuously with AE, aiming at detecting and locating environmentally-assisted damage mechanisms. The advantages of using AE in these situations are very clear. No other NDE methodology could provide this type of information reliably. Monitoring an area of a component, hidden behind reinforcement plates, under normal operating conditions, cost-effectively for 24 hours a day, 7 days a week is almost impossible with available conventional or even advanced NDE methods. This advantage becomes even more impressive if the entire component is to be monitored, searching for early stages of a damage mechanism, which could lead to (another) loss of containment. Current Federal and State Environmental and Safety Regulations (OSHA and EPA) drives the interest of using on-line AE monitoring for significant crack-like flaws, when cost effective and applicable.

Figure 5 shows an overhead piping system being continuously monitored with AE for detection of mechanically induced fatigue cracks.

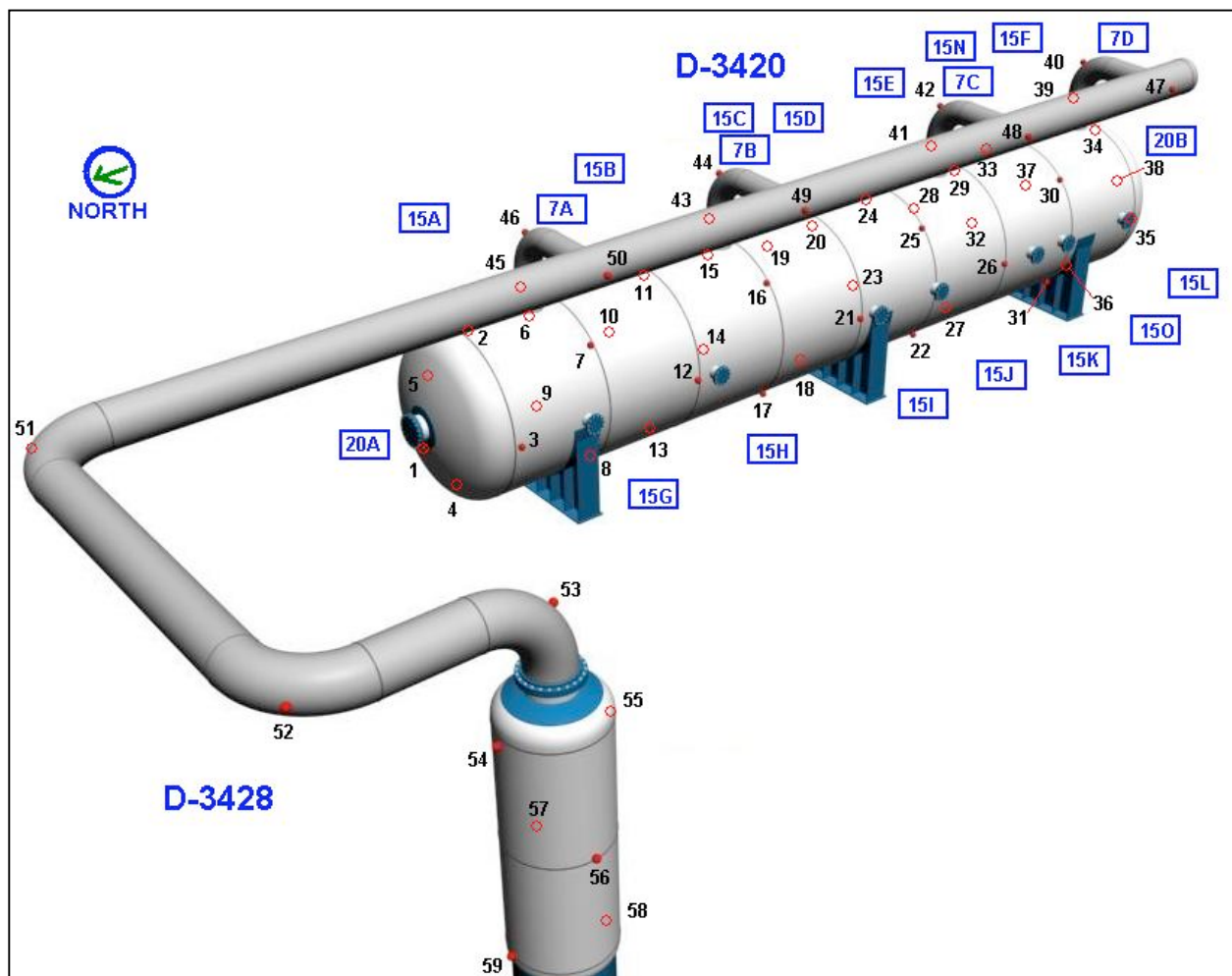


Fig. 4. Two steam drums and a section of a piping header being continuously monitored with AE, for internally driven damage mechanisms.

Conclusions

In the past, conventional AE testing was charged with relatively simple tasks. Established testing procedures allowed AE to develop a good reputation as an alternative to internal inspection of pressure vessels. However, other NDE testing methodologies developed and external inspection at relatively high speeds provided detection and sizing simultaneously. A wider than ever variety of alternative non-destructive testing techniques is currently available to reliability and maintenance professionals throughout the world.

AE monitoring is also evolving, and despite the continuing use of AE as a global inspection technique to avoid vessel entry, new applications are demanding AE to provide a new set of deliverables.

On-line monitoring of components exposed to risks associated with certain damage mechanisms offers AE an unique opportunity to serve facilities around the world in a new way.

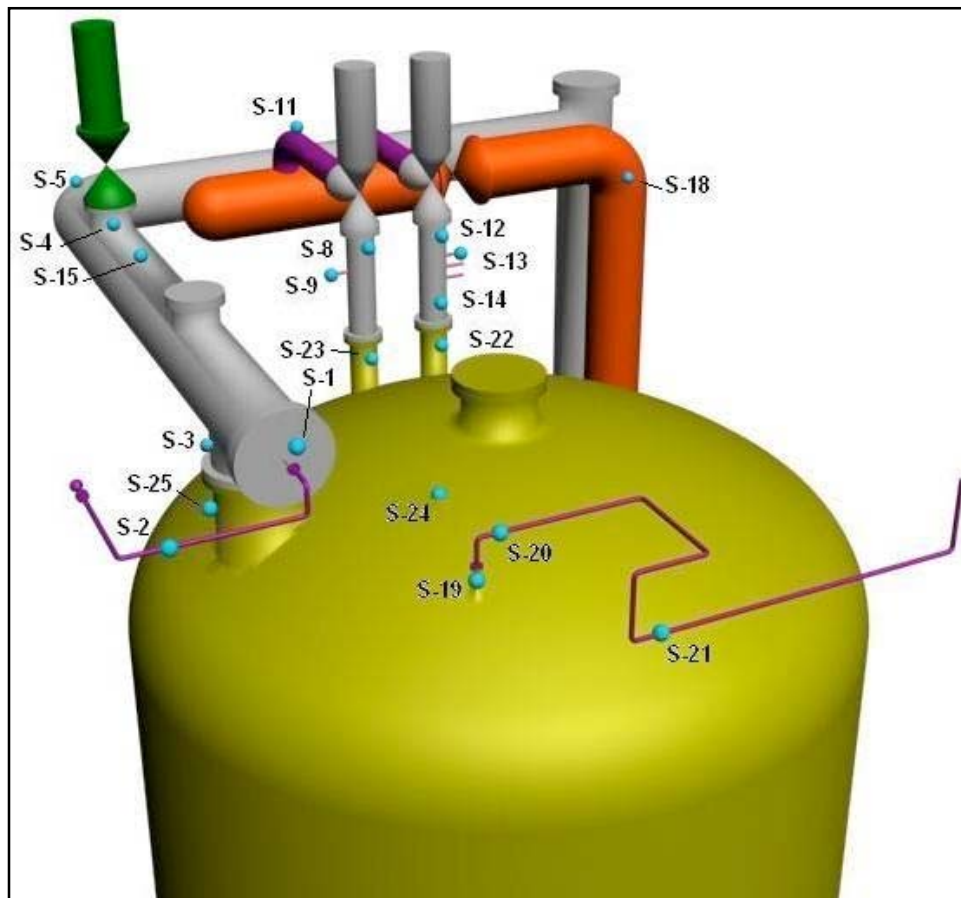


Fig. 5. An overhead piping system being continuously monitored with AE for detection of mechanically induced fatigue cracks.

Reference

1. ASTM E 569-97 – Standard Practice for acoustic emission monitoring of structures during controlled stimulation

NOVEL ACOUSTIC EMISSION SOURCE LOCATION

**RHYS PULLIN, MATTHEW BAXTER, MARK EATON, KAREN HOLFORD
and SAM EVANS**

Cardiff School of Engineering, The Parade, Newport Road, Cardiff, CF24 3AA, UK

Abstract

Source location is possibly the most attractive aspect of acoustic emission (AE) monitoring. Source location relies on the ability of several sensors to detect an AE event and locate the event using simple triangulation methods based on the time of arrival of the fastest propagating wave mode. Two assumptions are made in any source location calculation; the wave speed remains constant and that there is a direct path between sensor and source. This is rarely the case with many structures containing change in thicknesses, resulting in changes in propagation velocity and discontinuities, such as lugs or cut-outs, that alter propagation paths.

A novel technique, Delta-T mapping, that overcomes the problems of thickness changes and discontinuities has been developed. An outline of the novel technique and the results of two fatigue investigations, one with complex propagation paths and a further specimen with thickness changes are presented. Both investigations demonstrated that the Delta-T mapping is vastly superior to the current TOA technique.

Keywords: Source location, Delta-T mapping, fatigue fractures, complex geometries

Introduction

Source location is possibly the most attractive aspect of acoustic emission monitoring. If the location of an event is known, the number of possible source mechanisms is reduced as only certain mechanisms are associated with particular geometric features and conditions. In addition, identifying the location of an AE event can allow other non-destructive evaluation (NDE) techniques, such as dye penetrant or ultrasound, to be utilised.

Current source location techniques rely on the ability of several sensors to detect an AE event and locate the event using simple triangulation methods based on time-of-arrival (TOA) of the fastest propagating wave mode [1, 2]. However these source location methods are based on two assumptions; that wavespeed remains constant from source to sensor and that there is a direct wavepath between source and sensor.

When considering plate waves, invariably the case in bridges, pipes, pressure vessels and aerospace landing-gear modules, the velocity is dependant on thickness of the plate it is travelling in, meaning that wave velocity throughout a structure of changing plate thicknesses, will rarely be uniform. Furthermore, in composite structures wave velocity varies with the angle of propagation depending on the direction of travel when compared with composite lay-up. In addition, geometric features such as holes, lugs and structural discontinuities, often seen in real structures, can dramatically alter the wavepath.

These assumptions introduce errors in a source location measurement. In simple cases, these problems can be overcome with expert knowledge, assessment of wavepaths and intelligent sensor locations. However, these are estimations and cannot provide accurate results.

Recent methods aimed at improving the accuracy of the source location technique by alleviating the problems inherent in selection of a single wave velocity include modal analysis, a method based on energy attenuation and acoustic tomography.

Single-sensor source location [3, 4] relies on the measurement of the time difference between the arrivals of the two primary modes. However, it requires a detailed understanding of the dispersive nature of AE signals, and user a determination of the arrival times of the two modes, which can be open to interpretation. Furthermore, the arrival of the lower-amplitude, faster-propagating S_0 mode needs to be captured and visible when compared with background noise.

The use of energy attenuation has been investigated by Nivesrangsan et al. [5]. The methodology follows TOA, location replacing time difference with energy difference and wave velocity with an attenuation coefficient. However, as this method is based on the same principals as TOA source location, similar error sources apply.

A further method based on computerised tomography (CT) that was developed for medical applications has been presented by Schubert [6] and utilised algebraic reconstruction techniques (ART). The method is as follows

- Set up an array of sensors around an area of interest.
- Divided the area into a grid, with each grid square assigned an initial wave velocity.
- Conduct a series of simulated events, either by pulsing each of the sensors or by generating events within the grids.
- Use the known wavepath and elapsed time from source to sensor to re-evaluate the wave velocity assigned to each of the grid squares that the wavepath intersects using algorithms such as ART.
- Repeat the previous step until the wave velocity in each grid space has suitably converged. It is possible to use the wave velocity map to accurately locate and future events.

Any geometric features, such as holes, will cause an altered wave velocity to take account of the change in wavepath. However, in a further paper [7], results using this technique from an aluminium plate with a saw cut were presented. The array used was unable to detect the cut until it intersected at least one of the wavepaths between sensors, a possible disadvantage of this method.

Delta-T Source Location

In this paper, a novel method of source location, Delta-T, where an AE location array is mapped with an Hsu-Nielsen (H-N) source at known positions is presented. A more detailed description of the Delta-T technique can be found in [8]; however, a summary of the technique is provided below in five steps:

- *Determine area of interest.* Though Delta-T source location can provide complete coverage of a part or structure, it is best employed as a tool to improve source location around specific areas of expected fracture, which could be identified via finite element modelling.
- *Construct map system.* A grid is placed on the component over the area of interest and within which AE events will be located; the higher the resolution of the grid the greater the accuracy. It is possible to increase the resolution of the grid around features of interest; however, it should not be smaller than one wavelength, as this is the minimum location resolution. It should be noted that sources are located with reference to the grid and not the sensors.
- *Apply artificial source events to obtain time-of arrival data.* Artificial sources [9, 10] conducted at the nodes in the grid provide AE data for each sensor. Several sources at each node are required to provide an average result and to eliminate erroneous data. It is not essential to have AE data from every node in the grid because missing data points can be interpolated from surrounding nodes.

- *Calculate Delta-T Map.* From each artificial source, a difference in time of arrival or Delta-T is calculated for each sensor pair (an array of four sensors has six sensor pairs). The average Delta-T for each sensor pair at each node is stored in a map. These maps can be displayed as contour plots of equal Delta-T.
- *Compare Actual Data.* To locate an actual AE event, the Delta-T for each pair is calculated. A line or contour on each map corresponding to the calculated Delta-T can be identified. By overlaying results from each of the sensor pairs, a convergence point can be identified; the source location. As with time of arrival, a minimum of three sensors is required to provide a point location and more sensors will improve the location. In theory all lines will intersect at one location. However, in reality, this is not the case. Therefore, to estimate the source location, all of the convergence points can be calculated and a cluster analysis can be conducted on the points to determine the final location.

This paper presents two case studies demonstrating the developed novel source detection method.

Experimental Procedure

Figure 1 shows two fatigue test specimens, one with a variety of holes to interfere with direct wavepaths from source to sensor and another specimen with changing thicknesses to affect propagation velocities.

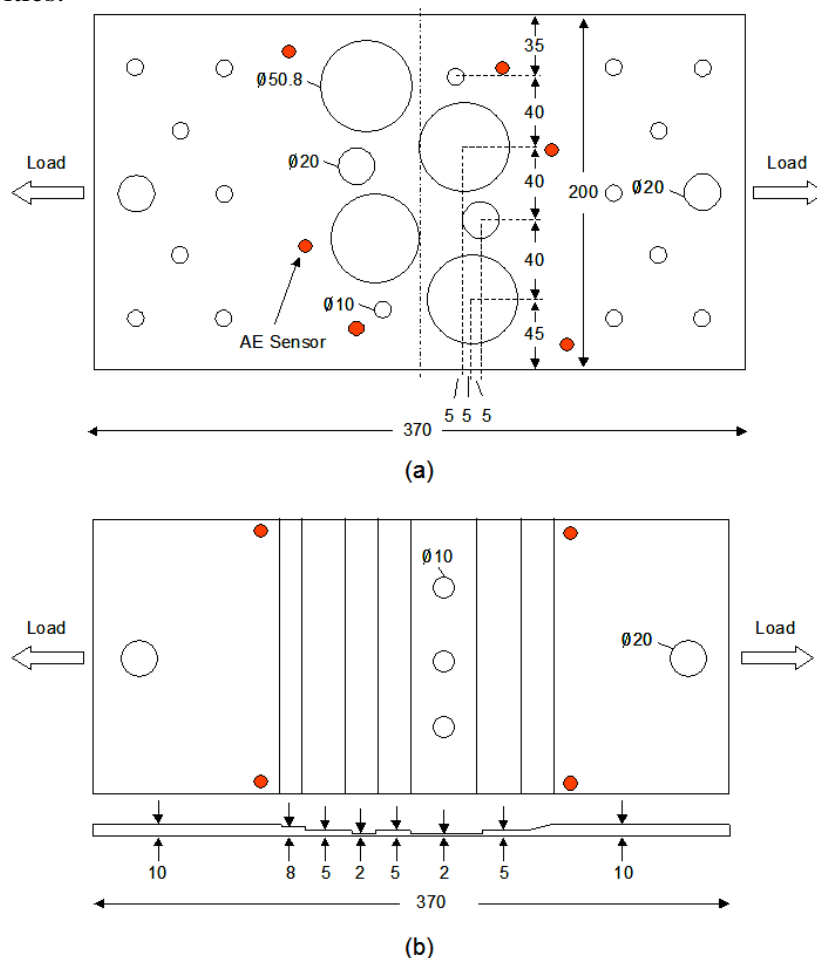


Fig. 1. Specimens for validation of developed source location technique. (a) Disruption of source to sensor propagation path; (b) Thickness change resulting in changes in propagation velocity (all dimensions in mm).

The specimen with numerous holes was made from 3-mm mild steel plate, but plate thicknesses were increased to 9 mm at the loading pins by the addition of two extra plates bolted to either side of the plate, to avoid failure at the loading pins. Physical Acoustics Limited (PAL) resonant sensors were mounted to the plates (as shown in Fig. 1 by filled circles), grease was used as an acoustic couplant and the sensors were held in position with magnetic clamps. The sensitivity of the mounted sensors was evaluated using the H-N source technique.

A 180 x 130 mm grid with a grid density of 10 mm and a 140 x 160 mm with a grid density of 20 mm were selected for the specimens with holes and steps, respectively. Five H-N sources were conducted at each available node to form the Delta-T grids. The specimens were fatigued under a load of 3.5 to 35 kN until failure. All AE feature data was recorded using a PAL MIS-TRAS system.

Results and Discussion

Response of all sensors to the H-N source was above 98 dB, demonstrating that all sensors were mounted correctly. A wave velocity for the first threshold crossing was determined as 4500 m·s⁻¹ in both the steel and composite specimens, and used for all TOA source-location calculations. The data from the H-N source events was used to create the Delta-T contour maps, as discussed previously. It is possible to create similar, theoretical maps for TOA using the above first threshold crossing wavespeed. Figure 2 displays a comparison between the Delta-T and TOA source location maps, for one sensor pair, for both specimens. By examining the Delta-T map, it is evident that the wavepaths are interrupted by the holes and to a lesser degree the change in thickness in the plates, which will cause errors in any source location calculation.

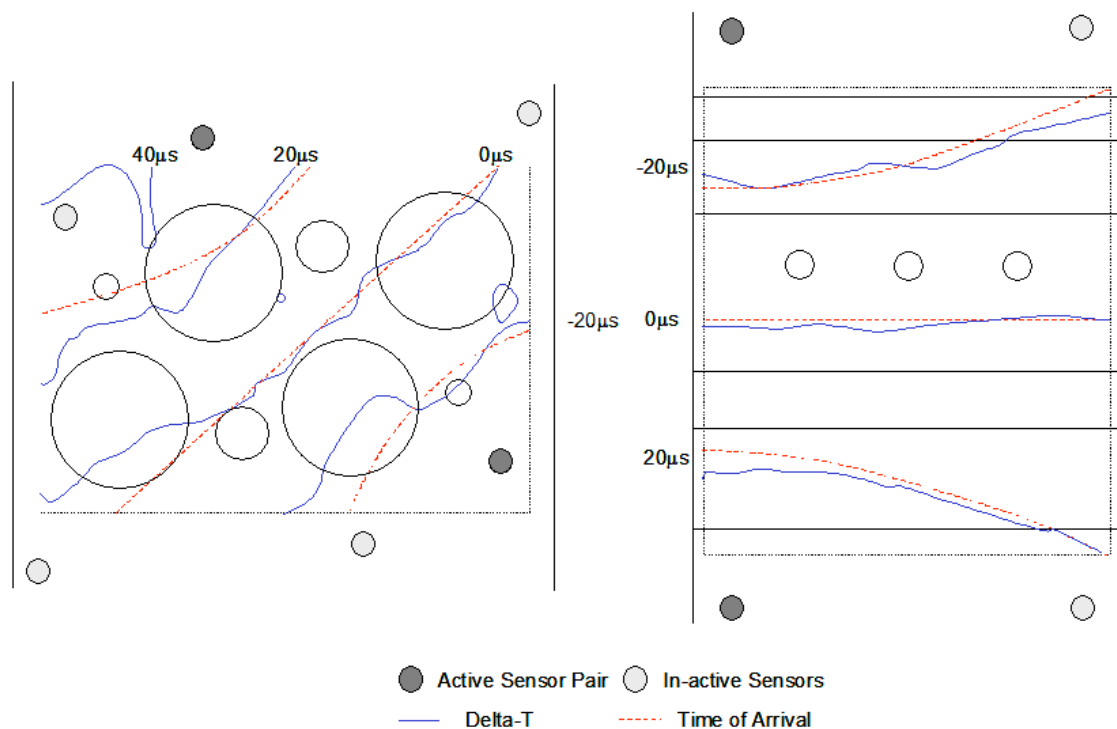


Fig. 2. Example of Delta-T source location maps for both specimens

Figure 3 shows a comparison of the TOA with the Delta-T location techniques of the detected signals for both specimens. The specimen geometry and the site of fracture initiation have been superimposed. The plots demonstrate how the Delta-T technique shows significant

improvement. In the specimen with holes, the TOA results (Fig. 3a) show four peaks of activity of above 70 events, whilst the Delta-T plot has only one such peak. Furthermore, the position of the peak cluster is much closer to the position of fracture. Figure 3c shows the TOA plot for the change-in-thickness plates. It can be seen that there is no single peak in close proximity to the fracture region whilst the Delta-T technique clearly identifies the fracture position, although it is not the peak of events.

Based on the location of the initiation of fracture and the closest peak cluster, the TOA and Delta-T techniques show errors of 15.5 and 8.0 mm, respectively, for the plate with holes, demonstrating a reduction in error of 48%. It is not possible to determine an error for the step plate as there is no cluster in reasonable proximity that could be defined as coming from the fracture.

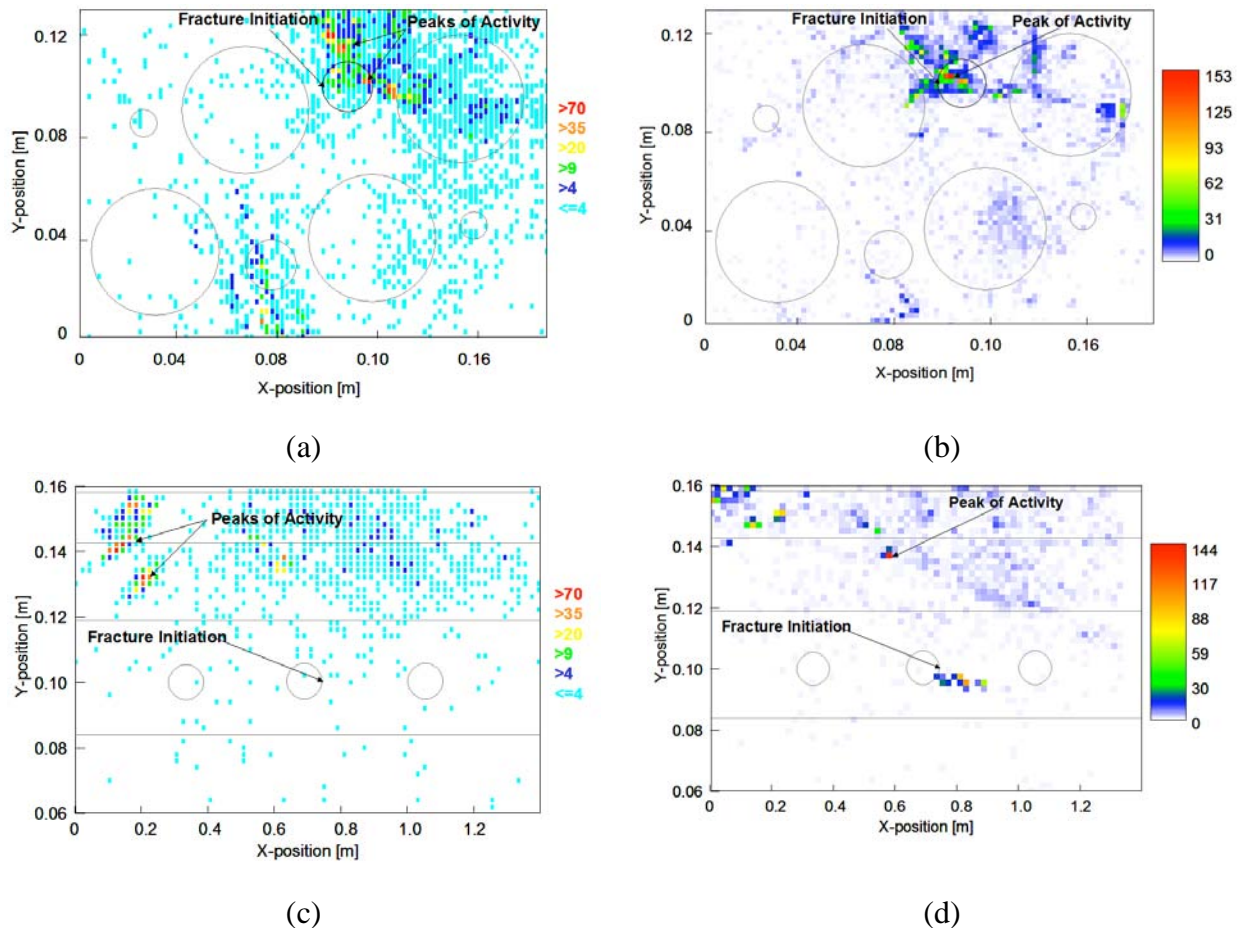


Fig. 3. Comparison of source location results from specimen with disruption of source to sensor propagation path. (a) Time of arrival, the specimen with holes; (b) Delta-T technique, the specimen with holes; (c) TOA, the specimen with steps; (d) Delta-T technique, the specimen with steps.

A further advantage of the Delta-T technique is that it has tighter source clusters. This can be seen when comparing the cluster sizes in Fig. 3a and b. Using the TOA technique (Fig. 3a) there are four clusters of >70 events whilst the Delta-T technique has only one cluster of >140 events. This suggests that if a spatial cluster were to be used as an indication of developing damage, the Delta-T method would identify it earlier.

Conclusions

Delta-T source location provides a novel approach for overcoming particular problems associated with source location in complex structures with some current techniques (TOA and Modal Analysis)

The completed fatigue investigations where there was a complex source to sensor propagation path and a change in propagation wave velocity have demonstrated that the Delta-T mapping technique is superior to the current TOA technique.

Acknowledgements

The authors wish to acknowledge the funding of this work by Messier-Dowty, the leading manufacturer of landing gears and landing gear components, and EPSRC. In addition, the technical support of Physical Acoustics Limited is acknowledged.

References

- [1] Miller, R. K. and McIntire, P. (1987). "Acoustic Emission Testing", *NDT Handbook*, Volume 5, American Society for Non-destructive Testing: p. 652
- [2] Rindorf, H. J. (1981). "Acoustic Emission Source Location in Theory and in Practice", *Bruel and Kjaer Technical Review*, **2**: 3-44.
- [3] Pullin, R., Holford, K. M. and Baxter, M. G. (2005). "Modal Analysis of Acoustic Emission Signals from Artificial and Fatigue Crack Sources in Aerospace Grade Steel", *Key Engineering Materials*, **293-294**, 217-224.
- [4] Holford, K. M. and Carter, D. C. (1999). "Acoustic Emission Source Location" *Key Engineering Materials*, **167-168**, 162-171.
- [5] Nivesangsan, P., Steel, J. A. and Reuben, R. L. (2005). "AE Mapping of Engines for Spatially-Located Time Series", *Mechanical Systems and Signal Processing*, **19**, (5), 1034-1054.
- [6] Schubert, F. (2004) "Basic Principles of Acoustic Emission Tomography" *Proc. 26th European Conference on Acoustic Emission Testing*, Berlin, Germany, vol. 2, pp. 693-708.
- [7] Schubert, F. (2006). "Tomography Techniques for Acoustic Emission Monitoring" *European Conference on Non-destructive Testing*, Berlin, Germany.
- [8] Baxter, M. G., Pullin, R., Holford, K. M. and Evans, S. L., (2007). "Delta T Source Location for Acoustic Emission" *Mechanical Systems and Signal Processing*, **21**, (3), 1512-1520.
- [9] ASTM, (1994). Standard guide for determining the reproducibility of acoustic emission sensor response, American Society for Testing and Materials, E 976
- [10] N.N. Hsu and F.R Breckenbridge, (1979). Characterization and Calibration of Acoustic Emission Sensors, *Materials Evaluation*, **39**, 60-68.

FUNDAMENTAL STUDIES OF SIGNAL STRENGTH AND SOURCE LOCATION USING SIMULATED AE SOURCES PRODUCED IN MODEL CORROSION PITS PLACED ON THE BOTTOM PLATE OF AN ABOVE-GROUND TANK

SAYURI MURAKAMI, RYO OGAWA, TAKUJI KOIKE,
MINORU YAMADA¹, SHIGENORI YUYAMA² and KYOJI HOMMA

Department of Mechanical Eng. and Intelligent Sys., The University of Electro-Communications, 1-5-1 Chofugaoka, Chofu, Tokyo, 182-8585 Japan; ¹National Research Institute of Fire and Disaster, 4-35-3 Jindaiji-higashi, Chofu, Tokyo 182-8508, Japan; ²Nippon Physical Acoustics Ltd., 2-17-10 Okamoto LK Bldg., Higashi, Shibuya, Tokyo 150-0011, Japan

Abstract

Present study reports effect of pit depth on AE signal strength due to the fracture of corrosion products or debonding of scales. AE signal strength detected in steel specimens with and without corrosion products was investigated by three-point bending tests. The results show that strong AE signals are generated in the specimen with corrosion product. Experiments to investigate effect of pit depth were performed using steel plates with holes mechanically drilled in two different sizes of remaining thickness, simulating corrosion pits. Signal strength detected by AE sensors placed on side plate of a tank depends on the remaining thickness because of the signal attenuation during propagation from the pit bottom to the plate surface. In addition, AE source location using a neural network was conducted by the use of artificial AE signals generated by pencil-lead breaks on the pit bottom. It was shown that the accuracy of the source location is independent of the signal strength in terms of amplitude, even if S/N ratio decreases to 20 dB.

Keywords: Corrosion, above-ground tank, neural networks

Introduction

Development of techniques to evaluate corrosion damages of bottom and annular plates (floor conditions) in above-ground tanks is urgently needed to protect the environment from contamination caused by leakage of hazardous products due to corrosion. Time-based maintenance has been legally required in Japan for tanks with a storage capacity greater than 1,000 kL. Tanks are opened and thickness data based on discrete point measurements is collected in time-based maintenance. However, localized thickness losses are difficult to find and assess. Pits due to corrosion should reduce the thickness locally and may result in leakage.

Acoustic emission (AE) testing based on a database collected with established test procedures and evaluation criteria has been widely used in the world as a standard test method for the evaluation of floor conditions in above-ground tanks in service. Since the early 1990's, a database on AE evaluation has been developed in Europe by opening and inspecting tanks after AE testing in order to evaluate tank bottom conditions [1]. The test procedure was introduced to the Japanese industries in 1999. Since then, an AE database for data evaluation has been developed to meet the Japanese regulation for tank maintenance. So far, the relationship between AE activity and the corrosion risk parameter (CRP) has been investigated, and a recommended practice has been issued by the High Pressure Institute in Japan [2].

There are two possible AE sources during the corrosion processes on the bottom of above-ground tank. One is hydrogen gas evolution in an acidic atmosphere, and the other is fracture of corrosion products. If chloride ions are present in the soil, the undersurface of the tank bottom becomes gradually acidic and corrosion is accelerated locally on the tank bottom [3-5]. Park et al. studied AE due to the hydrogen evolution generated by corrosion in an acidic atmosphere and confirmed that active corrosion under low pH conditions can be detected by using AE technique. They found a significant correlation between AE activity and corrosion rate [6]. However, AE due to the fracture of corrosion products has not been extensively studied so far [7]. Furthermore, the effect of remaining thickness on the signal strength detected by AE sensors placed on side plate of the tank has not been studied.

In the present study, AE signal strength detected in steel specimens with or without corrosion products has been investigated by three-point bending tests. Experiments to evaluate the effect of pit depth have been performed by using steel plates (150 x 100 x 6 mm) with holes mechanically drilled in two different sizes of remaining thickness, simulating corrosion pits. In addition, AE source location using the neural network, previously proposed by the authors [8-10], has been conducted by the use of artificial AE signals generated by pencil-lead breaks on the pit bottom.

Materials and Methods

AE measurement during the three-point bending test

Corrosion taking place on the internal or external surface of a tank bottom is a very serious problem of tanks in service. As corrosion progresses, the volume of corrosion products expands due to corrosion reaction. The layers of corrosion products are heavily loaded because of the weight of the tank and stored products. Fracture of corrosion products or debonding of scales should occur as corrosion progresses and produce AE.

In the present study, three-point bending tests are conducted to generate fracture of corrosion products, producing AE. AE signal strength detected by AE sensors are compared between steel specimens (60 x 300 x 5 mm) with and without corrosion products. A specimen without corrosion product and two specimens with corrosion product (corrosion specimen 1 and 2) were prepared for the tests. Note that the specimens with corrosion product were cut out from bottom plate of a tank out of service.

Instron 4505 tensile machine was used in the three-point bending tests. The span length was 230 mm. A PAC R3I AE sensor (resonant frequency: 30 kHz) was used, considering its use in field applications. The sensor was mounted on the specimen with a magnetic holder at the position 50 mm from a loading point. The specimen was loaded until the displacement due to loading was 10 mm.

AE measurement using an above-ground tank

An above-ground tank (out-of-service) was prepared by Japan Energy Corporation. Diameter, height, capacity, thickness of the bottom and side wall were 7.60 m, 7.43 m, 300 kL, 6 mm and 8 mm, respectively. Water was placed to 45 cm in height to insure the propagation of longitudinal AE waves (P-waves) in water. Four AE sensors (every 90°) were mounted with magnetic holders on the sidewall of the tank at the position 0.35 m from the annular plate. Couplant (silicone grease) was placed between the sensor surface and the tank surface to insure a good contact for wave transfer. AE equipment (μ DISPTM, PAC) was used to record AE signals detected by the AE sensors.

Model corrosion pit

A typical corrosion pit observed on the bottom plate of a tank is shown in Fig. 1. It causes localized thickness losses very rapidly, and may result in leakage. Model corrosion pits (8 mm in diameter) were made on steel plates (150 x 100 x 6 mm) by drilling. Pits with two different sizes of remaining thickness (ligament) were made, simulating different pit depth. The remaining thickness of the plate was 5 and 3 mm, respectively. The steel plates with the model pits were placed at 12 locations on the internal surface of the bottom plate of the tank filled with water. The locations are shown in Fig. 2. Note that a plastic cylinder was placed between the plate with the pits and the tank bottom such that an air layer prevented wave propagation from under the plate. Artificial AE sources due to the pencil-lead breaks were generated on the bottom of the pit.

AE waveform analysis and source location

To investigate effect of the remaining thickness on detected signal strength in terms of AE amplitude on the bottom plate of the tank, RMS voltage amplitude of artificial AE signals due to pencil-lead breaks were compared. 2H and 2B pencil-leads were used to generate artificial AE signals.

In the proposed AE source location using a neural network (NN) [8-10], a multilayer feed-forward NN trained by a back-propagation algorithm was used and a sigmoidal function was applied as the activation function of each node. Preliminary experiments were conducted to find suitable network architecture. The NN consists of four input nodes corresponding to arrival time differences at each sensor and two output nodes corresponding to locations on the bottom plate of the tank. Hidden nodes and layers were empirically set to 5 and 4, respectively. Arrival-time differences between different sensors were calculated by using theoretical wave velocity and the distance. The network was trained by the normalized time differences resulting from theoretical calculation and normalized two-dimensional coordinates.

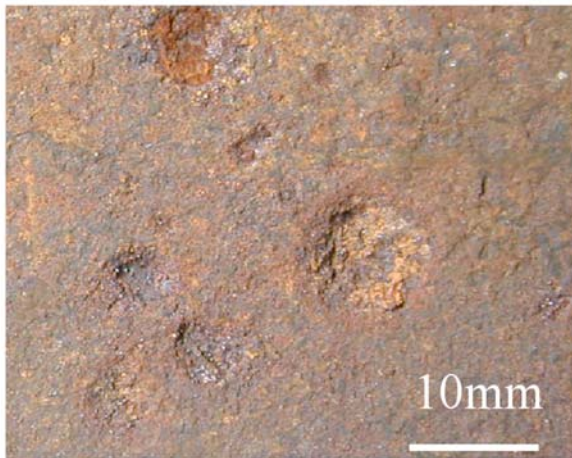


Fig. 1 Example of corrosion pit.

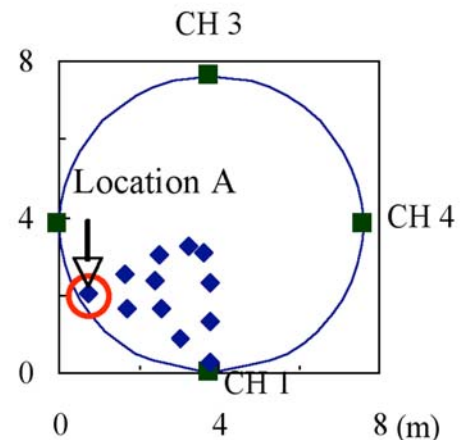


Fig. 2 Locations of steel plates with model pits.

Results and Discussion

Signal strength of AE generated by three-point bending tests

Three-point bending tests were carried out to investigate AE signal strength in both the specimen with and without corrosion product. All AE events detected during the tests for the specimen without corrosion product, corrosion specimens 1 and 2 were 469, 5081 and 5295, respectively. The cumulative numbers of AE events detected in the corrosion specimens were

~10-times greater than that in the specimen without corrosion. The RMS amplitude distribution for all events of each specimen is shown in Fig. 3. These graphs show that the RMS amplitude of AE signals generated from the specimen without the corrosion product are less than 100 mV while those generated in the corrosion specimens include RMS amplitude greater than 100 mV, and the percentages of the larger amplitudes are higher in the corrosion specimens. Debonding of scales was observed after the bending test in the corrosion specimen. The debonding may be the origin of the great AE amplitudes. RMS amplitudes detected in the specimen without corrosion product, the corrosion specimens and those due to pencil-lead breaks (2B) are compared in Fig. 4. The maximum value of RMS amplitude for each specimen is used for comparison. It is shown in the figure that the strength of AE signals generated in the corrosion specimens during the three-point bending test reaches almost the same level as that due to pencil-lead breaks. This indicates that very strong AE signals can be generated in the bottom plate with corrosion product in real tanks.

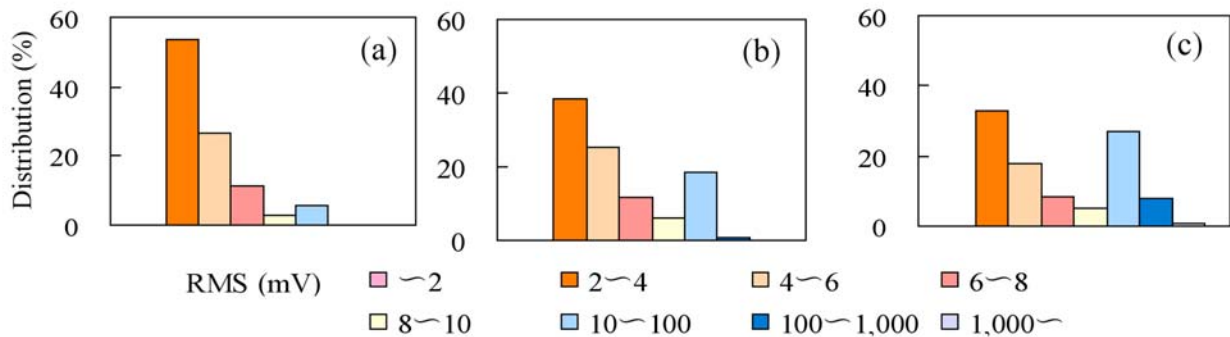


Fig. 3 RMS amplitude distribution for all events (a) Specimen without corrosion product (thickness: 5 mm, total number of event: 469) (b) Corrosion specimen 1 (thickness: 5 mm, total number of event: 5081) (c) Corrosion specimen 2 (thickness: 6 mm, total number of event: 5295).

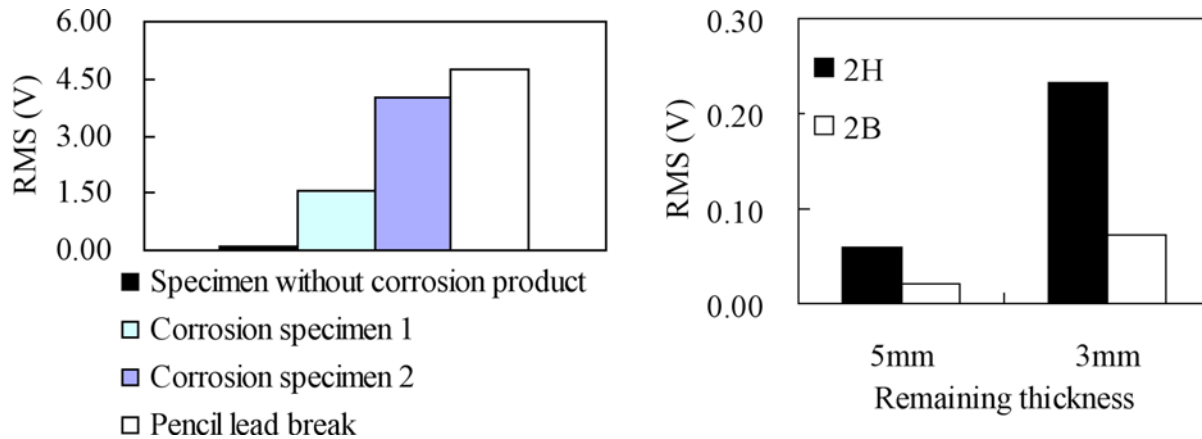


Fig. 4 RMS amplitude of maximum AE generated from each specimen and from pencil-lead breaks.

Fig. 5 Relationship between RMS amplitude and remaining thickness.

Effect of the remaining thickness on AE amplitude

RMS voltage amplitudes due to pencil-lead breaks were compared in order to evaluate the effect of the remaining thickness on the signal strength detected by the AE sensor placed on the sidewall. The pencil leads were broken at a distance of 70 cm from the AE sensor. Demonstrated in Fig. 5 are RMS amplitudes due to two different pencil leads (2H and 2B) for the

different remaining thickness. The remaining thickness demonstrates levels of the corrosion damage. The smaller thickness indicates greater damage. RMS amplitudes due to pencil-lead (2H) breaks inside bottom of the pits show that amplitude for the remaining thickness 3 mm is 3.9 times greater than that for 5 mm, while 3.6 times in case due to pencil-lead (2B) breaks. Thus, it is shown that detected signal strength depends on the remaining thickness, indicating that the greater the remaining thickness, the weaker the detected signals. In other words, it has been shown that the greater the remaining thickness, the greater the attenuation of the AE signal during the propagation.

Attenuation of AE waves in water

Attenuation of P-wave traveling in water has been investigated. Relationship between RMS amplitude and the distance from the source to the sensor is given in Fig. 6. Average RMS amplitudes due to both 2H and 2B leads are shown for the remaining thickness 3 mm and 5 mm. Attenuation of P wave in water is significant if the distance is smaller than 2m. However, the wave hardly attenuates if the distance exceeds 2m. The amplitude ratios of 2 m and 7 m to the 0.3 m are 18.0 % and 10.5 %, respectively in the case of the remaining thickness 3mm, while the ratios are 16.3 % and 12.2 %, respectively in the case of the thickness 5mm. Note that the S/N ratios of 2H and 2B at 7 m were 34.8 dB and 19.5 dB, respectively.

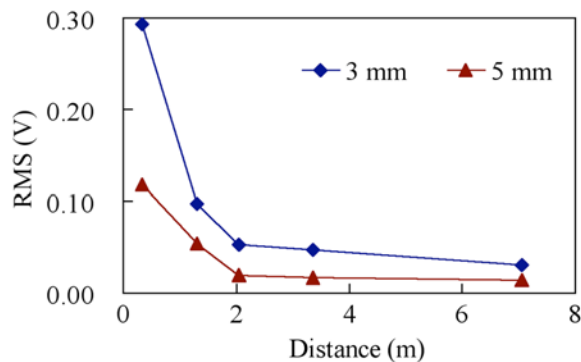


Fig. 6 RMS amplitude as a function of distance.

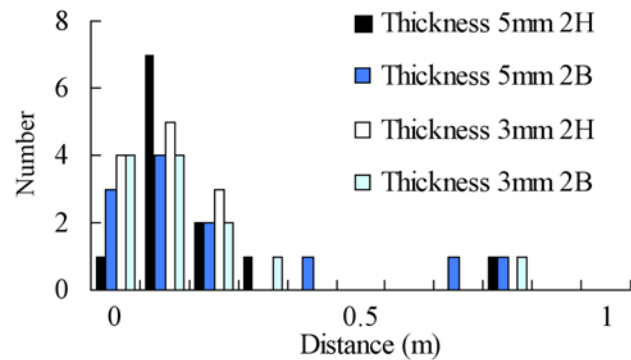


Fig. 7 Distribution of location error from the actual location.

AE source location

Arrival-time differences resulting from theoretical calculation were used as training data for the NN. Arrival times for effective data due to the artificial AE source were obtained from the threshold crossing set at 50% of the peak amplitude of the detected AE waveforms. The distribution of the located events with errors for each 10 cm range is exhibited in Fig. 7. The error average is around 0.3 m in all cases. Note that the maximum error for the remaining thickness 3 mm with 2H lead is 0.26 m, while it is about 0.85 m for other cases. The distance between the AE sources generated at location A in Fig. 2 and the AE sensor (CH 4) is about 7 m. The S/N ratio of the AE waveform due to the pencil-lead break (2B) was 19.5 dB in the test using the specimen with the pit (the remaining thickness: 5 mm). The location error in this case was about 0.3 m. Taking the diameter of the tank (7.60 m) into account, the location error is small enough for identification of the damaged area. In practical use, this accuracy range in source location should be good enough to perform further follow-up inspections for detailed information of the damaged area. Floor-scan inspection, for instance, is usually made for larger areas than this size during internal inspection. From these results, it can be concluded that the influence of signal strength (in terms of amplitude) on the source location error is small even if the S/N ratio decreases to about 20 dB.

Summary

The three-point bending tests found that AE signal strength in terms of RMS voltage amplitude from the specimen with corrosion product is greater than that from the specimen without the product. RMS amplitudes detected by the AE sensor placed on the sidewall of the tank due to pencil-lead (2H or 2B) breaks showed that it is greater when the remaining thickness is smaller. Since AE generated on the bottom of the pit attenuates during the propagation through the remaining part of the plate, signal strength detected by the sensor becomes greater as the remaining thickness becomes smaller. Thus, AE energy emitted into water becomes greater as the thickness becomes smaller. Attenuation of P waves in water is significant if the distance is smaller than 2 m. However, the waves hardly attenuate if the distance exceeds 2 m. S/N ratio of the detected AE signal due to the 2B pencil-lead break at 7 m from the AE sensor was about 20 dB. AE source location analysis leads to the conclusion that the influence of signal strength (in terms of amplitude) on the source location error is small even if the S/N ratio decreases to about 20 dB. It has been shown that AE source due to the fracture of corrosion products or debonding of scales can be located using an NN by an automated reading of the threshold crossing.

References

1. Cole, P. T. and Van de Loo, P. J., *Acoustic Emission-Beyond the Millenium*, Elsevier, 2000, pp. 169-178.
2. Yuyama, S., Yamada, M., Sekine, K., and Kitsukawa, S.: *Progress in AE XIII* (Proc. of 18th Intern. AE Symp.), Japanese Society for Non-Destructive Inspection, Aoyama Gakuin Univ., July 25-27, 2006, pp. 397-404.
3. Katoh, K., Suzumura, H., Ishimoto, H. and Yashiki, T., *Journal of High Pressure Institute of Japan*, **41**, (2), 2003, 55-63.
4. Katoh, K., Kojima, K., Katoh, C., Ishimoto, H. and Yashiki, T., *Journal of High Pressure Institute of Japan*, **42**, (2), 2004, 81-87.
5. Japan Society of Corrosion Engineering, *Corrosion Handbook*, Maruzen, Tokyo, 2002, pp. III-4-1-III-4-5. (in Japanese)
6. Park, S., Kitsukawa, S., Katoh, K., Yuyama, S., Maruyama, H. and Sekine, K., *Materials Transactions*, **46**, (11), 2005, 2490-2496.
7. Kanazawa, M., Cho, H. and Takemoto, M., *Zairyo-to-Kankyo*, **53**, 2004, 489-494. (in Japanese)
8. Maie, A., Homma, K. and Yuki, H., *Transactions of the Japan Society of Mechanical Engineers, Series A*, **65**, **634**, 1999, 1187-1192 (in Japanese).
9. Inaba, A., Homma, K., Murakami, S., Koike, T. and Yamada, M., *Transactions of the Japan Society of Mechanical Engineers, Series A*, **71**, (707), 2005, pp. 1046-1050 (in Japanese).
10. Murakami, S., Homma, K., Koike, T., Yamada, M. and Yuyama, S., *Journal of Solid Mechanics and Materials Engineering*, **1**, (7), 2007, 919-930.

LAMB MODAL REGIONS WITH SIGNIFICANT AE ENERGY IN A THICK STEEL PLATE

M. A. HAMSTAD

University of Denver, Dept. of Mechanical and Materials Engineering, Denver, CO 80208 USA

Abstract

Using a validated finite-element modeling code buried acoustic emission (AE) dipole point sources were operated at different depths below the top surface of a 25.4 mm thick steel plate. For each depth the out-of-plane displacements were obtained as a function of time at propagation distances up to 1016 mm. Modal regions that carried a significant portion of the AE energy were identified. Plots of propagation distance versus arrival times (from wavelet transform maximum values) were used to find group velocities at 102 kHz for either the A_0 or S_0 modes. These velocities were found to be very close to theory values. A method to identify the mode (and group velocity) that led to the wavelet transform maximum at 102 kHz was demonstrated for AE events at an unknown depth that were detected at four sensors in an array.

Keywords: Acoustic emission arrival times, AE dipoles, finite element modeling, wavelet transform, Lamb mode identification, thick plate, accurate location

Introduction

The author and co-workers have published a number of papers on the analysis of finite-element modeled (FEM) acoustic emission (AE) signals in a 4.7-mm-thick aluminum plate [1 - 4]. One focus of this work was the use of wavelet transform (WT) to obtain accurate arrival times of certain frequencies of the two fundamental modes. Since these arrival times were all associated with specific known group velocities, accurate source locations could be calculated for the dispersive AE signals even in the presence of significant electronic preamplifier noise [3].

The purpose of the research reported here was to determine Lamb wave modal regions that exhibit significant energy in a 25.4-mm-thick steel plate using a FEM database. The purpose also included the study of the use of a WT to extract accurate signal arrival times for calculation of source location. A recent publication [5] considered the question of the extraction of arrival times in nominal 15-mm-thick steel by WT. Experimental waveforms from both pressurization-activated sources and pencil lead breaks were obtained with resonant (150 kHz) AE sensors with some success and some difficulties for maximum propagation distances of up to 360 mm.

Finite Element Modeled AE Signal Database/WT Information

To create the FEM database used in this research, an axially symmetric (2D) code was primarily used for propagation distances up to 1016 mm (40 in.). The domain size was large to eliminate edge reflections. Some results with a 3D code were also used [6]. The validations of the explicit finite element codes can be found in published literature [7, 8].

The entire FEM signals were either left unfiltered or numerically processed with a 40 kHz high-pass filter or a 100 to 300 kHz bandpass filter. Subsequently all the signals were resampled to a larger time step of 0.1 μ s/point. The sources with a rise time of 2.3 μ s in the continuous mesh domain were dipoles using the "equivalent body force" concept for displacement discontinuities [9]. The source depths (center of the source) were 1.25, 4.73, 7.72, 10.71 and 12.7 mm. The signal propagation distances were 127, 254, 381 (maximum with 3D code), 508, 635, 762

and 1016 mm. The uniform cell sizes were 0.49 mm or smaller. The AE signals from single nodes provided the out-of-plane top-surface and bottom-surface displacement versus time corresponding to a perfect point-contact sensor (pseudo sensor). The use of bottom surface nodes extended the source depths to 14.69, 17.68, 20.67, and 24.15 mm. WT results [10] were used to enhance the identification of the AE signal Lamb modes and to obtain WT coefficient maximum values at certain frequencies.

Group Velocity Curves for Thick Steel Plate

Group velocity curves for steel [11, 12] are shown in Fig. 1 for the first five symmetric and anti-symmetric modes. It was desirable to consider propagation distances that were fairly large to more easily distinguish modes. To be able to relate the 2D code signal analysis results to in-plane sources, we consider comparisons of the displacement signals from out-of-plane with in-plane dipole sources at a propagation distance of 381 mm in the next section.

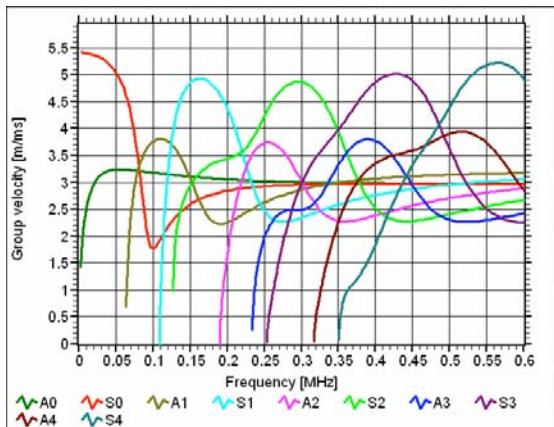


Fig. 1 Group velocities versus frequency for a steel plate of 25.4 mm thickness; first five symmetric and anti-symmetric modes [11, 12].

Modes Excited by Out-of-Plane and In-Plane Buried Dipoles

Figures 2 and 3 respectively show WT results for an out-of-plane and an in-plane (both 3D code) buried dipole at a depth of 7.72 mm below the top surface of the plate where the out-of-plane displacement was obtained at a propagation distance of 381 mm. The WT results were obtained from the signals after a 40 kHz high-pass filter. These two figures show that the modal intensity pattern is quite similar. Thus we can expect that certain results determined from the analysis of the signals with out-of-plane dipole sources can be transferred to in-plane dipole sources.

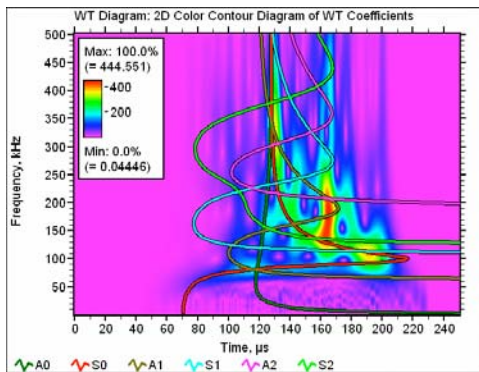


Fig. 2 WT for out-of-plane dipole at a depth of 7.72 mm below the surface, 40 kHz HP.

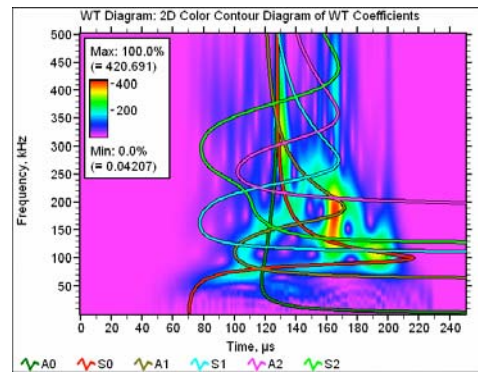


Fig. 3 WT for in-plane dipole at a depth of 7.72 mm below the surface, 40 kHz HP.

Displacement Signals and WT Results at 1016 mm Propagation Distance

Figures 4 - 6 respectively show at 1016 mm the out-or-plane displacement versus time as a function of source depth (relative to the sensor surface) for the conditions of no filtering, 40 kHz

high-pass and 100 to 300 kHz bandpass. Some WT results are shown in Figs. 7 - 9. First, as can be seen in Figs. 4 and 7 for sources near either surface, considerable energy is carried in the lowest frequency portion (less than 40 kHz) of the A_0 mode. These frequencies are below the frequencies normally used in AE monitoring. Second, Figs. 4 - 6 show that the signal levels increase gradually with increasing time with the highest amplitudes occurring later in the signals. Thus, use of threshold penetration for arrival times is likely to provide values at different velocities. Third, as indicated by the arrows in Figs. 4, 5 and 8, a Rayleigh wave (see Fig. 8 at frequencies above about 400 kHz) clearly appears only in the signal from a sensor on a surface when the source is close to that surface. Thus when real AE sources are on or near the inner surface of a pressure vessel, the signals obtained with sensors on the outer surface do not clearly exhibit a Rayleigh wave. Fourth, sources nearer the mid-plane of the plate had a WT maximum at about 102 kHz associated with the S_0 mode (see arrow in Fig. 9). WT results of all the displacement signals in Figs. 4 - 6 were examined to identify potential high intensity frequency/mode regions that might be used to determine mode arrival times.

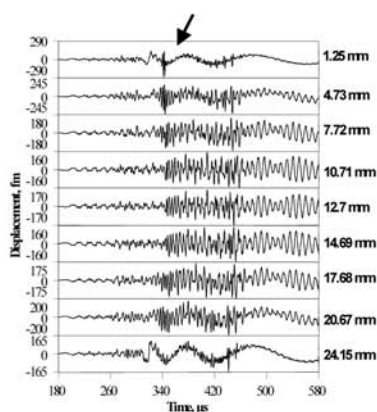


Fig. 4 Displ. vs. time at 1016 mm, out-of-plane source at depths shown, no filter.

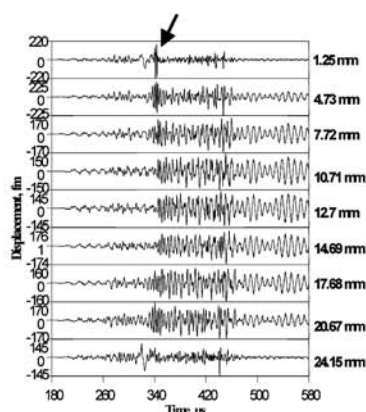


Fig. 5 Displ. vs. time at 1016 mm, out-of-plane source, 40 kHz HP.

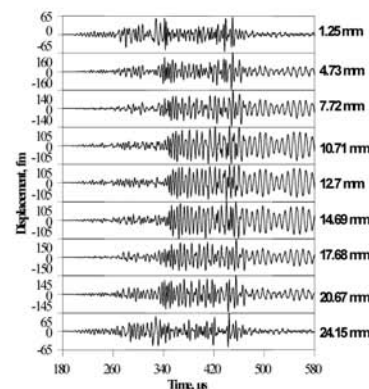


Fig. 6 Displ. vs. time at 1016 mm, out-of-plane source, 100 to 300 kHz.

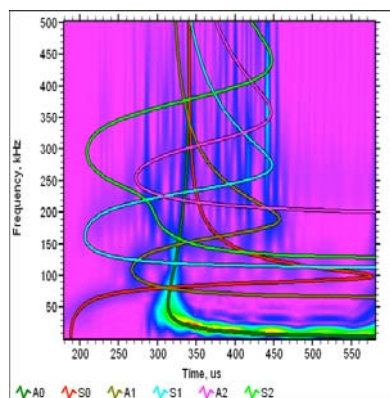


Fig. 7 WT of signal at 24.15 mm in Fig. 4; no filter; 0 to 500 kHz vertical scale.

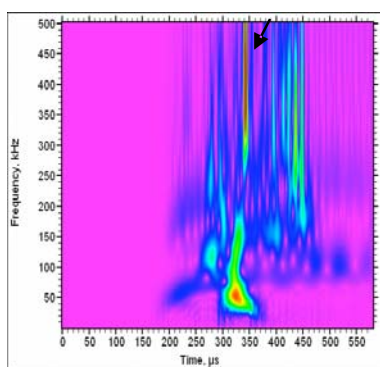


Fig. 8 WT of signal at 1.25 mm in Fig. 5; 40 kHz HP; 0 to 500 kHz vertical scale.

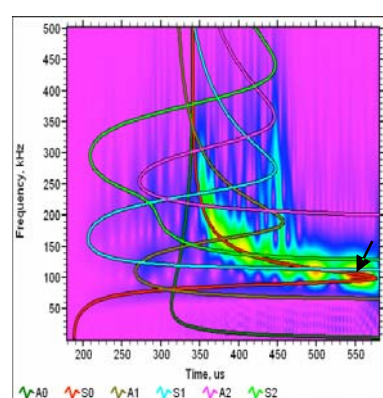


Fig. 9 WT of signal at 14.69 mm in Fig. 6; 100 to 300 kHz; 0 to 500 kHz vertical scale.

Useful Frequency/Mode Combinations to Determine Arrival Times

Since the highest intensity (largest WT coefficients) frequency/mode combinations change as a function of source depth, some priorities were used to identify a key combination: (i) select a

frequency applicable for all three of the frequency ranges; (ii) select a frequency/mode combination that covers a wide range of source depths; (iii) select a frequency so that possible modes have considerably different group velocities and (iv) select a frequency so the WT maximum corresponds to the mode arrivals.

To best meet the conditions listed above, the frequency selected was 102 kHz. This frequency can only (see Fig. 1) be associated with the A_0 , A_1 or the S_0 mode. It was determined that this choice could be used for all three frequency ranges. Further, the A_1 mode did not result in a maximum peak of the WT coefficients, and the velocities associated with the A_0 and S_0 mode peaks were widely separated at the 102-kHz frequency.

Table 2 provides a sample (not all results are shown) of the WT-maximum determined arrival times (at all propagation distances) and the modes for the 40 kHz high-pass data for different source depths. In addition, the table provides the group velocities as directly determined from the slope of a plot of propagation distances versus the arrival times. Finally, these “experimental” group velocities are compared to the theoretical velocities (last column). The results in Table 2 show that accurate group velocities can be determined from the arrival times of the peak in the WT magnitude at the 102-kHz frequency. Accurate group velocity results similar to Table 2 were obtained for the other two frequency ranges and all the depths.

Of special interest was the fact that the arrival time data points for 127-mm propagation distance fell on the linear line that defined the group velocity obtained from the FEM data. Further, the accurate results were found in the presence of wide variations in the signal durations (due to dispersions) for the different propagation distances. The main part of the signals varied in duration from about 50 μ s to about 400 μ s as the propagation distance increased from 127 mm to 1016 mm. Over this range of distances, the signal peak amplitudes decreased by 12 to 19 dB from the first distance to the last. These two large changes did not affect the determination of accurate arrival times.

Since the region of the S_0 group velocity curve that gave rise to the WT peak at 102 kHz is the same region that provided accurate arrival times for this mode at 522 kHz in the 4.7-mm-thick aluminum plate [1], Fig. 10 was created to show how this frequency changes with plate thickness for both steel and aluminum.

Table 2 WT peak arrival times (μ s) at 102 kHz with mode for 40 kHz high-pass data.

Source depth, mm	Propagation distance, mm							Group vel., mm/ μ s, from slope	Group vel., mm/ μ s, from theory
	127	254	381	508	635	762	1016		
1.25, A_0	41.9	78.5	123.	162.5	200.8	243.2	321.3	3.16	3.18
4.73, S_0	64.7	131.2	198.9	269.2	339.6	410.2	549.3	1.83	1.78
10.71, S_0	64.7	130.9	198.8	270.2	342.2	411.7	548.8	1.83	1.78
14.69, S_0	64.7	130.9	198.9	270.1	342.3	411.7	548.8	1.83	1.78
20.67, S_0	65.0	131.2	199.1	268.8	340.1	409.9	549.5	1.83	1.78
24.15, A_0	37.5	81.6	122.3	163.6	203.2	242.8	323.1	3.13	3.18

Application to Source Location and Related Mode Identification of the Single Frequency (102 kHz) Determined Arrival Times

In an experimental AE case, the source depth for each event is unknown, and a WT maximum-determined arrival time at 102 kHz could be associated with either the A_0 or the S_0 mode.

Hence, we examined a possible approach that would allow determination of the mode. It was assumed that the signals from the event were recorded at four different sensors in a location array. Using the available propagation distances, a series of cases were examined with different placements of the sensors around a fixed source location. Figure 11 shows a particular case of the arrangement of the sensors around a source location (indicated by X). For each sensor location the arrival times selected (40 kHz HP data) corresponded to those for two different source depths that provided data for the two possible modes (A_0 and S_0). Planar source location software [13] was used to calculate the location using each of the two possible group velocities (from the slope plots referred to earlier). From the results for each location calculation, the radius error from the actual to the calculated location was determined. It was found that the group velocity that gave the least radius error corresponded to the known actual mode that had led to the WT maximum-determined arrival times. For an example case, the sensor locations (x, y in mm) for sensors #1 – 4 respectively were [1410, 1356.4], [1011.1, 1204.8], [1697, 1942.3] and [906.8, 2219]. The relative arrival times in μs for the respective sensors were [A_0 mode: 0, 44.6, 122.3, 164.7] and [S_0 mode: 0, 67.7, 208.4, 279]. Table 3 shows the radius errors for each of the two possible group velocities. Due to the nature of the database used for these calculations the source location (x = 1219.2 mm, y = 1524 mm) was always the same for each case.

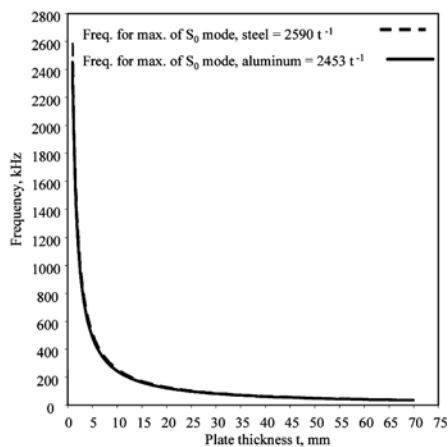


Fig. 10 Frequency of maximum WT intensity of the S_0 mode as a function of plate thickness for aluminum and steel plates.

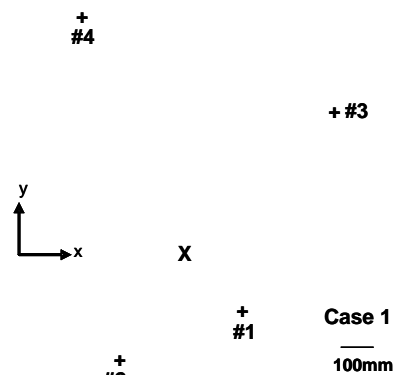


Fig. 11 Arrangement of sensors (#1, #2, #3, #4) around source location X (x = 1219.2 mm, y = 1524 mm). Scale shown as well as the directions of the x and y axis (origin not shown).

Table 3 Radius errors and uncertainty (“Lucy”)*.

Calculation conditions	Radius error, mm	“Lucy” values, mm
A_0 arrival times and A_0 velocity	9.5	2.2
A_0 arrival times and S_0 velocity	115	18
S_0 arrival times and A_0 velocity	241	15
S_0 arrival times and S_0 velocity	2	1.6

The source location software [13] automatically provided an “uncertainty” value for each location calculation. Table 3 also shows this “uncertainty” parameter (called “Lucy”) for the two possible group velocities. Clearly, the table shows the “Lucy” value is the smallest (bold values) for the correct velocity that resulted in the least radius error. Thus, small “Lucy” values can be used to identify the mode and associated group velocity. The method described here could be software automated. Thus, the use of non-resonant sensors could improve the accuracy of source location even in thick plates as has been shown in thin plates.

Conclusions

- For sources near the top or bottom surface of the 25.4-mm-thick plate, the most intense portion of the A_0 mode is at frequencies below those normally used in AE monitoring.
- For sources near a surface, the signal from a sensor on that surface exhibits a Rayleigh wave at frequencies above about 400 kHz
- The choice of a frequency of 102 kHz provides wavelet transform maximum-determined arrival times for mostly the S_0 mode as the depth of the source varies. For sources near a plate surface, the wavelet transform peak at this frequency corresponds to the A_0 mode.
- Over a wide range of propagation distances (127 to 1016 mm), filter ranges and source depths, the 102-kHz frequency wavelet transform peak provided accurate arrival times. The slope of plots of the propagation distance versus these arrival times provided group velocities very close to the theoretical values.
- For sources at an unknown depth recorded with at least a four-sensor array, the calculation of the planar location of the source from the WT peak arrival times (at 102 kHz) at each of the two possible group velocities yields two different locations. The lowest value of the “uncertainty” from the two source location calculations corresponds to the correct location and the correct mode (and associated group velocity).
- This method for the determination of the correct mode and associated group velocity could be automated to process digitized signals to significantly improve source location accuracy even in thick plates when non-resonant AE sensors are used.

Acknowledgements: The developments of the finite element codes and out-of-plane case runs by Dr. John Gary (NIST retired) are acknowledged. Filtering of the FEM results by Ms. Abbie O’Gallagher, NIST Boulder, CO is appreciated. Also the analysis efforts of Mr. Matthew Papa (University of Denver, Mechanical Engineering undergraduate) are appreciated. Finally, the private communications listed in the references are very highly appreciated.

References

1. M.A. Hamstad, K.S. Downs and A. O’Gallagher, J. of Acoustic Emission, **21**, 2003, pp. 70-94 and A1-A7.
2. K.S. Downs, M.A. Hamstad and A. O’Gallagher, J. of Acoustic Emission, **21**, 2003, pp. 52-69.
3. M.A. Hamstad and A. O’Gallagher, J. of Acoustic Emission, **23**, 2005, pp. 1- 24.
4. M.A. Hamstad and A. O’Gallagher, J. of Acoustic Emission, **22**, 2004, pp. 1-21, A1-A7.
5. Mulu Bayray and Franz Rauscheer, J. of Acoustic Emission, **22**, 2006, pp. 22-43.
6. M.A. Hamstad, Private communication, NIST, Boulder, CO, 2007.
7. M.A. Hamstad, J. Gary and A. O’Gallagher, J. of Acoustic Emission, **14**, 1996, pp. 103- 114.
8. M.A. Hamstad, A. O’Gallagher and J. Gary, J. of Acoustic Emission, **17**, 1999, pp. 97-110.
9. R. Burridge and L. Knopoff, Bulletin Seismic Society of America, **54**, 1964, pp. 1875-1914.
10. Vallen, J., Wavelet transform software version R2007.0309, Vallen-Systeme GmbH, Icking, Germany (2007). Available at <http://www.vallen.de/wavelet/index.html>.
11. H. Cho, Private communication, Aoyama Gakuin University, Shibuya, Tokyo, Japan, 2006.
12. Jochen Vallen and Gabriel Corneanu, Private communication, Vallen-Systeme GmbH, Icking, Germany, 2006.
13. Jochen Vallen, Private communication, Vallen-Systeme GmbH, Icking, Germany, 2001.

A SIMPLE METHOD TO COMPARE THE SENSITIVITY OF DIFFERENT AE SENSORS FOR TANK FLOOR TESTING

HARTMUT VALLEN, JOCHEN VALLEN and JENS FORKER

Vallen-Systeme GmbH, 82057 Icking, Germany

Abstract

AE testing of atmospheric storage tanks filled with liquid becomes more and more accepted. Sensors are attached to the tank wall and shall differentiate smallest amplitudes in the 25-45 kHz frequency range from the background noise. Different sensor models are offered for this application. Are these comparable regarding sensitivity and signal-to-noise ratio? This paper describes a reproducible method to compare such sensors. For continuous as well as for pulse excitation, a suitable setup and obtained results are described. Measuring the noise spectra helps to explain the influence of the frequency filtering on the signal-to-noise ratio.

Introduction

This paper addresses the needs of AE testers of atmospheric storage tanks of various sizes, who want to compare the sensitivity of different sensor models or sensors of same model using a simple method. The most important standards for AE sensor calibration are ISO 12713 (primary calibration) [1] and ISO 12714 (secondary calibration) [2]. Both standards are designed for calibration laboratories. They require a large and heavy calibration block. AE testers usually do not have access to such a calibration block. Additionally, ISO 12714 is recommended for the frequency range 100 kHz – 1 MHz, whereas tank testing is usually done in the frequency range 25-45 kHz. Hence, these standards are of no help for the AE tester. Other standards like EN 13477 [3] and ASTM E976 [4] are general and do not consider the fact that plate waves propagate in different modes.

To detect smallest AE signals, the sensor should have the largest possible signal-to-noise ratio (SNR). This means that for a certain excitation the sensor shall provide the largest possible signal voltage superposed with the smallest possible inherent noise.

For a sensitivity comparison one has to proceed as follows:

1. Excite both sensors in identical manner (frequency sweep) and strongly enough so that the noise can be neglected against the signal from the excitation. The output signal shall be $U_A(f)$.
2. Measure the inherent noise of the sensors (no excitation!). This is the output voltage U_R .
3. The SNR at given excitation is then: $SNR(f) = U_A(f)/U_R$. It might be of interest to calculate a SNR for peak values and one for RMS values.
4. The frequency response as well as the noise measurement shall be made with the same frequency filters as used for the tank test.
5. The sensor with the higher SNR can distinguish smaller excitations from the background noise. Hence, this is the more sensitive sensor.

Setup

For the comparison the following setup was used:

Function Generator (FG)

The function generator creates a sine wave voltage with adjustable frequency and amplitude or a pulse with selectable duration and amplitude, respectively. In our test we used model 33220A (Agilent).

Sensor Excitation

For a comparison, the sensors under test (SUT) need to be excited acoustically in exactly the same way. As emitter an ultrasonic transducer model V101 (Panametrics) was coupled face to face to one SUT using light machine oil as coupling agent. The emitter was driven by a frequency-swept sine wave and the AE signal amplitude from SUT was measured.

This method provides well reproducible results and is well suited for routine sensor verification. But the following objections could be raised:

- AE tank-floor testing analyzes burst AE and not continuous (sine wave) AE. A comparison should also consider burst excitation.
- Different SUT models could have different feedback on the V101 emitter and thereby tamper the comparison result.

Considering these objections, a second comparison was made using a pulse excitation via an aluminum rod of 610-mm length and 19-mm diameter with polished ends. Both excitation methods led to almost the same results for the frequency range 25-45 kHz.

Compared Sensor Models

We compared a Vallen VS30-SIC-46dB sensor (S/N 120) with another sensor, hereafter called XXX. Both sensors have an integral preamplifier requiring 28V DC supply voltage on the signal wire and 20.6 mm diameter. The following lists the differences.

Model	Length	Face	Connector
VS30-SIC-46dB	52.8mm	isolated ceramic plate	BNC at case
XXX	38.8mm	non-isolated metal plate	BNC with 1 m cable

Measurement Chain with Various Filters

For measurements we used Vallen AMSY-5 AE system with dual-channel AE processor ASIP-2, a 25-45 kHz band-pass for the first test, and a 25-100 kHz band-pass for a second test. These band-pass filters consist of digital high- and low-pass filters each with 48 dB/octave steepness. Figure 1 shows the response curves of the band-pass at 1 V_{PP} continuous sine wave at ASIP-2 input. Frequency sweep and RMS measurement were controlled by Vallen Sensor Tester software.

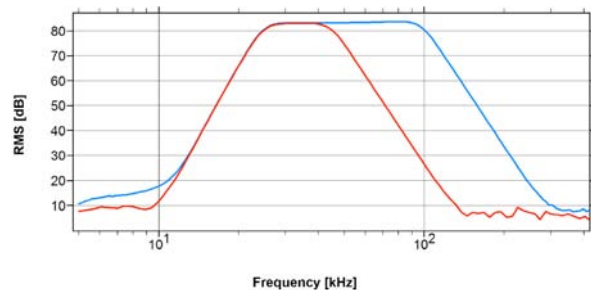


Fig. 1 Frequency response of the used filters.

Sensor Frequency Response

To obtain Figs. 2 and 3, the FG output (50 mV_{PP}, terminated externally with 50Ω) was connected to the V101, face-to-face with SUT. The red curves were taken with 25-45 kHz filter and the blue curves with 25-100 kHz filter in ASIP-2.

For the determination of the inherent noise of the SUT, we removed the acoustic excitation by disconnecting the V101 from the FG. We amplified the sensor output with an auxiliary amplifier by 40 dB, which allowed one to ignore the noise added by subsequent measurement stages. In this way the horizontal lines in orange (25-45 kHz) and green (25-100 kHz) were recorded.

During this noise measurement, we ensured that no acoustic noise sources like fans, human voices, or others could cause a distortion within the frequency range under evaluation. Both SUT were treated in exactly the same way.

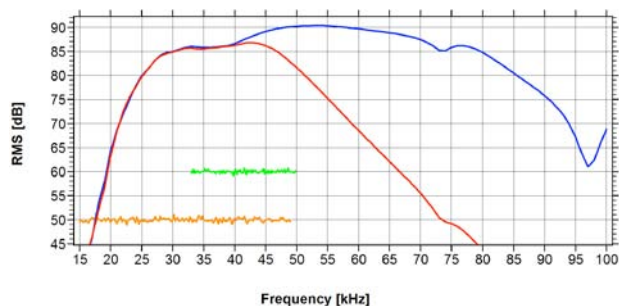


Fig. 2 Frequency response and noise of VS30-SIC-46 dB. 25-45 kHz: red and orange lines; 25-100 kHz: blue and green lines.

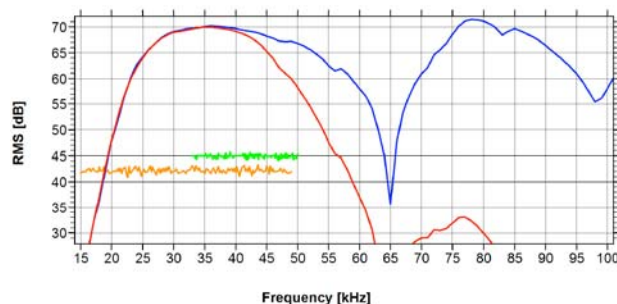


Fig. 3 Frequency response and noise of XXX. Line colors same as in Fig. 2.

The results are summarized in Table 1. They were deduced from the 4 lines of Figs. 2 and 3, whereby the noise has been corrected by the 40 dB post-amplification:

Table 1 Results for continuous sensor excitation.

Sensor:	VS30-SIC-46dB		XXX	
Filter [kHz]:	25-45	25-100	25-45	25-100
Maximum amplitude (RMS):	87 dB	90.5 dB	70 dB	72 dB
line color:	red	blue	red	blue
Frequency at max. ampl.:	35 kHz	53 kHz	35 kHz	78 kHz
RMS noise:	10 dB	20 dB	2.5 dB	5 dB
line color:	orange	green	orange	green
Signal-to-noise ratio SNR:	77 dB	70.5 dB	67.5 dB	67 dB
Difference wrt. XXX at 25 - 45 kHz:	9.5 dB	3 dB	0 dB	-0.5 dB

As can be seen from noise and maximum amplitude, the gain of the integral preamplifier of XXX is lower than that of the VS30-SIC-46dB, but the deciding factor is the SNR as this is independent of the gain. Results for continuous excitation and 25-45 kHz filter: VS30-SIC-46dB provides 17 dB more signal amplitude and 9.5 dB better SNR.

Using Burst Excitation

For XXX the exciting pulse amplitude was 5 V_P. For VS30-SIC-46dB the amplitude was reduced to 1 V_P because 5 V_P led to saturation due to the larger gain. Figure 4 shows the response of the VS30-SIC-46dB with 1-V_P excitation amplitude at V101, and Fig. 5 shows the response of XXX with 5 V_P at V101, both with 25-45 kHz filter. For the FFT, a 190-μs long Hamming window was used. Table 2 lists the maximum amplitude in the time domain (line 2), converted to dB (line 3), the maximum amplitude in the frequency domain (line 4). To compensate for the 5-V_P excitation of XXX, its line-2 value is divided by 5 (600/5 = 120 mV) and line 4 is reduced by 14 dB (97-14 = 83 dB). Table 2 also lists the noise in mV_P (line 5) and converted to dB (line 6). The noise values were recorded separately, in reference to the SUT output (before 40-dB amplification) and are maximum values (peaks), which occurred in a frequency of 1/s or less.

The resulting signal-noise-ratios are listed in line 7 (time domain) and line 8 (frequency domain). Scaling in Figs. 4-7 refers to the input voltage at the AE signal processor (ASIP-2).

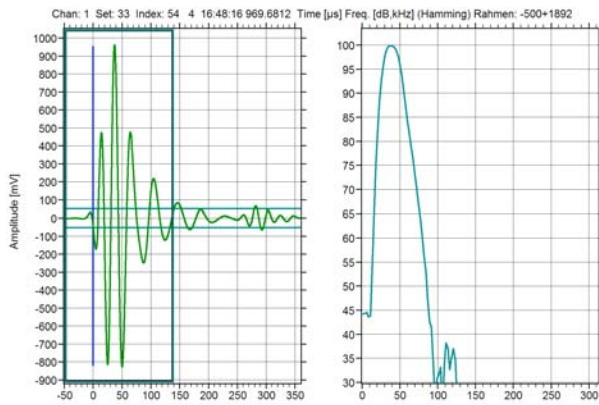


Fig. 4 Pulse response VS30-SIC-46dB, filter: 25-45 kHz, excitation $1 V_P \times 1 \mu s$. max. 940 mV in time domain or 100 dB in FFT. Noise: 0.58 mV_P.

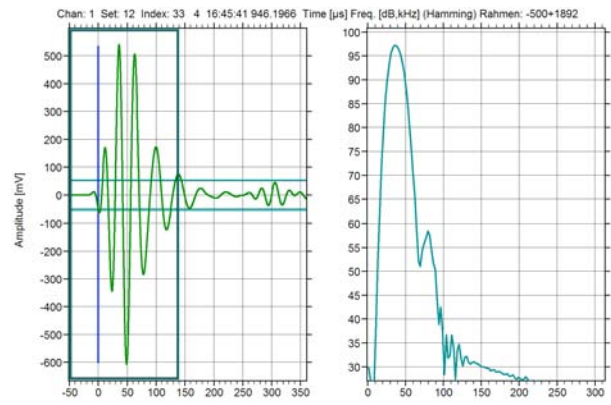


Fig. 5 Pulse response XXX, filter: 25-45 kHz, excitation $5 V_P \times 1 \mu s$. max. 600 mV in time domain, 97 dB in FFT. Noise: 0.20 mV_P.

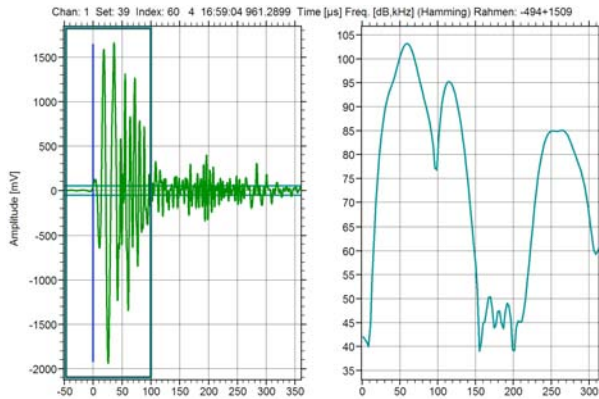


Fig. 6 Pulse response VS30-SIC-46dB, filter: 25-300 kHz, excitation $1 V_P \times 1 \mu s$. max. 1900 mV/103 dB at 60 kHz. Noise: 2.18 mV_P. Arrival of s_1 mode at $t = 30 \mu s$.

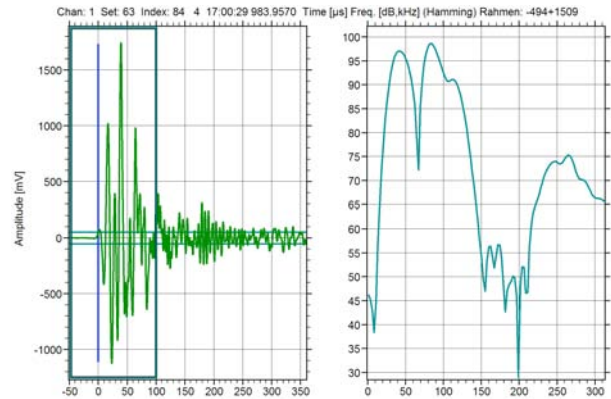


Fig. 7 pulse response XXX, filter: 25-300 kHz, excitation $5 V_P \times 1 \mu s$. Max. 1750 mV/98 dB at 80 kHz. Noise: 0.33 mV_P.

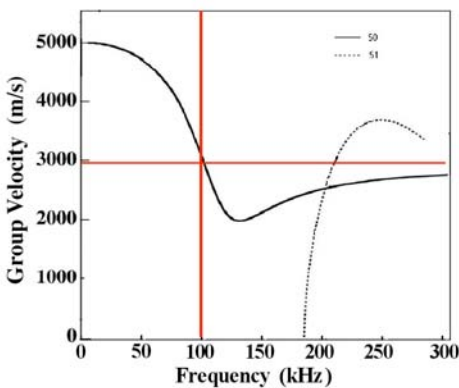


Fig. 8 Dispersion curves for 19 mm aluminum rod, according to [5].

Table 2 Burst excitation results with 25-45 kHz filter.

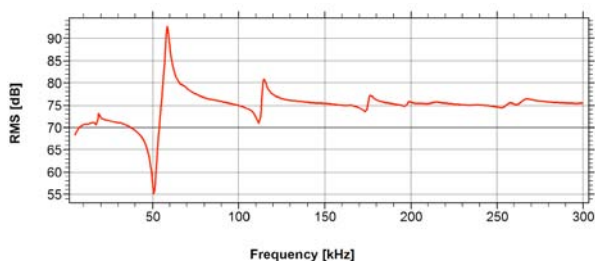
Line	Sensor:	VS30-SIC-46dB	XXX
<i>Measurements</i>			
2	max. Amplitude [mV _P]:	940	600/5V
3	max. Amplitude [dB]:	119.4	101.6
4	max. Amp (FFT) [dB]:	100	97-14
5	max. Noise [mV _P]:	0.58	0.2
6	max. Noise [dB]:	55.2	46
<i>Results:</i>			
7	SNR (mV _P) (3-6) in [dB]:	64.2	55.6
8	SNR (FFT) (4-6) in [dB]:	44.8	37.0

Figures 6 and 7 were taken with band-pass of 25-300 kHz. Figure 6 shows at approximately 30 μs the arrival of the s_1 mode, which travels with ~ 4000 m/s at 250 kHz according to Fig. 8. Considerable differences between the two sensor models are seen: VS30-SIC-46dB exhibits a resonance at ~ 60 kHz, where XXX exhibits resonances at 40 and 80 kHz and an anti-resonance

at 60 kHz. Due to the obscure influence of the s_1 mode, a direct comparison of Figs. 6 and 7 is not recommended.

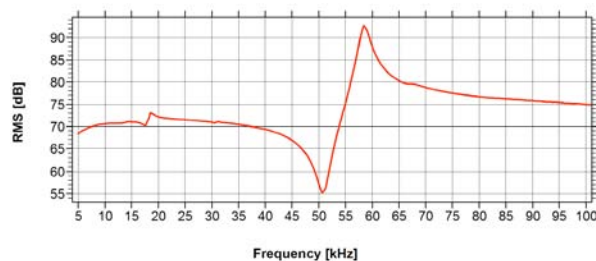
Result for burst excitation with 25-45 kHz filter: Table 2, line 3 indicates that VS30 delivers 17.8 dB more amplitude and line 8 shows 8.6 dB more SNR in time domain and 7.8 dB more in frequency domain. This result is very similar to continuous excitation.

Noise Spectra, Impedance and “Natural Frequency”



FG 100mV --> 10pF --> Sensor -->20cm --> preamp. 40dB --> ASIIPP (dummy filter)

Fig. 9 Impedance jumps of VS30-V (no integrated preamplifier).



FG 100mVpp --> 10pF --> Sensor -->20cm --> preamp. 40dB --> ASIIPP (dummy filter)

Fig. 10 Zoom of Fig. 9 around the natural frequency (58 kHz).

The frequency, at which a sensor shows a sudden *jump* in its impedance, is called *natural frequency* [6]. For obtaining an impedance curve (Figs. 9 and 10), a passive sensor must be used. A sine wave of 100 mV_{pp} from a function generator in series with 10 pF was fed in parallel to a sensor VS30-V (same piezo-element as VS30-SIC-46dB) connected to a preamplifier AEP4 (40 dB). Figure 9 shows the lowest impedance at 51 kHz, and the highest at 58 kHz. Peculiar with this frequency is, that the amplitude measured with sensor connected (Fig. 9: 94 dB) is higher than measured with the sensor disconnected (89 dB)! The impedance combination of both, sensor and preamplifier, generate a sharp resonance peak.

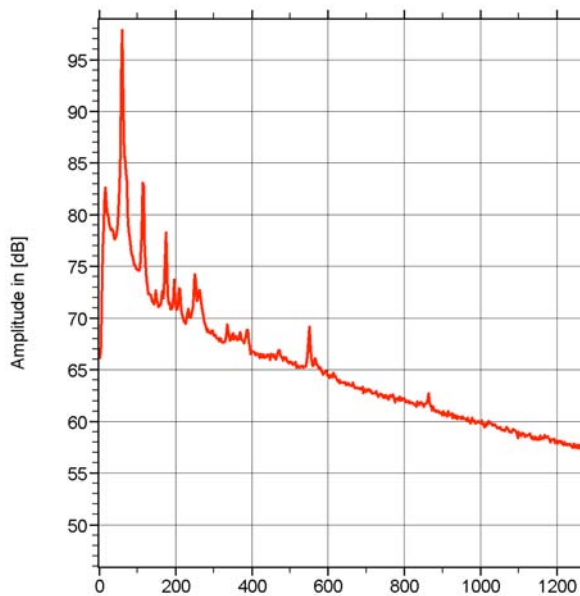


Fig. 11: Noise spectrum VS30-SIC-46dB (average of 1000 FFTs).

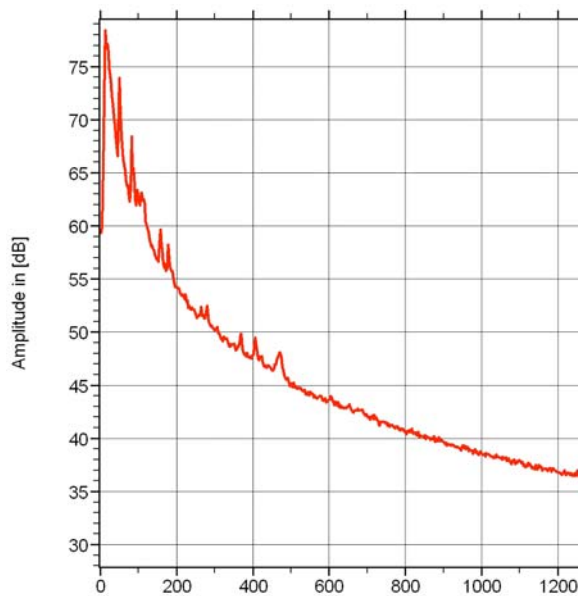


Fig. 12: Noise spectrum XXX (average of 1000 FFTs).

This peak can also be seen in the noise spectrum (Fig. 11) of a sensor with integrated preamplifier. This dominating peak in the noise spectrum is the reason for the increase of inherent noise when using the 25-100 kHz band-pass filter instead of 25-45 kHz. In both Figs. 9 and 11, further peaks at 112 kHz, 175 kHz and 270 kHz can be identified. XXX has its dominating peak in the noise spectrum below 25 kHz (Fig. 12). This explains why the noise of the XXX does not substantially increase with a 25-100 kHz band-pass filter.

The determination of a reproducible noise spectrum requires averaging the FFT over many measurements as the individual spectra of noise records scatter considerably. For Figs. 11 and 12, we averaged 1000 noise records using the Vallen FFT-Averager. The absolute scaling of Figs. 11 and 12 must not be compared. These figures shall just illustrate the different 'natural frequencies' and the effect of filter bandwidth on the noise of the filtered signal.

Conclusion

This report describes two setups to compare the sensitivity of different sensor models. One is with face-to-face coupling and continuous excitation, and the other with burst excitation via an aluminum rod. In both cases, the excitation is perpendicular to the sensitive area. When looking at the SNR (signal-to-noise ratio), the inherent noise and the noise spectra have to be considered.

Two sensor models have been compared. The result depends strongly on the used frequency range. For 25-45 kHz and identical excitation, one sensor model provides 17 dB more signal and about 9 dB better SNR than the other. For tank floor testing, the frequency range of 25-45 kHz is suited best. The more sensitive sensor model shows a natural frequency of 60 kHz. This causes a peak in the noise spectrum, which is excluded effectively by the 25-45 kHz band-pass filter.

References

- [1] *Non-destructive testing – Acoustic emission inspection – Primary calibration of transducers*, ISO 12713, ISO/TC135, 1998.
- [2] *Non-destructive testing – Acoustic emission inspection – Secondary calibration of acoustic emission sensors*, ISO 12714, ISO/TC135, 1999.
- [3] *Non-destructive testing – Acoustic emission – Equipment characterisation- Part 2: Verification of operating characteristics*, EN13477-2, CEN/TC138, 2001.
- [4] *Standard Guide for Determining the Reproducibility of Acoustic Emission Sensor Response*, ASTM E976 ASTM/E07.04, 2001.
- [5] J.L. Rose, *Ultrasonic Waves in Solid Media*, Cambridge University Press, ISBN 0 521 54889 6, 2004, p. 149+.
- [6] G. Gautschi, *Piezoelectric Sensorics*, Springer Verlag, ISBN 3-540-42259-5, 2002, p. 195+.

INVESTIGATION OF AE FROM A STEPPED CHEMICAL REACTION

SHAVKAT AZIMOV, ABDUKHOLIK LAKAEV, FARKHOD CHORIEV
and RICHARD NORDSTROM*

Laboratory of Physical Acoustics, the Physical-Technical Institute, Tajik Academy of Sciences,
Dushanbe, 734063 Tajikistan; *Portland State University, Portland, Oregon, USA

Abstract

AE can be monitored from and during chemical reactions. The term chemical acoustic emission (CAE) is sometimes used for this class of process. In contrast to most AE experiments, CAE experiments are largely reproducible. In this study, AE generated from a common commercial antacid is considered: aspirin with sodium bicarbonate (NaHCO_3) and citric acid ($\text{C}_6\text{H}_8\text{O}_7$) in water. Although AE can be compared to ratios of reactants on a qualitative basis, questions on the nature of generating source, propagation environment and interference noise effects abound. The simplicity of the base experiments belies some of the difficulties in obtaining concrete answers to these questions. To gain insight, tests varying the reactant ratios, the propagating media volume, reactant states were used. Also, we were interested in instrumentation effects, including a range of sensors and compatibility of AE results from instruments of different manufacturers.

The basic shape of the rate curve is repeatable over several factors, including sensor chosen, volume of water used, and starting reactant ratios, use of hit or count parameters or instrument manufacturer. Three rate periods were identified in this reaction. Typical of these tests included the first two minutes producing the strongest activity, a decreased rate (1/6th) for the next 2 minutes followed by a slow rate thereafter. Further details of these processes, as well as applications, are discussed.

Keywords: CAE, chemical reactions, chemical acoustic emission

Introduction

Monitoring chemical reactions with AE [1, 2] has been termed CAE for chemical acoustic emission. Past work have correlated the rate of AE generated with the amount of chemical reactants. A reaction of sodium bicarbonate and citric acid is reported in [1] and is continued here. This reaction takes place when tablets are placed in water, so the AE is detected through water.

This work takes an expanded look at the variables that affect the AE monitoring of the reaction reported in [1]. The questions posed concern many aspects of the AE test. What are the sources of AE in the reaction and what noise is present, be it background noise, interference or noise shadowing AE signals. How the actual reaction and the bubbles formed is one of the first queries. How does the propagation media affect the measured AE is another question. The size and the varying the paths for the bubble column are considered. Different sensors were tried. Rate analysis on all tests was performed, and some limited extensions of this were made.

Experimental Method

Description of Chosen Chemical Reaction

Experiments were performed at two laboratory sites. The reactants under study sodium bicarbonate (NaHCO_3) and citric acid ($\text{C}_6\text{H}_8\text{O}_7$) are readily available as a commercial antacid tablets. The reactants in each site were not identical, as can be seen in Table 1.

AE Test Equipment and Test Conditions

For the AE equipment, a Vallen-System AMSY5 was used for one set of experiments, while a PAC PCI-2 was used in the other. The results were comparable for the types of analysis that was used in these tests. Thresholds of 30 dB_{AE} were used except where noted. Most tests used 150-kHz resonant sensors (R15I, SE150-M), but 675 kHz (SE650-P) was also used. Also the bandwidths of the systems were nominally similar, from 100-900 kHz. The exception is when the 20-kHz or 2 MHz (SE2MEG-P) AE sensors were used, and correspondingly appropriate filters were used. See Tables 1 – 3 for test conditions.

Table 1: Variables considered in experimental work.

Commercial Identification	Composition*
UPSARIN UPSA	1000 mg Citric Acid 2000 mg Sodium Bicarbonate 325 mg Aspirin
Generic tablets distributed by Perrigo	1000 mg Citric Acid 1916 mg Sodium Bicarbonate 325 mg Aspirin

* These amounts were usually cut into quarters and all tests were repeated at least three times.

Table 2: Variables considered in experimental work.

Test Variable	Conditions Tried	Comments
Tablet Position	<ul style="list-style-type: none"> • Tablet Floats • Forced constraint to keep tablet at bottom • Tablets float or sink based on air bubbles • Tablets were also crushed into powder to disperse into test vessel 	As both tablets were near the density of water, on different experiments the tablets would either sink or float. Greater numbers of gas bubbles under the tablet were often observed when the tablet floated.
AE Sensor Contact	<ul style="list-style-type: none"> • On wall of glass flask • With sensor immersed • With sensor wearplate in contact with surface • Attached to the waveguide that is immersed in 	This is a practical consideration. It is usually advisable to treat common AE sensors as water resistant ONLY over short periods of time.
Volume of Water	From about 10 ml to 500 ml of water per 3500 mg total tablet size. For crushed tablets, weight ratios in the next table were tried	Interesting to demonstrate energy radiation issues in acoustic emission.
Height / Diameter	From about 1:10 to 10:1	Interesting to see how bubble column affects testing.

Table 3: Test Sequence – series 2.

Test	Volume	Additional Constraints
T1	500 ml	
T2	400 ml	
T3	300 ml	
T4	200 ml	
T5	100 ml	
T6	300 ml	held tablet under weight
T7	300 ml	held tablet in clamp
T8	repeated T7	

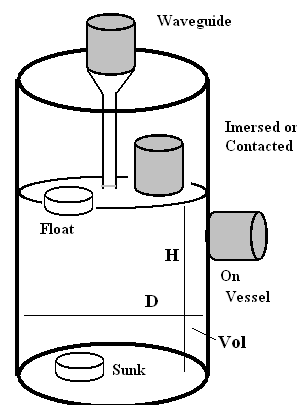


Fig. 1: Schematic of test conditions.

Table 4: Water to tablet ratios considered in powdered tablet tests.

Channel	1	2	3	4	5
Tablet Composition	~1 g	~0.5 g	~0.25 g	~0.125 g	~0.0625 g
Water Composition	15 ml	15 ml	15 ml	15 ml	15 ml

Results and Discussion

A typical result from tablet dissolution is shown in Fig. 2, showing four separate representations of a single test. Here is represented some of the feature common in most test variations and some noise issues. In initial tests, the tablet piece was dropped from a distance of several cm, which produced splash emission. In later tests, the tablet pieces were dropped from less than 1 cm to reduce this unwanted noise. The reaction is strongest at the beginning and decays steadily, suggestive of the rate of the chemical reaction [1]. The second peak was not present in all tests, but not uncommon either. In a few tests where the tablet was floated to the surface under the influence of bubbles being generated, the AE quantity increased dramatically.

The threshold did not usually qualitatively change the rate of AE, nor did the choice of AE hits, counts, or energy as seen in the figure where they are superimposed. If the threshold was moved low enough, but still above the electrical noise, some activity can be observed for hours, but the reaction activity is completed within 5 minutes in all cases. The cumulative amplitude distribution showed behavior consistent with the power law $N(A) = N_{\text{total}} (A/A_0)^{-b}$ where the b-value seen was 2.

Rate Analysis

As the reaction evolves, three periods are identified, as shown in the cumulative hit curve in Fig. 3. In this case, three constants are used to describe the rates; for this test, these were: $K_1=66.7$; $K_2=10.7$ and $K_3=0.01$. Typically, values of $K_1 > 50$ are expected, values of $K_3 < 1$ and intermediate values of K_2 .

Water Volume Comparison

By stepping the water volume downward (from 500 ml to 100 ml), it was hoped to demonstrate the most basic feature of the acoustic media. As would be expected, less volume dissipate the energy less and peak amplitude increased. One test in the series shown in Fig. 4, T2, shows the exceptional case where a tablet floated to the surface and produced a much greater level of AE.

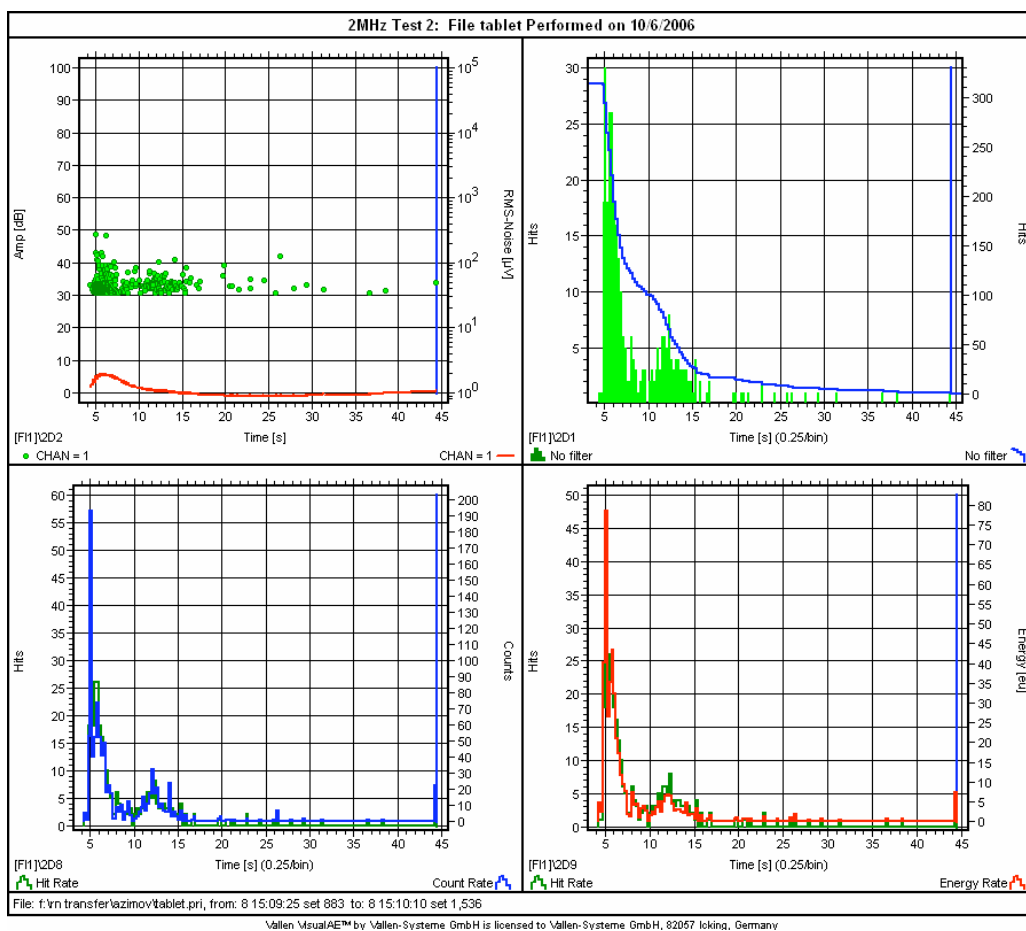


Fig. 2: Four representation of typical tablet dissolution.

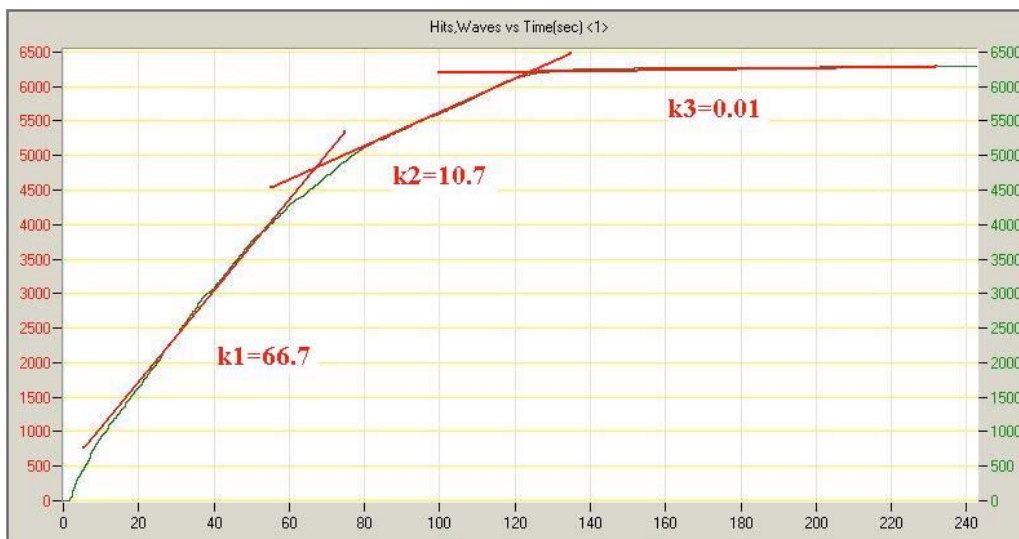


Fig. 3: Rate regions identified in a cumulative graph and fit to linear trends.

Bubble-Path Comparative Tests

To get an initial feel for how bubbles change the CAE, tests that were very similar except the bubble path were performed. In Fig. 5, on the left, is a shallow dish where the tablet is near the surface. On the right is a tall cylinder, with equal volume of water to the shallow dish, but where the tablet is on the bottom and bubbles must float to the surface.

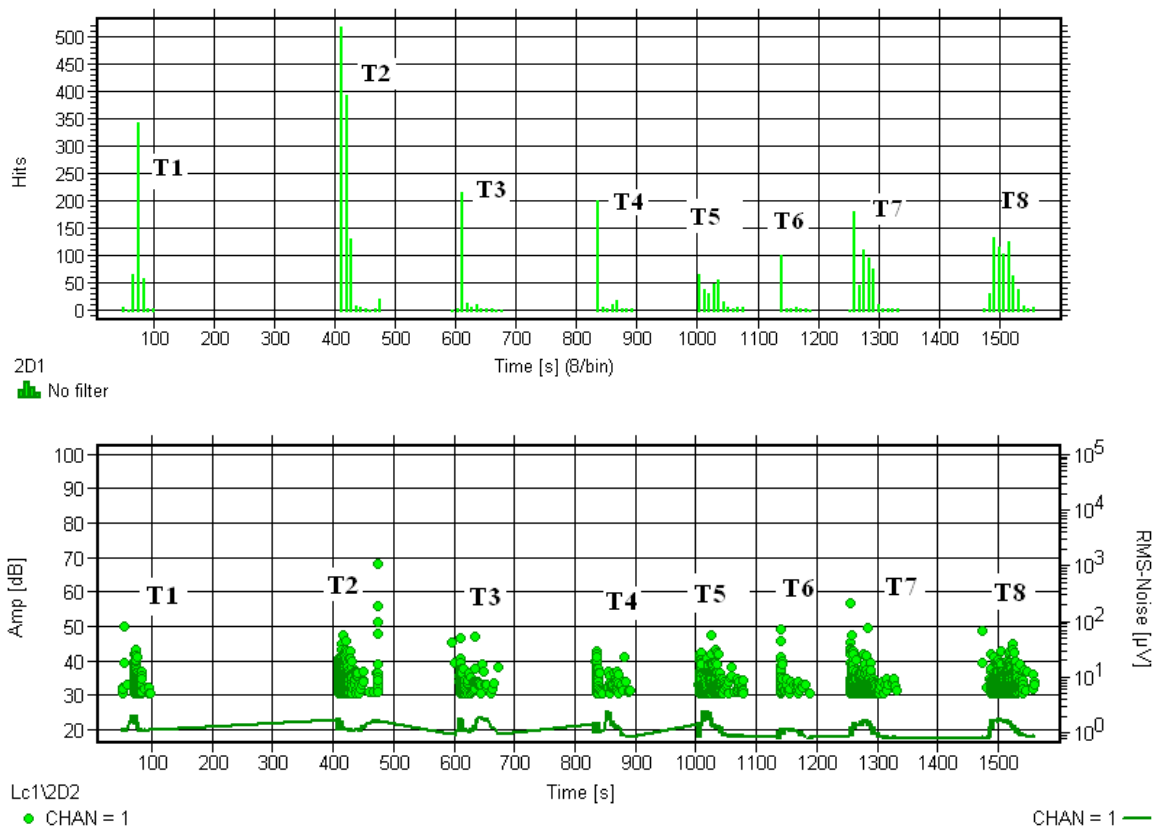


Fig. 4: AE rate and amplitude from tests in decreasing water proportions (see Table 2).

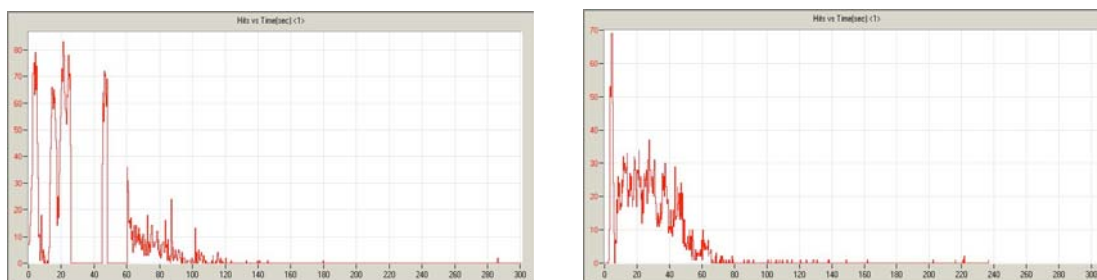


Fig. 5: AE rate from a shallow dish (left, no path for bubble flow) and a tall vessel (right, long path for bubble flow).

The shallow path shows interrupted features not seen in the tall cylinder. As opposed to suggesting that this indicates any differences in CAE generation, a more plausible suggestion can be hypothesized relating to the propagation. It appears that the bubbles are shadowing the AE sensor at points in the reaction. One additional observation, which would seem to support this is that the pattern of interruption in time is not repeatable.

Conclusion

A range of experiments have been conducted to monitor CAE with sodium bicarbonate and citric acid. A number of results have been found qualitatively:

- Sensors with main frequencies from 20 kHz to 2 MHz could all readily detect CAE
- The source of the CAE, based on these experiments, is consistent with the amounts of reaction constituents as in [1]. However, the influence of bubble generation has been dem-

onstrated as a factor, which should be further investigated. Splash, turbulence between bubbles and tablet or tablet sediment are also factors that could be observed experimentally.

- In these experiments, the propagation of AE is consistent with a diffuse wave propagation in the water

Work is continuing to improve and expand upon these experiments.

References

1. S.S. Azimov, "Acoustic Emission Rate as an Indicator of Chemical Reaction Rate," in *S.U. Umarov and Development of Physics in Tajikistan*, Dushanbe, 1998, pp. 88-90.
2. R. Belchamber, D. Betteridge, M. Collins, T. Lilley, C. Marczewski; A. Wade, *Analytical Chemistry*, **58**, 1986, 1873 – 1877.
3. S.N. Sakiev and S.S. Azimov, *Russian Journal of Physical-Chemical Mechanics of Materials (Physico-Khimicheskaja Mehanika Materialov)*, 1992, No. 4, 88-95.
4. Wade, A.P., Soulsbury, K.A., Chow, P.Y.T. and Brock, I.H., "Strategies for Characterization of Chemical Acoustic Emission Signals near the Conventional Detection Limit," *Analytical Chemica Acta*, **246**, 1991, 23-42.
5. Soulsbury, K.A., Wade, A.P., Sibbald, D., "A rules-based approach to classification of chemical acoustic emission signals," *Chemometrics and Intelligent Laboratory Systems*, **15**, 1992, 87-105.
6. Brock, I.H., Lee, O., Soulsbury, K.A., Wentzell, P.D., Sibbald, D., Wade, A.P., "Toolbox for chemical acoustic emission data acquisition and analysis," *Chemometrics and Intelligent Laboratory Systems*, **12**, 1992, 271-290.
7. Cao, Z., Wang, B., Wang K., Lin, H., "Chemical Acoustic Emissions from Gas Evolutin Processes Recorded by a Piezoelectric Transducer," *Sensors and Actuators B* **50**, 1998, 27-37.

EARLY FAULT DETECTION AT GEAR UNITS BY ACOUSTIC EMISSION AND WAVELET ANALYSIS

CHRISTIAN SCHEER, WILFRIED REIMCHE and FRIEDRICH-WILHELM BACH

Institute of Materials Science, Department of Non-Destructive Testing,
Leibniz Universität Hannover, An der Universität 2, 30823 Garbsen, Germany

Abstract

To secure the availability of machines and facilities, the reaction to damage initiation must be as fast as possible. Thus, early detection of damage initiation is crucial to the quick planning and execution of reconditioning measures. This helps minimize downtime and increase availability. Vibration analysis is a good tool for detecting faults and unacceptable operating conditions of machines at an early stage using spectral and correlation analysis. Detecting a defect in a machine by vibration analysis is however not possible before the degree of damage is already affecting its vibration characteristics. Using classical vibration analysis, especially the detection of cracks and their propagation in rotating shafts and gear wheels, is possible only with relatively short forecasting times before failure.

Early detection of cracks in shafts and gear wheels is possible by acquisition and analysis of acoustic emission (AE). Unlike accelerometers that capture the physical behavior of the component, an AE sensor is very sensitive at higher frequencies in order to detect ultrasonic impulses caused by changes within the material's structure like crack formation and crack propagation. At a gear wheel test bench, AE sensors were placed on the gearbox casing and additionally on the ends of the rotating shafts in order to detect defects at an early stage as well as enabling their location and the determination of the affected component.

Because of superimposed interferences, it is not sufficient to regard only the number and intensity of the emissions. Therefore, an additional evaluation of the short-time excitations in frequency domain is necessary using wavelet analysis. Compared with an FFT, wavelet analysis offers a higher resolution in time domain especially for high frequency events. The crack initiation and crack propagation at the root of a tooth shows early changes in the wavelet plot, which are periodic with rotational speed. Propagating pitting shows a different behavior. Both different faults show a characteristic development during the lifetime of a gear wheel.

Keywords: Wavelet analysis, condition monitoring, gear faults, rotating machinery, rotating sensors

Introduction

Due to increasing competition, companies are forced to introduce innovative production technologies rather than only relying on the evolution of established processes. The striving for economic production methods with short processing times as well as the more stringent requirements for properties of today's high performance components brings near-net-shape forming methods into the center of attention. The goal of the Collaborative Research Centre 489 (SFB 489) is to develop new technological, logistical, innovative as well as economic process chains, based on precision forging technology for the mass production of high performance components. One main target is to realize a considerable reduction of the entire process chain, which is founded on the integration of manufacturing steps as well as the substitution of metal cutting sequences by the employment of the precision forging technique [1].

Dynamic load test of components in the process chain "Precision Forging"

The high demands on technological properties of the precision forged components like gear wheels require tests at realistic operating conditions. Hence, one central point of the project is fixed by the diagnosis of components where the precision-forged gear wheels are tested in the gear test bench compared with conventionally machined components to analyze the running behavior. Additionally, the rate of wear and the development of damages have to be acquired and described. Another point is the determination of quality features, like the tooth flank strength and the tooth root strength, which is essential for the optimization of the component's properties and the manufacturing steps in the processing line [1].

Wavelet-analysis

Wavelet analysis provides a method of decomposing a recorded signal into a family of component parts. For general signal analysis, the objective is usually to extract frequency data from the signal and learn how its frequency composition changes with time. Besides the short-time-Fourier-transform (SFFT) the wavelet-transform is a method for the visualization of the time-frequency-intensity behavior. But in this case, it allows a higher resolution in time domain than the SFFT. In using the wavelet-transform, a so-called mother-wavelet has to be chosen, which is continuous in time and frequency and has an average value of zero. The wavelet-transform scales this mother-wavelet for each section of the signal to allow the best fit in frequency and amplitude. The two scaling factors plotted in time domain are the frequency and amplitude coefficients of the wavelet plot. The wavelet-transform has the advantage of showing low-frequency signal components as well as high-frequency components with a high resolution in time domain, even if they only arise for a short time [2, 3].

Acoustic emission analysis at rotating machinery

In addition to the instrumentation with accelerometers, one of the gearboxes was equipped with AE sensors at different measurement positions. At first, gear wheels were tested as can be seen in the right part of Fig. 1. For these tests, two AE sensors were placed on the two bearing housings, fixed bearing and loose bearing and a rotating AE sensor was placed at the end of the shaft with the test gear [4-6].

Further tests were performed using pinion shafts as displayed in the left part of Fig. 1. Another arrangement of sensors was used to enable location of AE events. At the corners of the gearbox, four sensors are placed in addition to two rotating ones at the ends of the shafts.

For data acquisition, a multi-channel AE measurement system was used using statistical methods to investigate AE properties like amplitude, energy, hits and counts. Additionally, the sensor signals were periodically obtained by a high-frequency transient measurement system to get transient data of several revolutions of the test shaft [7, 8].

During the first test measurements with different speeds and different loads, the influences of these parameters on the signal-to-noise ratio were identified and the thresholds for the AE amplitudes were set. Different loads ranging from 200 to 450 Nm showed no significant influences. For the following description of the fault initiation and propagation, only the information of the rotating AE sensor at the end of the test shaft is used. The other sensors showed no significant information about the condition of the test wheel because of their complex signal path. Figure 1 shows the arrangement of the different sensors and the transmission path from the teeth to the sensor. The mounting of an AE sensor directly on the gearwheel was not possible because of the shape and size of the gear wheel and the dimensions of the gearbox. Additionally, the connection of signal cables to a sensor directly on the gear wheel via the rotating shaft is quite difficult.

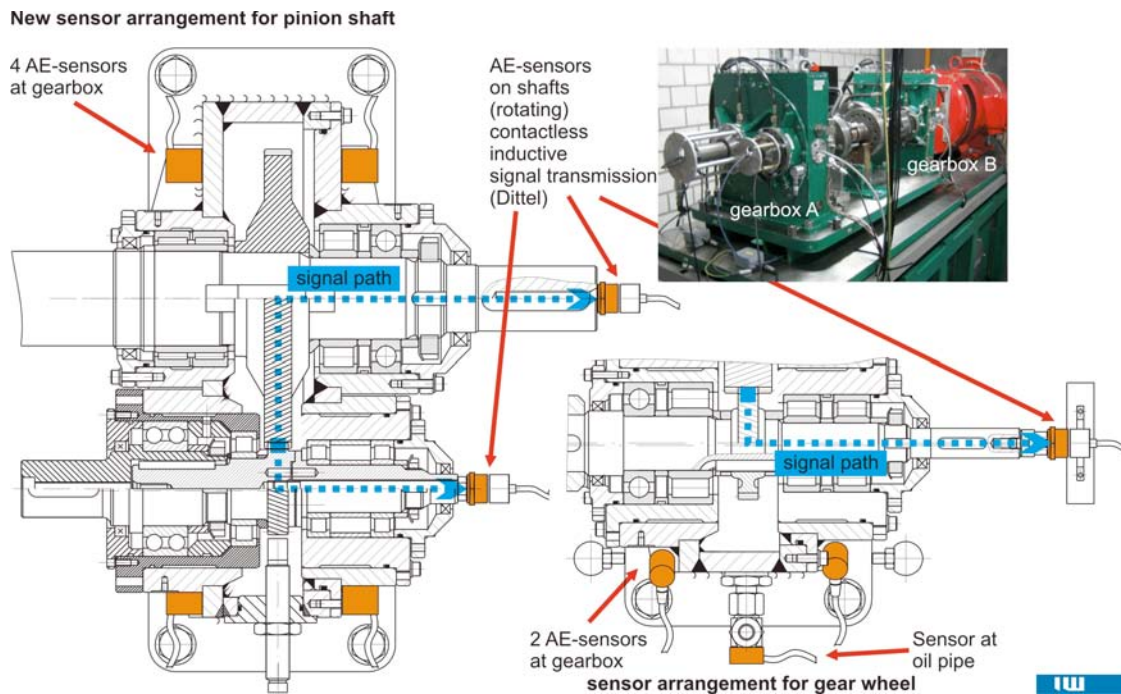


Fig. 1: Arrangement of AE-sensors at gearbox.

Detection of gear faults by AE analysis

The progression of the properties of an AE signal for the undisturbed reference condition after run-in, the crack initiation and propagation until the failure of the gear wheel and shut-down of the test bench is displayed in the upper half of Fig. 2. For the description of the AE signals, the number of hits is shown. In the upper part of the figure, the number of hits during the reference condition is very low, whereas in the diagram beneath the crack initiation can be detected by an increasing hit rate caused by the opening and closing of the crack during one revolution of the test wheel. With an increase of load cycles, the fracture of one half of the tooth occurs. Since the other half of the tooth is still carrying the load the test bench could be operated further.

Another example of the detection of gear faults is presented in the lower diagrams in Fig. 2. Here, the beginning and propagation of pitting at the teeth flanks is shown. Compared to the reference condition, there is an increase in the hit rate, which is not as large as in the case of a crack. Also the hit rate may decrease again, when pittings have developed. The propagation of pitting in the lower diagram of Fig. 2 shows this swelling progression more clearly.

More significant differences between crack development and pitting are visible in transient signals of the shaft sensor, logged over several revolutions of the shaft. An additional high-speed data acquisition card recorded these with 1-MHz acquisition rate through 250 ms. The amplitude of an AE sensor is influenced mainly by its main resonance ranges because of its non-linear behavior. To evaluate signal components out of these ranges, a transformation into frequency domain is necessary. Especially the wavelet-transform is a good means for this kind of high-frequency analysis with short-time events.

The time-frequency components of a crack development compared to the reference condition are displayed in the upper two diagrams of Fig. 3. The wavelet-transform is used here with the Morlet-wavelet as the mother-wavelet. The reference condition as well as the crack at a single tooth shows high amplitudes at about 100 kHz (resonance of the sensor, resp. the measurement chain). These quite low-frequency parts of the signals are not detected by the AE system because it uses a 120 kHz high-pass filter. The crack is clearly visible by short-time pulses in the

frequency range of 200-250 kHz. They appear at ca. 0.04 s intervals, which equals the rotational speed of 25 Hz. Six revolutions are displayed in the diagram and during each revolution, there is a short-time excitation at 200-250 kHz when the damaged tooth comes into mesh.

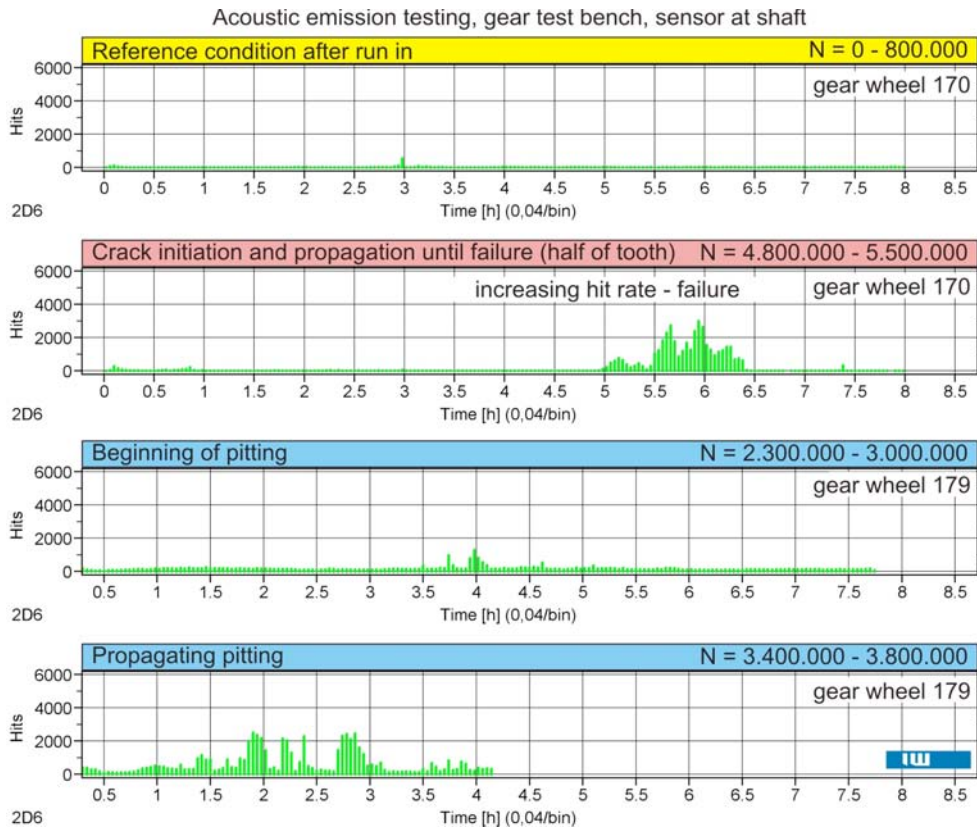


Fig. 2: AE data of reference, crack and pitting.

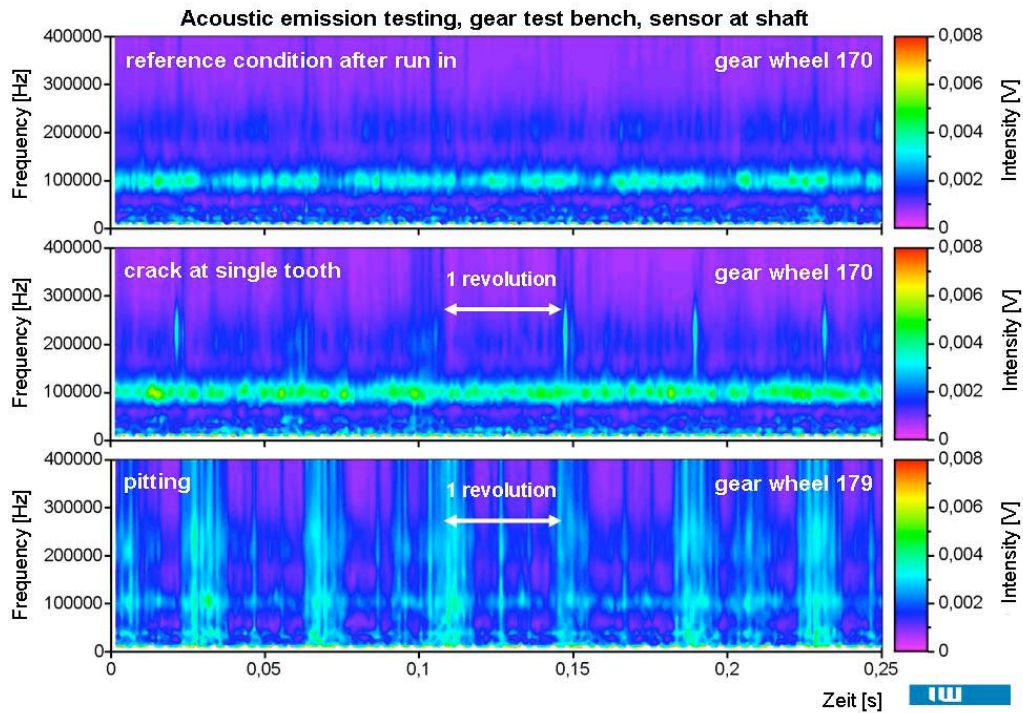


Fig. 3: Wavelets of reference, crack and pitting.

The behavior of pitting can be seen in the lower diagram of Fig. 3 in contrast to the crack development in the middle diagram. The dominant signal component at 100 kHz is visible in this plot, too. There is a much more broad-banded signal component visible over the whole frequency range up to 400 kHz, which lasts much longer than the excitation of the crack development. It is excited more than once per revolution because of the pitting development at several teeth simultaneously. When these teeth are in mesh, the pitting propagates and AE signals are generated.

Location of fault-specific events

Because of the high acquisition rates of up to several MHz, the location of AE signals is possible using run-time analysis of several sensor data. The sound waves propagate in concentric circles, resp. spheres, from the point of origin and can be detected by AE sensors. The maximum range of the sound waves depends upon the material properties, the geometric and surrounding conditions of the object and the number of surface contacts between different objects. At metal parts, these high-frequency sound waves may be detected beyond a distance of several meters.

The determination of the speed of sound, which is necessary for the location, is quite difficult for complex three-dimensional structures, because it varies dependent on different media and many contact surfaces. Performing this location of AE-events inside a gearbox, an averaged speed of sound is used. Further analysis of the signal paths, the materials and contact surfaces will improve this method.

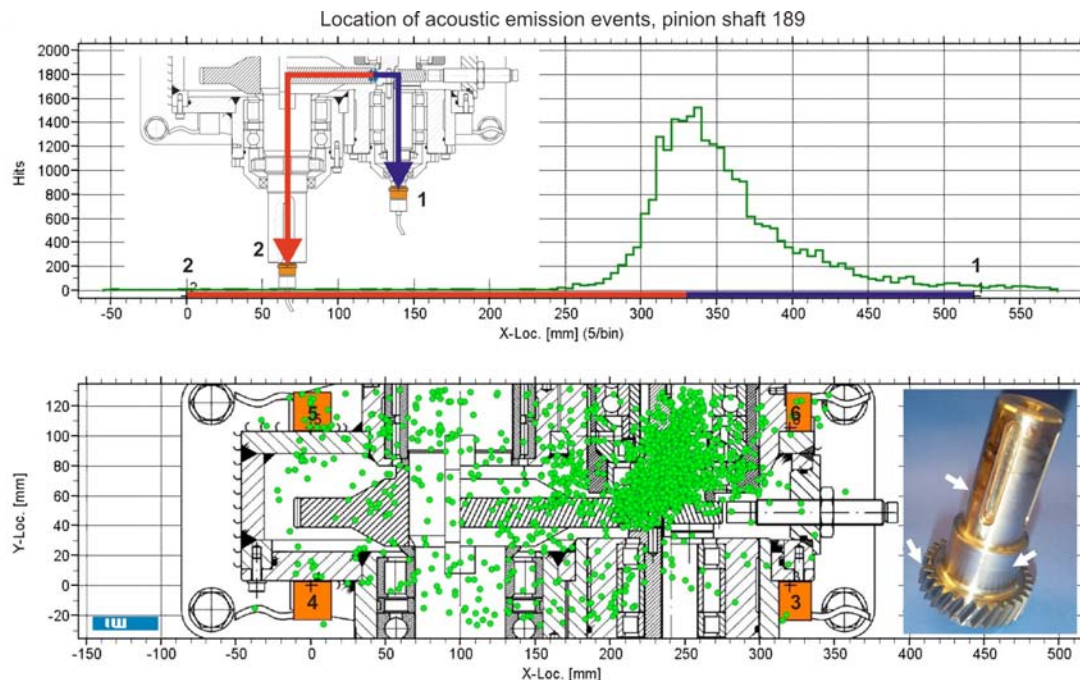


Fig. 4: Location of AE events inside the gearbox.

Four sensors at the corners of the gearbox near the shafts are used to locate AE-events inside the gearbox (Figs. 1 and 4). This enables a location on a sectional plane of the gearbox. Because of the good results of the shaft sensor, an additional rotating sensor was placed at the end of the second shaft to realize a linear location between these two sensors.

Additionally the gear test bench has been modified for a pinion shaft as another test object. The advantage to the gear wheel is the difference between signal path for the sensor and transmission path of the load (Fig. 1). This causes much less AE events by seizing in the fit and at the keys.

The locations of the AE events inside the gearbox are presented in Fig. 4. The linear location between sensor 1 and sensor 2 is visualized in the upper part of Fig. 4. A deviation of the hit maximum towards sensor 1 is clearly visible. The distances from the maximum to sensor 1 and sensor 2 identify the AE-events as coming from the teeth mesh. The location by the sensors at the gearbox shows a similar result. Using the sensors 3 to 6, there is an accumulation of AE events in the area of the teeth-mesh and at the roller bearing on the pinion shaft. The AE signals from the teeth mesh are generated by the teeth mesh itself as well as by the development of a crack. The AE signals in the bearing area are caused by seizures in the close fits and a wrong fit of the bearing inner ring (cf. Fig. 1).

Future work consists of filtering the AE data according to their location to improve the distinction between different gear faults, run-in effects, seizures and faults at other components like rolling element bearings.

Summary

Condition-based maintenance is a contribution to ensure the reliability of operation, high availability and efficiency of industrial machines and plants. This necessitates the acquisition of information about the condition of individual components.

The condition monitoring of the gear test bench at the Institute of Materials Science (IW) is achieved by vibration measurements to describe the operating condition and to detect the development of faults by analysis in both the time and frequency domains. Slow developing faults like pitting can be detected quite early by this method. The detection of cracks leading to tooth fractures is possible with a very short forecast time only.

The analysis of AE signals allows an early detection of cracks in the tooth root because of the crack propagation before the teeth mesh is disturbed and the vibration behavior changes.

The location of AE events enables the allocation to specific components inside the gearbox to improve the distinction between gear faults, run-in effects, seizures, and rolling-element bearing faults.

Acknowledgements: We express our sincere thanks to the German Research Foundation for the promotion of this work within the Collaborative Research Centre 489 “Process Chain for the Production of precision-forged High performance Components”.

References

1. Bach, Fr.-W.; Kerber, K.: Sonderforschungsbereich 489 „Prozesskette zur Herstellung präzisionsgeschmiedeter Hochleistungsbauteile“, www.sfb489.uni-hannover.de, 2006.
2. Misiti, M.; Misiti, Y.; Oppenheim, G.; Poggi, J.-M.: *Wavelet Toolbox User's Guide*, Mathworks, 2000.
3. AGU-Vallen Wavelet, wavelet transformation tool, Vallen-Systeme, Icking, 2005.
4. Toutountzakis, T.; Mba, D.: *NDT&E International*, **36**, (7), 471-477, 2003.
5. Tan, C. K., Irving, P., Mba, D.: Prognostic Potential of the Acoustic Emission Technique for Spur Gears, *Essential Technologies for Successful Prognostics*, 59th Meeting of the Society for Machinery Failure Prevention Technology, Virginia Beach, US, April 2005.
6. Sporer, A.: Hohe Sensibilität entwickeln, Acoustic-Emission-Systeme für die Schleifprozessüberwachung, Walter Dittel GmbH, Werkstatt und Betrieb 03/2006.
7. Vallen, H.: *Die Schallemissionsprüfung*, Castell-Verlag, 2003.
8. N.N.: *AMSY-5 Users Manual*, Vallen-Systeme GmbH, 2004.

NEURAL NETWORK ANALYSIS OF ACOUSTIC EMISSION SIGNALS FOR DRILL WEAR MONITORING

KRITSADA PRASOPCHAICHANA and OH-YANG KWON

Department of Mechanical Engineering, Inha University, Incheon 402-751, South Korea

Abstract

The objective of the study is to establish a strategy for tool-condition monitoring (TCM) that will lead to a more efficient and economical drill usage. Drill-wear monitoring has an important attribute in the automatic cutting processes as it can help prevent the damage of tools and workpieces, and optimize the drill usage. In this study, we present the architectures of a multi-layer feed-forward neural network with back-propagation training algorithm for the monitoring of drill wear condition. The input features to the neural networks were extracted from AE signals using the wavelet transform analysis. Training and testing were performed at a moderate range of cutting conditions in the dry drilling of steel plates. The results indicated that the extracted features from AE signals as the input to the supervised neural networks were effective for drill-wear monitoring and the output of the neural networks can be directly utilized for the planning of tool-life management.

Keywords: Neural network, back-propagation, drill wear, tool-condition monitoring (TCM)

Introduction

Various methods for tool-wear monitoring have been reported in the literature. Most of them are categorized by two main techniques [1, 2]. The first is the direct measurement of tool wear using optical methods, which can only be applied when cutting tools are not in process of cutting. The second is the indirect methods, which measure the relationship between the tool condition and the signals acquired depending on the sensors used. Among these, acoustic emission (AE) appears to be one of the most effective methods. The major advantage of AE monitoring is that the frequency range of AE signals can be much higher than the machine vibrations and environmental noise. In addition, it does not affect the cutting condition. But one of the most important features for AE signals is the additional signal processing, which extracts signal features from the signals detected under given cutting conditions [1-3]. The relationship between AE signals and the tool-wear condition is nonlinear so that the general mathematical relations cannot be used to map this relation [1]. Recent studies in the field of artificial neural networks have proven that they can be particularly useful in the modeling of nonlinear mapping and in the recognition of distinctive features from incomplete or chaotic input data [4-6].

TCM is an indispensable component for the prevention of the damage in machine tools and workpieces and the optimization of tool usage in the automated machining. Drill-wear condition is an important factor directly affecting the quality parameters of machined holes, such as hole roundness, centering, burr formation, and surface finish. Furthermore, under a certain cutting condition, wear development during drilling can reach the unacceptable levels, resulting in the damage of workpieces as well as machine tools and possibly in the production loss. Flank wear is widely used as the indication of the severity of drill-wear condition. Its progressive process is caused by the intimate frictional contact and the temperature elevated at the interface between the drill and the workpiece. Flank wear can be measured by using the average and the maximum wear land size, V_B and V_{Bmax} , as shown in Fig. 1.

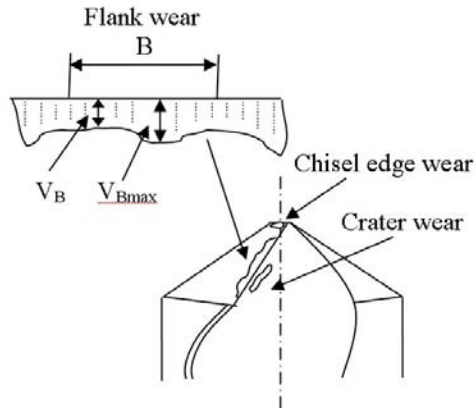


Fig. 1 A schematic of a typical twist drill with flank wear.

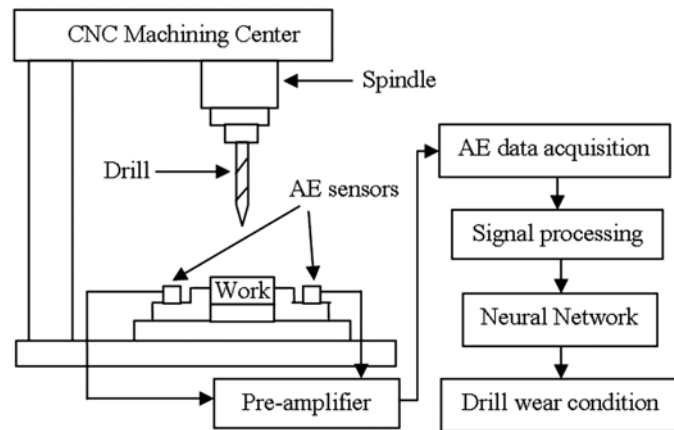


Fig. 2 Schematic diagram of the experiment set-up.

In this study, we have investigated the feasibility of using signals to train and test the neural networks for predicting the drill flank wear. Six neural network architectures were designed with different groups of input features. The inputs were extracted features from AE signals such as root-mean-square (RMS) voltages of the decomposed signals by discontinuous wavelet transform (DWT) and mean absolute wavelet coefficients by continuous wavelet transform (CWT).

Experimental procedures

Experiments were carried out on a machining center (HiMac-V100, Hyundai). Drills used were AISI M2 twist drills with 6-mm diameter and point angle of 118° . Workpieces were AISI 1055 steel plates of $120 \times 120 \times 25$ mm. The hardness of plates was measured to 215 H_B . Two AE sensors (B1025, Digital Wave) were mounted on the clamping fixture at the opposite side of each other as shown in Fig. 2. AE activities during drilling tests were monitored and recorded by using an AE data-acquisition board (Mistras2001, Physical Acoustics), with pre-amplification of 40 dB, band-pass filtering at 0.1-1.2 MHz and threshold of 50 dB. During each test, flank wear was measured by an optical microscope aided by a digital camera and an image processing software. Drilling tests were first performed at nine sets of cutting conditions with three cutting speeds (22, 26, 30 m/min) and three feed rates (0.13, 0.15, 0.17 mm/rev) without coolant, which were used for off-line training and testing. Three sets of cutting conditions were added later to check the validity of the neural networks with the features extracted from untrained data set. The cutting process was continued until the maximum allowable flank wear of $V_B = 0.3$ mm or the complete failure of a drill.

Signal analysis and feature extraction

Based on the analysis of AE sources, AE signals detected from metal cutting consist of the continuous and the transient signals, which have distinctly different characteristics [1]. Continuous signals are associated with shearing in the primary zone and wear on the tool face and the flank, while transient or burst signals are with either tool fracture or chip breakage. In this study, the input features to the neural networks were extracted from the continuous AE signals at the drilling depth of 2-5 mm using level-RMS values by DWT analysis and mean absolute wavelet coefficients by CWT analysis.

DWT level-RMS Analysis

In the DWT analysis, the signal is decomposed into the levels of approximations and details.

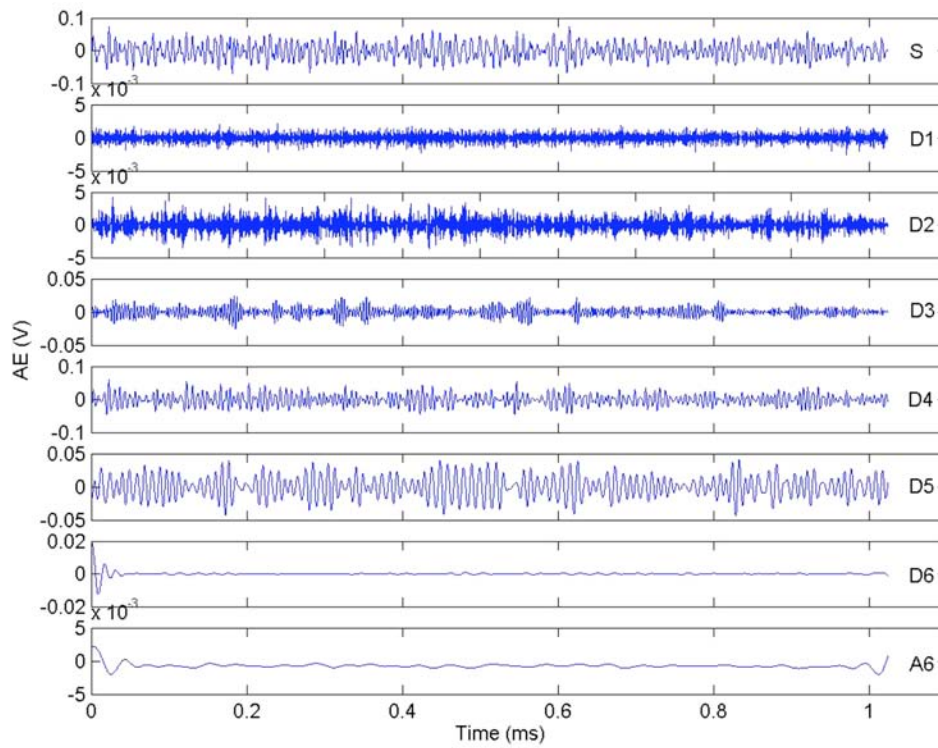


Fig. 3 Six-level wavelet decomposition of an AE signal.

The approximations are the high-scale, low-frequency components of the signal and the details are the low-scale, high-frequency components. The decomposition process can be iterated, with successive approximations being decomposed in turn, so that one signal is decomposed into many lower resolution components [7].

DWT was applied to selected continuous AE signals to decompose the original AE signal into its wavelet levels as shown in Fig. 3. Each level represents a certain frequency band. Decomposition was based on the ‘db20’ wavelet (a member of the Daubechies family) and six levels of iteration [7]. The RMS value of each frequency band level was used as the input features to describe different tool condition [2].

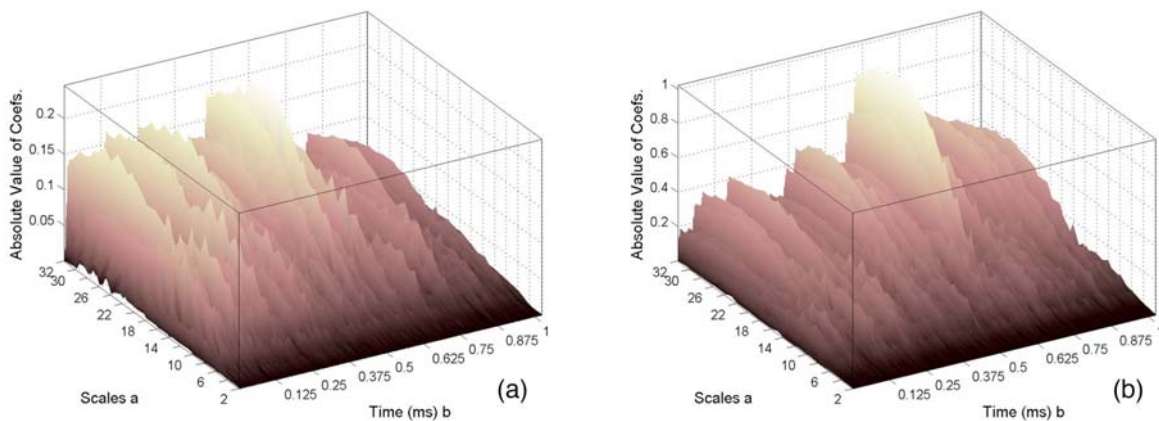


Fig. 4 3-D CWT coefficients surface for two cases of drill wear at the cutting speed of 26 m/min and the feed rate of 0.13 mm/rev. (a) $V_B = 0.000$ mm; (b) $V_B = 0.219$ mm.

CWT for Wavelet Coefficients

The CWT is defined as the sum over all time of the signal multiplied by scaled, shifted versions of the wavelet function. This process produces wavelet coefficients that are a function of

scale and position. The CWT coefficients represent how closely the wavelet is correlated with this section of the signal. The higher CWT coefficient value is, the more the similarity. The CWT coefficient $C(a,b)$ of a signal $f(t)$ is defined by [4, 7]

$$C(a,b) = \int_{-\infty}^{\infty} f(t) \frac{1}{\sqrt{a}} \psi^* \left(\frac{t-b}{a} \right) dt \tag{1}$$

where a represents scale, b represents position, ψ is the “mother” wavelet, and ψ^* is the complex conjugate of ψ .

A member of Daubechies wavelets family, ‘db20’, was selected as the mother wavelet for CWT in this study. In Fig. 4, three-dimensional plots of CWT coefficients for two cases of drill wear are presented in 16 scales (scale 2, 4, 6, ..., 32). The 16 mean absolute CWT coefficients were determined and used to describe the changing feature of the AE signals, which appeared to be influenced by the wear size and cutting conditions.

Neural networks

The architecture of a three-layer feed-forward back-propagation (FFBP) neural network was used in this study. This neural network used a hyperbolic-tangent sigmoid transfer function, which is a good trade off for the neural networks where speed is important and the exact shape of the transfer function is not [6]. In this study, the Levenberg-Marquardt algorithm is used in training neural networks in order to obtain neural networks with good generalization capability. This algorithm appears to be the fastest method for training moderate-sized feed-forward neural networks [6]. The learning process was stopped (i.e., neural network had converged) when the calculated output values were close to the desired target values within an acceptable mean-square error (MSE) value ($MSE < MSE_{goal} = 10^{-5}$).

Six neural network architectures as shown in Fig. 5 were designed as follows:

1. 1S-DWT: Input 7 DWT level-RMS values of AE signals from one sensor with different cutting conditions.
2. 1S-CWT: Input 16 mean absolute CWT coefficients of AE signals from one sensor with different cutting conditions.
3. 1S-All: Input 7 DWT level-RMS values and 16 mean absolute CWT coefficients of AE signals from one sensor with different cutting conditions.
4. 2S-DWT: Input 14 DWT level-RMS values of AE signals from two sensors and different cutting conditions.
5. 2S-CWT: Input 32 mean absolute CWT coefficients of AE signals from two sensors and different cutting conditions.
6. 2S-All: Input 14 DWT level-RMS values and 32 mean absolute CWT coefficients of AE signals from two sensors and different cutting conditions.

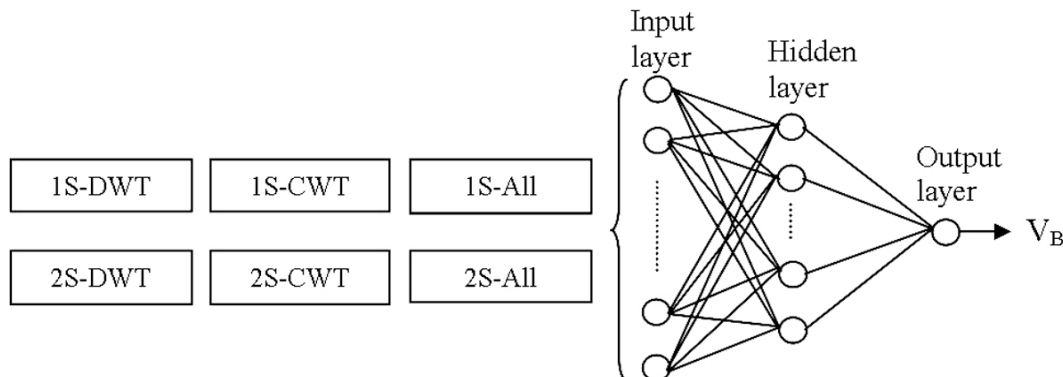


Fig. 5 Six neural network architectures

Table 1 Performance of neural networks with different architectures in the testing phase.

No. of sensor input	Drilling conditions		Percentage of correct predictions		
	Cutting speed (m/min)	Feed rate (mm/rev)	DWT level-RMS	Mean absolute CWT coefficients	All
One Sensor	22	0.13	82.64	72.94	78.92
	22	0.15	71.98	68.77	81.78
	22	0.17	90.20	85.67	91.19
	26	0.13	68.10	73.19	78.04
	26	0.15	60.77	87.68	85.32
	26	0.17	72.88	78.86	76.96
	30	0.13	73.36	74.38	73.39
	30	0.15	91.28	83.85	83.49
Average correct predictions			77.82	78.57	81.80
One Sensor*	24	0.18	73.78	69.78	73.44
	28	0.14	63.78	82.15	81.70
	32	0.12	78.00	68.73	78.41
Average correct predictions			71.86	73.55	77.88
Overall average correct predictions			76.33	77.31	80.82
Two Sensors	22	0.13	76.21	89.66	89.19
	22	0.15	85.55	76.90	88.68
	22	0.17	78.40	94.03	89.23
	26	0.13	78.97	91.23	97.07
	26	0.15	75.05	75.71	80.67
	26	0.17	94.54	87.40	88.99
	30	0.13	76.86	97.64	85.55
	30	0.15	89.46	74.48	84.54
Average correct predictions			82.22	84.31	87.51
Two Sensors*	24	0.18	89.56	87.31	79.76
	28	0.14	80.52	84.73	91.90
	32	0.12	72.12	71.80	84.14
Average correct predictions			80.74	81.28	85.27
Overall average correct predictions			81.85	83.55	86.95

* Untrained data sets; Signals from these conditions were not used in the training phase.

Results and discussion

Based on the above-mentioned neural network model for this study, the number of neurons to be used in the hidden layer of the architecture is critical in order to avoid either under-fitting or over-fitting the problem. In this study, the number of neurons in hidden layer was determined by a trial-and-error approach. Each network architecture was tested for the average MSE of 10 trials with the number of neurons from one (1) to twenty-five (25) and the minimum value out of 25 average MSE determined the number of neurons. The trial-and-error approach was repeated for each of the six architectures, and the number of neurons were determined as 6, 8, 5, 7, 5 and 14 for the architectures of 1S-All, 2S-All, 1S-DWT, 2S-DWT, 1S-CWT and 2S-CWT, respectively.

Table 1 shows a summary of the performance of the neural networks with different architectures during testing phase in terms of percentage of correct prediction. The testing phase helps the neural network architectures to generalize and increase its declaration accuracy. The results

indicate that neural networks with input features extracted from two sensors are more accurate than the networks with only one sensor input. The overall average correct predictions indicated that the best performance was obtained by the neural network architecture with input features from two sensors and both of the wavelet transforms, i.e. 2S-All. The performance of the architecture with input features by CWT is slightly higher than that by DWT, but the difference was almost negligible and within the range of statistical error bound.

In order to further verify the feasibility of using neural networks for the diagnosis of drill wear, the six architectures were tested with untrained data sets that were acquired under the drilling conditions different from those used for training the neural networks. The performance of three architectures with two sensors input was satisfactory, although it was less accurate than the performance for the cutting conditions used for training. When the performance of three architectures was tested with the input features from only one sensor input, the difference in the percentage of correct prediction between trained and untrained became much larger. Because the drilling position moved around within specimens, the distance from cutting source location to the sensor varied with the drilling of every hole. AE signal amplitude decreased in amplitude with the distance from source to sensor due to attenuation, which might affect the quality of input features extracted from the signal. This effect became less significant when the input features were extracted from the signals acquired by two sensors.

Conclusion

A multi-layer feed-forward neural network with back-propagation training algorithm was developed and applied to AE signal analysis to be used for drill-wear monitoring. The performance of six different neural network architectures was tested and found to be sensitive to the type of input data. The combination of DWT level-RMS voltage and mean absolute CWT coefficients as the input features resulted in the best performance to predict the drill-wear condition. In addition, neural networks with input features extracted from two sensors are more accurate than the networks with only one sensor input. These provided the 2S-All neural network architecture to obtain the best performance at a correct prediction of 87%. The results showed that once the neural network was properly trained, it becomes a powerful and reliable tool to solve the classification and pattern recognition problems of such AE signals as being acquired in the tool-condition monitoring applications.

References

1. X. Li, A brief review: acoustic emission method for tool wear monitoring during turning, *Int. J. Machine Tools & Manufacture*, **42**, 2002, 157-165.
2. X. Li and J. Wu, Wavelet analysis of acoustic emission signals in boring, *Proceeding of the Institute of Mechanical Engineers Part B*, **214**(5), 2000, 421-424.
3. J. Sun, G.S. Hong and M. Rahman, Identification of feature set for effective tool condition monitoring by acoustic emission sensing, *Int. J. Prod. Res.*, **42**(5), 2004, 901-918.
4. I. Abu-Mahfouz, Drill flank wear estimation using supervised vector quantization neural networks, *Neural Computing & Applications*, **14**, 2005, 167-175.
5. A.K. Singh, et al., Predicting drill wear using an artificial neural network, *Int. J. Adv. Manufacturing Technology*, **28**, 2006, 456-462.
6. H. Demuth and M. Beale, *Neural Network Toolbox User's Guide*, Version 3.0, Natick, MA, USA, The Math Works, Inc., 1998.
7. M. Misiti, Y. Misiti, G. Oppenheim and J.M. Poggi, *Wavelet Toolbox User's Guide*, Version 2.0, Natick, MA, USA, The Math Works, Inc., 2000.

EVALUATION OF IMPACT FORCE OF MELTED PARTICLE IN THERMAL SPRAYING PROCESS

MANABU ENOKI, KOICHI TANIGUCHI, SHIN OIKAWA, LEI SHEN,
MAKOTO WATANABE* and SELJI KURODA*

Department of Materials Engineering, The University of Tokyo, 7-3-1 Hongo, Bunkyo, Tokyo 113-8656, Japan; *Composites and Coating Center, National Institute of Materials Science, 1-2-1 Sengen, Tsukuba, Ibaraki 305-0047, Japan

Abstract

Coating technology has become important to enhance the material properties, such as heat resistance, wear, corrosion properties and so on. However, it is not easy to analyze the effect of coating parameters on the material properties because coating mechanism is very complicated and many processing parameters affect the properties. Mechanical behavior of impact particle in high-velocity oxy-fuel (HVOF) coating process was investigated by AE method. Each impact of a particle was clearly identified as an AE waveform using pin holes in coating process. Impact force of each particle was quantitatively evaluated by the analysis based on monopole force assumption, and it decreased as the ratio of melted particle.

Keywords: Plasma splay, coatings, process monitoring, impact force, melted particle

Introduction

Thermal spray is a process where material particle is heated, melted and stacked on the substrate. It is important to understand the condition of gas flow and melted particles in the region from nozzle to substrate. A particle is quickly heated and reacted and it traveled in the complicated and variable atmosphere. The process of formation of coating is complicated as there are numerous factors that control the condition of a coating layer. We need to analyze the phenomena of an impacting particle such as temperature, flight speed, spraying atmosphere and so on. Acoustic emission (AE) method is a unique technique to evaluate the time, size, location and mechanical mode of materials in real-time, and it is an important one among nondestructive evaluation (NDE) methods.

Impacting particles in various coating conditions were evaluated in high-velocity oxy-fuel (HVOF) coating process by AE method in this paper. The difference of coating parameters affects the degree of melted particles and shape of splats in the impact, and consequently it can be detectable as the difference of AE signals if the impact speed is constant. The object of this paper is to analyze the relationship between coating parameters and AE signals and obtain the simplified guidance for reliable formation of coating layer.

Experimental Procedures

Materials and Geometry

The thermal spraying equipment in the experiment consists of the controller (JP5000, TAFA), a spray gun, a powder feeder and gas bottles. Substrate was disk samples of SS400 steel with diameter of 70 mm and thickness of 15 mm. Coated surface was mirror-polished and status of impact particles after thermal spraying was observed by optical microscope and scanning electron microscope. Copper particles with diameter from 53 to 63 μm was used as spraying

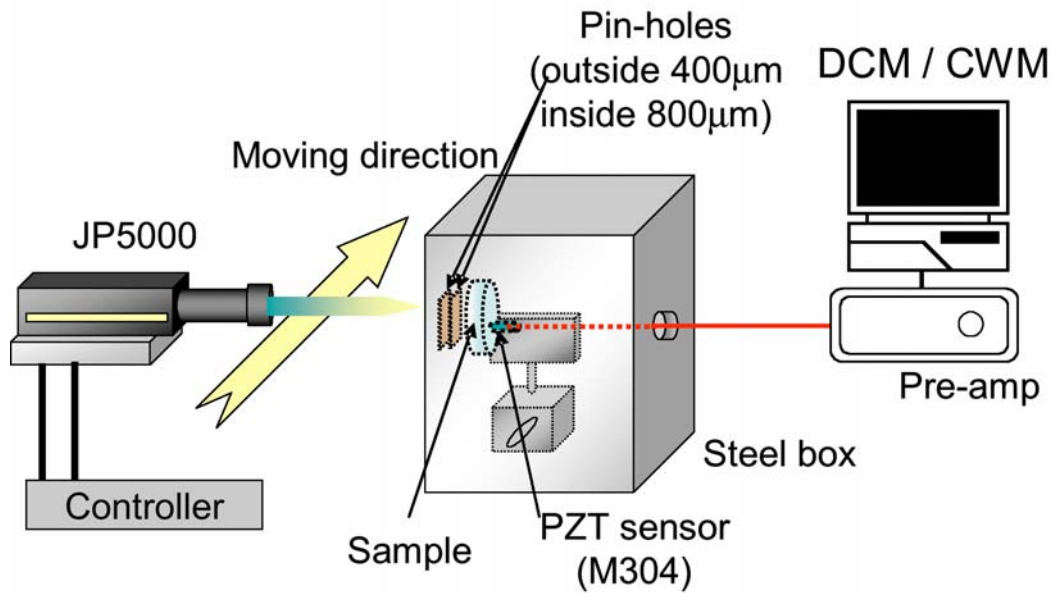


Fig.1 AE measurement setup for HVOF thermal spray process.

particles. Thermal spraying conditions in this experiment was the same as previously reported [1] because the status of melted particles was known. Combustion pressure was constant and fuel/oxygen ratio was changed from 0.46 to 0.86. Flight speed of particles was almost constant regardless fuel/oxygen ratio.

AE measurement

Schematic of AE measurement system is shown in Fig. 1. Sample was covered by steel box to reduce various noise to AE signals, and two pin-holes with diameter of 400 μm and 800 μm were also set in front of this box and the distance between holes was 1.5 mm. High sensitive AE sensor (M304, Fuji ceramics) was attached to the epicenter of impact particles, and AE signals after preamplification were recorded by both AE analyzer (DCM120, JT Toshi) and Continuous Wave Memory (CWM) system newly developed by our research group [2].

Analytical Procedures

Simulation of AE waveform

Impact of melted particles to the substrate in coating process is a complicated phenomenon. However, its mechanical behavior was considered in this paper; that is, impact force of melted particle and local thermal stress during cooling. Impact forces can be considered as monopole forces normal to the substrate, while thermal forces can be treated as dipole forces at the impact point if this stress is assumed to be axisymmetric. Wave propagation of AE was simulated by finite element method to evaluate the mechanical behavior at the impact in experiment from detected AE waveform. The disk sample with the same geometry as experimental substrate was divided to elements by pre-processor and wave propagation was calculated by commercial code (LS-DYNA, Livermore software technology). Pulse with length of 100 ns was used as input time function based on the previous result of impact simulation [3].

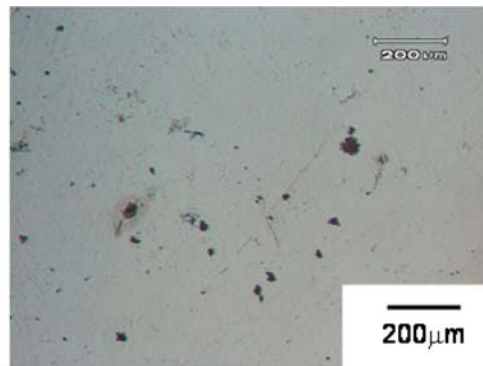
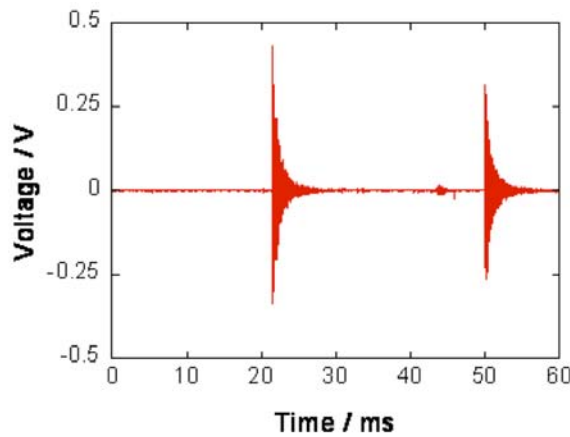


Fig. 2 Detected AE signals of fuel/oxygen ratio 0.46 (left), and surface observation (right).

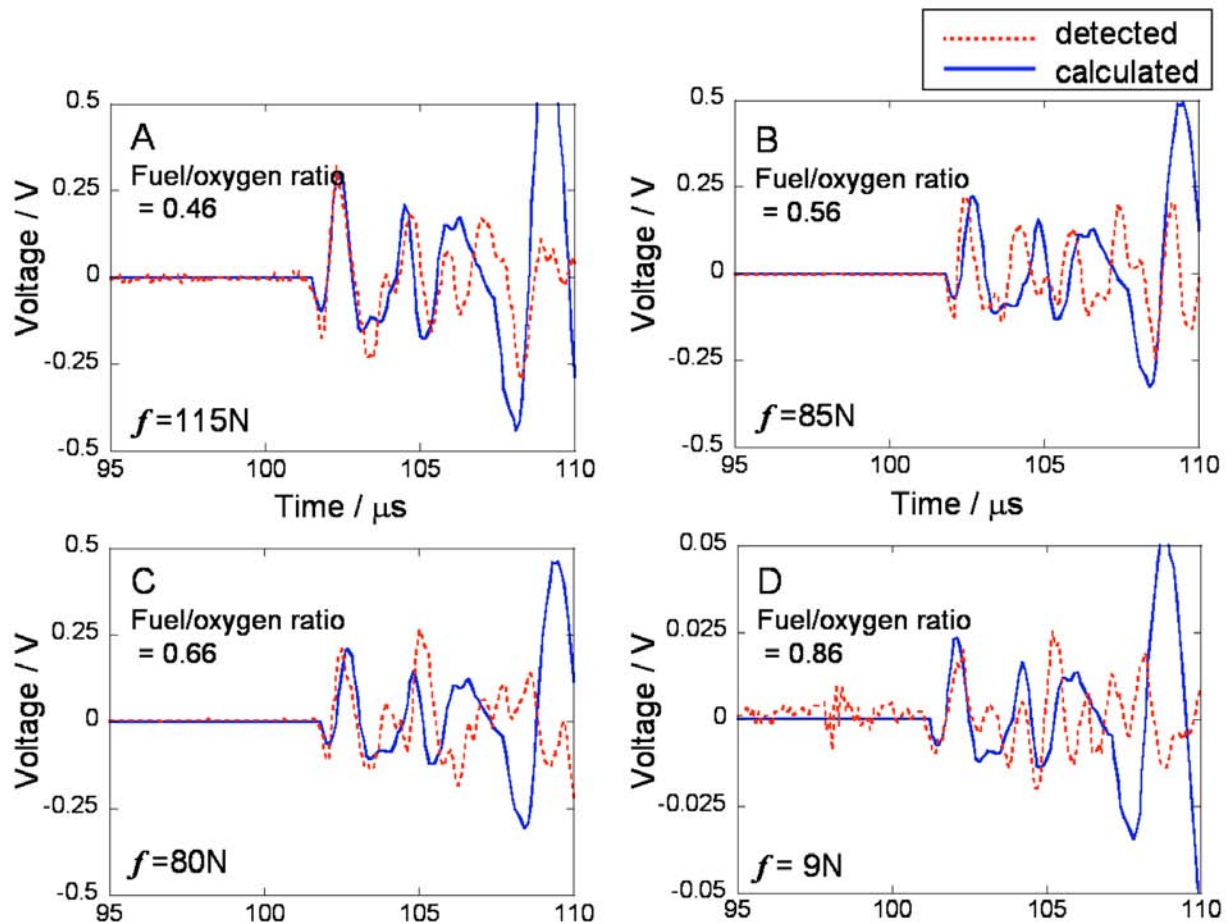


Fig. 3 Detected AE signals and calculated waveforms for each fuel/oxygen ratio.

Source analysis

As detected AE waveform includes the effect of wave propagation and characteristic of measuring system, the response function of measuring system was calculated using the simulated AE signal of pencil led breaking and the calculated waveform due to monopole force [4]. Detected AE waveform was compared to the simulated waveform including the response function of measuring system. Numerical software (MATLAB, MathWorks) was used for convolution and filtering of signals.

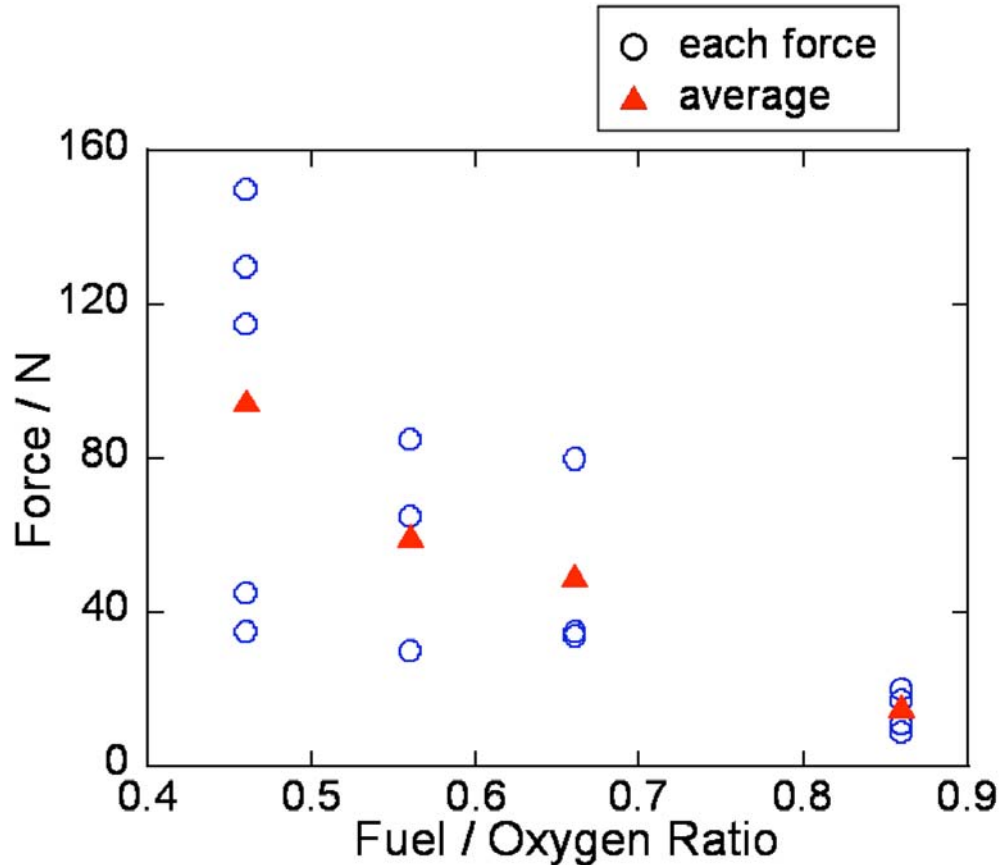


Fig. 4 Estimated impact force by AE source analysis for each fuel/oxygen ratio.

Results and Discussion

Detected AE signal and microphotograph of specimen for fuel/oxygen ratio of 0.46 is shown in Fig. 2. Relatively clear AE signals during coating process were obtained by noise prevention methods in spite of noisy environment. This waveform demonstrates two separated AE signals, and also two impact traces were observed at the surface of sample, which is shown in the right figure. The time period between AE signals was scattered, but it was less than ~60 ms in various coating conditions. Each mechanical behavior of impact could be analyzed by AE waveform because in most cases each AE signal was divided into a discrete waveform.

Let us consider the mechanical behavior of impact particle. As mentioned above, AE source can be treated as the combination of monopole force and dipole force. At first, the effect of dipole force was calculated based on the theoretical consideration. Dipole force due thermal stress can be represented as [5]

$$D = \frac{E}{(1-2\nu)} \cdot \alpha \cdot \delta T \cdot V \quad (1)$$

where E , ν , α , δT and V are Young's modulus, Poisson's ratio, thermal expansion coefficient, temperature difference and volume of source, respectively. If diameter of copper particle of 60 μm and approximate temperature difference during cooling of 1000K are substituted into Eq. (1), D is calculated as about 5×10^{-4} Nm. The simulated AE waveform due to this dipole force was calculated and compared to the experimental waveform. As the simulated dipole force was negligibly small, the effect of monopole was considered in the next section. This result may be

because AE signals were detected at the epicenter and dipole source gives small effect on the epicenter.

Impact forces were evaluated by the fitting of the detected AE signals and calculated waveforms convoluted with the response function of the measuring system, because the experimental signals were quite close to the calculated waveforms. Fitted results for each fuel/oxygen ratio are shown in Fig. 3. Estimated impact forces decreased as fuel/oxygen ratio was decreased, and is shown in Fig. 4. Melted particle ratio was strongly related to the fuel/oxygen ratio, and a small melted particle ratio corresponded to a small fuel/oxygen ratio [1]. This is because the increase of fuel/oxygen ratio induces the liquidation of particle. This fact was also confirmed by the impact force estimated from AE source analysis.

Conclusions

- (1) Each impact of particle during coating process was identified by AE measurement, because the number of AE signals was consistent with that of observed particles on the surface of the specimen.
- (2) Impact force of particle was estimated by AE source analysis based on monopole force assumption. The increase of melted particle ratio decreased impact force.

References

1. J. Kawakita et al.: Surf. Coating Technol., **200** (2006) 4414-4423.
2. K. Ito et al.: Mater. Trans., **48**(6) (2007) 1221-1226.
3. K. Yokoyama et al. : Mater. Trans., **47**(7) (2006) 1697-1702.
4. M. Enoki et al.: Int. J. Fract., **38** (1988) 295-310.
5. C. B. Scurby et al., *Laser Ultrasonics* (1990) 239.

INVESTIGATION OF ELASTIC VELOCITY IN ANISOTROPIC SHALE FOR CORRECTION OF HYPOCENTRAL LOCATION AND CHARACTERIZATION OF ACOUSTIC EMISSION EVENTS

N. DYAUR, I. BAYUK¹, Y. MOHAMED, G. KULLMANN and E. CHESNOKOV

Institute for Theoretical Geophysics, Oklahoma University, Norman, OK 73019 USA;

¹Schmidt Institute of Physics of the Earth RAS, 10 B. Gruzinskaya, Moscow, Russia

Abstract

A method of investigation of anisotropic shale samples for further study of acoustic emission (AE) caused by fracturing is presented. This method includes several steps: (1) selection of samples with no visible nature cracks or technologic cracks and choosing the zones of the shale to be prepared for fracturing experiment using the X-ray imaging method; (2) analysis of the mineralogical composition and microstructure of the shale with the scanning electron microscope; (3) measurements of compressional (V_p) and shear (V_s) wave velocities in the directions parallel, perpendicular and at 45° to the bedding plane in specimens of Barnett shale, which is necessary to characterize the velocity distribution and anisotropy type of rock under study; (4) determination of shale's stiffness from the velocities measured (two different techniques are suggested to be applied for the stiffness tensor determination).

Our study of Barnett shale samples with the method proposed allows us to conclude that the symmetry of the Barnett shale stiffness tensor is transversely isotropic. During the further experiment with fracturing of anisotropic specimens of Barnett shale, it is necessary to include these anisotropic parameters for the location of fracture with the help of AE.

Keywords: Barnett shale, elastic velocity, anisotropy, fracture location, stiffness tensor

Introduction

Fracture events are commonly accompanied by the acoustic emission (AE). The analysis of the AE gives a possibility to determine the location of an event. The AE analysis is usually carried out under the assumption that the medium is isotropic. However, when shales are considered, the anisotropy should be taken into account when analyzing the AE. In this work, we present our investigations of anisotropic specimens of Barnett shale before AE experiment with fracturing. Barnett shale is a sedimentary rock with fine structure of particles of minerals and rocks, microcracks and pores, which may have preferred orientation and influence on the elastic tensor of the shale. Wang [1] pointed out that all shales are intrinsically anisotropic and this anisotropy depends on porosity, compaction history, and, probably, of clay type.

In order to prepare a sample of the shale for fracturing experiment with registration of the AE it is necessary to know structure of the specimen and determine the space distribution of P- and S-wave velocity and type of anisotropy.

Experimental Procedures and Results

Our experimental procedure includes several steps described below.

Step 1. The X-ray imaging method

Using X-ray to provide an image of the cores, internal features have proven to be a useful

tool for the examination of core samples. It is the first step to eliminate or select samples, with or without visible features, depending on the needs of investigators. The image is a variation of gray tones, which are generated by the absorption or lack of absorption of the X-ray beam, as it passes through the sample under investigation (Fig. 1). With all controllable parameters maintained, X-ray energy and intensity, these gray tones are controlled by three factors, sample thickness, mineral density and porosity.

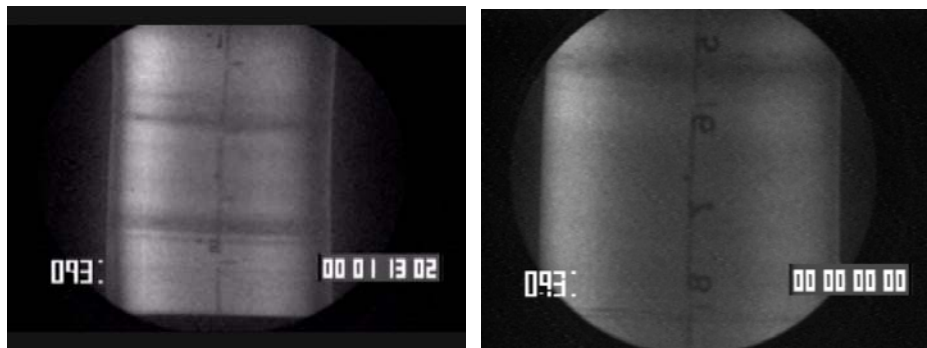


Fig. 1. Examples of X-ray image of Barnett shale taken from core. “Light” and “dark” X-ray zones are presented in the left picture, and “light” zone is mostly seen in the right picture.

The X-ray imaging process involves placing a core in a core-handling device used to rotate the core around its long axis while translating the core horizontally between an X-ray tube and imaging device. X-ray beam is transmitted through the core where its intensity is attenuated by an amount directly proportional to the thickness and density of the core. The attenuated X-ray beam then passes through a fluorescent screen in the X-ray imaging device that emits visible light when exposed to X-rays. The intensity of the emitted visible light is directly proportional to the intensity of the attenuated X-ray beam that has passed through the core. Spatial variations in density within the core result in spatial variations in visible light intensity creating a visible light image. This visible light image is captured by a CCD video camera, displayed in-motion and in real time on video monitor and recorded to the computer hard drive. Still frame or in-motion analog video images of particular interest can be captured, digitized, processes annotated, analyzed and output in a variety of formats.

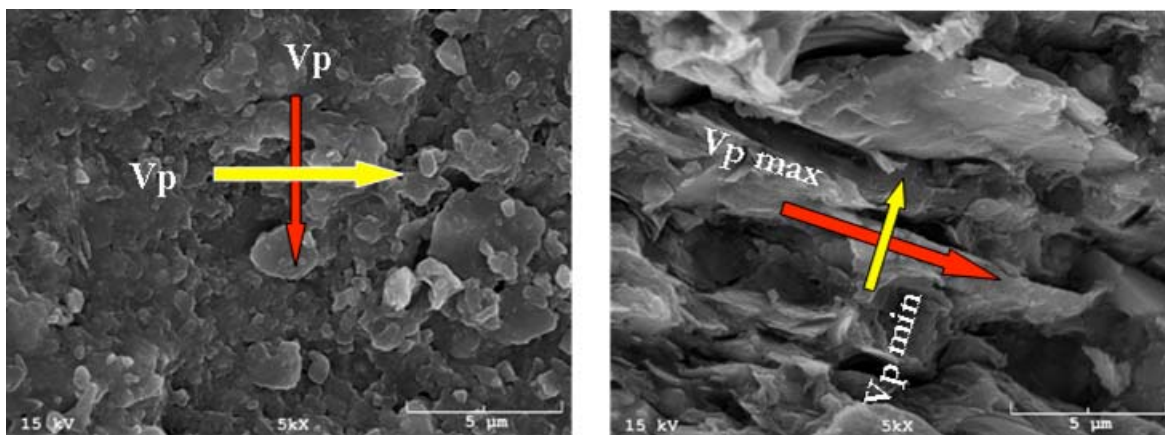


Fig. 2. SEM photos of a Barnett shale sample. The left image is a view of the bedding plane; Values of V_p velocities are almost the same in this plane. The right image is a view in the plane crossing the bedding planes. Velocities $V_{p\min}$ and $V_{p\max}$ (normal and parallel to bedding, respectively) are different and correspond to the microstructure of the shale.

Step 2. The study with SEM

The scanning electron microscope (SEM) gives us an idea about the mineralogical composition and microstructure of the shale, which should be used for better understanding of wave propagation character (Fig. 2). The shale SEM images present orientation of fine particles and minerals in the bedding direction. Wavelength of P-waves changes from 2.7 to 5.5 mm depending on propagating direction in the shale.

Comparing the mineralogical composition and X-ray image in the preliminary investigation of the Barnett shale, we found that the “light” zones are characterized by increased amounts of quartz and clay (or clay+mica) and reduced carbonate content, specifically calcite. The “dark” zones, on the contrary, contain significant carbonate content, specifically calcite, but reduced content of quartz and clay (or clay+mica). Densities of the “dark” zones are greater than those of the “light” zones. For example, the density of core specimen presented in Fig. 3 is 2.55 g/cm^3 for the “dark” zone and 2.41 g/cm^3 for the “light” zone. The shale has “dark” and “light” zones in X-ray images, which are parallel to the bedding plane. We have to use these zones together or separately choosing type of fracturing experiment in Barnett shale.

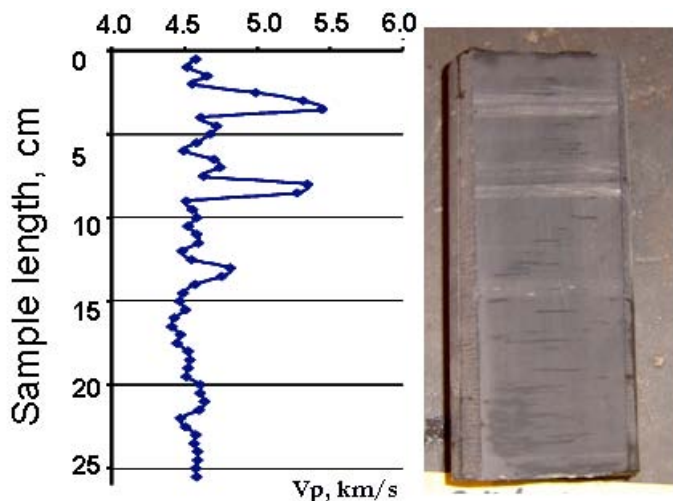


Fig. 3. Changes in compressional velocity along the Barnett shale core. The velocities were measured in the bedding plane in each 5 mm beginning from the core edge. The increased V_p values are related to zones rich in carbonate, which were found first by the X-ray imaging method. In the sample photo the “dark” X-ray zones appear as lighter (inversion of light).

Step 3. Velocity measurements

We applied the ultrasonic pulse transmission technique for the velocity measurements. The central frequency of P- and S- piezoelectric transducers was 1 MHz. The pulser was a high-voltage pulser-receiver. Commonly, we applied pulses of 50-100 v to a P- or S- transmitter, but sometimes the voltage was 200 v. We used an additional preamplifier in attenuating directions of samples. The digital sampling oscilloscope HS4 allows us to have sampling rate of 50 MHz. This means that the accuracy of picking time is 20 ns. Velocities were measured on the shale core of a diameter 101 mm and on shaped specimens of 20-mm thickness. The oriented core was used to obtain the azimuthal distributions of velocities and their dependence on the polar angle to characterize the type of Barnett shale anisotropy. To obtain the angle dependence of compressional (V_p) and shear (V_{s1} and V_{s2}) wave velocities, we used the oriented plugs or shaped samples of the Barnett shale.

The bedding plane of the shale is normal to the core axis. Some samples have calcite-filled fractures oriented in subvertical direction. The measurements in azimuthal directions (on the

bedding plane) were carried out in 22.5° interval. We found that the variations in V_p are small in this case. The estimation of the V_p plane (bedding) anisotropy factor showed variations from 0.5% to 3.8%. To understand the lateral anisotropy of shale we analyzed the polar diagrams of V_p at different scales. The small anisotropy in the horizontal plane can be explained by the influence of subvertical fracture orientation and preferable orientation of fracture formation. The possible explanation is the tectonic stress factor. In the direction normal to bedding, however, the difference in velocity is 60 - 90% and more, depending on many factors, specifically, on invisible microcracks. In the AE experiment, it is necessary to use these velocities to determine the sensors position relative to the axis of symmetry.

The velocities V_p and V_s have a strong correlation with the mineralogical composition and crack orientations. The ultrasonic signal has increasing amplitude in the directions parallel to crack orientation. The lowest amplitude is often observed in the directions normal to the crack plane and to the bedding plane. Similar correlation is observed for S_v -wave velocity in the shale. The polarization of this wave is perpendicular to bedding, in which the most part of particles and microcracks are oriented (see SEM image in Fig. 2). For the X-ray light zones, we obtained lower velocity and lower density, but larger porosity and clay contents. Inverse correlation of V_p , V_s for the X-ray dark zones of Barnett shale is observed.

Since shales are commonly considered as anisotropic rocks, their elastic properties are characterized by stiffness tensor having more than two independent parameters (the elasticity of isotropic rocks is completely described by two independent parameters). In order to find the stiffness tensor of Barnett shale samples, we measure the P- and S-wave velocities (V_p , V_{sh} , V_{sv}) in the directions parallel, perpendicular to the bedding plane and at 45° to the plane as shown in Fig. 4.

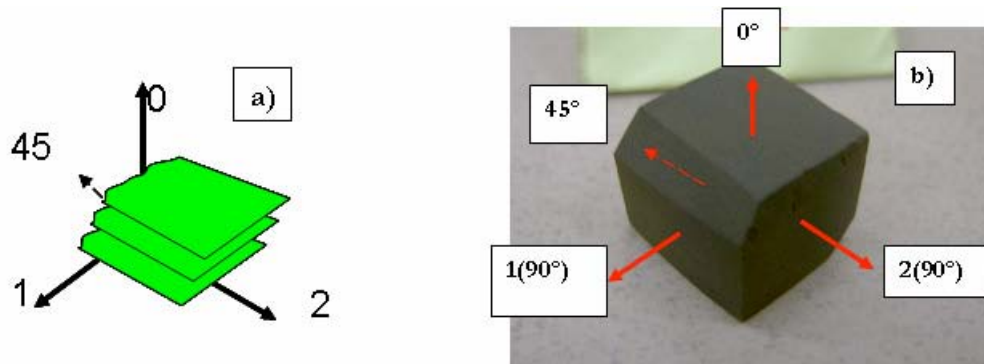


Fig. 4. Directions of P, Sh and S_v velocity measurements: a) schematic representations of the directions of velocity measurements relative to the vertical axis (1 and 2 are measurements in the bedding plane – 90°); b) shaped shale specimen prepared for the velocity measurements.

Step 4. Determination of shale's stiffness tensor

Two mutually perpendicular measurements of the velocities in the bedding plane allow us to conclude that the shale is of transversely isotropic symmetry with the vertical symmetry axis (VTI). The VTI stiffness tensor contains five independent constants: C_{11} , C_{33} , C_{44} , C_{66} , and C_{13} . The stiffness tensor of the Barnett shale has been determined using two different approaches. One of the approaches assumes the use of the Green-Christoffel equation [2], which gives a possibility to invert all of the components C_{ij} if the measurements at three directions relative to the bedding plane are available (at 0°, 90°, and 45°). This approach is commonly used in practice and can be considered as classical one.

However, our analysis shows that the errors in determination of the component C_{13} is greatly dependent on the errors in the velocity value found at 45° to the bedding and on the error of the

angle determination. Thus, the 1% errors in V_p , 3% errors in V_s in the aforementioned directions, and the error of only 2° in the “ 45° angle” may give the error in C_{13} reaching 30%. This can produce an error in the Thomsen parameter δ of up to 100%. Besides, sometimes a situation occurs when there is no possibility to measure some of the velocities needed for determination of the stiffness tensor components from the Green-Christoffel equation (due to considerable attenuation or small size of sample). In this case, we apply another approach for the stiffness tensor determination, which is based on the inverse problem solution with the help of the effective medium theory (EMT) [3].

According to this approach, we minimize a misfit between the experimental velocities and theoretical velocities found with the help of EMT method that is called generalized singular approximation method (GSA) [4, 5]. In the EMT, it is assumed that the wavelength is greater than a heterogeneity size (heterogeneities are mineral grains, pores, and cracks), and the stiffness tensor is determined as a so-called effective tensor, relating, via the Hook's law, the strain and stress fields averaged over sample volume. The effective stiffness tensor is a function of stiffnesses of all components, their shape, and orientation in space. Besides, the effective stiffness tensor is also dependent on medium' microstructure: connectivity of the mineral components and pores/cracks.

Applying the EMT, we model the shale as follows [3]. First, we insert clay platelets in the kerogen, whose elastic properties are known [6]. Then, we insert silt-sized minerals (quartz, feldspar, and so on) and grain-related pore/cracks having ellipsoidal shape. Then, using the information about the clay platelets orientation available from the thin section analysis, we rotate the clay platelets together with the grain-related voids around the vertical axis. We describe this rotation by the Gaussian law with zero means and a standard deviation. If significant elastic wave velocity anisotropy is observed in measurements, an additional system of thin horizontal cracks is inserted. The unknown parameters of this model are: kerogen content, shape (aspect ratio of ellipsoids) of grain-related voids and horizontal cracks, Gaussian standard deviation, and degree of pore/crack connectivity that is called friability factor in the GSA method. All these parameters are found from the minimization, which is carried out with bounds imposed on the unknown parameters. The bounds are commonly derived from the thin-section analysis. The mineral composition of shale is assumed to be known. The effective stiffness tensor of shale under study is calculated with the GSA method using the parameters providing the misfit minimum. Once the shale's stiffness tensor is determined, knowing the sample density, one can calculate the V_p and V_s velocities in any direction using the Green-Christoffel equation.

Figure 5 shows the V_p , V_{sv} , and V_{sh} velocity behavior in the polar plane of a Barnett shale sample calculated from the stiffness tensors found with measurements at angles 0° , 90° , and 45° to bedding, (1) from the classical approach, (2) from the misfit minimization. It also shows (3) the inverted velocity data from the misfit minimization using only the data from measurements at angles 0° and 90° . As seen, the minimization-based approach gives the velocity behavior very close to the classical one. The main idea here is to show the difference in inverted velocity behavior if we use, for minimization, velocity measurements at three angles (inverted blue curves) and only at 0° and 90° (inverted orange curves), since measurements at 45° are less reliable compared to those at 0° and 90° . As seen, the blue and orange curves are very close to one another and we can omit measurements at 45° in inversion if these measurements seem to be unreliable.

During the experiment with fracturing of anisotropic specimens of Barnett shale, it is necessary to use the shale's anisotropic stiffness tensor for the fracture location with AE and characterize the AE event.

The inverted parameters of shale's microstructure corresponding to the “blue curve” solution” are as follows: kerogen content is 2%, friability is 0.89 (note that in our model this factor varies from 0 to 1), aspect ratio of grain-related cracks is 0.022, Gaussian sigma (clay platelets

and cracks orientation relative Z axis) is 24° . This sample has the porosity of 13% and water-saturation of 2%. For this sample, good misfit between experimental and theoretical values is obtained without insertion of additional system of horizontal cracks. The resulting shale's stiffness tensor has the components (in GPa):

$C_{11} = 36.0$, $C_{33} = 12.1$, $C_{44} = 8.6$, $C_{66} = 18.2$, $C_{13} = 0.84$ and density of 2.39 g/cm^3 . In this case, the Thomsen's epsilon and gamma are 0.99 and 0.55, respectively.

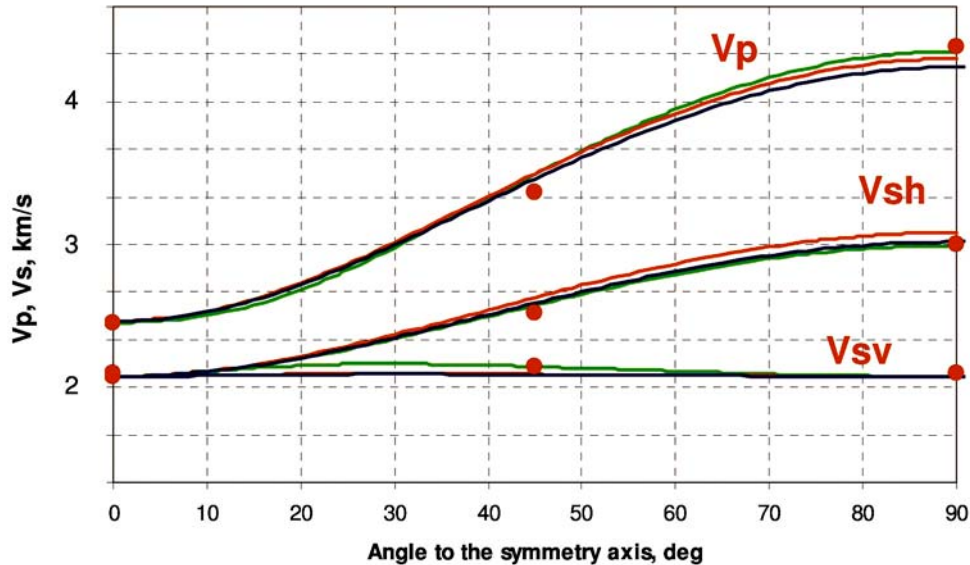


Fig. 5. Velocity behavior of V_p , V_{sv} and V_{sh} in the polar plane found from the velocity measurements at angles 0° , 90° , and 45° to bedding (1) from the classical approach (green curves); (2) from the misfit minimization (blue curves). Also shown is (3) from the misfit minimization from the velocity measurements at angles 0° and 90° to bedding (orange curves). Red circles show the experimental values. Sample N-1.

References

1. J. Wang, *Geophysics*, **67**, 2002, 1423-1440.
2. D.F. Auld, *Acoustic fields and waves in solids, Vol. 1*, Wiley, 1973. 423 p.
3. I. Bayuk, N. Dyauro, Y. Mohamed, M. Ammerman, and E. Chesnokov, *77th Annual International Meeting, SEG, Expanded Abstracts*, 2007a (in press).
4. I. Bayuk and E. Chesnokov, *Journal of Physics and Chemistry of the Earth*, **23**, 1998, 361-366.
5. I. Bayuk, M. Ammerman, and E. Chesnokov, *Geophysics*, **5**, 2007b (in press).
6. L. Vernik and X. Liu, *Geophysics*, **62**, 1997, 521-532.

SOURCE MECHANISMS OF ACOUSTIC EMISSION EVENTS BETWEEN LARGE UNDERGROUND CAVITIES IN A SALT MINE

GERD MANTHEI, JÜRGEN EISENBLÄTTER and THOMAS SPIES*

GMuG Gesellschaft für Materialprüfung und Geophysik, Dieselstraße 9, D-61231 Bad Nauheim, Germany. * Federal Institute for Geosciences and Natural Resources (BGR), Stilleweg 2, D-30655 Hannover, Germany

Abstract

Long-term acoustic emission measurements have been carried out in a salt mine in north-western Germany with the aim to investigate the micro- and macrofracturing processes in a region of a high degree of excavation. For ten years, the acoustic emission events were located by a network of 24 borehole sensors. Their mean rate is in the range of 60 to 100 events per hour. In order to get information about the source mechanisms, the moment tensor method has been applied to strong events, which were localized with good accuracy using more than 29 compressional-wave and shear-wave onsets. The selected events originated in a pillar between huge underground cavities.

The source mechanism of each acoustic emission event has been calculated considering the first motion of at least ten clearly discernible P-wave onsets. The moment tensor analysis figures out, that adjacent events show similar source mechanisms and similar orientations. This result seems plausible because the microcracks occur in the same stress field.

In this paper, we describe in detail how carefully the input data should be selected to get stable moment tensor solutions. We applied statistical methods to eliminate channels from the input data set which cause unstable solutions.

Keywords: Microcracking, rock salt, moment tensor method

Introduction

Since 1995 and 1997, acoustic emission (AE) measurements are carried out in the central section and the southern section, respectively, of the underground repository of Morsleben in a salt mine in northern Germany. Originally, each section was monitored by a network of 24 AE sensors covering an area of 150 m x 100 m x 120 m.

The aim of the AE measurements is to investigate the micro- and macrofracturing processes, which are important for the evaluation of the stability of cavities and the hydraulic integrity of the rock, especially in the case of an underground disposal of hazardous waste in salt rock. The AE events are automatically located using compressional-wave (P) and shear-wave (S) onsets, which are consistent with each other. The maximum amplitudes of the signals and the location of the events are used to calculate a measure of strength of the AE events analogous to the magnitude in seismology.

In this paper, the measured radiation patterns of AE sources, which were detected in the southern section, have been used to determine the fracture type and the orientation of the fracture planes utilizing the moment tensor method. This method requires good sensor coverage of all directions of the focal sphere. Actually, the spatial distributions of the AE sensor networks were designed for source location in a large region and not for determination of source parameters. Therefore, in most monitored regions, the coverage of the focal sphere by the sensor network

was only poor. AE events were selected from a region in the center of the network of the southern section where the coverage is best.

Figure 1 shows a plan view (horizontal projection) of the site. In this projection, the contours of the rooms and the main drift are marked by continuous lines (Rooms 2 and 3) and dashed lines (Rooms 9s and 9n). This mine section was excavated about 70 years ago in rock salt. Nuclear waste is stored in the two lower Rooms 2 and 3. A drift is located at a level between the upper and lower rooms. The average depth level of the cavities is about 500 m. 24 AE sensors (black dots) equipped with piezoelectric transducers are installed in boreholes of up to 30 m length, which were drilled from the drift (gray area) because the rooms are not accessible anymore. The central unit of the measuring system consists of a transient recorder monitoring the signals of the sensors (frequency range of 1 to 100 kHz), a computer controlling all actions of data acquisition and in-situ evaluation, and a modem for telecommunications.

Figure 2 shows in a perspective view of the cavities and the main drift (Rooms 9n and 9s and Disposal Rooms 2 and 3) 41,521 very strong events (yellow dots), which were located in a time period of approximately 5 years.

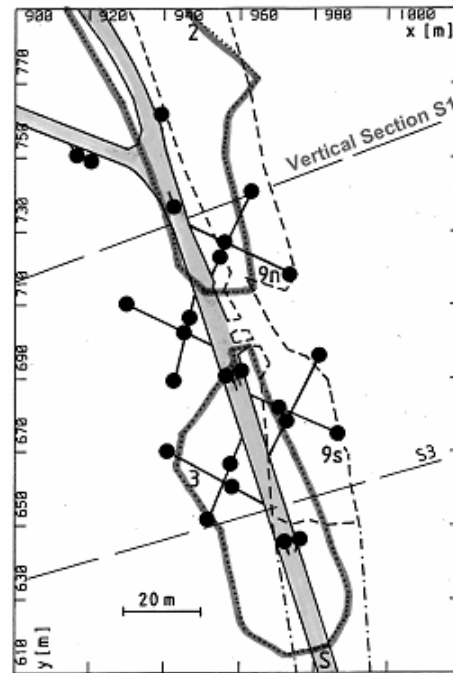


Fig. 1. Plan view of the two levels with Rooms 9n and 9s (dashed line) and Rooms 2 and 3 (bold continuous line) and the access drift (gray). The position of the borehole sensors are marked by black dots [1].

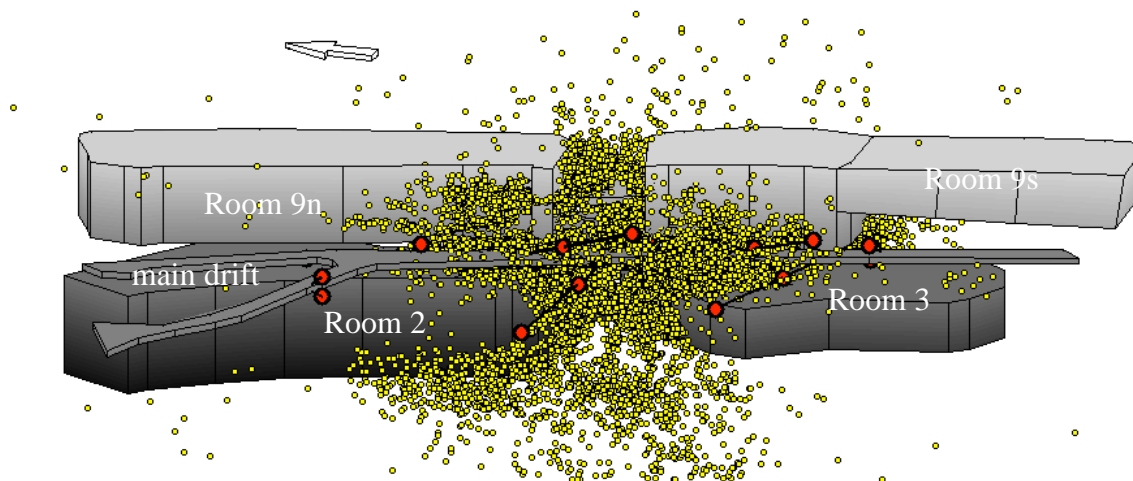


Fig. 2: Perspective view of cavities and the main drift at two levels (Rooms 9n and 9s and Disposal Rooms 2 and 3). The red dots indicate the AE sensors in boreholes, the yellow dots represent the locations of 41,521 AE events [1].

In the following, we will elucidate the extensive preparations to be made for a reliable moment tensor evaluation on the example of events selected from the northern region of the area

shown in Fig. 2, i.e. from a spatial interval of 20 m thickness around vertical section S1 (Fig. 1). In this interval 4,180 events are located.

Pre-processing and Extraction of Data

We applied the moment tensor method to a selection of events with clearly discernible P-wave onsets. Peak amplitudes and polarities of the first motion of the P-wave signal are the input data for the moment tensor calculations. We developed an interactive procedure for data extraction with visual inspection. The data extraction procedure involves the following steps:

- Only very strong events, which were precisely located using at least 30 consistent P- and S-wave arrivals, are selected.
- Band-pass filtering between 1 kHz and 60 kHz to remove high-frequency noise.
- Extraction of traces with a signal-to-noise ratio greater than 20.
- Determination of the P-wave first motion as the first minimum or maximum amplitude in a defined time window around the theoretical P-wave onsets.

Figure 3 shows windowed time traces aligned at the times of the first motion of the P wave. The numbers at the end of the traces refer to the incidence angle, the peak amplitude in Volt, and the length of the travel path. The following steps outline the treatment of data before moment tensor inversion calculations:

- Data were corrected for the measured sensor sensitivity and directivity.
- Geometrical wave attenuation and damping were considered.
- Traces where the incidence angle was greater than 80° were eliminated.
- Traces where the wave radiation is disturbed by large rooms or drifts are eliminated too.

After the data treatment, the over-determined equation system was solved for the six moment tensor components using singular-value decomposition (SVD).

Case Study of Moment Tensor Evaluation

In the following, the orientations of the principal axes obtained from the eigenvalues of the moment tensor are displayed. The eigenvectors of the largest, smallest, and intermediate eigenvalues give the directions of the T (or tensional) axis, the P (or compressional) axis, and the N (or null) axis, respectively.

Factors like small number of stations, insufficient sensor coverage, systematic measuring errors, and large variability in sensor coupling may lead to errors in the estimated source mechanisms.

There are two methods to estimate standard errors. In the first method, the standard errors of the moment tensor are estimated from the diagonal elements of the covariance matrix. This method postulates knowledge about measuring errors of the input data. If the measuring errors of the input data are unknown, which is the case in our measurements, the covariance matrix can be determined using the amplitude residuals.

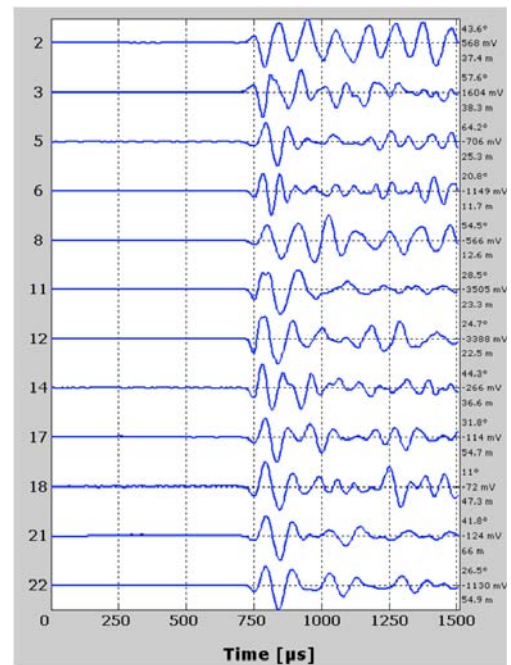


Fig. 3: Aligned P-wave onsets of an AE event located.

The second method is an application of the Jackknife test [2]. The Jackknife test is used to check the influence of a single sensor on the solution of the inversion calculations and to estimate their stability. In order to visualize and quantify the scatter of principal axes orientations, a bootstrap analysis was used. For each event, 250 moment tensor sets were generated by adding random errors to the moment tensor components within a confidence level of 99%, i.e., within 2.35 standard deviations obtained from the Jackknife test. The eigenvectors of all 250 moment tensors were calculated and their directions P, N, and T were plotted as small dots on an equal-area, lower hemisphere projection. Figure 4 shows such plots for the event of Fig. 3.

The plots in the upper row display calculations without channels 2, 3, 5, and 6 (from left to right), the plots in the second row display calculations without channels 8, 11, 12, and 14, and the plots in the third row display calculations without channels 17, 18, 21, and 22. The mean orientation and the scatter of the P, T, and N axes can be read from these plots. The solution with the smallest width of the confidence area is obviously that without channel 8 (the first plot in the second row), which consequently was excluded from the input data set in order to obtain stable solutions.

To quantify acceptable principal axes scattering, we derived stability criteria on a set of 50 randomly selected events.

Events were considered to be stable if the standard deviation of at least one of the three principal axes was less than 4°. Additionally the deviation between the observed and calculated first motion amplitudes must be less than 12%. If these conditions were not met, the event was rejected and not considered for interpretation.

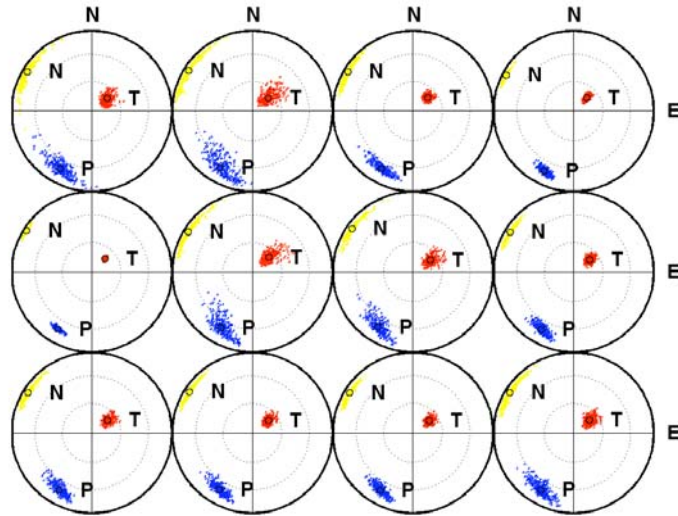


Fig. 4: Positions of the mean T, N, and P axes (big circles) and their confidence areas (small dots) estimated by the Jackknife test and bootstrap analysis without channels 2, 3, 5, and 6 (plots in the first row), without channels 8, 11, 12, and 14 (plots in the second row), and without channels 17, 18, 21, and 22 (plots in the third row).

Table 1: Moment tensors and standard errors obtained from covariance matrix diagonal elements (left-hand side) and from Jackknife test without Channel 8 (right-hand side).

$$M = \begin{pmatrix} -25.8 \pm 10 & 10.6 \pm 7.3 & 383.4 \pm 82.1 \\ 10.6 \pm 7.3 & 51.2 \pm 7.5 & 363.4 \pm 49.9 \\ 383.4 \pm 82.1 & 363.4 \pm 49.9 & 1373.7 \pm 277.1 \end{pmatrix} \quad M = \begin{pmatrix} -26.9 \pm 3.4 & 8.4 \pm 6.0 & 375.3 \pm 30.9 \\ 8.4 \pm 6.0 & 50.2 \pm 6.8 & 356.1 \pm 22.5 \\ 375.3 \pm 30.9 & 356.1 \pm 22.5 & 1340.7 \pm 106.1 \end{pmatrix}$$

Table 1 shows the moment tensor components and their standard errors obtained by both methods for the event in Fig. 3. Whereas the components are similar, the errors clearly differ. The standard errors are clearly smaller with the second method. This fact may be due to the number of measuring values, which are used by both methods: in the case of the first method only 11 equations, in the case of the second method 11x11=121 equations are used to calculate the same number of parameters (6 moment tensor components).

Results

Figure 5 displays the results of the moment tensor calculations of 53 events with stable moment tensor solutions in a perspective view in northeast direction together with the cavities and the main drift without the upper Room 9s (compare with Fig. 1). The events (yellow dots) are located in three separate regions. 18 events are located in Region I beneath the floor of the main drift. 20 and 15 events are located in Region II and III at the western wall and below the floor of Room 9n, respectively. This figure shows for each region the calculated P-wave radiation pattern in an equal-area, lower hemisphere projection (so-called beach balls). The red and blue areas indicate zones of dilatational and compressional first motion, respectively. The white lines in the beach balls indicate the nodal line. A closer look to Fig. 5 points out that adjacent events show similar radiation patterns. This means, that the source mechanisms and source orientations are the same. Furthermore, the radiation patterns of events in Region I show an extended area of dilatational first motion (red area) compared with events in Region II and III, which is an indication for an increased volumetric source component or tensile mechanism. Except some events in Region II, the nodal lines of the events in Region II and III are nearly identical.

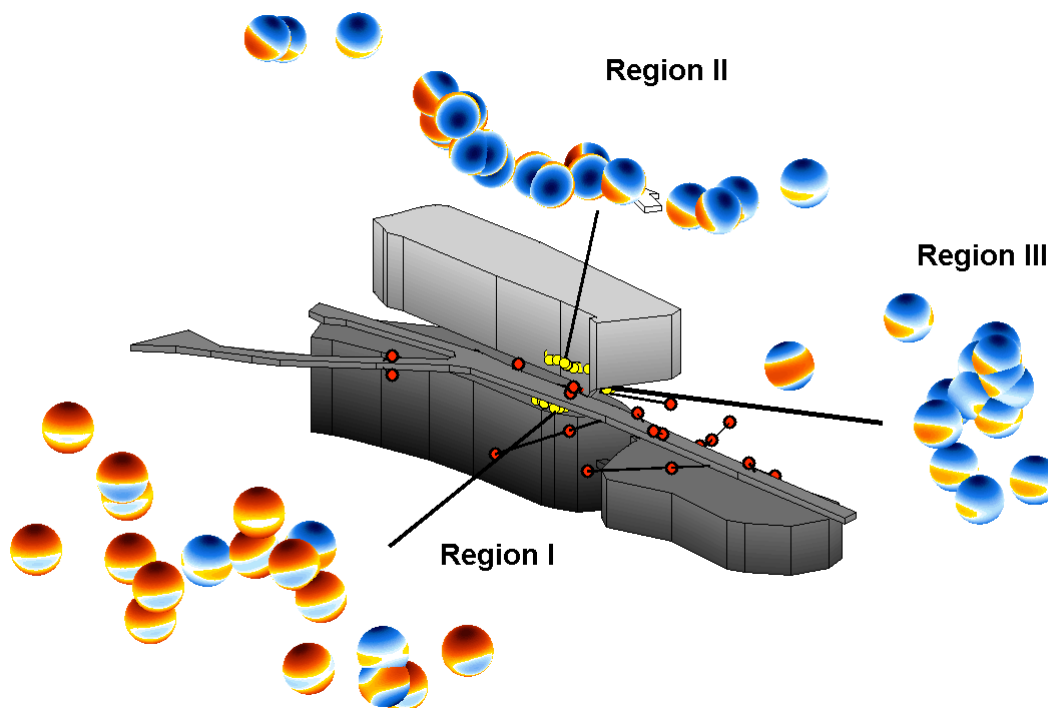


Fig. 5: Perspective view of cavities and the main drift at two levels (without Room 9s) with the P-wave radiation pattern of the investigated events in an equal-area, lower hemisphere projection (beach balls). The red and blue areas are indicating the dilatational and compressional first motion, respectively.

It should be mentioned that, generally, all events show two clearly discernible nodal lines, which enclose a flat angle below 90° . This result is an indication for more or less mixed mode mechanisms of both shear and tensile components, whereas an angle of 90° would indicate a pure shear source mechanism. The decomposition of the moment tensor into volumetric and deviatoric parts confirms this result. Whereas events in Region I and III show 20 to 25% lower shear source components and 20% higher volumetric source components than in Region II, events in Region II show high shear source components (approximately 50%) and low volumetric source components (below 20%).

Apart from a few events, most of the T (or tensional) axes tend to have approximately vertical direction in the range between 60° and 90° (measured from horizontal direction). The P (or compressional) axes have nearly horizontal direction.

Discussion

All evaluated events are located in zones of the highest AE activity in the northern part of the monitored area. In these zones, the AE events occur in "bandlike" structures between the corners of the upper and lower Rooms 9n and 2, respectively, as shown in Fig. 6 in a projection of all events, which include the smaller ones, within a 20-m interval to vertical Section S1 (see Fig. 1). This figure shows a more complete picture of the highly active zones (10,000 events in one month). Geomechanical finite element calculations [1] pointed out that the highest shear stresses and deformations exist in these zones. In addition, the calculations showed also that in these zones tensile stresses are to be expected. This combination of shear and tensile stresses will explain the observed high shear and volumetric source components.

The reason for the high microcrack activity in such "bandlike" structures is creep deformation with microcrack formation of the rock salt accompanied by dilatancy, which is in good agreement with significant volumetric source components. Similar results are known from rock specimen tests. The so-called extension fractures accumulate in zones of high shear stress, which form a cone of conjugate shear bands. In these highly damaged zones, the ultimate failure occurs by sliding [3, 4].

With respect to the practical application of these new tools to a radioactive waste disposal in rock, where zones of permeability for fluids are of utmost interest, it is to emphasize that a sufficiently large number of sensors should be positioned in such a way that all directions of the focal sphere are well covered. This is essential for the use of only P-wave first motions for location and moment tensor analysis. This is a question of accessibility for drilling wells for sensor installation. The sensors should be far enough from excavations and galleries so that the wave propagation will not be disturbed ("shaded") by excavated rooms and galleries.

References

- [1] T. Spies, J. Hesser, J. Eisenblätter and G. Eilers, *Proc. International Conference on Disposal Technologies and Concepts*, 2004, pp. 303-311.
- [2] B. Efron, and R. Tibshirani, *Statistical Science*, **1**, 1986, 54-77.
- [3] G. Herget: *Stresses in Rock*, A. A. Balkema/Rotterdam/Brookfield, 1988.
- [4] G. Manthei, *Bull. Seis. Soc. Amer. (BSSA)*, **95**, 2005, 1674-1700.

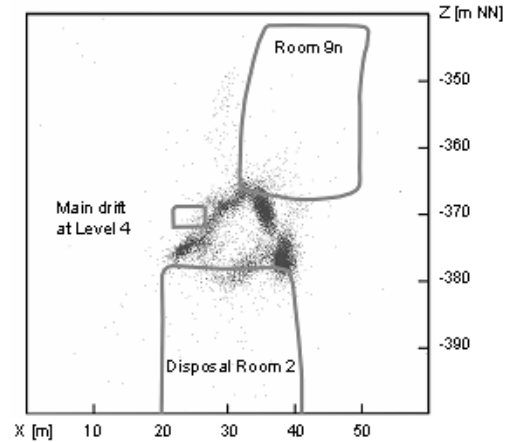


Fig. 6: Located AE events in vertical cross section S1 (see Fig. 1).

CLUSTERING ANALYSIS OF AE IN ROCK

N. IVERSON, C-S. KAO and J.F. LABUZ

Department of Civil Engineering, University of Minnesota, Minneapolis, MN 55455 USA

Abstract

Because failure of rock involves localization of microcracks, the location of acoustic emission (AE) can be used to track the failure process. In addition to the determination of event hypocenters, clustering analysis offers quantitative information to identify the characteristic of the spatial distribution of AE events. For example, an inspection of AE locations from a fracture test can be interpreted using the fractal dimension: three represents random events occurring in a volume while a fractal dimension of two signifies that the events have localized on a plane. A clustering algorithm is used to analyze laboratory tests performed on specimens undergoing tensile- or shear-type failure.

Keywords: Fractal dimension, clustering analysis, strength testing

Introduction

A common feature of failure in a quasi-brittle material such as rock is the development of microcracking, which releases energy in the form of elastic waves called acoustic emission (AE). The AE technique can be used to monitor the evolution of damage, through the entire volume, at various stages of loading. The coordinates of an acoustic source can be obtained from the arrival times of the P-wave at the receivers. The locations of AE provide a picture that forms a basis for the justification of mechanical models of damage and failure (Shah and Labuz, 1995).

Various algorithms for analysis of AE were developed and used to interpret failure of rock. Specimens were loaded with a closed-loop, servo-hydraulic frame and the data from LVDTs, strain gages, and a load cell were stored on a computer and time stamped for synchronizing with the events. The AE sensors were piezoelectric crystals connected to preamps and bonded to the specimen using a modified alkyl cyanoacrylate adhesive. One sensor was used as a trigger, with a threshold of 7 mV after amplification at 40 dB gain. The AE signals were recorded using four, two-channel high-speed digitizers with a 100- μ s recording window and then sent to a computer and stored for later analysis. The digitizers recorded at 40 Msamples per second. A pretrigger region was included to ensure capture of the first arrival; this pretrigger was set at 50 μ s. Eight AE sensors were used to record event data.

AE Locations

The unknowns for a three-dimensional location are the three AE source coordinates and the time of source inception, assuming that the P-wave velocity is known. However, the quadratic nature of the distance equation requires a minimum of five receivers to remove any ambiguity in optimizing the source location. The optimization is achieved by minimizing the residual in a least-squares sense using the Levenberg-Marquardt technique:

$$\varepsilon^2 = \sum_{i=1}^{\#_of_Sensors} \left(\left[\frac{\sqrt{(x_i - x)^2 + (y_i - y)^2 + (z_i - z)^2}}{c} + t_o - t_i \right]^2 \right) \quad (1)$$

where ε is the error; x , y , and z are the coordinates of the AE event; x_i , y_i , and z_i are the coordinates of the i^{th} sensor; c is the P-wave velocity; t_o is the time of the event; and t_i is the arrival time at the i^{th} sensor (e.g. Salamon and Wiebol, 1974).

To find the relative arrival time, the waveform was checked to see when the signal passed a designated threshold value, which was determined from the standard deviation of the noise of channel for each sensor. The mean amplitude and standard deviation of the noise during the pre-trigger period was calculated. The threshold was then set at three times the standard deviation from the mean. When the threshold value was exceeded the point was stored as the trigger point. The data was then scanned preceding the trigger point until the point in which the channel's mean value was obtained prior to this trigger point; this point was then used for the potential arrival of the event. The next 120 points were checked to see if the trigger threshold was crossed three more times during that interval. If the threshold had indeed been exceeded three subsequent times, the point was then stored as the arrival time. About 50 - 75% of the total events were located within 5-mm error. The error for each event was calculated by checking the goodness of fit between the sensors as the distance from the calculated location and the estimated arrival times.

Clustering Analysis

One way of describing a geometric figure is by its fractal dimension, which can be thought of as the number of variables required to describe a shape. For example, a line has a fractal dimension of one, a plane has a fractal dimension of two, and a volume has a fractal dimension of three (Mandelbrot, 1983). The use of fractal analysis to monitor the evolution of the failure process is reasonable because a fractal dimension of three represents random events occurring in a volume and a fractal dimension of two signifies that the events have localized on a failure plane (Hirata et al., 1987; Smalley et al., 1987).

The process used to obtain the fractal dimension is the correlation integral, which compares the proximity of events to one another:

$$C(r) = \frac{2}{N(N-1)} N_R(R < r) \quad (2)$$

where $N_R(R < r)$ = the amount of pairs (p_i, p_j) with a distance smaller than r (e.g. Knox, 1963; Williams, 1983). The correlation integral can then be used to calculate the fractal dimension (FD):

$$C(r) = r^{FD} \quad (3)$$

By varying the value for r , a plot can be made to represent the changing value of the correlation integral versus the distance r . The fractal dimension is the slope of the function on a log-log plot, as shown in Fig. 1.

To demonstrate the clustering analysis, three sets of 100 data points, which can be thought of as AE locations, were placed randomly (i) in a volume (Fig. 1a), (ii) on the surface of a sphere (Fig. 1b), and (iii) along a line (Fig. 1c). The clustering analysis was performed, and the corresponding fractal dimensions were 3.0, 2.0, and 1.0, respectively. In laboratory tests associated with failure of rock, a common second order feature is a mode I fracture or a shear band, and the fractal dimension offers the possibility to identify localization of deformation.

Experimental Results

Three Point Bend Tests

The first series of experiments involved tensile failure through mode I fracture. Specimens of Serena sandstone were loaded in the three point bend configuration. The beams were cut to a length of 310 mm, a width of 80 mm, and a thickness of 32 mm. The distance between supports was 300 mm. A strain-gage based displacement transducer with a gage length of 20 mm was

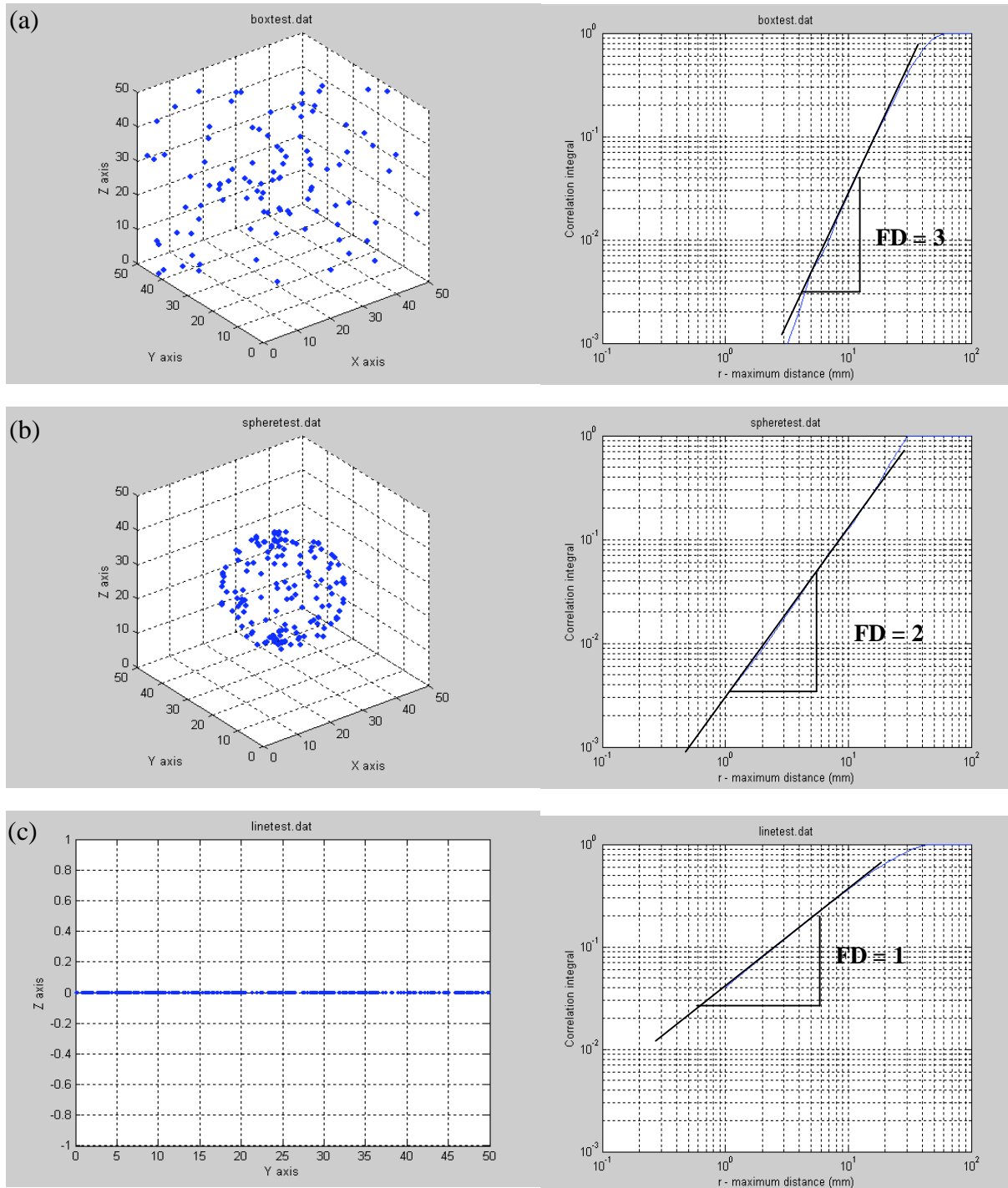


Fig. 1. Points randomly distributed (a) in a volume, (b) on a surface of a sphere, (c) along a line.

placed at the center position to measure the crack mouth opening displacement (CMOD), which was used as the control signal within the closed-loop, servo-hydraulic load frame.

Figure 2 shows the located events at different stages of loading, as indicated by the % of peak load (the load ratio). A migration of AE with load was observed and the AE tracked the propagation of the crack. Note that the boundary of the beam was smooth—there was no notch.

The clustering analysis showed that the fractal dimension started at about 2.3, with a steady decrease during the test (Fig. 3). Even with a smooth boundary, localization in the form of an intrinsic zone produced a natural stress concentration near the bottom of the specimen, and some localization of AE was observed. A crack initiated and propagated in a similar fashion to a notched specimen (Labuz and Biolzi, 1998). The fractal dimension before peak started at 2.3, although there were very few events (< 50) prior to peak. Nevertheless, FD dropped from 2.3 to 2.0 after peak load as the fracture propagated.

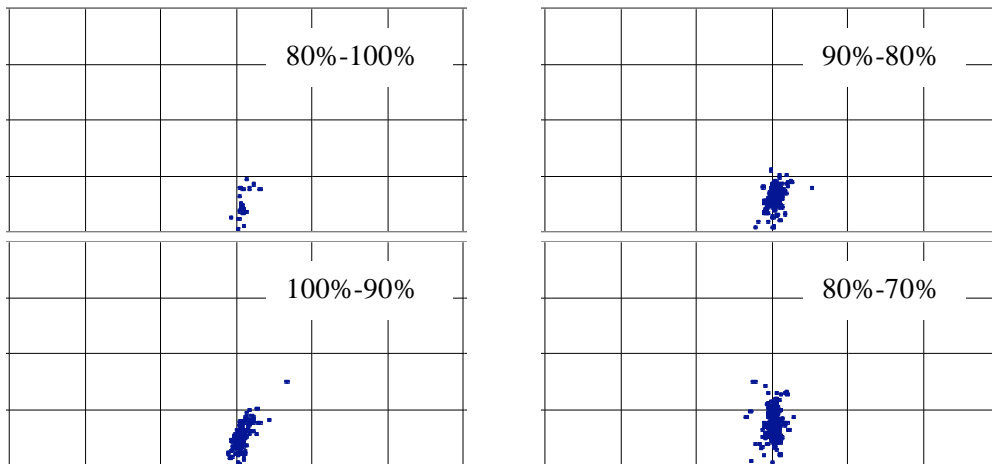


Fig. 2. AE events in beam with no notch at different load ratios.

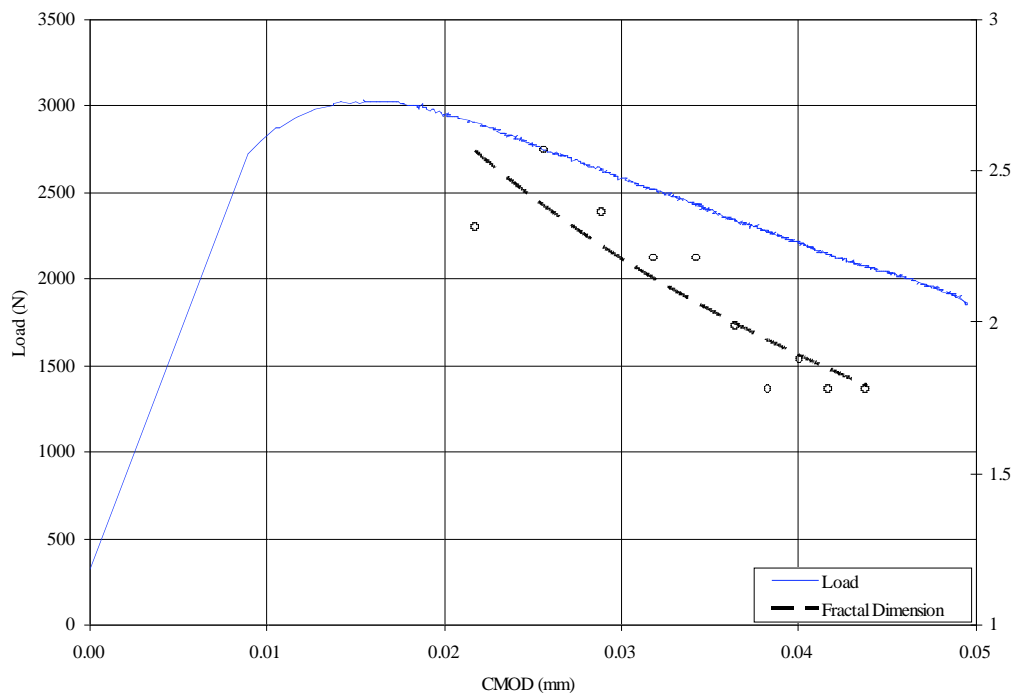


Fig. 3. Load history and fractal dimension for beam with no notch.

Biaxial Test

A plane-strain (biaxial) compression apparatus (Drescher et al. 1990; Riedell and Labuz 2007) was used to examine shear banding in Berea sandstone. The apparatus allows the failure plane to develop and propagate in an unrestricted manner by attaching a low friction linear bearing to the upper platen. Plane-strain deformation is enforced by a thick-walled steel cylinder called the biaxial frame. Eight AE sensors were mounted on the specimen to capture the events.

The AE event locations were plotted in load increments and compared from successive load ranges, as shown in Fig. 4. The AE seemed fairly sporadic and concentrated toward the center of the specimen. As peak load was reached, however, the pattern changed. The amount of events occurring away from the center increased and focused above and left of center. It appeared that the shear band was propagating (Riedel and Labuz, 2007).

The clustering analysis was applied to the AE locations from the biaxial experiment. The FD started at a value of 2.6, but it dropped in the post-peak region reaching a value of 2.3 before terminating the test (Fig. 5).

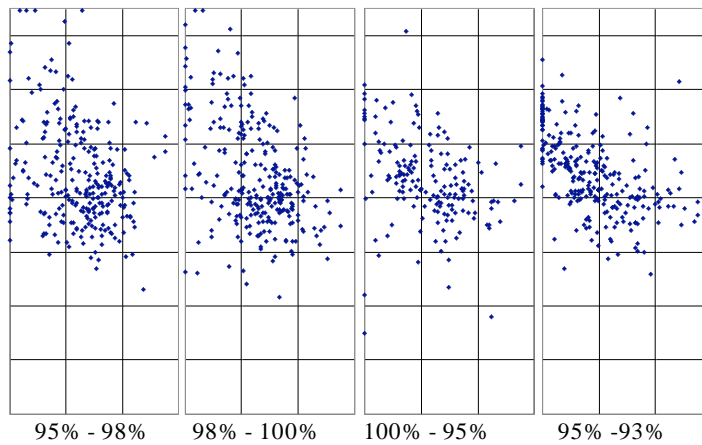


Fig. 4. AE events in biaxial specimen (BSXL13).

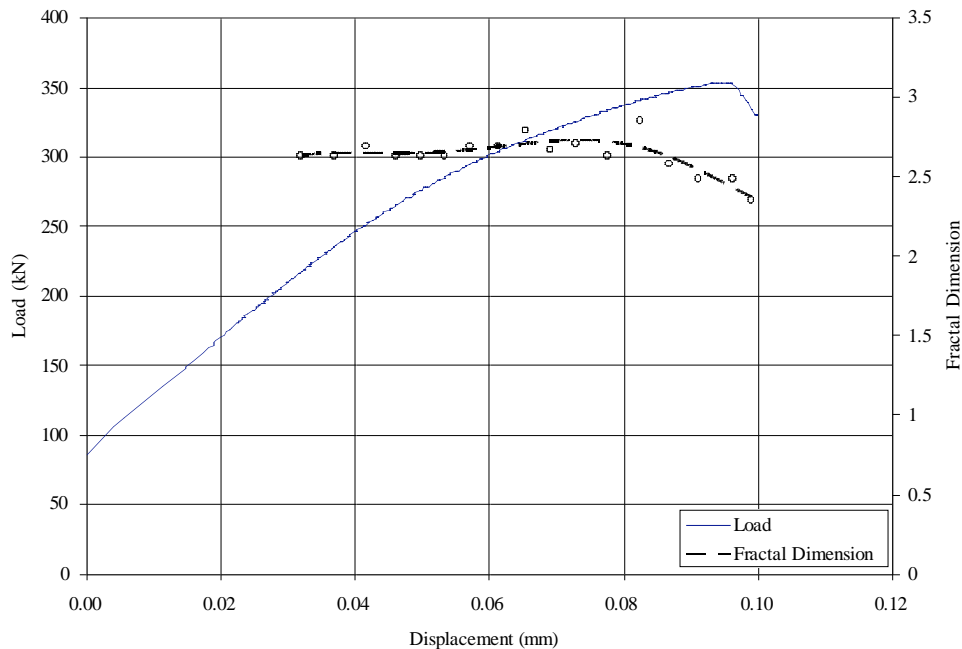


Fig. 5. Load history and fractal dimension for the biaxial test (BSXL13).

Conclusions

This research was focused on the development of numerical methods to analyze AE data. Specifically, a location algorithm for estimating the source hypocenter was used to map the failure process of rock under tensile and shear type loading. A clustering analysis based on fractal theory provided a quantitative method for describing the transition from random microcracking to localized failure.

The distribution of events within an increment of load has a fractal structure that can be characterized by a fractal dimension FD, where a reduction in FD indicates clustering of hypocenters. A parametric study was used to provide a visual interpretation of a fractal dimension between three (random events) and two (localization of events on a plane). The algorithms developed were used to interpret AE data from various experiments on rock. The results for the beams with a smooth boundary (no notch) showed that near peak load the fractal dimension was about 2.3, and approached 2.0 in the post-peak phase of loading as crack propagation occurred. Confined, plane strain compression tests involving shear-type failure showed that the fractal dimension was approximately 2.6 before peak load, and as the test progressed and shear banding developed, the fractal dimension decreased to around 2.3.

References

1. A. Drescher, I. Vardoulakis, and C. Han, *Geotech. Testing J. ASTM* **13**, 1990, 226-234.
2. T. Hirata, T. Satoh, and K. Ito, *Geophysical Journal of Research, Astronomical Society*, **90**, 1987, 369-374.
3. G. Knox, *British Journal of Preventive and Social Medicine*, **17**, 1963, 17-24.
4. J.F. Labuz and L. Biolzi, *Int. J. Solids Struct.*, **35**, 1998, 4191-4204
5. B.B. Mandelbrot, *The fractal geometry of nature*, W.H. Freeman, 1983, 468p.
6. M.D.G. Salomon and G.A. Wiebol, *Rock Mech.*, **6**, 1974, 141-166.
7. J.J. Riedel and J.F. Labuz, *Int. J. Num. Anal. Meth. Geomech.* **31**, 2007, 1281-1299.
8. K.R. Shah and J.F. Labuz, *J. Geophys. Res.*, **100** (B8)2/3, 1995, 15527-15539.
9. R.F. Smalley Jr., J.-L. Chatelain, D.L. Turcotte, and R. Prevot, *Bulletin of the Seismological Society of America*, **77**(4), 1987, 1368-1381.
10. G.W. Williams, Time-space clustering of disease, in *Statistical Methods for Cancer Studies*, R.G. Cornell, editor, New York, 1984. Marcel Dekker, Inc.

ON INVESTIGATING MICROCRACK EVENTS AT COCR ALLOY AND ACRYLIC CEMENT INTERFACE IN SHEAR STRENGTH TESTS

GANG QI and BIN ZHANG

Medical Acoustic Research Laboratory, Department of Mechanical Engineering, The University of Memphis, Memphis, TN 38152, USA.

Abstract

This work examined microcrack event initiation and formation in shear strength tests of stem cement interface encountered commonly in cemented total hip replacement (or total hip arthroplasty, THA). It was found that although the strength of this interface could be increased significantly from about 4 MPa to over 9 MPa, it resulted in a consequence of surprisingly early microcrack event onset at stress levels of 0.108, 0.273, and 0.303 MPa for the satin-finished, grit-blasted, and plasma-sprayed stem surfaces, respectively. Roughened stem surface creates significantly greater microcrack activities in both preyield and yield loading stages, which could result in worrisome debris production during fatigue loading. The data from this work may help explain the contradictory clinical outcomes. According to the most recent work, it appears that these microcrack activities are more likely a major contributor to the aseptic loosening in the cemented femoral component in THA.

Keywords: PMMA bone cement, surface roughness, stem-cement interface, microdamages

Introduction

The stem-cement interface is considered as a primary site leading to eventual clinical loosening of cemented total joint replacements. Many potential influencing factors, such as extant porosity and gaps at the stem-cement interface [1-6], controlling the polymerization front of the curing cement [3, 7, 8], cement viscosity [9] and stem-surface roughness and coating [3, 10-13]. Of these factors, surface roughness has the greatest influence on the mating strength of stem-cement interface. However, the debate remains of whether to roughen, semi-roughen or not roughens the stem surface. For instance, it was reported that a roughened stem surface showed poor outcomes [14-17], while others reported that there was no significant difference between roughened and smooth (polished or satin) stem surfaces [18, 19].

The objectives of this study are: (1) to characterize microcrack activities at the stem-cement interface; (2) to correlate microcrack activity characteristics with classical mechanical measurements; and (3) to provide a means that can be used to predict mechanical behavior of the stem-cement interface. To accomplish these objectives, an acoustic emission technique (AE) was used that is capable of measuring the initiation, distribution, and accumulation of microcrack activities and associated energy in the loading process without the knowledge of the state of stress [20-22].

Method

Thirty-one stem-cement interface sandwich specimens were prepared for this study. Of these, 12 had a grit-blasted finish ($R_a=3.9 \mu\text{m}$), 10 had a satin finish ($R_a=0.85 \mu\text{m}$), and 9 had a plasma-sprayed finish ($R_a=9.29 \mu\text{m}$). The final finished size of the stem bars was $5.9 \times 11.1 \times 125 \text{ mm}$. The surface treatments of these bars were glass-bead blasting (satin finish), alumina-grit blasting (grit blasted), or CoCr plasma spray (plasma sprayed). The surface roughness of the stem, R_a , were measured using a contact profilometer (Surfcom 1800D, Zeiss) with a travel and cutoff length of 15 mm and 5 mm, respectively. The PMMA bone cement (VersaBond™, Smith & Nephew Inc., Memphis, TN) were mixed for 40 – 50 sec and introduced to a rectangular mold over the CoCr alloy bars in a medium viscosity state. Specimens were allowed to cure for over 48 h in the mold before released. The edges were sanded to remove any excess cement. The prepared specimens were subject to shear-strength tests under the regime shown in Fig. 1, in which the cement bar was clamped on both narrow sides with the bottom end supported. A quasi-static loading (Instron 4465) was applied to the top surface of the stem bar at a crosshead rate of 1 mm/min. Each shear-strength test was monitored using an AE system (ASMY-5, Vallen-Systeme GmbH, Germany). The AE sensors (Physical Acoustics, Inc., Princeton, NJ) have resonant and operating frequencies of 140 kHz, and 125 to 750 kHz, respectively. Five sensors were attached to the specimen surfaces with glue applied around their peripheries and silicon grease applied centrally for proper acoustic coupling (Fig. 1). The AE signals were conditioned first by preamplifiers (AEP4, 40 dB, Vallen-Systeme GmbH, Germany), and then fed to the AE system. All the post-test AE data was processed by an in-house developed program (MapCrack©, at the Medical Acoustic Research Lab, the University of Memphis).

In this work, we categorize the standard quasi-static load in the following specified stages: 1) preyield - when the applied load is below yielding level, and 2) yield - when the applied load is between yield and slightly beyond the ultimate load.

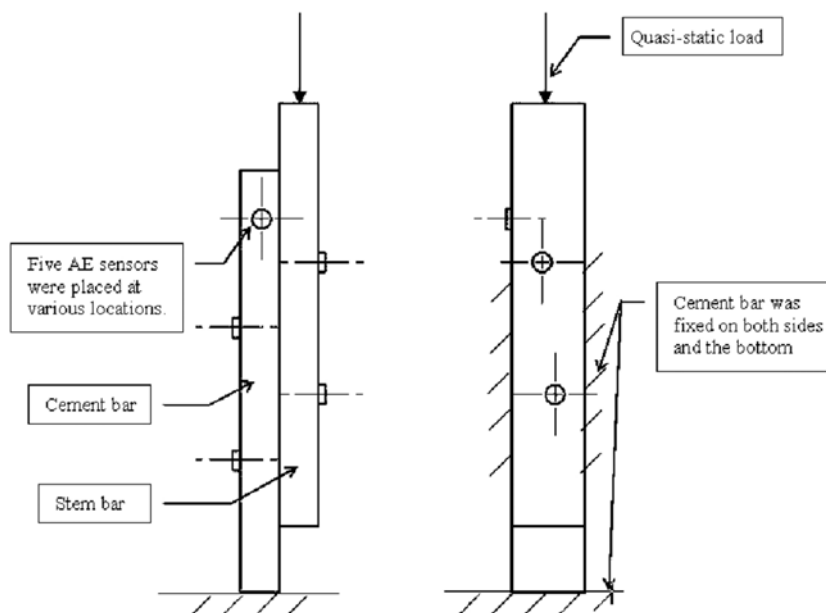


Fig. 1. Stem-cement interface strength test regime.

Results

Measurements of surface roughness, R_a , apparent interface shear strength, microcrack activity onset stress, and the stress ratio were tabulated in Table 1.

Table 1. Surface roughness, apparent shears strength, microcrack activity onset stress, and stress ratio.

Surface finish	Roughness R_a , μm	Shear strength, MPa	Onset stress, MPa	Stress ratio (onset/max), %
Satin finished	0.85 ± 0.03	0.377 ± 0.056	0.108 ± 0.031	25.842 ± 6.229
Grit blasted	3.95 ± 0.15	1.915 ± 0.107	0.273 ± 0.034	15.200 ± 2.335
Plasma sprayed	9.29 ± 0.29	9.480 ± 0.317	0.300 ± 0.085	3.237 ± 0.882

The cumulative microcrack activities in the three loading stage are summarized in Table 2. Statistical tests showed that there are significant differences of microcrack intensity between the smooth and roughened interfaces in the preyield loading stage. When examining the quantity of microcrack activities in the preyield stage relative to the microcrack activities in preyield and yield stages, the ratios are 51%, 32%, and 27% in the plasma-sprayed, grit-blasted, and satin-finished surfaces, respectively (Table 2).

Table 2. Microcrack activities, intensities, and average microcrack energy in the preyield and yield loading stages, and preyield activities to preyield and yield activities ratios.

Surface finish	Microcracks	Preyield stage	Yield stage	Ratio of preyield to preyield + yield stages
Satin finish	# of activities	642 ± 304	1036 ± 310	27.42 ± 5.80
	Activity intensity, #/mm ²	0.999 ± 0.426	1.810 ± 0.541	---
	Average activity energy, eu	112.799 ± 36.171	323.336 ± 74.397	---
Grit blasted	# of activities	1519 ± 397	2624 ± 235	31.87 ± 6.20
	Activity intensity, #/mm ²	3.197 ± 0.727	4.587 ± 0.411	---
	Average activity energy, eu	8.424 ± 1.131	69.207 ± 18.421	---
Plasma sprayed	# of activities	5436 ± 930	5028 ± 581	50.64 ± 4.31
	Activity intensity, #/mm ²	15.650 ± 2.818	13.909 ± 1.760	---
	Average activity energy, eu	7.914 ± 1.458	127.805 ± 30.632	---

SEM observations of the stem and the corresponding mating cement surfaces indicate that there is a clear distinction between the amount of breakage of cement fragments in the stem surfaces (indicated by the dark areas in Fig. 2). There is only one dark area found in satin-finished specimen (indicated by an arrow; Fig. 2a). The cross section observations did not show any substantial microcracks that appeared to be due to the shear rupture.

Conclusion

This work investigated microcrack activities at the clinically significant femur stem and cement interface. It was found that:

- Microcrack activities could onset at a surprisingly low stress level, 0.108 ± 0.031 , 0.273 ± 0.034 , and 0.300 ± 0.085 MPa for the satin finished, grit blasted, and plasma sprayed interface groups, which are much lower than previously thought.

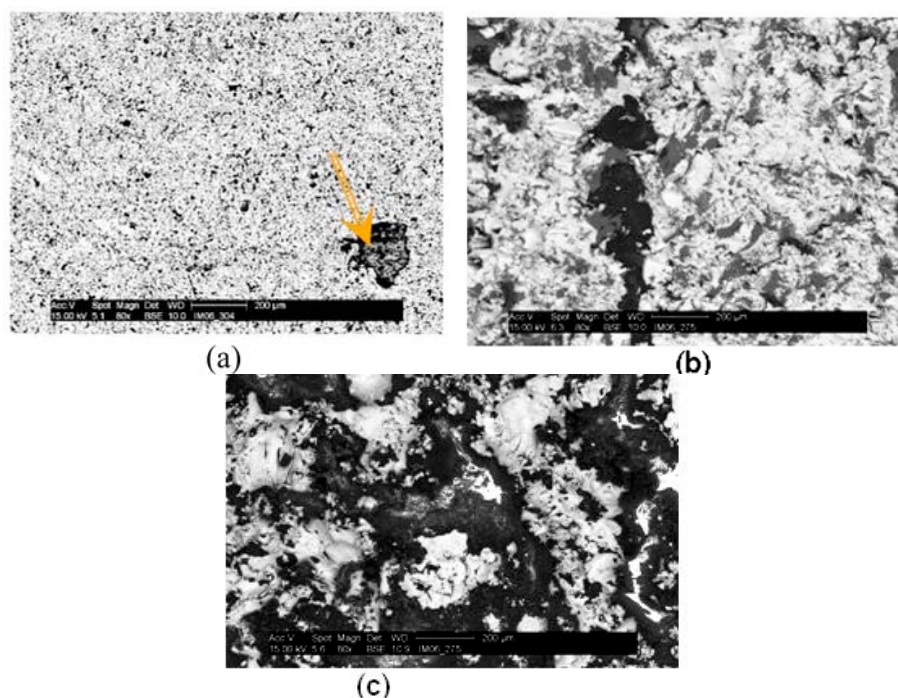


Fig. 2. Post-test stem surface morphology. The light and dark areas are the metal and the broken interlocked cement, respectively, (a: satin finish, b: grit blasted, and c: plasma sprayed).

- There was a significantly greater microcrack intensity in the roughened stem interface than that in the satin interface.
- The average microcrack activity energy was significantly greater in the satin finished interface than that in the roughened interfaces, which indicated the failure mechanism in the satin finished interface is the “true interface debonding,” whereas the roughened interfaces are dominated by the breakages of interlocked cement fragments.

Acknowledgment: This work was supported by NIH AR051119, the bone cement was supplied by Smith & Nephew, Inc. Memphis, TN, USA.

References

- [1] Wang JS, Taylor M, Flivik G, Lidgren L. Factors affecting the static shear strength of the prosthetic stem–bone cement interface. *J. Mater. Sci. Mater. Med.* 2003, **14**: 55– 61.
- [2] Mann KA, Damron LA, Miller MA, Race A, Clarke MT, Cleary RJ. Stem-cement porosity may explain early loosening of cemented femoral hip components: Experimental-computational in vitro study. *J. Orthop Res.* 2006 Dec, **5**.
- [3] Bishop NE, Ferguson S, Tepic S. Porosity reduction in bone cement at the cement–stem interface. *J Bone Joint Surg* 1996, **78-B**: 349–57.
- [4] Race A, Miller MA, Ayers DC, Cleary RJ, Mann KA. The influence of surface roughness on stem–cement gaps. *J Bone Jnt Surg* 2002, **84B**, 1199 –1204.
- [5] Race A, Miller MA, Clarke MT, Mann KA. Cement-implant interface gaps explain the poor results of CMW3 for femoral stem fixation: A cadaver study of migration, fatigue and mantle morphology. *Acta Orthop.* 2005 Oct; **76**(5): 679-87.
- [6] Wang JS, Franzen H, Lidgren L. Interface gap after implantation of a cemented femoral stem in pigs. *Acta Ortho Scand* 1999; **70**: 234–9.

- [7] Damron LA, Kim DG, Mann KA. Fatigue debonding of the roughened stem-cement interface: effects of surface roughness and stem heating conditions. *J Biomed Mater Res Part B: Appl Biomater.*, **78B**: 181–188, 2006
- [8] Dall DM, Miles AW, Juby G. Accelerated polymerization of acrylic bone cement using preheated implants. *Clin Orthop Relat Res* 1986; **211**:148 –150.
- [9] Mann KA, Damron LA, Race A, Ayers DC. Early cementing does not increase debond energy of grit blasted interfaces. *J Orthop Res* 2004; **22**: 822– 827.
- [10] Crowninshield RD, Jennings JD, Laurent ML, Maloney WJ. Cemented femoral component surface finish mechanics. *Clin Orthop Relat Res.* 1998 Oct; **355**: 90-102.
- [11] Barb W, Park JB, Kenner GH, von Recum AF. Intramedullary fixation of artificial hip joints with bone cement-precoated implants. I. Interfacial strengths. *J Biomed Mater Res.* 1982 Jul; **16**(4): 447-58.
- [12] Bundy KJ, Penn RW. The effect of surface preparation on metal/bone cement interfacial strength. *J. Biomed. Mater. Res.* 1987 Jun; **21**(6): 773-805.
- [13] Davies JP, Singer G, Harris WH. The effect of a thin coating of polymethylmethacrylate on the torsional fatigue strength of the cement-metal interface. *J. Appl. Biomater.* 1992 Spring; **3**(1): 45-9.
- [14] Collis DK, Mohler CG. Loosening rates and bone lysis with rough finished and polished stems. *Clin. Orthop. Rel. Res.* 1998; **355**: 113–122.
- [15] Della Valle AMG, Zoppi A, Peterson MGE, Salvati EA. Surface finish affects the clinical and radiographic performance of a modern cemented femoral stem. In: Surgeons AAoO, editor. 2005 Annual Meeting. Washington, D.C.: American Academy of Orthopaedic Surgeons; P028.
- [16] Ong A, Wong KL, Lai M, Garino JP, Steinberg ME. Early failure of precoated femoral components in primary total hip arthroplasty. *J Bone Joint Surg Am* 2002; **84A**: 786 –792.
- [17] Della Valle AG, Rana A, Nestor B, Bostrom M, Westrich G, Salvati EA. Metallic shedding, surface finish changes, and extensive femoral osteolysis in the loose Spectron EF stem. *Clin. Orthop. Relat. Res.* 2006 Jan; **442**: 165-70.
- [18] Rasquinha VJ, Ranawat CS, Dua V, Ranawat AS, Rodriguez JA. A prospective, randomized, double-blind study of smooth versus rough stems using cement fixation: Minimum 5-year follow-up. *J. Arthroplasty* 2004; **19**(Suppl 2): 2–9.
- [19] Vail TP, Goetz D, Tanzer M, Fisher DA, Mohler CG, Callaghan JJ. A prospective randomized trial of cemented femoral components with polished versus grit-blasted surface finish and identical stem geometry. *J. Arthroplasty* 2003; **18**(Suppl 1): 95–102.
- [20] Qi G, Li J, Mann KA, Mouchon WP, Hamstad MA, Salehi A, Whitten SA. 3D real time methodology monitoring cement failures in THA. *J. Biomed. Mater. Res. A.* 2004 Dec 1; **71**(3): 391-402.
- [21] Qi G, Li J, Mouchon WP, Lewis G. Defect-induced fatigue microcrack formation in cement mantle. *J. Biomed. Mater. Res, A.* 2005 Nov 1; **75**(2): 414-24.
- [22] Qi G, Pujol J, Fan Z. 3-D AE visualization of bone-cement fatigue locations. *J. Biomed. Mater. Res.* 2000 Nov; **52**(2): 256-60.

REVIEW OF ACOUSTIC EMISSION IN CHINA

GONGTIAN SHEN, GUANG DAI¹ and SHIFENG LIU²

China Special Equipment Inspection and Research Center, Beijing 100027, China;

¹Department of Mechanical Eng., Daqing Petroleum Institute, Heilongjiang 163318, China;
Soundwel Corporation, Beijing 100029, China

Abstract

Acoustic emission technique was started in the end of 1960s in China. Now there are more than 40 universities and institutes and 150 people engaged in acoustic emission research and application in China. There are more than 60 inspection organizations and 350 level II and III personnel engaged in acoustic emission testing service for pressure equipment, aircraft and steel structure. The research and application fields include equipment developing and manufacturing, AE signals analysis and processing, metal, composite, metallic structure, pressure vessel, aircraft structure, concrete, rock and so on. This paper introduces the history, organization, research and application area of acoustic emission in China.

Historical Background

Acoustic emission technique was introduced into China in 1969. From 1972 to 1974, Metals Institute of The Academy of Sciences of China performed research on acoustic emission characters of metallic deformation and fracture. Many researchers used acoustic emission to monitor and measure cracking and growth of crack in steel in the second half part of 1970s [1].

In 1980s AE research and application found a rapid development with the main objective of service testing for metallic pressure vessel [2 - 5]. From then more than 2000 large pressure vessels have been tested by China Special Equipment Inspection and Research Center (CSEI), the Hefei General Machine Institute, the Wuhan Safety and Environmental Protection Institute, the Daqing Petroleum Institute (DPI). AE research and application on aircraft structure, composites, rocks and magneto-acoustic emission also has been intensively carried out by Beijing Institute of Aeronautical Materials, Beijing Research Institute of Materials and Technology, First Research Institute of Air Force, Wuhan University and so on.

The first single channel AE instrument was developed by Shenyang Computer Research Institute in China in 1976. From then two channels and four channels AE instruments were manufactured and sold in the 1980s. The 36 channels acoustic emission instrument was developed in 1986. The first multi-channel acoustic emission instrument based on PC/AT bus and Windows software was developed by CSEI in 1996. The first digital multi-channel acoustic emission instrument based on acoustic emission signal wave acquisition was developed in 2000 [6].

Chinese Committee on AE

The Chinese Committee on Acoustic Emission (CCAIE) was formed in 1978 as one technical committee of the Chinese Society for NDT. The committee chairman and members are changed every 4 years. The committee chairman can hold the position maximum two 4-years. In 2000, Prof. Guang Dai from DPI became Chairman, a position he still holds. There are 37 members in CCAIE. Meetings were held in every summer.

The First National Acoustic Emission Conference was held in Huangshan Mountain in 1979. Until now 11 National Acoustic Emission Conferences have been held. The time and place of

conferences are as follows:

No.	Date	Place
1	July, 1979	Huangshan, Anhui Province
2	April, 1983	Guilin, Guangxi Province
3	Nov., 1986	Changchun, Jilin Province
4	Aug., 1989	Qingdao, Shandong Province
5	Sept., 1993	Zhangjiajie, Hunan Province
6	Oct., 1995	Emeishan, Sichuan Province
7	Oct., 1997	Beijing
8	June, 1999	Shanghai
9	Aug., 2001	Chengdu, Sichuan Province
10	July, 2004	Daqing, Heilongjiang Province
11	July, 2006	Hangzhou, Zhejiang Province

Starting with the 5th conference, the conferences have been held biennially. The number of the delegates is usually between 50 and 80. The proceedings usually collect 40 to 60 papers. The delegates from USA, Germany and Japan attended the 7th, 10th and 11th Conference in China.

Present Situation [7 – 13]

Organization and Personnel

Now there are more than 40 universities, colleges and institutes engaged in acoustic emission research and application in China. There are more than 60 inspection organizations personnel engaged in acoustic emission testing service for pressure equipment, aircraft and steel structure.

Two NDT personnel notify bodies have started to qualify and certify AE personnel since 1998 in China. One is belong to General Administration of Quality Supervision, Inspection and Quarantine (AQSIQ). 8 level III and 280 level II AE personnel have been qualified and certified by AQSIQ. The testing objects of these AE personnel are special equipment including in boiler, pressure vessel, pressure piping, elevator, crane, ropeway and amusement ride. Another one is belong to Committee of Scientific and Technical Industry for National Defense (CSTIND). 4 level III and 80 level II AE personnel have been qualified and certified by CSTIND. The testing objects of these AE personnel are aeronautical facilities, space equipment, weapons and nuclear industrial equipment.

AE Equipment

About more than 40 sets of 32 or over channels AE instruments, more than 60 sets of 8 to 24 channels AE instruments and more than 100 sets of 1 to 4 channels AE instruments are in-service in China. Many multi-channel AE instruments are imported from PAC of USA and Vallen Corporation of Germany recent years. There are two domestic companies manufacturing AE instruments. One is Beijing Crahesion Science and Trade Corporation Limited (BCSTC). The other one is Soundwel Corporation. They all produce multi-channel digital AE instruments and have very large business in China.

AE Standards

10 AE standards have been drafted and 9 have been published. These standards are listed as follows:

GB/T 12604.4-2004 Non-destructive testing - Terminology - Terms used in acoustic emission testing

GB/T 18182-2000 Acoustic emission examination and evaluation of metallic pressure vessels

GB/T 19800-2005 Non-destructive testing - Acoustic emission inspection - Primary calibration of transducers

GB/T 19801-2005 Non-destructive testing - Acoustic emission inspection - Secondary calibration of acoustic emission sensors

GJB 2044-1994 Acoustic emission testing of Titanium alloy pressure vessels

JB/T 8283-1999 Acoustic emission instrument –Equipment characterisation testing

JB/T7667-1995 Acoustic emission testing and evaluation of in-service pressure vessels

JB/T6916-1993 Acoustic emission testing and evaluation of in-service high pressure cylinders

QJ 2914-1996 Acoustic emission testing of composite structures

JB/T XXXX Non-destructive testing - Acoustic emission testing and evaluation of atmospheric pressure metal storage tanks (draft)

AE Signals Analysis and processing methods

The employed methods include normal AE parameters analysis, time's difference AE source location, correlation figure analysis, modern spectrum analysis, pattern recognition analysis, artificial neural network pattern recognition, fuzzy analysis and grey correlation analysis.

Research and Application Fields

The research and application include in metals, composites, metallic structures, pressure vessels, pressure pipeline, atmospheric pressure storage tanks, aircraft structures, concrete, rock, wood materials, magneto-acoustic emission, manufacturing process monitoring and so on.

Main Research and Application Works

Pressure Vessels Testing

The most important activities in AE testing in China have been run in the scope of pressure vessel safety research and evaluation since 1980. Now more than 50 inspection agencies are engaged in pressure vessel testing with AE [14-18]. Almost 80% of the multi-channel AE instruments are used as pressure vessel testing. More than 1000 large size pressure vessels are tested every year. CSEI is the largest inspection organization for pressure vessels [19-26]. According to the different situations of pressure vessels, AE testing destinations are classified as following five types:

- AE testing of new metallic pressure vessel (MPV) during proof hydrostatic pressure test: This testing destination include in monitoring the leakage to prevent the catastrophic failure of pressure vessel, evaluating the structural integrity and finding the unknown flaw cracking and growing.

- AE testing and defect assessment of in-service MPV: There are many welding defects such as porosity, slag inclusion, non-fusion, lack of penetration in the pressure vessels manufactured in 1970s in China due to there were no strict quality control systems. How to handle these welding defects is very difficult for the in-service pressure vessels inspection The repair of all the welding defects is expensive and need a long time. The conventional non-destructive testing methods such as ultrasonic test and radiographic test need a long time and are difficult to distinguish activities of defects. Fracture mechanics assessment need to know the exact size of the defect. In eventually, it was found that AE testing is a most effective method for the welding defect assessment of in-service pressure vessel. The cracking and growth of defects, slag inclusion fracture, residual stress releasing, oxide scales peeling off, structural friction and leakage can be

distinguished by through using time's difference AE source location, modern spectrum analysis, pattern recognition analysis, artificial neural network pattern recognition and grey correlation analysis [25-29].

- AE on-line monitoring and safety evaluation of MPV: According to relevant administration and supervision regulations of pressure vessel in China, in-service pressure vessels should be stopped to being performed inspection and test for each 6 years. But sometimes the production cannot be stopped. AE on-line monitoring is used to evaluate the safety situation and extend the operating period of pressure vessels. In addition, AE on-line monitoring is frequently used to monitor the active situation of known welding defects for in-service pressure vessels.

- Acoustic emission test and safety evaluation of wrapped multi-layer pressure vessel (WMPV): Wrapped multi-layer thick wall cylindrical pressure vessel is one of the most structures used by high pressure vessels in the world. Due to there are many advantages included high ductility, high safety, low fabricated condition and so on, a larger number of WMPV have been fabricated and used in China since 1958. Hydrogen and nitrogen gas cylindrical pressure vessel is one of the most WMPV used in China. However, due to the structural character of WMPV, their in-service inspection and testing is very difficult for ultrasonic and radiographic test. For WMPV, due to a lot of acoustic emission signals should be produced by friction between layers during load and fall the signals from flaws into oblivion, it was held that acoustic emission test is not applicable to WMPV. However, after performing acoustic emission test for 14 wrapped multilayer cylindrical Nitrogen gas tank through two times load and many times hold load, it was found that there are much more AE signals of WMPV than single layer pressure vessel in the first loading, but the AE character of WMPV is the same as single layer pressure vessel in the second loading. Now the AE testing technique of WMPV has been developed. Until now more than 500 WMPVs have been tested and evaluated.

- Composite pressure vessel (CPV): Not like MPV, there is very few number of CPV in China. The 44th Institute of Aerospace Industry Co. has performed AE testing for dozens of CPV.

Aircraft Structures

In this field, AE is applied to monitor the produce and growth of fatigue crack in aircraft structure. The work has been done by the Beijing Institute of Aeronautical Materials since 1983 [2]. A group led by Geng [30], The First Research Institute of the Air Force, has performed many AE tests for the fatigue test of airplane. They passed through to introduce some new AE parameters based on the normal AE parameters to discriminate fatigue cracking signals in a bulkhead bolt from a number of friction noise signals.

Metals

The research works for metallic AE characteristics are mainly focused on the deformation, fracture and fatigue of steel and aluminum alloy in China [1-13]. One of the destinations is to investigate the deformation and fracture mechanism of metals. Another destination is to obtain basic data for pressure vessel and metallic structure AE test.

Composites

The main research fields are the deformation and fracture AE features of composites in China [5-7]. Those materials include SiC fiber reinforced Al matrix composite, SiC particulate reinforced Al matrix composite, carbon fiber reinforced polyimide composite, Kevlar/epoxy composites and so on. The AE characters of carbon fiber reinforced polyimide composite during

heating and solidifying also was tested [31].

Concrete

Ji, University of Science and Technology Beijing, has done a systematic study for the AE characters of concrete in his dissertation of Ph.D. [32]. After combining the acoustic emission characteristics of concrete with mechanical process and fracture damage features, he put forward a conception of nonlinear characteristics of acoustic emission process of concrete materials. Cheng, North Communication University, has established an AE testing method for assessing quality of concrete sleeper of railway [33].

Rocks

The main application is to measure the geostress with AE in geology, seism and petroleum exploration fields. The Institute of Petroleum Exploration in Beijing has measured the direction of principal stress of ten oil fields by through of measuring the sonic speed of core [8]. The Institute of Geomechanics and Institute of Crustal Dynamics measured the magnitude of maximum principal geostress in rock specimen under uniaxial loading condition by AE Kaiser Effect[9].

Magneto-acoustic Emission

Magneto-acoustic emission (MAE) for ferromagnetic materials has been investigated since 1984 in China. After studying the magnet-oacoustic emission characteristics of grain oriented Fe-Si alloy, Shen and Xu found that the motion of 180° magnetic domain walls can generate acoustic emission signals [34,35]. The MAE and Barkhausen noise of Ni and carbon steel also has been studied [36-38]. Ma et al. investigated the stress influence on MAE.

Pressure Pipeline Leakage Testing

Acoustic emission technique has been used to monitor the leakage and locate the leakage point for underground pressure pipeline recent years. CSEI and Soundwel Corporation have cooperated to develop an underground pressure pipeline leakage point location testing system based on wavelet analysis and correlation location technique.

Atmospheric Pressure Storage Tanks Bottom Corrosion Testing

The bottom corrosion testing research and application for atmospheric pressure storage tanks have been performed by CSEI, Daqing Petroleum Institute and Zhejiang Special Equipment Inspection Institute recent five years. The testing standard has been drafted by a team led by Shen and wait for final approval by government. More than 50 big oil storage tanks have been tested for every year [11 - 13].

Wood Materials

Nanjing Forestry University studied on the acoustic emission characteristics of tensile fracture for particleboard and wood-plastic composites [13]. It is concluded that different particleboard and wood-plastic composites has different acoustic emission characteristics. The result shows that AE technique can be applied in damage detection for particleboard and wood-plastic composites.

Conclusion

(1) At present, there are about 360 qualified AE personnel, 150 AE researchers, 60 AE testing organizations, 40 universities and institutes engaged in AE research in China. Due to a large number of in-service pressure equipment and many new big engineering projects under construction, China not only has large requirement for AE instrument, but also for advanced techniques and AE testing service.

(2) The research and application fields are very wide in China. The main research fields are metals, composites, concrete, rock, wood materials, magneto-acoustic emission and manufacturing process monitoring. The main mature application fields are pressure vessels testing, atmospheric pressure storage tanks bottom corrosion testing and aircraft structures testing.

(3) The manufacture and sales of AE instruments are also successful in China. The domestic manufacturers can possess about 40% market.

References

1. The proceedings of the 1st National AE Conference, Huangshan, China, July, 1979.
2. The proceedings of the 2nd National AE Conference, Guilin, China, April, 1983.
3. The proceedings of the 3rd National AE Conference, Changchun, China, Nov., 1986.
4. The proceedings of the 4th National AE Conference, Qingdao, China, August, 1989.
5. R.G. Geng, Recent Development of Acoustic Emission: Twenty-year Review of Chinese Society for Nondestructive Testing, *Nondestructive Testing*, **20** (6), June 1998, 151-154.
6. G.T. Shen et al., Acoustic Emission Progress in China: - Celebration for the 25th anniversary of Chinese Society for NDT, *Nondestructive Testing*, **25** (6), June 2003, 302-307.
7. The proceedings of the 5th National AE Conference, Zhangjiajie, China, September 1993.
8. The proceedings of the 6th National AE Conference, Emeishan, China, Oct. 1995.
9. The proceedings of the 7th National AE Conference, Beijing, China, Oct. 1997.
10. The proceedings of the 8th National AE Conference, Shanghai, China, June 1999.
11. The proceedings of the 9th National AE Conference, Chengdu, China, Aug. 2001.
12. The proceedings of the 10th National AE Conference, Daqing, China, July 2004.
13. The proceedings of the 11th National AE Conference, Hangzhou, China, July 2006.
14. G. Dai, et al: "AE monitoring and studying of signal analysis method for large spherical tanks with insulating layer", *Progress in Acoustic Emission VI*, 11th Intl Acoustic Emission Symposium, JSNDI, Sendai, Japan, 1992.
15. G. Dai, et al: "AE monitoring and strain measurement for testing pressure vessel with artificial prefabricated flaw", *Progress in Acoustic Emission VI*, 11th Intl Acoustic Emission Symp., JSNDI, Sendai, Japan, 1992.
16. G. Dai, et al: "AE monitoring and data analysis for large spherical tanks", *NDT&E Intl*, 1993, **26** (6), 287-290.
17. G. Dai, et al: "AE testing of a low-alloy steel pressure vessel", *NDT&E Intl*, 1993, **26** (6), 291-294.
18. L. Li, et al: "Location technique of acoustic emission for spherical pressure vessel", *Proceedings of 14th WCNDT*, New Delhi, Dec.8-13, 1996.
19. Gongtian Shen, Shifeng Liu, Yaoguang Wan and Qingru Duan: "The correlation between active defects and source location in acoustic emission test of metal pressure vessels", *Progress in Acoustic Emission IV*, 9th Intl Acoustic Emission Symp., JSNDI, Kobe Japan, 1988.
20. Shifeng Liu, Gongtian Shen, Yaoguang Wan and Qingru Duan: "Application of AE technique during in-service pressure vessel inspection", *the World Meeting on AE*, March 20-22, 1989, Charlotte, North Caroline, USA.

21. Shifeng Liu, Yaoguang Wan, Gongtian Shen and Qingru Duan: "AE inspection and defect assessment for metal pressure vessels", *Intl J. of Pressure Vessel and Piping*, **38**, 57-67, 1989.
22. Shifeng Liu, Yaoguang Wan, Gongtian Shen and Qingru Duan: "AE defect assessment for pressure vessels", *Proceedings of the 12th Word Conf. on Nondestructive Testing*, April 23-28, 1989, Amsterdam, The Netherlands.
23. S.F. Liu, Y.G. Wan, G.T. Shen and Q.R. Duan: "Acoustic emission monitoring for pressure vessel", *The 7th Intl Pressure Vessel Conf.*, Dusseldorf, Germany, 31st May-5th June 1992.
24. G.T. Shen et al.: "Acoustic Emission Test and Safety Evaluation of Wrapped Multilayer Pressure Vessel", *China Boiler and Pressure Vessel Safety (English Edition)*, 1995, **2**, 68-73.
25. G.T. Shen, B.X. Li, Q.R. Duan and S.F. Liu: "Acoustic Emission Sources of Field Pressure Vessel Test", *Progress in Acoustic Emission VIII*, 13th Intl Acoustic Emission Symp., JSNDI, Nara, Japan, 1996.
26. S.F. Liu, G.T. Shen, et al: "Modern spectral analysis of waveform acoustic emission data", *Proceedings of 14th WCNDT*, New Delhi, Dec. 8-13, 1996.
27. G. Dai, "The acoustic emission characteristics and fuzzy comprehensive analysis of active defects for the pressure vessel in service", *Dissertation of Ph.D.*, Zhejiang University, January 1996.
28. S.F. Liu, "Spectral analysis and artificial neural network pattern recognition of weld defect acoustic emission data", *Dissertation of Ph.D.*, Tsinghua University, July 1996.
29. G.T. Shen, "The characteristics and discriminating methods of acoustic emission sources for metallic pressure vessel", *Dissertation of Ph.D.*, Tsinghua University, February 1998.
30. R.S. Geng, et al.: "Evaluation of fatigue crack growth in bulkhead bolt of an aircraft using acoustic emission", *Proceedings of 14th WCNDT*, New Delhi, Dec. 8-13, 1996. pp. 2379-2382.
31. G.T. Shen et al., *The Investigation of Acoustic Emission Characterization during heating and solidifying for carbon fiber reinforced polyimide composite*, *Nondestructive Testing*, **20** (5), May, 1998, 126-128.
32. H.G. Ji, "Acoustic emission characteristics of concrete damage", *Dissertation of Ph.D.*, Northeast University, November, 1996.
33. Y.R. Cheng, et al., "Acoustic emission, a tool for assessing quality of prestressed concrete sleeper", *Intl Symp. on Engineering Concrete*, Nanjing, China, 1991, pp. 1873-1877.
34. G.T. Shen, Y.H. Xu and S.F. Liu: "Magnetomechanical acoustic emission in grain oriented and non-oriented Fe-Si alloy", *Progress in Acoustic Emission IV*, 9th International Acoustic Emission Symposium, Japanese Society for Non-destructive Inspection, Kobe, Japan, 1988.
35. Y.H. Xu, G.T. Shen, et al.: "An investigation on magnetoacoustic emission of ferromagnetic materials with 180° magnetic domain wall", *J. of Magnetism and Magnetic Materials* **127**, 1993, 169-180.
36. X.R. Mu, G.T. Shen, et al.: "The influence of microstructure on MAE and BN of dual-phase steel", *Progress in Acoustic Emission IV*, 9th International Acoustic Emission Symp., JSNDI, Kobe, Japan, 1988.
37. R. Hill, R.S. Geng et al., *NDT&E Intl.* **24** (4), 1991, 179-186.
38. R. Hill and R.S. Geng, "Assessment of weld and material defects using acoustic and electromagnetic Barkhausen emission", *Progress in Acoustic Emission VII*, The 12th Intl Acoustic Emission Symp., JSNDI, Sapporo, Japan, 1994.

AN INVESTIGATION OF FREQUENCY AS AN ACOUSTIC EMISSION SIGNAL DISCRIMINATOR IN CARBON FIBRE COMPOSITE MATERIALS

MARK EATON, KAREN HOLFORD, CAROL FEATHERSTON and RHYS PULLIN
Cardiff School of Engineering, Cardiff University, Cardiff, CF24 3AA, UK

Abstract

This work considers the use of frequency content as a discriminating factor for AE signals from carbon fibre composites. An artificial AE source generated by a conical transducer was used to investigate the effects of specimen geometry and sensor response on the frequency content of recorded signals. Additionally, AE signals were recorded from different damage mechanisms in tensile and beam buckling coupon specimens. The peak frequency content was used to examine signals resulting from the different damage modes observed and observations were in general agreement with previous research studies. However, it was shown that great care is required when using peak frequency content as a discriminating factor because geometry and sensor response have a significant effect on the frequency content of a recorded signal.

Keywords: Composites, signal discrimination, frequency.

Introduction

The use of composite materials has become widespread in aerospace and automotive applications because of their high specific stiffness and they are increasingly used in safety critical structures. In light of this, it is essential that the continued integrity of composite components is ensured under long-term use. Many different damage mechanisms, such as delamination and matrix cracking, can occur in composite materials, which may not be detected visually but can dramatically reduce the ultimate failure load of a component. The prediction of damage type and its onset is difficult due to the possible variations in component lay-ups and manufacturing processes. As such it is very desirable to be able to detect and discriminate between AE signals from different damage mechanisms in composite materials.

A variation of source relaxation time has been shown for different damage mechanisms in glass fibre/epoxy [1] and it is commonly believed that this will result in AE signals with different frequency content. A number of researchers have attempted to utilise frequency content as a discriminating factor for AE signals [2-4]. The results are in good agreement with all researchers finding matrix failures such as matrix cracking and delamination producing signals with low frequency content ($\sim < 150$ kHz) and fibre failures producing signals with high frequency content ($\sim > 300$ kHz).

Experimental Procedure

The investigation of the effects of specimen geometry and sensor response on frequency content was conducted on a 1500 x 500 x 2.16 mm carbon fibre/epoxy plate manufactured from Advanced Composites Group (ACG) MTM28-1/HS uni-directional (UD) pre-preg with a $(0,90)_{4S}$ lay-up. The artificial source consisted of an in-house manufactured broadband conical transducer provided by the National Physical Laboratory, UK. The resulting signals were recorded by two Physical Acoustics Corp. (PAC) S9208 broadband sensors. The sensors were arranged along the

0° material direction at the centre of the plate such that one sensor was adjacent to the conical transducer and the other was at a distance of 200 mm. The sensors were coupled with ultrasound gel and mounted with magnetic clamps. A sensitivity test was conducted using a Hsu-Nielsen source each time a sensor was mounted, to ensure adequate coupling was achieved. A PAC “wavegen” 1410 board provided a 160V single-cycle square-wave with frequency varying from 100-900 kHz at 100 kHz intervals, to drive the conical transducer. The test was then conducted with the sensors in opposite positions. The same tests were then repeated with two PAC WD wideband sensors. AE monitoring was conducted throughout all tests using a PAC PCI-2 system at 10 MSPS.

Six tensile specimens measuring 240 x 30 x 1.08 mm were manufactured from ACG's HTM45/HS UD pre-preg with (0)₈ and (0,90)_{2S} lay-ups. To suppress grip noise and minimise slippage, aluminium end tabs were bonded to the specimens reducing the unsupported length to 150mm. The specimens were instrumented with a single PAC WDi sensor mounted at the centre using electrical tape with brown grease as a couplant and loaded to failure under displacement control at a rate of 0.125 mm·min⁻¹.

Six beam buckling specimens were also manufactured from HTM45/HS UD pre-preg with measurements of 200 x 30 x 2.16 mm and lay-ups of (±45)_{4S} and (0,90)_{4S}. The specimens were subject to an in-plane compressive load along their length. This is facilitated by a loading cage that provides built-in supports at each end, reducing the unsupported length to 170 mm, and ensuring the supports remain aligned throughout the test. The specimens were loaded to failure at 0.5 mm·min⁻¹ and 1 mm·min⁻¹ for the (0,90)_{4S} and (±45)_{4S} lay-ups, respectively. Two PAC WD sensors were mounted using electric tape with brown grease as a couplant at ¼ and ¾ of the unsupported length to correspond with the two points of inflection.

Results and Discussion

The waveforms and power spectra of the signals recorded by two S9208s adjacent to the conical transducer are shown in Fig. 1a and b for driving pulses of 100 kHz, 500 kHz and 900 kHz. The response of both sensors to a 100-kHz driving pulse shows that most of the energy in the signal is contained below 100 kHz. As the frequency of the driving pulse increases so the frequency content of the recorded signal expands to higher frequencies. The response to a 500-kHz artificial source shows that the frequency content of the signals has increased with most of the energy contained below 400 kHz and very little energy is seen above 600 kHz. However as the frequency of the driving pulse is increased above 500 kHz, there is little increase in the frequency content of the signal, which can be seen in the response to a 900 kHz source where, again, most of the energy is contained below 400 kHz and very little is seen above 600 kHz.

When the sensors are moved away from the conical transducer the response becomes very different. Figure 2a and b show the recorded signals and their power spectra for both the S9208 sensors mounted at a distance of 200 mm from the conical transducer with driving pulse frequencies of 100, 500 and 900 kHz. Both the S₀ and A₀ fundamental plate modes are observed in all the waveforms recorded at 200 mm. The response of the S9208 sensors to a 100-kHz driving pulse has an A₀ mode that is much larger than the S₀ mode. This is reflected in the power spectra by most of the energy being contained below 100 kHz, due to the lower frequency of the A₀ mode. The half-cycle times for the peak of the A₀ modes equate to frequencies of approximately 52 kHz and 55 kHz for S9208-1 and 2, respectively. The 500-kHz and 900-kHz driving pulses generate a response with S₀ and A₀ modes of similar amplitudes; this is reflected by the observation of higher frequency peaks in their power spectra between 200 kHz and 500 kHz. The two regions of frequency content can be attributed to the fundamental plate-wave modes, A₀ and S₀. This is ratified by the half-cycle times of the peak cycles of the S₀ and A₀ modes from S9208-1

for a 500-kHz source, which have corresponding frequencies of 374 kHz and 39 kHz, respectively, suggesting that geometry has a considerable effect on the frequency content of a signal.

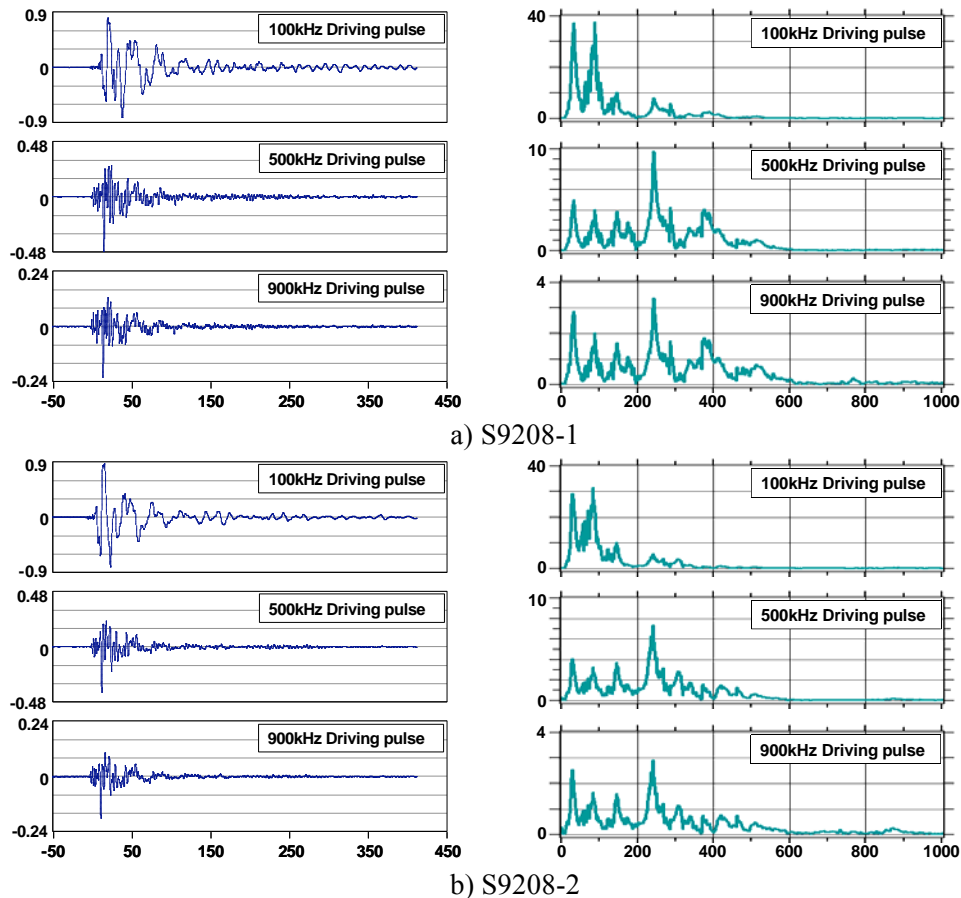


Fig. 1 Waveforms and their power spectra recorded by S9208s adjacent to the source, presented in V versus μs and mV versus kHz, respectively.

The response of two WD sensors mounted adjacent to the conical transducer is presented in Fig. 3a and b for driving pulse frequencies of 100, 500 and 900 kHz, respectively. The WD's response to a 100-kHz driving pulse contains most of its energy below 150 kHz, which is similar to the response of the S9208 sensors to the same source. As observed in the S9208s response, the frequency content of the recorded signal expands to higher frequencies as the driving pulse frequency is increased. For a 500-kHz driving pulse, the majority of the signal energy is contained below 600 kHz. For a driving pulse of 900 kHz, there is still very little energy contained above 600 kHz. The increase in higher frequency content is thought to be an attribute of the sensor because it is not observed for the broadband S9208 sensors and indeed the WD is known to have a peak in sensitivity at approximately 525 kHz. The observation of most interest from this test is the difference in response between the two WD sensors to the same source. It can be seen in Fig. 3b that the two WD sensors have a considerably different response to a 500-kHz driving pulse. The signal recorded by WD-1 has more low frequency content than that of WD-2 and its peak is at approximately 100 kHz, whereas WD-2 has more higher frequency content with significant content observed at approximately 475 kHz and 550 kHz. This demonstrates how the response of a sensor can affect the frequency content of a recorded signal and how the response can vary, even among sensors of the same model.

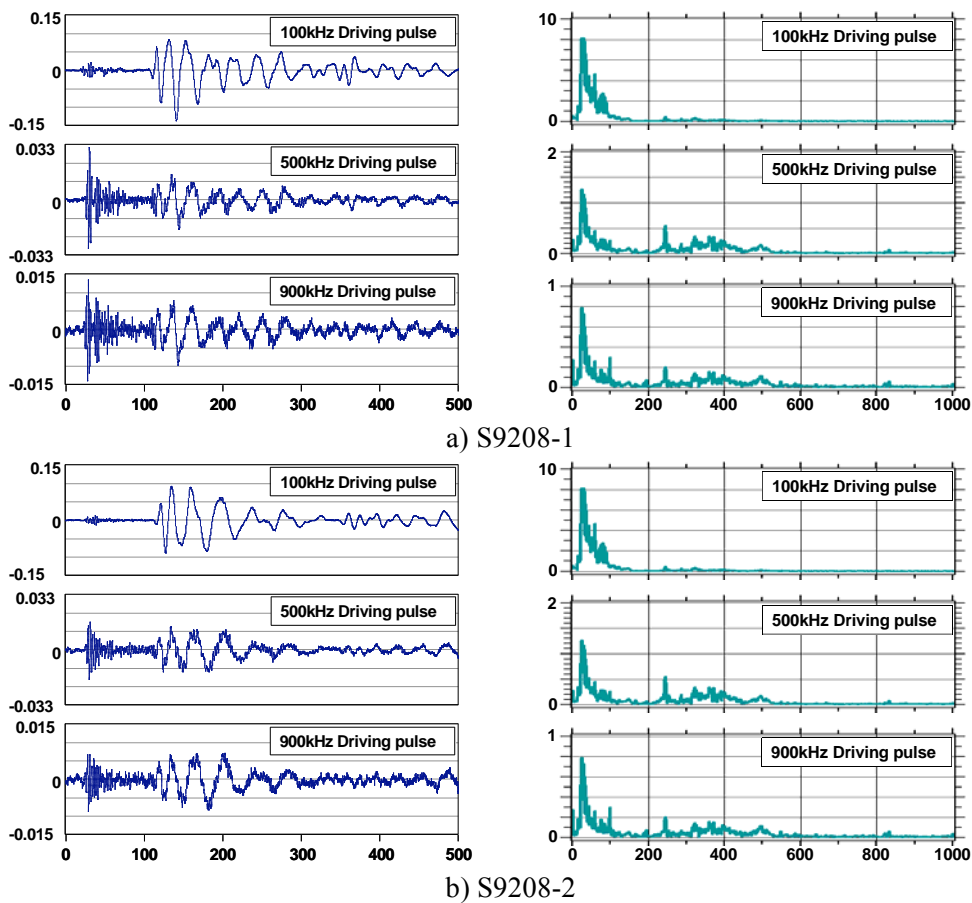


Fig. 2 Waveforms and their power spectra recorded by S9208s 200 mm from the source, presented in V versus μ s and mV versus kHz, respectively.

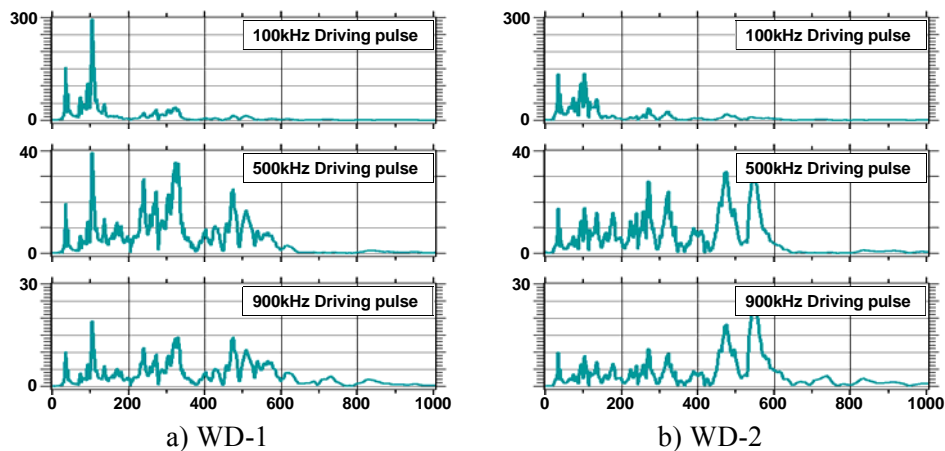


Fig. 3 Power spectra recorded by WD sensors adjacent to the source, presented in mV versus kHz.

The power spectra, recorded by the two WD sensors mounted at a distance of 200 mm from the conical transducer are shown in Fig. 4a and b for source driving pulses of 100, 500 and 900 kHz. Both the fundamental plate-wave modes are observed in a signal recorded from a 100 kHz driving pulse, but as the frequency of the driving pulse increases, the A_0 mode rapidly diminishes and for a 500-kHz driving pulse, it is no longer observed. The power spectra of these signals have three distinctive peaks occurring at approximately 100, 275 and 550 kHz. The amplitudes

of these peaks also vary with driving pulse frequency. As expected more energy is contained at lower frequencies for a low frequency driving pulse and more energy is contained at higher frequencies for a higher frequency driving pulse. The lower and middle frequency peaks are again attributed to the A_0 and S_0 modes in accordance with the S9208 results. As the A_0 mode loses amplitude with increasing driving pulse frequency, a corresponding reduction in the amplitude of the low frequency peak in the power spectrum is observed. The higher frequency peak centred about 550 kHz is again considered to be an artefact of the sensor. Additionally, it appears that the frequency content at this level is very different for the two WD sensors, suggesting that the frequency response of the two sensors is different. A difference in sensor response such as this could lead to confusion when considering frequency as a discriminating factor. For example, the two power spectra seen in Fig. 4a and b for a 500-kHz driving pulse both have a peak frequency of approximately 275 kHz. WD-1 has a very dominant peak at 275 kHz, whereas WD-2 has a peak at 275 kHz, whose amplitude is only slightly larger than that of the peak at 550 kHz. It is clear that a small variation in the source could quite easily produce a significantly different result from sensor WD-2. It is interesting to note that other researchers [2-4] all observed frequencies in low, medium and high frequency bands using PAC WD sensors that correspond to the three frequency peaks of 100 kHz, 275 kHz and 550 kHz.

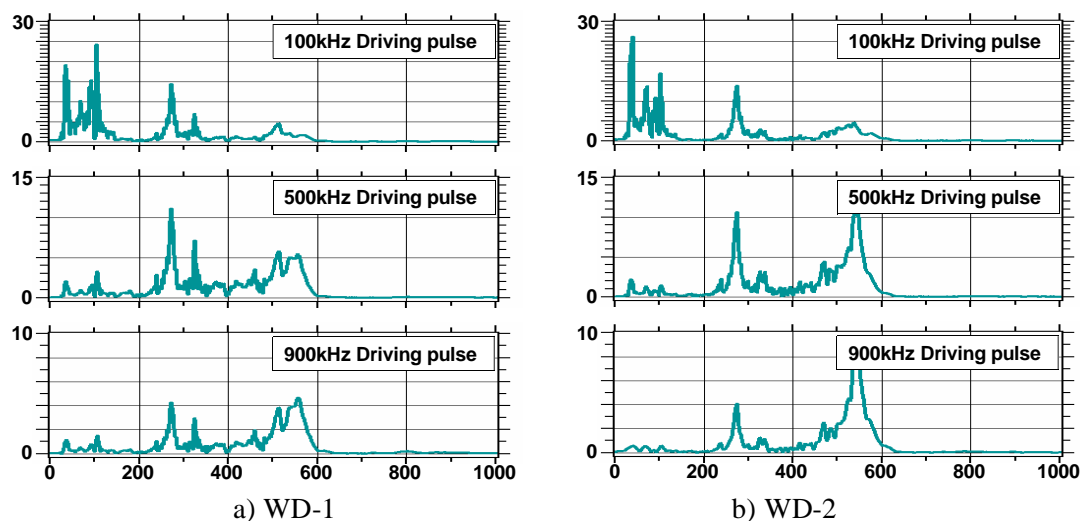


Fig. 4 Power spectra recorded by WDs 200mm from the source, presented in mV versus kHz.

Figure 5a and b present the frequency analysis of two tensile specimens having $(0,90)_{2S}$ and $(0)_8$ lay-ups, respectively. The hits for each test are separated using the peak frequency recorded by AEWin into three frequency bands 0-150 kHz, 150-400 kHz and >400 kHz. The hits within each band are then plotted cumulatively against time. The low frequency band for the $(0,90)_{2S}$ specimen is clearly dominant and this corresponds to large amounts of matrix damage observed. The $(0)_8$ specimen is expected to have less matrix damage and more fibre failure, concurrently the frequency analysis shows the higher frequency band to be dominant for this type of specimen.

The frequency analysis for a representative curvature specimen is presented in Fig. 6a and b for channel 1 and 2, respectively. The damage observed in the specimen was predominantly matrix failure, which is represented by the presence of numerous low frequency hits on both channels. However, the activity in the middle and high frequency bands is completely different on both channels. For channel 1 (Fig. 6a), the most activity is seen in the middle band and the least activity is seen in the higher band, whereas for channel 2 (Fig. 6b) the most activity is seen in the high frequency band and the least activity is seen in the middle frequency band. Indeed, the rate

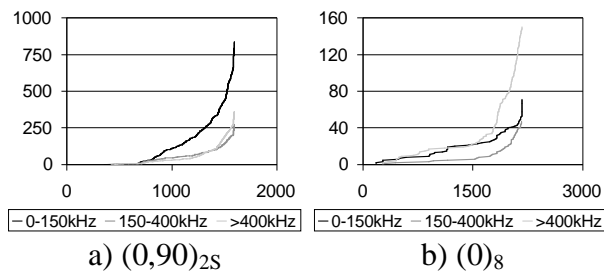


Fig. 5 Frequency analysis of tensile specimens, presented in cumulative hits versus time (s).

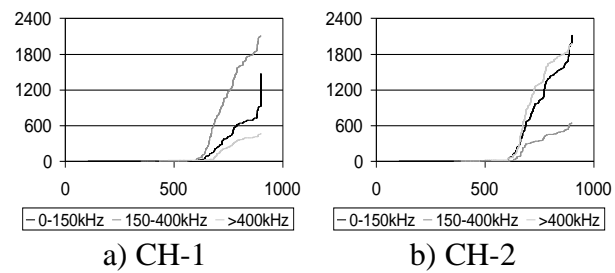


Fig. 6 Frequency analysis of a beam buckling specimen with $(0,90)_{4S}$ lay-up, presented in cumulative hits versus time (s).

of hits recorded on channel 1 between 150-400 kHz is very similar to that of hits recorded above 400 kHz on channel 2 and vice versa. The two WD sensors used for these tests are the same two sensors used in the first part of this work to assess the sensor response to different frequency sources. Figure 4 shows how the different sensors can produce a different response to the same source. In particular the 500-kHz source shows that for the same source the peak frequency might lie in either the 150-400 kHz band or the >400 kHz band depending on the sensor, highlighting the effects that sensor response can have on the frequency content of a signal and the potential confusion it can cause.

Conclusions

It has been shown that peak frequency content of an AE signal can be used to provide some information about its source. However it has been demonstrated how the overriding effects of specimen geometry and sensor response can produce misleading results. As such this technique should be approached with great care and an understanding of the wave propagation and sensor response for a specific case is essential.

Acknowledgements: The authors would like to thank Dr. Pete Theobald from the National Physical Laboratory (NPL) for the loan of the conical transducer.

References

1. H. Suzuki, M. Takemoto, K. Ono, J. Acoustic Emission, **14**, 1996, 35-50.
2. J. Bohse, Composites Science and Technology, **60**, 2000, 1213-1226.
3. C. R. Ramirez-Jimenez, N. Papadakis, N. Reynolds, T. H. Gan, P. Purnell, M. Pharaoh, Composites Science and Technology, **64**, 2004, 1819-1827.
4. P. J. de Groot, P. A. M. Wijnen, R. B. F. Janssen, Composites Science and Technology, **55**, 1995, 405-412.

MONITORING THE EVOLUTION OF INDIVIDUAL AE SOURCES IN CYCLICALLY LOADED FRP COMPOSITES

RUNAR UNNTHORSSON, THOMAS P. RUNARSSON and MAGNUS T. JONSSON

Department of Mechanical & Industrial Engineering, University of Iceland, Reykjavik, Iceland

Abstract

An experimental methodology for tracking the locations of multiple individual sources of acoustic emission (AE), in cyclically loaded fiber reinforced polymers (FRP), is presented. The approach is developed, discussed, and demonstrated using AE data measured during the fatigue testing of an assembled CFRP prosthetic foot. The results are presented as 2D images where paths show evolution of AE sources. From these paths, the locations of the AE sources in each fatigue cycle can be tracked. Hence, this methodology makes it possible to monitor damage growth and to identify AE sources. The technique forms the basis for further study which otherwise would be difficult to accomplish due to the overwhelming number of sources with similar characteristics. As a result a useful tool for monitoring and evaluating the health of a composite is developed.

Keywords: Source tracking, carbon fiber, composites, fatigue

Introduction

Carbon Fiber Reinforced Polymer (CFRP) composites have many interesting properties such as high strength-to-weight ratio and excellent corrosion and fatigue tolerance. Despite this, damage in composites develops early in service [1-4] and continues to accumulate throughout the service life. The fatigue tolerance can be attributed to resistance to inhomogeneous damage growth, which is a property of highly inhomogeneous materials [3]. The high damage tolerance of composites means that composites are able to meet their in-service requirements for prolonged period of time while damage accumulates and grows. Consequently, there is a definite need to detect, monitor and evaluate individual damages. A system, which enables successful diagnosis and prognosis, can possibly be used to extend the service life and to prevent catastrophic failure.

The type and the location of damages are random and the fatigue behavior changes with different lamina sequences, geometry and loading conditions. For these reasons, and the fact that testing of composites shows a high experimental scatter [3, 5], fatigue modeling of composites is generally a formidable task. Existing fatigue models are based on certain materials, laminate sequences and loading conditions [1, 6, 7]. Due to these restrictions, the models cannot generally be extended to composites, which have different lay-up or are used under different loading conditions. Under repetitive or cyclic loading conditions, AE is emitted from both damage progression and from cumulated damage; i.e., rubbing of delaminated surfaces. As a result, multiple AE transients with varying amplitude, duration, and frequency are emitted in each cycle and many are emitted simultaneously. Furthermore, the values of the AE signal features from cumulated damage usually fall in the same range as the ones from damage growth [4, 8]. Waveform based parameters such as ring down count, amplitude, and energy have been used for the detection of damage; i.e., delamination, matrix cracking, debonding, fiber cracking, and fiber pull-out [8-12]. For this reason, an intuitive approach to monitoring is to keep track of one or more waveform parameters, which characterize the AE from the source of interest. Each parameter will follow a probability distribution, which changes when the source (damage) changes. Because of the

parameter fluctuations and the high rate of AE with similar parameter values, waveform parameters alone are not sufficient for distinguishing between sources. Additional indication is therefore needed. If each source emits an AE at the same load level in each cycle, then the load level of AE occurrence is sufficient to distinguish between the sources. However, as the delamination cracks grow, the load level of occurrence changes.

The methodology presented in this paper uses both the time of occurrence and the AE amplitude in each cycle for monitoring the evolution of many individual AE sources simultaneously. From the resulting images, one can locate interesting AE sources for further study, or for tracking, which otherwise would be difficult to accomplish due to the overwhelming number of sources with similar characteristics.

The remainder of the paper is organized as follows. In section 2 the proposed methodology is developed and in section 3, it is demonstrated and discussed by applying it to AE data, which has been studied before by the authors in [13]. Finally, a conclusion of the work is presented.

Methodology

This section describes the proposed experimental methodology, which is a graphical tool developed for tracking the locations of individual AE sources. It was designed for monitoring objects subjected to repetitive loading conditions. By using the images generated by the methodology, one can monitor the evolution of individual AE sources and locate interesting AE signals for further study. Figure 1 shows a schematic overview of the methodology.

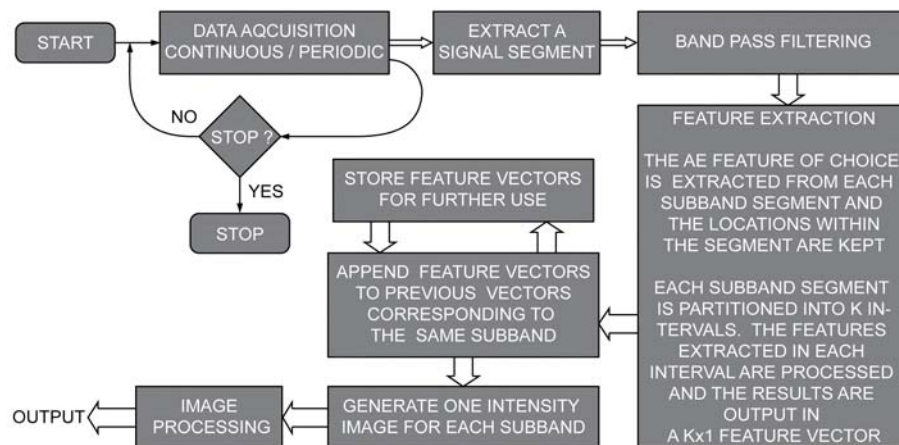


Fig. 1. Schematic overview of the proposed experimental methodology.

The first step of the approach is to split the AE signal into segments of length equal to the period of one cycle. If the AE signal is not continuously acquired, i.e., measured periodically, then care must be taken to ensure that the segments all start at the same phase of each cycle. A reference signal, such as displacement or load, can be measured simultaneously and used for segmenting. In the next step, each segment is bandpass filtered into N subbands. The user selects the type of filtering, number of subbands (N), and the individual subband bandwidths. Figure 2 illustrates these two steps.

In the third step, a feature vector is generated from each subband segment. Each feature vector is generated in two stages. In the first stage, the AE feature of interest is extracted from the segment. Both the positions within the segment and the feature values are logged.

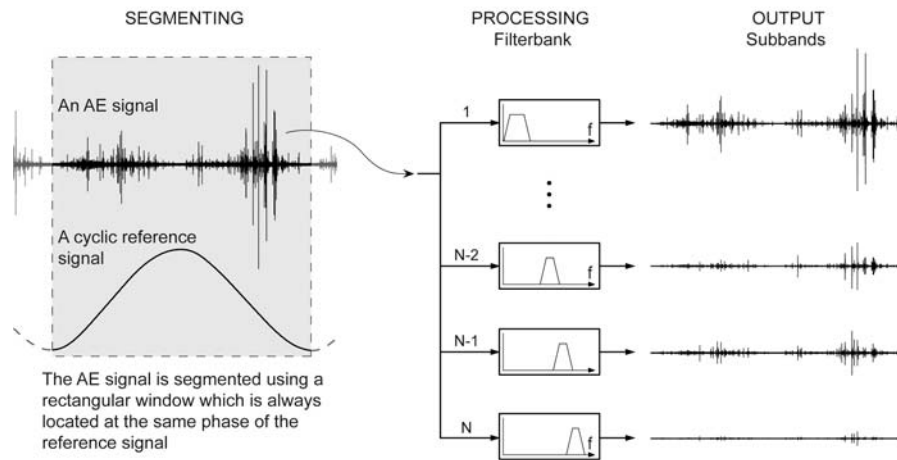


Fig. 2. The AE signal is segmented and each segment is split into N subbands.

In the second stage, the segment is partitioned into K intervals and the features extracted within each interval are processed. The user selects the number of intervals, K . The results from the processing are output as a feature vector ($K \times 1$). Depending on the processing in the second stage, the first stage can in some cases be omitted; i.e., when the energy in each interval is computed, or the maximum amplitude. In order to illustrate how a feature vector is generated, the maximum amplitude in each interval was chosen. Figure 3 explains the procedure. Each subband segment is first rectified and partitioned into K intervals and then the maximum amplitude within the interval is found; i.e., a piecewise constant envelope is generated. The envelope is then down-sampled by a factor L/K , where L is the length of the subband segment. The resulting feature vector contains one sample from each interval of the envelope. The amplitude filtering and down-sampling process extracts the amplitude of the strongest transient in each interval. Hence, the tracking capability is limited by this filtering. However, since the filtering is performed in all the subbands the tracking ability is improved because the AE energy from different sources often resides in different subbands. The down sampling also helps keep the data manageable since the number of samples acquired during one fatigue cycle can be high.

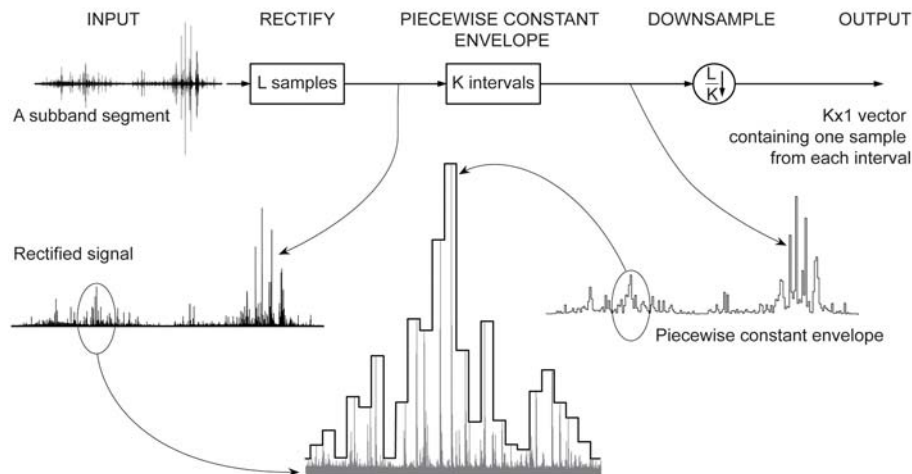


Fig. 3. For each subband segment, new feature vector is computed by first rectifying the signal, then computing a piecewise constant envelope, and finally down sampling the envelope.

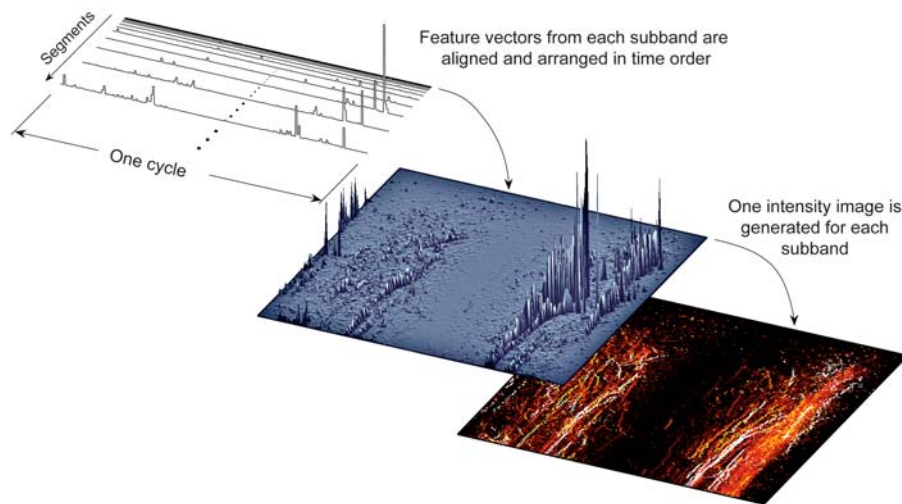


Fig. 4. For each subband, new feature vectors are appended to previous vectors and an intensity image is generated.

In the fourth step, each new feature vector is appended to previous vectors from the same subband and an intensity image is generated. Figure 4 illustrates this procedure. In the fifth and the last step, image processing is performed in order to enhance the images and to make the paths more prominent.

Experimental Procedures and Results

In order to demonstrate the methodology outlined above, it was applied to an experimental data measured during fatigue testing of an assembled CFRP prosthetic foot made by Össur hf. The foot was placed in the test machine and two actuators were used to apply amplitude controlled cyclic loading at 1 Hz. One actuator applied load to the forefoot and the other to the heel. The foot was cyclically tested until a 10% change in displacement, with respect to initial value, was observed for either actuator. Figure 5 shows a schematic representation of the experimental setup.

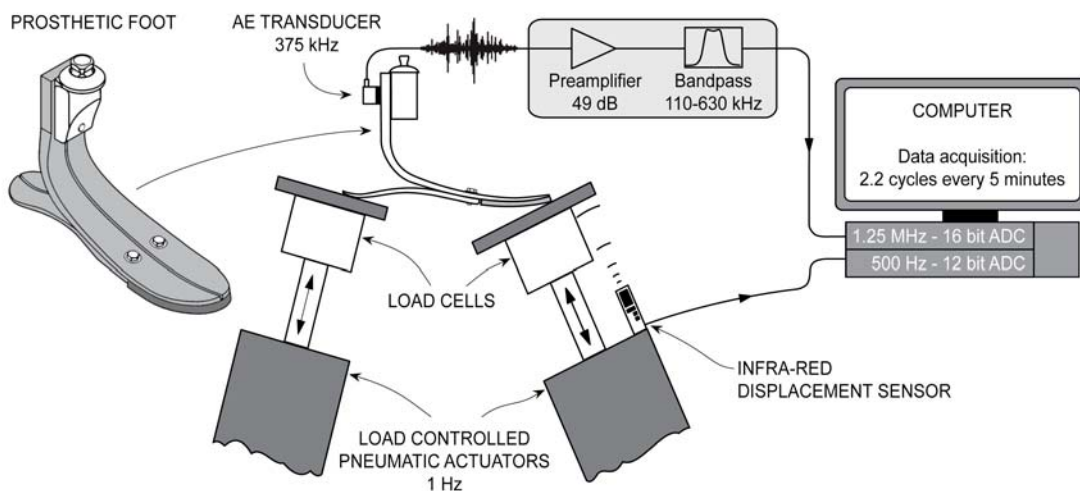


Fig. 5. A schematic representation of the experimental setup.

The AE signal and the position of the forefoot's actuator were measured simultaneously for 2.2 seconds every 5 minutes throughout the test. The sampling rates were set to 1.25 MHz and 500 Hz, respectively, for the AE and the position measurements. The L-Gage Q50 infra-red displacement sensor from Banner Engineering was used for the position measurements of the actuator loading the forefoot. For measuring the AE signals, the VS375-M AE transducer and the AEP3 preamplifier from Vallen Systeme GmbH were used. The preamplifier was equipped with 110-kHz high-pass and 630-kHz low-pass filters. The gain was set to 49 dB. The output from the preamplifier was fed to a 16-bit A/D converter for a full waveform digitization. For further information about the experimental setup the reader is referred to [13]. The position measurements were used for reference when the AE signal was segmented. Each AE measurement was trimmed so that it represented exactly one fatigue cycle, starting at the lowest position of the forefoot's actuator. Elliptical bandpass filters, each with 33-kHz bandwidth, were used to decompose the AE signal above 100 kHz into subbands. The bandpass filtering was performed using a phaseless filtering in order to avoid phase delay [14].

Each subband segment was divided into $K = 200$ intervals before computing the piecewise constant envelope. Figure 6 shows the resulting intensity image for the 133-166 kHz subband and also the evolution of the AE energy and the AE hit count from each segment. Intensity images are a convenient way to visualize the range of data; i.e., the higher the amplitude, the brighter the image pixels. The last two were computed from the unfiltered AE signal. The AE energy is the sum of the signal's values squared. The AE hits were determined using a short-term Fourier transform-based approach [13]. By comparing the evolution of the energy, and the AE hit count, to the subband images, one can gain better understanding of the changes, which are occurring in the material. An example is the energy spike, which occurred at segment no. 130. This spike was due to the formation of a new damage. After this spike, the signal's energy provided no further information about the damage evolution. However, from the subband images, the beginning of two new paths can be observed at segment 130 and their evolution can be monitored up to segment no. 239 where an apparent increase in AE amplitude can be seen. At segment 239, a half of the foot delaminated but the 10% displacement failure criterion was not met.

Figure 7 shows the resulting images for the 266-300 kHz (left) and 366-400 kHz (right) subbands. The evolution of some of the sources is present in both images; i.e., these sources emit AE signals, which lie in both subbands. The evolution of other sources is present in either image and not matched in the other. By studying different subbands, one can possibly detect band-limited AE and distinguish between two damages that emit AE signals at the same time but are evolving in different directions, as can be seen by comparing the circled paths in the left and right images of Fig. 7.

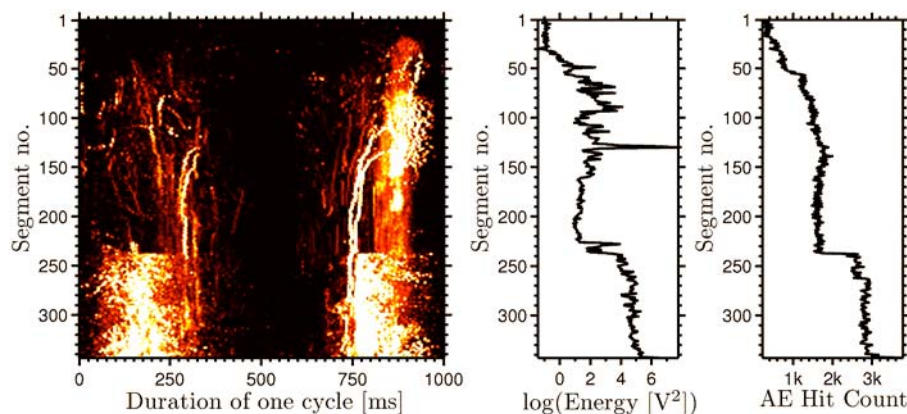


Fig. 6. The resulting images for the 133-166 kHz subband.

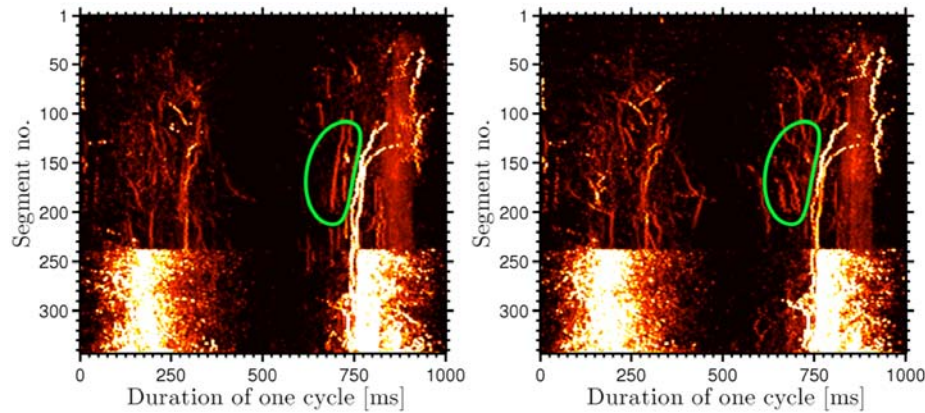


Fig. 7. The resulting images for the 266-300 kHz (left) and 366-400 kHz (right) subbands.

Conclusions

An experimental methodology for tracking the evolution of individual AE sources while monitoring cyclically loaded objects was presented. The decomposition of the AE signal into subbands enables the detection of band limited sources which otherwise would possibly go undetected. The methodology is a graphical tool, which aids with the monitoring and interpretation of AE data and should be a welcome addition to the toolbox of any engineer involved in AE monitoring of cyclically loaded objects.

Acknowledgements: The authors gratefully acknowledge Össur hf. for providing samples and access to their testing facilities. The work of the first author was supported by grants from: The RANNIS Research Fund, and the University of Iceland Research Fund.

References

1. J. Degrieck and W. V. Paepegem, *Applied Mechanics Reviews*, **54**, 2001, 279-300.
2. W. Van Paepegem and J. Degrieck, *International Journal of Fatigue*, **24**, 2002, 747-762.
3. H. G. Halverson, W. A. Curtin, and K. L. Reifsnider, *International Journal of Fatigue*, **19**, 1997, 369-377.
4. Y. A. Dzenis and J. Qian, *International Journal of Solids and Structures*, **38**, 2001, 1831-1854.
5. J. Baram, *Experimental Mechanics*, **33**, 1993, 189-194.
6. K. P. Dyer and D. H. Isaac, *Composites Part B: Engineering*, **29**, 1998, 725-733.
7. M. Knops and C. Bogle, *Composites Science and Technology*, **66**, 2006, 616-625.
8. D. Tsamtsakis, M. Wevers, and P. De Meester, *Journal of Reinforced Plastics and Composites*, **17**, 1998, 1185-1201.
9. M. Giordano, A. Calabro, C. Esposito, A. D'Amore, and L. Nicolais, *Composites Science and Technology*, **58**, 1998, 1923-1928.
10. M. Wevers, *NDT and E International*, **30**, 1997, 99-106.
11. H. Nayeb-Hashemi, P. Kasomino, and N. Saniei, *Journal of Nondestructive Evaluation*, **18**, 1999, 127-137.
12. E. R. Green, *Journal of Nondestructive Evaluation*, **17**, 1998, 117-127.
13. R. Unnthorsson, T. P. Runarsson, and M. T. Jonsson, *International Journal of Fatigue*, doi:10.1016/j.ijfatigue.2007.02.024, 2007.
14. C. A. Mercer. Prosig Inc., 2001.

NEURAL NETWORK BURST PRESSURE PREDICTION IN COMPOSITE OVERWRAPPED PRESSURE VESSELS

ERIC v. K. HILL, SETH-ANDREW T. DION, JUSTIN O. KARL,
NICHOLAS S. SPIVEY and JAMES L. WALKER II*

Aerospace Engineering Department, Embry-Riddle Aeronautical University, Daytona Beach, FL 32114 USA; *Non-Destructive Evaluation Branch, NASA Marshall Space Flight Center, AL 35812 USA

Abstract

Acoustic emission data were collected during the hydro-burst testing of eleven 380-mm (15")-diameter filament-wound composite over-wrapped pressure vessels. A neural-network burst pressure prediction was generated from the resulting AE amplitude data. The bottles shared commonality of graphite fiber, epoxy resin, and cure time. Individual bottles varied by cure mode (rotisserie versus static oven curing), types of inflicted damage, temperature of the pressurizing medium, and pressurization scheme. Three categorical variables were selected to represent undamaged bottles, impact damaged bottles, and bottles with lacerated hoop fibers. This categorization along with the removal of the AE data from the disbonding noise between the aluminum liner and the composite over-wrap allowed the prediction of burst pressures in all three sets of bottles using a single back-propagation neural network. Here, the worst-case error was 3.38%.

Keywords: Amplitude distribution, back-propagation, burst pressure prediction, composites, filament-wound, graphite/epoxy, neural networks, nondestructive evaluation, pressure vessel.

Introduction

Acoustic Emission

Acoustic emission (AE) is a nondestructive evaluation method that involves instrumenting a specimen with piezoelectric transducers and recording parametric representations of the waveform data from flaw growth activity in order to perform a structural integrity analysis. Analysis of the AE data allows for the determination of failure mechanisms that are active in the specimen. Consequently, it also contains information concerning the structural integrity.

Burst Pressure Prediction

The prediction of burst pressures in both damaged and undamaged filament wound composite pressure vessels has been previously accomplished using linear multivariate statistical analysis and back-propagation neural networks [1-3]. The goal of this research was to utilize a back-propagation neural network to make burst pressure predictions on 380-mm-diameter graphite/epoxy filament-wound composite over-wrapped pressure vessels (COPVs, otherwise known as bottles) that were varied in the method of cure, type of damage, temperature, and pressurization scheme. What made this research different from its predecessors was that the disbonding of the composite over-wrap from the aluminum liner generated multiple-hit AE data (noise), which had nothing to do with the structural integrity of the vessels. This precluded a straightforward solution similar to those obtained previously until the noise data were eliminated.

Neural Networks

Artificial neural networks are a diverse set of robust mathematical tools used to classify data into clusters, recognize patterns, process signals, and do predictive modeling and forecasting. Here, an unsupervised SOM neural network was used to classify the composite failure mechanisms that occur during pressurization. The back-propagation architecture is a feed-forward design that was subsequently employed for making supervised burst pressure predictions.

Kohonen Self Organizing Map (SOM)

In composite structures, the amplitude frequencies [of occurrence] generated during damage progression can be grouped and classified into failure mechanisms. For small data sets, these mechanisms can be seen as “humps” in the AE amplitude distributions. Figure 1 shows the amplitude distribution for bottle SN002, an impact damaged graphite/epoxy COPV used for training the back-propagation network, which appears to have four humps. This number of failure mechanisms (four) was confirmed by classifying the AE amplitude data with a Kohonen self-organizing map (SOM) neural network.

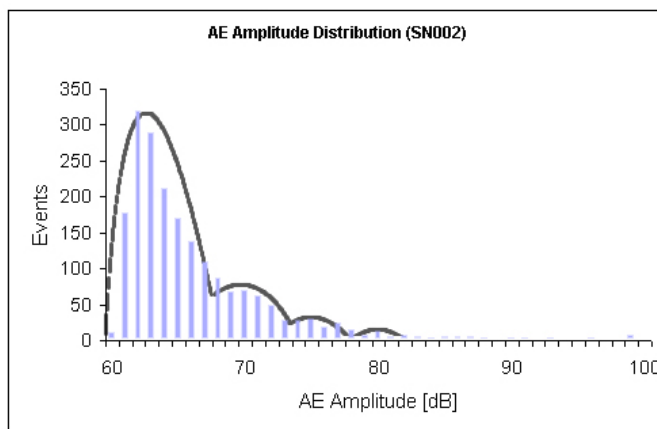


Fig. 1 AE amplitude distribution for COPV SN002.

Back-propagation

The back-propagation neural network is a feed-forward, supervised neural network, that is to say, it does not return a feedback signal to itself during each training pass, and it is necessary to train the network on a known solution before applying it to a new case. This is called supervised learning. A back-propagation neural network is typically constructed with an input layer, one or more hidden layers (each composed of multiple neurons) for mapping, and an output layer.

Experimental Procedure

Pressure Vessels

Eleven 380-mm-diameter filament-wound COPVs were wet-wound on a filament winder. The bottles were thin-walled aluminum cylinders over-wrapped with graphite fibers and epoxy resin. The winding sequence was 3 inner-hoop plies, followed by 2 helical layers, and then 2 outer-hoop plies. Eight of the bottles were rotated at slow speeds (rotisserie style) during oven curing; three were oven cured without rotation. Four of the COPVs were tested at ambient temperature, while the remaining seven experienced cryogenic temperatures. Due to the nature of piezoelectric materials, it was thought that the large variation in temperatures would have a significant effect on transducer output voltage, as well as adding to the brittle nature of the composite material.

Varying amounts of artificial damage were inflicted on the bottles in the form of impacts from both blunt and sharp tups, as well as with the cutting of hoop fibers: five tows were cut in the mid-hoop ply and five in the first outer-hoop ply. The strain rate was also varied non-systematically in that the pressurization scheme used on each bottle test varied in both duration and number of pressurization ramps/holds; thus, no two bottles were pressurized alike.

The amount of diversity in some of these variables and the small number of bottles would not allow for statistical analysis of the effects of each variable. Therefore, neural networks were employed as the primary method of data analysis. Table 1 summarizes the test variables along with the failure or burst pressures.

Table 1 Summary of graphite/epoxy COPV variables and burst pressures.

S/N	Damage	Cure Type	Test Temperature	Burst Pressure [psig]
002	Impacted	Static	Cryogenic	1880
003	Impacted	Rotisserie	Cryogenic	2004
005	None	Rotisserie	Ambient	2960
009	None	Static	Cryogenic	2544
010	None	Static	Cryogenic	2460
013	None	Rotisserie	Ambient	2874
014	None	Rotisserie	Cryogenic	2390
018	Lacerated	Rotisserie	Ambient	2864
020	Impacted	Rotisserie	Cryogenic	1967
025	Lacerated	Rotisserie	Cryogenic	2393
026	Lacerated	Rotisserie	Ambient	2675

AE Data Collection

Acoustic emission data were successfully collected from all seven of the bottles in the test set. A multi-channel Physical Acoustics Corporation (PAC) AE analyzer was used to record the AE flaw growth data from seven AE channels, each representing a transducer at a unique location on the test bottles. This data acquisition unit also allowed for a separate parametric input, which was used to record a voltage signal representative of the pressure in the test specimen. Figure 2 shows a schematic diagram of the test setup.

Six PAC-R15 AE transducers were mounted equidistant around the circumference of the top and bottom hoop windings on each bottle. The seventh transducer was mounted near the upper polar boss on the helically wound portion of the bottles. In the ambient temperature tests, hot-melt glue was used to bond each transducer and provide acoustical coupling between the transducer and the specimen. For the cryogenic tests, high-aqueous vacuum grease and a mechanical housing were used to couple the transducers to the bottles. The data sampling threshold was set to record all AE hits that had an amplitude of 60 dB or greater.

AE Data Filtering

Even though constraints such as amplitude threshold, peak definition time (PDT=100 μ s), hit definition time (HDT=500 μ s), and hit lockout time (HLT=500 μ s) were applied to the AE sampling, considerable noise and multiple-hit data were still present in the raw data sets. HDT is the minimum time that an AE event must have to be recorded, and the combination of HDT and HLT determines the maximum time for an event before it is considered to be a multiple-hit event [4]. These settings work in real-time as data are recorded.

Multiple-hit data occur when many AE waveforms reach the transducer closely spaced in time, one after another (in a condition of buffer overrun or in the cases where HDT and HLT are

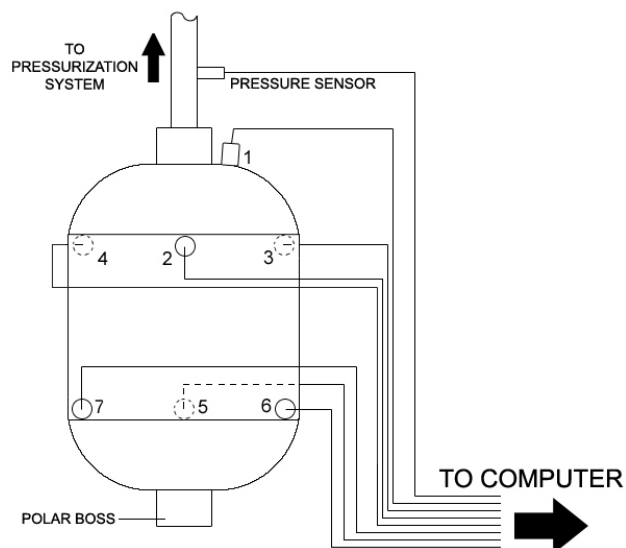


Fig. 2 Sensor positioning and test setup.

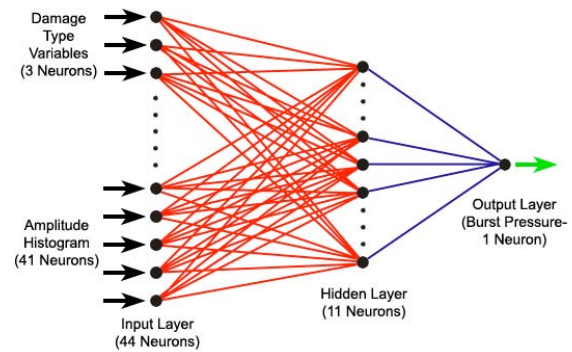


Fig. 3 Network architecture.

not properly set). This results in a long artificial waveform that is actually comprised of several shorter waveforms, which will have vastly different AE parameters than single-hit data. In this case, the multiple-hit data are probably the result of composite disbonding from the aluminum liner, a failure mechanism which should not affect the burst pressure.

In order to remove these multiple hits from the recorded data set, it was determined that any AE hits having durations longer than 100 ms were to be removed. Rise time, the waveform parameter that represents the time-to-peak of the waveform, was used to further remove suspected multiple hit data. Long rise times typically indicate multiple hits logged together. Thus, any hit with a rise time of greater than 25 ms was also removed from the data set. The AE energy parameter is a measure of the area under the rectified waveform envelope. In the case of these data, many hits were reported by the data acquisition system to have zero energy. These hits were also discarded under the assumption that they were noise.

The final filter applied to the data was to select those data points to be used in the actual burst pressure prediction. After removing all of the data prior to the start of pressurization (the acquisition hardware recorded AE parameter data before pressurization commenced), it was decided that the first 2000 data points would provide a sufficient sample size for the neural network to train on while still taking only those data that were acquired at or below 20% of the anticipated burst pressure. In general, damage is inflicted on composite bottles during any pressurization cycle; therefore, the goal was to predict on data taken at low proof pressures.

Using the final edited data set from each bottle, a frequency distribution of the amplitudes was extracted for training and testing of the back-propagation neural network. The histogram representation of an amplitude distribution for bottle S/N 002 can be seen in Fig. 1, and the amplitude distributions from the edited data for all eleven bottles are summarized in Table 2. The neural network was trained to analyze the subtle differences in the distributions from each bottle and match them to the damage type and burst pressures provided in the training set.

Results

Network Architecture

The back-propagation neural network used herein [4] had the architecture shown in Fig. 3. The input for each bottle consisted of a 1 x 44 dimensional vector with 3 entries representing the damage categories (001 undamaged; 010 impacted; and 100 lacerated) plus 41 integers repre-

Table 2 Finalized amplitude distribution frequencies (with **categorical variables** in bold).

S/N	Amplitude Distribution Frequency Data	Burst Pressure [psig]
002	010 2 11 177 319 289 212 171 139 109 87 69 70 63 50 29 29 30 19 24 16 7 13 68 6 3 6 5 5 3 1 4 3 1 3 1 0 3 2 0 7 0	1880
003	010 2 66 452 461 268 171 130 89 76 44 37 40 25 35 20 13 17 11 4 10 7 2 4 1 2 4 2 0 0 0 1 0 2 0 0 0 0 0 0 1 4 1	2004
005	001 1 169 148 121 115 95 123 88 81 78 62 59 74 53 53 58 61 47 46 52 58 38 48 43 34 29 31 28 21 21 21 10 7 7 4 6 7 0 3 1 0 0	2960
009	001 1 39 360 452 285 177 119 88 82 70 46 42 31 40 28 32 20 13 9 8 8 6 4 6 7 7 3 1 4 3 3 0 2 0 0 0 1 0 0 0 4 0	2544
010	001 1 47 337 400 298 194 114 112 75 58 58 55 34 44 32 29 20 19 10 8 8 5 10 8 4 1 1 2 6 2 1 1 0 1 1 0 1 1 1 1 1 0	2460
013	001 1 71 401 380 254 169 96 76 67 61 42 44 49 42 29 23 33 16 16 16 21 15 15 12 9 7 4 10 8 7 3 0 3 0 0 1 0 0 0 0 0 0	2874
014	001 1 67 477 475 309 193 98 66 54 29 47 22 25 24 13 2 10 9 10 7 4 9 4 4 1 2 3 1 3 4 0 5 3 1 1 1 0 1 0 2 1 3	2390
018	100 3 225 222 211 176 160 136 137 99 98 80 85 67 54 2 44 40 23 19 21 15 15 5 2 6 4 2 0 0 0 1 0 0 0 0 0 1 0 0 0 0 0	2864
020	010 16 212 369 301 230 179 147 99 95 65 47 42 30 35 25 12 12 8 13 7 10 5 4 0 5 1 7 4 2 3 1 2 0 1 2 0 0 0 0 5 4	1967
025	100 3 30 224 309 294 216 176 132 102 99 76 63 39 48 36 26 19 18 15 12 10 13 8 6 5 0 3 0 0 1 0 2 5 0 1 1 1 1 1 0 0 7 2	2393
026	100 3 13 108 166 199 199 205 173 167 135 103 107 86 66 58 47 29 29 35 15 16 5 8 8 5 1 3 2 3 3 1 0 1 1 1 0 1 0 0 0 1 0	2675

sending the frequency distribution of amplitudes from 60 to 100 dB (Table 2). The actual burst pressure was also supplied as an input for error calculation at the output.

Each neuron in the hidden layer contains a hyperbolic-tangent activation or transfer function that can be used to approximate the shape of the amplitude distributions. A large number of neurons can be used together to approximate compound and/or discontinuous curves that will fit the training data well, but if trained too closely, the back-propagation neural network may not predict accurately on the test data. Too few neurons in the hidden layer will result in loosely fit curves that will not correspond well to the training or test data. Using this approach, it was found that 11 neurons in the hidden layer offered the network that would best fit both the training and the test data.

Training the Network

The back-propagation neural network, generated using Neuralware's NeuralWorks Professional II Plus software package, was trained on a total of seven COPVs, including bottles from each of the three damage categories (Table 3). The training set was chosen so that a high and low burst pressure COPV from each damage category was included. The undamaged category also included a midrange burst pressure bottle. Thus, the epoch size was seven or the total number of bottles in the training set.

After numerous experimental iterations, the optimum network architecture and input parameters were determined [4]. The learning rule was the normalized cumulative delta, and the optimal learning coefficient for the network was found to be 0.30 with a momentum of 0.40. This relatively large learning coefficient allowed the network to train very quickly and to learn in only 71 cycles. Because the network trained so quickly, bias neurons were not employed to speed up the training process. Transition points and learning coefficient ratios were not important either because the default transition point of 5000 cycles was never reached, while the F' offset was set at 0.10.

A root-mean-square (RMS) error value on the seven COPVs in the training set is computed by the software after every training cycle to determine how well the network has trained. Here the RMS error convergence was set at 7%. This means that training was considered complete when the network-training curve was within an RMS error of 7% of the training data. It was found that a higher convergence criterion left the network too loosely fit to the training data, and a lower convergence criterion forced tighter fitting of the training data but poorer fitting of the test data.

Burst Pressure Predictions

Finally, the trained network was used to predict burst pressures for both the training and test sets. Table 3 shows a summary of the prediction results on all the COPVs. The maximum prediction error in the seven bottle training set was -2.78%, and the maximum error in the four bottle test set was 3.38%. All of these values were well within the goal of predicting the burst pressures to within a $\pm 5\%$ error.

Table 3 Summary of training and test results

S/N	Damage	Purpose	Burst Pressure [psig]	Predicted Burst Pressure [psig]	Error [%]
002	Impacted	Train	1880	1827.597	-2.78
003	Impacted	Train	2004	1964.115	-1.99
005	None	Test	2760	2853.188	3.38
009	None	Train	2544	2584.266	1.58
010	None	Test	2460	2432.273	-1.12
013	None	Train	2874	2791.009	-2.88
014	None	Train	2390	2358.271	-1.32
018	Lacerated	Train	2864	2869.181	0.18
020	Impacted	Test	1967	1999.875	1.67
025	Lacerated	Train	2393	2369.740	-0.97
026	Lacerated	Test	2675	2643.174	-1.19

Conclusions

The worst-case prediction error of 3.38% was low, and the network trained quickly in spite of the many test variables involved. If there were any variations in the amplitude distribution data due to cure mode, temperature, and pressurization scheme, they were automatically taken into account by the back-propagation neural network. The fact that network training was accomplished in only 71 cycles attests to the effectiveness of preprocessing or editing the AE data to remove the multiple-hit data and other noise.

References

1. E.v.K. Hill, J.L. Walker II, and G.H. Rowell, *Materials Evaluation*, **54**, 1996, pp. 744-748.
2. J.L. Walker, S.S. Russell, G.L. Workman, and E.v.K. Hill, *Materials Evaluation*, **55**, 1997, pp. 903-907.
3. M.E. Fisher and E.v.K. Hill, *Materials Evaluation*, **56**, 1998, pp. 1395-1401.
4. S.-A. T. Dion, MSAE Thesis, Embry-Riddle Aeronautical U., Daytona Beach, 2006.

ULTIMATE STRENGTH PREDICTION IN FIBERGLASS/EPOXY BEAMS USING ACOUSTIC EMISSION AMPLITUDE DATA

ERIC v. K. HILL, MICHELE D. DORFMAN* and YI ZHAO

Aerospace Engineering Department, Embry-Riddle Aeronautical University, Daytona Beach, FL 32114 USA; *Lockheed Martin Aeronautics Company, P.O. Box 748, Mail Zone 4271 Fort Worth, TX 76101 USA

Abstract

The research presented herein demonstrates the prediction of ultimate strengths in composite beams subjected to three-point bending using a neural network analysis of AE amplitude distribution data. Fifteen unidirectional fiberglass/epoxy beams were loaded to failure using a three-point bend test fixture. AE amplitude distribution data taken during loading up to a proof load of 80% of the average ultimate load were used as inputs for a back-propagation neural network. The network was trained on the proof load amplitude distributions from seven beams, and tested on the remaining eight. This resulted in a worst-case ultimate-load prediction error of 4.3%. A second analysis was performed using a Kohonen self-organizing map and multivariate statistical analysis. The Kohonen self-organizing map was utilized to classify the AE data into failure mechanisms. Then multivariate statistical analysis was performed using the number of hits associated with each failure mechanism to develop a prediction equation. Here the worst-case ultimate-load prediction error was -11.34%. The difference in the prediction errors is due to the intolerance of statistical analyses to noisy data; hence, the use of a back-propagation neural network is recommended when noisy data are involved.

Keywords: Acoustic emission amplitude distribution data, back-propagation and Kohonen self-organizing map (SOM) neural networks, failure mechanisms, fiberglass/epoxy beams, multivariate statistical analysis, three-point bending, ultimate strength prediction

Introduction

Previous research has shown that acoustic emission (AE) amplitude distribution data combined with the use of neural networks can be used to create a prediction model for ultimate loads/stresses in various applications. Fatzinger and Hill [1] tested a set of ten fiberglass/epoxy I-beams end-loaded in cantilever fashion with a hydraulic ram. Two of these beams were manufactured using a different resin type. AE amplitude distribution data taken during loading up to 50% of the theoretical ultimate load were used as inputs for a prediction neural network. The network, trained on five beams (one from the different resin type), was able to predict ultimate loads in the remaining five beams with a worst-case error of -10.6%. A classification neural network was subsequently utilized to sort the AE data into failure mechanisms. Then, a multivariate statistical analysis was performed using the percentage of AE hits associated with each failure mechanism along with the epoxy type to develop a prediction equation for ultimate load. The multivariate statistical analysis resulted in a prediction equation that had a worst-case error of +36.0%.

Current Approach

The approach employed herein was similar to that described above, except that here the 15''

(381 mm)-long beams were rectangular in cross section and loaded transversely in three-point bending [2]. Fifteen unidirectional fiberglass/epoxy beams were loaded to failure in an MTS load frame using a three-point bend test fixture with a span set at 7" (188 mm). Physical Acoustics Corporation R15I transducers were mounted onto the test specimens 1.5" (38 mm) from each end. AE amplitude distribution data taken during loading up to 80% of the average ultimate load were used as inputs for a prediction neural network. The network was trained on the amplitude data from seven beams, and tested on the remaining eight. A second analysis was performed using a classification neural network and multivariate statistical analysis. The classification network was utilized to categorize the five AE parameters (amplitude, duration, counts, rise time, and energy) into failure mechanisms. Then multivariate statistical analysis was performed using the number of hits associated with each failure mechanism to develop a prediction equation.

Neural Networks

Back-propagation

A back-propagation neural network is a multilayered, supervised, feed-forward network, as shown in Fig. 1, used here to predict ultimate loads. This type of network learns the relationship between the given input and the target output vector by minimizing the difference between the target and actual output vectors. The learning process consists of two stages. In the first stage, the input vectors are fed through the network to generate an output response vector. In the second stage, the output error is computed for each input based upon the target output values. The network error is then reduced by propagating error adjustments back to the network connection weights.

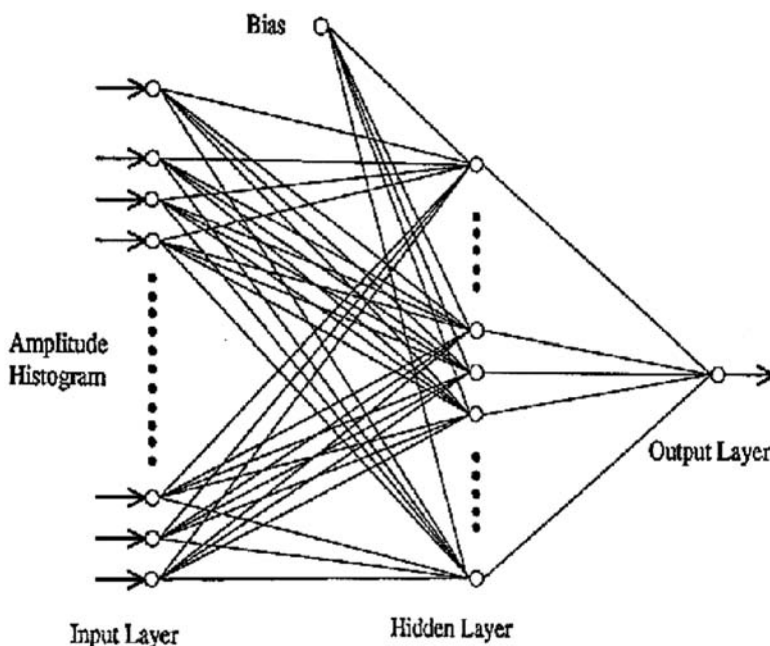


Fig. 1 Back-propagation neural network

Kohonen Self Organizing Map

A Kohonen self organizing map (SOM) is a single layered, unsupervised, competitive neural network, as shown in Figure 2, used here to classify AE data into failure mechanisms. A SOM is a neural network that sorts data into different categories from multi-dimensional inputs. When trained properly, a SOM can take data that is difficult to separate accurately, and divide it into different groups with common characteristics.

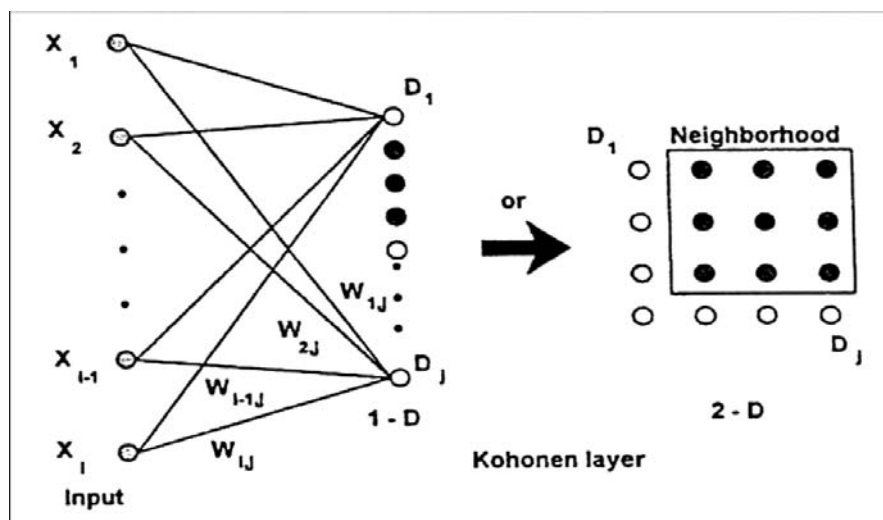


Fig. 2 Kohonen self organizing map

Ultimate Strength Prediction

Back-propagation Prediction

NeuralWorks Professional II/Plus software by NeuralWare was used to create a series of back-propagation neural networks that were optimized to predict the ultimate failure load using 80% proof load AE amplitude distribution data [2]. Architecturally, the optimum network consisted of a 61-neuron input layer for the amplitude frequencies of occurrence (hits), a 13-neuron hidden layer for mapping, and a single neuron output layer for predicting the ultimate load. The normalized-cumulative-delta rule was used for learning with a hyperbolic-tangent activation or transfer function. The learning coefficient for the input layer was 0.30 and for the hidden layer was 0.15 with a transition ratio of 0.35 applied every 7000 training cycles, while the F' offset was set at 0.05.

Fifteen beam specimens were tested in all with each neural network being trained on 7 specimens (Table 1) and tested on the remaining 8 specimens (Table 2). The amplitude data set from each beam was entered three times (bootstrapped) in random order to help the software learn on a larger set of data. Thus, the epoch size was $3 \times 7 = 21$. It should also be noted that the training set included the high and low values of ultimate load in order for it to predict correctly [1]. Lastly, the network was trained until the RMS error of the output converged to 3%.

The resulting back-propagation neural-network ultimate load predictions are summarized in Table 3. As can be seen (highlighted), the back-propagation neural network was able to predict the ultimate loads with a worst-case error of 4.34%. Note that all the errors on the training data are less than 1%, while those for the test data are all less than 5%. These minimal errors are the result of optimizing the back-propagation neural-network architecture and settings plus the iterative optimization process involved in its training: searching for the minimum error solution.

Kohonen Self-Organizing Map Classification of Failure Mechanisms

Next, a series of Kohonen self-organizing maps (SOMs) were generated using the NeuralWorks Professional II/Plus software to classify the AE parameter data (amplitude, duration, and energy) into failure mechanisms [2]. Architecturally, the optimum SOM consisted of a 3-neuron input layer for AE amplitude, duration and energy and a 4×1 Kohonen layer for processing. It was used to classify the AE data taken up to 80% of the average ultimate load into the expected four failure mechanisms [3]. The failure mechanism results listed in Table 4 thus became the inputs to the statistical analysis.

Table 1 Training set.

Specimen ID	Ultimate Load (lbs)	Amplitude Distribution Data
MDD3-1	336	3 9 6 2 4 2 0 0 1 0 2 0 0 0 1 0 0 1 0 1 0
MDD4-2	372.5	4 1 7 1 4 1 0 1 0 1 1 1 2 7 9 7 6 3 1 7 3 7 1 1 2 6 1 1 1 0 0 1 0
MDD2-3	357.5	2 0 2 7 3 0 2 3 2 2 1 5 1 3 1 4 1 2 9 1 0 1 0 1 1 5 9 7 2 4 6 2 5 2 2 3 0 1 2 0 1 0
MDD1-2	312.5	1 4 1 8 1 8 9 1 2 9 1 0 1 4 1 5 1 1 5 1 4 1 2 5 1 4 8 1 3 2 2 2 2 4 1 0 3 3 3 1 2 0 1 0 0 1 0 0 1 0
MDD4-3	392.5	7 1 0 9 7 8 2 5 3 1 4 2 1 2 2 2 3 4 4 3 4 1 3 4 5 0 2 0 0 2 0 1 2 1 1 1 0
MDD5-2	375	2 2 4 3 2 2 1 2 1 3 1 1 2 0 1 0 0 1 0 1 0
MDD5-3	365	4 1 2 7 6 5 3 1 2 3 1 1 0 0 1 1 0 1 1 0 1 3 0 0 0 0 1 0

Table 2 Testing set.

Specimen ID	Ultimate Load (lbs)	Amplitude Distribution Data
MDD1-1	375	6 9 1 0 2 9 4 4 4 2 3 4 3 1 2 1 2 1 2 1 2 2 3 1 0 1 0
MDD3-2	312.5	1 4 1 9 2 4 1 3 1 6 1 2 9 5 4 6 5 2 4 9 3 5 4 7 4 2 3 2 3 2 3 0 0 0 0 1 0 0 0 0 1 0 1 2 0
MDD2-2	365	5 1 1 1 5 8 9 8 5 9 7 6 1 0 3 3 3 4 4 4 3 3 3 4 5 5 2 3 4 2 3 2 2 2 1 2 1 1 0 0 0 1 0
MDD1-3	327.5	9 1 5 8 1 4 1 0 1 2 9 3 5 5 3 5 2 1 1 1 2 1 1 0 1 1 0
MDD3-3	340	3 1 4 1 1 6 7 7 7 1 1 0 0 1 0 2 0 0 1 0 1 0 0 1 1 0
MDD4-1	363	3 4 7 5 3 5 3 1 2 0 1 0 0 0 0 1 0 0 0 0 0 0 1 0 0 1 2 0
MDD2-1	372.5	1 3 4 2 4 1 1 0 1 3 2 0 1 0 0 0 0 0 1 2 3 0
MDD5-1	367.5	0 5 2 1 2 1 1 0 1 1 0 1 2 1 0 1 1 2 1 0 1 2 0 0 0 1 1 0

Table 3 Back-propagation neural network results.

	Specimen ID	Actual Load (lbs)	Predicted Load (lbs)	% Error
Training Data	MDD3-1	336	333.6	-0.72
	MDD4-2	372.5	372.5	-0.01
	MDD2-3	357.5	357.6	0.03
	MDD1-2	312.5	312.0	-0.16
	MDD4-3	392.5	392.7	0.06
	MDD5-2	375	378.1	0.83
Test Data	MDD5-3	365	364.9	-0.02
	MDD1-1	375	359.4	-4.15
	MDD3-2	312.5	326.0	4.34
	MDD2-2	365	354.2	-2.97
	MDD1-3	327.5	334.5	2.14
	MDD3-3	340	325.5	-4.26
	MDD4-1	363	361.9	-0.31
	MDD2-1	372.5	378.8	1.69
MDD5-1	367.5	383.1	4.25	

Table 4 Multiple linear-regression inputs.

Specimen ID	Number of Hits per Mechanism				Actual Load (lbs)
	Mechanism 1	Mechanism 2	Mechanism 3	Mechanism 4	
MDD1-1	33	24	18	4	375
MDD1-2	62	72	56	20	312.5
MDD1-3	51	41	16	1	327.5
MDD2-1	12	9	7	1	372.5
MDD2-2	45	40	31	38	365
MDD2-3	108	85	63	11	357.5
MDD3-1	24	4	4	0	336
MDD3-2	77	45	43	15	312.5
MDD3-3	40	18	5	1	340
MDD4-1	21	13	2	3	363
MDD4-2	51	57	32	2	372.5
MDD4-3	34	25	26	21	392.5
MDD5-1	9	5	11	3	367.5
MDD5-2	10	13	6	0	375
MDD5-3	31	14	8	1	365

Multivariate Statistical Analysis Prediction

Statgraphics Plus was the program used to calculate the coefficients of the prediction equation. Multiple linear-regression analysis based on the above input data yielded the following approximate (neglecting the Mech3 and Mech4 terms) ultimate load prediction equation [2]:

$$\text{Predicted Load} = 372.96 - 0.687 \text{ Mech1} + 0.214 \text{ Mech2}.$$

From this equation the ultimate load was predicted for each specimen using the number of hits per failure mechanism as the independent variables. The predicted results can be seen in Table 5. Here the worst-case prediction error was -11.34%, almost three times as large as that obtained with the back-propagation neural network.

Table 5 Multiple linear regression analysis results

Specimen ID	Actual Load (lbs)	Predicted Load (lbs)	% Error
MDD1-1	375	355.4	-5.22
MDD1-2	312.5	345.8	10.65
MDD1-3	327.5	346.7	5.86
MDD2-1	372.5	366.6	-1.57
MDD2-2	365	350.6	-3.94
MDD2-3	357.5	317.0	-11.34
MDD3-1	336	357.3	6.35
MDD3-2	312.5	329.7	5.50
MDD3-3	340	349.3	2.74
MDD4-1	363	361.3	-0.46
MDD4-2	372.5	350.1	-6.01
MDD4-3	392.5	355.0	-9.57
MDD5-1	367.5	367.8	0.09
MDD5-2	375	368.9	-1.63
MDD5-3	365	354.7	-2.83

Conclusions

- The back-propagation neural network successfully predicted the ultimate loads in unidirectional fiberglass/epoxy beams subjected to three-point bending from the AE amplitude data taken up to a proof load of 80% of the average ultimate load.
- The Kohonen self-organizing map appeared to successfully classify the AE data into 4 failure mechanisms using the AE parameters amplitude, duration and energy only.
- Multivariate statistical analysis using the number of hits associated with each failure mechanism predicted ultimate failure loads successfully but with much larger errors than the back-propagation neural network.
- The back-propagation neural network provided better prediction results than the multivariate statistical analysis because the latter is inherently sensitive to noisy or sparse data whereas the iterative back-propagation algorithm is not.

References

1. E.C. Fatzinger and E.v.K. Hill, *J. of Testing and Evaluation*, **33**, 2005, 8 p. (on-line).
2. M.D. Dorfman, MSAE Thesis, Embry-Riddle Aeronautical U., Daytona Beach, 2004.
3. L.J. Graham, *1980 Paper Summaries, ASNT National Spring Conference*, ASNT, 1980, pp. 74-79.

ANALYSIS OF ACOUSTIC EMISSION FROM IMPACT AND FRACTURE OF CFRP LAMINATES

KANJI ONO, YOSHIHIRO MIZUTANI¹ and MIKIO TAKEMOTO²

Department of Materials Science and Engineering, UCLA, Los Angeles, CA 90095-1595, USA;

¹Tokyo Institute of Technology, Ookayama, Meguro, Tokyo 152-8552, Japan; ²Faculty of Science and Engineering, Aoyama Gakuin University, Sagamihara, Kanagawa 229-8558, Japan

Abstract

The impact damage of CFRP plates under impact load was evaluated using recording of AE, load and strain history. The threshold or critical impact force to cause internal damage in cross-ply CFRP laminates was determined using dynamic surface strain and Lamb-wave AE along with the impact force history. Loading was conducted in SACMA-type impact tests at 0.8 and 1-m/s velocity. Four types of cross-ply CFRP plates ($[0_n^o/90_n^o]_s$, $n = 4-10$) are impacted with a spherical steel-tup, 16 mm diameter. Surface strain of a test laminate is measured using a strain gage. Lamb-wave AE signals were detected by small AE sensors on both surfaces. Polarity of AE signals detected by both sensors are compared in investigating the progression of fracture. Only impact-induced AE (or Impact-AE) is obtained when the impact tup contacts the specimen at a lower speed. When internal fracture occurs, both Impact-AE and fracture-induced AE (Fracture-AE) were detected. The nature of Fracture-AE is examined in this study in conjunction with ultrasonic C-scan and surface evaluation. AE monitoring on both surfaces enabled us to clearly separate the S_0 and A_0 modes of Lamb-wave AE signals. Most of strong AE signals correlated with matrix fracture source, while other damages had no associated distinctive events.

Keywords: Impact-AE, fracture-AE, CFRP laminates, impact damage threshold

Introduction

Carbon-fiber reinforced plastics (CFRPs) are useful in a wide range of applications due to their high specific strength and stiffness. However, they are prone to impact damage even under modest hits. SACMA-type impact test is often used for investigating impact fracture of CFRPs [1]. Only load history and tup velocity are taken during the test, after which samples are subjected to compression testing. We added AE monitoring and strain sensing to the SACMA tests and obtained the impact damage threshold for CFRP plates [2]. In so doing, in lieu of limited data, i.e., maximum impact load, impact duration and energy, we found details of the dynamic fracture processes in the form of Lamb-wave AE signals as well as displacement and surface strain history. Two types of AE signals were identified; Impact-AE and Fracture-AE. Only a limited number of previous studies have been reported on impact damages with little materials analysis [3-6], despite abundant CFRP studies of compression after impact are known.

In this study, waveforms of Lamb-wave AE signals due to internal damage in cross-ply CFRP laminates are examined, in conjunction with dynamic surface strain and the impact force history measured during SACMA-type impact tests. In particular, two-surface sensing [7-9] allowed us to evaluate mode types of detected signals. Additionally, failure modes were examined using microscopic studies to determine crack length and types and using ultrasonic C-scan to reveal the extent of delamination. Results are compared to the observations during quasi-static tests of the same CFRP.

Specimen and Experimental Setup

A large-size plate of $([0_n/90_n]_s, n = 4, 6, 8, 10)$ was prepared by laminating pre-pregs. Carbon fibers were pitch-based XN-50 from Nippon Graphite Fiber with the nominal modulus of 490 GPa. Rectangular specimens with $150 \text{ mm}^L \times 100 \text{ mm}^W$ were cut with the fiber directions (0°) on the top surface along the longitudinal (or X-) direction. Impact tests used Dynatup 8250 from Instron Corp., which satisfied SACMA SRM 2R-94 standard. Impact load was applied at the center of a specimen via a hemispherical steel tup of 16-mm diameter, weighing 3.61 kg [2]. The edges of the specimen were clamped all around by steel flanges. Four small AE sensors (Physical Acoustic Corp.: Type Pico) were mounted on both surfaces at 32-mm from the impact point in the X-direction. Polarity of AE signals detected by both sensors are compared for investigating the progression of fracture. A top AE sensor was used for determining the damage initiation. Outputs of two of the AE sensors were amplified 40 dB and filtered by a band-pass filter of 200 kHz to 1.2 MHz for eliminating large-amplitude low-frequency AE due to impact. The other two outputs were recorded directly at 10-1200 kHz bandwidth. As signal saturation occurred with amplification, all the analysis here used only direct-recording data. These signals were digitized by 2 PAC MISTRAS boards at the sampling interval of 500 ns over 10.2 ms, and stored in computers. The strain gage was attached on the top surface at the 32-mm from the impact point. Outputs of the strain gage and the load cell on the impact tup were digitized at the sampling interval of $1 \mu\text{s}$ over 60-ms period. The strain gage data was used for deciding impact damage threshold and timing. See [2] for other information. The tup displacement was dynamically recorded with a strain-gaged leaf-spring and used for velocity measurement.

Impact tests for four types of cross-ply CFRP plates ($[0_n/90_n]_s$) were conducted at two impact velocities (nominally 0.8 and 1 m/s) by controlling the height of the tup. Impact test for the 40-ply plate at 0.8 m/s was omitted, because no damage was observed at 1.0-m/s impact test. Details of quasi-static tests of similar CFRP plates were reported earlier and most fracture mechanisms are expected to operate under dynamic conditions as well.

Two-surface Sensing

In thin plates, Lamb waves are usually detected as AE signals. Figure 1 gives examples of 20- μs -long waveforms from in-plane (IP) and out-of-plane (OP) pencil-lead breaks. Two Pico sensors were placed on opposite faces of a 3.2-mm thick stainless steel plate, 50 mm from an edge. For comparison, the left figure is for an IP source with two sensors on the same side.

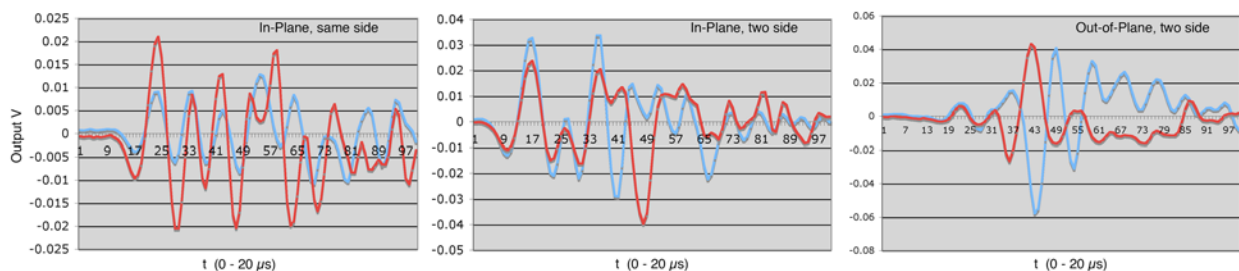


Fig. 1 Lamb waves from IP/OP pencil-lead break sources. Two Pico receivers were used.

Two Pico sensors on the same side showed similar wave character for the first 7 peaks, but differences became prominent after $\sim 8 \mu\text{s}$. The first $3.6\text{-}\mu\text{s}$ portion is S_0 mode, but the arrival of A_0 mode cannot be discerned from these waveforms. IP source detected on two sides produced

nearly same waveforms for the first 6 peaks ($\sim 8 \mu\text{s}$), indicating this part is S_0 mode. OP source (1 mm from the edge) showed the initial 4 peaks at the same phase, followed by 5 peaks at the opposite phases. The opposite phase waves are A_0 mode, while the initial part is S_0 mode. Such OP sources are often considered to generate primarily flexural modes, but this source was close to the edge and reflection contributed to the symmetric mode, albeit weaker.

It is clear that, with the two-side monitoring, we can distinguish symmetric (typically S_0) mode for the in-phase waves, while out-of-phase waves are asymmetric, flexural (typically A_0) mode. In CFRP plates used here, the calculated wave speed of S_0 mode varies widely; it is only about 15% faster than that of A_0 mode moving over the entire thickness at 500 kHz, and here the temporal separation of the two modes from a single source is not readily visible. However, faster propagating S_0 mode along the 0° -fibers exists with the measured velocity of 8-10 mm/ μs without much dispersion. When S_0 mode or A_0 mode is found by itself, a distinct source is expected to have been active. See [7, 8] for more discussion on two-surface sensing.

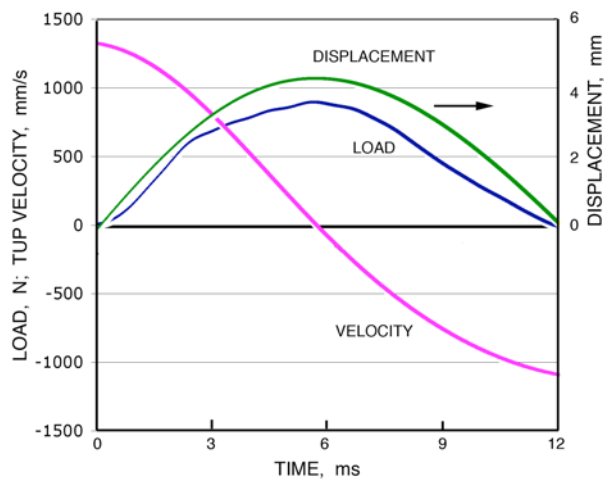


Fig. 2 Impact force-displacement-velocity vs. t for 16-ply CFRP at 1 m/s nominal velocity.

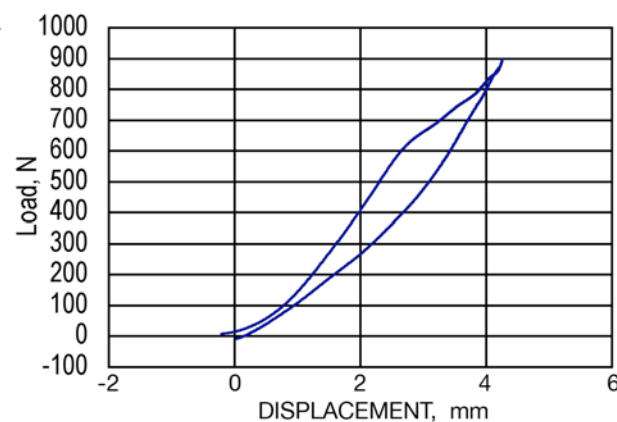


Fig. 3 Impact force vs. displacement plot of 16-ply CFRP at 1 m/s nom. impact velocity.

Impact History and Impact Damage

Measured impact force-displacement-velocity values are plotted against time in Fig. 2 for a 16-ply sample, hit at a nominal velocity of 1 m/s. The velocity at contact was 1.3 m/s, decreasing to zero at the peak load, from which point the tup reversed the direction as the load was reduced. The load vs. displacement plot is given in Fig. 3, which indicates the elastic loading and a sudden slope decrease (-45%) at 600 N, where damage initiated. A corresponding loading rate reduction is seen in Fig. 2. Most of bending displacement recovered upon unloading and the initial unload slope was unchanged from the load slope, implying minimal damage to the elastic stiffness of the plate. Directly recorded AE signals from Pico sensors are shown in Fig. 4. Early signals at 0.4 to 2.4 ms are Impact-AE (IAE) signals and have the flexural wave character. Fracture-AE (FAE) signals start at ~ 2.5 ms with 14 major events.

The first F-AE event coincides with the slope change of the load-time and load-displacement curves (cf. Figs. 2 and 3). This signal consists of a pair of S_0 and A_0 packets at 2.54 ms (Fig. 5a). The S_0 packet was 20- μs long, indicating the presence of fast through-fiber mode. This signal has a strong A_0 component, which is six times stronger than the S_0 packet preceding it (in p-to-p values). Most (11 of 14) of the recognizable AE events seen in Fig. 4 are of the type with both S_0 and A_0 components (Fig. 5a) and are marked with an asterisk. This signal type is almost identical

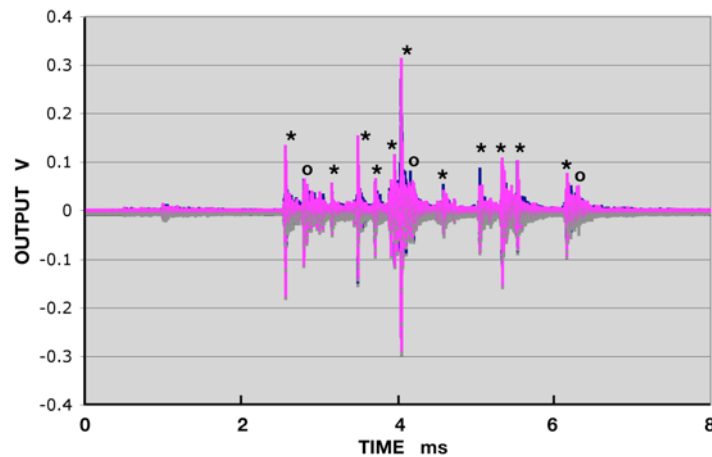


Fig. 4 Direct recording of AE signals from bottom sensor. 16-ply sample hit nominally at 1 m/s. Most of top sensor signals are hidden.

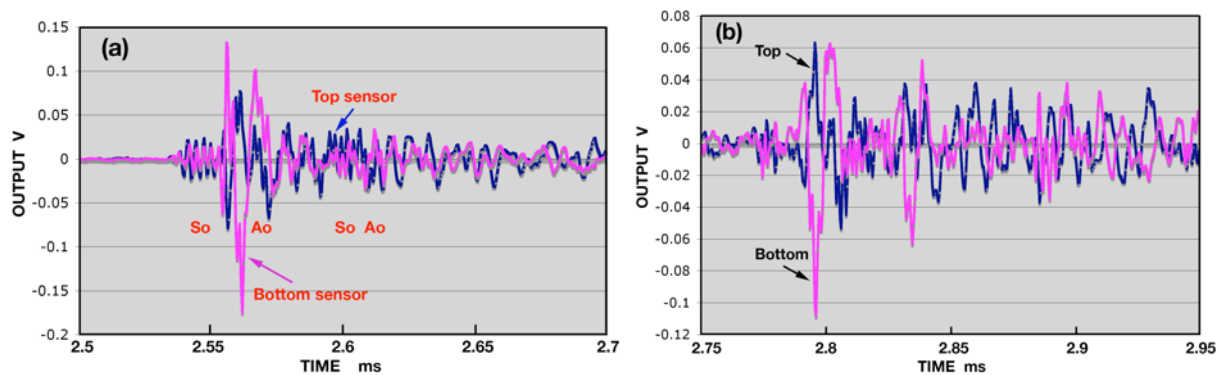


Fig. 5 The first two major events in Fig. 4, each shown in 200- μ s long segment for 2 sensors.

to Type-D signal detected in the static tests of the same CFRP reported earlier [6, 7]. It was attributed to matrix fracture, found on the bottom surface under the impact point, splitting 0° -fibers. This signal type (-D) was weaker, but similar in appearance to Type-A signal in the static testing, which was very strong ($>2.5 V_{pp}$) and was attributed to fiber fracture, which was observed on the top surface in real time using a video camera.

The second event starting at 2.77 ms (Fig. 5b) is mostly comprised of A_0 packets when top and bottom sensor signals have reasonable similarity (with inverting). We found three such signals, marked with an "o" in this test and referred to as Type-D'. Overall, these two events (Fig. 5a and b) resemble each other. The second type appears to be of the same origin as the first except the weaker S_0 portion was disturbed by interference from the remnants of prior waves.

In this sample, a large matrix crack (53-mm long) was found on the bottom surface. The cross-sectional view of the plate (Fig. 6) shows this crack at the top. Delamination and fiber fracture are also observed in the middle layer. Delamination was extensive according to the observation by an air-coupled ultrasonic C-scan image (Fig. 7). The extent of damage spreads to as large as 42 x 15 mm double-tree shape area.

It is significant to note that, in dynamic tests, Type-D (and -D') signals were prevalent, but not so strong ($0.6 V_{pp}$ maximum). This implies that the matrix crack proceeded stepwise under dynamic loading, although this is counter-intuitive. Stepwise development of the matrix crack is likely to be induced by the underlying fibers, which may have to be fractured to allow matrix crack propagation. In other test samples, delamination occurred between bottom- 0° and 90° plies, and stepwise matrix crack growth was implied from AE findings. This point needs more study.

Another notable fact is the lack of AE signals that can be traced to the large delamination observed. All the major events are associated with the matrix crack and only the trailing parts of signals can explain delamination. It is feasible to recognize another signal type at 2.6 ms in Fig. 5a is, where a pair of S_0 and A_0 packets of similar amplitude are observed. This is characteristic of Type-C AE signals reported earlier for delamination between CFRP plies. This type is difficult to discern on waveform plots as many signals of various origins overlap as a rule. As the remaining waveform plots were surveyed, apparent S_0 and A_0 packets are also seen continually. However, distinct patterns fail to emerge. Despite extensive delamination observed, we found no distinctive AE type. It is likely that delamination developed continually without any sudden displacement jump. Under static loading, in contrast, nearly 20% of identified signals were Type-C, attributed to delamination. Also missing are signals (Type-B) previously assigned to transverse cracks (37% in the static test). These appear to constitute mostly A_0 -mode signals that followed strong Type-D signals. These differences between static and dynamic tests are expected due to visco-elastic nature of polymeric fracture processes, which require further examination.

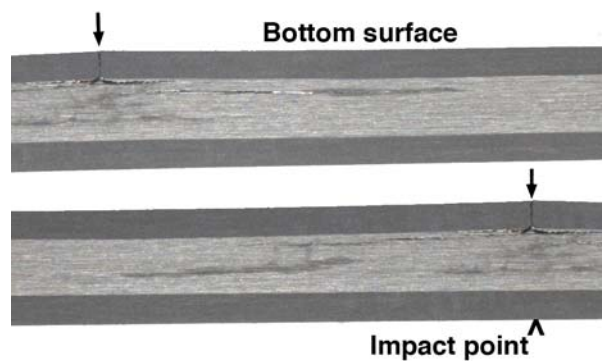


Fig. 6 Cross-section of the 16-ply sample with arrow pointing to the matrix crack.

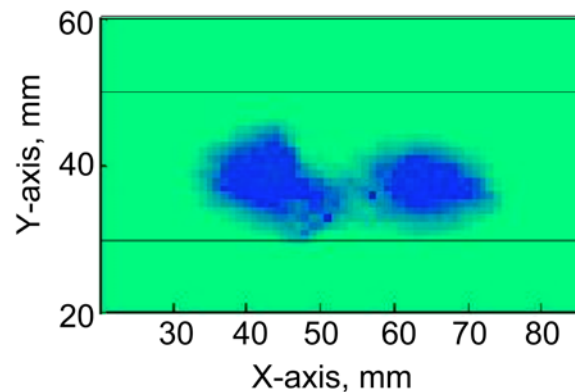


Fig. 7 Ultrasonic C-scan image of damaged area.

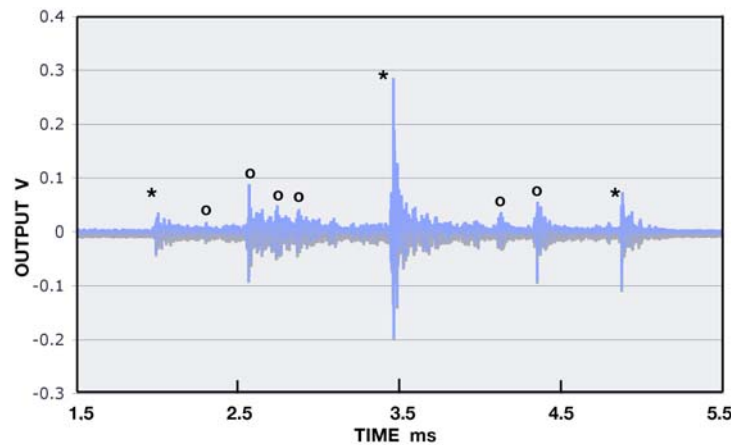


Fig. 8 F-AE signals of a 24-ply plate sample impacted at 1 m/s.

Three of six samples impacted at 1 m/s showed similar AE behavior described above. That is, over 60% of events were of Type-D and most of the remainder were Type-D'. The AE behavior of two other samples (24-ply and 32-ply plates, also impacted at 1 m/s) was slightly different as shown in Fig. 8. (Last one, 40-ply plate did not produce F-AE.) The first F-AE signal was detected at 2 ms and was of Type D (denoted with *) as before and the strongest signal was also of Type-D (at 3.45 ms). In this sample, more A_0 -only Type-D' signals were observed as marked by

an “o”. In the 32-ply sample, the ratio of D’ to D was the same; i.e., 2 : 1. In both cases, duration of F-AE observation was shorter (3 or 2 ms) than the 16-ply samples (~4 ms) due to higher stiffness of thicker plates. Thus, there are more overlaps of signals between strong events, probably converting Type-D into Type-D’.

Waveform of Type-D signal was previously simulated using the same CFRP and a line-focused laser pulse [6, 7]. Results are shown in Fig. 9, where the setup is at left, the waveform at center and its wavelet transform at right. The similarity of this waveform with that of Type-D is evident, including the period of the S_0 packet preceding the A_0 packet (20 μ s) and the ratio of A_0 to S_0 amplitude (5.4 : 1). The frequency of the S_0 packet was higher in the simulation, reflecting the nature of the fast rise laser source. In the simulated waves, it is 500-600 kHz, whereas the S_0 frequency in Fig. 5 was 250-400 kHz. Observed A_0 frequency of ~140 kHz was comparable to the simulated A_0 packet frequency. It is noted here that the frequency of A_0 waves due to I-AE was much lower at 20-40 kHz.

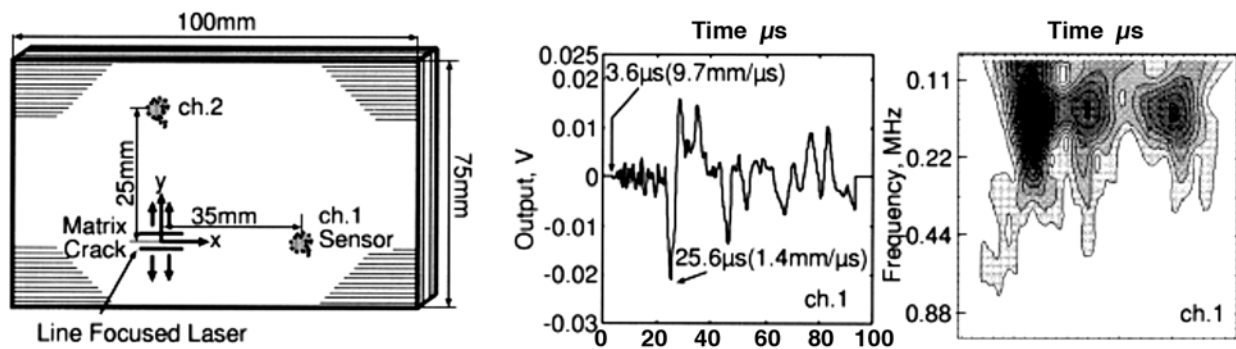


Fig. 9 Laser simulation of matrix cracking on the bottom surface using focused laser beam parallel to the 0° fibers. Pico sensor was 35 mm away (3 mm further than the present experiment).

Conclusions

This study reports on the utility of two-surface sensing in differentiating symmetric and asymmetric Lamb-wave modes. The method was applied to the monitoring of AE during the impact of CFRP plates of four different thicknesses. Different failure modes were seen under dynamic loading in comparison to quasi-static loading. A large matrix crack on the back surface and extensive delamination were the main features. AE signals attributable to matrix crack propagation were predominantly detected, while those due to delamination could not be discerned clearly. This was in marked contrast with the static case, where 4 separate failure mechanisms were correlated to 4 AE-signal types.

References

- 1) SRM 2R-94, SACMA Recommended Test Method for C.A.I., SACMA
- 2) Y. Mizutani, K. Ono and M. Takemoto, *Progress in AE XI*, 2002, JSNDI, Tokyo, pp. 23-30.
- 3) S.I. Ochiai, K.Q. Lew and J.E. Green, *J. of Acoustic Emission*, **1** (3), (1982), 191-192.
- 4) N. Liu, et al., *Key Engineering Materials*, **167-168** (1999), 43-54.
- 5) W.H. Prosser, M.R. Gorman and D.H. Humes, *J. of Acoustic Emission*, **17**, (1999), 29-36.
- 6) A. K. Mal, F. Shih, and S. Banerjee, *Proceedings of SPIE - Smart Nondestructive Evaluation and Health Monitoring of Structural and Biological Systems II*, Vol. 5047, 2003, pp. 1-12.
- 7) Y. Mizutani, K. Nagashima, M. Takemoto, K. Ono, *Proc. of AECM-6*, ASNT, pp. 114-123.
- 8) Y. Mizutani, K. Nagashima, M. Takemoto and K. Ono, *NDT and E. Intl.*, **33-2** (2000), 101.
- 9) Y. Mizutani, Doctoral Dissertation, Aoyama Gakuin Univ., 2000. 137 p.

ON USING AE-HIT PATTERNS FOR MONITORING CYCLICALLY LOADED CFRP

RUNAR UNNTHORSSON, THOMAS P. RUNARSSON and MAGNUS T. JONSSON

Department of Mechanical & Industrial Engineering, University of Iceland, Reykjavik, Iceland

Abstract

This paper presents the results of a study where AE-hit patterns are used for monitoring the location of AE sources. The AE-hit patterns contain information about the spacing between hits and other additional information about the hits, e.g., the amplitude. A methodology for detecting AE hits and coding the information is developed. A procedure for searching for AE-hit patterns in the coded representation and for processing the search results is also presented. The approach is demonstrated using experimental AE data acquired during fatigue cyclic testing of an assembled CFRP prosthetic foot. The results of this study show that the AE-hit patterns can be used to track the evolution of AE sources. Additionally, the results show that by adding the peak amplitude of AE hits to the hit patterns, the tracking of AE sources is improved significantly.

Keywords: Source tracking, hit patterns, carbon fiber, composites, fatigue

Introduction

The research idea behind this study is to investigate whether damages in carbon fiber-reinforced polymers (CFRP) generate characteristic sequences of AE hits, which could be used to monitor damage progression. In [1] the authors used the peak hit amplitude for tracking the locations of evolving AE sources within fatigue cycles. The purpose of this study was to evaluate whether better results could be obtained by monitoring the temporal AE-hit patterns.

One of the fundamental elements of music is rhythm. Rhythm can be determined by the relation between note accents (attack) and the rests between notes [2]. The term can be used to refer to either a repetitive pulse, or a beat, which is repeated throughout the music or a temporal pattern of pulses. The modeling and the interpretation of temporal patterns are of interest to people working in different disciplines. In the field of music information retrieval rhythm-based features have been extracted from audio and used for classifying music styles [3], i.e., blues, disco, polka, etc. In the field of computational neuroscience, patterns in spike trains are studied in order to understand the “language of the brain”[4].

The first step of working with temporal patterns is to determine the pulses. Once they have been determined, the rest, or duration, between them can also be determined and the results can be coded into features and processed. The detection of pulses starts usually with the processing of the signal in order to make the detection more accurate. The resulting signal is called a detection function and it can be in any domain of interest, e.g., time domain, frequency domain, and time-scale/time-frequency domain. An example of a detection function is one made using a model called a *rhythm track* [5]. The rhythm-track model is based on the assumption that the audio can be considered to be a random signal and the signal's energy increases significantly when a pulse occurs. The rhythm track can be created using several methods; e.g., by using the signal's instantaneous energy in the time- and the frequency domains [5, 6]. The pulses are detected from the detection function. The peaks in the detection function do not all correspond to the onset of pulses, consequently, several approaches have been used to identify those that do;

e.g., by using fixed threshold and peak-picking [6]. The approach taken here uses the signal's envelope as the detection function and hits are determined by peak-picking.

Interpreting hit patterns is a non-trivial task. Similar patterns can be generated differently, e.g., closely spaced hits can either be due to rapid AE release or due to multiple AE simultaneously emitted from the numerous AE sources in the material. In addition, the signal can be affected by processes, such as reflection and attenuation. The attenuation can be caused by geometric spreading, dispersion, internal friction, and scattering [7]. During the progressive degradation process of a cyclically loaded CFRP composite material, the damage mechanisms in the material grow and some evolve into different mechanisms [8]; i.e., delamination as a result of the coalescence of matrix cracks. By monitoring the evolution of hit patterns, and detecting changes, the inception of critical damage mechanisms can possibly be detected before the onset of catastrophic failure.

Methodology

This section describes and discusses the methodology used for locating the AE hits and the procedure for coding the results into a compact form. The procedure for searching and locating hit patterns in the coded representation is also described and discussed.

The aim is to monitor the location of evolving AE sources within fatigue cycles. Hence, the first step is to split the AE signal into segments of length equal to the period of one fatigue cycle. The AE hits are then determined from a detection function. The detection function is generated by converting the AE signal into decibels (dB). The logarithm transformation changes the dynamic range of the signal by enhancing low values, while compressing high values. The transformation is useful when the transducer cannot be placed at the location of damage and the AE signal suffers from high attenuation. Furthermore, the transformation makes it possible to use one setting for detecting both high and low amplitude hits.

The hits are detected and located by peak picking of the detection function. The peak picking is performed by an algorithm, which incrementally removes peaks and valleys that have peak-to-peak values below a threshold, T_{pp} , starting with the smallest ones [9]. The threshold controls the sensitivity of the approach. If the sensitivity is increased then smaller pulsations in the AE signal will be detected as hits.

Once the hits have been located, the results are coded into a coding vector. The structure of the coding vector can be accomplished in many different ways. Figure 1 outlines one possible structure of the coding vector, in which the coded inter-spike intervals (ISI) can be used with additional information. The information is coded and put in a vector, which is placed in between each coded ISI. Hence, each hit is represented by a substring in the coding vector.

In this study, two different coding approaches are investigated. The first uses only ISI coding and the second combines the ISI coding with a coded representation of the peak amplitude. The coding of the ISI is made by first logarithmically transforming (Log_{10}) the time between the peak amplitudes of successive hits, measured in milliseconds. The results are then shifted, scaled, and rounded so that each interval is represented by integers between $-N_{\text{ISI}}$ and -1 . The coding of the peak amplitudes is performed similarly. The amplitudes are logarithmically transformed (Log_{10}), shifted, scaled, and rounded so they are represented by integers ranging from 1 to N_{AMP} .

The procedure for searching for hit patterns in the coding vector is illustrated in Fig. 2. Before starting the search, the user must choose the lengths of the hit patterns. The lengths must be integer multiples of the substring length. The locations where a pattern, H_P , is observed are stored in an observations vector, O_P , where $P = 1 \dots N_P$ and N_P is the number of hit patterns. The observation vector is of same length as the original AE signal segment and initially contains only

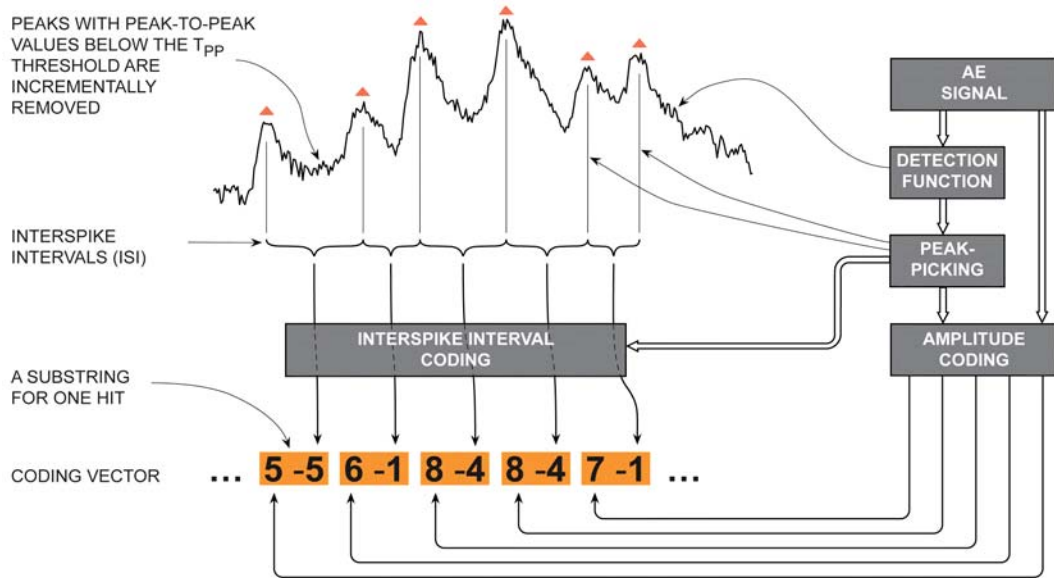


Fig. 1. The generation of the coding vector illustrated using substrings with coded amplitude and coded ISI.

zeros. The locations where a pattern, H_p , is observed within the AE signal are indicated by ones (1) in the observation vector. The vector is then partitioned into K intervals and the number of observations in each interval is counted. The results are put into a feature vector which has K entries.

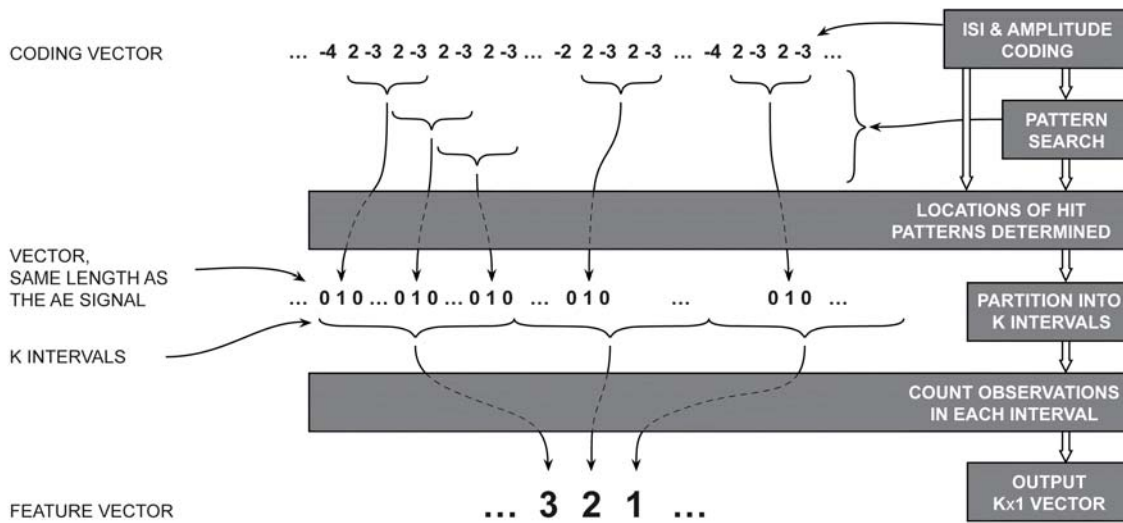


Fig. 2. The procedure for finding hit patterns and processing the results into a feature vector.

Results.

The test specimen, the test setup, and the experimental procedure used in this study, were described in references [1] and [9]. The experimental data and the graphical tool presented in [1] were used for studying the evolution of AE hit patterns. The same settings were used for the subband filtering. The peak-to-peak threshold, T_{pp} , was adjusted for each subband, so the average number of amplitude pulses in the first 5 measurements was around 10.000; i.e., average

pulse duration was 0.1 ms. The values of N_{ISI} and N_{AMP} were both set to 10 and $K = 200$ intervals were used when computing the feature vectors. Two different coding representations were studied: one using only ISI information and another using both ISI and the peak amplitude of the hits.

ISI coding

Approximately 60 patterns were obtained for each subband using ISI coding. However, only a handful of the patterns provided images which could be used to track the locations of the AE sources within the fatigue cycles. The two intensity images in Fig. 3 show the results obtained by logging the locations where two different patterns were observed. The prominent paths observed in both images show that the ISI is a characteristic feature of certain AE sources and it can be used to locate interesting AE sources for further study, or for tracking. Half of the foot delaminated at segment no. 239, but the displacement failure criterion was not met [6]. Due to the rubbing of the delaminated surfaces high number of AE hits with similar ISI were emitted. As a consequence, only few paths can be identified from the remaining segments.

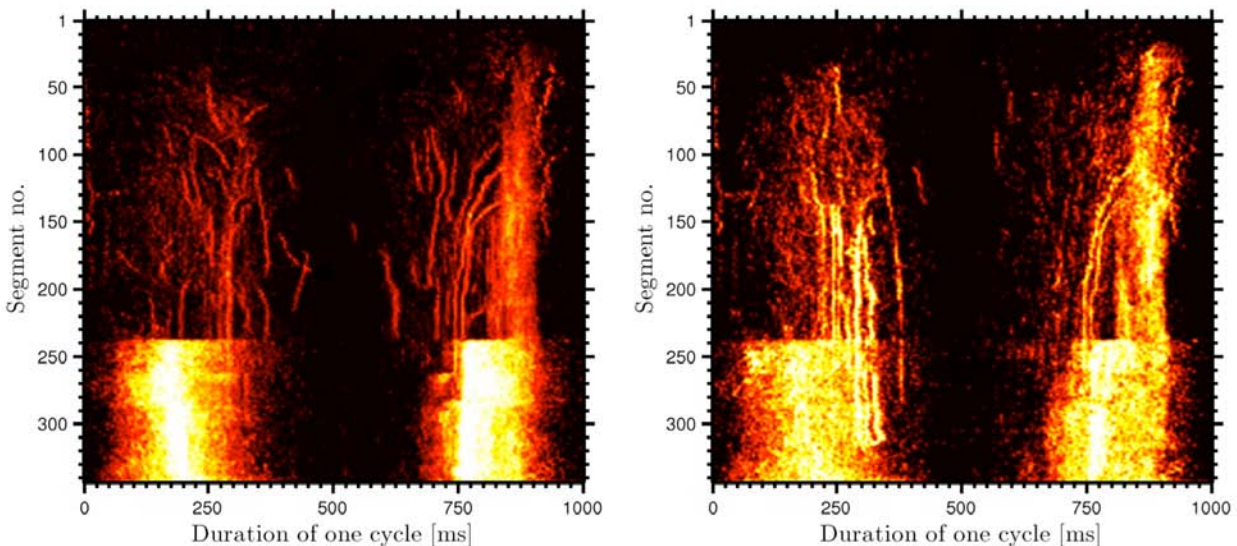


Fig. 3. The resulting images for two patterns using only ISI coding: one computed in the 333-366 kHz (left) and other computed in 133-166 kHz (right) subbands.

ISI/peak amplitude coding

By combining the ISI information with the peak amplitude of each hit, the total number of patterns increased up to approximately 600 patterns for each subband. The increase is a function of the number of quantization levels used for the amplitude, N_{AMP} . By visually inspecting the evolution of patterns and selecting patterns that show evolving trends, a composite image can be made which enables better understanding of the evolving damages in the material.

Figure 4 shows such an image, made by picking out, overlaying, and enhancing paths from 28 patterns. The patterns were handpicked from all subbands. The image on the right side of Fig. 4 shows the evolution of the AE energy in each segment. The AE energy was computed from the unfiltered AE signal by summing up the signal's values squared.

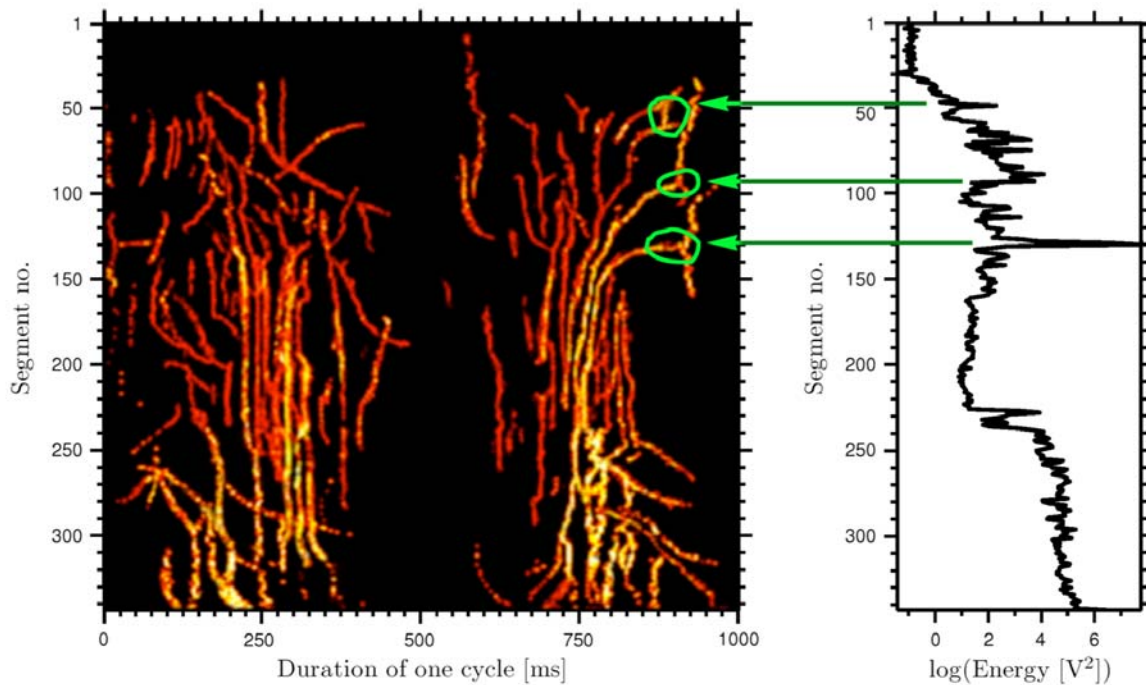


Fig. 4. A composite image made by overlaying and enhancing the results from 28 patterns (left) and the evolution of the signal's energy from each segment (right).

A comparison of the intensity images in Fig. 3 to the intensity image in Fig. 4 reveals that the addition of the peak amplitude makes it possible to track the evolution of several AE sources after segment no. 239. The tracking improvement can also be observed by comparing the 765-1000 ms region of the images. In this region of the fatigue cycle, the initiation of 3 paths can be observed (circled). These three paths can be monitored up to segment no. 239 where half of the foot delaminated.

In the 765-1000 ms interval strong AE signals were emitted from splinters [9]. Splinters, or tear outs, on the sides were commonly observed on the foot component in the area from the mid-foot to the ankle. The reason for the formation of splinters was the varying width of the foot components. The ends of the cut fibers were only held together by the matrix, which eventually failed due to repeated compression and tension loading. The splinter for this foot was located at the lower half of the foot component, i.e., below centre line. This caused the splinter to push out during upward movement of the toe's actuator (loading) and snap back during unloading, often producing an audible sound.

The reliability of the additional paths obtained by the combining the ISI and the peak amplitude in the pattern coding can be evaluated by comparing the paths which can be obtained using both coding approaches. Based on this evaluation method, the additional paths must be considered to be significant.

Conclusions

In this paper, we developed a methodology for detecting AE hits and for coding information extracted from the detected hits, i.e., the duration between hit peaks. We also developed a procedure for searching for AE-hit patterns in the coded representation and for processing the search results. The approach was then demonstrated using experimental AE data acquired during the fatigue testing of an assembled CFRP prosthetic foot.

The results show that the information provided by the inter-spike intervals (ISI) of the AE hits alone can be used to track the locations of AE sources. This is especially interesting since the study of ISI as a feature to track AE sources has, to the best of our knowledge, not been studied previously. In [1] the authors proposed a graphical tool for tracking the locations of AE sources in cyclically loaded objects. The tool was demonstrated by using the maximum amplitude in each interval of the cycle as a feature to track. This tool was also used here for tracking AE sources. The results obtained by using only ISI information are similar to the results presented by the authors in [1].

A significant improvement in the source tracking was accomplished by combining the ISI information with the peak amplitude of each hit. The addition of the peak amplitude makes it possible to track sources when there is very high AE activity, for example once delamination has occurred. The reason for this is the additional information provided by the amplitude of the AE hits, which produces a higher number of AE-hit patterns. This increase in the number of patterns is because the observations of patterns with certain ISI coding were divided between several patterns; i.e., patterns with the same ISI coding but different amplitude coding. Hence, the amplitude addition worked like a filtering.

Currently, selecting useful hit patterns for AE tracking is done manually by visual inspection. It is unlikely that the same patterns will be useful for other test specimens. It would be, therefore, useful to develop a technique for the automatic selection of useful patterns.

Finally, the experimental data used for this study was obtained during multi-axial cyclic loading of an assembled (bolted) complex-shaped composite. Hence, it is concluded that the approach used here can be successfully applied in a real world setting.

Acknowledgements: The authors gratefully acknowledge Össur hf. for providing samples and access to their testing facilities. The work of the first author was supported by grants from: The RANNIS Research Fund, the Icelandic Research Fund for Graduate Students, and the University of Iceland Research Fund.

References

1. R. Unnthorsson, T. P. Runarsson, and M. T. Jonsson, in "*Proceedings of the Sixth International Conference on Acoustic Emission*" (Kanji Ono, ed.), AEWG, 2007, Lake Tahoe, Nevada, USA.
2. H. F. Olson, *Music, physics and engineering*, Dover Publications 1967, 460 p.
3. S. Dixon, E. Pampalk, and G. Widmer, in "*International Symposium on Music Information Retrieval*", ISMIR, 2003.
4. F. Rieke, D. Warland, R. de Ruyter van Steveninck, and W. Bialek, *Spikes: Exploring the Neural Code (Computational Neuroscience)*, The MIT Press, 1997, 395 p.
5. W. A. Sethares, R. D. Morris, and J. C. Sethares, *Speech and Audio Processing*, IEEE Transactions on **13**, 2005, 275-285.
6. J. P. Bello, L. Daudet, S. Abdallah, C. Duxbury, M. Davies, and M. B. Sandler, *Speech and Audio Processing*, IEEE Transactions on, **13**, 2005, 1035-1047.
7. W. H. Prosser, in "*Proceedings of the SPIE conference on Nondestructive Evaluation Techniques for Aging Infrastructure and Manufacturing: Materials and Composites*", December 2-5, 1996, Scottsdale, Arizona, pp. 146-153.
8. E. K. Gamstedt and B. A. Sjögren, *Composites Science and Technology*, **59**, 1999, 167-178.
9. R. Unnthorsson, T. P. Runarsson, and M. T. Jonsson, *International Journal of Fatigue*, doi:10.1016/j.ijfatigue.2007.02.024, 2007.

ANALYSIS OF THE HYDROGEN DEGRADATION OF LOW-ALLOY STEEL BY ACOUSTIC EMISSION

KRYSTIAN PARADOWSKI, WOJCIECH SPYCHALSKI,
KRYSTYNA LUBLINSKA and KRZYSZTOF J. KURZYDŁOWSKI

Faculty of Materials Science and Engineering, Warsaw University of Technology,
02-507 Warsaw, Poland

Abstract

The hydrogen effect of low-alloy steels applied to the petrochemical, chemical and energy industry is the phenomenon, which significantly influences the integrity and safety of industrial installations. Hydrogen degradation with other operating conditions, the elevated temperature, pressure and stress, produced many material defects in micro- and macro-scale. It is critical to determine the influence of degradation factors on mechanical properties of structural materials to assure safe operation. For the precise assessment by the AE, it is necessary to perform AE study in laboratory conditions and collect experimental data, which will provide information for analysis of AE measurements in the service conditions.

The study was performed on a 13CrMo4-5 steel with or without hydrogen charging. The AE signals were measured during loading applied by a testing machine. The AE study was compared to the investigation carried out by scanning electron microscopy, which showed many changes in the microstructure of material after hydrogen charging. The hydrogen charging was realized by cathode polarization. This presentation shows the results of laboratory study on the application of the AE testing during modified mechanical tests to evaluate the material degradation under the hydrogen influence and operating conditions.

Keywords: Low-alloy steel, degradation, hydrogen

Hydrogen Degradation

Systematic rise of interest in the use of hydrogen in different branches of the industry may be seen in recent years. Hydrogen is used for energetic purposes (as fuel, in synthetic fuel production processes involving coal liquefaction method, in refinery hydrogen processes) and non-energetic (as a raw material in chemical industry, as reducing gas in metallurgy). In the case of the oil refining industry, the desire of stepping up production of engine fuels is related to the inevitability of intensification of crude oil processing. It calls for starting new hydro-cracking or hydro-desulfurizing installations, and for launching new hydrogen generating plant. The material applied must show high resistance to the destructive influence of hydrogen. The degree of hydrogen degradation varies and depends on many factors (e.g., structural, mechanical). In the case of steel, hydrogen damage may reveal itself as delayed hydrogen cracking, degradation of mechanical properties, especially ductility, and can change microstructures and create bubbles filled with molecular hydrogen, methane or hydrogen sulfide. Intensity of the material degradation caused by hydrogen saturation, depends considerably on the speed of diffusion of hydrogen in the given type of steel, as well as on the metal's ability to dissolve hydrogen. Hydrogen penetration through the low-alloy steels is very high because of high coefficient of hydrogen diffusion through the crystal lattice of iron. Hydrogen can also be transported through the core of dislocation or grain boundaries, which greatly increases its penetration [1, 2]. The process of hydrogen destruction of metals and its alloys is complex and therefore it is not

possible to determine one form of hydrogen degradation. Predicting the form of hydrogen destruction or the degree of its intensity, and suggesting universal parameters allowing for prediction of deterioration of any material, without detailed experiments that match each case, is not possible. Aggressive thermo-mechanical conditions, to which materials are subjected under real operating conditions and the presence of hydrogen, create real danger of hydrogen degradation taking place. Those materials may undergo high temperature hydrogen attack, but their hydrogenation may take place at ambient temperature as well, e.g., in petrochemical installations where in real corrosive conditions, we also deal with hydrogen penetration.

Experimental Procedures and Results

The study was performed on a low-alloy steel 13CrMo4-5 (1Cr-1/2Mo). Results of experiments performed on the steel in the initial state, after cathodic hydrogen charging and after exposure to operating conditions were compared in this study. The hydrogen charging was by cathode polarization in a 0.5M-H₂SO₄ solution with the addition of 5 mg/dm³ As₂O₃, to promote hydrogen penetration at ambient temperature. The current density used was 20 mA/cm² for an exposure time of 3 hrs. The samples in the exposed state were taken from cut-outs of an industrial pipe, used for 10 years. This pipe was selected by performing non-destructive testing (NDT) that detected the reasonable hydrogen degradation. The substance transported through the pipe contained hydrocarbons, hydrogen, water and sulfur-containing fuel and had higher concentrations of H₂S. The maximum operating temperature of the pipe reached 60°C.

In order to show the effect of hydrogen on the microstructure, microscopic observations were carried out by using a scanning electron microscope (SEM). Samples selected for examination were chemically etched with 4% Nital. In order to determine the degree of material degradation, hardness tests, tensile tests and fracture toughness tests were performed. Hardness tests were conducted with Rockwell (A scale) and Vickers (HV5) methods. Tensile tests were performed at ambient temperature, with a strain rate of 4.17×10^{-4} [s⁻¹]. Fracture toughness tests were performed at ambient temperature with compact-type samples.

Acoustic emission (AE) examinations were performed during two different, modified mechanical tests, which were carried out with the help of the static loading machine of 5 kN maximum force. The first of them consisted in loading of the tested surface of the material with 5-mm diameter ball indenter. In order to perform this test specially designed test set-up was employed, which allowed for attaching AE sensor on the ball indenter. The maximum force during test was 0.6 kN. The second test was performed on compact-type samples for plane strain fracture toughness test with pre-cracks made before tests. Pre-cracks were made with the varying load method at 20-Hz frequency. The lowering of the force amplitude below 3 kN was the criterion for the pre-crack test end. The length of the pre-crack in the samples for AE tests was about 5 mm. During AE measurements, two AE sensors (150-kHz resonant frequency) were employed, mounted opposite on the sample surfaces parallel to the pre-crack plane. The maximum force during tests equaled 5 kN. Schematics of the AE tests together with the results are given later. Analysis of the registered AE signals is given as the diagrams of amplitude [dB] vs. time, which were correlated with the force graph. Those results were related to force vs. cumulative number of events (AE hits) graph, in order to show Kaiser and Felicity effect.

Mechanical Tests

Hardness tests did not reveal differences between materials in the initial state and after cathodic hydrogen charging and after exposure to operating conditions. Tensile test results demonstrated slight decrease of plasticity of material after exposure to the operating conditions of 5~10% in relation to the starting material. Yet all determined strength parameters of tested

materials fulfilled all standard guidelines for steel types tested. In the case of fracture toughness tests, the sample size did not meet the criterion of plane strain state [3, 4]. For all cases, the plastic zone size at the crack tip was greater than 5% of the specimen thickness and crack surface morphologies indicated significant ductility. Additionally, the material subjected to operating conditions developed macroscopic structural defects, making further test impossible (Fig. 1). Microstructural defects under the cyclic loads increased to the critical size and stopped the crack propagation. Microstructure examination performed revealed numerous micro-structural changes in the degraded materials. The microphotograph showing changes in hydrogen charged material is displayed in Fig. 2.

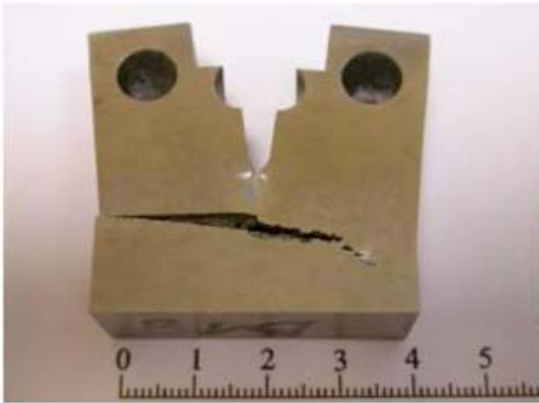


Fig. 1. Sample after fracture toughness test, material taken from a pipe.

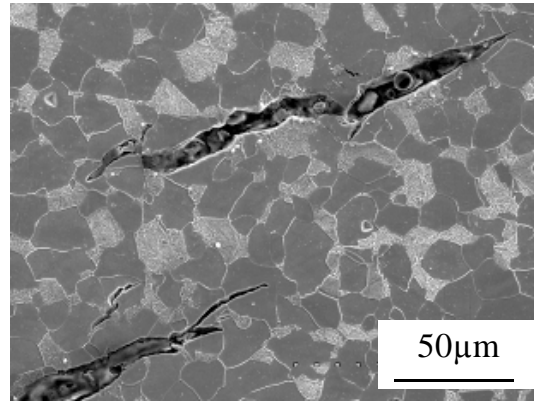


Fig. 2. Microstructural changes in hydrogen charged material.

In connection with problems described above, it was stated that quantitative determination of the degree of degradation of studied materials with the help of the mechanical tests performed is not possible.

Acoustic Emission Study

AE study, using indenter, was performed during cyclic material loading in two measurement sequences shown in Figs. 3 and 4. In the case of the hydrogen charged material (under laboratory conditions), the number of accumulated AE hits was 123 (Fig. 3).

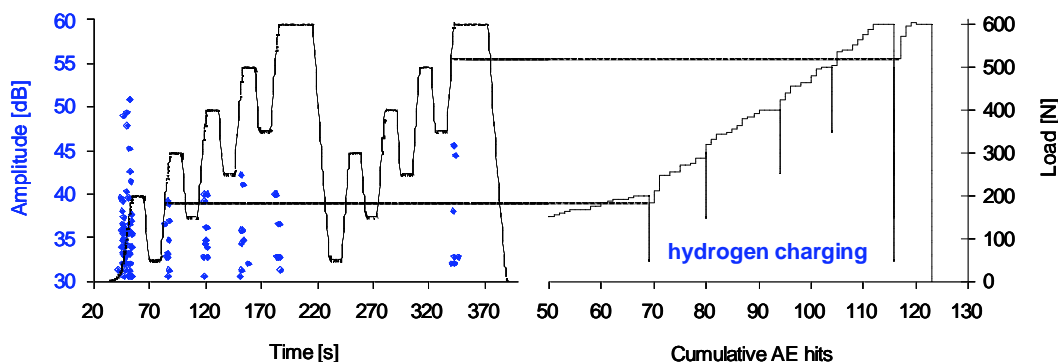


Fig. 3. AE measurement results of hydrogen charged material during indenter loading

The cumulative AE hits vs. force curve (Fig. 3) shows the presence of the Felicity effect during repeated loading of the material between 320 s and 370 s of the test with Felicity ratio of 0.87. In the case of the material after exposure, a higher acoustic activity was registered with clear Felicity effect (Fig. 4) during second measurement sequence. Cumulative AE hits reached

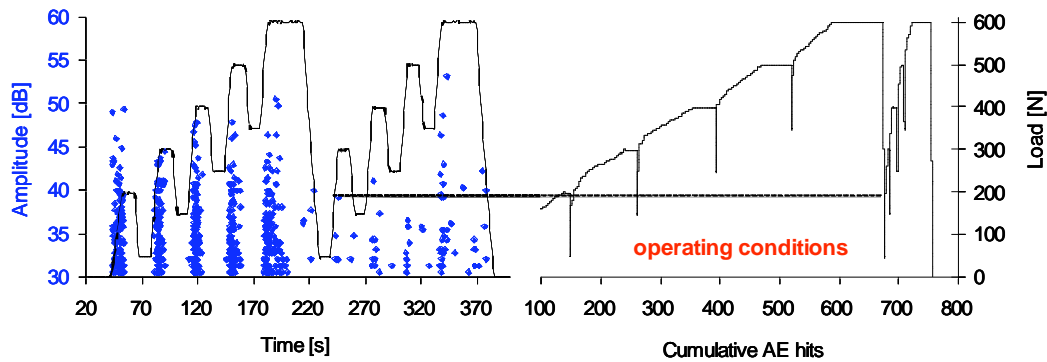


Fig. 4. AE measurement results of material after exploitation during indenter loading.

758, and Felicity ratio equaled 0.35. Material after exploitation characterized itself with higher acoustic activity during loading. In the case of the material, in the initial state, the number of cumulative AE hits was 101 and the Felicity effect was not detected.

In order to compare the results obtained for all three materials, relationship between severity and historic index is shown in Fig. 5. This clearly reveals the difference between AE recorded for degraded materials and material in the initial state.

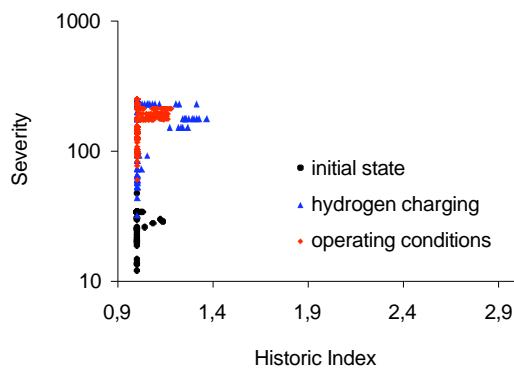


Fig. 5. Dependence of historic index on severity for materials loaded with indenter.

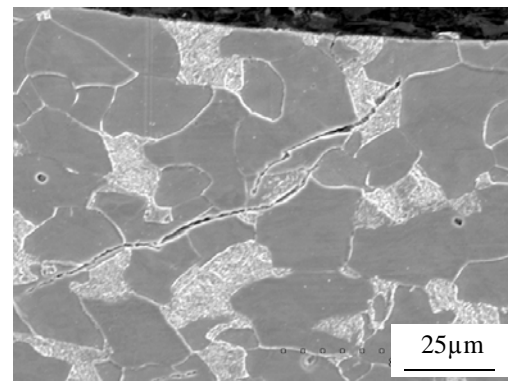


Fig. 6. SEM examination test of the hydrogen charged material, area under indentation with visible crack.

Though comparable number of signals recorded in the case of the hydrogen charged material and material in the initial state, severity values show, that these signals are of higher energy than those registered in the material in the initial state. SEM inspections performed on the material cross section under indentation surface revealed the presence of the cracks in the degraded materials (Fig. 6). Cracks recorded may be the potential reason of increased AE activity during indentation tests.

AE tests of the compact samples with pre-cracks were performed during loading of the material according to the schematic shown in Figs. 7 and 8. One should note that the samples were subjected to hydrogen charging after pre-cracks were made. It could intensified the hydrogen-induced degradation at the pre-crack tip as comparing to specimens cut from the material after operating conditions. The atomic hydrogen during cathodic charging derived from metal-environment surface reaction diffuses to microstructural heterogeneities at the crack-tip such as voids and microcracks, recombines to the molecular form, and builds up a very high internal pressure [5]. Felicity ratio of the hydrogen charged samples prepared for fracture toughness test equaled 0.27.

Characteristic of the material after exposure to operating conditions, as compared to other materials is the presence of AE during load decreases in the first and last cycles. Felicity ratio of the material after exposure amounted to 0.43. In the case of the material in the initial state number of AE hits recorded amounted to 83, and Kaiser effect was observed. Material after hydrogen charging produced more AE signals in the first part of the test, than the material after exposure. The different extent of the material degradation at the crack-tip could influence AE activity during the first loading to the maximum. Higher number of cumulated AE hits 1412 (Fig. 7) relative to the material after exposure to operating conditions confirms this fact. This number for the material after exposure was 573 (Fig. 8).

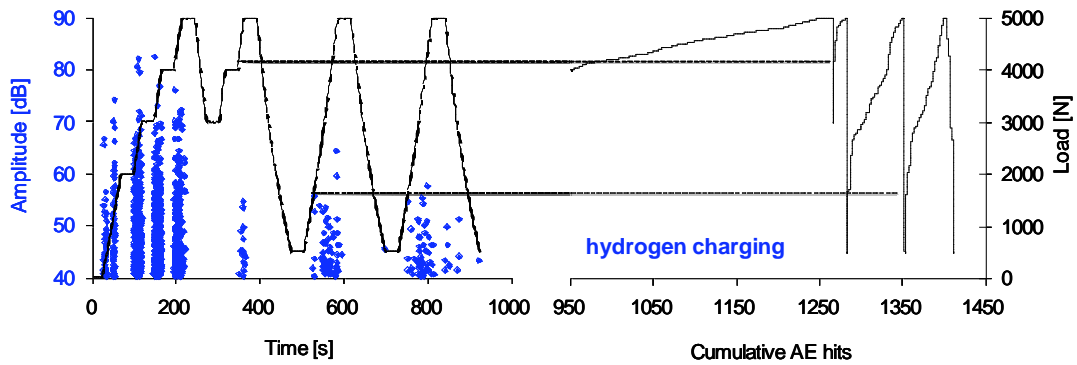


Fig. 7. AE measurement results of the hydrogen charged samples for fracture toughness test.

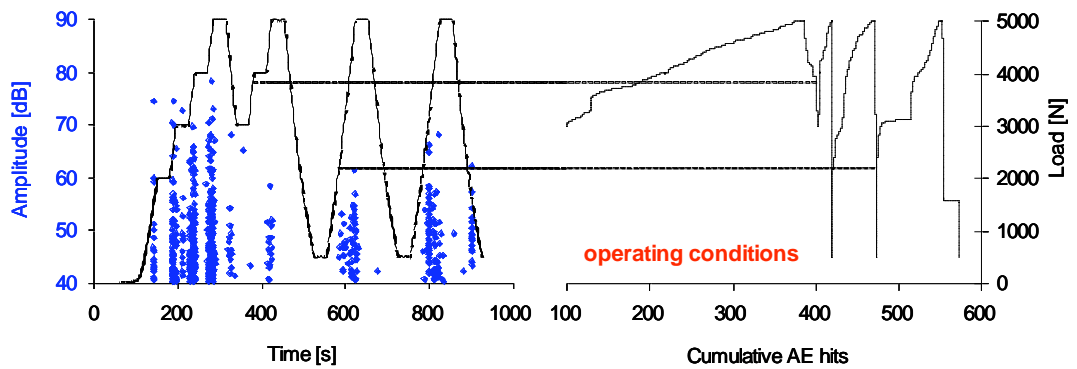


Fig. 8. AE measurement, during loading, results of the samples for fracture toughness test from the material after exposure to operating conditions.

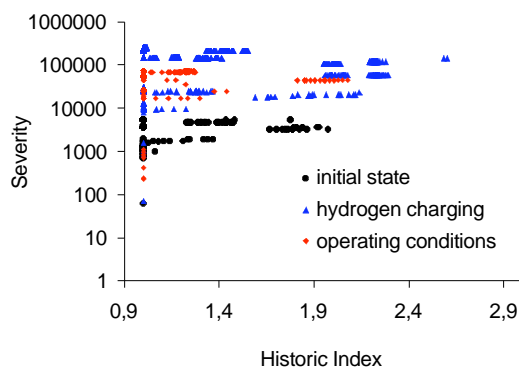


Fig. 9. Dependence of historic index on severity recorded on samples prepared for fracture toughness tests.

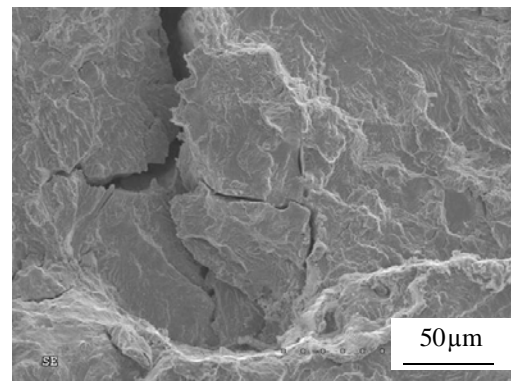


Fig. 10. Fracture of the sample prepared for fracture toughness test from the material after exposure.

Comparison of the test results performed on the compact samples is shown in Fig. 9, which illustrates meaningful rise of severity value for material in the degraded state. In Fig. 10, one can see fracture of the sample made of the material after exposure, with visible micro-cracks characteristic of degraded material. Microscopic examination revealed change of the fracture character from ductile for samples in the initial state, to locally brittle and mixed brittle – ductile (partly brittle for samples exposed to degradation).

Summary

Standard mechanical tests do not always allow the estimation of the degradation of the material exposed to operating conditions with hydrogen environment. The use of acoustic emission in connection with modified mechanical examinations showed significant differences in AE signals recorded. Suggested method of examination was devised on the basis of numerous tests conducted on the material charged with hydrogen under laboratory conditions. On this basis a series of tests were performed on the material taken from cut-out of the pipe operated under real life conditions. This clearly revealed the differences in AE signals recorded in relation to material in the initial state.

Acknowledgement: This work was supported by the Polish Committee for Scientific Research as research project N507/033 31/0813.

References

1. P. Timmins, *Solutions to Hydrogen Attack in Steels*, ASM, Mat. Park, OH USA, 1997.
2. J.P. Hirth, in *Hydrogen Degradation of Ferrous Alloys*, ed. R.A. Oriani, J.P. Hirth, M. Smialowski, Noyes Pub. 1985, p. 131.
3. S.D. Antolovich, *An Introduction to Fracture Mechanics*, ASM Metals Handbook, Vol. 19, 1997, p. 375.
4. J.D. Landes, *Fracture Toughness Testing*, ASM Metals Handbook, Vol. 19, 1997, p. 402.
5. P.S. Pao, *Mechanisms of Corrosion Fatigue*, ASM Metals Handbook, Vol. 19, 1997, p. 186.

AE ANALYSIS OF TRANSFORMED MARTENSITE VOLUME

VIJAY PAWAR, WILLIAM WOOD and RICHARD NORDSTROM

Department of Mechanical and Materials Engineering,
Portland State University, OR 97201, USA

Abstract

When alloys are modified, experimentally determining the new martensite phase transition points during cooling may be obtained using a Gleeble with cross-strain dilatometer type measurements. The resolution of these measurements is limited. Although acoustic emission (AE) is much more sensitive to the martensite phase transitions, significant temperature gradients in specimens prevent a reasonably accurate correlation between the AE start and stop and the phase start and finish. Two steps are taken here to improve the possibilities with AE. First, specimens are designed with regions of steep temperature gradients to control transformed martensite volumes and to limit temperature variation. Second, the AE-rms is correlated to predicted martensite volume range following work by Van Bohemian.

These experiments were realized on 4340 steel with resistance heating from a Gleeble. Both lateral strain (dilation) and AE are recorded from the martensite transformation. "Hat" specimen, and later double hat specimens are used to force steep temperature drops across hat shoulders. Larger ratios of hat diameters gave the best control over martensite volume.

Scatter is the issue that dominates the correlation between the volume of transformed martensite and AE power. The main source of scatter was inconsistency of the acoustic energy transfer from test to test.

Keywords: Martensite transformation, transformed martensite volume

Introduction

Martensite transformation in steels occurs during cool-down from the austenite (face-centered-cubic) phase to the martensite (body-centered-tetragonal) phase. During this phase transformation, the crystallographic volume increases by about 4%.

Detection of AE from martensite transformation was one of the earliest published accounts of recording AE [1, 2]. Both threshold-based [3] and continuous [6-10] AE monitoring have been successful in detecting AE from the martensite transformation. When the martensite transformation occurs because of mechanically induced strain, it has also been detected [4]. When the type of transformation for an alloy is in doubt, AE has been used as evidence of the martensitic transformation [5].

Gleeble-based lateral strain measurements are useful for measuring the start and finish of martensite transformation. The AE response is highly accurate as to when it occurs, but because of temperature gradients in test samples, the time of AE occurrence is not specific to one temperature or even a sufficiently small range of temperatures. For AE to determine the actual martensite start and finish temperatures, the temperature gradient must be controlled within the desired temperature tolerances. The first objective is to control the volume of transformed martensite. Van Bohemian [6-10] published some interesting predictions on how much martensite has transformed based on the total AE power (derived from AE-rms). The second objective is to see if the controlled volume of transformed martensite accurately correlates to AE-power from specimen to specimen, and what factors limit the accuracy.

Experimental

All tests used 4340 steel. A soak of 900°C for 60 seconds transforms ferrite to austenite during heat treatment and insures complete dissolution of all prior ferrite and carbides. After this soak, martensite transformation will occur during cool-down or quenching in the range of 175°C to 300°C.

The Gleeble is a resistive-heating thermo-mechanical process simulation testing machine manufactured by Dynamic Systems Inc. Specimens for the Gleeble are usually of uniform cross-section, either circular or square. The temperature can be programmed through feedback of a single thermocouple, typically placed in the middle of the specimen. As both ends of the specimens are gripped with water cooled copper jaws, the specimen experiences a pronounced temperature profile along its axis. Here, the specimen configuration was changed to a “hat” (Fig. 1, dimensions in table 1) to better control the temperature profile. With the hat geometry, the temperature profile will be disjoint with a steep temperature change across the hat shoulder. Although a soak temperature near 900°C was desired across the entire hat, in this phase of the work the goal at the edge of the shoulder of 727°C was sought. Any volume of the specimen that does not see this temperature will not produce martensite on cool-down. This approximation will overestimate the martensite volume as complete austenitization will require much higher temperatures.

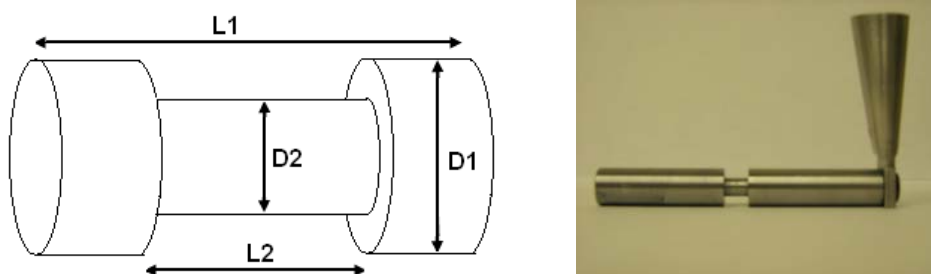


Fig. 1. So-called “hat” specimen for Gleeble, and waveguide attached to later specimens.

One or more chromel-alumel (type K) thermocouples are welded to the specimen. One thermocouple acts as control and is placed in the center of the specimen. The acoustic emission system was an AMSY-5. The lateral strain (also called cross-strain or C-strain) was recorded with the AE-rms. In the first two series of tests, the AE sensor (150 kHz) is placed on the copper jaws. The jaws and the specimen are held in contact through mechanical force alone. Couplant was not used between jaw interfaces because it could interrupt the conduction path. For the third series of tests, the AE procedure utilized a detachable waveguide. In the first tests, coupling sensitivity checks [7] were performed near the sensor. In the third test series of tests, checks were made on the waveguide and in the middle of the test, both before and after testing.

Table 1. Dimensions and details of hat specimen tests.

Test Series	Overall	Details
1	<ul style="list-style-type: none"> • D1:D2 of 3:2 • Vary L2 from 6-18 mm • One specimen without a hat 	L1 = 90 mm, D1= 12 mm, D2= 8 mm. Length between copper jaws = 25 mm. AE sensor mounted on copper jaws
2	Reduce specimens to D1:D2 of 2:1	Same except D2 = 6 mm
3	<ul style="list-style-type: none"> • Keep D1:D2 of 2:1 • Keep L2 fixed at 6 mm • Vary D1 from 12 to 6 mm 	AE sensor mounted on waveguide Also tried some two step specimens

Results and Discussion

Detecting and Analyzing Transformed Martensite with AE and Strain

Figure 2A shows the C-strain (left axis) and AE-rms (right axis) from one cycle. The first 100 s of the test show the heating and temperature soak; at about 50 s into the cycle the soak temperature transition can be seen. During this first 100 s, the resistance heating is active, which generates noise seen in the AE-rms; and when the active heating is turned off, the AE-rms can be seen to return to the background levels. The martensite phase transformation occurs after 100 s, as seen in Fig. 2A where the AE increases and the C-strain sees an inflection.

The total AE power was calculated from the square of the AE-rms, subtracting the noise component as was done in [10] and seen in Fig. 2B. Total AE power is taken as the area under the curve. A background noise level within one decimal place could be estimated from the noise at the end of the graph. However, choosing the value of AE-noise², which levels the total AE-power curve before and after the test was found to be good to three decimal places.

The main difference between C-strain and AE-rms recordings of martensitic transformations is that C-strain detects the process at only one plane, while the AE detects any transformation occurring anywhere in the specimen. The C-strain, mounted in the center of the specimen, will be the last part of the specimen to reach the martensitic start temperature. AE detects the martensite before the C-strain gage as seen previously in [12].

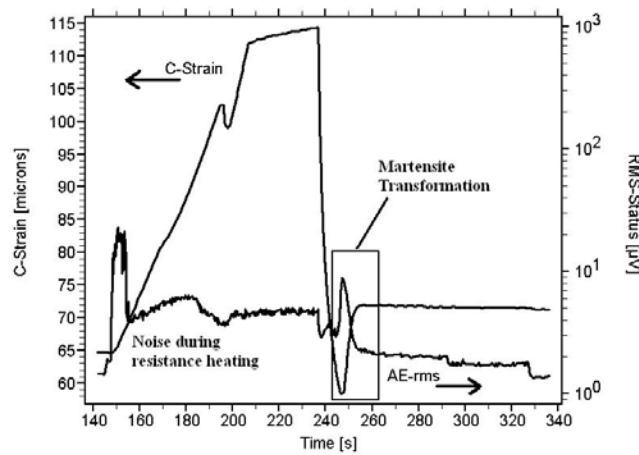


Fig. 2A C-strain and AE-rms from entire heating-cooling cycle.

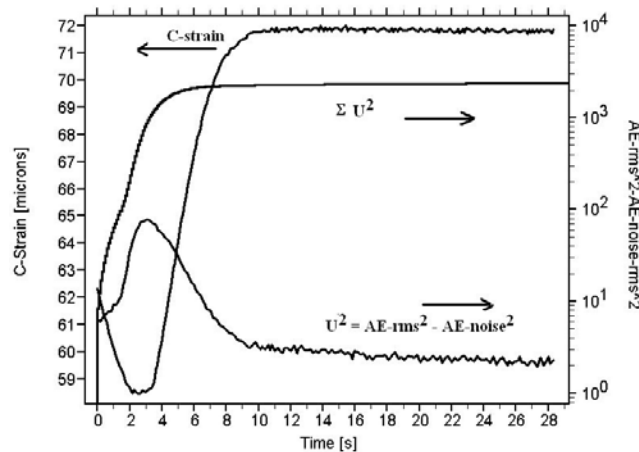


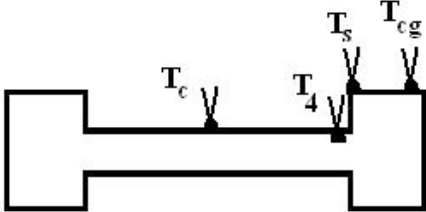
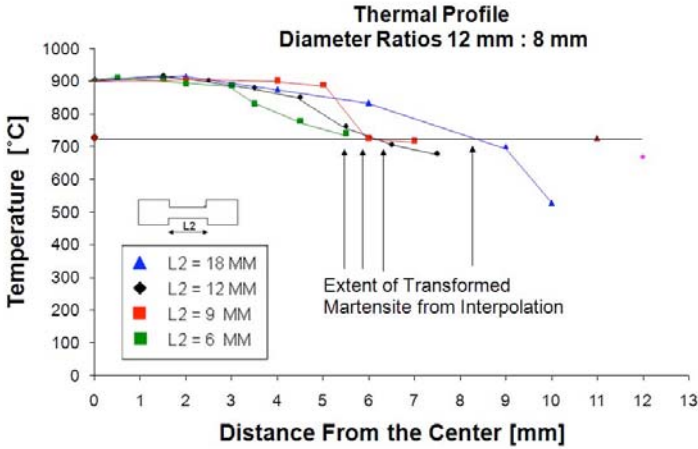
Fig. 2B. AE-power derivation during martensite transformation.

Controlling Transformed Martensite Volume

Table 2 shows measured temperatures inside (T_4) and outside (T_s) the hat shoulders when $T_C = 900^\circ\text{C}$ for various geometries. More complete temperature profiles for some tests are shown in Fig. 3. For this phase of the work, the target tolerances were to get a floor temperature of 727°C to fall in the shoulder region (between T_4 and T_s) during soak, although tighter tolerance would be desirable in further work. In these cases, the transformed martensite volumes were taken as the hat volumes. In other cases, the transformed martensite volume was estimated as the volume within the region where the temperature profile intercepted the austenitizing temperature.

The volume of transformed martensite was estimated by finding the positions, which exceed the austenitizing temperature and taking the volume within this temperature zone as the transformed martensite volume. With the best hat-specimen geometries, the hat volume equals the transformed martensite volume (the austenite limit falls within the shoulder) and there is a small variation of temperature across the soak.

Table 2. Temperatures across hat shoulder and relations to desired austenitizing range.

 <p>Fig. 3A Thermocouple positions for Table 2.</p>	Length L2 [mm]	Ratio of Diameters D1:D2 [mm:mm]	T_4 [°C]	T_s [°C]
<p>T_C Center Thermocouple (900°C at soak) T_4 Temperature at inside the shoulder T_s Temperature at outside the shoulder T_{cg} Temperature at the copper grips ($T_{cg} = 20^\circ\text{C}$)</p>	18	12:8	700	528
 <p>Thermal Profile Diameter Ratios 12 mm : 8 mm</p> <p>Temperature [°C]</p> <p>Distance From the Center [mm]</p> <p>Extent of Transformed Martensite from Interpolation</p> <p>Legend: ▲ L2 = 18 MM ◆ L2 = 12 MM ■ L2 = 9 MM ■ L2 = 6 MM</p>	12	12:8	726	720
	9	12:8	852	763
	6	12:8	888	832
	18	12:6	520	371
	12	12:6	544	430
	9	12:6	695	540
	6	12:6	796	643
<p><i>Outside Desired Martensite Transformation Range</i></p>	6	10:5	690	540
<p>Desired Temperature Range</p>	5.5	6:3	690	580

AE as a Function of Martensite Volume

Figure 4 shows total AE power plotted against the estimated volume of martensite. Scatter is much more obvious than the hoped-for trend. About 50 of the 100 tests can be distinguished, with many data points actually lie on top of each other (less than 0.5% difference), even in the first test series. The highest level of reproducibility was achieved when tests were run one after the next, which required no jaw adjustments (tightening). The waveguide was used in an attempt to remove this source of scatter altogether.

Effects of the specimen geometry on how much acoustic energy is transferred to the specimen is a concern for the AE power to volume trend.

In correlating AE power to transformed martensite volume as in [10], scatter from specimen to specimen was significant. Among the lessons learned: the acoustic path must be as consistent as possible (which significantly reduces scatter) and the simulated AE should be monitored in a linear fashion to the degree of accuracy of the correlation (linear, with energy) as opposed to general AE practice which allows logarithmic accounting of peak amplitude [11].

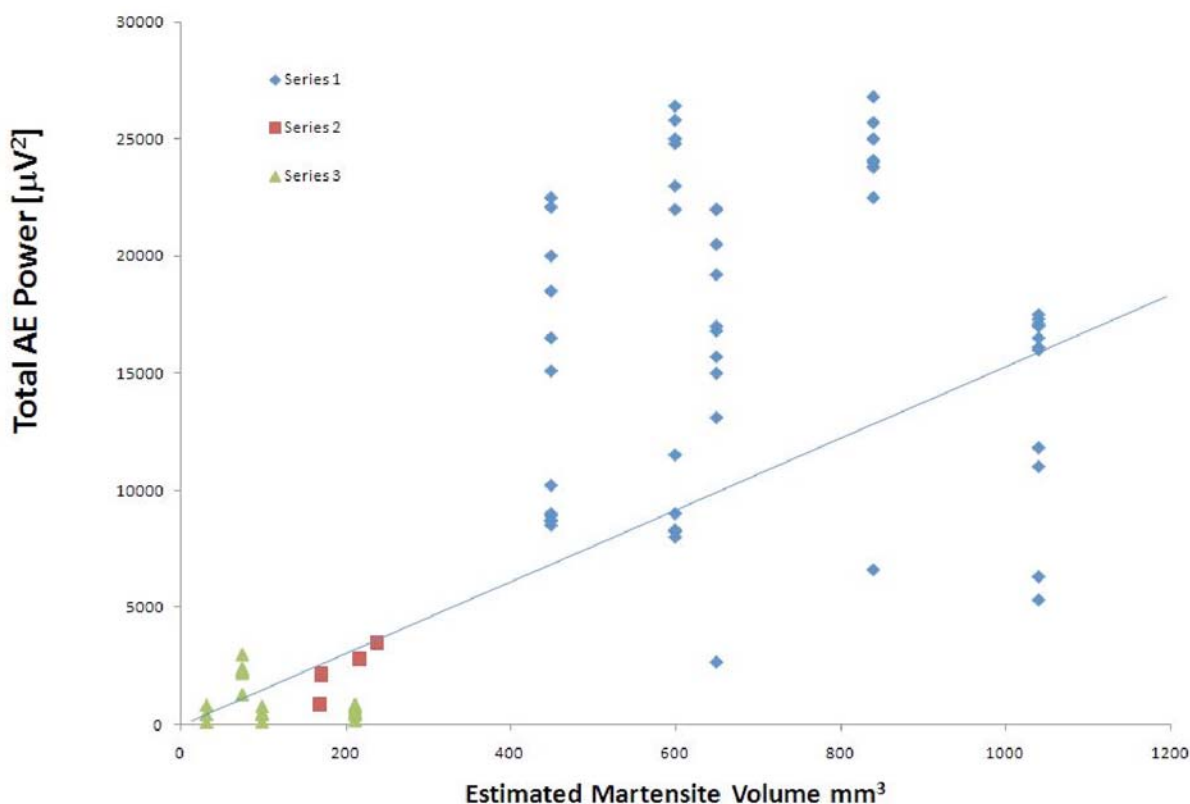


Fig. 4. Total AE power against estimated martensite volume.

Conclusion

To control transformed martensite volume a hat Gleeble specimen was used. Only two of the geometries met the first phase goal of accepting a range of temperatures between a lower limit to desired soak of 727-900°C within the hat region. Double hat specimens provided multiple gradients and this approach appears to be the best way to proceed to get tighter tolerances on temperature range in the controlled volume.

Scatter makes the correlation between total-rms power and martensite volume look weak. Efforts to control the amount of scatter are necessary to make use of this relationship.

References

1. F. Forster, E. Scheil, *Zeitschrift Metallkunde*, **28** (9), 1936, 245-247. Translated by Thwaite and Wanner in *J. of Acoustic Emission*, **14**, 1996, vi-viii.
2. F. Forster, *Materials Evaluation*, **41**, 1983, 1477-1488.
3. G.R. Speich, R.M. Fisher, *Acoustic Emission ASTM*, STP 505, 1972, pp. 140-151.
4. T. Yasuda, D. Tani, H. Nishino, K. Yoshida, *J. of Acoustic Emission*, **24**, 2006, 153-160.
5. C.K. Mukhopadhyay, K.V. Kasiviswanathan, T. Jayakumar, B. Raj, *Scripta Metallurgica et Materialia*, **30**, 1994, 303-307.
6. S.M.C. van Bohemen, J. Sietsma, M.J.M. Hermans, I.M. Richardson, *Philosophical Magazine*, **85** (16), 1, 2005, 1791-1804.
7. S.M.C. van Bohemen, J. Sietsma, M.J.M. Hermans, I.M. Richardson, *Acta Materialia*, **51**, 2003, 4183-4196.
8. S.M.C. van Bohemen, M.J.M. Hermans, G. den Ouden and I.M. Richardson, *Journal of Physics D*, **35**, 2002, 1889-1894.
9. S.M.C. van Bohemen, M.J.M. Hermans and G. den Ouden, *Journal of Physics D*, **34**, 2001, 3312-3317.
10. S.M.C. van Bohemen, "An acoustic emission study of martensitic and bainitic transformations in carbon steel", Delft University Press, 2004, 165 pages.
11. ASTM Standard E 650-97.
12. R. Nordstrom, W. Wood, J. Keegan, "AE Experience from Gleeble Testing of Steels," presented at AEWG-44, 2001.

HYDROGEN RELATED BRITTLE CRACKING OF METASTABLE TYPE-304 STAINLESS STEEL

HIDEO CHO and MIKIO TAKEMOTO

Faculty of Science and Engineering, Aoyama Gakuin University,
5-10-1 Fuchinobe, Sagamihara, Kanagawa 229-8558, Japan

Abstract

Among stainless steels, Type-316 steel is stable and shows high resistance to hydrogen-induced brittle cracking, but the meta-stable Type-304 steel shows a high susceptibility to the hydrogen-induced embrittlement and cracking. Mechanism of hydrogen-induced brittle cracking of the Type-304 steel was studied by AE monitoring under various combination of static and dynamic elastic and plastic deformations in a charging solution at room temperature and 80°C. Here, the hydrogen was supplied before and during tensile testing. We detected a number of AE signals from the Type-304 steel with hydrogen charging during dynamic plastic deformation at room temperature and observed hydrogen-induced cracks, while no AE for the Type-304 charged by hydrogen and deformed at 80°C. Maximum load of the Type-304 steel with hydrogen charging decreased to 30% that of the steel without charging. Type-304 steel, hydrogen charged after being quenched in liquid nitrogen, produced few AE during tensile loading at room temperature. We detected no AE from Type-316 steel during plastic deformation in charging solution at both temperatures. Hydrogen-induced brittle fracture of Type-304 steel was confirmed to be induced by both gliding dislocations and deformation-induced lath martensite. Hydrogen is supposed to be transferred to the martensite by gliding dislocations accompanying protons.

Keywords: Meta-stable austenitic stainless steel, hydrogen induced brittle fracture, strain induced martensite, gliding dislocation

Introduction

Meta-stable austenitic stainless steels are known to be susceptible to hydrogen embrittlement. Many researchers reported that strain-induced martensite suffered hydrogen embrittlement [1, 2]. Fracture type was intergranular (IG). Carpenter et al. reported that AE signals from sensitized Type-304 steel, during tensile loading in a charging solution, were produced by the IG-cracks caused by the grain boundary separation. Here the IG-cracking occurred when hydrogen charging was continued till the maximum load. They proposed a transport model by moving dislocations [3, 4]. Direct demonstration of this model is impossible at present, even if we use any kind of advanced analysis equipments. Collection of reliable data, which can or cannot support this model, is needed.

In this report, we studied the hydrogen embrittlement of Type-304 and -316 steels by monitoring AE during quasi-static loading in a charging solution at 25°C and 80°C.

Experimental procedure

We used commercially available Type-304 and -316 stainless steels. Chemical composition is shown in Table 1. Test specimens of Fig. 1 were prepared by an electro-discharge machine

to produce identical specimens. Width in gage section was controlled to 15 mm. A notch with the tip radius of 0.2 mm was induced on one side. These samples were abraded by silicon carbide abrasive papers of 150, 300, 400, 600, 800, 1000 and 1500 mesh, and mirror polished by aluminum oxide powder. The specimen was sensitized at 650°C for 24 hours in low-pressure furnace after solution treatment at 1050°C for 1 hour, and quenched in water. The specimen was sealed by rubber-based coating material, except for the exposure area of 15 mm x 10 mm. Hydrogen was charged in an H₂SO₄ solution of pH:2, at cathodic current density of 1 mA/cm² using a potentio-galvanostat.

We monitored AE using four small AE sensors (PAC, Type-PICO), which were mounted on the sample as they make a line. Outputs of two sensors (channels

2 and 3 in the gage section) were amplified by a pre-amplifier (Gain: 40 dB) and fed to a personal computer. Two more sensors (channels 1 and 4 on the shoulder) were used to discriminate the friction noise from the signals. We monitored the crack propagation by a CCD camera.

Table 1 Chemical composition of austenitic stainless steel used (mass %).

	C	Si	Mn	P	S	Ni	Cr	Fe
Type 304	0.05	0.61	1.56	0.04	0.024	8.55	18.2	balanced
Type 316	0.05	0.57	0.82	0.02	0.0006	11.3	17.5	balanced

Experimental results

Tensile loading in charging solution

Tensile load was applied to Type-304 specimen in a charging solution using crosshead control method, in the following sequence: (1) Increase the load at constant crosshead speed. (2) When a small load drop (~0.1 kN, probably from the start of cracking) was detected, crosshead was stopped and held. (3) Then, monitor the load decrease for 3 hour.

In these tests, hydrogen charging was started with the loading. The crosshead speed was varied between 0.05 mm/min to 0.4 mm/min. Figure 2 shows the load-time diagram at crosshead speeds of 0.4, 0.2, 0.1 and 0.05 mm/min for the sensitized Type-304 specimen at 25°C. A fine smooth line indicates that of a non-charged specimen at crosshead speed of 0.1 mm/min. Five specimens show different behavior in the plastic range. The specimens hydrogen-charged during loading showed extensive load decay. Initial decay and the total load decay were larger at higher loading rates. The curve of the charged specimen at crosshead speed of 0.1 mm/min agrees fairly well that of the non-charged specimen, but deviates slightly at large loads. The maximum load reached was 5 to 6.5 kN. The maximum load increased with an increase of crosshead speeds.

Figure 3 shows changes of cumulative AE counts with time. Detected AE signals were classified by their frequency characteristics into two types (Type-A and -B) as shown in Fig. 4. Type-A was detected after the maximum load and showed broad frequency components. In contrast, Type-B was detected throughout loading. Frequency spectrum of the Type-B showed a limited frequency component and resembles the noise from hydrogen gas evolution in SCC [5]. We selected Type-A as the crack signal. We detected many signals during load increasing period, but few signals during the initial portion of the load decay. For two samples with crosshead speeds of 0.2 and 0.4 mm/min, we again detected signals during rapid load decay

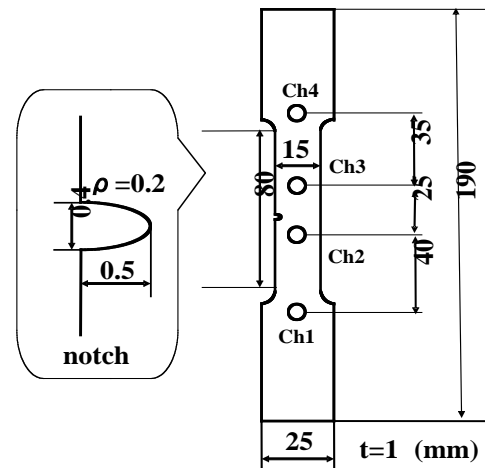


Fig. 1 Schematic of specimen and sensor location.

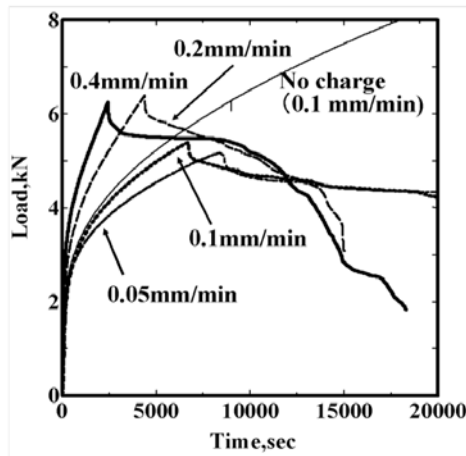


Fig. 2 Load - time diagram for the sensitized Type-304 specimens with various crosshead speeds in a charging solution.

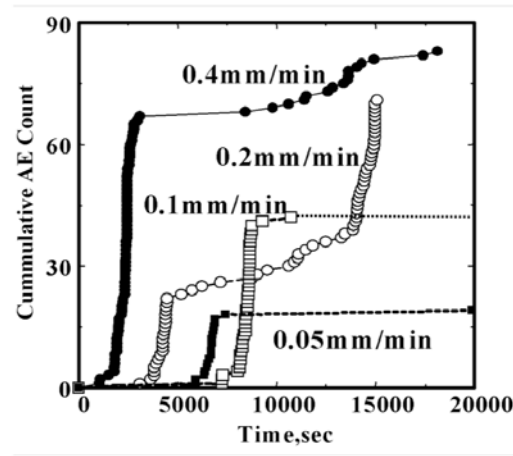


Fig. 3 Cumulative AE counts for the sensitized Type-304 specimens with various crosshead speeds in a charging solution.

period after incubation times. However, we did not detect AE during load decay for two specimens with lower crosshead speeds of 0.05 and 0.1 mm/min. Detail mechanism of AE generation rate and its dependency on the crosshead speed is a future problem.

Figure 5 shows CDD images of crack progression. White spots in the image are hydrogen gas bubbles. Timing of crack progression from the notch bottom agreed roughly with the first AE timing at 1,100 s, as shown by the photo (a) at 1,800 s. We observed a crack with large opening at the maximum load (photo (c)), but after that, a fine crack during load decay (photo (d)).

Figure 6 shows post-test SEM of the sample with the crosshead speed of 0.1 mm/min. We observed a number of IG-cracks and falling-off of grains around the notch. Here the falling-off of grains was caused by the grain boundary separation. As these cracks were considered to be caused by strain-induced martensite, we measured ferrite amount near the main crack using a ferrite meter. It was measured as 7%. Figure 7 shows fracture surface of another sample loaded to final fracture in the same charging condition. We observed both dimple and cleavage fracture surfaces, and deep grooves along the elongated grains.

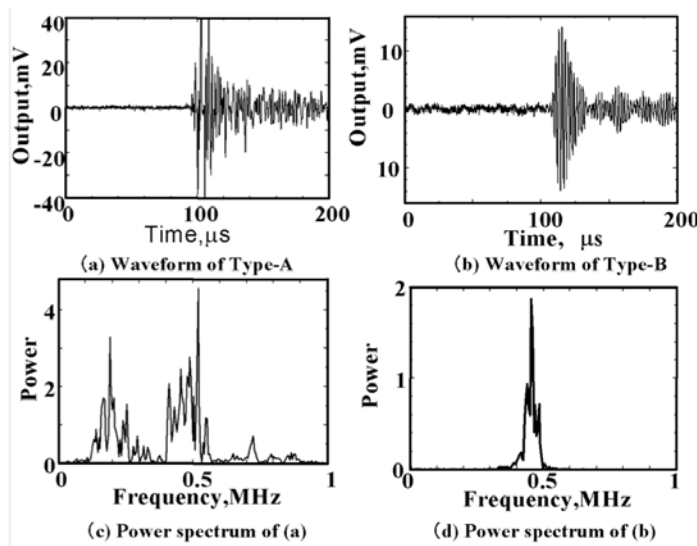


Fig. 4 Two types of AE signals detected and their power spectra.

Effect of strain-induced martensite on hydrogen induced cracking

We studied effect of strain induced martensite on the hydrogen-induced cracking using Type-304 and -316 steels. Transition temperature (M_d) of austenite to martensite of the Type-304 steel is 30°C, so we then compared the crack susceptibilities of the Type-304 steel at 25 and 80°C. We deformed the sensitized Type-304 sample, with charging at 80°C (0.1 mm/min) and detected no AE. The maximum load was not reached in loading up to 6 kN, while we observed

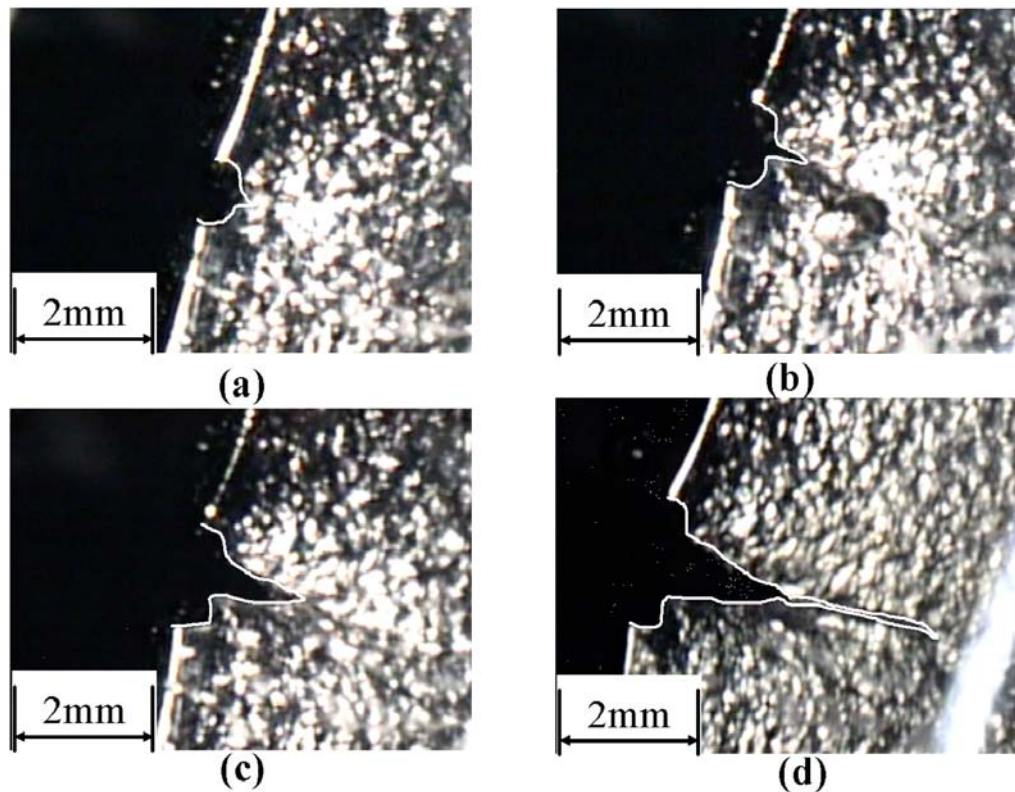


Fig. 5 CCD images of crack propagation of the sensitized Type-304 specimen with crosshead speed of 0.4 mm/min in charging solution. (a):1800 s (after detection of first AE) (b):2300 s (c):2440 s (at max load) (d)13200 s.

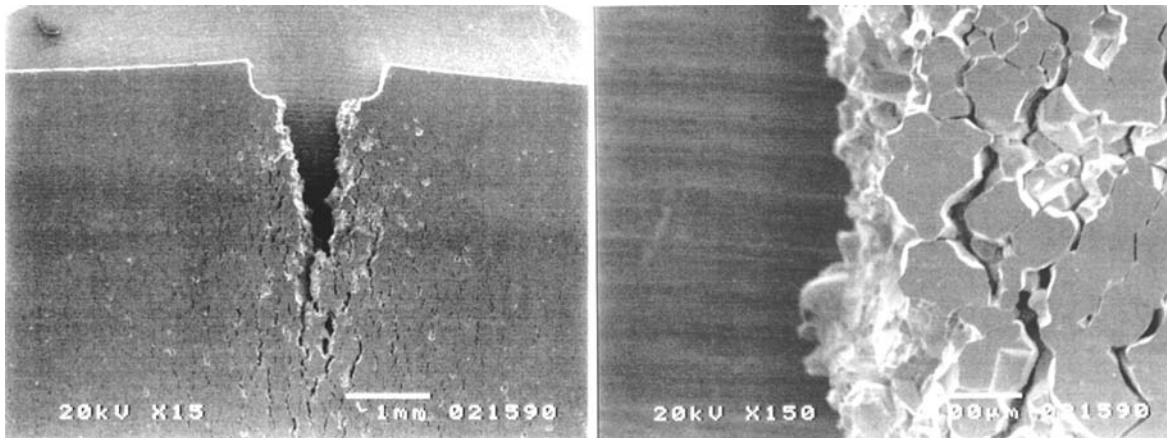


Fig. 6 SEM images of the sensitized type-304 specimen surface around the notch with crosshead speed of 0.1 mm/min at 25°C in charging solution.

high AE activity and the maximum load of 5.3 kN for the loading at 25°C (Fig. 3). Martensite amount was measured as below 1.0%. This result implies that the martensite is a necessary factor to cause the hydrogen-induced cracking.

The M_d temperature of the Type-316 steel is -28°C, and this steel produces no strain-induced martensite at 25°C. In order to confirm this, the sensitized Type-316 steel was tensile tested in the charging solution at 25°C, by the same method as in the previous section. This steel produced three AE during the loading to 6 kN, indicating no susceptibility to hydrogen-induced cracking, as shown in Fig. 8.

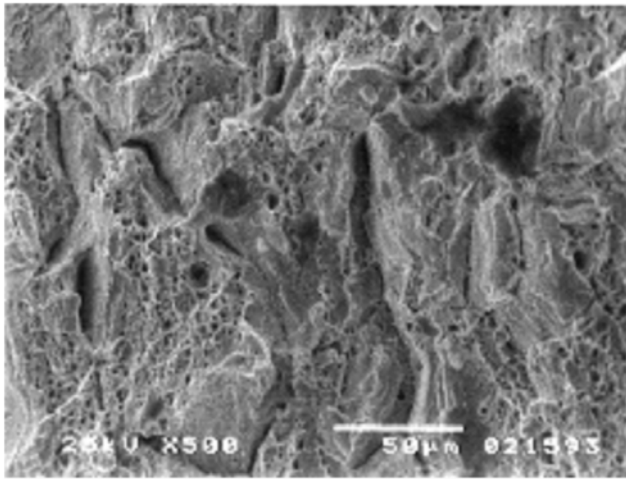


Fig. 7 Fracture surface of the sensitized sample with crosshead speed of 0.1 mm/min at 25°C in charging solution. Both dimple and cleavage fracture surfaces are shown.

Effect of Hydrogen charging and thermal martensite

Experimental data of previous sections suggested an importance of both the martensite and gliding dislocations during plastic deformation. The test in this section intends to confirm these. We attempted AE monitoring from the sensitized, and then nitrogen quenched and pre-charged Type-304 steel during tensile loading in air. Hydrogen was charged for 144 hr at current density of 10 mA/cm² (charge amount of 5184 C/cm²) prior to the loading. This specimen possesses thermally-induced martensite of approximately 15% near the notch bottom.

Figure 9 shows load-time curves of the quenched and pre-charged specimens in air. We detected no AE and no crack. Thermally-induced martensite increased the yield load by approximately 14% over that of the sensitized Type-304 steel without hydrogen charge, but is immune from the hydrogen-induced cracking. This implies that simultaneous supply of protons and generation of dislocation are needed for hydrogen-assisted cracking.

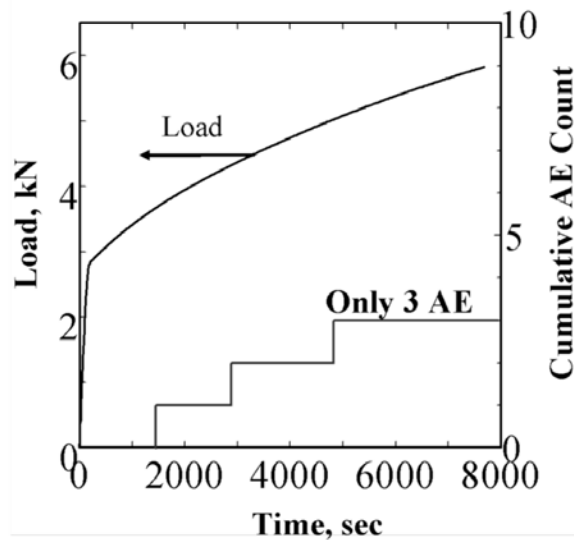


Fig. 8 Load-time diagram and cumulative AE count for sensitized 316 specimens with charging at 25°C.

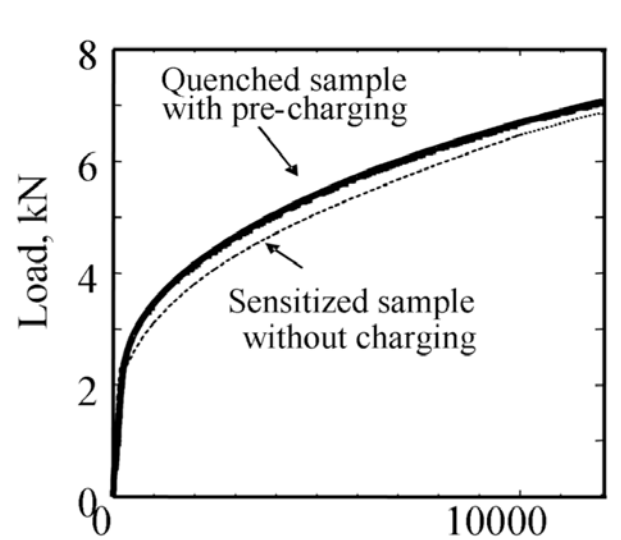


Fig. 9 Load-time diagram for the pre-charged sample quenched in liquid nitrogen in air. For comparison, sensitized sample without charging was shown.

Discussion

The martensite is necessary condition for hydrogen-induced cracking but not the sufficient condition, as demonstrated by the last section's experiment using quenched samples. Figures 2 and 3 imply that both the gliding dislocation by dynamic plastic deformation and the strain-induced martensite, and of course the diffusible protons, are necessary for hydrogen embrittlement. The grain boundary separation occurs when these three condition were simultaneously satisfied. These results agree with the results by Carpenter et al. [4]. We, however, could not explain the complicated AE behavior during load decay in Fig. 3. These must be explained based on the rate process of proton diffusion and martensite formation. Unsolved problems are 1) How the protons are transferred to the martensite at the tip of notch and growing crack, and 2) How the martensite distributes in the austenitic grains.

Diffusion coefficient of proton in the austenitic phase is as low as 10^{-12} cm²/s, million times smaller than (10^{-6} cm²/s) in the ferritic phase. Thus the proton can not quickly diffuse through the austenitic grains. Fast and sufficient supplement of protons to the martensite will be possible by gliding dislocation accompanying the protons or self diffusion through the martensite. This cannot be studied by any type of advanced analysis equipment at present, but we can compare the crack velocity and proton diffusion rate under controlled stress intensity. The second problem includes a contentious martensite path for proton diffusion and the grain boundary separation. The grain boundary separation can be explained by the martensite formation along the chromium depleted zone. Distribution of the martensite, and possibly the initiation of crack, will be revealed by the advance analysis equipment.

We recently observed frequent grain boundary separations in polythionic APC-SCC of sensitized Type-304 steel [5]. AE were detected when the steel suffered the grain boundary separation. Detailed mechanism is not well understood. There is a possibility of hydrogen-induced grain boundary separation in the APC-SCC.

Conclusion

In order to study the mechanism of hydrogen embrittlement of austenitic stainless steel, we monitored AE. Results are summarized below:

- 1) We detected AE and crack for the sensitized type 304 when it is exposed to both the dynamic plastic deformation and hydrogen charging simultaneously. Much AE were continuously emitted during plastic loading at higher cross head speeds.
- 2) Experiment suggests that hydrogen assisted cracking occurs when sufficient protons were transferred to the strain induced martensite. Diffusion path and trap site of protons have to be studied in future.

References

- [1] M. L. Holzworth, *Corrosion*, **25**, 1968, 107.
- [2] N. Otani, S. Asano, Y. Fujishima and Y Yamamasu, *J. Japan Inst. Metals*, **37**, 1972, 746.
- [3] S.H. Carpenter and D. R. Smith, *Metallurgical transaction A*, **21A**, 1990, 1933.
- [4] S.H. Carpenter, K. Ono and D. Armentrout, *Progress in Acoustic Emission XIII*, 2006, p. 55.
- [5] A. Yonezu, H. Cho and M. Takemoto, *Progress in Acoustic Emission XIII*, 2006, p. 489.

CHARACTERIZATION OF TITANIUM HYDRIDES USING A HYBRID TECHNIQUE OF AE AND FEM DURING INDENTATION TEST

YOSHIHIRO TANIYAMA, HIDEO CHO, MIKIO TAKEMOTO
and GEN NAKAYAMA*

Faculty of Science and Engineering, Aoyama Gakuin University, Fuchinobe, Sagamihara, Kanagawa 229-8558, Japan; *Research Laboratory, Ishikawajima Harima Heavy Industry, Shin-nakahara, Isogo, Yokohama, Kanagawa, 235-8501, Japan

Abstract

Pure titanium (Gr.1) and titanium-0.6 mass% palladium (Gr.17) are prone to produce brittle hydrides when they absorb hydrogen. This research studied structures and mechanical characteristics of two hydrides in Gr.1 and Gr.17. Fracture strength of thin hydrides was measured by a hybrid method of AE and FEM during micro-indentation. We determined the threshold indentation load to cause the Mode-I fracture during Vickers indentation by AE monitoring and then computed the critical strain to cause the Mode-I fracture by the FEM. Utilizing the stress and strain curves of base metals and hydrides obtained by a dual indentation method, the fracture strain of the Gr.17 hydride is calculated as half that of the Gr.1 hydride. X-ray diffraction revealed that the Gr.1 and Gr.17 hydrides are $TiH_{1.971}$ and TiH_2 , respectively. Palladium in Gr.17 contributes to produce hard and brittle hydride with higher hydrogen content.

Keywords: Titanium hydride, mechanical property, fracture strain and strength, indentation, critical indentation force, FEM, Mode-I crack

Introduction

Study is underway to assess the endurance capability of titanium-clad overpack of high-level radioactive waste in deep underground water. The overpack will be exposed to oxygen-free 3.5% NaCl solution. Thus, pure titanium (Gr.1) and titanium-palladium (Gr.17) are likely to produce brittle hydrides by the cathodic current density (proton reduction) corresponding to the passivation holding current density. We previously reported both the fracture behavior and fracture dynamics of Gr.1 hydride [1]. Measurement of mechanical properties of hydrides is, however, difficult since the hydrides are thinner than 100 μm . We used a hybrid technique of AE and FEM during Vickers indentation on the thin hydrides.

This study reports AE results on the progression of micro-cracks in growing hydrides in a simulated underground environment. Next we report the mechanical properties of Gr.1 and Gr.17 hydrides using an indentation technique. AE was successfully utilized to determine the critical indentation load to cause the Mode-I fracture in the hydrides. Mechanical properties of Gr.1 and Gr.17 hydrides were found to be much different, due to chemical compositions of the hydrides.

AE from micro-fractures in growing titanium hydrides

Experimental method

The amount of hydrogen charge to the overpack in underground environment is calculated to be 10 MC/m² for 60,000 years storage [2]. We supplied the specimens with hydrogen at cathode

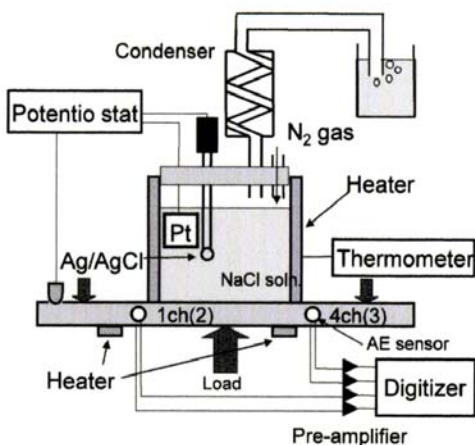


Fig. 1 Experimental setup for hydrogen charging and AE monitoring for Ti.

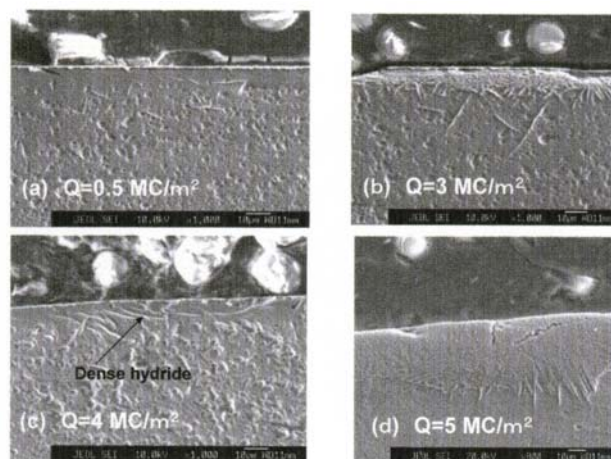


Fig. 2 Changes of the Gr.17 hydrides with hydrogen charge.

current density of 10 A/m^2 in a 0.6 mol/l NaCl solution purged by nitrogen gas at 70°C . The amount of hydrogen charging was 1, 3, 5, 6.5 and 10 MC/m^2 .

Figure 1 shows the hydrogen charging and AE monitoring method for plate-shaped Ti specimens of 11-mm thickness, 50-mm width and 145-mm length. The specimen was subjected to three-point bending with surface tensile stress of 200 MPa. AE was monitored by four resonant-type small sensors (PAC: Type-PICO) mounted on the side surfaces of the specimen. Sensor outputs were amplified 40 dB by pre-amplifiers and fed to a personal computer.

Chemical composition of Gr.1 titanium is 0.01 mass% C-0.0007H-0.031O-0.0005N-0.032Fe and $<0.02\text{Pd}$. That of the Gr.17 is 0.014 mass% C-0.0007H-0.09O-0.003N-0.035Fe and 0.062Pd.

Growth behavior of hydrides

We studied growth behavior of Gr.17 hydride as seen in Fig. 2. Below 0.5 MC/cm^2 , we observed needle-shaped hydrides as shown in photo (a). Above 3 MC/m^2 , the needle shaped hydrides coalesce and forms colonies of dense layer of $10\text{-}\mu\text{m}$ thickness. Characteristic features of Gr.17 hydride are that these are non-uniform and irregular in shape. Above 4 MC/m^2 , plate-shaped hydride layer is produced. At 5 MC/m^2 , the hydride layer grows to thick plates of $20 \mu\text{m}$ as shown in (d). Thickness of Gr.17 hydride does not exceed $150 \mu\text{m}$ at 10 MC/m^2 , but the hydrides tend to crack by themselves.

Figure 3 shows changes of cumulative AE counts with hydrogen charge for Gr.1 and Gr.17 Ti. In Gr.1 Ti, AE counts increased gradually till the charge amount of 6 MC/m^2 and rapidly increased above 6 MC/m^2 , while it increased rapidly above 4.5 MC/m^2 for Gr.17 Ti. Sources of AE were located using both the arrival-time difference of the So-wave and sheet velocity of 5990 m/s . All 33 events with strong So-wave were located in the corrosion cell. Figure 4 compares the transverse structure of two hydrides produced in Gr.1 and Gr.17 Ti at 10 MC/m^2 . Thickness of Gr.17 hydride layers reached approximately $120 \mu\text{m}$, while that of Gr.1 hydride is $10 \mu\text{m}$. For Gr.17 hydride, we observed dish-shaped shallow exfoliation. It is noted that crack morphology changes depending on the geometry and mechanical properties of the hydrides. We sometimes observed vertical and/or slant cracks.

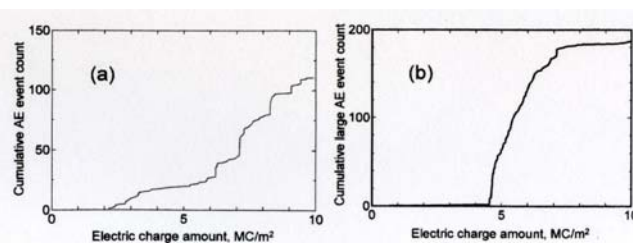


Fig. 3 Changes of cumulative AE counts with H charging to Gr.1 Ti (a) and Gr.17 Ti (b).

Mechanical properties of Ti and hydrides

We first studied whether the Gr.17 hydride suffers median crack by micro-indentation. We observed no median crack, but slight extrusion around the periphery of the Vickers indentation, indicating that the hydride is not so brittle like ceramics, but possesses some extent of ductility.

Next, we measured the stress-strain curves of the substrates and hydrides using a dual indentation method. Indentation load: F vs. penetration depth: h curves were first obtained using a dynamic micro-indentation machine (Shimadzu, DUH-W201). Figure 5 compares the F vs. h curves of Gr.1 and Gr. 17 Ti, using two indenters with different tip-angle. Details of the dual indentation method can be found elsewhere [3, 4]. It estimates the Young's modulus: E , yield strength: σ_y , strength coefficient: R and work hardening coefficient: n of the stress-strain curves with $\sigma = R\epsilon^n$ in the plastic region.

Figure 6 compares the σ - ϵ curves of Gr.1 and Gr.17 Ti. Three parameters: E , R and n are shown in the figure. The fracture strains (38% for Gr. 1 and 54% for Gr.17) of the base metals were determined by the tensile tests. Experimental σ - ϵ curves agreed quiet well with those predicted by the dual indentation method.

Fracture strains of the hydrides

We determined the fracture strains by inducing a fine Mode-I crack using a new indentation machine. We studied whether the Mode-I crack can be induced by Vickers indentation, using a commercial indentation machine (HVM-2000). Figure 7 shows examples of cracks induced into thin hydride layer of Gr.1 Ti. The upper figure shows the crack induced by loading up to 15 N, and the lower by loading to 20 N. The vertical crack is produced by tensile stress induced by the indentation, and is the Mode-I crack. Large loading of 20 N produced both the partial exfoliation and subsequent Mode-II cracks as well the Mode-I crack. These data indicates that we can determine the critical strain to induce the Mode-I crack by FEM method, if we can correctly determine the critical load or the critical penetration depth correctly.

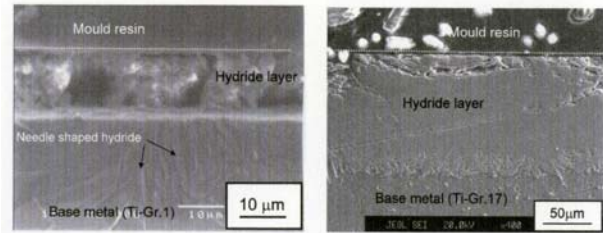


Fig. 4 Transverse SEM of Gr.1 (left) and Gr.17 hydrides after charging 10 MC/m².

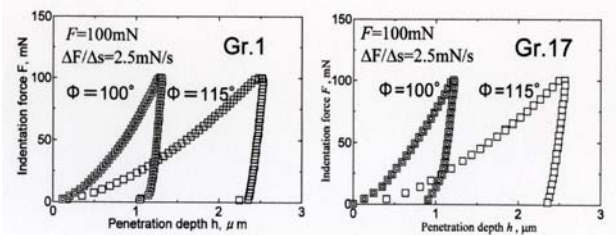


Fig. 5 Indentation force F vs. penetration depth h curves of Gr.1 and Gr.17 substrates by the dual indentation method.

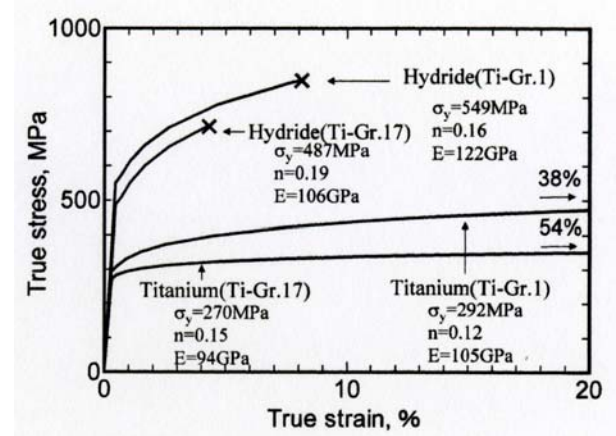


Fig. 6 σ - ϵ curves of substrates and hydrides by the dual indentation method.

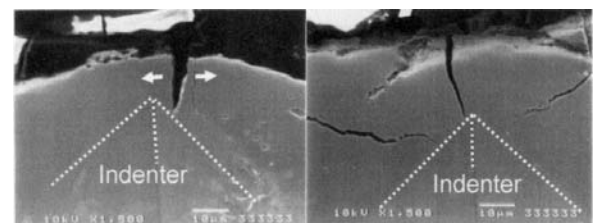


Fig. 7 Cracks induced in the hydride by Vickers indentation at 15 N (left) and 20 N (right).

The commercial indentation machine, however, does not measure the F vs. h curve. Thus, we developed a new indentation machine, which can measure the F vs. h curve and used AE system to monitor the critical load to cause the first Mode-I crack.

The new indentation machine was constructed by modifying the micro-servo testing machine (Shimadzu, Microservo MNT-1000NB-10). We controlled the load using a feedback program developed in laboratory and monitored the penetration depth by an eddy-current displacement meter to the accuracy of $0.1 \mu\text{m}$. Construction of sliding device of the sample from a microscope to the indentation machine was difficult. Positioning accuracy of this device is not so good as hoped for.

The critical load to cause the first Mode-I cracks was monitored by AE. We mounted two small sensors (PAC, Type-PICO) on the two counter surfaces. Output of the sensors were amplified by 60 dB and fed to a personal computer. AE from friction between the indenter and hydride were separated from AE by the Mode-I crack, using the polarization distribution of the first arriving So-mode waves [4]. The Lamb waves with the same So polarity was diagnosed as the AE from the Mode-I crack. Amplification of 60 dB is needed since the Mode-I crack is generally less than $5 \mu\text{m}$ and emitted weak Lamb waves.

Figure 8 compares the F vs. h curves for Gr.1 and Gr.17 hydrides. Vertical triangles near the curves indicate the first AE timing from the Mode-I cracks. The critical load to cause the first Mode-I crack is determined as 19.6 N for Gr.1 hydride and 7.4 N for Gr.17 hydride. We previously reported the critical load of 16 N for Gr.1 hydride [1]. Larger critical load and penetration depth for Gr.1 hydride than those for Gr.17 hydride indicates that Gr.1 hydride is less brittle.

Figure 9 shows the Mode-I cracks in two hydrides. Due to poor positioning capability of the sliding device developed, indentation location could not be accurately determined. Short crack of $8.6\text{-}\mu\text{m}$ length was induced in Gr.1 hydride when the indenter reached the hydride. FEM analysis was performed in the region surrounded by dashed line. Here, the triangle by solid line designates the ridge of the indenter. Center of the indentation was originally indented in the base metal. Figure 10 shows elements of quarter model for 3-dimensional FEM. Lower left corner of the triangle corresponds the center of the tip of the indenter. We computed the strain ϵ_{33} in the direction of X_3 using the package software of MARC and MENTAT.

The strains ϵ_{33} were computed using the F vs. h curves of both substrates and hydrides by changing the penetration depth (displacement controlling condition). Figure 11 shows the results. Detail strain distribution in the X_2 direction is shown in Fig. 12. The strain ϵ_{33} is lower at interface of the base metal/hydride, but increases toward the free surface. The critical strain is determined as 0.081 and 0.043 for Gr.1 hydride and Gr.17 hydride, respectively.

Deviation of the critical load to cause the Mode-I crack in Gr.1 hydride was studied by two graduate students (A and B) for three years. The student A reported the critical load of 16 N and 20. Student B reported, using another sample prepared by the same hydrogen charging condition, 19.6 N (this study). Average critical load for Gr.1 hydride is 18.5 N. Thus, the critical strain of 0.081 for Gr.1 hydride, obtained using 19.6 N, is supposed to be close to the critical strain computed using the average critical load of 18.5 N. Student B attempted to obtain more data for Gr.17 hydride, but could not, since the location accuracy of the sliding device was poor. He

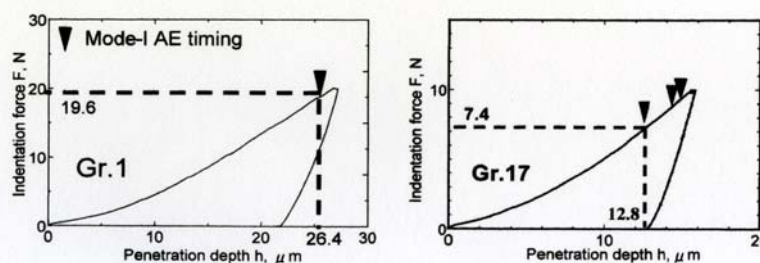


Fig. 8 F vs. h curves for Gr.1 and Gr.17 hydrides with timing of AE from the Mode-I crack

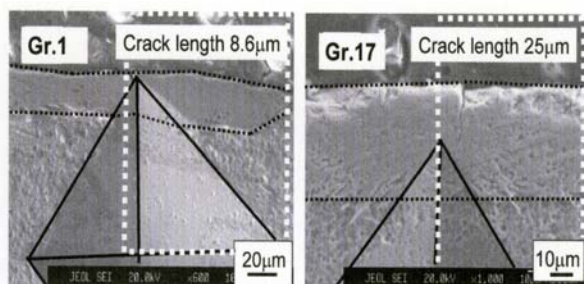


Fig. 9 SEM photos with the Mode-I cracks, indentations and region for FEM analysis.

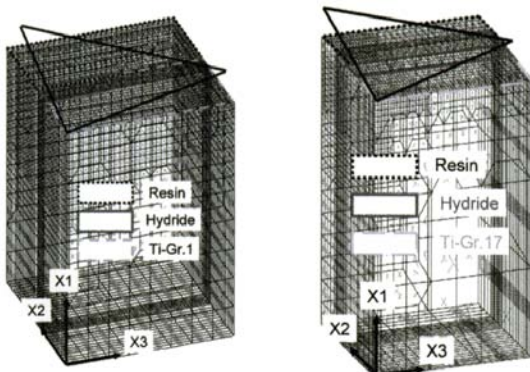


Fig. 10 Elements of quarter model for three dimensional FEM for strain computation during indentation.

could not induce the Mode-I crack in the hydride. Thus we cannot discuss the correct critical load of Gr.17 hydride. We examined propriety of the FEM method. Figure 13 compares the experimental F vs. h curve with that by the FEM. Though the curve by the FEM is slightly lower than the experimental data, there observed a fairly good agreement, indicating a reliable simulation of experiment by FEM.

The stress-strain curves in the final form were already presented in Fig. 7. Both the fracture strength and strain of Gr.17 hydride are smaller than those of Gr.1 hydride. This difference was thought to be due to chemical composition of the hydrides. We studied chemical composition of the hydrides by X-ray diffraction method and observed a broad diffraction peaks at around 98.6° for Gr.1 hydride and that at around 62.8° for Gr.17 hydride. According to the ASTM code 07-0370, Gr.1 hydride was determined as $TiH_{1.971}$ and Gr.17 hydride as TiH_2 . Brittleness of Gr.17 hydride appears to be due to its higher hydrogen concentration. From Fig. 8, we note three AE signals from the Mode-I cracks for Gr.17 hydride. This suggests that surface layer of the brittle Gr.17 hydride suffers small exfoliations following the first Mode-I crack. Another example is in the Fig. 5. We observed small multi-layer exfoliations in thin surface layer of the Gr.17 hydride.

Conclusion

In order to study the mechanical properties of hydrides produced in pure titanium (Gr.1) and titanium-0.06 mass% paradium alloys (Gr.17), a hybrid method of AE and FEM was utilized for indentation test.

Results obtained are summarized as below.

- 1) Gr.1 titanium emitted AEs by cracking at charges of more than 6 MC/m^2 , while Gr.17 Ti emitted abrupt AE at 4.5 MC/m^2 . Thickness of the hydride layer of Gr.17 at 10 MC/m^2 reached approximately $120 \mu\text{m}$, while that of Gr.1 is $10 \mu\text{m}$.
- 2) Stress-strain curves of Gr. 1 and Gr.17 Ti and hydrides were estimated by dual indentation method. There observed a good agreement between the estimated and measured for the substrates.
- 3) Fracture strain of the hydrides were estimated using a new indnetation machine and FEM. Critical indentation load to cause the Mode-I crack was correctly determeind by AE monitoring. Fracture strain of Gr.1 hydride was calculated as 8.1%, while that of Gr.17 hydride as 4.3%. The Gr.17 hydride is more brittle than the Gr.1 hydride. Chemical

composition of the Gr.17 hydride was measured as TiH_2 , and that of the Gr.1 hydride as $TiH_{1.971}$ by the X-ray diffraction method.

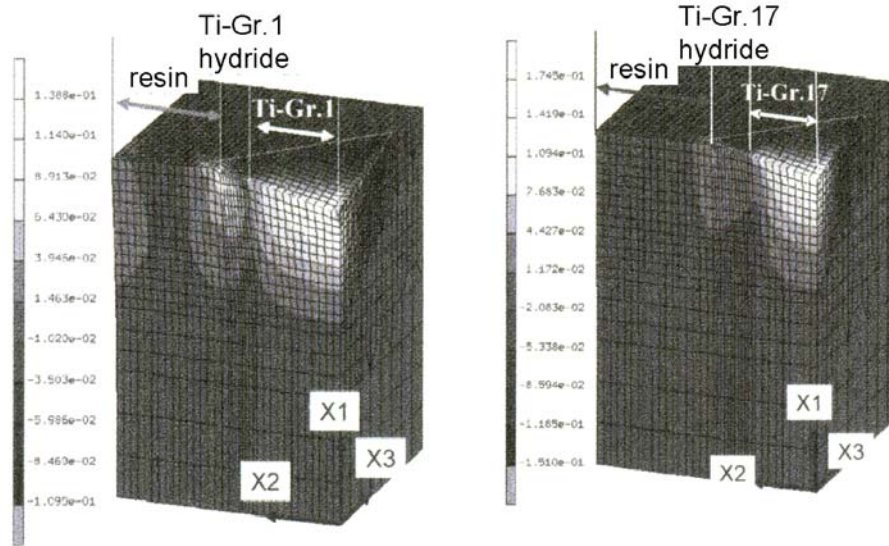


Fig. 11 Strain distribution around the Vickers indentation computed by 3-dimensional FEM.

References

- [1] Y. Taniyama, T. Matsuo, H. Cho, M. Takemoto and G. Nakayama, *Progress of Acoustic Emission XIII*, 2006, pp. 295-302.
- [2] G. Nakayama, N. Nakamura, Y. Fukaya, M. Akashi, H. Ueda, *European Federation of Corrosion Publications*, Number 36, pp. 373-394, NANEY (2003)
- [3] M. Dao, N. Chollacoop, K.J. Van Vliet, T.A. Venkatesh and S. Suresh, *Acta Mater.*, **49**, 2002, 3899.
- [4] Ayman A. Salem, Surya R. Kalidindi, Roger D. Doherty: *Acta Materialia*, **51**, (2003) 4225-4237.

CAN WE USE AE TECHNIQUE FOR SOIL CORROSION MONITORING OF UNDERGROUND PIPELINE?

- MONITORING LIMIT OF AE SIGNALS FROM RUST FRACTURE BY SOIL CORROSION -

HIDEO CHO and MIKIO TAKEMOTO

Faculty of Science and Engineering, Aoyama Gakuin University,
5-10-1, Fuchinobe, Sagamihara, Kanagawa 229-8558, Japan

Abstract

Most pipelines in Japan have been used for the past 30 years or more. AE method is expected to estimate the corrosion zone. We first studied AE activity of the rust produced by 10-week soil corrosion. Next, we studied attenuation of cylinder wave by the rust-prevention tape and wet soil. Finally, we report AE activity of the steel pipe subjected to soil corrosion for 20 years. For this pipe, AE signals were monitored for a short period using low-frequency AE sensors mounted close to the rust. We, however, cannot predict the active period of the rust. Thus, AE monitoring from the rust fractures of underground pipes is limited for short distances less than one meter. It takes a long time to monitor the AE signals from soil-produced rust.

Keywords: Underground pipe line, soil corrosion, cylinder wave, attenuation, rust fracture

Introduction

Underground pipelines in Japan were constructed during the time before Tokyo Olympics in 1964. Corrosion of the underground pipes is becoming serious problems both in chemical plants and public utilities. Japanese companies are recently inspecting the wall reduction of the underground pipelines using a guided-wave inspection system. This system generates strong F- or T-mode cylinder waves using piezoelectric or electromagnetic transducers and detects the waves reflected by wall reduction. The guided waves, however, cannot propagate more than 2 m for underground straight pipes due to large attenuation of the cylinder waves [1, 2].

Acoustic emission (AE) technology cannot monitor the wall reduction, but can estimate the corrosion zone, if we can detect AE signals from rust fracture. Strong requirement to the AE technique is the detection of localized corrosion of the pipelines, due to local damage to the rust prevention tape and asphalt cloth. AE activity of the rust produced by soil corrosion (soil-produced rust, hereafter) is considered to be different from the rust produced by atmospheric corrosion (atmosphere-produced rust). We first compared AE activities of the soil- and atmosphere-produced rust using steel plates exposed to weathering. AE activities of these plates under mechanical loading and thermal cycles were studied. Next, we studied attenuation of the cylinder waves by wet soil and new rust-prevention tape. Lastly, we monitored AE signals from a steel pipe with thick rust produced by underground corrosion for 20 year.

Structure of the Rust Produced by Soil and Atmospheric Corrosion

We prepared 250 steel plates (45-mm wide, 90-mm long and 2-mm thick), subjecting them to soil or atmospheric corrosion for 2, 5 and 10 weeks. The soil-produced rust was prepared by burying the plates in two types of soils. One is the so-called "red-soil" and another "black soil".

The former is pasty and the latter is muddy when they absorb water. These soils correspond to two layers of the four-layered loam of volcanic trass in Tokyo area [3]. The soil is slightly acidic. The plates are coated by the rust-prevention adhesive tapes except the center portion of 20-mm square on one side, and buried in the soils.

The soil-produced rust was very hard and well adhered to the steel even after brushing by a fine brass wire brush. Thick rust of 1 mm or more were produced over 60% of the exposed area. In contrast, the plates exposed to the atmospheric corrosion produced thin rust, which were easily removed by brushing. Thick rust more than 0.5 mm were produced on only 5% of the exposed area.

As shown in Fig. 1 (transverse EPMA of the soil-produced rust), the rust contains a number of soil elements (SiO₂, Al₂O₃, Fe₂O₃ and less CaO, MgO, NaO and K₂O) in addition to the iron oxides (Fe₂O₃ and Fe₃O₄) shown as [Fe and O]. We observed a number of branched cracks in the soil-produced rust.

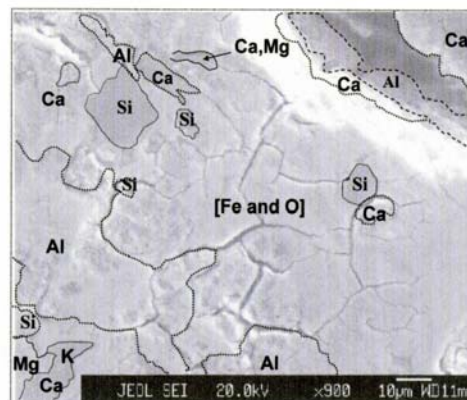


Fig. 1 Distribution map of elements in the soil-produced rust produced by soil corrosion.

AE Activities of the Rust

AE activity by three-point bending

AE signals during three-point bending with the span distance of 30 mm were monitored by four small resonant sensors (PAC, Type-PICO) mounted on four corners of 30-mm square. Strain at loading point was measured by a strain gage mounted on the base metal, and is increased up to 0.2%. Sensor outputs were amplified 60 dB, and stored in a computer as digital data.

Figure 2 shows nine diagrams of cumulative AE event counts and strains for three rust produced by 2, 5 and 10 weeks exposure. Average temperature of June was 22°C with 140 mm rain and that of July was 25°C with 170 mm rain. Average amplitude of the F-mode Lamb waves is also shown in the diagrams. The plates with atmospheric rust produced 100 events after 5-week exposure, while those buried in the red soil produced 600 events after 2-week exposure. Vertical arrows near the curves indicate the threshold strain, above which AE signals were continuously detected. The threshold strains are much smaller for the plates buried in the soils. This plate produced AE signals continuously at strains above 0.022%. It is noted, however, that the amplitude is almost identical for the atmosphere- and soil-produced rust. AE activities in term of the event counts are much higher for the soil-produced rust. This suggests that the external loading such as internal gas pressure to the underground gas pipelines is effective for monitoring the integrity loss.

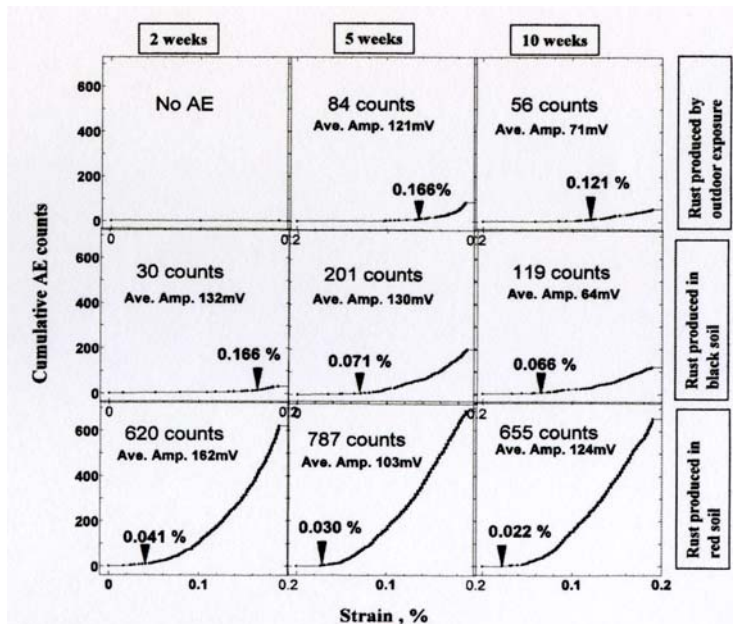


Fig. 2 Cumulative AE counts with applied strain for the steel plates exposed to soil and atmospheric corrosion.

AE activity the rusts by wet and dry cycles

Any steel plates, dried in a room after removal from exposure site, did not produce AE during thermal cycles between 25° to 40°C. These results suggest that drying of the rust must be avoided to measure the AE activity. Unfortunately, we dried all samples in room air and kept them in a desiccator, so we wondered what type of test methods we should use. After trials of many types of tests, we decided to measure the AE activity after immersing them in water for one day. We detected a few AE during the first heating, but no AE during second heating.

Figure 3 shows changes of the cumulative AE counts and average amplitude with exposure time. These show a strange change. Strong AE signals were produced after 5-week exposure, while the amplitude of AE signals decreased at 10-week exposure. There also observed no clear difference in both the amplitudes and event counts of the rust produced by atmospheric and soil corrosion. Atmosphere-produced rust produced strong AE, as seen in 5-week data. It is again noted that the result obtained by the proposed method does not necessary represent the AE activity of the rust as they are in natural weathering. AE activity must be measured at the site of a structure.

As the rust grows slowly and is generally brittle, large cracks rarely occur just after frequent large cracks. This is studied by another test and shown in Fig. 4. This figure shows change of cumulative event counts and amplitude of Lamb waves during natural drying of the rust produced by black soil by 4-week exposure. Drying is done in air-conditioned room at 27°C. We observed vigorous AE signals with large amplitude during natural drying. This strongly indicates that AE must be monitored during the drying period of grown rust. It is, however, almost impossible to estimate the drying timing of the rust in the soil. Underground pipelines (1-m depth) are almost always in wet condition. If we dry the pipeline using inert hot gas, we can perhaps monitor the integrity loss of underground pipelines. This technique was once used for the field test of corroded pipes with cooperation with steel-making company. Result was inconclusive since the corroded pipes were once dried before being buried.

Attenuation of the Cylinder Waves by Rust Prevention Tape and Wet Soil

We measured the attenuation. Accurate attenuation measurement of the cylinder waves is difficult. We have to use an advanced method for calculating the energy of the separated mode [4]. We, thus, measured an apparent attenuation using the amplitudes of the L- and F-modes. Even in this method, a problem often arises for the F-mode wave, since the amplitude of the F-mode changes along the pipe circumference [5]. Figure 5 shows a method for measuring the attenuation. Method A is for measuring the attenuation by the rust-prevention tape (JIS Z1901, 0.4-mm

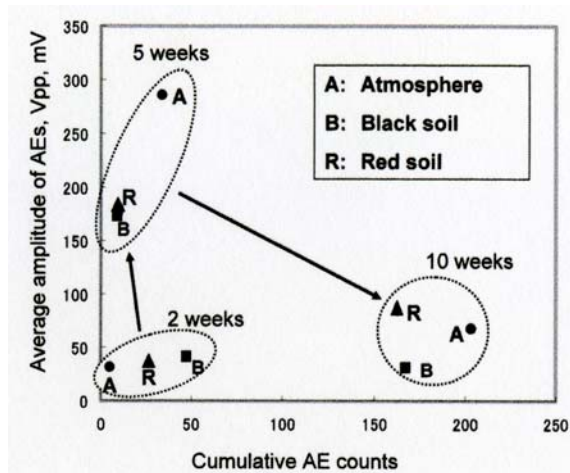


Fig. 3 Changes of event counts and average amplitude of AE signals from rusts.

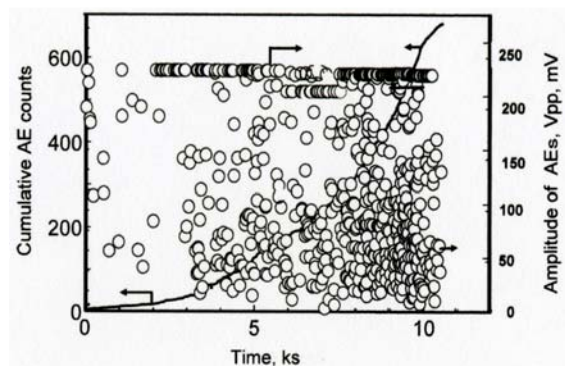


Fig. 4 Changes of cumulative event counts and amplitude during drying.

thick polyvinyl chloride adhesive tape), and method B for that by the wet black soil with 40 mass% water. The cylinder wave was excited by a 100-kHz PZT transmitter of 80-mm diameter mounted to the right end surface and monitored by three AE sensors (PAC, Type-PICO) mounted at angel of 0°, 120° and 240°. Attenuation was measured by changing the width of the double wrapped tape and wet soil in the right portion.

The left of Fig. 6 shows changes of the amplitude of L- and F- modes with the length of the tape. Surprising is that the average attenuation (-12.7 dB/m) of the L-mode by the tape is larger than that (-6.8 dB/m) of the F-mode wave. The attenuation by the wet soil is much smaller than that by the rust-prevention tape. Another interesting finding, for the wet soil, is that the average attenuation (-3.8 dB/m) of the F-mode wave is larger than that (-0.8 dB/m) of the L-mode.

These data suggest that the attenuation by the new tape becomes hazard to AE monitoring. In another word, if AE is detected, it means the rust-prevention tape is aged. This timing may coincide with the timing of corrosion initiation of the coated pipeline. We also attempted to measure the attenuation with the asphalt cloth, but could not measure it due to too large attenuation.

AE Monitoring of the Steel Pipe Buried for 20 Years

This pipe was made of plain-carbon steel, 39-mm diameter, with polyethylene coating. The pipe was buried in soil for 20 years and some parts had through-wall corrosion. A 1-m section of the pipe with thick rust was tested. Figure 7 shows the steel pipe after removing the coating. It had ~2-mm thick rust over 100 mm long at the mid portion. The center 300 mm of this pipe was again buried in wet black soil for 4 months using a plastic box before AE monitoring. The soil was allowed to naturally dry, but was kept wet by supplying 1000 ml water every 2 weeks. This operation was meant to revive the rust activity.

AE was monitored using three types of sensors, i.e., PAC Type R15 (150 kHz resonant frequency, channels 1 and 6), PAC Type-PICO (450 kHz, channels 2 and 5) and JT (broadband sensor up to 1 MHz, channels 3 and 4). All sensors were located

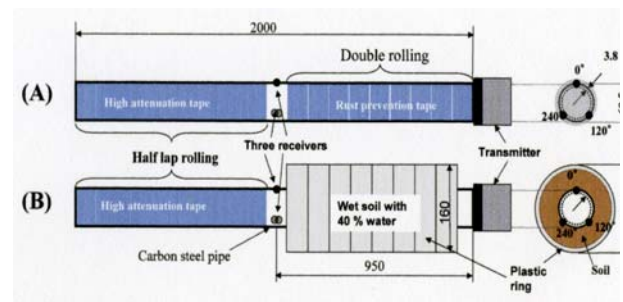


Fig. 5 Method for measuring the attenuation of cylinder wave due to the rust-prevention tape and wet soil.

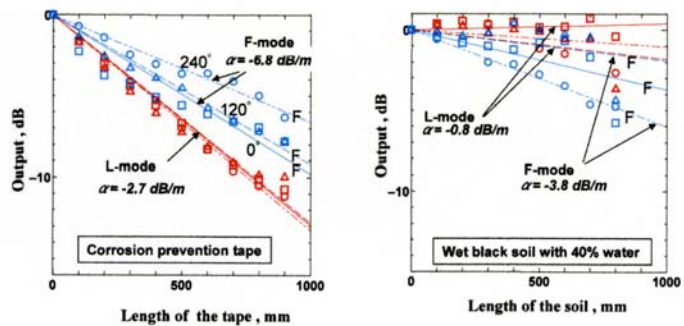


Fig. 6 Output of L- and F-mode cylinder waves vs. length of the attenuator. The left is by the corrosion-prevention tape and the right by the wet soil.

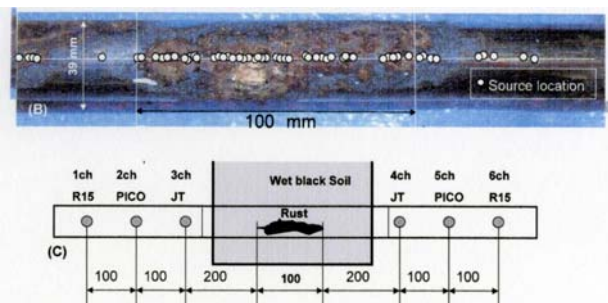


Fig. 7 A steel pipe buried for 20 years (the upper) and monitoring method of AE from the pipe in black soil. White dots indicate located AE.

within 450 mm from the thick rust. Outputs of the JT sensor were amplified 60 dB, but those of other sensors were amplified 40 dB.

We monitored AE from the pipe wrapped by the rust-prevention tape for 2 days, but detected no AE. Then we monitored AE of bare pipe. Figure 8 shows change of cumulative event counts and corrosion potential with time over one day. Vertical open arrows indicate the timing of water supply of 300 ml. We detected few AE after water supply at 5-10, 40-50 and 75-80 ks. This suggested that we cannot monitor the integrity loss of the pipe by short-time AE monitoring.

Next we attempted another experiment 2 weeks later. We monitored AE during thermal cycles. The soil was 15 times heated and cooled by on-off operations of an infrared lamp during 2.5 days. Both the corrosion potential and AE were monitored simultaneously. Water (300 ml) was supplied 3 times (vertical open arrows). Figure 9 shows change of corrosion potential, temperature and cumulative event counts during thermal cycles. We detected an abrupt AE at around 140-160 ks, after 10 heat cycles, but no AE after this. This timing corresponds with shifting of corrosion potential to noble direction. However, we cannot predict this timing. Difficulty in damage monitoring of the underground structure is the estimation of such timing.

Source locations of AE, estimated using the arrival times of the F-mode waves, are shown in Fig. 7. 27 of 70 events were located in the zone with thick rust as shown by white circles in the upper photo. Waveforms of the AE detected at 122 ks are shown in Fig. 10. Amplifications are shown in each figure. Output amplitudes of the sensors (Ch. 1, 2 and 3) mounted on the left half of the pipe are higher than those on the right half (Ch. 4, 5 and 6), indicating the rust fractures occurred at the left portion of the 100-mm long rust. This gives us important information, i.e., large attenuation of the cylinder wave by wet soil. This attenuation appears to be much larger than that (-3.8 dB/m) in the Fig. 6. The reason is not well understood, but appears to be soil thickness. It was 50 mm in Fig. 5 and 300 mm in Fig. 7.

Other information on the resonance frequencies of the sensors are as follows. Amplitude of the two PICO sensor outputs is much weaker compared to those of the R15 sensors. Frequency components of the F-mode detected by the JT sensor are from 80 to 100 kHz. In order to monitor AE from underground pipes, we need to use sensors with resonance frequency lower than 80 kHz. Another important point is wrong sensor layout. We mounted all sensors on the upper line of the pipe where the rust is produced. This layout appears to be wrong. We have to determine the sensor position, at which we can monitor the strong AE in advance.

Our conclusion from these tests is that AE monitoring of underground pipes over long distance is very difficult due to the large attenuation of the cylinder waves and the capricious nature of rusts. Monitoring distance of AE for the underground pipe may be limited to less than 1 m

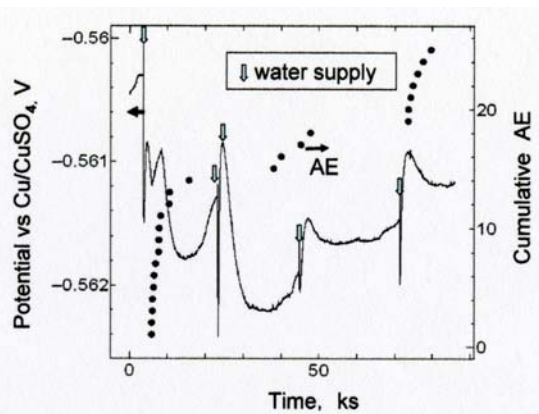


Fig. 8 Corrosion potential and AE of the rusted pipe from natural drying of wet soil.

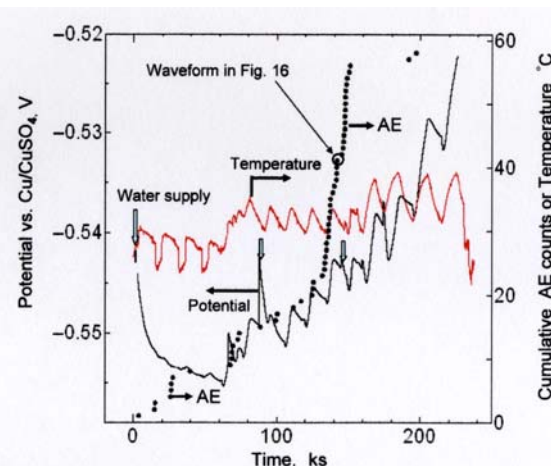


Fig. 9 Corrosion potential, temp. and AE from the rusted pipe during thermal cycles.

even if we use high amplification with resonant sensors at lower frequencies. When we detect AE from underground pipes, it means the pipes are under severe corrosion attack. Source location is not necessary since the sensors must be mounted close the corrosion zone.

Conclusion

We studied structure and AE activities of rust produced by soil corrosion and measured attenuation of the cylinder waves by wet soil and rust-prevention tape. Monitoring of AE from the corroded pipe with thick rust taught us important information on the integrity loss monitoring of underground pipe by AE. Results obtained are summarized below.

- 1) The rust produced by the soil corrosion grows thicker including soil elements and emits AE at being subjected to mechanical loading. The rust loses their AE activities once they were dried. AE activity of the survived rusts, however, changes in quite complicated manner, independent of the exposure period.
- 2) Attenuation of the cylinder waves by new rust-prevention tapes is larger than that by the wet soil. As the amplitude of the F-mode changes by sensor position on the pipe circumference, we have to determine the appropriate sensor position, which can measure the cylinder waves with higher sensitivity.
- 3) We monitored AE from the steel pipe with thick rust produced by the soil corrosion for 20 years. Few AE were detected in a limited period during thermal cycles. However, we cannot estimate the timing of rapid emissions of AE. Integrity loss monitoring of the underground pipe by conventional AE technique appears to be difficult due to large attenuation and capricious nature of the rust, and needs advanced inexpensive system, which makes a long-term monitoring possible. External loading may be effective for exciting the rust by fracturing.

References

- [1] Report by research committee on guided wave testing, J. Jpn. Soc. Nondestructive Inspection (in Japanese), **54**, 2005, 596-602.
- [2] T. Ikeda, R. Kinbara, M. Miyazawa, I. Matsuoka and M. Fujiwara, J. Jpn. Soc. Nondestructive Inspection (in Japanese), **54**, 2005, 595.
- [3] Earth Science Group, Cyclopedia of Earth Sciences. Heibon-sha (1996).
- [4] H. Kasama, M. Takemoto and K. Ono, J. Jpn. Soc. Nondestructive Inspection (in Japanese), **49**, 2000, 269.
- [5] H. Nishino, S. Takashina, F. Uchida and M. Takemoto, Jpn. J. Appl. Phys. **40**, 2001, 364.
- [6] D.C. Gazis, J. Acoust. Soc. Am. **31**, 1959, 568.

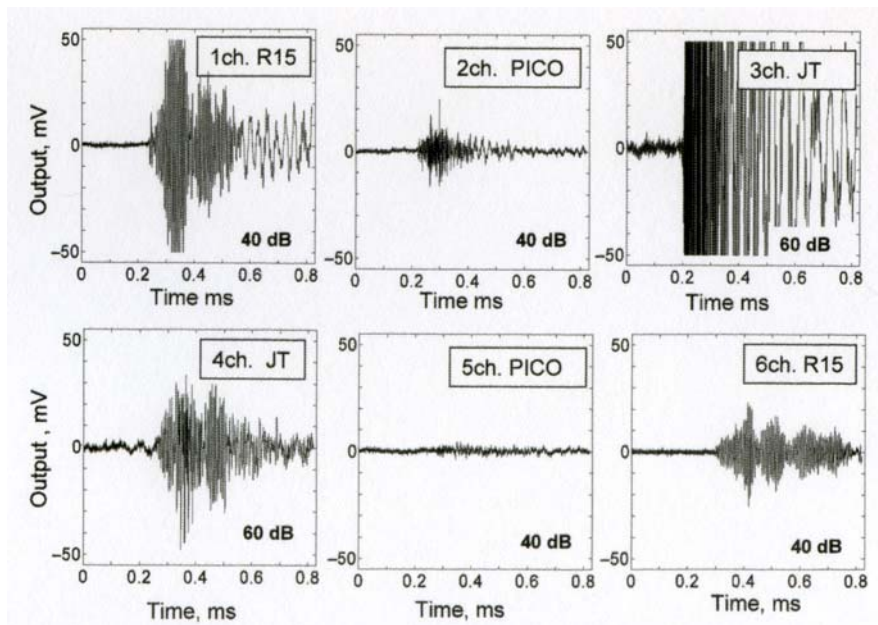


Fig. 10 Waveforms of cylinder wave signals detected at 122 ks by 6 sensors mounted at different locations near the rust.

DEVELOPMENT OF AN ACOUSTIC EMISSION DIAGNOSIS OF STEEL-CONCRETE COMPOSITE DECKING

MITSUHIRO SHIGEISHI and MASAYASU OHTSU

Department of Civil & Environmental Eng., Kumamoto University, Kumamoto 860-8555, Japan

Abstract

In recent years, the steel and concrete composite slabs have been increasingly adopted as decking of bridges. Inspections of the concrete condition of such composite slabs are relatively difficult tasks because the steel plates hide the concrete body. The establishment of an inspection method for these structures is urgently required for the security of traffics on the bridges. The aim of this research is to develop a non-destructive inspection method of the steel-concrete composite slab using AE technique. The AE measurements were implemented through a wheel load running test using an actual size specimen of Robinson-type steel-concrete composite slab. As a result, variation of AE activities and characteristics of the AE waveform parameters reveal the fatigue progression of the specimen. In addition to fatigue, rain-water infiltration into the slab from the surface crack is a matter of concern because it can lead to fast deterioration of the slab. The wheel load running test of the slab specimen with infiltration of water into the surface crack was carried out. From the results of AE events observation, the detectability of AE measurement for the infiltration of water into the slab was verified.

Keywords: Bridges, fatigue, wheel load, water infiltration, steel-concrete composite slab

Introduction

Acoustic emission (AE) provides unique capabilities for the continuous monitoring and non-destructive evaluation of the structural health and functioning of bridges. A sparse array of AE sensors is used to detect and locate active damage and damage-related processes. Convincing arguments for using AE arise in monitoring a bridge. No other monitoring method has either the sensitivity of AE to detect damage processes, or the ability to locate remote damage. AE can detect damage that other methods cannot, and can detect the damage long before it becomes critical. AE monitors the bridge using only a small number of lightweight, inexpensive, low-power, rugged sensors with almost no need for operator intervention. Finally, AE can be easily implemented on bridges that are already in service.

In the early stage, AE has been utilized for survey of defects in steel bridge structures [1]. Probably the first application of AE for testing bridges was done by Pollock and Smith in 1971 [2]. They demonstrated that signals recorded in the field could be associated with test results on laboratory specimens. Since that, many researchers collected data on many steel bridges. However, in concrete bridge, it is uncommon that the AE measurement is utilized. A significant portion of the deterioration of highway bridges is due to corrosion of the reinforcing steel in concrete bridge slabs. In Japan, many studies on the application of the AE measurement to concrete bridge inspection have been conducted to improve the inspection efficiency [3].

Steel-concrete composite slab

Recently, the demand for increasing traffic volume and providing higher durability has become stronger, so steel-concrete composite (SCC) slabs have been adopted in more cases. Figure

1 shows the work of a typical SCC slab, which is generally known as Robinson slab. Concrete body is bonded with steel bottom plates by steel studs that are welded to the steel plates. Transverse ribs are installed to reduce the deflection caused by the dead load during the hardening process of the concrete.

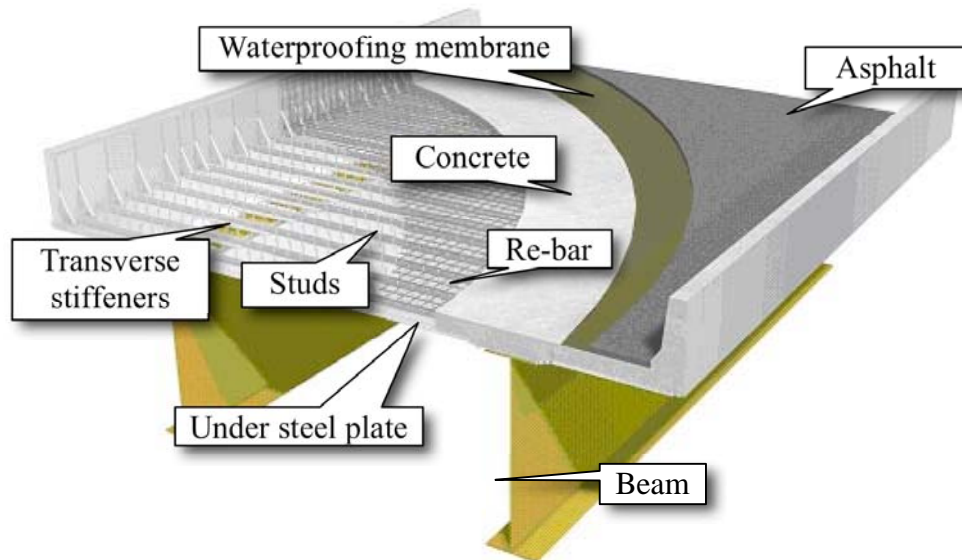


Fig. 1 Sketch of a typical SCC slab (Robinson slab).

However, on SCC slabs, unlike on reinforced concrete or prestressed concrete slabs, visual inspection of concrete condition is difficult because the steel plates are installed under the paved concrete. Therefore, establishment of concrete inspection methods is urgently required. This study focuses on AE technique, which is one of nondestructive inspection methods, and aims at development of an inspection method for this Robinson-type SCC slabs using by AE technique.



Fig. 2 Detail of bottom side of a typical SCC slab.

The authors have been making AE measurement for SCC beam and slab specimens under static and cyclic loading [4], and identifying the characteristics in typical AE waveform parameters of SCC structures damaged by the bending load. In this study, AE measurements on SCC slab were carried out under moving wheel loading, which was aimed for reproducing more

precisely behavior of the actual road bridge slab. We also examined the applicability of AE technique for the evaluation of damage in actual bridge inspection.

This paper also describes the fluctuations of AE activities owing to water infiltration into the concrete part through the top surface cracks. Water infiltration is a critical issue. As water reaches down to the bottom, it would corrode the steel plate rapidly and the durability of SCC slabs is shortened. Therefore, establishing methods to detect the water infiltration into SCC slab is desired.

Experimental Procedure and Results

Steel/concrete composite slab specimen

A two-thirds (2/3) part of the Robinson-type SCC slab for an actual bridge was made as a test specimen. The specimen has the dimension of 2300 x 4500 x 160 mm. The thickness of the concrete part and the bottom steel plate were 154 mm and 6 mm, respectively, as shown in Fig. 3. The test specimen has reproduced the actual slab construction and has a junction by the splice plate and the bolted connection.

Acoustic emission measurement

Eight AE sensors were attached on the bottom surface of the steel plate. AE sensors have resonance frequency at 150 kHz and those were general type for the AE measurement of steel structure. The AE sensors were placed so that the sensors can detect more AE events accurately (Fig. 3). The AE sensors were fixed by using silicone-grease couplant and magnet holders. The signal was amplified 40 dB by pre-amplifier and the threshold for storing the data of the analyzed AE wave parameters was set to 100 μ V defined at the sensor output.

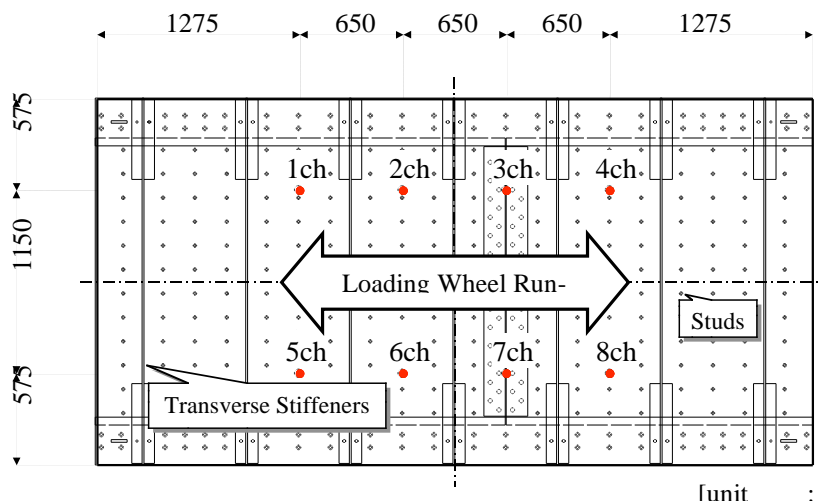


Fig. 3 Sketch of the SCC slab specimen and AE sensor positions (●).

Running wheel loading procedure

In the moving wheel loading test, a crack penetrating through the slab was formed at the middle of the beam specimen between the supports by applying a negative flexural load. Therefore, AE measurement should be also made under the similar condition in this research. In advance, the pre-bending load was applied to the center of the slab (Fig. 4) so that the cracks occurred on the top surface of the slab at mid-span. Then, the composite slab specimen has become vulnerable to be damaged by water infiltration from the top surface.

Figure 4 also shows the process of loading. In the first 100,000 cycles, the wheel load was 120 kN. The axle load was raised to 160 kN in a 20 kN step every 100,000 cycles.

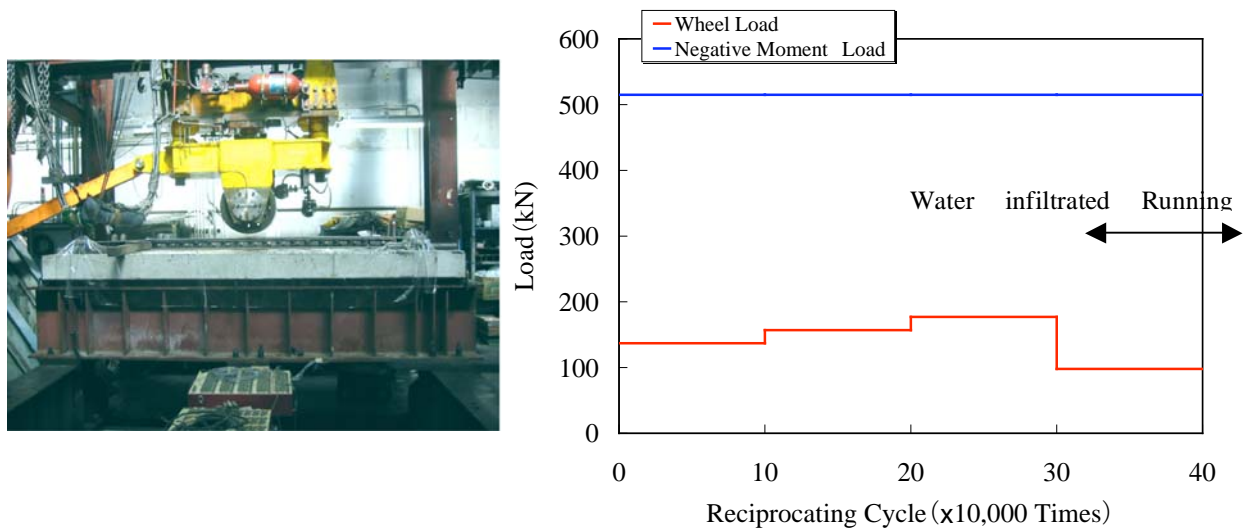


Fig. 4 Wheel loading test condition and procedure of the loading test.

Results and Discussion

At the end of the 300,000 cycles, the slab suffered substantial damage as shown in Fig. 5. Subsequently, the running wheel loading test was continued at lower axle load for another 100,000 cycles, while supplying water on the top surface of the slab to infiltrate into the concrete through the cracks.

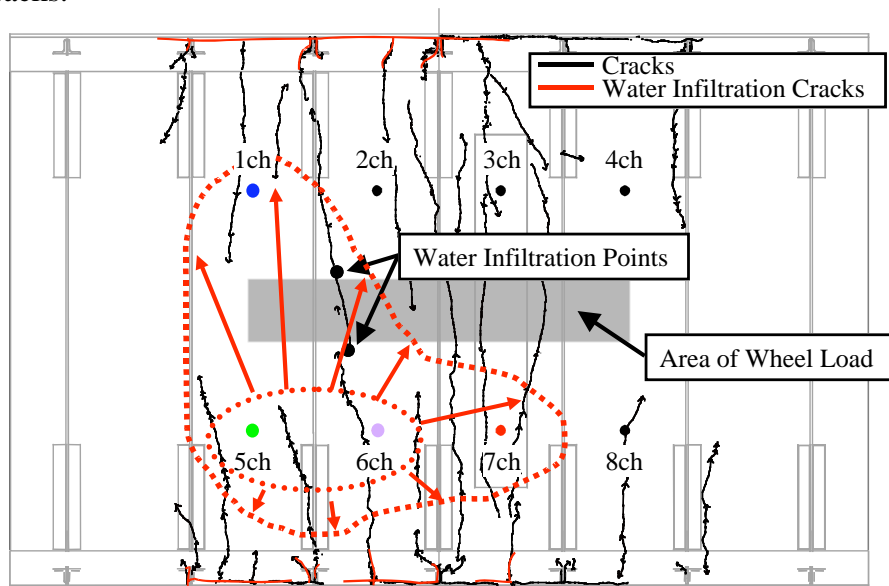


Fig. 5 Situation of the water infiltration (upper) and water seeping through a crack.

AE was measured for 15 minutes at certain intervals during moving wheel loading to verify fluctuations of AE characteristics. AE detected during the test is indicated in Fig. 6 using the relationship between the durations and counts of waves, which were general AE parameters calculated from the waveform [5].

At the start of wheel running test with water-feeding (a), the correlation between the AE parameters, the duration and the counts were nearly proportional to each other. After 500 cycles of wheel motion after water infiltration began (b), the duration was longer but the count was low at sensors 5 and 6. Similar phenomena were observed at sensors 1 and 7 in AE measurement after 2000 cycles (c) and after 4800 cycles (d).

Based on the AE results, the water infiltration progress was evaluated as red dotted line as shown in Figure 5. The AE sensors were located near the cracks through which water was allowed to infiltrate. Water infiltration through other cracks was also confirmed as shown in Figure 5.

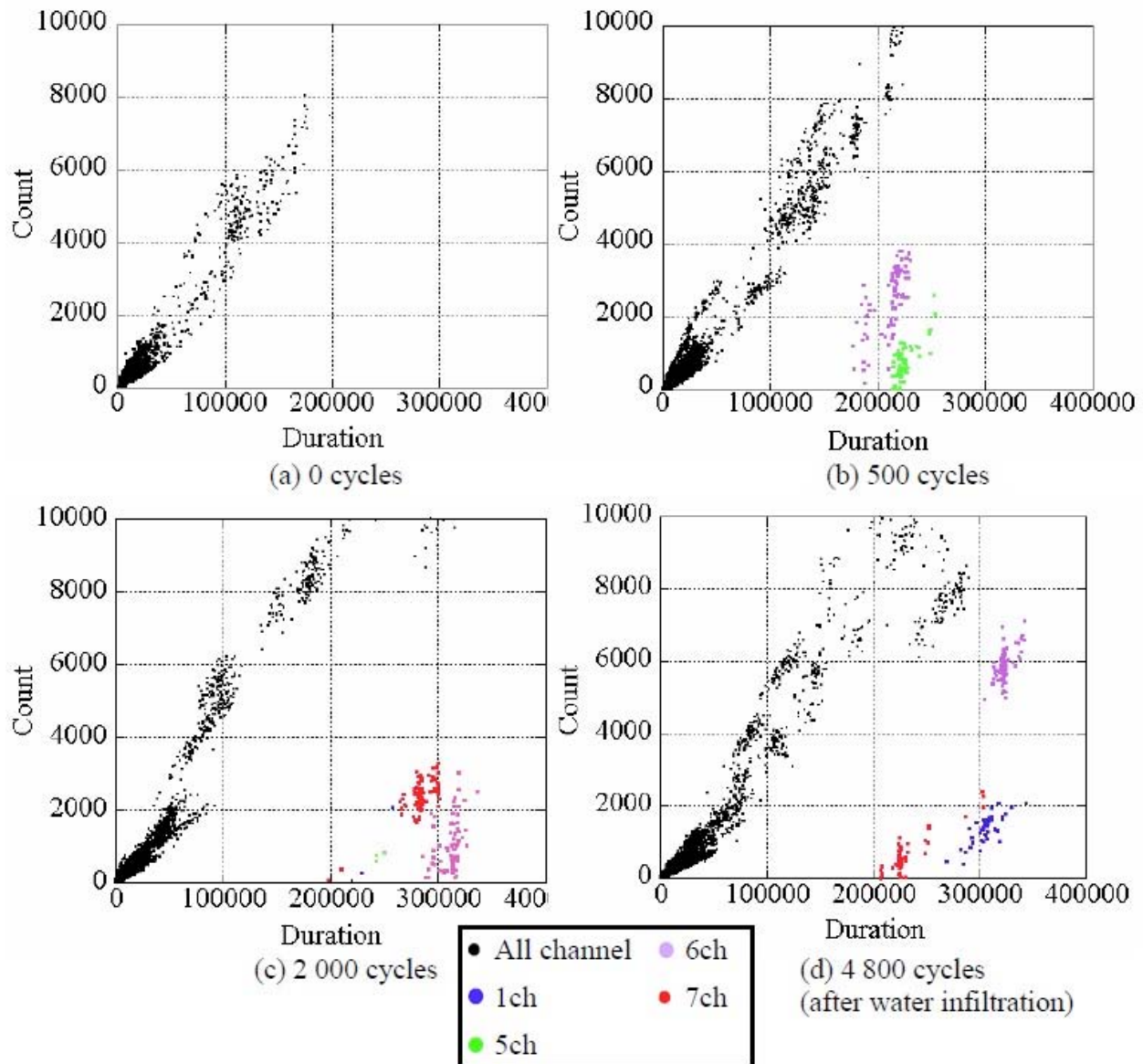


Fig. 6 Relationship between duration and count of detected AE.

The specimen was cut into four sections after the end of the fatigue test. Cracks penetrating to the steel plate and water infiltration were found as shown in Fig. 7. No water infiltration was found near the AE sensors 4 and 8. As a result of the above observation, it was suggested that AE characteristics during water infiltration could be easily verified by using the duration and the count of waves.

Closing Remarks

The test revealed that water infiltration through cracks, a matter of grave concern for steel-concrete composite slabs, can be verified using AE technique.

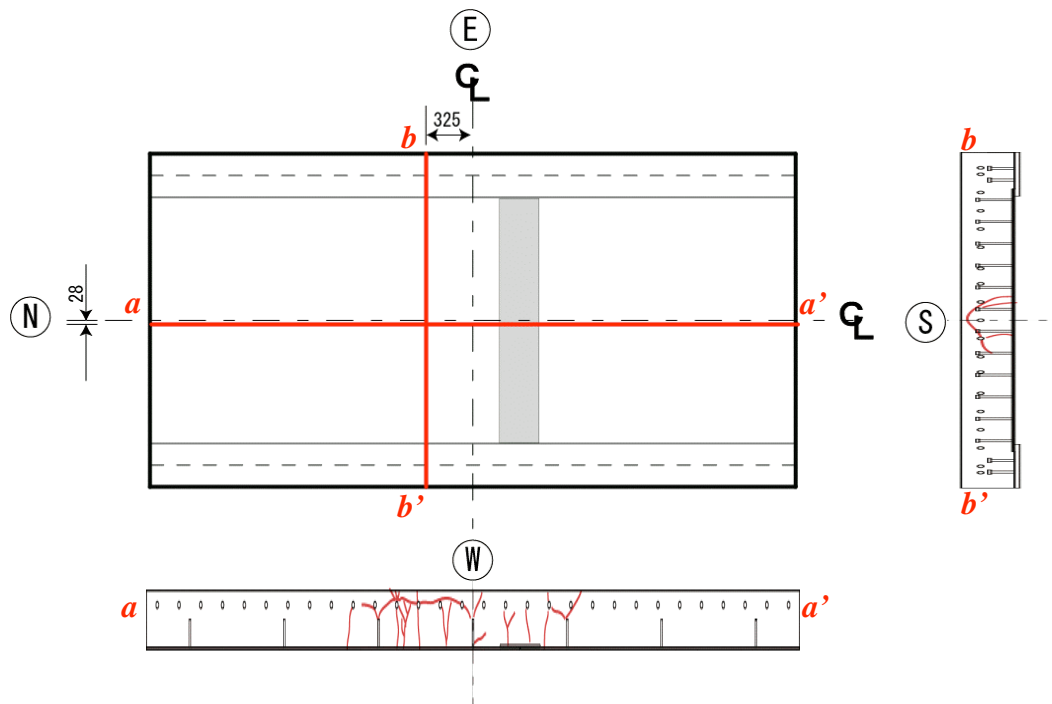


Fig. 7 Internal crack situation by cutting the specimen.

Water infiltration progress can be observed by AE parameter distribution in correlation between the duration and the threshold-crossing counts of the AE wave. The hit number of AE events with lower counts and longer duration indicates the progress of the water infiltration into the concrete body through the surface cracks due to the wheel running reciprocation. Moreover, the location of the AE sensor that detects such AE could give the progress of the water infiltration area.

In the future, traffic noise in the measurement of actual structures and optimal positioning of sensors are to be investigated.

References

1. *Method and apparatus for structural monitoring with acoustic emission and using pattern recognition*, United States Patent 4535629, 1985.
2. A.A. Pollock and B. Smith, "Stress-Wave Emission Monitoring of a Military Bridge," *Nondestructive Testing*, **30**, 1971, pp. 348-353.
3. *Recommended Practice for In Situ Monitoring of Concrete Structures by Acoustic Emission*, NDIS-2421, Japanese Society for Non-Destructive Inspection, 2000.
4. T. Ito, M. Shigeishi, and M. Ohtsu, "Acoustic emission in fatigue process of steel plate-concrete composite slabs," *Proceedings of the 16th International Acoustic Emission Symposium*, Japanese Society for Non-Destructive Inspection, 2002, pp. 133-137.
5. A.A. Pollock, "Acoustic emission inspection," *Metals Handbook*, ASM International, 1989, pp. 278-294.

DEFECT DEVELOPMENT AND FAILURE EVALUATION IN PRESTRESSED CONCRETE GIRDER BY ACOUSTIC EMISSION

MALGORZATA KALICKA

Department of Civil Engineering, Kielce University of Technology,
Aleja Tysiąclecia PP 7, 25-314 Kielce, Poland

Abstract

Acoustic emission behavior during proof loading of pre-stressed concrete girders was analyzed using supervised pattern recognition. Classes that grouped AE signals characterize deterioration evolution in girder. The girders were divided into zones and AE analysis was performed for each zone. AE activity of virgin girder was compared to AE activity of cracked girder. The zones with the strongest AE were selected and their responsibility in damage evolution in girder is studied. It was noticed that high loaded zones of girder not always coincide with strong AE activity zones. Moreover, we noticed that zones with a similar crack density exhibit different AE activities. The failure events that lead to girder collapse and AE signals produced by these events are analyzed.

Keywords: Pre-stressed concrete girder, pattern recognition analysis, deterioration mechanism

Introduction

Proof tests of 6 full-scale pre-stressed concrete girders have been made using a health monitoring procedure. Details concerning this procedure were presented during AEWG-49 and are given in [1]. The basic testing technique is acoustic emission (AE). AE signals were classified employing NOESIS supervised pattern recognition (SPR) procedure [2]. Different types of AE sources characterized the deterioration mechanisms. We used zonal method for AE sources localization. The performed studies confirmed the SPR method's usefulness for detection, classification and source localization that are produced by destructive processes in girders. Employing reference AE signals, it is possible to identify the possible deterioration mechanisms.

However, tests performed so far indicated a variety of AE behavior of girders during proof tests, even when their structures and loading modes were similar or even the same. Acoustic activity in girder zones differs from expected ones concerning intensity and severity of deterioration processes; i.e. classes of AE sources. The results indicated that there is no simple way for health monitoring performance, residual-life and loading-capacity prediction and influence of damages introduced earlier on service-life evaluation. In addition, we do not know if AE technique can detect the "critical event" that leads to girder collapse and warning against incipient failure. These problems were not studied extensively yet and this paper aims at elucidating some of them on the basis of AE results recorded during proof tests on two prestressed girders. AE activity is demonstrated on point diagrams, where AE signal strength is plotted against time. The loading sequence consists with a number of steps. The number of steps changes from 8 to 20 depending of loading capacity of girders (see [1]). The AE events recorded during each step are added and presented vs. time of the longest step. The colors and points' shape indicate AE source classes and severity codes of damage processes in accordance with Table 1.

Table 1. AE signals classification.

No. of AE class	C4	C0	C1	C3	C5	C2	C6
Point patterns	○	□	◆	▼	▲	●	+
Severity code	1	2	3	4	5	6	7

Experimental Procedures and Results

We utilized standard AE instrumentation. The 12-channel MISTRAS or 24-channel SAMOS systems from PAC were used along with DECI 55-kHz sensors. For each signal, we recorded 12 signal parameters. Details concerning AE location mode, signals classification, expected deterioration mechanisms in girders, the length of zones and reference signal parameters, see [1].

The first tested girder was 18.8 m in length double-tee WBS under four-point bending. The girder was divided into 11 zones. The zone 6 was bent while loading points were situated in zones 5 and 7 and shearing loads were added. We were interested in AE activity differences for a virgin girder and damaged one in the same loading ranges. The girder was loaded from 0 to 600 kN unloaded to 0 and reloaded to the same load. This load was twice the load of first crack appearance. AE activity for whole girder is presented in Fig. 1.

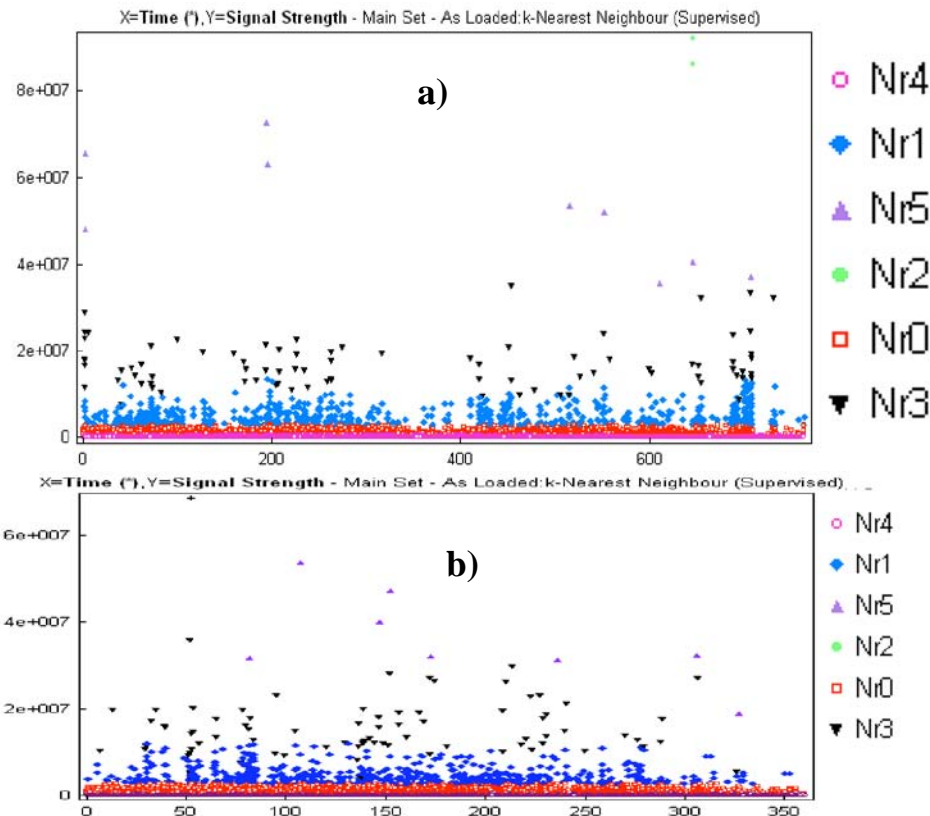


Fig. 1 a) AE activity in WBS girder during first loading from 0 to 600 kN; b) second loading.

Number of hits during first loading in all classes for virgin girder exceeded the hits number during reloading. Signal strength during first loading was higher. On both diagrams C1-blue, C3-black and C5-purple sources indicate crack initiation and propagation accompanied by some plastic deformation of wires. Results show that damage in the form of cracks and plastic

deformation of reinforcement have little influence on AE activity. This AE behavior was observed in other girders too. The exception is when new class of AE sources with higher strength takes place.

The second T-shape girder was 26.5 m long. For AE source location, it was divided into 12 zones as shown in Fig. 2. Work with this girder analyzed AE activity evolution in zones and its relationship to cracks and deterioration processes. This analysis concerned AE hits recorded during load increase in the range from 0 to 996 kN; i.e. up to ~70% of the collapse load.

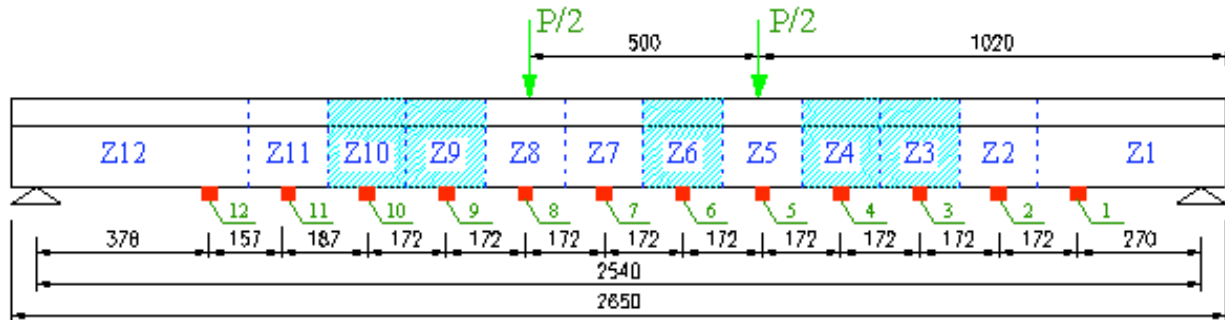


Fig. 2. Scheme of T girder with sensors and zones location.

Intensive AE activity took place in 5 of 12 zones. These are shaded in Fig. 2. Zones Z3 and Z4 were symmetrically situated to zones Z9 and Z10. Both bending moment and shear force loaded all four of them. However, only in Z9 and Z10 appeared AE signals that belonged to C5 that suggests plastic deformation of wires. Different AE behavior may take place because of torsion in the left side of girder. Observation of larger crack-mouth openings and differences in crack inclination (vertical in the left side and sloped on the right) supports this suggestion. The reasons may be internal inhomogeneity or/and lateral slenderness of girder.

Only bending moment loaded zones Z6 and Z7. While Z6 produced strong AE, the activity in Z7 was significantly weaker. Similar numbers and length of cracks existed in both (see Fig. 3).

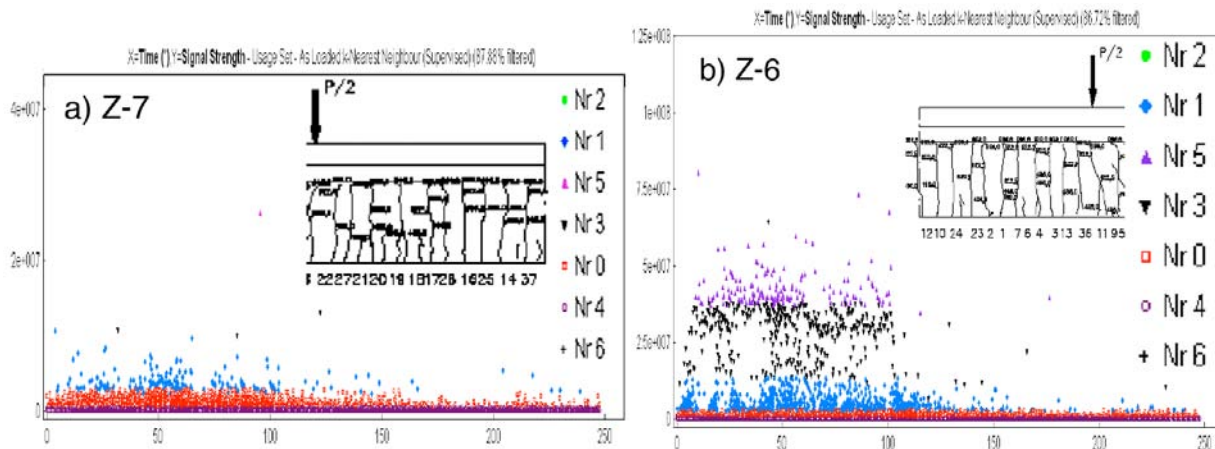


Fig. 3. AE activity and cracks distribution in neighbor zones of T girder, load range 0 – 996 kN.

Loading was increased to up to 90% of the collapse load and this increased the intensity of AE activity in all zones. The strongest one was still in zones Z3, Z4, Z6, Z9 and Z10, however. The AE activity exhibited an intermittent nature even in the most active zones. Example is demonstrated in Fig. 4, where recorded hits are demonstrated in zones Z9 during load ranges 934-996 kN and 1186-1245 kN.

The five zones Z3, Z4, Z6, Z9 and Z10 exhibited strong AE activity. This activity was at the same level while in other zones it was clearly lower. Thus, the five zones were “hot spots” (HS) of girder that have to be monitored for structural health evaluation. To find HS of other girders we monitored them at lower load equals to ~15% of predicted collapse load. The HS demonstrated themselves by elevated AE activity although these hits were in classes C0 and C4 only.

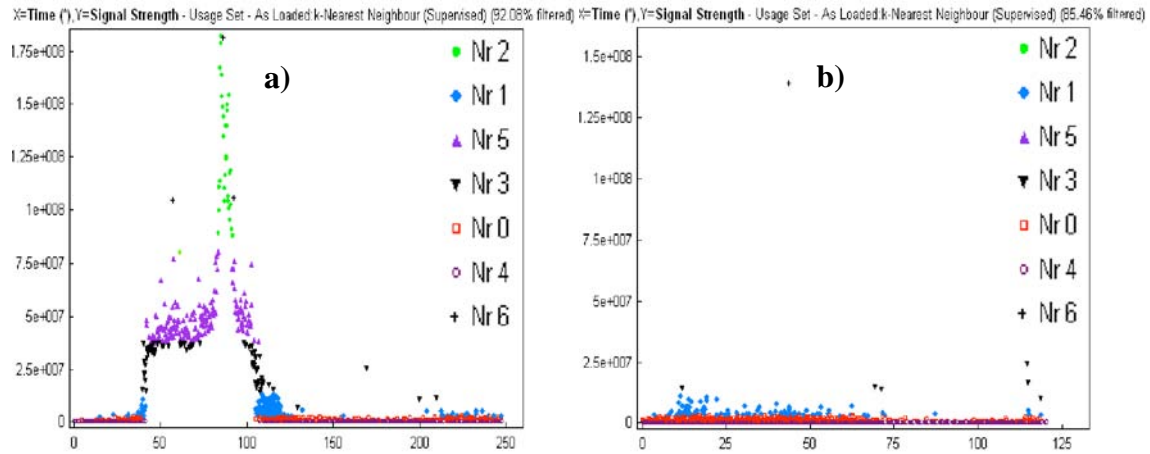


Fig. 4. AE activity in zone Z9; a) loading range 934-996 kN, b) loading range 1186-1245 kN.

Performing studies on deterioration development in prestressed girders, there is a question whether it is possible to detect the critical event that leads to girder collapse with the help AE technique. Can AE activity warn us early enough against failure? Our research demonstrates that girder fracture frequently takes place in zones with low AE activity, although these cross-sections were heavily loaded. We present one example concerning the 18.8-m-long WBS girder, which had collapsed at the load of 681 kN. The diagrams in Fig. 5 show AE activity in two neighbor zones – Z6 where failure took place and Z7 where AE activity was high.

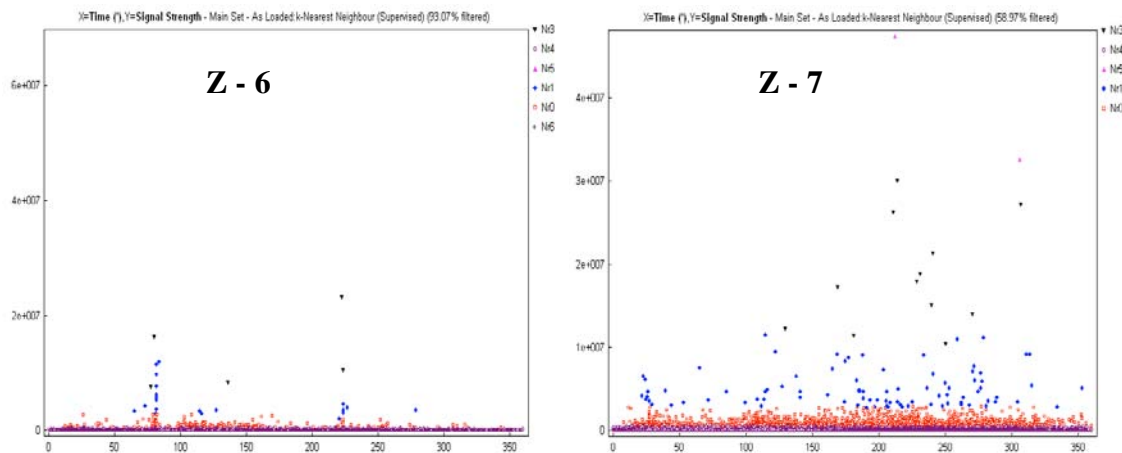


Fig. 5. AE activity in zones Z6 and Z7.

Careful AE monitoring in zones did not provide signs of incipient failure. AE events record during loading range from 640 to 681 kN, that is up to fracture, can be seen in Fig. 6. During more than 90% of this loading time AE was a typical one and did not indicate coming collapse of the beam. About 20 sec before collapse (corresponding to 2.5 kN below the collapse load) some increases in AE activity (in the form of blue points) can be seen. Such signals are produced by

concrete crack initiation. High-energy signals can be seen only during girder collapse. Thus, AE cannot warn against failure early enough to protect the girder during the proof loading. However, when the girder becomes a part of structure, AE indicates and localizes its collapse clearly by a spike that contains hits from all high-energy classes.

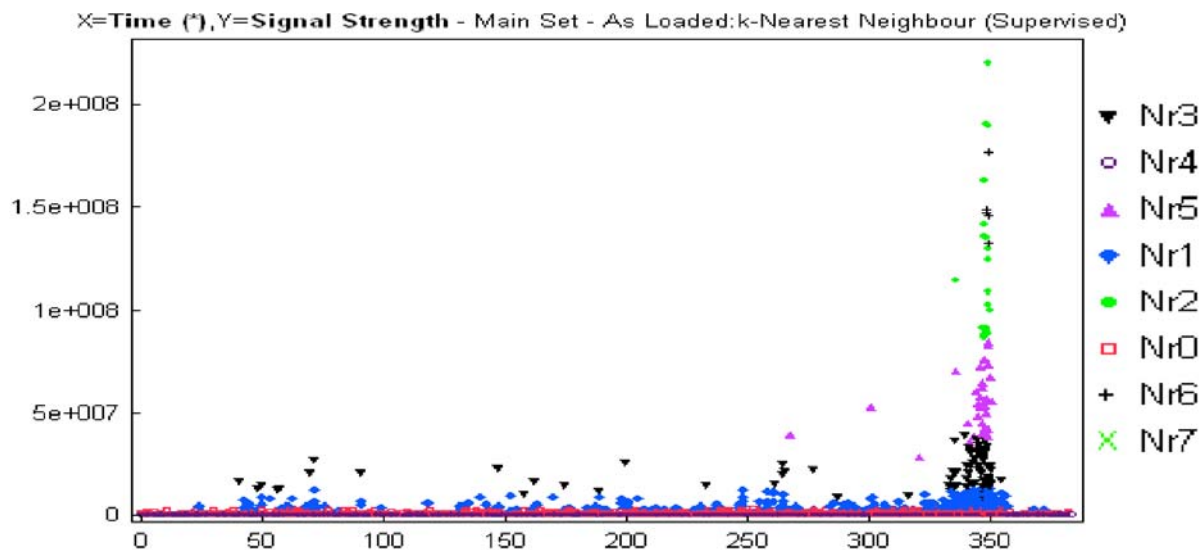


Fig. 6. AE activity in the WBS girder from 640 kN to collapse at 681 kN.

It is necessary to describe the mechanisms that resulted in the failure of the pre-stressed girders tested. Most of tested girders collapsed as a result of concrete compression. Just before failure in compressive part of girder a local plastic deformation is observed in the form of tiny slip lines. Weak AE accompanies this plastic deformation that is indicated by blue diamonds. Because of limited “concrete plasticity” of strain under 0.3%, this plastic deformation leads to fracture in a short time and girder collapse. The above mechanism took place in the WBS girder, while the “critical event” for the T girder was lateral buckling. Both processes need only several seconds and AE technique cannot detect the incipient failure early enough.

However, both critical events took place as a result of destructive processes leading to stress redistribution in the girders. The cracks in concrete shifted the neutral layer of the beam toward compressive zone (roughly it is situated at the crack tips) and the area of compressive part of the beam is reduced while the compressive stress increases. Wires take the loading in the tensioned zone of the cross-section. When girder loading increases, the stress in wires can equals their yielding stress and stress redistribution in zones of the girder takes place. This process accelerates the failure of the girder.

Buckling may initiate the girder collapse as well. The equation that determines the lateral buckling critical load is:

$$P_{cr} = \frac{\beta \sqrt{EJ_z} \sqrt{GJ_t}}{l^2}$$

where: EJ_z is bending rigidity with respect to vertical axis and GJ_t torsional rigidity. Material modules, moment of inertia and torsion constant depends on concrete deterioration and neutral layer position. In addition, the torsional rigidity decreases with the number of damaged zones increasing. Thus, the buckling critical load can be decreased significantly.

Although the critical events of failure cannot be indicated by AE monitoring, all the deterioration processes that control it, like microcracks in concrete, crack initiation and propagation, plastic deformation of wires and concrete crumbling can be characterized with the help of AE

SPR analysis. Blue (C1) and black (C3) points indicate the intermediate damage while purple (C5) and green (C2) points show heavy damage. Results of this study on girder suggest that AE events appearance in classes C5 or C2 systematically indicates severe damage of a girder that may have to be replaced.

Discussion and concluding remarks

A set of proof tests on pre-stressed concrete girders have been made with AE monitoring. AE SPR analysis was employed for AE signal classification and used in the characterization of the deterioration evolution in the girders. Especially, the AE behavior was analyzed and can influence the results interpretation for health assessment.

AE activity during proof loads of a virgin girder concerning both number of hits and strength of signals was stronger in comparison with AE activity of the same girder after serious cracking and reloading. It was noticed that in girder zones with the same loading, AE activity differs significantly. Therefore, it is recommended to localize HS and monitor them at first. Usually numbers of HS do not change with loading and HS keeps high AE activity all the time.

In bent and sheared zones, we observed stronger AE than in zones loaded in bending only. However, we do not find a relationship between AE activity and number and length of cracks. Similar cracked zones can exhibit different AE. Even at high loads AE activity in zones exhibit intermittent nature. This necessitates monitoring time to be long enough during all field AE tests.

The performed proof loadings of pre-stressed concrete girders underline the complexity in deterioration development. The AE behavior of similar girders can be quite different. Therefore to evaluate the health condition of a girder and especially bridges on the basis of AE monitoring an experienced staff familiar with AE equipment, AE data processing is necessary. Database of previously monitored structures and reference signals play a key role as well.

This study on pre-stressed girders shows that the critical events of girder collapse are compression failure of girder concrete or lateral buckling. Both of these processes may produce only weak AE activity over a short period of time. These hits are difficult for separation from other AE activities. Thus AE cannot be used for warning against collapsed.

However, AE-SPR analysis is a suitable tool for monitoring the deterioration development and for the assessment of damage severity in order to prevent the collapse of pre-stressed concrete girders and bridges. All stages of deterioration development can be estimated. C5 and C2 classes of AE signals indicate the dangerous deterioration according to the database built from our previously performed tests.

Acknowledgements: This work was supported by the Ministry of Science and Higher Education, Research Grant No 132/E-368/SPB/COST/T-07/DWM93/2004-2007.

References

1. L. Gołaski, G. Świt, M. Kalicka, Kanji Ono, J. Acoustic Emission, **24**, 2006, 187-195
2. A. Anastasopoulos, J. Acoustic Emission, **23**, 2005, 318-330.

ACOUSTIC EMISSION OF FULL SCALE CONCRETE BEAMS FOR EVALUATION OF JOINT EFFECT

D. G. AGGELIS, T. SHIOTANI, S. MOMOKI and M. TERAZAWA*

Research Institute of Technology, Tobishima Corporation, 5472 Kimagase, Noda, Chiba, 270-0222, Japan; *Civil Engineering Headquarters, Tobishima Corporation, Sanbancho, Chiyoda, Tokyo, 102-8332, Japan

Abstract

The present paper discusses the mechanical and acoustic emission (AE) behavior of two large reinforced concrete beams. One was constructed in two parts, which were assembled later to evaluate the behavior of the joint. The beams were tested in four-point bending. It is found that the structural performance of the two beams is quite different but at initial loading stages, strain and deflection measurements do not show significant discrepancy. On the contrary, AE parameters indicate that the damage accumulation happens earlier in the assembled beam. This is confirmed by the calculated sources of AE events, which are close to the construction joints. The results show that AE is a suitable technique to monitor the fracture process of structures and yields valuable information that cannot be obtained at the early stages of damage by any other method.

Keywords: Bending, structural integrity characterization, cracks, fracture process

Introduction

The number of aging concrete structures increases continuously worldwide. The damage assessment and maintenance are essential in order to secure or even extend the safe service life of these structures. One of the techniques used for the characterization of their structural integrity is acoustic emission (AE).

Overstraining of a material results in cracking, giving rise to elastic waves propagating to all directions. These transient waves (AE signals) can be detected by AE sensors attached to the surface of the material. The advantage of AE is the recording of the damage process during the entire load history, which enables us to determine the onset of fracture and to follow all the subsequent stages. In laboratory studies, AE parameters have been correlated with the damage process [1-11]. There are also applications of AE in actual structures with the aim of damage or repair evaluation [2, 6, 12-15]. Important parameters of AE are the number of AE signals (hits), events and their peak amplitude. At the early stages of damage, the number of emissions is limited and their intensity is low. As the stress increases and the damage propagates, the number of emissions becomes larger as well as their amplitude [2, 3, 6, 9, 12].

For damage quantification purposes, certain indices have been proposed. In addition to AE when a material or structure is stressed, the behavior during unloading is also crucial. When the material is intact, the AE activity during unloading is of low intensity. For damaged material though, the emission continues even during unloading. The number of AE events during unloading divided by the number of events during the whole cycle is defined as the calm ratio and values near zero indicate intact material condition [6, 13-16].

Another index comes from the "improved *b*-value" analysis of the amplitude distribution of the events [17]. Generally, a large scale fracture corresponds to large AE amplitude; however,

the use of the amplitude alone is inappropriate because of the increased material attenuation after damage accumulation. In this respect, the amplitudes are studied through their cumulative distribution that changes with the progression of damage. It has been confirmed that extensive cracking is accompanied by a severe drop in the Ib -value [2, 15, 17-19].

In this paper, the AE behavior of full-scale reinforced concrete beams under 4-point bending is discussed. The aim is the comparison between two different construction methods. The location of the AE events revealed the sensitive areas of each design that acted as crack sources. The AE indices also predicted which beam would exhibit higher ultimate strength even from the first cycle of the loading process.

Experimental procedure

Concrete beams

The length of the beams was 6.5 m while the cross section was 0.65 m (height) by 1 m (width). They consisted of two layers of concrete. The lower layer had a thickness of 150 mm and after the complete hydration of this layer, the second layer was cast on top with no reinforcement. The basic difference of the two beams was the construction process. Beam A was constructed in two steps, i.e., each layer was cast as one piece. In contrast, the bottom layer of beam B was constructed in two separate parts that were then joined during the casting of the upper layer; see Fig. 1. The advantage of beam B is easier handling, but the structural performance should be evaluated first. The beams were loaded in a four-point-bending test. The span between the supports was 6 m, as seen in Fig. 2. The test consisted of 5 loading cycles: the first two were up to 500 kN, the third and fourth up to 750 kN and the last loading is to failure.

Acoustic emission monitoring

Twelve R6 sensors of Physical Acoustics (PAC) were employed for the AE monitoring. They were attached using wax on the positions 1-12, as shown in Fig. 2. The signal was pre-amplified 40 dB, digitized with a sampling rate of 1 MHz and stored in a 16-channel PAC-DiSP system. Apart from the analysis of parameters and waveforms, the software AEWIn of PAC provided automatic, real-time event source location.

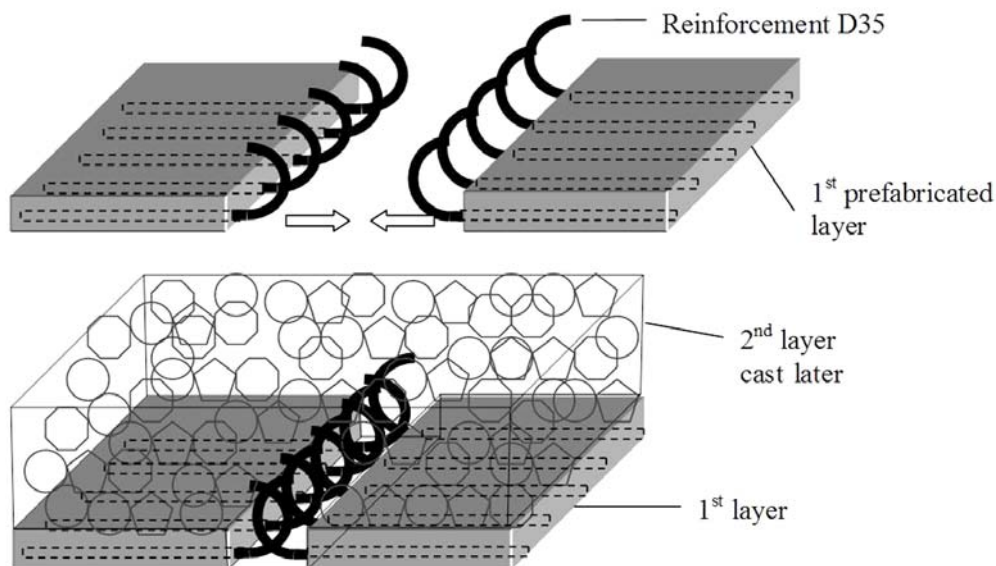


Fig. 1 Detail of the assembly of beam B.

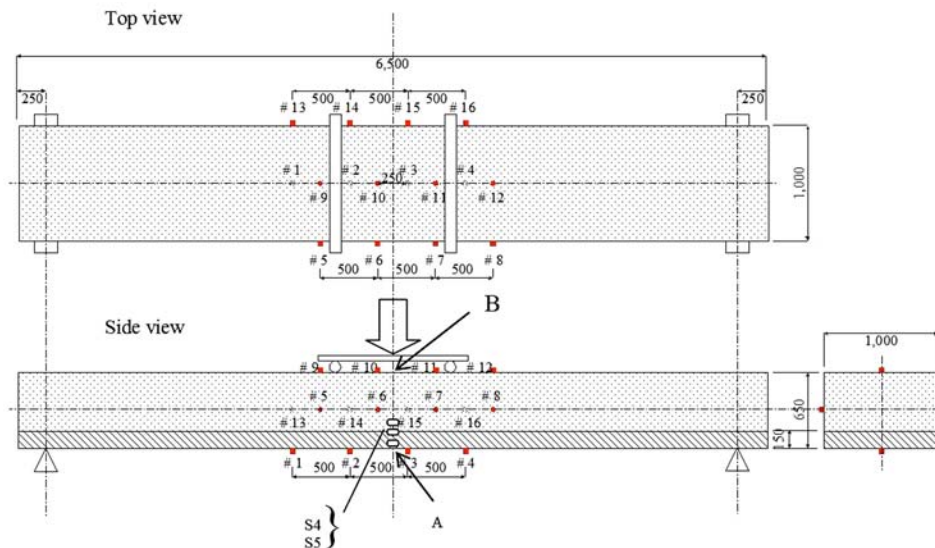


Fig. 2 Geometry of the experiment and sensor location (unit: mm).

Results and Discussion

Figure 3 shows the cumulative AE events along with the applied load for beams A and B. During any cycle the events increase, reaching for beam B a number more than double that of A, indicating more intense cracking. More important though, is the value of AE indices, like the calm ratio. In Table 1, the numbers of events during loading and unloading of steps 1 and 3 are presented. The activity of B was intense even from the first unloading. The number of the events during unloading was almost of the same order with loading, leading to a calm ratio of 0.39. This value is related with high degree of damage in relevant works [6, 12-16] and shows that the damage of beam B was extensive even from the first loading cycle. Beam B constantly exhibited higher calm ratio values for all stages, as shown by the results of step 3 in Table 1. At this step, beam A also exhibited high calm ratio (0.23), implying that it was seriously damaged as well.

The calm ratio indicated that beam B started to develop damage much earlier than A, something that could not be evaluated by strain or deflection data. This early damage led eventually to a lower maximum load of beam B (approx. 10%, as seen in Fig. 3)

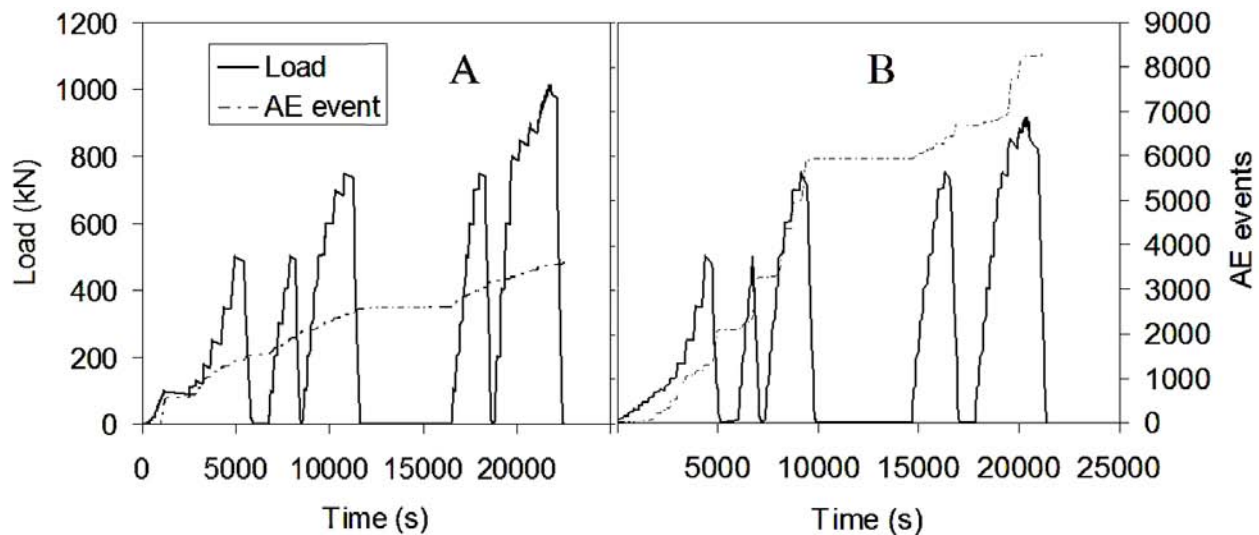


Fig. 3 Time history of load and cumulative AE events.

Table 1 Number of events for different loading steps and calm ratios.

	Beam A			Beam B		
	Loading	Unloading	Calm ratio	Loading	Unloading	Calm ratio
1 st step (500kN)	1412	121	0.079	1286	807	0.386
3 rd step (750kN)	390	117	0.230	1718	934	0.352

Source location

Figure 4 shows the locations of the events for the first loading and unloading step for both beams along with the pattern of surface cracks developed. The events are indicated by circles, the center of which is the location of the source and the diameter stands for the amplitude of the first detected hit. Beam A exhibits widely distributed events over the whole monitored area. During unloading, the number of events is lower indicating minor damage.

In beam B, most of the events are located above the position of the left joint. This means that the joint contributed to local stress concentration leading to accumulation of cracks. Even more indicative is the behavior during unloading. It is clear that a large number of events were nucleated again from the area above the construction joint, most of them with high intensity, implying damage accumulation. This led to the lower strength for beam B.

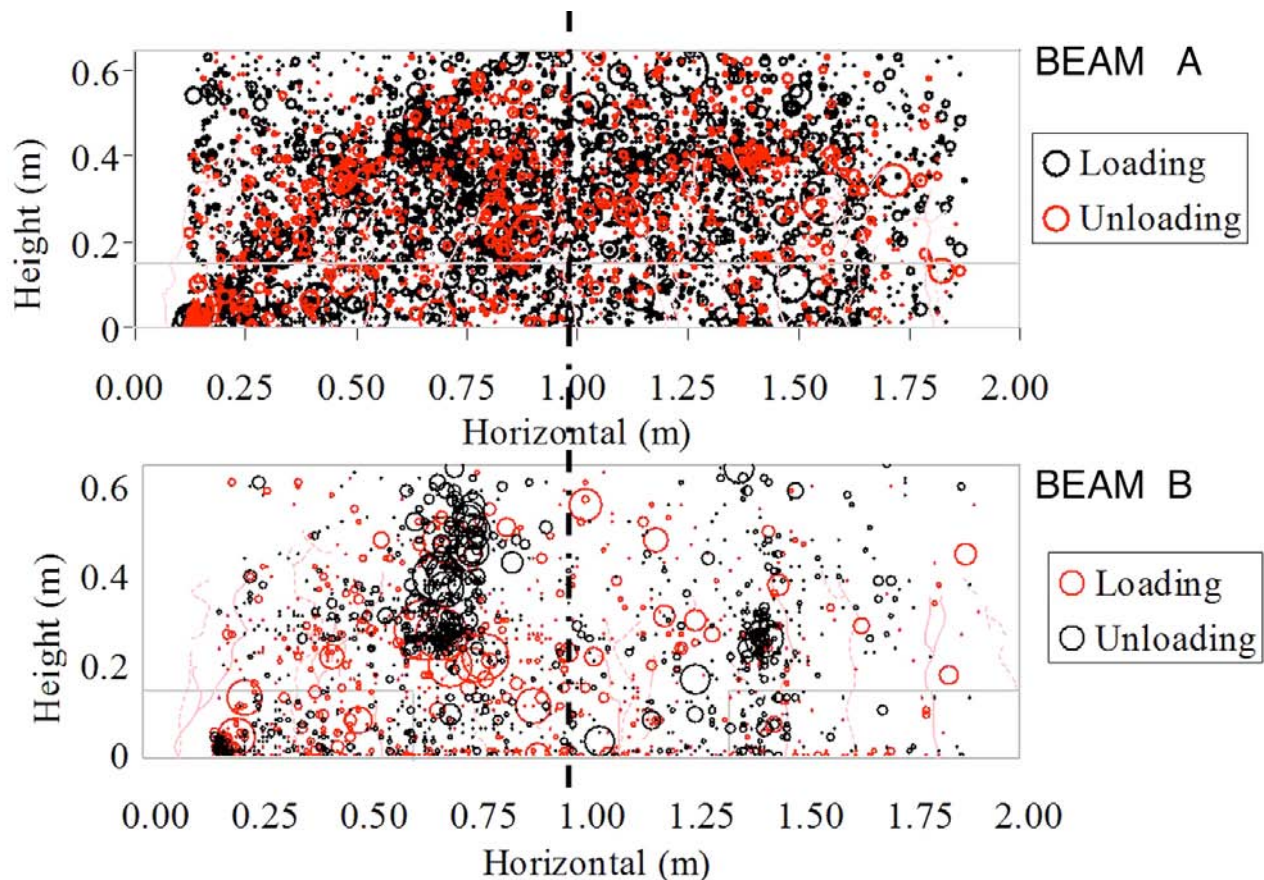


Fig. 4 Locations of AE events and surface crack pattern for the 1st loading cycle for beams A and B. The solid lines denote cracks observed on the front side and dashed lines on the rear side. The dash-dot line denotes the centerline of the specimens.

Ib-value

The AE event amplitude distribution changes with time as extensive cracking develops. When strain gauges are in the vicinity of a crack, a sudden change can be seen in the strain behavior as well. Such a case is presented in Fig. 5 for beam B. The strain histories of two strain gauges (S4 and S5 of Fig. 2) are shown for the first 2 hours of the experiment. After about 2000 s, the strain readings started to change direction and in the time span of 3800 to 4250 s they exhibited sharp drops, while the load was still monotonically increasing. This behavior was recorded on multiple strain gauges, showing that it was due to cracking and not due to a failure of a single strain gauge.

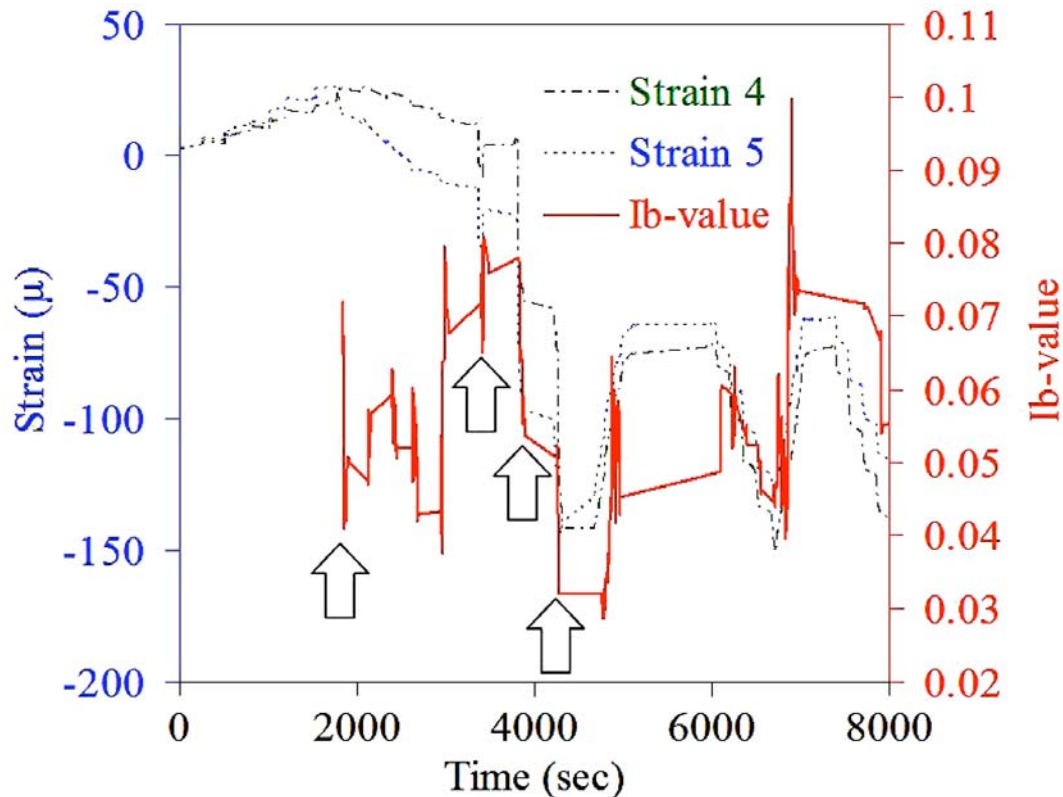


Fig. 5. Time history of (a) strain and (b) *Ib*-values for beam B.

The *Ib*-value history exhibited many points of fluctuation during the experiment, indicating different cracking events, see Fig. 5. Note that the *Ib*-values presented were calculated from AE events of the zone 0.70 m to 1.05 m, which includes the strain gauge positions, see Fig. 4. A large drop of *Ib*-value occurred at the moment when the strain readings changed direction (~2000 s; 1st arrow). Three sharp drops of the strain (2nd to 4th arrows) happened at 3300~ 4200 s, accompanied by large drops of *Ib*-value. These effects are the consequences of cracking of the beam.

Furthermore, the *Ib*-value dropped below 0.05 at many instances. This value has been established as indicative of extensive damage [2, 15, 17]. *Ib*-value below 0.05 is another indication of the severe condition of the beam, even from the first loading cycle in beam B.

Conclusions

The AE activity of two full-scale concrete beams is reported. One (beam B) had a construction joint in order to evaluate relative performance. AE results showed that the joint

acted as crack initiator, and significant damage was accumulated in their vicinity from the early stages of loading. This damage was indicated by the location of AE events, while the activity during unloading, quantified by the calm ratio, confirmed the extent of damage from the early stages of loading. As a result, the beam with a joint had 10% lower ultimate load. The AE amplitude distribution quantified by the I_b -value, indicated the crack propagation events, something that strain and deflection meters cannot monitor unless the fracture occurs in their vicinity. AE analysis shows the ability to monitor a large volume, with real time crack localization as well as correlation of cracking process with the applied load even from the early stages of damage.

References

- 1) T. Shiotani, J. Bisschop, J.G.M. Van Mier, *Engineering Fracture Mechanics*, **70**(12), 2003, 1509-1525.
- 2) T. Shiotani, M. Ohtsu, K. Ikeda, *Construction and Building Materials*, **15**(5-6), 2001, 235-246.
- 3) B. Schechinger, T. Vogel, *Construction and Building Materials*, **21**(3), 2007, 483-490.
- 4) M. Shigeishi, M. Ohtsu, Identification of acoustic emission sources by using SiGMA-2D moment tensor analysis. *Acoustic Emission: Standards and Technology Update*, ASTM STP 1353, Vahaviolos SJ, ed. American Society for Testing and Materials, 1999, 175-188.
- 5) M. Ohtsu, T. Suzuki, *Journal of Acoustic Emission*, **22**, 2004, 30-38.
- 6) M. Ohtsu, M. Uchida, T. Okamoto, S. Yuyama, *ACI Structural Journal*, **99**(4), 2002, 411-417.
- 7) H. Mihashi, N. Nomura, S. Niiseki, *Cement and Concrete Research*, **21**, 1991, 737-744.
- 8) C. Grosse, H. Reinhardt, T. Dahm, *NDT&E Int*, **30**(4), 1997, 223-230.
- 9) T. Shiotani, M. Shigeishi, M. Ohtsu, *Construction and Building Materials*, **13**, 1999, 73-85.
- 10) C. U. Grosse, F. Finck, *Cement and Concrete Composites*, **28**(4), 2006, 330-336.
- 11) T. C. Triantafyllou, C. G. Papanikolaou, *Materials and Structures*, **39**(1), 2006, 93-103.
- 12) T. Shiotani, Y. Nakanishi, K. Iwaki, X. Luo, H. Haya, *Journal of Acoustic Emission*, **23**, 2005, 260-271.
- 13) T. Shiotani, D. G. Aggelis, Damage quantification of aging concrete structures by means of NDT, *Proc. of Structural Faults and Repair-2006*, June 13-15, Edinburgh, 2006, (in CD).
- 14) T. Shiotani, X. Luo, H. Haya, *Journal of Acoustic Emission*, **24**, 2006, 205-214.
- 15) T. Shiotani, Y. Nakanishi, X. Luo, H. Haya, *Journal of Acoustic Emission*, **22**, 2004, 39-48.
- 16) S. Colombo, M. C. Forde, I. G. Main, M. Shigeishi, *Construction and Building Materials*, **19**, 2005, 746-754.
- 17) T. Shiotani, K. Fujii, T. Aoki, K. Amou, *Prog. Acoust. Emiss VII*, 1994, 529-534.
- 18) J. H. Kurz, F. Finck, C. U. Grosse, H. W. Reinhardt, *Structural Health Monitoring*, **5**, 2006, 69-81.
- 19) S. Colombo, I. G. Main, M. C. Forde, *Journal of Materials in Civil Engineering-ASCE*, **15**(3), 2003, 280-286.

ACOUSTIC EMISSION AND X-RAY TOMOGRAPHY IMAGING OF SHEAR FRACTURE FORMATION IN LARGE REINFORCED CONCRETE BEAM

TATYANA KATSAGA and R. PAUL YOUNG

Civil Engineering Department, Lassonde Institute, University of Toronto, Toronto, Canada

Abstract

This study investigates the mechanisms of shear fracture formation in a large shear-critical reinforced concrete beam with large coarse aggregates by using acoustic emission (AE) and computed tomography (CT) techniques. AE and elastic wave velocities were measured using the Hyperion GigaRAM AE Recorder developed for ultra-detailed investigation of brittle fracture and failure of rock and rock-like materials. The analysis revealed complex spatial and temporal fracture development during the slow quasi-static fracture process. When AE events are related to cracks and concrete microstructure via CT images, they show how coarse aggregates influence fracture nucleation and development. Fractured aggregates are found at the place of fracture nucleation, and large aggregate particles cause non-uniform fracture propagation. Predominant microcrack mechanisms were revealed for different stages of fracture formation.

Keywords: X-ray computed tomography, concrete, aggregates, shear fracture

Introduction

Fractures in concrete are directly influenced by the complexity of concrete microstructure in all aspects from nucleation and propagation to surface roughness formation. Researchers have studied the influence using different techniques and approaches. One approach is to measure and analyze the fractal dimension of concrete fracture surfaces depending on the kind of aggregate [1] or the maximum aggregate size [2]. A correlation was found between fractal dimension and fracture toughness. Another approach involves non-destructive 3D studies using AE techniques [3-5]. These studies show how concrete microstructure influences fracture process zone, fracture energy and fracture toughness. Additionally, advanced AE techniques can be used to define AE source mechanisms [6-8].

Detailed nondestructive investigation of cracks inside materials becomes possible with the development of X-ray computed tomography (CT) techniques. Landis et al. [9] calculated fracture energy using the actual surface area of internal cracks using CT data collected during loading. Chen et al. [5] compared cracking paths, obtained by X-ray inspection, in concrete with different maximum aggregate size, and found that widths of the crack zone increase with increasing maximum aggregate size. Young et al. [10] combined CT imagery and AE to relate physical features within the sample to AE locations and phases of micro-scale damage.

In this study, in order to gain improved insight into 3D micro-mechanics of failure, AE techniques were employed during the shear failure testing of large reinforced concrete beam. The recorded AE event source locations were related to high resolution X-ray CT images obtained from core samples extracted from the beam after testing. Further, various aspects of failure were studied by analyzing the AE mechanism evolution throughout the fracture formation.

Experimental Procedure and Data Processing

A large, lightly-reinforced normal-strength concrete beam with large coarse aggregates (max size = 55 mm) was loaded to shear failure in a three-point bending test using the Baldwin test frame at the University of Toronto [11]. The specimen, designed to be shear-critical, was 9000 mm long, 1510 mm tall, 300 mm wide, and was supported on rollers spaced at 8100 mm apart.

AE setup

One half of the specimen was instrumented with AE sensors to record acoustic emissions induced from micro-cracking during loading. The concentrated array of 24 sensors, 16 receivers (V103, Panametrics) and 8 pulsers (R15, PAC) was designed to investigate diagonal shear fracture development before failure and was installed on the surface of the beam using special holders screwed into the concrete (Fig. 1a). The monitoring parameters were selected, based on the results of pencil-lead break or artificial shot (ultrasonic pulse) tests: 60 dB pre-amplification and 10 MHz sampling frequency.

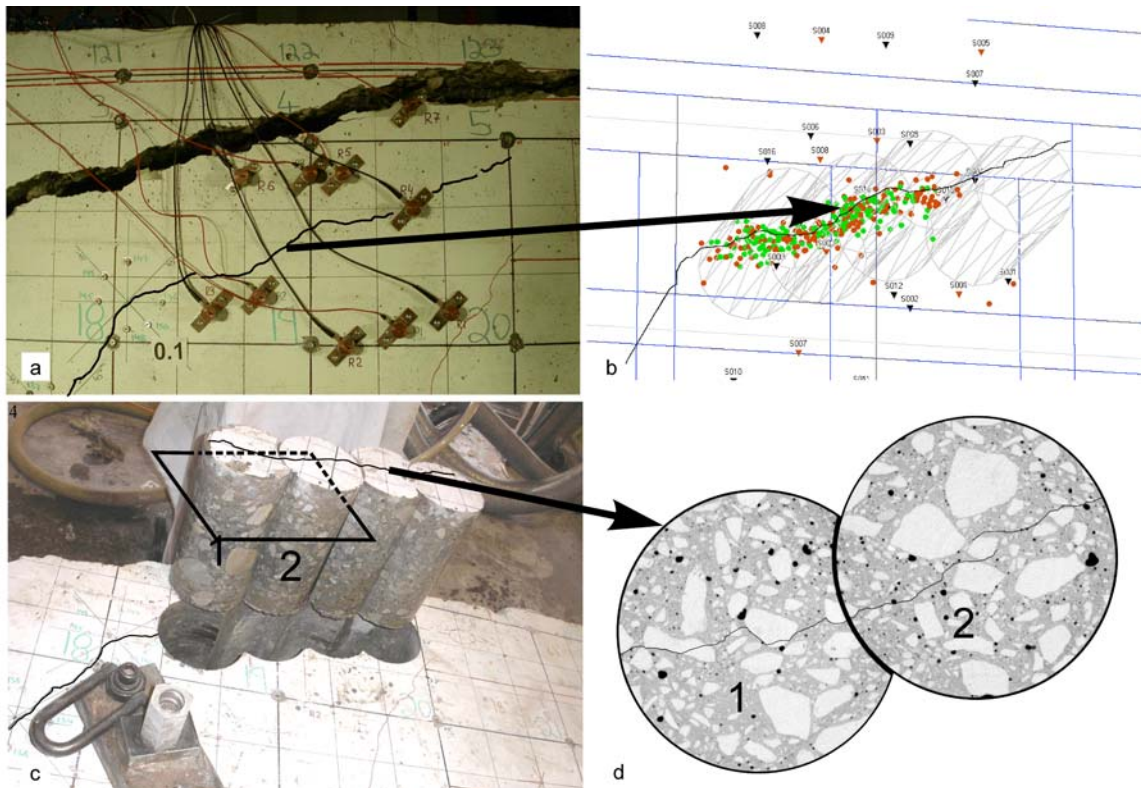


Fig. 1 (a) Beam with array of sensors after testing (front view); (b) AE activity related to slow fracture below final; (c) 300-mm cores extracted from the beam: the jagged black line identifies fracturing that has occurred in the cores; (d) CT images for two cores (section view).

Signals from the sensors were recorded using a 16-channel recording system called the Giga Recorder. The unique feature of this equipment is the ability to continuously monitor, in great detail, critical periods of acoustic activity during failure. Continuous waveforms can be sampled at rates up to 10 MHz on 16 channels, with durations up to 4 minutes long. These waveforms capture all AE events emitted during the recorded period and allow for the detailed investigation of failure. Traditional triggered data was also recorded throughout the entire experiment. The Giga Recorder approach is described in detail by Thompson et al. [12].

Computed tomography imaging

After the failure of the beam, four core samples were extracted from the beam with the segments of the fracture that preceded the final fracture. Position for the coring was defined based on AE event locations (Fig. 1b, c). Two samples were sent to the University of Texas for high-resolution X-ray CT [13]. The samples were imaged separately using the high-energy scanning system, which was designed for scanning large samples. Horizontal CT images were taken at 1 mm intervals across the sample diameter with resolution of 1024x1024 pixels (Fig. 1d) and clearly show the microstructure of the concrete including the aggregates, fractures and air voids.

Data processing

InSite [14] software was employed to analyze AE events and velocity data. Before AE data processing, P-wave velocities were defined, assuming straight raypaths between pulsers and receivers. Wave velocities transmitted through concrete beam did not show any preferred direction in velocity variations; so a homogeneous-isotropic velocity structure was assumed throughout the concrete volume. A combination of Simplex and Geiger methods was used for locating AE events. A custom Visual Basic application was developed to study the CT scan images in precise relation to the AE locations in AutoCAD. Events were filtered by ± 7 -mm slices from the plane of the image and were superimposed into this image.

To analyze the evolution of microcrack mechanisms during shear fracture formation, P-wave first-motion polarities were defined and analysed using a first motion polarity method (Zang et al., 1998):

$$pol = \frac{1}{k} \sum_{i=1}^k sign(A^i)$$

where A is the first motion amplitude and k is the number of sensors. In this study, positive polarity represents compressional pulses initiated by tensile fractures. Events are considered as tensile if $0.25 < pol < 1$; shear if $-0.25 < pol < 0.25$; implosion or collapsed events if $-0.25 < pol < -1$.

Results and Discussion

AE locations

AE source locations, divided into time periods A to E, are presented on Fig. 2 from the top point of view. Events for each time period are shown in different color. Symbol sizes are scaled according to their event magnitude. Periods A, B and 36 seconds of period C show triggered AE events, while the rest of period C, periods D and E show AE events extracted from continuous waveforms. AE locations exhibited non-uniform event distribution along the fracture surface width. During period A, 5 isolated events occur in the space ahead of the fracture front. During period B, several events nucleate at the position near to the front surface of the beam. Period C showed AE event development in two directions: forward and sideways, across the width of the beam in a narrow band leaving uncracked concrete between the band and the primary fracture front. During period D, the sideways fracture connected with the primary fracture front and propagated a few cm forward. Overall, 121 events were located. At the end of period D, microcracking is throughout region of eventual fracture surface. Period E showed 120 events occurring due to the shearing of the cracked surfaces at the fracture.

AE locations and crack topography

Studying CT images and AE events together allows the investigation of the relationship between fracturing and concrete properties. Figure 3a shows the first AE event nucleation at the level 70 mm during period B and Fig. 3b the secondary nucleation at the level 195 mm during period C. It is interesting to observe that both nucleations associate with aggregate fracturing.

Stronger than the surrounding material, aggregate particles cause stress concentration and trigger fracture nucleation. AE event accumulation was also found at the positions where fracture changed its direction (Fig. 3c).

Combination of CT images and AE events revealed the reason of non-uniform spatial fracture development during period C. Large particles of coarse aggregate were found on both sides from the AE band. These large aggregates locally strengthened material so the fracture was forced to propagate only between aggregates.

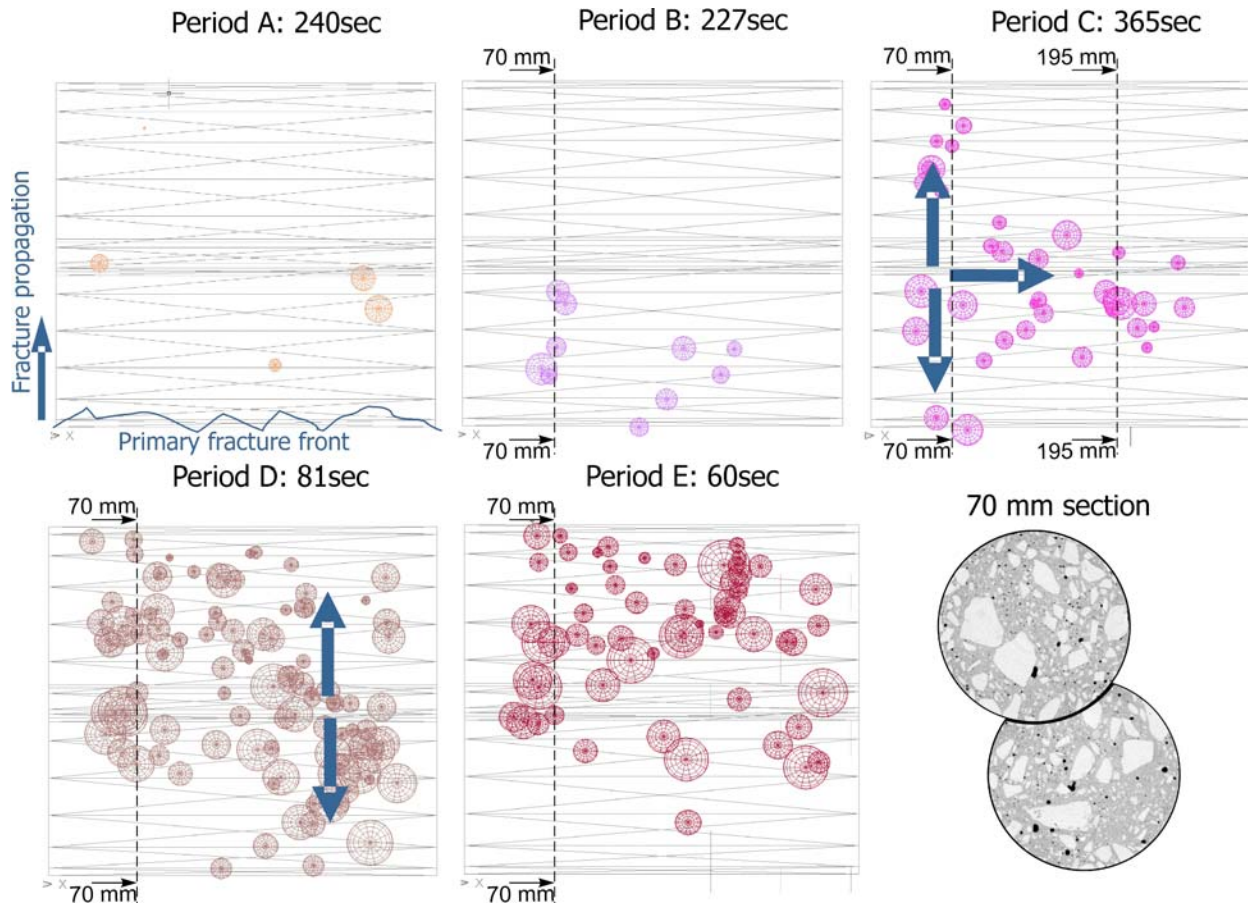


Fig. 2 AE source locations for different periods of fracture propagation.

AE Focal Mechanism

Table 1 combines the results of mechanism analysis and Fig. 4 shows examples of fault plane solutions. Moment tensors were analyzed for selected complex events with the equal number of positive and negative polarities.

The events during Period A, which signify fracture nucleation, are dominantly tensile. The number of tensile events decrease and the number of shear events increase with the fracture development. The implosion events are rare and there is no pattern of their occurrence. The shear events release the largest amount of energy and produce high magnitude events. Predominant number of shear events indicates the final stage of the fracture development.

Figure 4 shows the evolution of events and their mechanisms in 70 mm section. AE mechanisms are based on fault plane solutions obtained using first motion polarities. Tensile cracks (#2639, #2654, #2729, #2836) and one larger CLVD (compensated linear vector dipole) event (#2668) initiate the fracture. CLVD event occurred at the place where aggregate was fractured at the edge. Tensile events also appear during the next period ahead the fracture (#3336, #3496,

#3538, #3566, #3606). It was found that subsequent events that occurred close to the preceding events are shear events. For example, shear event #3328 (period C) appeared next to events #2639 and #2654 (Period B). Events occurred during Periods D and E are predominantly shear events.

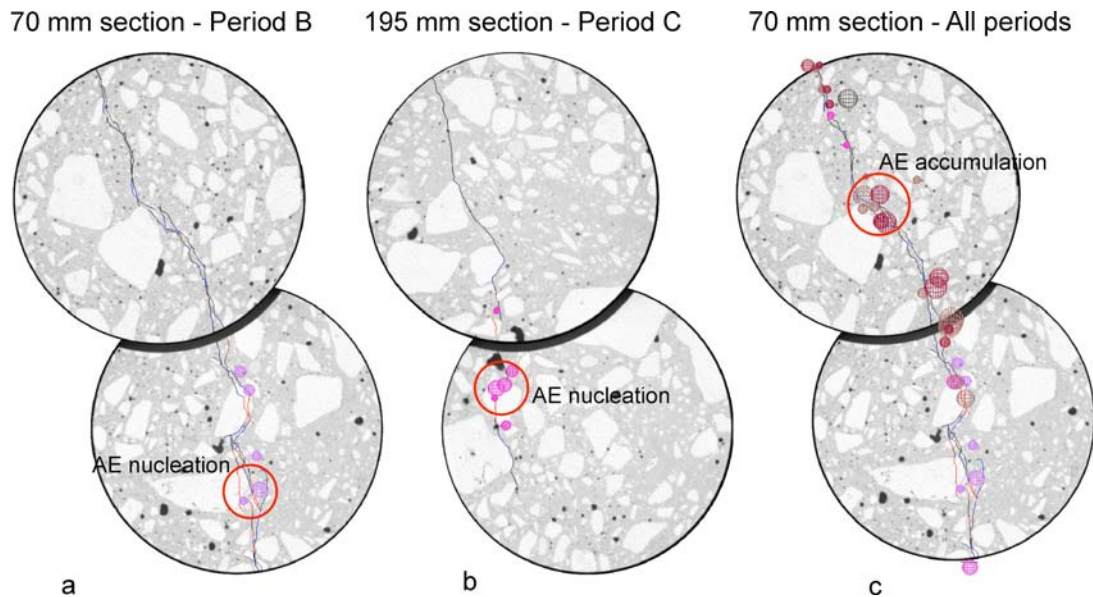


Fig. 3 CT images and corresponding AE events for different sections.

Table 1. Variation of event types with fracture development

Periods of fracture propagation	Duration sec	Number of events	Mechanism		
			Tensile %	Shear %	Implosion %
Period A	240	5	80	20	0
Period B	227	11	67	33	0
Period C	365	39	58	33	8
Period D	81	121	49	32	19
Period E	60	120	25	66	9

Conclusion

The combination of CT and AE imaging gives a unique opportunity to study AE events in relation to the microstructure of material. The AE event locations revealed complex non-uniform spatial and temporal fracture development in the concrete with the large aggregates at the slow quasi-static stage of fracture propagation. The high-resolution CT images resulted in detailed images of the concrete microstructure including the aggregates, cracks and air voids.

As expected, the cracks on the CT images showed a close correlation with AE events. Analysing the temporal and spatial evolution of AE events in relation to the CT images allows the precise reconstruction of the failure sequence. Coarse aggregates are shown to play an important role in fracture nucleation and development: aggregate fracturing is found at the place of fracture nucleation and non-uniform fracture propagation is explained by the influence of large pieces of aggregates. AE event accumulation takes place when the fracture changes its direction.

AE mechanism analysis revealed that new fracture development associates mainly with tensile events and subsequent events at the nearest position are shear events. During fracture development, the number of tensile events decreases and the number of shear events becomes dominant (66%) due to shearing of cracked surfaces. Therefore, studying the predominant mechanisms during monitoring or inspection can be helpful in defining the stage of fracture development.

The overall results of the work show that the combination of AE and CT imaging provides an extremely effective tool for the investigation of the process of fracture formation in materials with complicated microstructure.

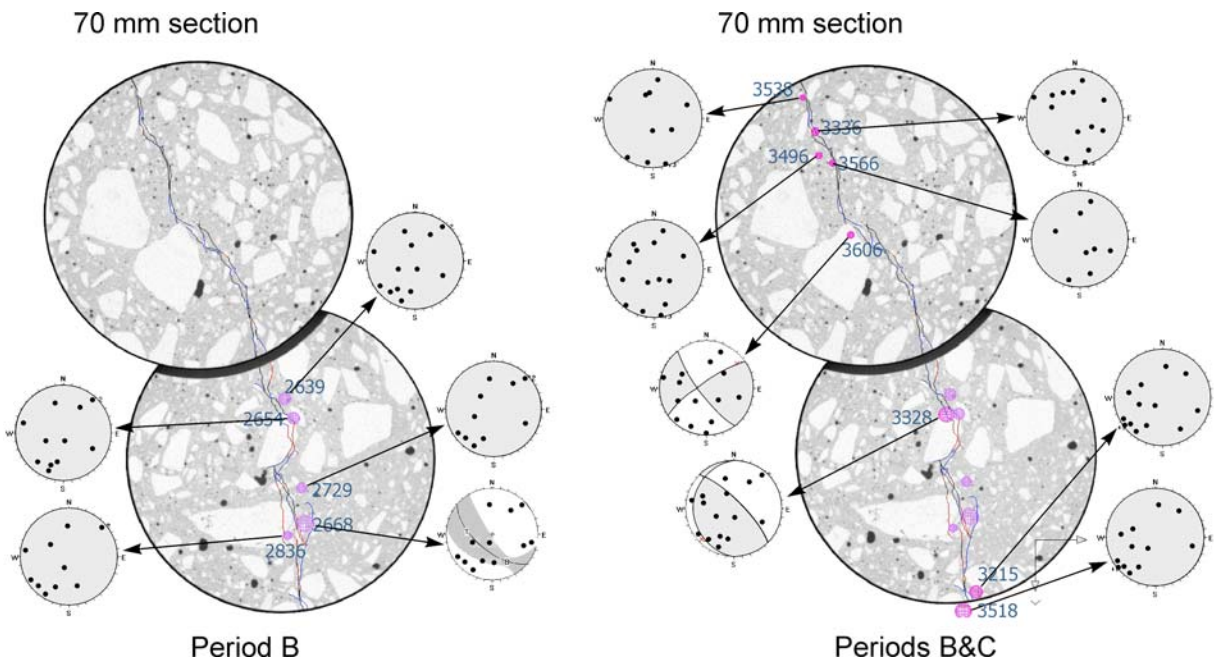


Fig. 4 CT images, corresponding AE events and their fault plane solutions: shaded regions on the fault plane solutions represent compression.

References

1. A.M. Brandt, G. Prokopski, *J. Mater. Sci.*, **28**, 1993, 4762-4766.
2. M.A. Issa, M.S. Islam, and A. Chudnovsky, *Eng. Fract. Mech.*, **70**, 2003, 125-137.
3. H. Mihashi, N. Nomura, and S. Niiseki, *Cement Concrete Res.*, **21**, 1991, 737-744.
4. E.N. Landis and S.P. Shah, *Advn. Cem. Bas. Mat.*, **2:3**, 1995, 105-118.
5. B. Chen and J. Liu, *Constr. Build. Mater.*, **18:8**, 2004, 585-590.
6. A. Zang, F.C. Wagner, S. Stanchits, G. Dresen, R. Andresen, and M.A. Haidekker, *Geophys. J. Int.*, **135**, 1998, 1113-1130.
7. M. Ohtsu, T. Okamoto, and S. Yuyama, *ACI Struct. J.*, **95:2**, 1998, 87-95.
8. C.U. Grosse, H.W. Reinhardt, and F. Finck, *J. Mater. Civil Eng.*, **15:3**, 2003, 274-279.
9. E.N. Landis and E.N. Nagy, *Engineering Fracture Mechanics*, **65**, 2000, 223-234.
10. R.P. Young and B.D. Thompson, *Proc. 11th International Congress on Rock Mechanics*, Lisbon, 2007.
11. E.G. Sherwood, E.C. Bentz, and M.P. Collins, *ACI Struct. J.*, **104:2**, 2007, 180-190.
12. B.D. Thompson, R.P. Young, and D.A. Lockner, *Pure Appl. Geophys.*, **163:5-6**, 2006, 995-1019.
13. R.A. Ketcham and W.D. Carlson, *Computers & Geosciences*, **27**, 2001, 381-400.
14. Applied Seismology Consultants. <http://www.seismology.org/insite.aspx>. Cited July 31, 2007.

GLOBAL MONITORING OF CONCRETE BRIDGE USING ACOUSTIC EMISSION

T. SHIOTANI, D. G. AGGELIS and O. MAKISHIMA*

Research Institute of Technology, Tobishima Corporation, 5472 Kimagase, Noda, Chiba, 270-0222, Japan; *Civil Engineering Headquarters, Tobishima Corporation, Sanbancho, Chiyoda, Tokyo, 102-8332, Japan

Abstract

Global monitoring of civil structures is a demanding challenge for engineers. Acoustic emission (AE) is one of the techniques that have the potential to inspect large volumes with transducers placed in strategic locations of the structure. In this paper, the AE technique is used to characterize the structural condition of a concrete bridge. The evaluation of AE activity leads to information about any specific part of the structure that requires attention. Consequently, more detailed examination can be conducted once the target area is selected. In this study, surface wave investigation was subsequently performed to detail the condition of the target area.

Keywords: Concrete structures, damage assessment, global monitoring, surface wave velocity.

Introduction

The deterioration of civil infrastructure worldwide calls for effective methods for damage evaluation. One of them, AE monitoring technique, uses signals generated within the structure, which are due to crack growth under stress, as well as secondary emissions due to friction of crack interfaces. This unique monitoring technique parameterizes the fracture/failure process, and distinguishes it from other nondestructive tests. This is the only one capable of real-time mapping of fracture processes. In addition to real-time source identification from the acquired AE signals, the energy level or “magnitude” of the detected signals can be evaluated, and provides immediate evidence of the degree of damage. A particular engineering advantage of the AE technique is its efficiency for global monitoring since a large and complex structure can be monitored with a limited number of sensors. Consequently, the most crucial part of the structure can be targeted with a more detailed AE monitoring for quantification of AE indices [1-4], or using other suitable techniques [5]. Results obtained from the AE testing depend highly on many external parameters such as the applied load and loading rate, the properties of the material and the type of structure. These factors restrict the development of comprehensively applicable tools. Additionally, due to the complex composition of most civil structures, AE waveforms depend on their propagation path from the source to the sensors [6]. However, in any case, valuable information can be extracted concerning which part of the structure has sustained the most severe deterioration.

In the specific case presented herein, a 45-m bridge span is under examination. Preliminary investigations of surface-crack observation and physical tests of excavated cores did not reveal any extensive damage. The cores can characterize only the area where they were extracted and the surface observation cannot reveal internal damage. Therefore, further monitoring was conducted with AE technique. The AE testing was performed by applying stress with the mobile load of a heavy vehicle. Based on the AE activity the part of structure more likely to exhibit higher degree of damage than the other areas in the longitudinal direction was selected for the

detailed investigation. A similar application on a much smaller scale was reported in [2]. A surface ultrasonic examination, which is indicative of the quality [7, 8], followed in order to investigate the pulse velocity of concrete at the area of interest.

Experimental Procedure

For the AE monitoring, 28 sensors were attached in all to the bottom surface of the bridge using a wax. They were placed on the longitudinal axis of the bridge with a separation of 1.4 m as shown in Fig. 1. Specifically, the sensitive AE sensors to concrete structures, R6 of PAC, were used. These sensors exhibit nominally the maximum sensitivity at 60 kHz and are widely used for concrete monitoring. The detected AE signals were pre-amplified by 40 dB and acquired by two synchronized data acquisition systems, namely a 16-channel DiSP and a 12-channel Mistras of PAC. Strain gauges were also placed in three locations on the top surface of the bridge, as shown in Fig. 1.

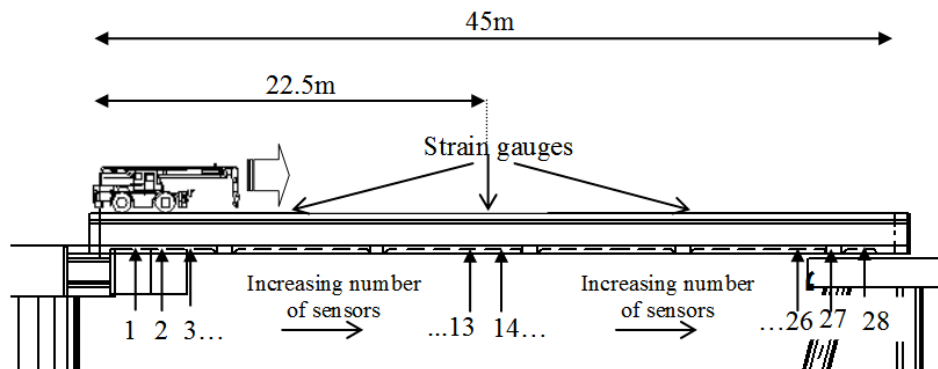


Fig. 1. Representation of the crane passing over the bridge and sensor location.

Acoustic Emission Activity

Damage indices

The interpretation of the detected AE activity is not always easy. This is the reason why different indices have been suggested and applied for the purpose of damage quantification. As stated earlier, when a material or structure is stressed, AE is produced. Additionally, the behavior during unloading is also crucial. In case the material is intact (or the applied load is low), the AE activity during unloading is of low intensity. For damaged material, the emission continues even during unloading. The number of AE hits during unloading divided by the number of hits during the whole cycle is defined as the calm ratio and values near zero indicate intact material condition [2, 4, 9].

Another index comes from the analysis of the amplitude distribution of AE events, or so called the improved *b*-value analysis [1, 4]. Although a large-scale fracture in general corresponds to large AE peak amplitude, the use of the amplitude solely can be misleading. This is because the accumulated damage increases the materials' attenuation rate due to scattering at the cracks. Therefore, even a high amplitude signal will be severely attenuated before being recorded by the sensors. In this respect, the amplitudes are studied through their cumulative distribution that uniquely changes as the damage is accumulated. Specifically, the gradient of the distribution is calculated. With the evolution of damage, this slope decreases, meaning simply that the ratio of the large energy AE events to that of the small relatively increases in the total population of AE events. It has been confirmed that at the moments of extensive cracking, the *Ib*-value exhibits severe drops [10-14].

AE monitoring results

The load for the AE monitoring was applied by a 20-ton crane vehicle, which passed three times over the bridge with a constant speed of approximately 0.5 m/s, as seen in Fig. 1. As the crane moved over the bridge, the strain and stress fields changed. The compressive strain measured on the top surface of the bridge at the mid-span can be seen in Fig. 2. The maximum strain was recorded at 88 s, when the vehicle was in the middle of the span, suggesting the highest tensile stress at the bottom layer of the structure. In the same figure, the cumulative number of AE hits recorded by all the sensors is depicted for one passage. It can be seen that the rate of AE hits was more intensive before the crane reached the center of the bridge at 88 s. Up to that moment, more than 70% of the total number of hits was recorded, implying that more active sources were located in the first half of the bridge.

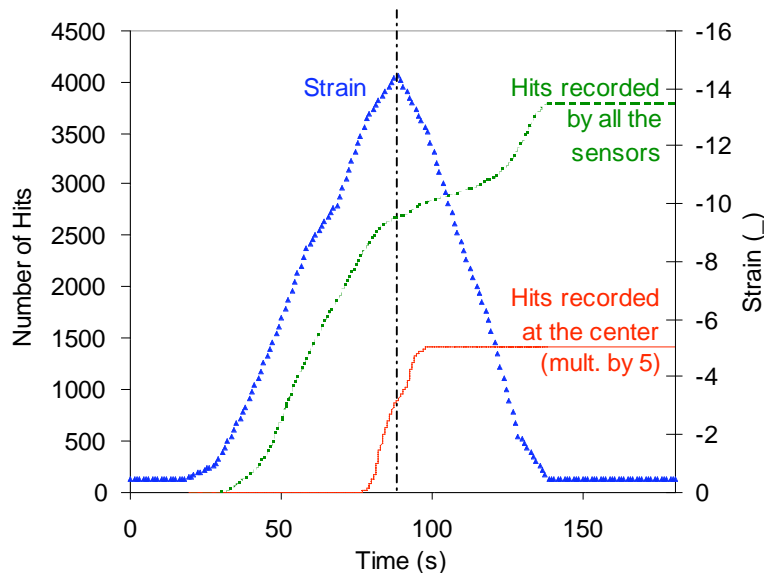


Fig. 2. Time history of strain at the center and cumulative AE hits during crane passage.

As stated, in order to calculate the calm ratio, the AE activity should be correlated with a measured mechanical parameter. In this case, this was conducted using the measured strain at the middle point and the AE activity of the center part, recorded by the two sensors placed closest to the center (13 and 14 of Fig. 1). The activity of these sensors and AE hits of all sensors combined are plotted in Fig. 2. For clarity, the middle sensor hits are multiplied by a factor of 5. The hits of the middle sensors started at 74.5 s as the crane was approaching, and the last hit was recorded 10 s after the crane had passed over the bridge center, showing the intensive AE activity even during unloading. The number of hits for three different trips of the crane and the resulting calm ratios are presented in Table 1. The calm ratios concerning the center part of the bridge range from 0.3 to 0.45 for any individual passage of the crane, indicating serious damage according to past studies [2, 11, 12, 16, 17]. The attenuation rate of the material was measured at 7.0 dB/m and the average first hit amplitude reaching a sensor was 54 dB. Accordingly, the sensors can capture hits originating at least 2 m away. Considering also the separation of 1.4 m between sensors 13 and 14, one can assume that this calm ratio is characteristic of a span of 4 to 5 m in the middle of the bridge.

Ib-value analysis

In Fig. 3, the *Ib*-values based on the AE events located at different zones of the bridge are plotted for the three different passages of the crane. The span was divided into 12 zones of

Table 1. Number of AE events for different stages of loading and calm ratios.

Trip	Loading	Unloading	Calm ratio
1	175	146	0.455
3	409	179	0.304
5	295	208	0.414

3 m each, in order to allow the number of events for the *Ib*-value calculation. Specifically, the total number of events to be considered for the calculation of the *Ib*-value should be above 50 [1, 10-14]. The number of events for the same zones is also shown in the chart. It is evident that some areas of the structure exhibited larger number of events than others as seen in Fig. 3 and the *Ib*-value is calculated for the zones only exhibiting more than 50 events. Focusing on the *Ib*-values, it is seen that they vary between 0.05 and 0.13. According to established correlations, values above 0.2 imply the intact condition, between 0.1 and 0.2 suggests the moderate damage and it is becoming more intense as the *Ib*-value decreases below 0.1 [1, 2, 12]. This shows that a large part of the structure is deteriorated. While the limited AE activity of the rest does not allow the evaluation of this parameter, there were not many active sources in that area.

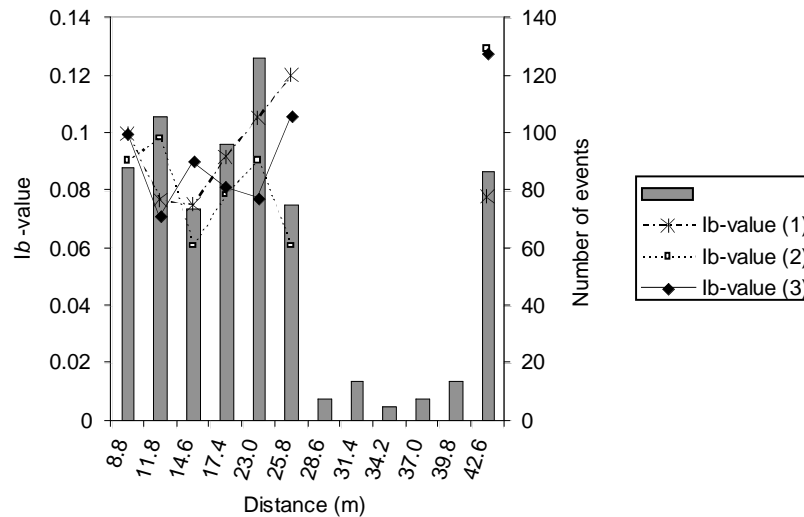


Fig. 3. *Ib*-values for three different trips of the crane and indicative AE events for the first trip.

Velocity measurements

In order to make a more detailed examination of the active area of AE activity, wave velocity measurements were made. Velocity has been established as an indicator of concrete quality for many decades and it is accepted that velocity above 4000 m/s indicates high quality, while below 3000 m/s suggests poor quality [7, 17].

For the velocity measurement, nine AE sensors were used in an arrangement of three parallel arrays of three. The separation distance was 1.5 m, resulting in an examined area of 3 m by 3 m, see Fig. 4. The excitation was conducted by pencil-lead break near the location of each transducer. Therefore, each time, one sensor was used as trigger for the acquisition and eight as receivers. In this way, a number of intersected paths were examined, and the results can be considered more representative of the area and more reliable than single measurement between two points. The velocity was measured by the time of the first detectable disturbance of each waveform, which corresponds to the onset of longitudinal waves.

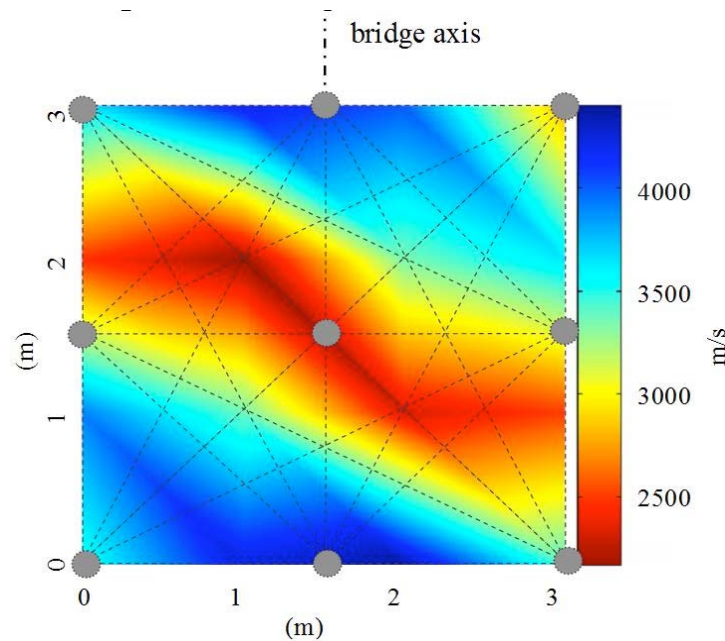


Fig. 4. Velocity structure of the bottom surface of the concrete bridge. The positions of the transducers are indicated by circle and the examined wave paths by dashed lines.

The transit times of the individual paths, along with the sensor positions were supplied to a suitable tomography program [18]. This way the visualization of the velocity structure was obtained and the information of which parts of the surface area exhibit lower velocity than others was obtained as shown in Fig. 4. From this figure, considerable discrepancies of the wave velocity were found within the area of 9 m^2 . Specifically, a zone approximately in the center of the selected area exhibited velocities close 2500 m/s , while other areas had velocity higher than 4000 m/s . Presumably there is a certain defect in this area although the cause inducing the AE activity has yet to be identified. Concrete cracks, delaminations of different layers (e.g. asphalt on concrete) or friction between the tendon ducts and matrix concrete are possible origin contributing to the AE observed. Follow-up investigations focusing on this weak area will clarify the source. This sequential investigation started with AE activity followed by detailed measurements of ultrasonic velocity is useful in characterizing the quality of large-scale concrete structures.

Conclusions

In this paper, the suitability of acoustic emission to monitor large concrete structures is presented. The AE technique was initially used to select the most deteriorated area based on the number of AE events and the values of quantification indices like the calm ratio and Ib -value. The subsequently conducted ultrasonic examination exhibited very low velocities confirming that the area indicated by AE activity was actually deteriorated. This shows the potential of AE testing as a global monitoring for examination of large volumes using a limited number of sensors. Even if AE indices or parameters cannot be directly correlated with the degree of damage, they suggest which part of the structure needs further and detailed investigations. Subsequently, wave velocity measurements were conducted allowing a more general evaluation through the reported correlations between velocity and concrete quality. It is suggested that the combination of such stress wave techniques as AE and surface wave examination can assess the degree of damage of large civil structures that so far has been difficult to attain.

References

- 1) T. Shiotani, K. Fujii, T. Aoki, K. Amou, Evaluation of progressive failure using AE sources and improved b -value on slope model tests, *Prog. Acoust. Emiss VII*, (1994), JSNDI, Tokyo, pp. 529-534.
- 2) M. Ohtsu, M. Uchida, T. Okamoto, S. Yuyama, Damage assessment of reinforced concrete beams qualified by acoustic emission. *ACI Structural Journal*, **99**(4), (2002), 411-417.
- 3) C. Grosse, H. Reinhardt, T. Dahm. Localization and classification of fracture types in concrete with quantitative acoustic emission measurement techniques. *NDT&E Int*, **30**(4), (1997), 223–230.
- 4) T. Shiotani, Evaluation of long-term stability for rock slope by means of acoustic emission technique, *NDT&E Int*, **39**(3), (2006), 217-228.
- 5) V. M. Malhotra, N. J. Carino (Eds.), *CRC Handbook on Nondestructive Testing of Concrete*, (1991), CRC Press, Florida.
- 6) B. Schechinger, T. Vogel, Acoustic emission for monitoring a reinforced concrete beam subject to four-point-bending, *Construction and Building Materials*, **21**(3), (2007), 483-490.
- 7) T. R. Naik, V. M. Malhotra, The ultrasonic pulse velocity method, in: Malhotra, V. M., Carino N. J., (Eds.), *CRC Handbook on Nondestructive Testing of Concrete*, (1991), CRC Press, Florida.
- 8) T. Gudra, B. Stawinski, Non-destructive characterization of concrete using surface waves, *NDT&E Int*, **33**, (2000), 1-6.
- 9) S. Colombo, M. C. Forde, I. G. Main, M. Shigeishi, Predicting the ultimate bending capacity of concrete beams from the “relaxation ratio” analysis of AE signals, *Construction and Building Materials*, **19**, (2005), 746-754.
- 10) T. Shiotani, M. Ohtsu, K. Ikeda, Detection and evaluation of AE waves due to rock deformation, *Construction and Building Materials*, **15**(5-6), (2001), 235-246.
- 11) T. Shiotani, Y. Nakanishi, X. Luo, H. Haya, T. Inaba, Damage evaluation for railway structures by means of acoustic emission, *Key Engineering Materials*, **270-273**, (2004), 1622-1630.
- 12) T. Shiotani, Y. Nakanishi, X. Luo, H. Haya, Damage assessment in deteriorated railway sub-structures using AE technique, *Journal of Acoustic Emission*, **22**, (2004), 39-48.
- 13) J. H. Kurz, F. Finck, C. U. Grosse, H. W. Reinhardt, Stress drop and stress redistribution in concrete quantified over time by the b -value analysis, *Structural Health Monitoring*, **5**, (2006), 69-81.
- 14) S. Colombo, I. G. Main, M. C. Forde, Assessing Damage of Reinforced Concrete Beam Using “ b -value” Analysis of Acoustic Emission Signals, *Journal of Materials in Civil Engineering-ASCE*, **15**(3), (2003), 280-286.
- 15) T. Shiotani, D. G. Aggelis, Damage quantification of aging concrete structures by means of NDT, *Proc. of Structural Faults and Repair-2006*, June 13-15, Edinburgh, (in CD).
- 16) T. Shiotani, X. Luo, H. Haya, Damage diagnosis of railway concrete structures by means of one-dimensional AE sources, *Journal of Acoustic Emission*, **24**, (2006), 205-214.
- 17) M. F. Kaplan, The effects of age and water/cement ratio upon the relation between ultrasonic pulse velocity and compressive strength. *Mag. Concr. Res.*, **11**(32), (1959) 85–92.
- 18) Y. Kobayashi, H. Shiojiri, T. Shiotani, Damage identification using seismic travel time tomography on the basis of evolutionary wave velocity distribution model, *Proc. Structural Faults and Repair-2006*, June 13-15, Edinburgh. (in CD).

MAPPING OF WHEEL FLANGE RUBBING ON RAIL USING AE: LABORATORY TEST

N. A. THAKKAR, R. L. REUBEN and J. A. STEEL

Mechanical Engineering, School of Engineering and Physical Sciences, Heriot-Watt University,
Riccarton, Edinburgh, Scotland EH14 4AS UK

Abstract

Abnormal contact stresses between wheels and rails can give rise to excessive rail wear and, in more extreme cases, to rolling contact fatigue (RCF) and gauge corner cracking (GCC). The independent investigation into the Hatfield train disaster in the UK, whose primary cause was a rail defect, highlighted the need for improved awareness of the condition of railway rails. This work is aimed, not specifically at detecting rail cracks, but at monitoring the intensity of contact between wheel and rail using acoustic emission with a view to making an in-service update of estimated remanent life.

A test-rig has been built in order to simulate rail-wheel contact, providing for variations in normal contact force and rolling speed, and allowing the simulation of a range of defects in a way that would not be possible at full scale. In this paper, wheel flange rubbing on the rail (a precursor to GCC) has been simulated and monitored using acoustic emission (AE).

A simple analytical model for AE arising from normal wheel contact has been used to locate parts of the track where a wheel flange is rubbing on the rail. The method works by comparing AE peaks above normal with natural defects with and without the additional defect of flange rubbing, calculating a cross-correlation function, whose peakedness is an indication of how well correlated the defects are with the AE peaks. In all cases, cross-correlations were better when rubbing was present indicating that flange rubbing can be detected even in the face of natural defects.

Keywords: Rail/wheel interaction, structural integrity monitoring.

Introduction

Fracture of railway rails can have serious consequences [1], and some shallow angle defects cannot easily be identified even by the most advanced NDT defect detection techniques [2]. Contact stresses are responsible for rail defects and Miller [3] has identified the main factors affecting contact stresses as external load, traction force, and rail-wheel contact area. Contact area and hence the stress between rail and wheel had been measured as a function of load using ultrasonic NDT although this has not yet been used to establish the exposure to wear and surface fatigue under a range of conditions, such as load, speed and surface lubrication [4, 5]. More detailed mechanics analyses based on contact stresses (e.g., Ringsberg and Josefson [6]) have established the conditions for RCF initiation on rail heads.

Acoustic emission monitoring has been applied to a number of contact problems, such as bearings and defects, and has been found to be sensitive to bearing defects [7] and gear defects [8] in reciprocating and rotating machineries. Contacts involving curved surfaces lead to particular issues with durability and, given that contact between a ball bearing and race and between rails and wheel have some similarities [9], it is reasonable to suppose that AE monitoring can be used to examine the rail-wheel interaction and perhaps also be sensitive to surface and subsurface condition. It has already been claimed that fatigue initiation and propagation in rolling

contact fatigue (RCF) can be detected using AE, Guo *et al.* [10]. Equally, it has been found that ultrasound is not useful for identifying gauge corner cracking in rails and even the eddy current technique is not able to find all individual rail surface defects [2].

The principle of this work is that AE can be used to determine whether the contact between a rail and wheel is “normal” or abnormal, abnormalities being defined as rough areas of the rail surface, out-of-round wheels, poor flange conformity or misshapen rails. Being able to do this would allow a rail-mounted sensor to be used to count the contact cycles in terms of intensity as well as number in a way that could not be derived from traffic figures alone, thus supplementing rail maintenance management systems. In earlier work, Thakkar *et al.* [11] devised an analytical model for the particular experimental set-up used, which describes the AE level from normal rolling using some simple AE propagation coefficients derived from pencil-lead break tests on the track. This model was used to identify areas on the track where natural surface defects cause additional AE in a similar way to defect identification in bearings and gear teeth. In this paper, a parallel set of experiments is reported, using the same track surface condition, but with an eccentricity of the wheel trajectory in relation to the track, so that flange rubbing takes place over a controlled length of the track.

Experimental Procedure

The test rig (Fig. 1b, c) consisted of a circular track round which a single wheel was driven using a motor at the centre of the track and a rigid arm, to which the wheel was attached. To obtain a rubbing effect of the wheel flange on the track, the motor shaft was displaced by about 2.4 mm (Fig. 1a) from the centre of the circular track. The variation of contact around the circumference was therefore mostly “normal” with an arc, within which the flange comes into contact with the rail, reaches a maximum contact load and then comes out of contact with the rail.

PAC Micro-80D AE sensors and PAC type 1220A preamplifiers (dual gain 40dB-60dB) were mounted on one side of the joint in the circular track (Fig. 1b) and connected to an NI 6115 data acquisition board used to collect raw AE data.

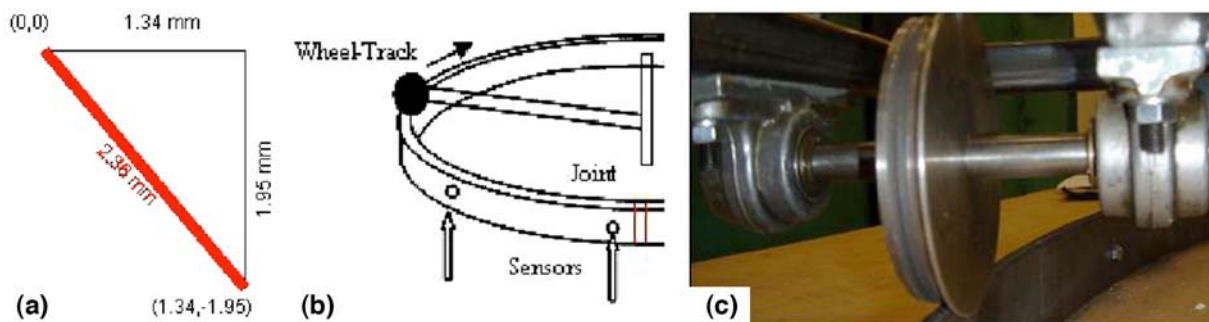


Fig. 1: (a) Motor shaft displacement, (b) Sensor positions on rail, (c) Wheel flange rubbing on rail.

The sensors were mounted on the web of the rail at 0.1 m and 1 m from the joint, the sensor nearest the joint being used as the trigger sensor and the other to collect the data for processing. The mounting points were cleaned with sand paper and vacuum grease was used as a couplant with the sensors being held against the surface using magnetic clamps. Data was acquired at 2.5 MHz, for 5 million samples corresponding to 2-seconds recording time in which the wheel moves, for a speed of 3.5 ms^{-1} , 7 m including the pre-trigger distance (0.14 m), completing more than a full revolution of the test rig (5.4 m circumference). Four different wheel speeds (1 ms^{-1} ,

1.5 ms⁻¹, 3 ms⁻¹ and 3.5 ms⁻¹) were used and four different contact loads (4 kg, 5 kg, 6 kg and 6.5 kg) were applied. Five records were taken for every wheel speed and load giving a total 80 records under 16 different conditions. The track was made from 50 mm×6.25 mm profiled mild steel bar cold bent into the circular shape and joined by a simulated fish plate with a 3 mm gap. The wheel was of cylindrical shape of diameter 90 mm with a flange on the inner edge and was mounted on two rolling element bearings (Fig. 1c).

A dial gauge was mounted on the supporting arm (Fig. 2a) to measure the position of the rail relative to the motor shaft after displacement (Fig. 1a) and measurements of the radial distance between the rail and the arm tip taken at regular intervals around the track circumference. The actual fitted (through measured points) and nominal circles are shown to scale in Fig. 2b, the nominal circle being the one, which assumes the design radius of 850 mm and a centre at (0,0). Figure 2c shows the same data with the radial coordinate amplified by subtracting 840 mm from each radial value, and shows the flange contact zone, which corresponds to distances of 1.4 to 2.4 metres from the joint.

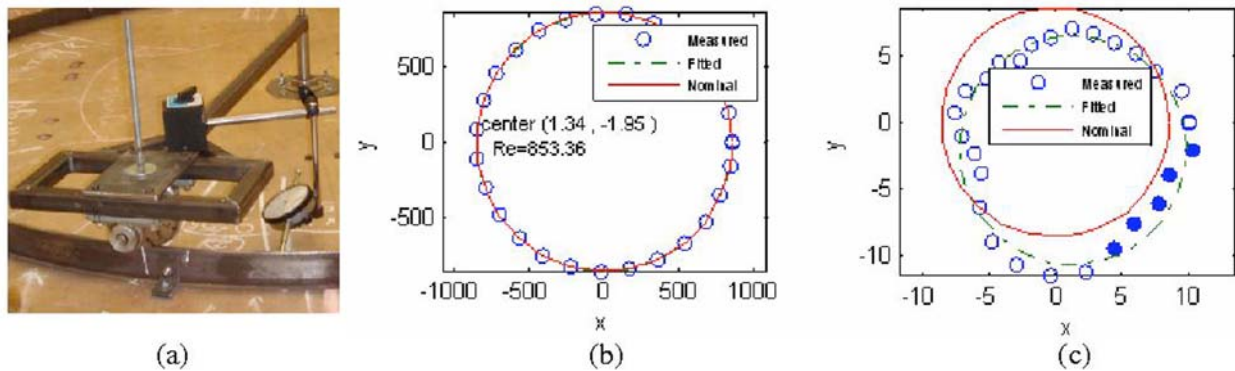


Fig. 2. (a) Dial gauge on supporting arm, and measured points and fitted and nominal circles, (b) at full scale and (c) with amplified radial scale

Results and analysis

A simple attenuation model has been developed [11], which treats the wheel as a moving source generating AE energy, E_0 . The energy, E_t , recorded at a fixed sensor at a circumferential position x_1 or x_2 relative to the wheel for the wheel approaching and travelling away from the sensor is given by equations 1 and 2, respectively:

$$E_t = E_0 e^{-kx_1} + RE_0 e^{-k((c_2-x_1)+c_2)} + RE_0 e^{-k(c_1-(c_2-x_1)+(c_1-c_2))} + TE_0 e^{-k(c_1-x_1)} + TE_0 e^{-k(c_1+x_1)} \tag{1}$$

$$E_t = E_0 e^{-kx_2} + RE_0 e^{-k(x_2+c_2+c_2)} + RE_0 e^{-k(c_1-(c_2+x_2)+(c_1-c_2))} + TE_0 e^{-k(c_1-x_2)} + TE_0 e^{-k(c_1+x_2)} \tag{2}$$

The model considers various paths from the wheel to the sensor. The attenuation coefficient ($k = -0.57$ dB/m), reflection coefficient ($R = 48\%$) and transmission coefficient ($T = 25\%$) were measured using separate pencil-lead break tests with a four-sensor array, leaving a single unknown (E_0), which can be varied to produce a best-fit level of the model. Comparing the circumferential variation in AE with the best-fit model allows the identification of areas where there is an indication of abnormal contact. Figure 3 shows five independent measurements of the rms averaged AE (averaging time 0.01 s) along with the fitted normal contact curves for one example of a wheel velocity of 3.5 ms⁻¹ and a preload of 4 kg. As can be seen, the signal is significantly and consistently above the model fit in the flange rubbing zone, highlighted by black fill, between D1 and D2.

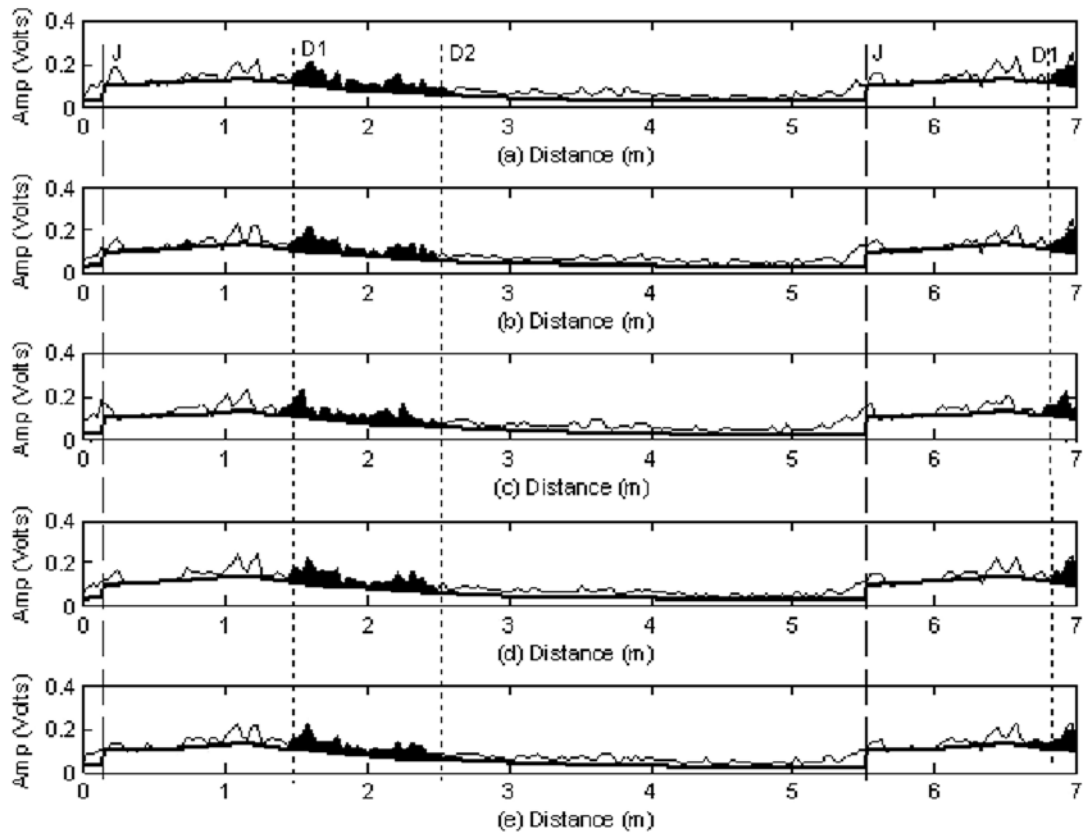


Fig. 3: Measured rms AE at a wheel speed of 3.5 m/s. — rms AE; - - - analytical model.

The dashed lines marked with “J” are the positions where the wheel passes over the joint and here spikes are evident due to wheel impact on the joint. The location of the joint in the AE record is an important part of the curve-fitting process as it allows the discontinuity between Eq. 1 and Eq. 2 to be identified. At the example wheel speed of 3.5 ms^{-1} , the wheel arrives twice at the sensor during each record.

In the earlier work [11], the natural defects on the surface of the rail were measured and Fig. 4 shows their intensity, measured as the total length of defect per 0.1-m length of track alongside the rms AE above background noise again averaged per 0.1-m length of track for each of the five records at the example condition of 3.5-ms^{-1} wheel speed and 4-kg load. Figure 5 shows the corresponding autocorrelation function for each of the five records with their corresponding kurtosis values, ranging from 1.9 to 2.07. Figure 6 shows the defect intensity distribution with flange rubbing added, along with the corresponding AE signal above normal rolling. Figure 7 shows the cross-correlations for the flange-rubbing case along with the corresponding values of kurtosis (1.66 to 1.88) for comparison with Fig. 5, again for the example condition. As can be seen, the kurtosis is improved over the case without flange rubbing.

Applying the same approach to the remaining speeds at a 4-kg load yields similar results, and Fig. 8 shows the averaged value of kurtosis for the five records at each condition. It is clear that the average kurtosis is always smaller with flange rubbing, indicating a more peaked cross-correlation function, although the difference is more marked at the lowest speed, where the kurtosis is generally higher, indicating generally poorer cross-correlation. It is suspected that the poor correlation for low speeds is partly due to the fact that a complete revolution is not acquired in the low-speed records and, more importantly, to the fact that the sensitivity to natural defects is low at low speeds; this is also the case for low loads. Whereas the effect of speed and load on

sensitivity to natural defects is a matter for future investigation, it appears at present that the sensitivity to flange rubbing is not affected as much by the experimental conditions.

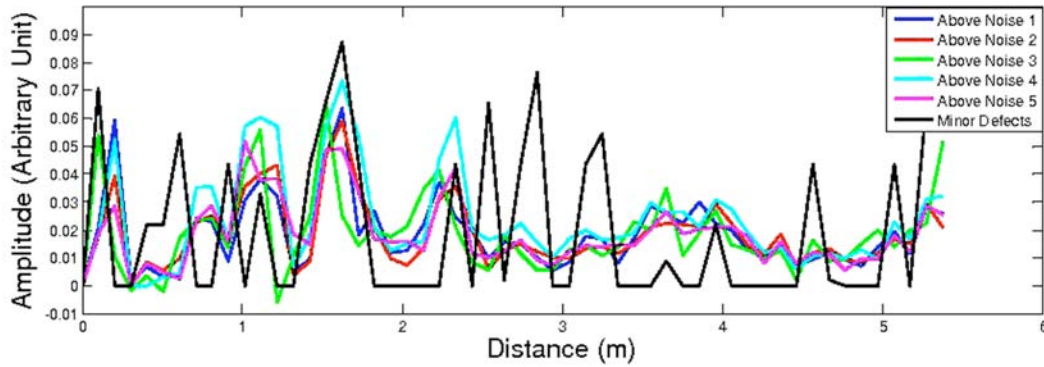


Fig. 4: Signal above normal and defect intensity without flange rubbing.

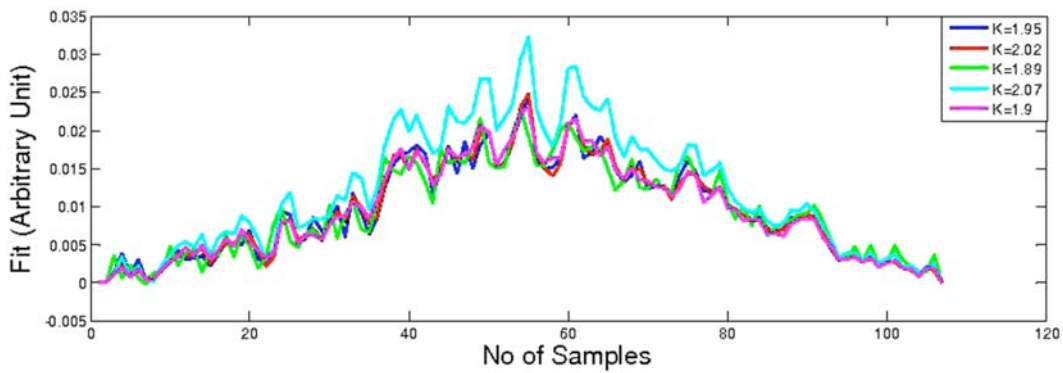


Fig. 5: Cross correlation between defect intensity and AE above normal without flange rubbing.

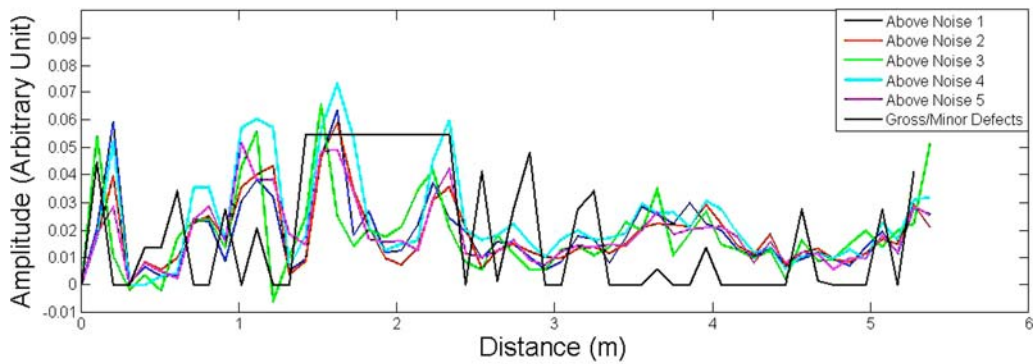


Fig. 6: Signal above normal and defect intensity with flange rubbing.

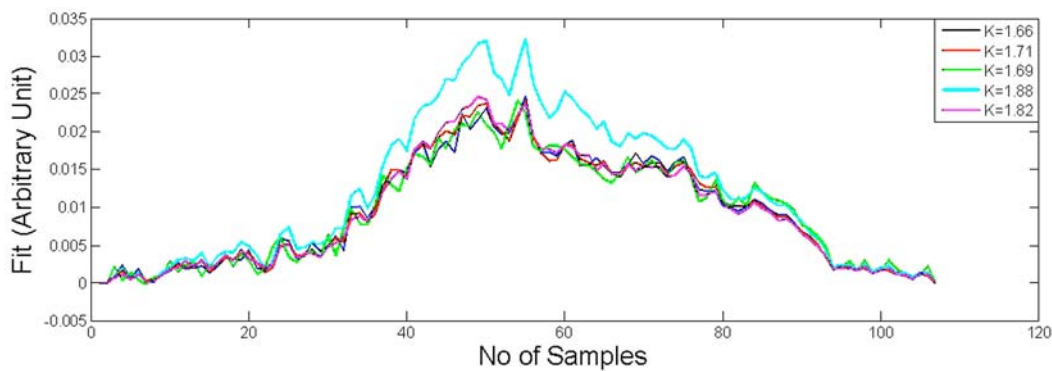


Fig. 7: Cross correlation between defect intensity and AE above normal with flange rubbing.

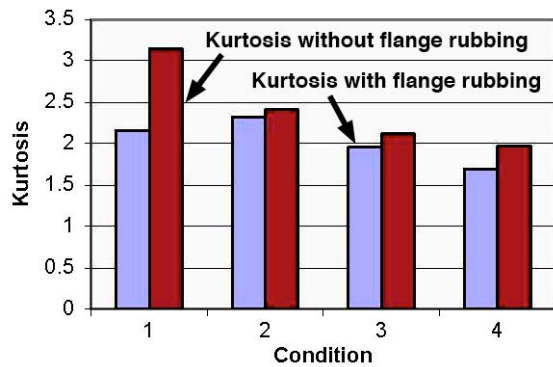


Fig. 8: Kurtosis with and without flange rubbing for all wheel speeds at 4-kg load. (Conditions 1-4, 1 ms^{-1} , 1.5 ms^{-1} , 3 ms^{-1} and 3.5 ms^{-1} , respectively)

Conclusions

Using a simple model of AE for normal rolling and correlating the AE signal above the model value with a measure of defect intensity per unit length of track, the following conclusions can be drawn.

1. The signal-above-normal-rolling can be correlated with the intensity of natural defects and flange rubbing can be treated as defect of unit intensity.
2. The correlation is improved when flange rubbing is present and the correlations persist for flange rubbing under conditions where it is poor for natural defects.
3. The effect of experimental conditions (speed and load) on defect sensitivity is matter for future investigation.

References

1. Office of Rail Regulation (ORR). "Train derailment at Hatfield: A final report by the independent investigation board", (UK) Health and Safety Executive, July 2006.
2. Bruzelius, K., Mba, D., "An intial investigation on the potential applicability of acoustic emission on rail track fault detection", *NDT & E International*, **37**, 2004, 507-516.
3. Miller, K. J., "Structural integrity – whose responsibility?", *Proceedings IMechE, Part L*, **217**(1), 2003, 1-22.
4. Pau, M., Aymerich, F. and Ginesu, F. "Ultrasonic measurements of nominal contact area and contact pressure in a wheel-rail system", *Proceedings of IMechE, Part F*, **214**, 2000, 231-243.
5. Pau, M. "Ultrasonic waves for effective assessment of wheel-rail contact anomalies", *Proceedings of IMechE*, **219**, 2005, 79-90.
6. Ringsberg, J. W. and Josefson, B. L. "Finite element analysis of rolling contact fatigue crack initiation in rails", *Proceedings of IMechE, Part F*, **215**, 2001, 243-259.
7. Morhain, A. and Mba, D. "Bearing defect diagnosis and acoustic emission", *Proceedings IMechE, Part J*, **217**(4), 2003, 257-272.
8. Toutountzakis, T. and Mba, D. "Observation of acoustic emission activity during gear defect diagnosis", *NDT & E International*, **36**(7), 2003, 471-477.
9. Kalker, J.J. "Survey of wheel-rail rolling contact theory", *Vehicle System Dynamics*, **8**(4), 1979, 317-358.
10. Guo, Y. B. and Schwach, D. W. "An experimental investigation of white layer on rolling contact fatigue using acoustic emission technique", *International Journal of Fatigue*, **27**(9), 2005, 1051-1061.
11. Thakkar N. A., Reuben, R. L., Steel, J. A. "Rail-wheel interaction and defect location using acoustic emission: a laboratory study", *Mechanical Systems and Signal Processing*, submitted, 2007.

CONTRIBUTIONS OF ACOUSTIC EMISSION TO STRESS CORROSION CRACKING RESEARCH

MIKIO TAKEMOTO

Research Center for Thermal Spray, Kanmeta Engineering Co. Osaka, Japan;
Faculty of Science and Engineering, Aoyama Gakuin University,
Fuchinobe, Sagamihara, Kanagawa 229-8558, Japan

Abstract

This paper surveys how AE techniques have been utilized to study and monitor stress corrosion cracking (SCC) by reviewing both the literature and experimental data at Aoyama Gakuin University for the past 35 years. The author started AE research in 1984, expecting that “the source analysis technique of AE will be powerful tool to study the SCC mechanism”; in particular, “whether the SCC is caused by active path corrosion (APC) or by a mutual action of corrosion and mechanical fracture”. This paper deals with APC-SCC of Type-304 steel by chloride, fluoride solutions and polythionic acid, carbon steels by hot nitrite solutions and brass by ammonia, but not the delayed fracture of high-strength steels, which produce vigorous AE due to hydrogen cracking.

We have studied SCC mechanisms using AE systems developed in-house and a corrosion potential fluctuation technique. No AE from transgranular (TG)-SCC of Type-304 steel in concentrated hot chloride solution was detected and this strongly suggests that the TG-SCC is caused by the APC. The progression of chloride TG-SCC yields no primary AE, but we can monitor secondary AE from hydrogen gas evolution and fractures of the rust produced in SCC. In contrast, intergranular (IG)-SCC of sensitized Type-304 steels by dilute fluoride-chloride solutions and polythionic acid solutions emit primary AE due to fast fracture. We also observed falling-off of grains by the grain boundary separation along with AE. Here, AE is produced by mechanical separation of the grain boundaries attacked by advancing corrosion. IG-SCC of carbon steel by hot nitrite and brass by ammonia produced strong AE. However, it is difficult to separate AE by the fracture of thick passivation films from the primary AE by the grain boundary separation. Finally, the author discusses what have remained as the future problems in understanding the APC-SCC.

Introduction

SCC of austenitic stainless steels had been important problems since they were used as the corrosion resistant material after the Second World War. SCC of Type-304 and -316 steels by chloride-bearing solutions as well by high-temperature water are serious problems in chemical and nuclear plants. SCC is well-known to be caused by mutual action of material, environment and stress. Electrochemical reaction plays an important role determining the propagation rates of the SCC.

The author started as a corrosion researcher, studying the chloride SCC of Type-304 steel during the 1970s, and came in the field of AE research in 1984. My motivation to the AE research was “the source wave analysis technique will be a powerful tool to study the SCC mechanism”. It is remembered that the source analysis technique had been actively developed in the 1980s. In the field of corrosion, there was a hot argument on “whether the SCC is caused by the anodic dissolution or by the mutual action of dissolution and mechanical fracture”. There was, however, no experimental data to demonstrate either of these hypotheses. My expectation to the AE method was “AE can clearly reveal whether discontinuous brittle fracture is involved in the APC-SCC and if so, we can study the source dynamics”. In spite of intensive studies, we could not detect AE signals from transgranular (TG)-type SCC of non-sensitized

Type-304 steel in concentrated hot chloride solution. No AE, however, gave us important information on the mechanism of the TG-SCC.

In the first portion of this paper, the author briefly introduces the APC-SCC and what had been discovered in the 1960s and 70s based on the literature survey, and discusses whether the mechanical fracture is involved in the chloride SCC of Type-304 steel based on our data. We are recently using a hybrid technique of AE and corrosion potential fluctuation (CPF), and found some interesting information on the AE mechanism of intergranular (IG)-SCC. The IG-SCC of sensitized Type-304 steel in dilute fluoride and polythionic acid solutions emits primary AE due to the grain boundary separation. The author discusses "How primarily AE is produced and what are the primary and secondary AE?"

Difficulty of AE techniques arises when we study the SCC of carbon steel in hot nitrite and brass in ammonia. These materials produce thick oxide films and the fracture of the thick films produces vigorous AE. Such AE cannot be separated from those by the grain boundary separation.

The author discusses only the APC-SCC and does not discuss the delayed fracture (hydrogen embrittlement) of high-strength steels, which produces strong AE signals. He, however, has to discuss the role of hydrogen in the APC-SCC as needed and will briefly discuss what remain as future problems.

What Is the APC-SCC and What Had Been Discovered?

Naming of "Stress Corrosion Cracking" appears to give confusion to field engineers, who are not familiar with SCC. Some textbooks include the delayed fracture in the category of "SCC". Field engineers consider that the SCC produces AE, since it is "*cracking*". If SCC is produced by the corrosion along active path (APC), it does not produce primary AE or AE signal. Joseph Kaiser called the SCC as "Stress Corrosion" in the 1950s [1]. This naming appears to be correct, since the SCC is mostly controlled by the corrosion originated and accelerated by stress.

Typical APC-SCC of Type-304 steel in chloride bearing solutions is TG-type. The SCC by high-temperature light water in BWR nuclear power plants is also the APC-SCC [2], but IG-type. The IG-SCC is also caused by dilute fluoride and tetra-thionic ($\text{H}_2\text{S}_4\text{O}_6$) solutions at room temperature [3], and produces tremendous falling-off of grains by the grain boundary separation. The APC-SCC occurs at noble corrosion potentials, in which fast anodic dissolution of metal can take place, while the delayed fracture occurs in the active potential range where a reduction reaction of proton takes place. Thus, it is important to know the corrosion potential to determine whether hydrogen is associated in the APC-SCC and to estimate the corrosion rate.

The APC-SCC occurs when a passivation film (oxy-hydroxide film) protects the base metal from general corrosion. Then, the base metal suffers a rapid anodic dissolution when the passivation film is locally broken by stress. Anodic current density of base metal without the passivation film reaches 1 A/cm^2 , which corresponds to the crack velocity of $1 \mu\text{m/s}$. A plate of 1 cm thickness is completely destroyed in only 3 hours. It is reminded that the crack velocity by the APC is quiet fast.

The Faradic reaction has been considered in SCC mechanism for a long time. In this model, electrons produced by anodic dissolution ($\text{M} \rightarrow \text{M}^{+z} + z\text{e}^-$) are consumed by the reduction reaction of dissolved oxygen ($\text{O}_2 + 2\text{H}_2\text{O} + 4\text{e}^- \rightarrow 4\text{OH}^-$ and $4\text{H}^+ + \text{O}_2 + 4\text{e}^- \rightarrow 2\text{H}_2\text{O}$) and/or the reduction reaction of protons ($2\text{H}^+ + 2\text{e}^- \rightarrow \text{H}_2$). Indeed, we can observe continuous evolution of hydrogen gas bubbles from SCC in concentrated chloride solutions. The pH in SCC is generally lower than 2 due to hydrolysis reaction of metallic chlorides. The cathodic reaction in the progressing SCC becomes the proton reduction. Thus, hydrogen cannot be ignored even in the APC-SCC.

Recently, non-Faradic reaction model can successfully explain the fluctuation of corrosion potential (CPF) in the APC-SCC [4]. In the non-Faradic model (see Fig. 1), electrons produced by the anodic reaction were once charged in a condenser (Helmholtz double layer), and gradually consumed by the reduction reaction of dissolved oxygen and cause so-called RD-type fluctuation. Here, the RD-type CPF means that the corrosion potential rapidly shifts to active direction and gradually recovers to original noble potential. The rapid shift to active direction implies a rapid increase of anodic current due to the film fracture. When proton reduction reaction occurs in the SCC, we cannot detect the RD-type CPF. This technique is now becoming a powerful tool to monitor the early stage of the APC-SCC.

It is noted that there are two types of the passivation films. One is a self-passivation film, which is produced by reaction with water in air, and another a thick oxide film produced by oxidation reaction with special solutions. The former in austenitic stainless steels is a very thin film of less than 1 nm. The latter are often called as the precipitation-type oxide film and de-alloyed layer in binary alloys, and generally thickens (few tens to hundreds μm) and brittle. Typical examples are the tarnish film (Cu₂O) on brass in ammonia, and magnetite film (Fe₃O₄) on carbon steel in hot nitrate solution. We often detect AE from the fracture of these films, but cannot monitor the AE from the fracture of the self-passivation film.

A research group on the SCC of binary alloy claimed that the fast SCC velocity (3×10^{-5} m/s) of brass cannot be explained by the APC [5]. They used AE technique for studying SCC mechanism. Newman's group [6] first discussed timings of AE and fluctuation of anodic current as shown in Fig. 2. Their research is highly regarded as the first one for the CPF. It is important, however, to separate AE into the primary and secondary AE, based on the waveform analysis. The primary AE makes an important contribution to study SCC mechanism. The secondary AE include AE from gas bubbles, fracture of thick passivation films and oxides in SCC. The secondary AE is often used to detect SCC in process plants [7]. The primary AE is, in this paper, defined as the AE, which directly relates to the crack propagation velocity.

Chloride SCC in the 1960's and 70's were studied using a boiling 42 mass% MgCl₂ solution (146°C in the U.S. and 145°C in Japan as standard solutions by NACE and JIS) and made the AE monitoring difficult, due to boiling noise. Okada [8] first studied AE from APC-SCC in a boiling 42% MgCl₂ solution in 1974, and reported no AE from the APC-SCC, but AE from delayed fracture. For the last 20 years, this solution has been scarcely used in Japan. When we use a dilute (but still concentrated compared to the sea water) and non-boiling MgCl₂ solution such as 30% MgCl₂ solution at 90°C, we can detect clear RD-type CPF and sometimes AE, without being disturbed by noise.

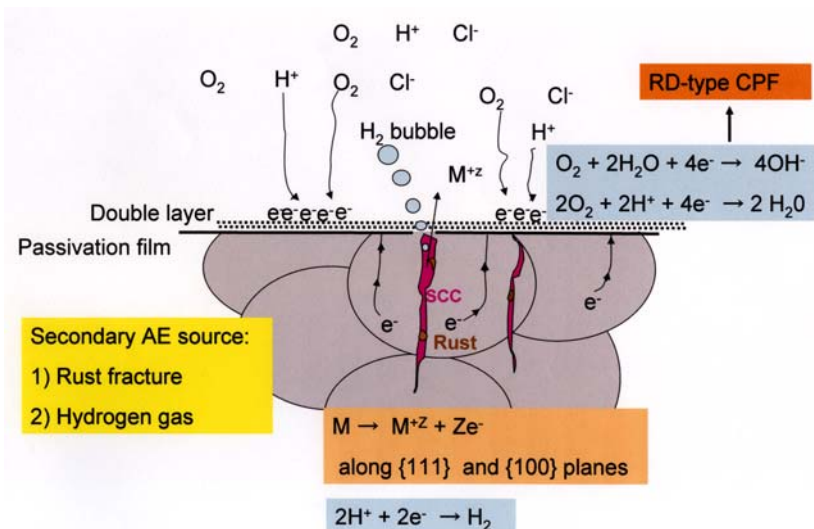


Fig. 1 Non-Faradic electrochemical model for TG-SCC of Type-304 steel in chloride solution and AE source.

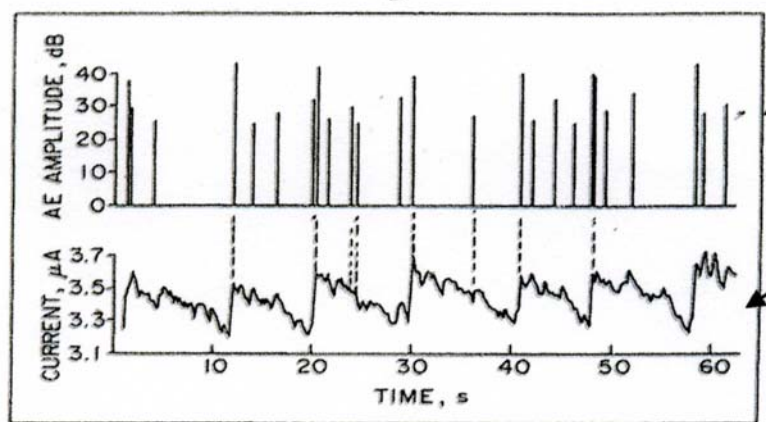


Fig. 2 Timing of AE and current fluctuation at zero potential of brass in a 1 mol/l NaNO₂ solution. [6]

Role of Passivation Film in SCC

Mechanical behavior of the self-passivation and precipitation-type film is important for discussing the SCC mechanism and susceptibility. The author estimated the mechanical characteristics of these films by studying the threshold stress criteria of the chloride SCC of Type-304 steel pipes and nitrate SCC of low carbon steels [9-11]. The hot nitrate solution produces thick magnetite film. Threshold stress criteria are compared in principal stress diagrams (Fig. 3). Threshold stress of Type-304 steel is arranged by the equivalent stress of the Von-Mises shear strain energy, which is valid for ductile materials, while the SCC criterion of the carbon steel is by the maximum principal stress.

Left locus of Fig. 3 implies that the passivation film on the Type-304 steel is ductile and SCC is caused by break-down of the self-passivation film. In contrast, the precipitation-type film (right locus) is brittle and fractures by the principal tensile stress. Ammonia-SCC of brass obeys the maximum principal stress criteria. Figure 4 shows surface photographs of carbon steel and brass after tensile loading with (bottom) and without (top) precipitation-type film. With no film, wavy slip lines for carbon steel and cross slips for brass were observed. These occur in the direction of the maximum shear stress or 45° to the loading direction (horizontal direction of the photos). For the metals with precipitation-type film, we observed IG cracks along the steel grain boundaries (left bottom) and fine TG cracks within grains of the brass. Fracture of these films produces AE since the films are thick and brittle. Figure 5 shows step-wise elongation and AE timing (\blacktriangledown) of carbon steel with and without the precipitation-film in

silicone oil at 100°C . We detected AE at the timing of the film rupture, which occurs at step-wise elongation due to the serration. These AE signals are regarded as the secondary AE, not the primary AE due to corrosion reactions.

In case of chloride SCC of Type-304 steel, we observed very clear slip lines in the direction of maximum shear stress, but detected no AE from the film fracture. Figure 6 shows initiation of chloride SCC in Type-304 pipe subjected to torsional loading [11]. Shear stresses are acting both in the vertical and horizontal directions. It can be seen that slip lines are attacked and appear as parallel black lines. We can see corrosion pits along slip steps. Pickering [12] proposed an initiation model of chloride SCC as shown in Fig. 7. His model suggests that the corrosion pits were connected by ductile fracture, indicating a mutual action of corrosion and mechanical fracture. However, our observation in the boiling MgCl_2 solution (Fig. 6) did not catch the progression of corrosion pits. The corrosion pits stop their growth. In these photos, SCC is observed along grain boundary (a) and as slant black bold lines (b and c). They propagate from the grain boundary into neighboring grains in the direction normal to the maximum principal tensile stress.

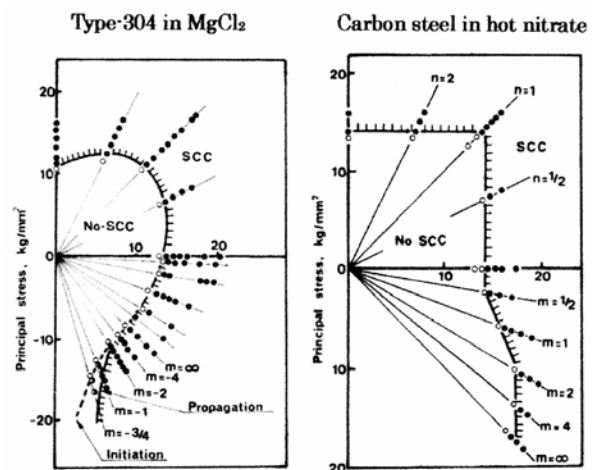


Fig. 3 Threshold stress locus of chloride SCC of Type-304 in boiling 42% MgCl_2 solution (the left) and nitrate SCC of carbon steel in (60% $\text{Ca}(\text{NO}_3)_2$ + 3% NH_3NO_4) solution at 100°C .

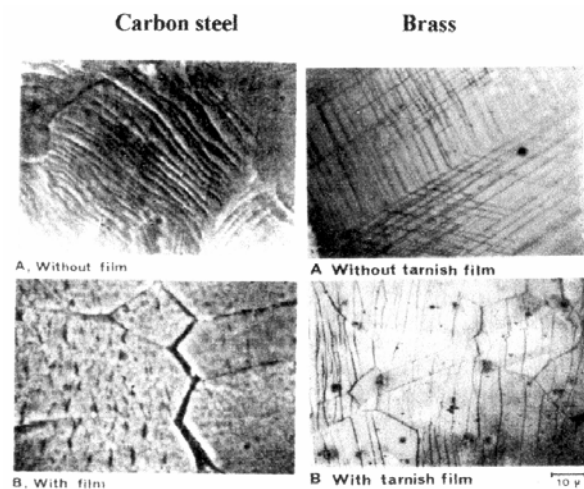


Fig. 4 Surface photos of carbon steel and brass without (the upper) and with the precipitation type thick films.

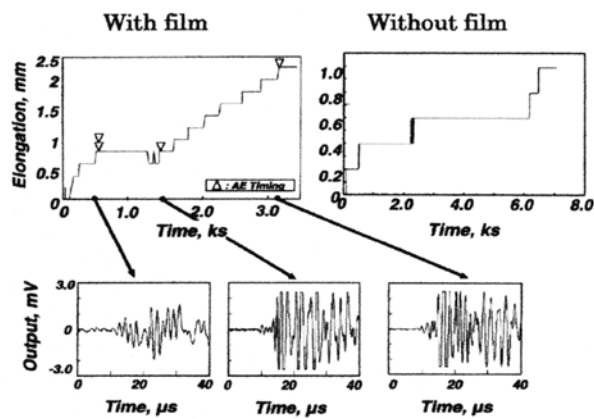


Fig. 5 AE from fracture of thick Fe_3O_4 film and no AE from bare carbon steel in silicone oil at 100°C .

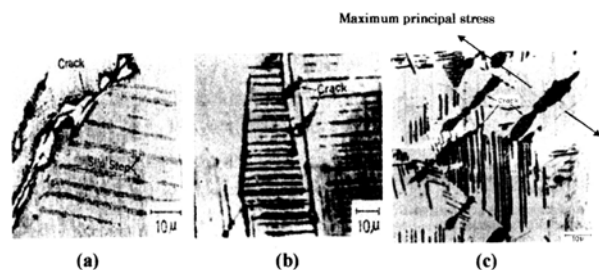


Fig. 6 Initiation of TG-SCC observed in boiling MgCl_2 solution for Type-304 pipe subjected to torsional loading.

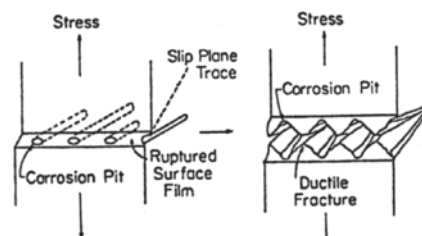


Fig. 7 A model for mutual action of corrosion and ductile fracture by Pickering [12].

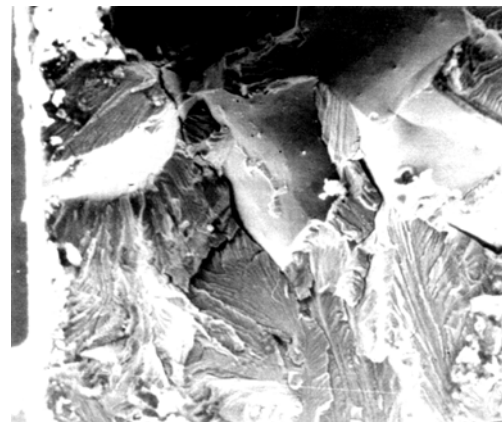


Fig. 8 Fracture surface of chloride SCC of non-sensitized Type-304 pipe subjected to torsional loading.

Both the sensitized and non-sensitized Type-304 steels suffer TG-SCC in concentrated chloride solutions. However, TG-SCC changed to IG-SCC when torsional loading was applied [10]. Figure 8 is the fracture surface showing both TG and IG cracks in non-sensitized Type-304 pipe subjected to the torsional loading. Both TG cleavage cracks with river-patterns and IG cracks with smooth grain boundaries were observed. It should be, however, noted that the smooth grain boundary has some irregular protuberance like extrusions. These are considered to be the source of the primarily AE in the IG-SCC.

AE From Chloride SCC

We have repeated many SCC tests of non-sensitized Type-304 steel in 35%- MgCl_2 solution at 90°C (no boiling), but could not detect any AE signal from TG-SCC even with 80-dB amplification [13]. This lack of AE observation suggests that the TG-SCC of Type-304 steel in chloride solutions is caused by APC mechanism of entirely chemical nature, and no cleavage fracture is associated with the TG-SCC.

Using sensitized Type-304 plates in 1999, we detected a few and weak Lamb AE signals before the final fracture. We next monitored both the AE and CPF from sensitized Type-304 thin plates in non-boiling solutions [13]. As shown in Fig. 9, AE signals were detected when large and frequent RD-type CPFs in Zones II and III. Detail analyses of AE and CPF in Fig. 10 showed that the potential shifted to active direction a few seconds after the timing of AE observations (\blacktriangledown). These AE signals were generated by fast cracks with source rise time of $0.7\text{--}1\ \mu\text{s}$. This source parameter was estimated by the waveform matching of the So-mode Lamb waves. This finding strongly suggests the mechanical separation of grain boundary. We again detected both the RD-type CPF and cylinder wave AE signals during an early stage of IG-SCC in the HAZ of butt-welded Type-304 pipes, as shown in Fig. 11.

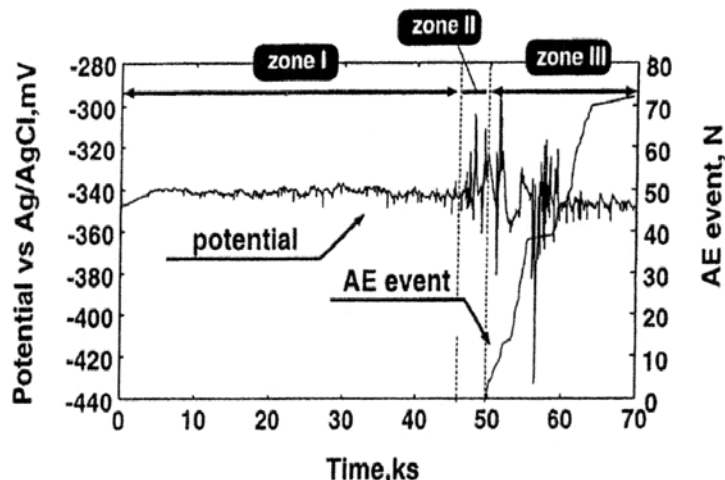


Fig. 9 Change of cumulative AE events and CPF during chloride SCC.

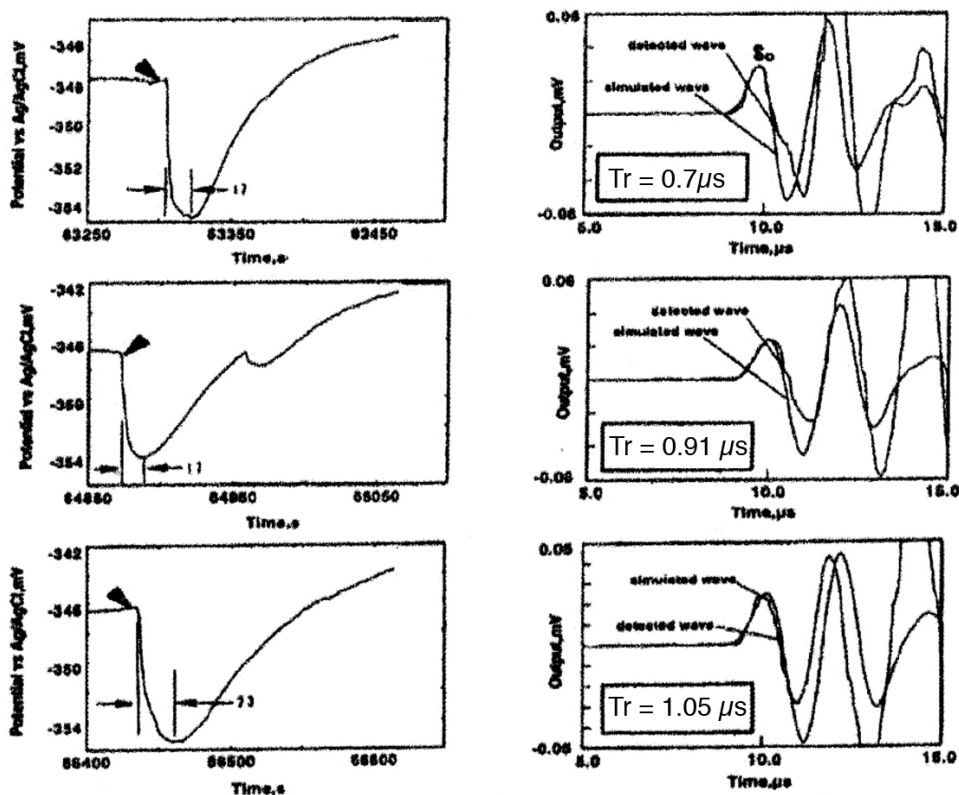


Fig. 10 Timing of AE (triangles) and RD-type CPF (left). Waveform matching of the So-mode Lamb wave for source analysis (right).

Figure 12 shows falling-off of grains from the surface of the HAZ [14]. The grain boundary separation is the only AE source since AE monitoring was performed during SCC initiation, during which there is no hydrogen gas evolution or rust fracture. It is noted, however, that the timing of AE and CPF in Figs. 10 and 11 is not same; i.e., almost the same timing in Fig. 10 and late AE in Fig. 11. This is probably because the sources for the AE and CPF are different. The solution temperature and stress levels were also different. In order to differentiate and clarify microscopic fracture mechanisms, accurate source location of AE and CPF is needed and this is a future challenge.

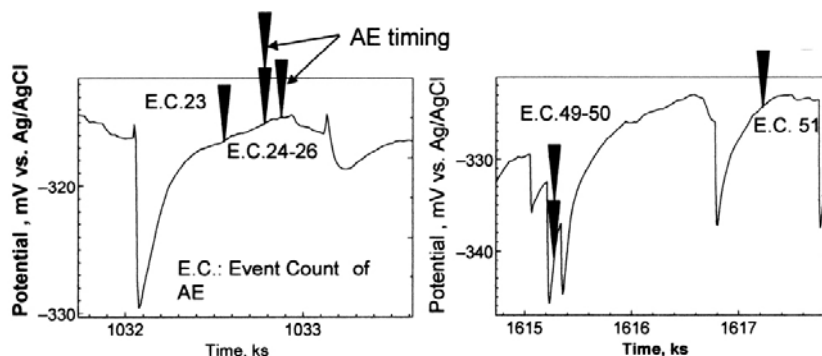


Fig. 11 Timing of AE and RD-type CFP from IG-SCC of Type-304 pipe weld in 35% MgCl₂ solution.

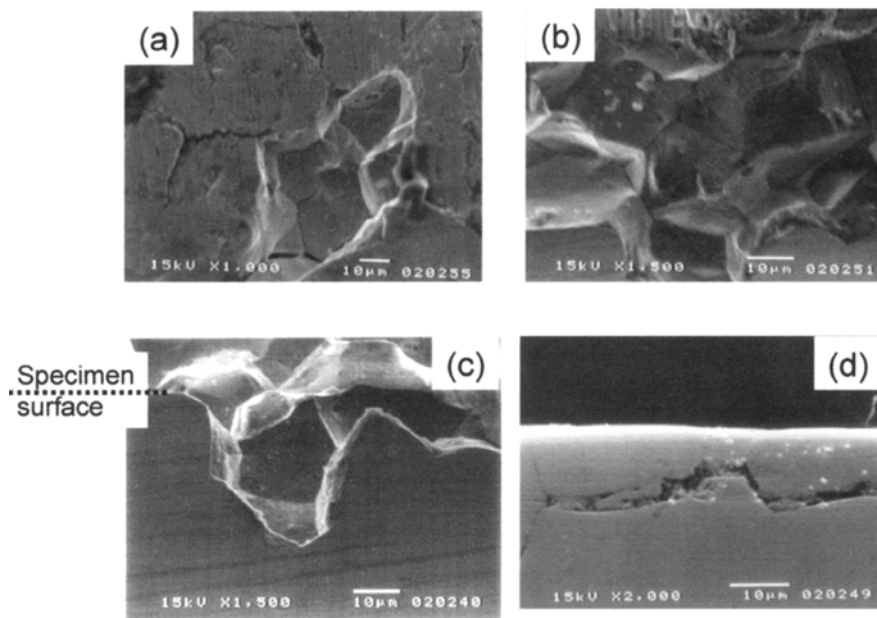


Fig. 12 Top- (a,b) and side- (c,d) surface SEM of IG-SCC of 304 pipe weld in MgCl₂ solution.

AE from IG-SCC by Fluoride and Tetra-thionic Acid

IG-SCC of sensitized Type-304 steel in tetra-thionic acid ($H_2S_4O_6$ at pH=2) and fluoride solution [15] produce strong AE signals. Tetra-thionic acid ($H_2S_4O_6$) is readily produced by the reaction of FeS with water, and is the most detrimental for sensitized Type 304 steel. Fluoride solutions are also detrimental for sensitized stainless steel, more so than the chloride solutions [15]. Either of them causes typical IG-SCC and produces strong AE at room temperature.

We monitored bulk-wave AE from IG-SCC using a CT specimens in 1993 [3]. In the early 1990s, we established a combined AE detection-analysis system (called ADAS) of source location, source simulation and moment tensor analyses [16]. Figure 13 shows the AE monitoring system with 8 sensors. Seven sensors (#1 to #7, PAC, PICO) were for the source location and moment tensor analyses. Sensor #8 (displacement-type sensor, Dunegan S9208) measured the out-of-plane displacement of the bulk waves utilized for source dynamics study. Concentration of these solutions was as low of 1000 ppm. Figure 14 shows AE timing during a CERT (constant extension-rate test) of the CT specimen at room temperature.

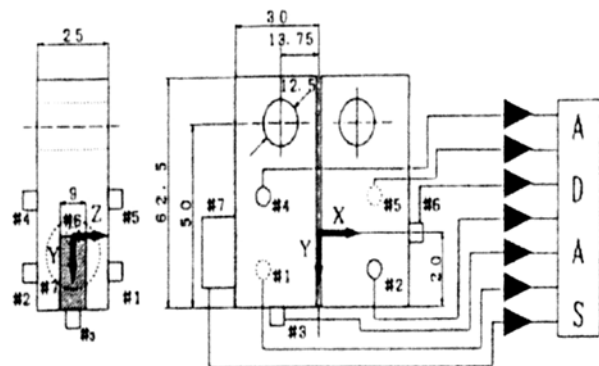


Fig. 13 AE monitoring from IG-SCC of a CT specimen for source wave analysis.

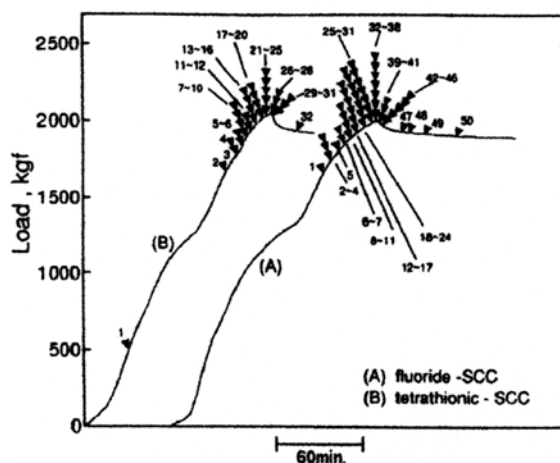


Fig. 14 AE timing during CERT of the CT specimen in fluoride and tetra-thionic solution at room temperature.

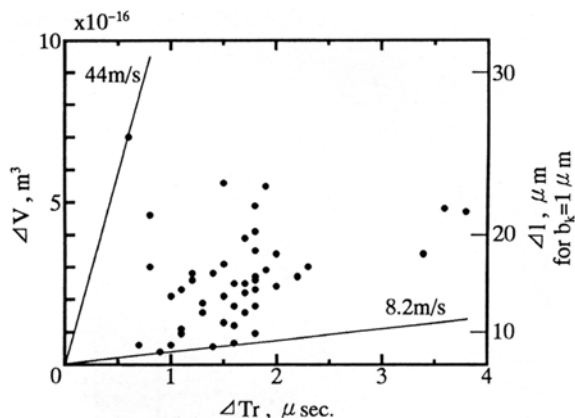


Fig. 15 Source parameters, source volume and rise time, of fluoride SCC of sensitized Type-304 steel. Crack velocity = 8.2 – 44 m/s.

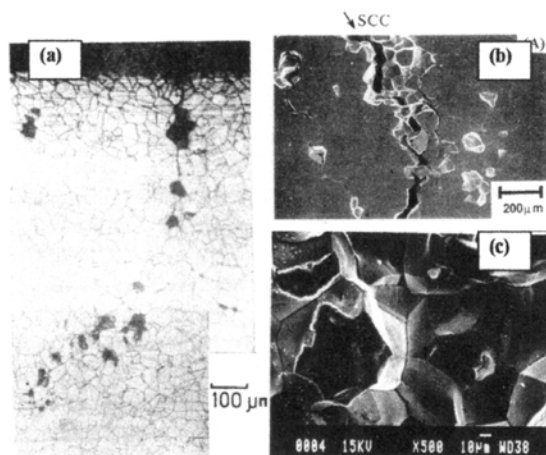


Fig. 16 IG-SCC with falling-off of grains by fluoride (left) and tetra-thionic acid (right) solution at room temperature.

Room temperature test is quite suitable to AE monitoring. We detected a number of AE signals, at around the general yielding (loading was stopped at this point). Using the moment tensor analysis, AE signals from Mode-I (crack-opening) AE signals with tensile ratio higher than 80% were shown by solid triangles. Source parameters of AE signals from the fluoride-SCC are shown in Fig. 15. Here, the parameters were obtained by waveform matching of the P-waves using the theoretical Green's function of the second kind. SCC velocities were estimated to be from 8 to 44 m/s. SCC velocity by tetra-thionic acid was also estimated as 10 to 36 m/s. Crack size, estimated by assuming a crack opening of 1 μm, was less than 20 μm. Another SCC experiment using plate specimens relying on the analysis of the So-Lamb waves showed the fracture velocities from 7 to 30 m/s.

In the IG-SCC due to tetra-thionic acid and fluoride solutions, an especially noteworthy feature is the frequent falling-off of the grains as shown in Fig. 16. This is less prominent in chloride solutions, but is produced very frequently by the co-existence of trace of fluorine (100 ppm) and chlorine (1000 ppm) ions. Fluorine ions strongly accelerate the grain boundary separation and chlorine ions promote pitting. The ASTM recognized the harmfulness of fluorine ions to environmental SCC from early 1980s, but this has been obscure in Japan.

Crack Velocity of Grain Boundary Separation and Delayed Fracture

Comparison of micro-crack velocities in the IG-SCC and delayed fracture of high-strength steels often supplies us with important information on the mechanism of the cracks. The maximum velocity (approximately 40 m/s) of the grain boundary separation in the IG-SCC of meta-stable, sensitized Type-304 steel coincides with the lowest velocity of the delayed fracture of high strength steels [17]. Thus, there is a possibility of delayed micro-fracture of the strain-induced martensite and the chromium depleted zone in the tetra-thionic acid solution (pH=2), but the delayed fracture is almost impossible in neutral fluoride solution.

Carpenter et al. [18] reported AE from grain boundary separation for the sensitized Type-304 steel subjected to simultaneous plastic deformation and hydrogen charging. In that system, AE was attributed to grain boundary separation due to hydrogen embrittlement. Accurate source location with a μm -precision enables a detailed study of the grain boundary separation mechanisms, but it is out of the current AE technology.

Intergranular Corrosion ahead of IG-SCC

We are studying how far the intergranular corrosion progressed ahead of the crack tip. This is a serious issue in sizing of IG-SCC in nuclear power plants. Figure 17 shows the stress-strain curve with AE timing during ambient bending of the specimen pre-exposed to the polythionic IG-SCC induced at tensile strain of 1.4%. The specimen was washed after the SCC pre-exposure and thoroughly dried. We detected strong Mode-I AE signals (\blacktriangledown) during a subsequent 3-point bending in air. Figure 18 shows SEM of IG-SCC at 1.6% strain. We observed IG-SCC with crack tips surrounded by two red ellipses at 1.4% (the strain, at which SCC test was done). After applying 1.6% strain, grain boundary separation becomes apparent as shown by white arrows. This strongly indicates that the grain boundaries ahead of IG-SCC had been attacked by advancing corrosion. Here, the active path is assumed as the Cr-depleted zone and/or strain-induced martensite existing at the grain boundary.

Source Model of AE in IG-SCC of Sensitized Type-304

The author prepared two schematic drawings for feasible models of AE sources in IG-SCC. These models are constructed based on the grain boundary attack by advancing corrosion. Figure 19 represents the AE sources for the IG-SCC by fluoride and polythionic acid solutions, and Fig. 20 for the IG-SCC by concentrated chloride solutions. As shown by symbols $\leftarrow//\rightarrow$, mechanical separation occurs in limited portions of the grain boundary. The separated portions correspond to the grain boundaries not corroded previously. Their fraction is large for IG-SCC by fluoride and polythionic acid solutions, but small for IG-SCC by concentrated chloride solutions. This is because the chloride solution attacks only the grain boundary with large misorientations of $\{111\}$ planes.

Recall the extrusion-like protuberance in Fig. 8. These are supposed to be the intact (non-corroded) portions of the grain boundary. Cohesion strength of the intact portions is expected to be lower than regular grain boundary. This may be induced by either stress sorption of specific anions [10] or hydrogen embrittlement [18].

AE from IG-SCC of Carbon Steel in Hot Nitrate Solution

We monitored vigorous Lamb-wave AE and CPF from low-carbon steel plates in non-boiling nitrate solution (100°C) [19]. Most AE signals detected in noble potential range were diagnosed as the AE by the film fracture due to the serration (Fig. 5). We also detected a few AE at later stage, during which SCC propagated and potential shifted to active range. However, these were supposed to be produced by fracture of thick film produced on the sidewall of IG-SCC, since the estimated crack volume is very small. The IG-SCC of carbon steel does not produce any falling-off of grains. Stress sorption model was proposed for the IG-SCC in this system [20], but experimental research of this

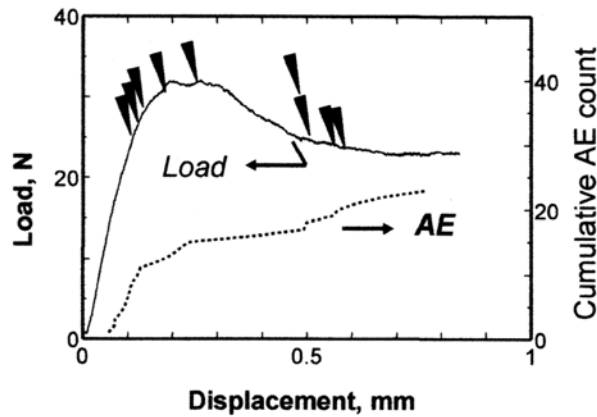


Fig. 17 AE detected during bending of dried specimen with polythionic IG-SCC.

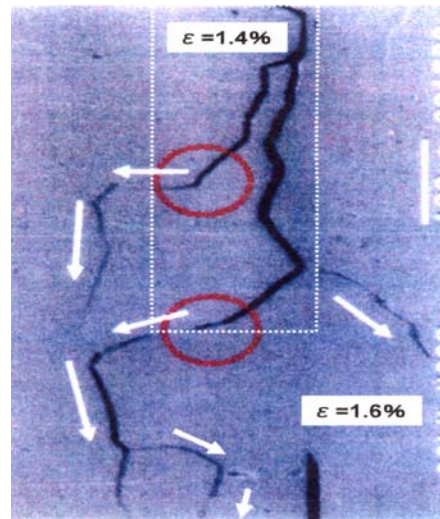


Fig. 18 Extension of polythionic IG-SCC by applying strains in air.

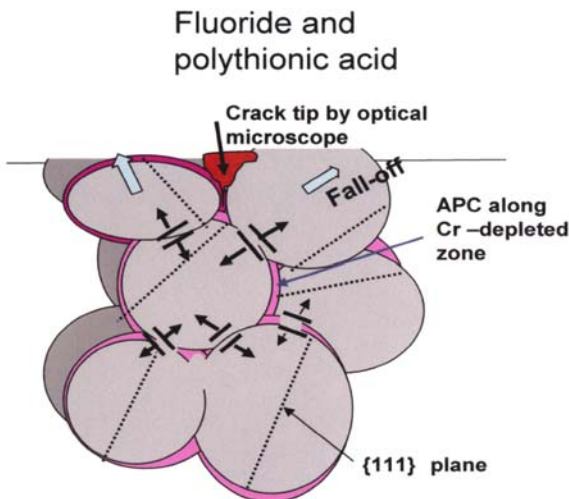


Fig. 19 AE source due to the grain boundary separation caused by IG-SCC of sensitized Type-304 steel in fluoride and polythionic acid solutions.

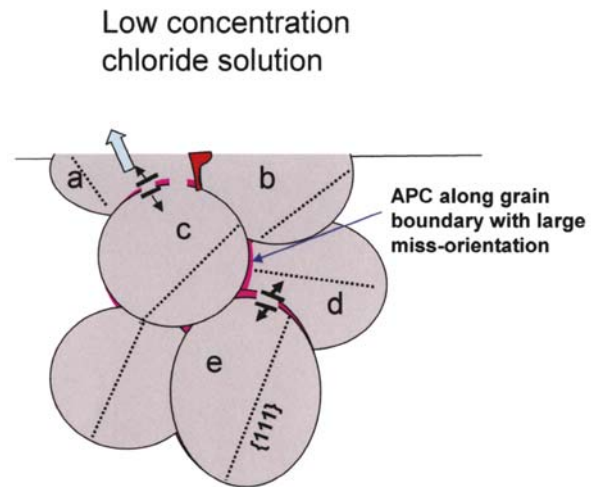


Fig. 20 AE source due to the grain boundary separation caused by IG-SCC of sensitized Type-304 steel in concentrated chloride solution.

model has not been performed so far. AE technique can monitor the progression of the IG-SCC, but appears to be difficult to study detailed mechanisms.

What Remain as Future Problems?

There appears to be no unified mechanism, which can explain the SCC in various combinations of metals and environment. Followings are unsolved problems and will be future challenge.

- 1) Why does the different material-environmental combination cause different fracture type of TG and IG? What is the active path(s) in the TG-SCC and IG-SCC?
- 2) Why does the Type-304 steel suffer TG-SCC in the concentrated chloride solution even if it is sensitized, where weak grain boundaries should be susceptible to IG-SCC? This needs an advanced understanding of

- grain-boundary chemistry to study the active path.
- 3) Why does the Type-304 steel suffer TG-SCC in the concentrated chloride solution even if it is sensitized, where weak grain boundaries should be susceptible to IG-SCC? This needs an advanced understanding of grain-boundary chemistry to study the active path.
 - 4) Why is the TG-SCC of 2) partially converted to the IG-SCC under biaxial stress state (role of shear stress component)? This needs advanced micro-mechano-chemical techniques.
 - 5) Concerning the mechanism, accurate source location of AE and CPF is needed to study the grain-boundary separation mechanism. How is the grain boundary cohesion strength lowered by what chemical reaction?

Conclusion

Advanced AE techniques can listen to what is happening in the SCC, and can make important contributions to corrosion research. However, we have to diligently understand what AE techniques can and cannot do.

Both the TG-SCC and IG-SCC of austenitic stainless steels appears to be caused by anodic dissolution along active path (APC). A few AE signals from IG-SCC indicate small-size mechanical separation of grain boundary.

The author could not go into the counter-measures to SCC in this article. It is, however, acknowledged that most SCC of field equipment are caused by the residual tensile stresses induced by welding and material processing, and can be easily mitigated by converting the tensile residual stresses to compressive stresses.

One hundred years were needed to understand the mechanism of the boiler embrittlement due to caustic SCC. Sixty years passed since Dr. Joseph Kaiser studied the Stress Corrosion by AE. He could not analyze the waveform, but we can do this at present. However, we will still need quite an advanced AE system with both extremely high source location precision and source dynamics capabilities in order to pinpoint SCC mechanisms.

References

- [1] H.M. Tensi, *Proceeding of 26th European Conference on Acoustic Emission*, Vol. 1, 2004, Berlin, pp. 1-18.
- [2] S. Suzuki, Documents of first meeting for advanced SCC evaluation standard, Tokyo Inst. Tech, 2004, p. 19.
- [3] M. Takemoto, T. Nakazawa, *Corrosion Engineering in Japanese*, **44**, 1995, 166-173.
- [4] H. Inoue, *Corrosion Engineering*, **52**, 2003, 444-451. (in Japanese)
- [5] D.G. Chakrapani and E.N. Pugh, *Metall. Trans*, **6A**, 1975, 1155-1163.
- [6] K. Sieradzki and R.C. Newman, *Phil. Magazine*, **51**, 1985, 95-132.
- [7] A. Yonezu, K. Ito, K. Morozumi, H. Cho and M. Takemoto, *Corrosion Engineering*, **54**, 2005, 329-336. (in Japanese)
- [8] H. Okada, K. Yukawa and H. Tamura, *Corrosion*, **30**, 1974, 253-255.
- [9] M. Takemoto and Y. Aoki, *Corrosion Engineering*, **31**, 1982, 753-759. (in Japanese)
- [10] M. Takemoto, *Corrosion Engineering*, **35**, 1986, 78-82. (in Japanese)
- [11] M. Takemoto, *Corrosion Engineering*, **32**, 1983, 3-8. (in Japanese)
- [12] H.W. Pickering and P.R. Swann, *Corrosion*, **19**, 1963, 373.
- [13] S. Fujimoto and M. Takemoto, *Corrosion Engineering*, **53**, 2004, 309-316. (in Japanese)
- [14] A. Yonezu, H. Cho and M. Takemoto, *Advanced Material Research*, **13**, 2006, 243-250.
- [15] M. Takemoto, T. Shinohara and M. Shirai, *Corrosion Engineering*, **36**, 1987, 210-218. (in Japanese)
- [16] M. Takemoto, Y. Hayashi and M. Takemoto, *Corrosion Engineering*, **43**, 1994, 570-579. (in Japanese)
- [17] Y. Hayashi, M. Takemoto and M. Takemoto, *NACE, CORROSION'94*, 1994, Paper No. 220.
- [18] S.H. Carpenter, K. Ono and D. Armentrout, *Progress in Acoustic Emission XIII*, (2006), pp. 55-60.
- [19] M. Takemoto, H. Cho and K. Ono, *26th European Conf. on Acoustic Emission*, Vol. 2. 2004, Berlin, pp. 617-629.
- [20] H.H. Uhlig and J.S. Avas, *J. Trans., ASME*, **56**, 1952, 361.